Bilgi Toplumu Teknolojileri için Anten Sistemleri ve Algılayıcılar

Proje No: 107E090 (COST IC0603)

Prof.Dr. Özlem Aydın Çivi

Y.Doç.Dr. Lale Alatan

Doç.Dr. Şimşek Demir

Prof. Dr. Altunkan Hızal

Y.Müh. Caner Güçlü

Y. Müh. Aykut Cihangir

Y. Müh. Nihan Gökalp

Kasım 2010

ANKARA

ÖNSÖZ

107E090 projesi kapsamında, yeniden şekillendirilebilir anten, elektronik taramalı dizi anten ve yansıtıcı dizi anten tasarımı, üretimi ve ölçümleri yapılmıştır. X-band Sur Biçimli dizi antende varaktör diyotlar kullanılarak huzmenin elektronik tarama yapabileceği gösterilmiştir. MM-Dalga sabit genişlikli ve doğrusal sönümlenen yarık antenler tasarlanıp, üretilmiş ve antenin şeklinin bu iki yapı arasında değiştirilmesi durumunda ışıma örüntüsünün değiştirilebileceği gösterilmiştir. K ve Ka bantlarında bağımsız çalışabilen, RF MEMS anahtarlarla yeniden yapılandırılabilir özellik kazandırılmış, ayrık halka elemanlı dairesel polarizasyonlu yansıtıcı dizi anten tasarlanmış, üretilmiş ve ölçülmüştür.

Bu proje, COST IC0603 projesine katılım kapsamında, TÜBİTAK tarafından desteklenmiştir. COST proje toplantılarına katılım ve Araştırma Görevlisi Caner Güçlü'nün katıldığı Kısa Dönemli Bilimsel Çalışma (Short Term Scientific Mission) COST IC0603 projesi tarafından karşılanmıştır.

İÇİNDEKİLER

TABLO LİSTESİ

ŞEKİL LİSTESİ

ÖZET

Bu proje kapsamında, özellikle milimetre-dalga frekanslarında çalışan yeniden şekillendirilebilir anten, elektronik taramalı dizi anten ve yansıtıcı dizi anten tasarımı, üretimi ve ölçümleri yapılmıştır. Yeniden şekillendirilebilirlik özelliği için farklı teknolojiler kullanılmıştır.

Huzmesi yönlendirilebilen sur biçimli mikroşerit yürüyen dalga anten dizisi X-bant uygulamalarında kullanılmak üzere tasarlamış, üretilmiş ve ölçülmüştür. Antenin ana huzmesinin istenilen yöne elektronik olarak döndürülebilmesini sağlayabilmek için mikroşerit hat üzerinde gerekli faz değişimini sağlayacak varaktör diyotlar kullanılmıştır. Yapılan EM benzetim ve ölçümler sonucu sur biçimli anten dizisinde, ana huzmenin diyot kontrolü ile tasarlandığı gibi 10^{o} lik bir açı taraması yapabildiği gösterilmiştir. Bu kavram kanıtlaması şeklinde bir çalışmadır; huzmenin daha büyük açı aralığında tarama yapması için tasarımda yapılması gereken değişiklikler belirtilmiştir.

MM-Dalga sabit genişlikli ve doğrusal sönümlenen yarık antenler tasarlanıp, üretilmiş ve antenin şeklinin, optik uyarımla bu iki yapı arasında değiştirilmesinin sağlanması durumunda ışıma örüntüsünün değiştirilebileceği gösterilmiştir.

Proje kapsamında gerçekleştirilen bir diğer çalışmada da K ve Ka bantlarında bağımsız çalışabilen, RF MEMS anahtarlarla huzmesi elektronik olarak döndürülebilen dairesel polarizasyonlu yansıtıcı dizi anten tasarlanmış, üretilmiş ve ölçülmüştür. Çift frekanslı (24.4 GHz ve 35.5 GHz) dizi iç içe geçmiş farklı boyutlarda iki ayrık-halka dizisi şeklinde tasarlanmıştır. Huzme döndürme amacıyla her bir ayrık halkanın açısal konumunu RF MEMS anahtarlarla ayarlayarak, dairesel polarizasyonlu dalgaların fazları kontrol edilmektedir. Anten ODTÜ MEMS merkezinde geliştirilen yüzey mikro-işleme süreciyle üretilmiştir. Işıma örüntüleri ölçülmüş ve benzetim sonuçlarıyla karşılaştırılmıştır. Ölçümlerle, ana huzmenin, tasarlandığı gibi, Ka bandında 35°'ye, K bandında 24°'ye döndürülebildiği gösterilmiştir.

Proje çalışmalarından sur biçimli mikroşerit anten dizisiyle ilgili hazırlanan makale *Microwave and Optical Technology Letters* adlı dergide yayınlanmak üzere kabul edilmiştir. Yansıtıcı dizi antenle ilgili makale de hazırlık sürecindedir. Saygın konferanslarda yedi bildiri sunulmuştur. Ayrıca, proje kapsamında üç yüksek lisans tez çalışması tamamlanmıştır.

Anahtar Kelimeler: Yeniden şekillendirilebilir antenler, sönümlenen yarık antenler, faz dizili antenler, yansıtıcı antenler, RF MEMS anahtarlar, RF MEMS antenler

ABSTRACT

In this project, reconfigurable antenna, beam steering array and reflectarray have been designed, produced and measured, especially in mm-wave frequencies. To provide reconfigurability, different technologies have been considered.

X-band electronically scanning meanderline microstrip traveling wave antenna array has been designed, produced and measured. To rotate the antenna beam to the desired direction, microstrip meander line has been loaded by varactor diodes that provide required phase shift values. EM simulations and rdiation pattern measurements of the meanderline antenna have demonstrated that the antenna has the capability to scan 10° with the control of varactors as designed. This is a proof-of-concept type study; alternative configurations to increase the scan range have also been discussed.

MM-wave tapered slot antennas with a constant width and linear taper have been designed, produced and measured. It has been demonstrated that if the shape of the tapered slot antenna can be changed between constant width and linear taper structures by means of optical excitation, radiation pattern reconfigurability can be obtained.

In another study accomplished in this project, electronically scanning circularly polarized reflectarray working independently in K and Ka bands has been designed, produced and measured. Dual band (24.4 GHz and 35.5 GHz) reflectarray has been designed as an interlaced array of split rings of two different sizes. In order to steer the beam, the phase of the incident circularly polarized wave is controlled by RF MEMS switches that modify the angular orientation of split-rings individually. The antenna has fabricated by using surface micromachining process developed in METU MEMS Center. Radiation patterns of the antenna are measured and compared with the simulations. It has been shown that the reflectarray is capable of beam switching to 35° in Ka band, 24° in K band as required.

One journal paper on meanderline antenna has been accepted to be published in *Microwave and Optical Technology Letters*. Preparation of manuscript on reflectarray is under progress. Seven conference papers have been presented in well known Conferences. Furthermore, three Master Thesis studies have been accomplished during the project.

Keywords: Reconfigurable antennas, tapered slot antennas, phased arrays, reflectarrays, RF MEMS switches, RF MEMS antennas

1. GİRİŞ

ASSIST - Antenna Systems & Sensors for Information Society Technologies (Bilgi Toplumu Teknolojileri için Anten Sistemleri ve Algılayıcılar) başlıklı COST IC0603 aksiyonu bilgi toplumu için vazgeçilmez olan kablosuz iletişim sistemlerinin yeni gereksinimlerini karşılayacak ve sağlık, biyoloji, tüketici elektroniği, radyo astronomi, çevre gozleme gibi sistemler için yeni antenler geliştirilmesi, bu tür karışık ortamlarda antenlerin modellenmesi, tasarımı ve üretilip ölçülmesi gibi geniş bir alanda çalışmaları kapsamaktadır. COST IC0603 projesi incelendiğinde, yeni sistemlerde milimetrik dalga ve daha yüksek frekanslarda çalışan antenlere ve bunları üretebilecek teknolojilere gereksinim duyulduğu görülmektedir. Ayrıca, yeniden şekillendirilebilirlik (reconfigurability) aynı antenin birden çok sistem için kullanılmasına olanak sağladığı için, kablosuz iletişim cihazlarında antenin kapladığı hacmin ve maliyetin azaltılması açısından önemlidir. Mikroişlemeye dayalı MEMS (Mikro-Elektro-Mekanik Sistemler) teknolojisi hem yüksek frekansta çalışan antenlerin hassas bir şekilde üretilebilmesine hem de yeniden şekillendirilebilir yapıların üretilmesine olanak sağladığı için bu aksiyon çerçevesinde kullanılması/çalışılması proje kapsamında yer almıştır. Bunlara dayanarak, 107E090 nolu projede, COST IC0603 kapsamında, özellikle milimetre-dalga frekanslarında çalışan yeniden şekillendirilebilir anten, dizi anten ve yansıtıcı dizi anten tasarımı, üretimi ve ölçümleri yapılmıştır.

Proje kapsamında ilk olarak, huzmesi yönlendirilebilen sur biçimli mikroşerit yürüyen dalga anten dizisi X-band uygulamalarında kullanılmak üzere tasarlanmış, üretilmiş ve ölçülmüştür. Antenin ana huzmesinin istenilen yöne elektronik olarak döndürülmesi için mikroşerit hat üzerinde gerekli faz değişimini sağlayacak varaktör diyotlar kullanılmıştır. Yapılan EM benzetim ve ölçümler sonucu sur biçimli anten dizisinde, ana huzmenin diyot kontrolü ile tasarlandığı gibi 10^{o} lik bir açı taraması yapabildiği gösterilmiştir. Bu kavram kanıtlaması şeklinde bir çalışmadır; huzmenin daha büyük açı aralığında tarama yapması için tasarımda yapılması gereken değişiklikler belirtilmiştir. Bu çalışmanın ayrıntıları Bölüm 2'de verilmiştir.

MM-Dalga sabit genişlikli yarık anten ve doğrusal sönümlenen yarık antenler tasarlanıp, üretilmiştir. Anten şeklinin bu iki yapı arasında optik uyarımla değiştirilebilmesi durumunda, ışıma örüntüsünün değiştirilebileceği kavramsal olarak gösterilmiştir. Yapılan parametrik çalışma, antenlerin üretim ve ölçüm sonuçları Bölüm 3'de verilmiştir.

Proje kapsamında gerçekleştirilen bir diğer çalışmada, K ve Ka bantlarında bağımsız çalışabilen, RF MEMS anahtarlarla huzmesi elektronik olarak döndürülebilen dairesel polarizasyonlu yansıtıcı dizi anten tasarlanmış, üretilmiş ve ölçülmüştür. Çift frekanslı (24.4 GHz ve 35.5 GHz) dizi iç içe geçmiş farklı boyutlarda iki ayrık-halka dizisi şeklinde

tasarlanmıştır. Huzme döndürme amacıyla her bir ayrık halkanın açısal konumunu RF MEMS anahtarlarla ayarlayarak, dairesel polarizasyonlu dalgaların fazları kontrol edilmektedir. Anten ODTÜ MEMS merkezinde geliştirilen yüzey mikro-işleme süreciyle üretilmiştir. Işıma örüntüleri ölçülmüş ve benzetim sonuçlarıyla karşılaştırılmıştır. Ölçümlerle, ana huzmenin, tasarlandığı gibi Ka bandında 35°'ye, K bandında 24°'ye döndürülebildiği gösterilmiştir. Bu çalışmanın ayrıntıları Bölüm 4'te sunulmuştur.

Proje süresince, RF MEMS üretim sürecinin daha iyileştirilmesi için çalışmalar yapılmış, ve başarılı adımlar ODTÜ RFMEMS üretim sürecine eklenmiştir. Üretim sürecinin son durumu Bölüm 5'te özetlenmiştir.

Ayrıca proje kapsamında, 26.5 ve 35 GHz'de çalışan çift frekanslı yarık anten tasarımı, üretimi ve ölçümü yapılmıştır, (GÖKALP 2009). Bu antenin çift frekansta çalışması için, RADANT firmasından alınmış, paketli RF MEMS anahtarlar kullanılarak yarığın boyu değiştirilmiştir. Bu anten, 104E041 projesi kapsamında tasarlanan çift frekanslı dizinin elemanı olarak kullanılmıştır. Bu anten elemanı ve diziyle ilgili çalışmalar ve elde edilen sonuçlar 104E041 projesi sonuç raporunda verildiğinden bu raporda yeniden verilmemiştir, (AYDIN CIVI 2010).

2. HUZMESİ DÖNDÜRÜLEBİLEN VARAKTÖRLÜ SUR BİÇİMLİ MİKROŞERİT ANTEN DİZİSİ

2.1 Giriş

Günümüzde mikroşerit antenler düşük üretim maliyetleri, sisteme kolay entegre edilmeleri, hafif ve düzlemsel olmaları, huzme şekillendirici sistemlerle beraber kullanılabilmeleri nedeniyle askeri ve endüstriyel alanlarda sıkça tercih edilmektedir. Bu avantajlarının yanı sıra yürüyen dalga anten dizileri yüksek kazançları, düşük yan huzme değerleri ve ayarlanabilen polarizasyon özellikleri ile radar uygulamaları için uygun anten tipleri arasıda yer almaktadır (DURAL 1983, RATMON 1991, TIURI 1974). Raporun bu bölümünde, X band radar uygulamalarında kullanılabilecek ana huzmesi yönlendirilebilen sur biçimli yürüyen dalga anten dizisinin tasarım, üretim ve ölçüm aşamaları anlatılmaktadır. Huzmenin yönlendirilmesi, mikroşerit hattın üzerine varaktör diyot yerleştirilerek sağlanmıştır. Tasarlanan ve üretilen anten dizisinin fiziksel ve elektriksel özellikleri Bölüm 2.2'de, ölçüm sonuçları ve değerlendirilmesi ise Bölüm 2.3'de verilmektedir.

2.2 Sur Biçimli Mikroşerit Anten Dizisinin Tasarımı ve EM Benzetim Sonuçları

Bu proje kapsamında geliştirilmiş ışınım huzmesi yönlendirilebilen yürüyen dalga anten dizisi sekiz adet sur biçimli yapıdan oluşmaktadır, sekiz adet varaktör diyot Şekil 1'de görüldüğü gibi sur dizilerinin üzerine bulunmaktadır. Anten dizisinin çalışma frekansı X-bant radar uygulamalarına uygun olacak biçimde 10 GHz seçilmiştir. Anten taban malzemesi olarak yüksek frekansta çalışan, düşük kayıplı 15 mil kalınlığında dielektrik sabiti 2.2 olan Rogers 5880 Duroid kullanılmıştır. Yürüyen dalga anten dizisi 50-Ω yükle sonlandırılarak anten sonuna ulaşan dalganın geri yansıması engellenmektedir. Anten dizisinde kullanılan varaktör diyotlar DC gerilim ile kontrol edilebilen ve kapasitansları uygulanan gerilim ile orantılı olarak değişebilen yapılardır. Mikroşerit anten dizisi varaktör diyotlarla yüklenerek ışınım huzmesinin istenilen doğrultuya yönlendirilmesi sağlanmıştır.

Sur biçimli mikroşerit anten dizisinin birim elemanı, Şekil 2'de verilen dört köşeli sur biçimli yapıdan oluşmaktadır. Köşelerdeki keskin geçişler geri dönüş kaybını arttırmaktadır, (DURAL 1983). Bu kaybı azaltmak amacıyla köşeler kesikli yapılandırılmıştır. Sur biçimli mikroşerit anten dizisinde ışıma, bu köşelerin eşdeğer manyetik akımlarla modellenmesiyle açıklanabilir (DURAL 1983). Mikroşerit üzerindeki manyetik akımın köşenin iç ve dış kenarlarında ilerlerken aldığı yol farklıdır. Sur biçimli mikroşerit antenin ışıma özellikleri, polarizasyonu Şekil 2-b' de gösterilen birim elemanın *s*, *l* ve *d* değerleri ile belirlenebilmektedir. Örneğin,

s=λ/2, l=λ/4 ve d=3λ/4 değerleri için yayılan manyetik alanın yatay ve dikey bileşenleri arasında doksan derecelik bir faz farkı oluşur ve dairesel polarizasyon elde edilir. Bu çalışmada tasarlanan anten dikey polarizasyondadır.

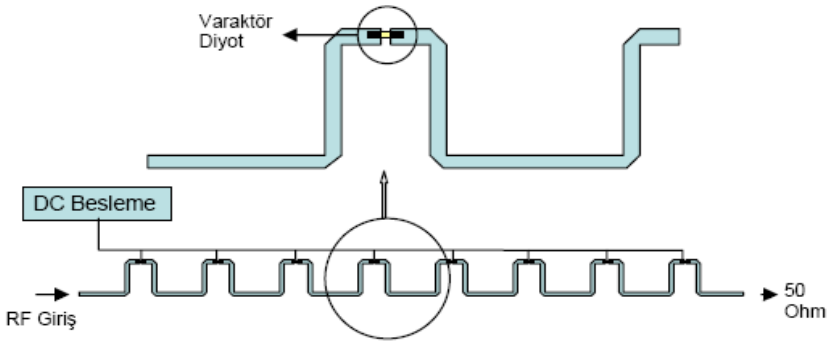

Şekil 1. Işınım huzmesi yönlendirilebilen varaktörlü mikroşerit anten dizisi

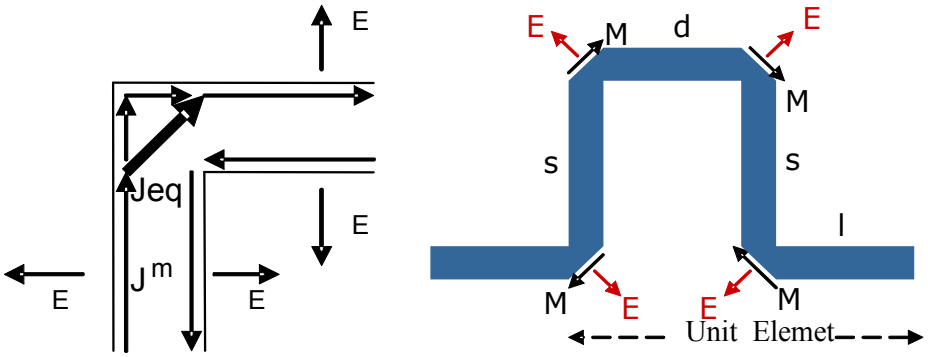

Şekil 2. (a) Sur biçimli anten dizisindeki köşe yapısında eşdeğer akım dağılımı (b) Dört köşeli sur biçimli anten dizisinin birim elemanı

Antenin *d* uzunluğunu değiştirerek, ana huzmeyi istenilen yöne yönlendirmek mümkündür. Anten dizisindeki birim eleman sayısı arttıkça anten dizisinin kazancı artar, yan huzmeleri küçülür ve anten dizisinin sonundaki 50-Ω yüke ulaşan sinyal seviyesi azalır.

Bu çalışmada anten elemanının elektriksel boyu, üzerine takılan varaktör diyotlar ile ayarlanmaktadır. Bu anten dizisinde kullanılan varaktör diyotlar kapasitans değerleri 0.3 pF'tan 2.4 pF'a kadar değişebilen MICROSEMI MPV2100-206'dır. 0 volt besleme voltajı altında 2.4 pF, 20 volt besleme voltajı altında 0.3 pF kapasitans değerini sağlayabilmektedir. Diyotun farklı gerilim altında sağladığı faz değerlerinin ölçülebilmesi için varaktör diyot 50-Ω mikroşerit hat üzerine Şekil 3'de görüldüğü gibi yerleştirilmiştir. Diyota 0-25 Volt arası DC gerilim uygulanarak diyodun sağladığı faz değişimi elde edilmiş ve Şekil 4'de verilmiştir.

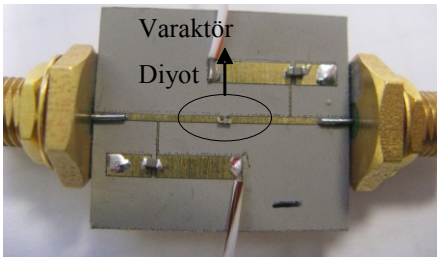

Şekil 3. 50 Ω Mikroşerit hat üzerine yerleştirilmiş Microsemi MPV2100 varaktör diyot besleme devresi

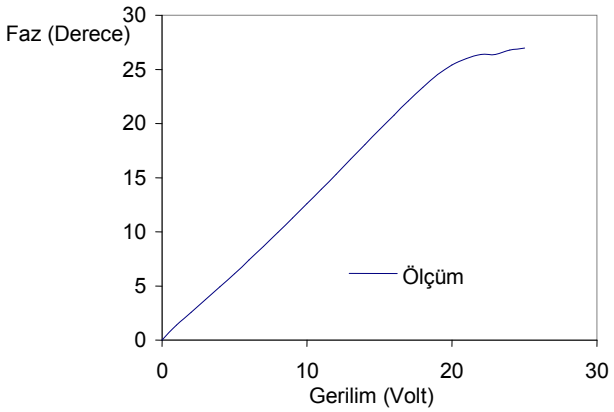

Şekil 4. Varaktör diyotun farklı besleme gerilimleri altında sağladığı faz değişimi

Anten dizisinin tasarımında Momentler Yöntemini (MoM) kullanan Ansoft Designer v3, Elektromanyetik benzetim yazılımı kullanılmıştır. Varaktör diyotların kapasitans değerlerinin S-parametreleri elektromanyetik analizi yapılan mikroşerit yapıların üzerine yerleştirilmiştir. Farklı kapasitans değerleri için anten dizisinin S-parametresi değerleri Şekil 5'de gösterilmiştir. Bu sonuçlara göre 10 GHz'de anten dizisinin S_{11} değeri -10 dB'nin altındadır. S_{21} değeri ise -3 dB civarındadır. Farklı kapasitans değerleri için ana huzmenin yönü elektromanyetik simülasyonlarla gözlenmiştir. Bu simülasyon sonuçlarına göre varaktör diyot'un kapasitans değeri 0.3 - 2.4 pF arasında değişirken ışınım huzmesi 30°'den 19°'ye, yani yaklaşık 10° dönmektedir. Işınım huzmesinin kapasitans değerlerine göre dönüşü

Şekil 8'de gösterilmiştir.

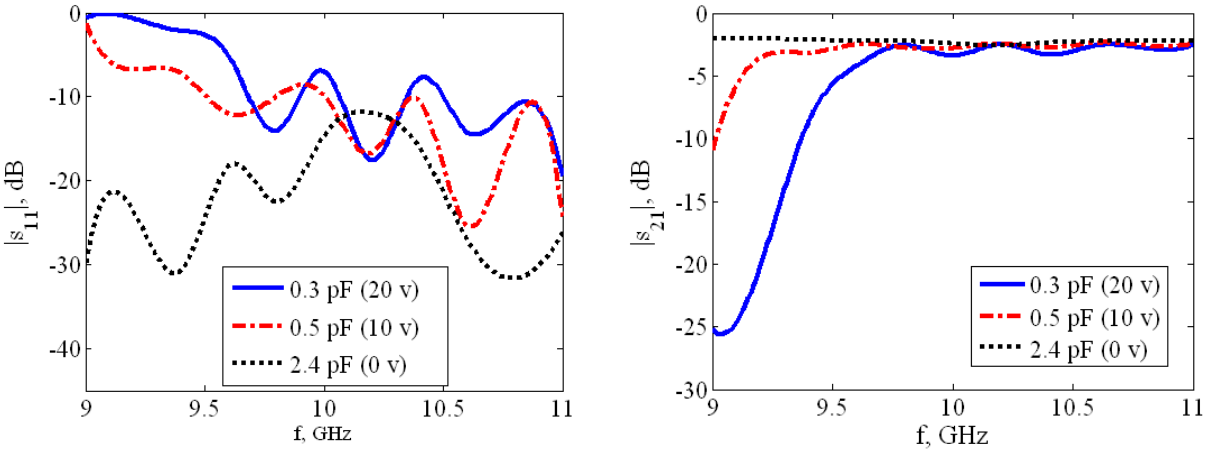

Şekil 5. Simulasyonlarda elde edilen S11 ve S21 değerleri

2.3 Dizinin Üretimi ve Ölçüm Sonuçları

Bölüm 2.2'de tasarımı verilen anten dizisi, düşük kayıplı 15 mil kalınlığında dielektrik sabiti 2.2 olan Rogers 5880 Duroid üzerine üretilmiştir. Şekil 6'da üretilen varaktör diyotlu anten dizisi görülmektedir.

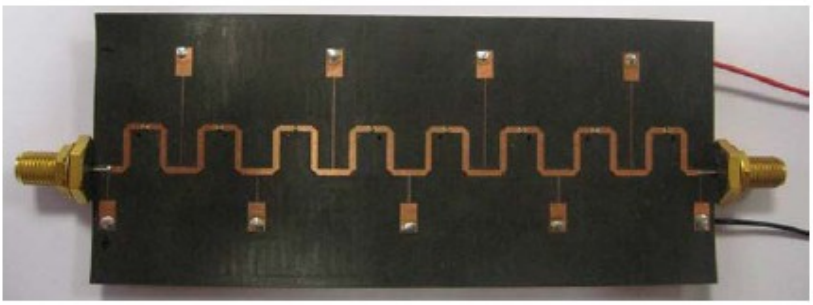

Şekil 6. Prototip olarak üretilen ışınım huzmesi yönlendirilebilen anten dizisi

Varaktör diyotları beslemek için, Şekil 6'da görüldüğü gibi, iki parçalı mikroşerit hatlar kullanılmıştır. Besleme hatlarının, anten performansına etkisini azaltmak için, önce 100Ω çeyrek dalga boyu hat, sonra 50 Ω çeyrek dalga boyunun tek katı uzunlukta hatlar kullanılmıştır. 50 Ω'luk hatların sonunda via yardımıyla antenin arkasına geçilmiş ve besleme telleri bağlanmıştır.

Anten dizisinin S-parametreleri, farklı voltaj değerleri için ölçülmüş ve ölçüm sonuçları Şekil 7'de sunulmuştur. S-parametresi ölçüm sonuçları 10 GHz'de antenin geri dönüş kaybının -10 dB'nin altında olduğunu ve varaktör diyotların araya girim kayıplarının 7 dB civarında olduğunu göstermektedir.

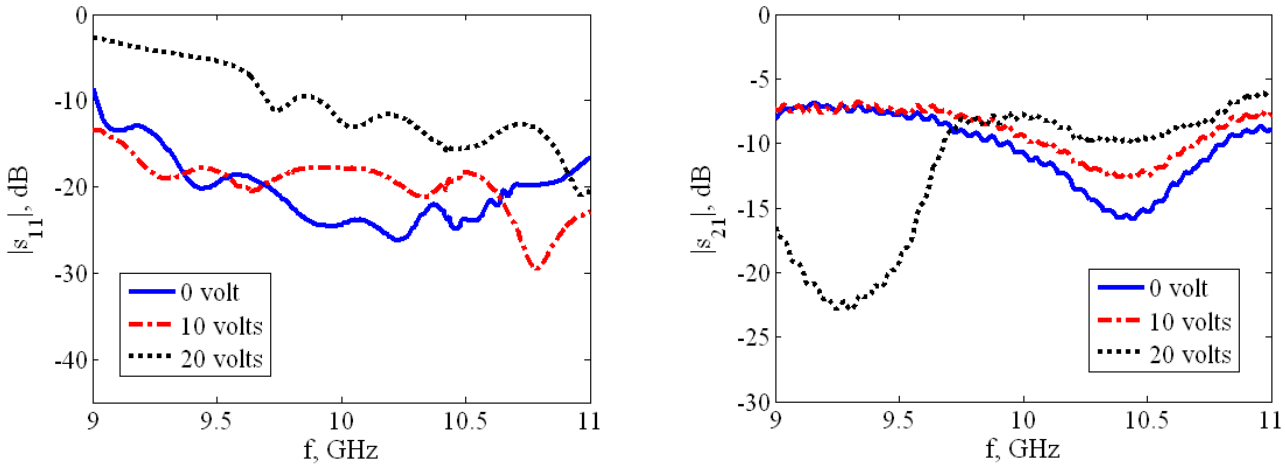

Şekil 7. Ölçülen S11 ve S21 değerleri

Anten dizisinin ışınım huzmesi, 10 GHz'de E-düzleminde, farklı gerilim değerleri için ölçülmüştür. Farklı gerilim değerleri için elektrik alan ölçüm sonuçları, EM benzetim sonuçlarıyla karşılaştırmalı olarak Şekil 8'de gösterilmektedir. Görüldüğü gibi benzetimlerle ölçüm sonuçları uyuşmaktadır. Benztimlerde olduğu gibi ölçümde de antenin ışınım huzmesi 10°'den fazla dönmektedir. Arama ve izleme radarlarında anten mekanik olarak yancada döndürülürken, doğrulama için ana huzmenin birkaç derece döndürülmesi gerekebilmektedir. Üretilen bu anten bu tür uygulamalarda kullanılabilir. Ayrıca tek bir varaktör diyot yerine 90° hibrit varaktör diyotlarla yüklenerek daha fazla faz değişimi sağlanabilir (CHENG 2006), bu da daha geniş bir aralıkta huzmenin döndürülebilmesini sağlar.

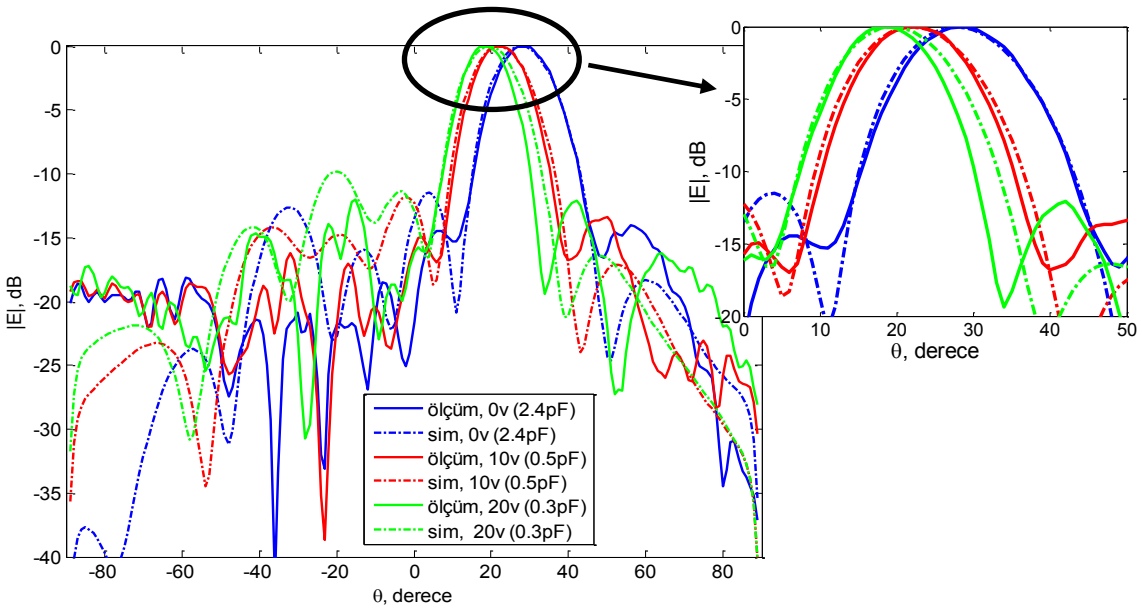

Şekil 8. Farklı DC gerilim değerleri için 10GHz'de anten dizisinin elektrik alanının benzetim ve ölçüm sonuçları (θ anten düzlemine dik doğrultudan ölçülmektedir)

3. YENİDEN ŞEKİLLENDİRİLEBİLİR MİLİMETRE DALGA SÖNÜMLENEN YARIK ANTEN

3.1 GİRİŞ

Bu bölümde sunulan çalışmada, sönümlenen yarık antenlerin fiziksel özelliklerinin ışıma örüntüsüne etkilerini araştırmak ve iki farklı sönümlenme tipi arasında yapılacak geçişlerle ışıma örüntüsünde yeniden şekillendirilebilirlik elde edilebilme olasılığını araştırmak hedeflenmiştir. Bu kapsamda, iki yarık anten tipi arasında öncelikle elektromanyetik benzetim sonuçları ile karşılaştırmalı analiz yapılmış ve elde edilen sonuçların doğruluğunun belirlenmesi amacıyla her iki anten tipinden de ikişer adet anten üretilerek yankısız odada ışıma örüntüsü ölçümleri gerçekleştirilmiştir.

Sönümlenen yarık antenler, bir dielektrik malzeme üzerine kazınmış ve uzunluk boyunca genişleyen bir yarık iletim hattından oluşur ve uçtan ışıma karakteristiğine sahiptir. Elektromanyetik dalgalar, yarık iletim hattını oluşturan ve genişleyen metal yüzeyler arasında yüzeyden ayrılıp havada yayılmaya başlayana kadar hareket eder. Bu özellikleri sayesinde dar huzme genişliği ve yüksek yönlülüğe sahiptir. Anten beslemesi ve anten arasındaki geçişe de bağlı olarak geniş bir bantta çalışabilirler. Anten kazancı, antenin elektriksel uzunluğuyla doğru orantılı olarak değişmektedir.

Sönümlenen yarık antenler, yürüyen dalga antenler kategorisinin yavaş dalga alt kategorisine giren antenlerdir. Bu sebeple yarık üzerindeki faz dağılımı anten boyunca sabit olarak kabul edilemez (BALANIS, 1982).

Temel olarak üç çeşit sönümlenen yarık antenden bahsedilebilir. Bu anten çeşitleri yarığın sönümlenme biçimine göre adlandırılır ve Şekil 9'da gösterilmiştir.

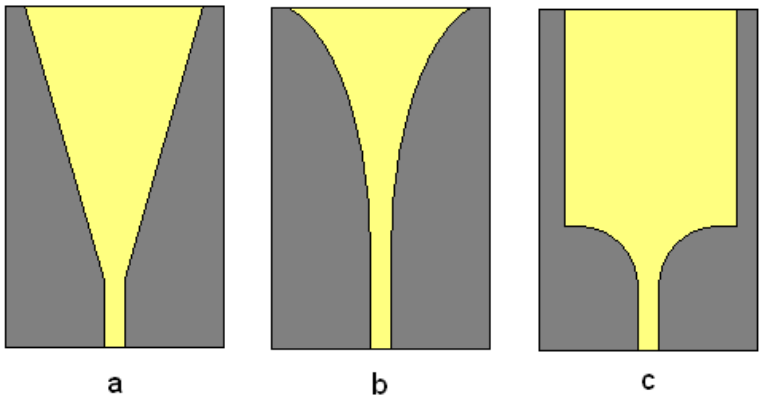

Şekil 9. Sönümlenen Yarık Anten Çeşitleri a) Doğrusal Sönümlenen Yarık Anten b) Üstel Sönümlenen Yarık Anten c) Sabit Genişlikli Yarık Anten

Bu üç sönümlenen yarık antenin, aynı anten uzunluğu ve anten parametreleri için ışıma örüntüleri karşılaştırıldığında, üstel sönümlenen yarık antenin en geniş huzmeye, sabit genişlikli yarık antenin ise en dar huzmeye sahip olduğu görülür. Yan huzme seviyesi ise, beklendiği üzere, üstel sönümlenen yarık antende en az, sabit genişlikli yarık antende ise en fazladır. Bu sebeple doğrusal sönümlenen yarık anten ile sabit genişlikli yarık anten arasında gerçekleşecek bir geçiş, yan huzme seviyesi ve ana huzme genişliği açısından yeniden şekillendirilebilirlik sağlayacaktır. Bu çalışma kapsamında doğrusal sönümlenen yarık anten ve sabit genişlikli yarık antenler ayrı ayrı analiz edilmiş ve ışıma özellikleri karşılaştırılmıştır.

Sönümlenen yarık antenler, ışıma için yarık iletim hatları kullandığından genellikle besleme iletim hattı tipi ve yarık iletim hattı arasında bir geçiş tasarlanması gereklidir. Bu geçiş tasarımları iki ana başlık altında değerlendirilebilir (SYEDA, 2003). Bu geçiş tiplerinden ilki, iki iletim hattı arasında fiziksel bağın olmadığı elektromanyetik bağlaşımlı geçişlerdir. Örnek olarak Şekil 10'daki gibi mikroşerit hat-yarık hat geçişi verilebilir.

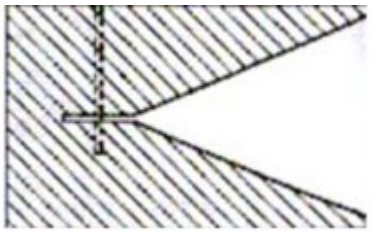

Şekil 10. Elektromanyetik bağlaşımlı mikroşerit-yarık hat geçişi

Diğer bir geçiş tipi de iki hat arasında fiziksel bağa ihtiyaç duyan doğrudan bağlaşımlı geçişlerdir. Bu tip bir örnek Şekil 11'de görülen eş düzlemli dalga kılavuzu-yarık hat geçişidir.

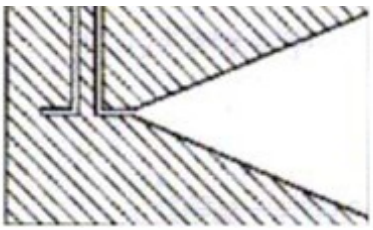

Şekil 11. Doğrudan bağlaşımlı eş düzlemli dalga kılavuzu-yarık hat geçişi

Bölüm 3.2'de sönümlenen yarık antenlerin farklı parametrelerini değiştirerek ışıma örüntüsüne etkileri tartışılmaktadır. Üretim ve ölçüm sonuçları Bölüm 3.3'de verilmektedir.

3.2 Sönümlenen Anten Işıma Örüntüsü Üzerine Parametrik Çalışma

Sönümlenen yarık antenler, dielektrik tabaka kalınlığı ve dielektrik sabiti belli bir oranı sağladığı sürece yürüyen dalga özelliklerini korurlar. Etkili kalınlık (t_{eff}) parametresi aşağıdaki denklemde verilmiştir.

$$\frac{t_{eff}}{\lambda_0} = \left(\sqrt{\varepsilon_r} - 1\right)\frac{t}{\lambda_0}$$

Bu denklemde t_{eff} etkili kalınlığı, ε_r dielektrik sabitini, t substrat kalınlığını ve λ_0 dalgaboyunu ifade etmektedir. Sönümlenen yarık antenlerin, yürüyen dalga özelliklerini koruması için

$$0.005 \le \frac{t_{eff}}{\lambda_0} \le 0.03$$

değerinin sağlanması gereklidir. Laboratuvarımızda bulunan malzemeler arasından ROGERS RO5880 malzemeden kalınlığı 0.51mm olan tabakanın kullanılması uygun bulunmuştur.

3.2.1 Mikroşerit Hat-Yarık Hat Geçişi Tasarımı

Antenin besleme hattı olarak mikroşerit iletim hattı kullanılmasına karar verilmiştir. Bu sebeple mikroşerit hattan yarık iletim hattına geçiş yapısı tasarlanması gerekmiştir. Bu geçiş için, Şekil 12'de verilen, dielektriğin iki yüzündeki mikroşerit ve yarık hattın birbirini dik olarak kestiği elektromanyetik bağlaşımlı geçiş değerlendirilmiştir (SCHUPPERT, 1998).

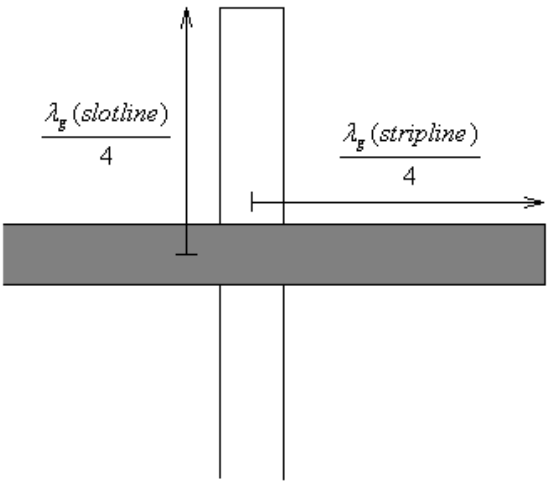

Şekil 12. Mikroşerit-Yarık hat geçişi

Bu geçişte, dielektrik tabakanın farklı yüzeylerinde olan mikroşerit hat ve yarık hat birbirlerini dik açıyla kesmekte ve birbirlerinden çeyrek kılavuzlu dalgaboyu kadar uzağa erişmektedirler. Aynı zamanda anten beslemesi olduğu için mikroşerit hattın empedansı 50Ω

olarak seçilmiştir. Yarık hattın empedansını belirleyen faktör ise yarık genişliğidir. Çok büyük empedanslar elde etmemek için yarık hat kalınlığı üretilebilecek en küçük kalınlık olan 0.254 mm olarak seçilmiş ve bu da, Ek-1'de verilen formüller çerçevesinde 152.76Ω empedansa karşılık gelmiştir.

Mikroşerit hat ve yarık hatların empedans eşlemesi için, geniş bantta düşük kayıp elde etmek için Chebyshev empedans dönüştürücü kullanılmıştır. Buna göre mikroşerit antenin besleme empedansı olan 50Ω ile yük empedansı olan yarık hat empedansı (152.76Ω) arasında, Şekil 13'de görüldüğü gibi, üç kademeli bir dönüştürücü tasarlanmıştır.

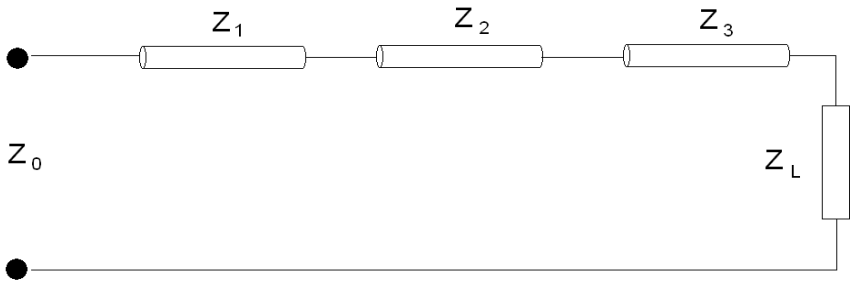

Şekil 13. Chebyshev Empedans Dönüştürücü

Ek-2'de verilen formüller ışığında Z_0=50Ω ve Z_L=152.76Ω alınarak Z_1, Z_2 ve Z_3 empedansları sırasıyla 61.01Ω, 87.39Ω ve 125.19Ω olarak hesaplanmıştır. Bu empedanslar, 50Ω'luk giriş mikroşerit hattının sonuna arka arkaya bağlanan farklı kalınlıklarda çeyrek kılavuzlu dalga boyu uzunluğunda üç mikroşerit parça ile sağlanmıştır. Bu empedanslara karşılık gelen mikroşerit kalınlığı ve çeyrek kılavuzlu dalgaboyu uzunlukları Ek-1'deki formüllere göre hesaplanmıştır. Ayrıca HFSS EM benzetim yazılımında da mikroşerit yapılar modellenmiş ve kullanılacak değerler daha doğru bir şekilde bulunmuştur. Elde edilen değerler Tablo 1'de sunulmaktadır.

Tablo 1. Mikroşerit Hat Boyutları

	Hesaplanan Değerler		**Benzetimden Çıkan Değerler**	
	Kalınlık	$\lambda_g/4$	Şerit Genişliği	$\lambda_g/4$
Z_0=50 Ω	1.58 mm	1.56 mm	1.58 mm	1.54 mm
Z_1=61.01 Ω	1.16 mm	1.58 mm	1.08 mm	1.56 mm
Z_2=87.39 Ω	0.6 mm	1.61 mm	0.54 mm	1.60 mm
Z_3=125.19 Ω	0.26 mm	1.63 mm	0.2 mm	1.63 mm

Benzetimden çıkan değerler ile modellenen iki geçiş, Şekil 14 ve Şekil 15'te verildiği gibi, HFSS yazılımında uç uca bağlanmış ve geri dönüş kaybı ve geçiş kaybı parametreleri incelenmiştir.

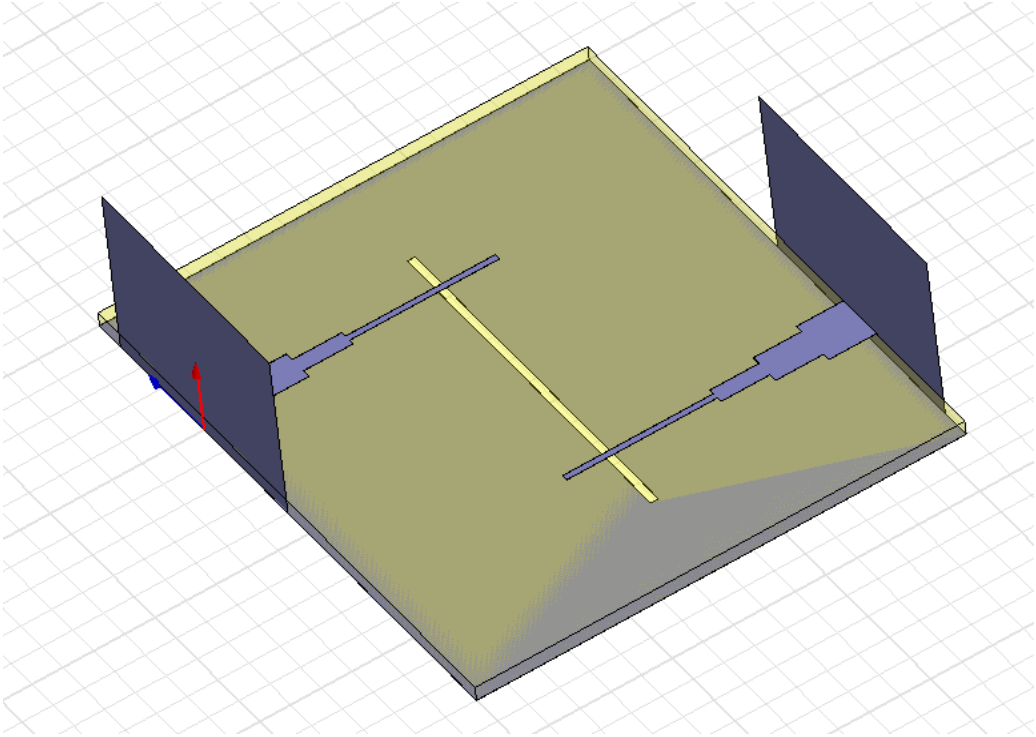

Şekil 14. Geçiş EM benzetim modeli

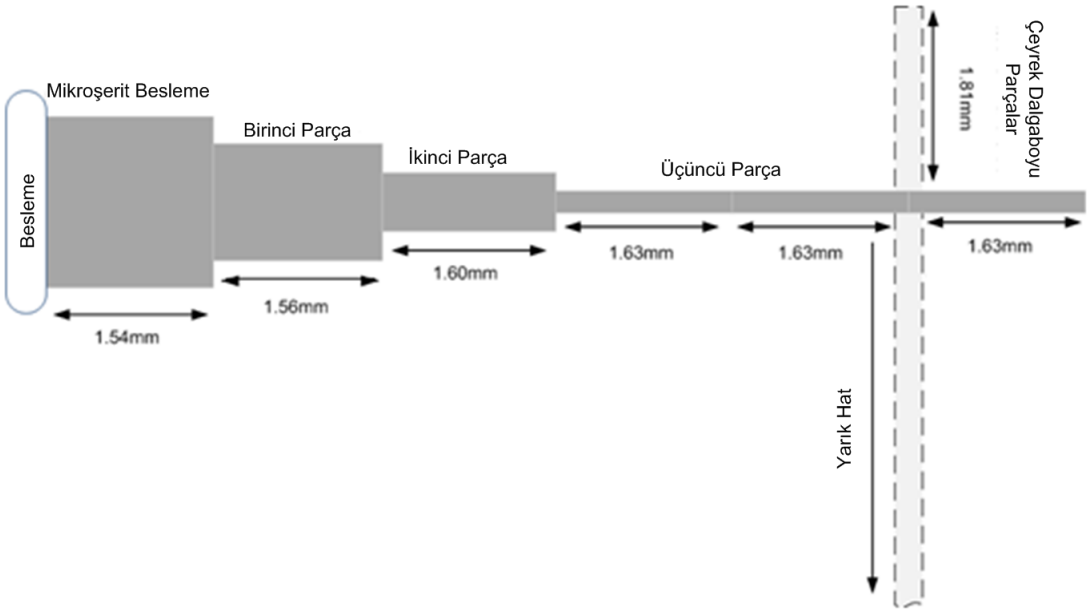

Şekil 15. Geçiş fiziksel boyutları

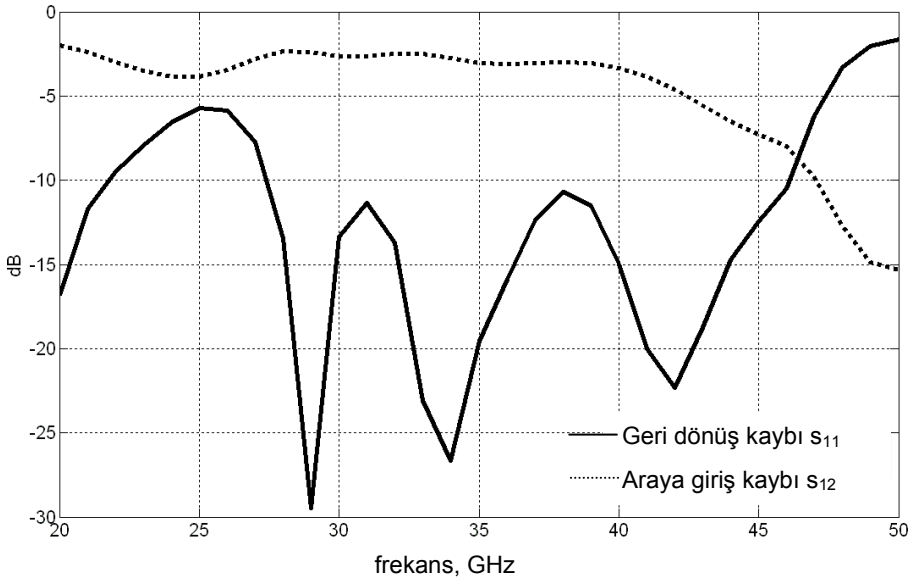

Şekil 16. Geçiş kayıpları

Şekil 16'da görüldüğü üzere, geçiş 27-40GHz arasında -10dB'den düşük geri dönüş kaybı ve 3 dB'den düşük araya giriş kaybı vermektedir.

3.2.2 Doğrusal Sönümlenen Yarık Antenin Parametrik Analizi

Bir doğrusal yarık antenin ışıma karakteristiğini etkileyen temel olarak üç parametre vardır. Bu parametreler anten uzunluğu (L), açıklık genişliği (W) ve toprak uzantısıdır (H). Bu parametreler Şekil 17'de gösterilmiştir.

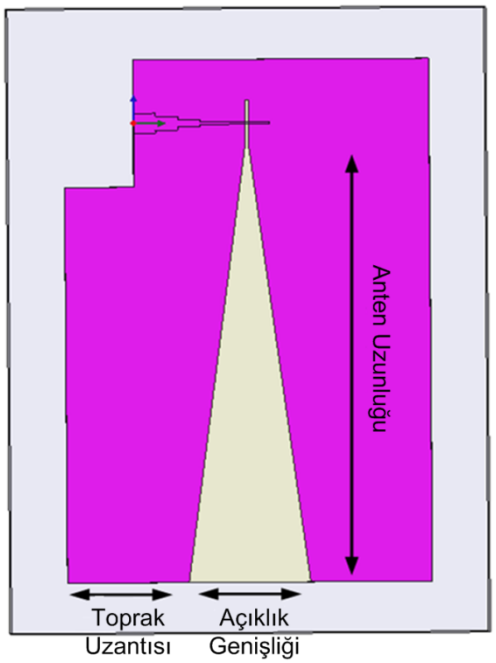

Şekil 17. Doğrusal sönümlenen yarık anten parametreleri

Parametrik analizde, bu parametrelerin ikisi sabit tutulup diğeri değiştirilerek, değişen parametrenin yarım güç huzme genişlikleri ve yan huzme seviyelerindeki değişim incelenmiştir.

Merkez frekansta, uçtan ışıma karakteristiği elde etmek için anten uzunluğunun 3 dalgaboyundan uzun olması gereklidir (KOKSAL, 1997). Bu nedenle anten uzunluğu olarak 3, 4, 5 ve 6 dalgaboyu uzunlukları parametrik çalışma kapsamına alınmıştır. Antenin verimli ışıma yapması için ise, açıklık genişliği yarım dalgaboyundan uzun olmalıdır (YNGVESSON, 1985). Bu nedenle, analizlerde açıklık genişliği 0.5 ve 1 dalgaboyu olarak alınmıştır. Toprak uzantısı olarak da 1, 1.5 ve 2 dalgaboyu değerlendirilmiştir. Parametrik çalışmalarda anten beslemesi olarak mikroşerit anten ve tasarlanan geçiş yapısı kullanılmıştır. EM Benzetimler HFSS yazılımında yapılmıştır. Parametrik çalışma sonuçları Tablo 2'de verilmiştir.

Tablo 2. Doğrusal Sönümlenen Yarık Anten Parametrik Analiz Sonuçları

W/λ_0	H/λ_0	L/λ_0	Yönlülük (dB)	E-Yüzeyi YGHG (derece)	H-Yüzeyi TGHG (derece)	E-Yüzeyi YLS (dB)	H-Yüzeyi YLS (dB)
0.5	1	3	10,24	26	34	-4,19	-8,92
		4	10,03	37	27	-7,53	-8,54
		5	8,96	48	22	-5,38	-5,74
		6	8,13	44	21	-3,85	-1,35
	1.5	3	9,5	40	32	-7,41	-7,62
		4	10,2	30	27	-7,02	-7,82
		5	9,72	34	24	-6,92	-7,57
		6	8,06	45	21	-5,82	-5,52
	2	3	8,91	45	32	-6,85	-7,04
		4	10	33	28	-8	-6,02
		5	10,28	23	26	-4,74	-5,15
		6	9,13	25	23	-4,25	-3,59
1	1	3	11,72	26	34	-15,05	-9,16
		4	12,51	24	30	-12,15	-9,64

		5	12,83	23	26	-12,73	-9,82
		6	12,14	23	26	-12,56	-8,97
	1.5	3	10,94	38	33	-12,96	-8,13
		4	12,05	28	29	-13,04	-7,84
		5	12,65	24	26	-16,94	-7,63
		6	12,55	22	23	-15,77	-7,66
	2	3	10,94	40	34	-13,49	-8,95
		4	11,49	34	27	-14,49	-8,5
		5	12,31	29	26	-15,27	-7,02
		6	12,69	21	25	-16,55	-6,29

Görüldüğü üzere anten uzunluğunun artmasıyla E-düzlemi ve H-düzleminde yarım güç huzme genişlikleri azalmıştır. Anten uzunluğu ile huzme genişliği ters orantılı olduğundan bu beklenen bir durumdur. Yan huzme seviyeleri incelendiğine ise H-düzlemindeki yan huzme seviyesinin antenin uzaması ile arttığı görülmüştür. Bu durum da, açıklıktaki elektrik alanın dağılımı ile açıklanabilir. Şekil 18'den görüldüğü gibi, açıklık genişliği daraldıkça açıklıktaki elektrik alan daha tekbiçimli hale gelir. Bu nedenle H-düzleminde daha dar huzme genişliği ve daha yüksek yan huzme seviyesi gözlenir.

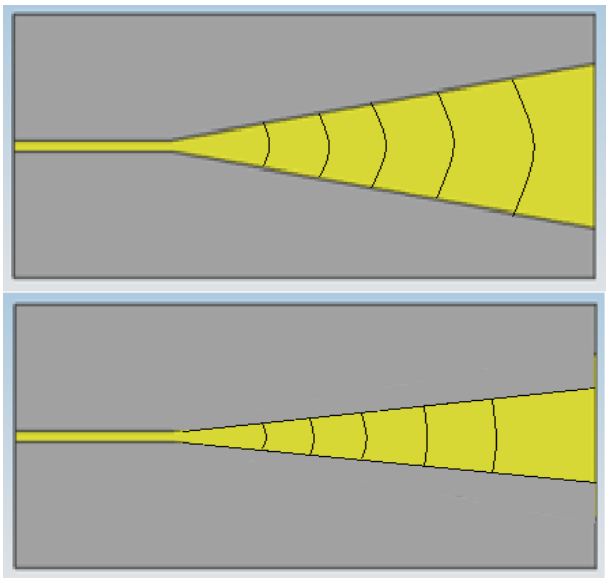

Şekil 18. Açıklıktaki elektrik alanın genişliğe göre dağılımı

Açıklık genişliğinin artması, E-düzleminde daha düşük huzme genişliği ve daha düşük yan huzme seviyesine neden olmaktadır. H-düzleminde ise açıklıktaki elektrik alan dağılımından dolayı huzme genişliği artarken yan huzme seviyesi azalmaktadır.

Toprak uzantısının ise örüntüde genellenebilecek bir değişikliğe yol açmadığı görülmüştür.

3.2.3 Sabit Genişlikli Yarık Anten Parametrik Çalışması

Sabit genişlikli yarık anten için de doğrusal sönümlenen yarık antende değiştirilen parametreler değiştirilerek parametrik çalışma yapılmıştır. Parametrik çalışma sonuçları Tablo 3'te özetlenmiştir.

Tablo 3 Sabit Genişlikli Yarık Anten Parametrik Analiz Sonuçları

W/ λ_0	H/ λ_0	L/ λ_0	Yönlülük (dB)	E-Yüzeyi YGHG (derece)	H-Yüzeyi TGHG (derece)	E-Yüzeyi YLS (dB)	H-Yüzeyi YLS (dB)
0.5	1	3	10,77	23	34	-8,12	-9,9
		4	11,06	22	28	-4,77	-11,23
		5	10,55	21	23	-3,31	-9,66
		6	9,08	48	18	-6,99	-5,21
	1.5	3	9,72	35	32	-8,63	-7,35
		4	10,49	22	26	-8,18	-7,77
		5	10,92	19	23	-8,18	-8,05
		6	10,6	19	20	-5,98	-8,76
	2	3	9,04	41	31	-7,57	-7,55
		4	9,71	32	25	-8,3	-5,73
		5	10,58	21	22	-6,29	-4,32
		6	11	15	21	-5,86	-4,38
1	1	3	9,71	20	32	-8,87	-6,85
		4	10,54	18	29	-8,09	-8
		5	11,14	16	25	-7,68	-9,88

		6	11,16	15	23	-4,78	-12,56
	1.5	3	8,55	32	29	-9,51	-5,62
		4	9,31	23	25	-7,27	-4,71
		5	10,05	17	23	-6,97	-4,72
		6	10,81	14	22	-5,34	-6,91
	2	3	8,66	30	30	-9,32	-7,08
		4	8,54	28	25	-7,82	-6
		5	9,06	26	21	-7,07	-4,05
		6	10,19	18	21	-5,88	-3,26

Görüldüğü üzere anten uzunluğu arttıkça huzme genişlikleri beklendiği üzere daralmakta E-düzlemi yan huzme seviyesi artmaktadır.

Açıklık genişliğinin artması E- düzleminde hem huzme genişliğini hem de yan huzme seviyesini azaltmaktadır. H- düzleminde ise yan huzme seviyesi açıklık genişliği ile doğru orantılıdır.

Toprak uzantısının artması ise, H-düzlemi yan huzme seviyesini artırmakta, diğer parametrelere etki etmemektedir.

Parametrik analizleri yapılan tüm antenler 35GHz olan merkez frekansında -10dB'den düşük geri dönüş kaybı vermektedir.

Antenlerin ışıma örüntü bantları incelendiğinde, 30-40GHz frekans bandında benzer ışıma ışıma örüntüleri gösterdiği gözlenmiştir. Üç frekansta da antenin uçtan ışıma özelliği korunmaktadır. Şekil 19 ve Şekil 20'de doğrusal sönümlenen yarık antenin E ve H-düzlemlerinde 30, 35 ve 40GHz frekanslarındaki ışıma örüntüleri verilmiştir.

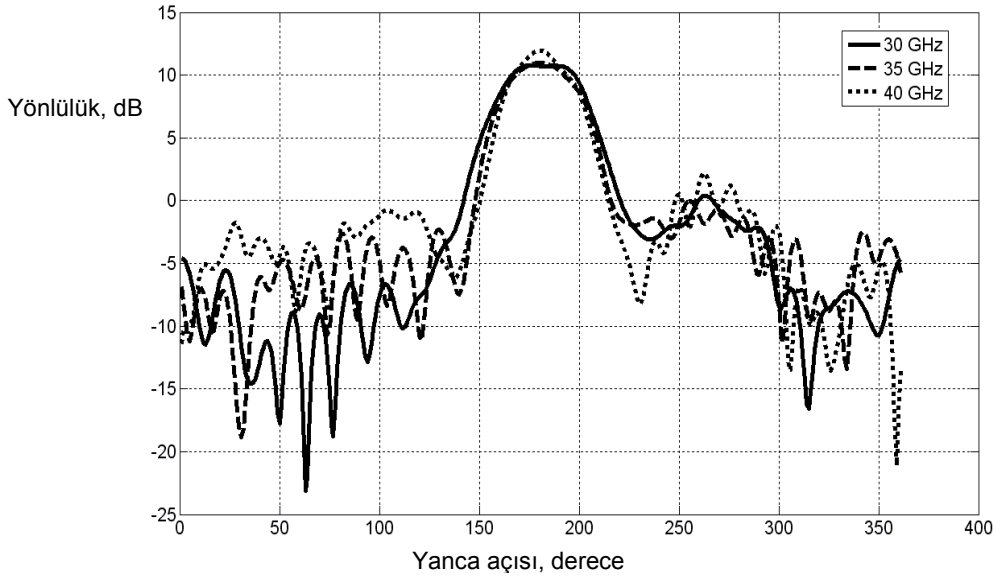

Şekil 19. Doğrusal Sönümlenen Yarık Anten E-Yüzeyi Işıma Örüntüsü (L/ λ_0=3, W/ λ_0=1, H/ λ_0=2)

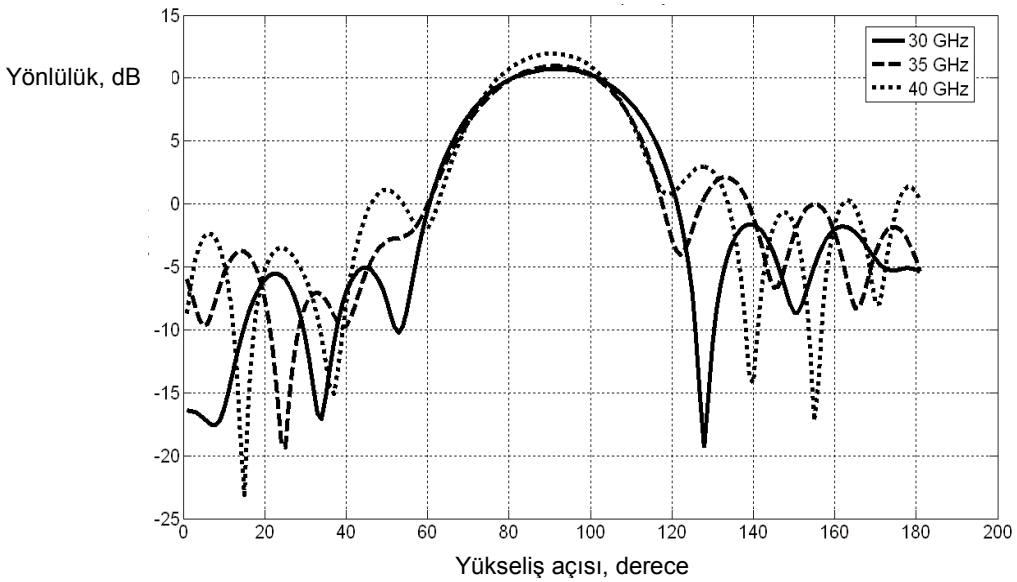

Şekil 20. Doğrusal Sönümlenen Yarık Anten H-Yüzeyi Işıma Örüntüsü

Şekil 21 ve Şekil 22'de sabit genişlikli yarık antenin 30, 35 ve 40 GHz frekanslarındaki E ve H-düzlemi ışıma örüntüleri verilmiştir. Görüldüğü üzere anten 10 GHz'lik bantta ışıma özelliklerini korumaktadır.

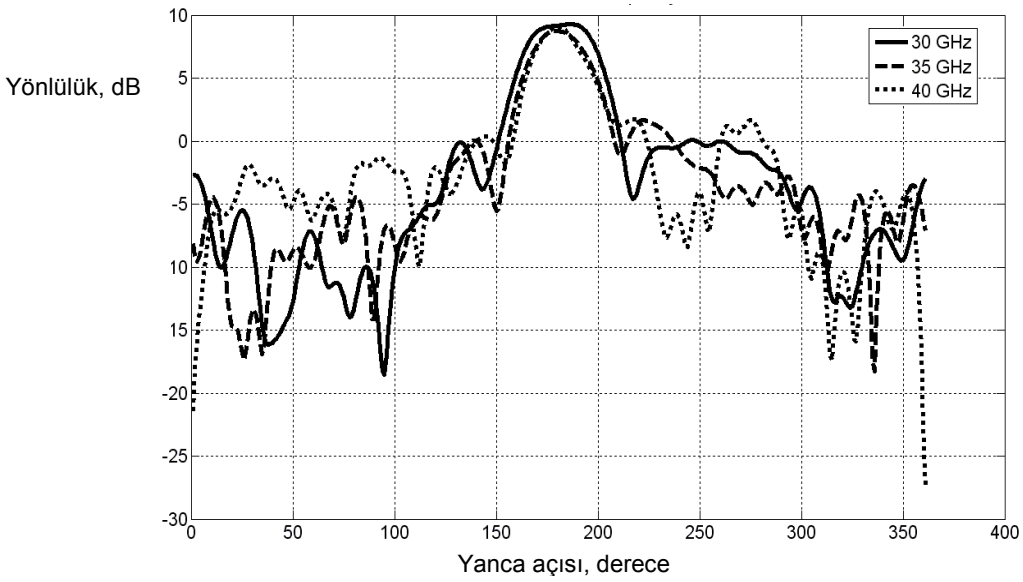

Şekil 21. Sabit Genişlikli Yarık Anten E-Yüzeyi Işıma Örüntüsü

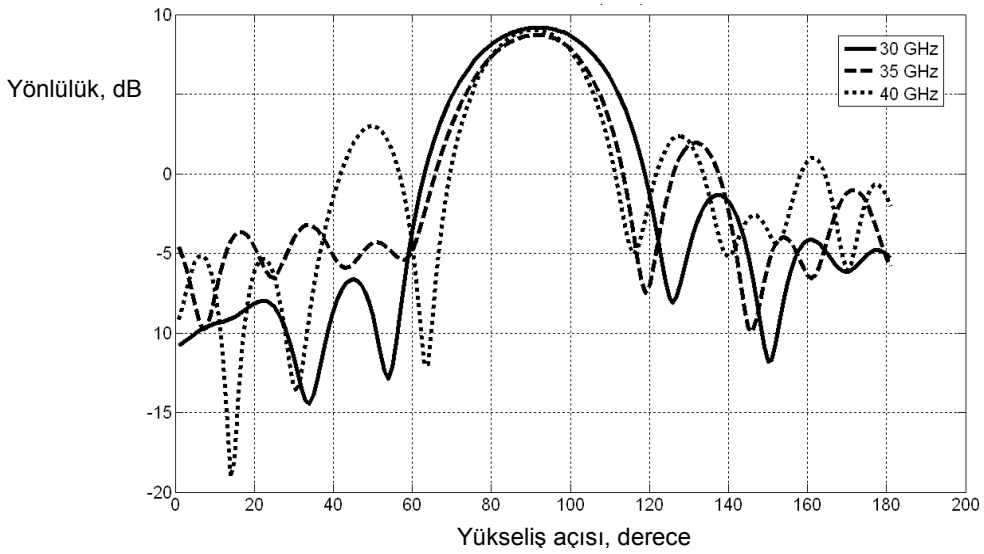

Şekil 22. Sabit Genişlikli Yarık Anten H-Yüzeyi Işıma Örüntüsü

3.2.4.Doğrusal Sönümlenen Yarık Anten-Sabit Genişlikli Yarık Anten Örüntü Karşılaştırması

Bu bölümde, aynı fiziksel parametrelere sahip doğrusal sönümlenen ve sabit genişlikli yarık antenlerin ışıma örüntüleri birbirleriyle karşılaştırılmıştır. Bu karşılaştırmadaki amaç, iki anten tipinden birinin daha geniş huzme genişliğine ve daha düşük yan huzme seviyesine, diğerinin ise daha dar huzme genişliğine ve daha yüksek yan huzme seviyesine sahip olduğunu göstererek, iki anten tipi arasında yeniden şekillendirilebilirlik elde edilebileceğinin gösterilmesidir. Buna göre doğrusal sönümlenen yarık antenden, sabit genişlikli yarık antene geçişte yan huzme seviyesinin artması karşılığında huzme genişliği daralacaktır.

Şekil 23‘de yeniden şekillendirilebilir bu antenin geometrisi verilmiştir.

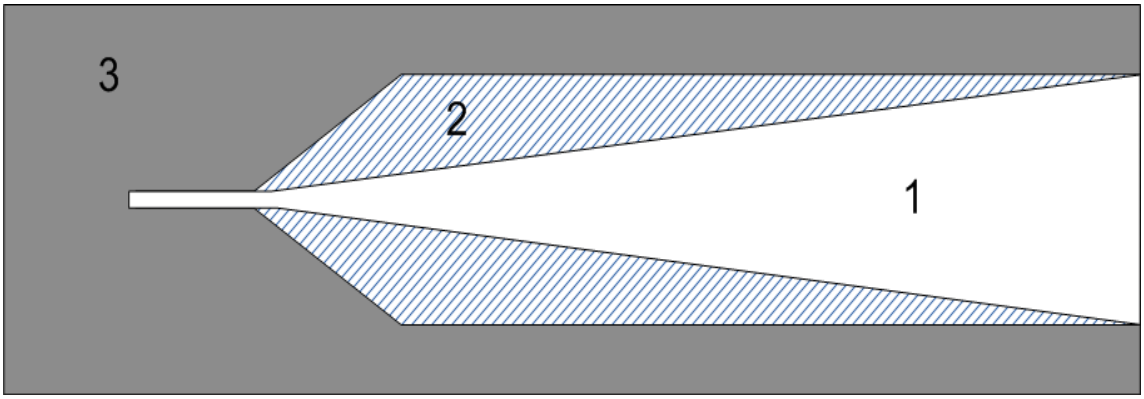

Şekil 23. Yeniden Şekillendirilebilir Anten Geometrisi

“1” ile işaretlenmiş bölge dielektrik tabakayı, “2” ile işaretlenmiş bölge optik uyarı ile metal olarak davranacak malzemeyi, “3” numaralı bölge ise metal yüzeyi göstermektedir. Buna göre “2” ile numaralanmış bölge uyarılmadığında sabit genişlikli yarık anten, uyarıldığında ise doğrusal sönümlenen yarık anten yapısı oluşacak ve yan huzme seviyesinde azalma ve huzmede genişleme görülecektir.

Tablo 4 Doğrusal Sönümlenen-Sabit Genişlikli Yarık Anten Karşılaştırması

			Doğrusal Sönümlenen Yarık Anten				**Sabit Genişlikli Yarık Anten**				**Huzme Daralması (derece)**		**Yan Huzme Artması (dB)**	
L/λ_0	W/λ_0	H/λ_0	$YGHG_E$	$YGHG_H$	YLS_E	YLS_E	$YGHG_E$	$YGHG_H$	YLS_E	YLS_E	$YGHG_E$	$YGHG_H$	YLS_E	YLS_E
		1	26	34	-4,19	-8,92	23	34	-8,12	-9,9	3	0	-3,93	-0,98
		1,5	40	32	-7,41	-7,62	28	32	-8,63	-7,35	12	0	-1,22	0,27
	0,5	2	45	32	-6,85	-7,04	41	31	-7,57	-7,55	4	1	-0,72	-0,51
		1	26	34	-15,0	-9,16	20	32	-8,87	-6,85	6	2	6,18	2,31
		1,5	38	33	-12,9	-8,13	32	29	-9,51	-5,62	6	4	3,45	2,51
3	1	2	40	34	-13,4	-8,95	30	30	-9,32	-7,08	10	4	4,17	1,87
		1	37	27	-7,53	-8,54	22	28	-4,77	-11,2	15	-1	2,76	-2,69
		1,5	30	27	-7,02	-7,82	22	26	-8,18	-7,77	8	1	-1,16	0,05
4	0,5	2	33	28	-8	-6,02	32	25	-8,3	-5,73	1	3	-0,3	0,29

		1	24	30	-12,1	-9,64	18	29	-8,09	-8	6	1	4,06	1,64
		1,5	28	29	-13,0	-7,84	23	25	-7,27	-4,71	5	4	5,77	3,13
	1	2	34	27	-14,4	-8,5	28	25	-7,82	-6	6	2	6,67	2,5
		1	48	22	-5,38	-5,74	21	23	-3,31	-9,66	27	-1	2,07	-3,92
		1,5	34	24	-6,92	-7,57	19	23	-8,18	-8,05	15	1	-1,26	-0,48
	0,5	2	23	26	-4,74	-5,15	21	22	-6,29	-4,32	2	4	-1,55	0,83
		1	23	26	-12,7	-9,82	16	25	-7,68	-9,88	7	1	5,05	-0,06
		1,5	24	26	-16,9	-7,63	17	23	-6,97	-4,72	7	3	9,97	2,91
5	1	2	29	26	-15,2	-7,02	26	21	-7,07	-4,05	3	5	8,2	2,97
		1	44	21	-3,85	-1,35	48	18	-6,99	-5,21	-4	3	-3,14	-3,86
		1,5	45	21	-5,82	-5,52	19	20	-5,98	-8,76	26	1	-0,16	-3,24
	0,5	2	25	23	-4,25	-3,59	15	21	-5,86	-4,38	10	2	-1,61	-0,79
		1	23	26	-12,5	-8,97	15	23	-4,78	-12,5	8	3	7,78	-3,59
		1,5	22	23	-15,7	-7,66	14	22	-5,34	-6,91	8	1	10,43	0,75
6	1	2	21	25	-16,5	-6,29	18	21	-5,88	-3,26	3	4	10,67	3,03

Tablo 4'ten görüldüğü üzere birden fazla konfigürasyonda kayda değer bir huzme genişliği değişikliği, yan huzme seviyesi karşılığında elde edilebilmektedir.

Şekil 24 ve Şekil 25'de $L=3\lambda_0$, $W=1\lambda_0$ ve $H=2\lambda_0$ için doğrusal sönümlenen ve sabit genişlikli yarık anten örüntü karşılaştırması verilmiştir.

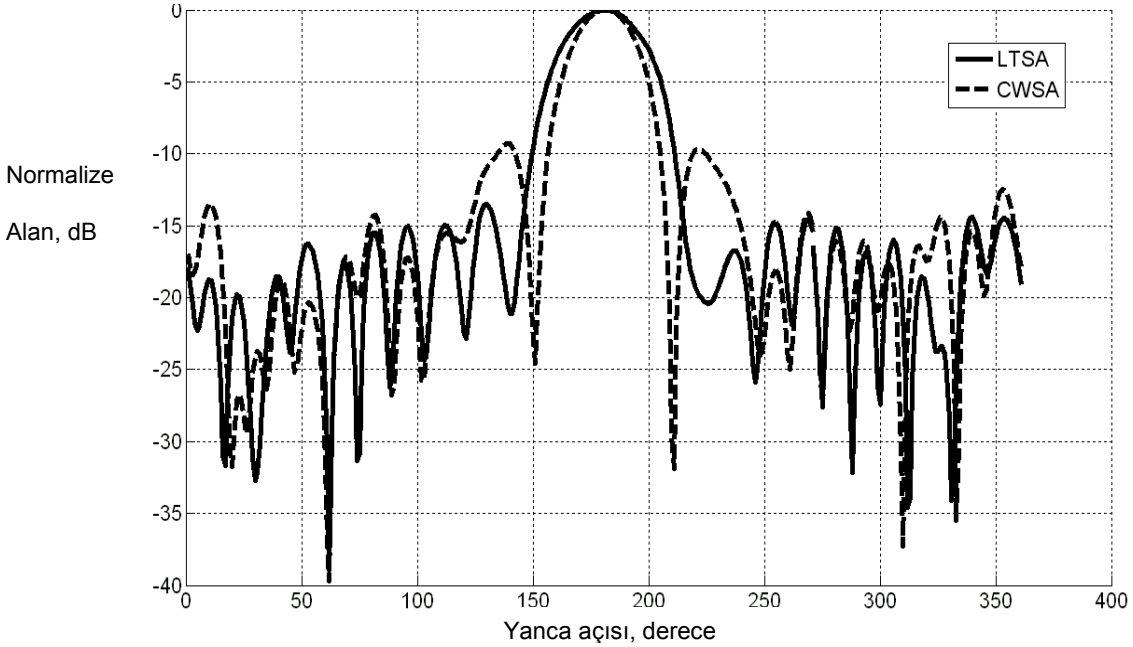

Şekil 24. Doğrusal Sönümlenen-Sabit Genişlikli Yarık Anten E-Yüzeyi Örüntü Karşılaştırması

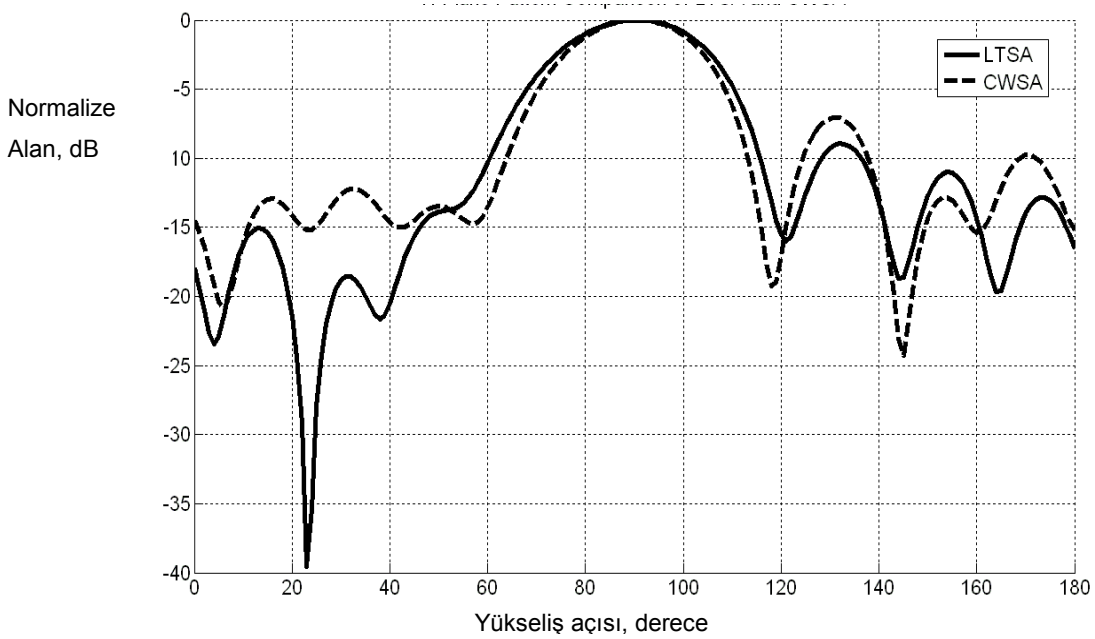

Şekil 25. Doğrusal Sönümlenen-Sabit Genişlikli Yarık Anten H-Yüzeyi Örüntü Karşılaştırması

Görüldüğü gibi anten tipleri arasındaki geçişlerde iki yüzeyde de huzme genişliğinde ve yan huzme seviyesinde değişiklik görülmüştür.

3.3 Üretim ve Ölçüm Sonuçları

Antenlerin üretimi aşamasında, mikroşerit-yarık hat geçişindeki empedans eşleyicinin son mikroşerit bölümünün üretim için çok dar olduğu ve kullanılan dielektrik tabakanın kazıma işlemi için uygun olmadığı görülmüştür. Üretilebilir bir anten tasarımı yapabilmek için,

dielektrik tabaka RO4003 olarak değiştirilmiştir. Yeni tasarımda mikroşerit-yarık hat geçişi için empedans dönüştürücü gerektirmeyen ve daha geniş bir mikroşerit kalınlığına sahip bir geçiş yapısı tasarlanmıştır. Bu geçişin de HFSS yazılımında EM benzetimi yapılmıştır. Benzetim sonucu Şekil 26'da gösterilmiştir.

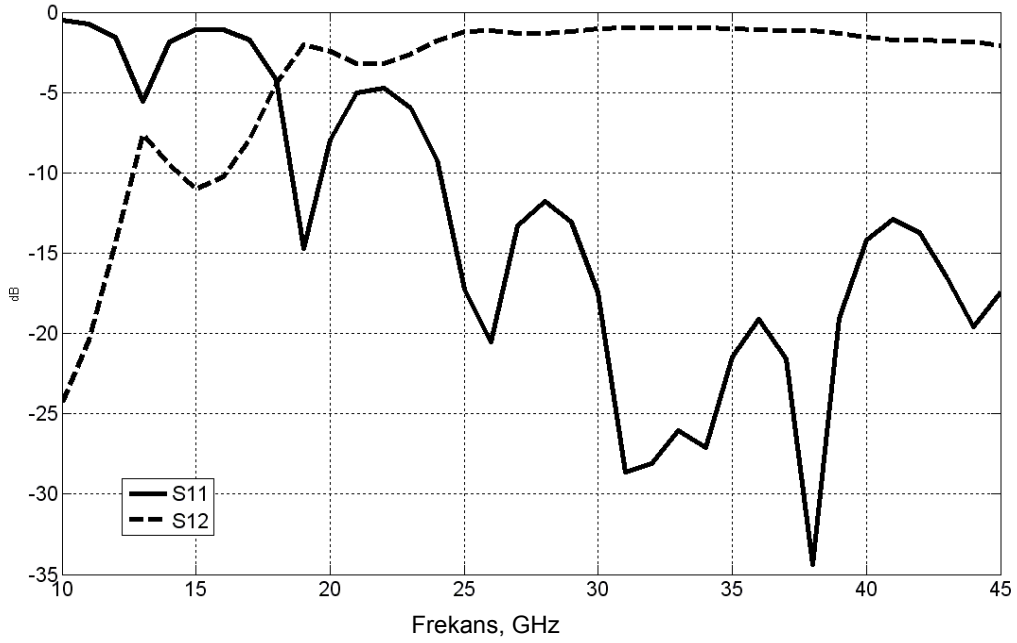

Şekil 26. Mikroşerit-Yarık Hat Geçişi Geri Dönüş ve Geçiş Kaybı

Bu geçiş 25-45 GHz frekans bandında 2 dB'den düşük geçiş kaybı ve -10 dB'den az geri dönüş kaybına sahiptir.

Ölçümler için bu geçişi kullanan dört anten üretilmiştir. Bunlardan ikisi doğrusal sönümlenen, ikisi sabit genişlikli yarık antendir. Üretilen antenlerin fotoğrafları Şekil 27'de verilmiştir. Bu antenlerin fiziksel özellikleri:

- $L=3\lambda_0$, $W=1\lambda_0$, $H=2\lambda_0$ Doğrusal Sönümlenen Yarık Anten
- $L=3\lambda_0$, $W=1\lambda_0$, $H=2\lambda_0$ Sabit Genişlikli Yarık Anten
- $L=4\lambda_0$, $W=1\lambda_0$, $H=1.5\lambda_0$ Doğrusal Sönümlenen Yarık Anten
- $L=4\lambda_0$, $W=1\lambda_0$, $H=1.5\lambda_0$ Sabit Genişlikli Yarık Anten

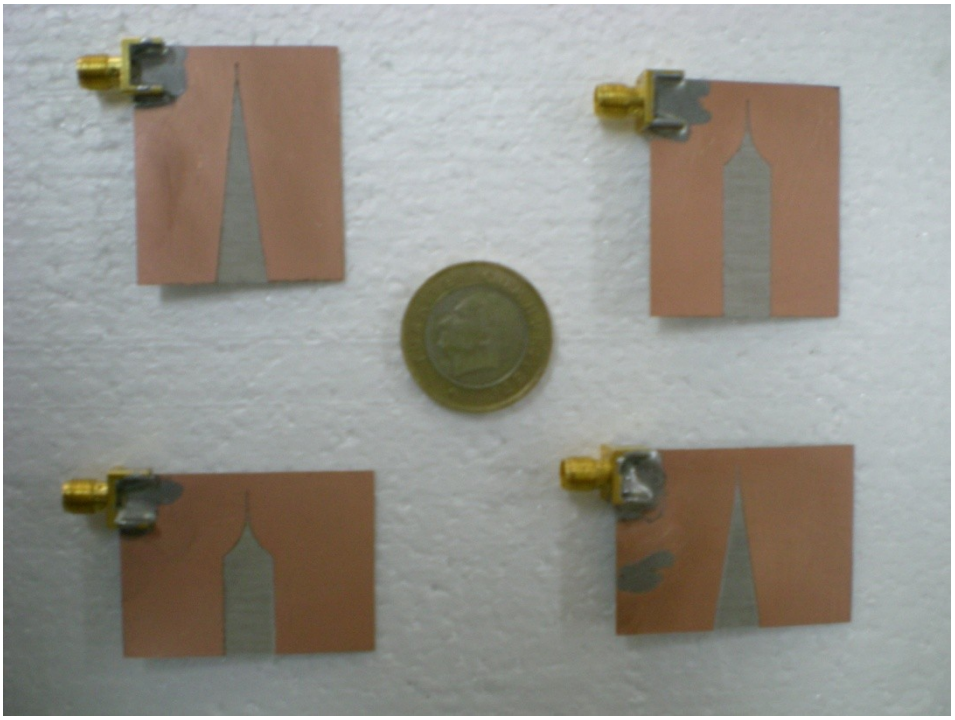

Şekil 27. Üretilen Antenler

Üretilen antenlerin ışıma örüntüleri, yankısız odada E ve H-düzlemlerinde ölçülmüştür. Doğrusal sönümlenen antenler için alınan ölçüm sonuçları ve aynı antenler için alınmış benzetim sonuçları Şekil 28 ve Şekil 29'da verilmektedir.

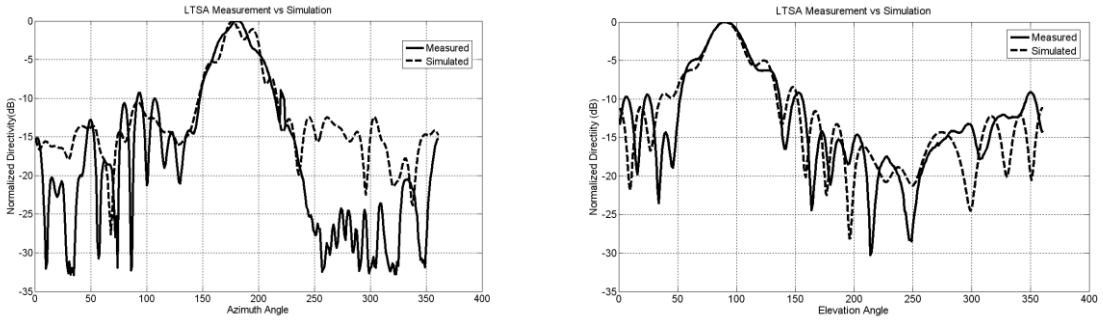

Şekil 28. Doğrusal Sönümlenen Anten E ve H- Düzlemi Işıma Örüntüleri (L=3λ_0, W=1λ_0, H=2λ_0)

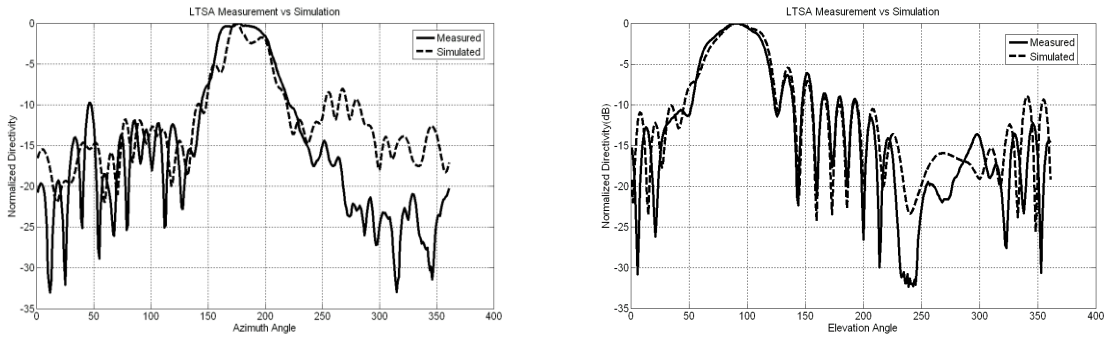

Şekil 29. Doğrusal Sönümlenen Anten E ve H- Düzlemi Işıma Örüntüleri (L=4λ_0, W=1λ_0, H=1.5λ_0)

Görüldüğü üzere, EM benzetim sonuçları ve anten ölçüm sonuçları birbiriyle uyuşmaktadır. Farkın görüldüğü tek bölge E-düzleminde 230-360^0 arasındaki bölgedir. Her iki antende de bu farkın görülmesi ve ölçüm sonucunda bu bölgede daha düşük ışıma görülmesi, farkın ölçüm sırasında anteni tutan süngerden kaynaklandığını işaret etmektedir. Aynı şekilde sabit genişlikli anten ölçüm-benzetim sonucu karşılaştırması da Şekil 30 ve Şekil 31'de verilmiştir.

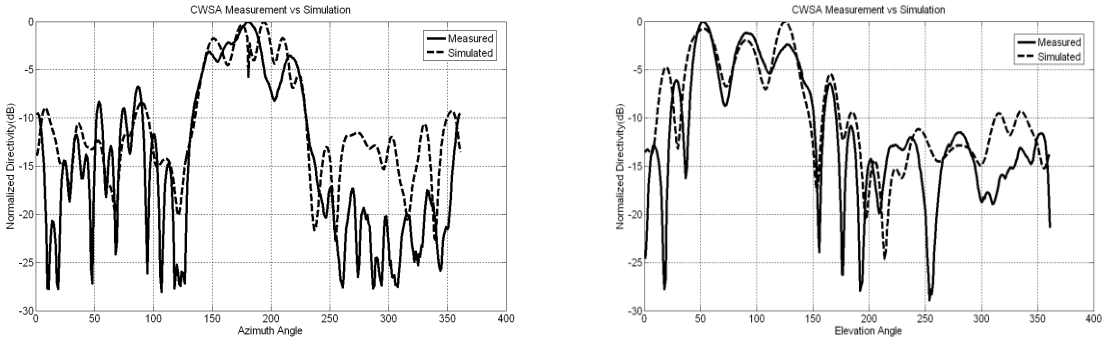

Şekil 30. Sabit Genişlikli Yarık Anten E ve H-Düzlemi Işıma Örüntüleri (L=3λ_0, W=1λ_0, H=2λ_0)

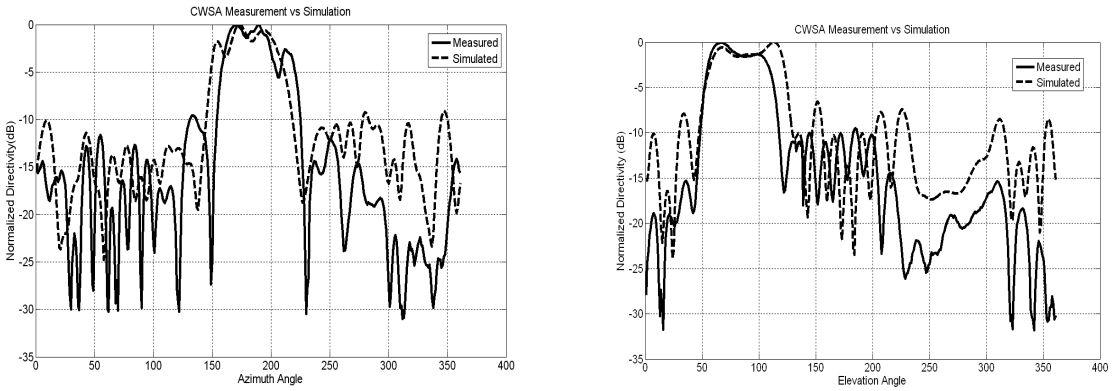

Şekil 31. Sabit Genişlikli Yarık Anten E ve H- Düzlemi Işıma Örüntüleri (L=4λ_0, W=1λ_0, H=1.5λ_0)

Sabit genişlikli yarık antende de ölçüm sonucu ve benzetim sonucu yine E-düzlemindeki aynı bölge haricinde birbiriyle tutmaktadır. Ölçümdeki farklılığın sabit genişlikli yarık antende de aynı bölgede görülmesi sorunun destek köpüğünden kaynaklanması ihtimalini güçlendirmektedir.

4. ÇİFT BANTLI AYRIK HALKA YANSITICI DİZİ ANTENİ

4.1 Giriş

Yansıtıcı dizi anteni geçmişi 60'lı yıllara kadar uzanan bir anten türüdür (BERRY 1963). Temel nitelikleri bakımından, faz dizili antenler ile yansıtıcı çanak antenlerin birleşimi olarak ortaya çıkmıştır. Yansıtıcı dizi anteni, Şekil 32'de görüldüğü gibi, düzlemsel bir yüzeye yerleştirilmiş baskı anten elemanlarından ve bu yüzeyi aydınlatan bir besleme anteninden oluşmaktadır. Baskı anten elemanlarının geometrisi, açısı, büyüklüğü ve benzeri özellikleri ayarlanarak, farklı yansıma açıları elde edilebilmektedir. Böylece, yansıyan dalganın ilerleme yönünü belirleyecek şekilde, yansıyan dalganın anten yüzeyindeki faz dağılımı ayarlanabilir. MEMS anahtar/faz kaydırıcı, varaktör ve benzeri elemanlarla bir araya getirilerek yeniden şekillendirilebilir yansıtıcı dizi antenler elde edilebilir. Bu sayede ışınım örüntüsü, çalışma frekansı dinamik şekilde değiştirilebilir.

İlk yansıtıcı dizi anteni örneği 1970'lerde üretilmiştir, bu ilk örnek tek ucu kısa devre haline getirilmiş dalga kılavuzlarından oluşmaktadır (MALAGASİ 1978). Günümüzde, yüzey mikroişleme teknolojisinin gelişmesiyle çeşitli taban malzemeler üzerinde, yeniden şekillendirilebilir mikroşerit yansıtıcı anten uygulamaları yapılmaktadır (BAYRAKTAR 2010).

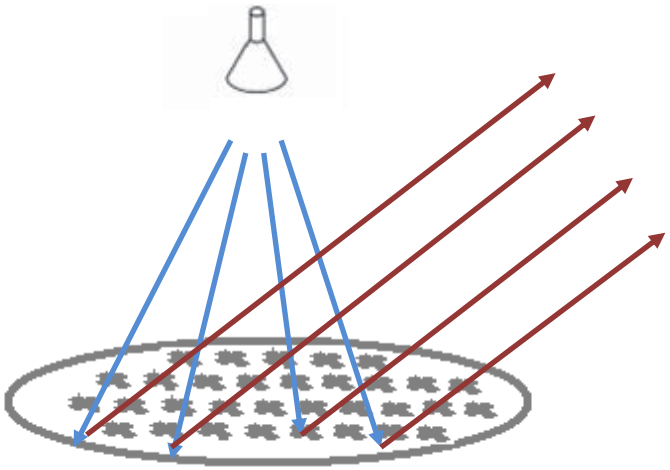

Şekil 32. Yansıtıcı dizi anten yüzeyinde fazların ayarlanması

Bu proje kapsamında tasarlanan yansıtıcı dizi anteni, ayrık halka elemanlarından oluşmaktadır. Faz kontrolü ise dönüşsel faz konrol prensibi ile sağlanmaktadır. Benzer prensipte yapılar daha önce birkaç kez yansıtıcı dizi uygulamalarında kullanılmıştır (HUANG 1997, HAN 2004, MARTYNYUK 2004, STRASSNER 2004). Fakat, bu uygulamaların tamamı sabit ışıma örüntüsü verecek şekilde tasarlanmıştır, yeniden şekillendirilebilir bir yapı söz

konusu değildir. Dönüşsel faz kontrol ilkesine göre, yansıtıcı elemana diresel polarizasyonlu bir dalga gönderildiğinde, yansıyan dalganın gelen ile aynı dairesel polarizasyonlu bileşeninin fazı elemanın açısal konumu ile doğru orantılıdır. Dolayısıyla halkanın ayrık kısmı döndürülerek, huzmeyi döndürmek için gerekli faz farkları elde edilebilir. Bunu gerçekleştirebilmek için bu çalışmada, ayrık halkaların üzerinde 60° fiziksel açı farkıyla MEMS anahtarlar yerleştirilmiştir. Bu anahtarlar 3 adet karşılıklı çift meydana getirmekte, 3 çiftin ikisi kapalı birisi açık tutularak, halkanın ayrığının 60° fiziksel dönüşü sağlanmaktadır. Antenin iki farklı frekansta çalışması için, K ve Ka bantlarında yansıyan dalganın fazını ayrı ayrı kontrol etmek üzere, farklı boyutta ayrık halkalardan oluşan, birbirine geçmiş bir şekilde yerleştirilmiş iki ayrık halka dizisi tasarlanmıştır. Tasarlanan anten, 4inç çapında 0.5mm kalınlığında kuvartz tabanda 24.4 GHz'te çalışan 109 ve 35.5 GHz'te çalışan 112 halkadan oluşmaktadır. Elemanlar arasındaki 120° ardışık faz farkı sayesinde, antenin, Ka ve K bantlarında ana huzmeyi 35° ve 24° dereceye döndürme yeteneği vardır. Bu anten, araştırmacıların bilgisi dahilinde, iki frekansta bağımsız huzme yönlendirme yeteneğine sahip ilk yansıtıcı anten tasarımıdır. Bölüm 4.2'de dönüşsel faz kontrol ilkesi anlatılmaktadır. Ayrıca, ilkenin çalışmasını göstermek amacıyla tek frekanslı dairesel polarizasyonlu yansıtıcı dizi antenin karakteristiği incelenmektedir. Çift frekansta çalışan dizi birim hücresinin tasarımı ve EM benzetim sonuçları Bölüm 4.3'te verilmektedir. Dizide kullanılan MEMS anahtar Bölüm 4.4'de sunulmuştur. Üretilen anten ve antenin ölçüm sonuçları Bölüm 4.5'te verilmektedir.

4.2 Ayrık Halka Elemanı ve Tek Frekans Uygulaması

Bu bölümde, öncelikle dönüşsel faz kontrol ilkesi anlatılmaktadır. Şekil 33'de görüldüğü gibi bir ayrık halka elemanı ele alınmış ve ayrık kısmı döndürüldüğünde, bu elemandan yansıyan dairesel polarizasyonlu dalganın fazının nasıl değiştiği ilgili formüllerle çıkartılmıştır.

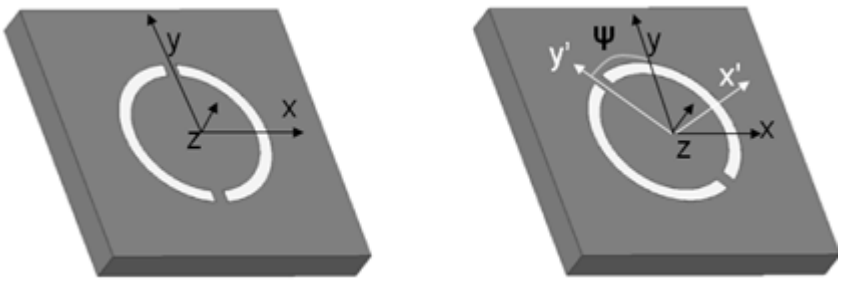

Şekil 33. Yansıtıcı elemanın dönüşünün gösterimi

Şekil 33'de görüldüğü üzere üslü koordinat sistemi, ayrık halkanın üzerinde bulunmaktadır. Eğer ayrık halkaya dairesel polarizasyonlu bir dalga gönderdiğimizde yansıyan dalganın ifadesini biliyorsak; ayrık halka elemanı orijin etrafında döndüğünde üslü koordinatlarda yansıma ifadesinin aynı kalacağı görülür. Üssüz koordinat siztemi (yani sabit duran sistem) çerçevesinde bakıldığında yansıma tepkisinin ne olacağı, üslü ve üssü koordinat sistemleri arasında kartezyen ileri ve geri dönüşümlerle bulunabilir.

Ayrık halkanın üzerine, denklem (1)'deki gibi bir dairesel polarizasyonlu dalganın geldiğini varsayalım:

$$\overrightarrow{E^{gelen}} = (\hat{a}_x \pm j\,\hat{a}_y)E^0\, e^{jz} \tag{1}$$

Bu durumda, yansıyan dalga ifadesi aşağıdaki gibi yazılabilir:

$$\overrightarrow{E^{yansıyan}} = 0.5E^0\Gamma_{eş-pol.}(\hat{a}_x \mp j\,\hat{a}_y)e^{\pm j2\psi}e^{-jz} + 0.5E^0\Gamma_{çap.-pol.}(\hat{a}_x \pm j\,\hat{a}_y)\,e^{-jz} \tag{2}$$

Denklem (2)'den de görüldüğü gibi, yansıyan dalga eş ve çapraz dairesel polarizasyonlu iki bileşenden oluşur. Bu bileşenlerin, gelen dalga ile eş polarizasyonlu olanında, fiziksel dönüş açısının iki katına denk gelen bir faz görülmektedir. Bir diğer deyişle, yansıyan dalganın eş polarizasyonlu bileşeninin fazı ayrık halkanın dönüş açısıyla doğru orantılıdır. Bu, dönüşsel faz kontrol prensibi olarak adlandırılır. Bu sayede, çapraz polarizasyonun bastırıldığı bir frekans aralığı bulunabilen yansıtıcı yüzeylerde, yansıyan dalganın fazının doğrusal olarak kontrol edilmesi mümkündür.

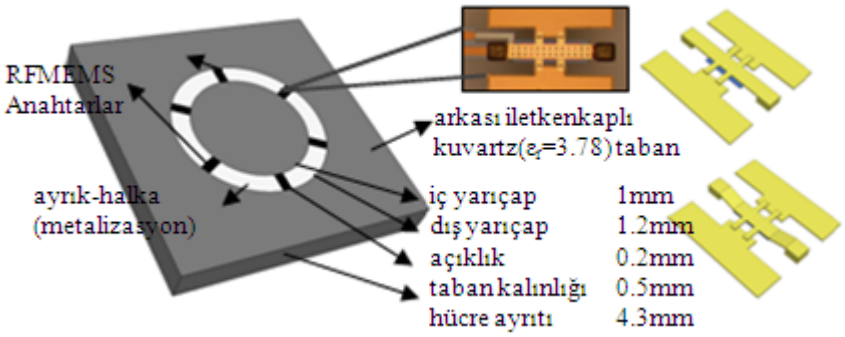

Şekil 34. Tek frekanslı örnek yapı ve üzerine yerleştirilecek MEMS anahtar

Şekil 34'de tek frekansta çalışmak üzere tasarlanan yapı ve MEMS anahtarlarla bütünleştirme için temsili gösterim bulunmaktadır. Eleman 0.5 mm kalınlığında arkası metal kaplı kuvartz taban üzerine tasarlanmıştır. Ayrık halka elemanı, belli bir frekans bandında

yansıyan çapraz polarizasyonlu alan bileşenini bastırmaktadır. Işınsal simetrisi sayesinde MEMS anahtarlar yerleştirilerek dönüş etkisi yaratılmasını kolaylaştırmıştır.

Birim eleman HFSS programında tasarlanmıştır. Sonsuz elemanlı dizi varsayımı ile, periyodik sınır koşulları ve Floquet Dalga gönderimi ile EM benzetimler yapılarak, çapraz polarizasyonun bastırıldığı frekans aralığı berlirlenmiştir. Birim hücreye sağ el dairesel polarizasyonlu dalga gönderilmiş ve elde edilen yansıma katsayısının eş (sağ el) ve çapraz (sol el) polarizasyonlu bileşenleri frekansa göre Şekil 35 (a)' da verilmiştir. Görüldüğü üzere, belli bir frekans aralığında çapraz polarizasyonlu dalga bastırılmaktadır. Bu frekans aralığı antenin çalışma bandını belirlemektedir.

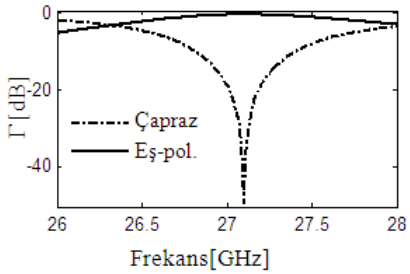

(a)

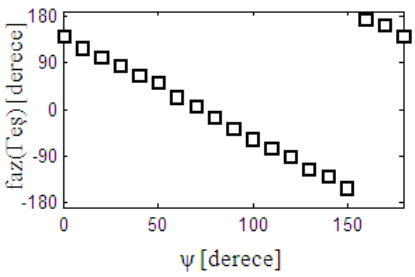

(b)

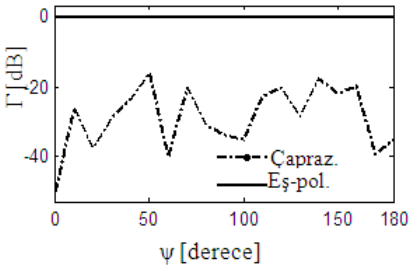

(c)

Şekil 35. Tek frekanslı yapının benzetim sonuçları, (a) frekans yanıtı, (b) fazın dönüş açısına bağlılığı, (c) farklı açısal konumlar için çapraz polarizasyon seviyesi.

Çalışma frekansında yapılan benzetimlerde, ayrık halkanın farklı açısal konumları için yansıyan dalganın çapraz polarizasyon bastırma yeteneği ve yansıyan eş polarizasyonlu dalganın fazı elde edilmiş ve Şekil 35 (b) ve (c)'de, fiziksel dönüş açısına göre çizdirilmiştir. Sonuçlar çok açıkça göstermektedir ki, tasarlanan ayrık halka, çalışma frekansı olan 27.4 GHz'te farklı dönüşsel konumlardayken çapraz polarizasyon -20 dB'den iyi bastırılmıştır, ve yansıyan dalganın fazı doğrusal olarak, 360°'lik aralıkta değiştirilebilmektedir.

4.3 Çift Frekansta Çalışan Eleman

İki ayrı frekansta çalışan bir yansıtıcı dizi anten elemanı elde etmek için bir önceki kısımda çalışması gösterilmiş olan elemanlardan iki farklı boyutta kullanmak gerekmektedir. Akla gelen iki seçenek, ya iç içe, ya da yansıtıcı anten elemanına köşeli merkezli yerleştirmektir. Yapıların üzerine MEMS anahtarların koyulacağı göz önünde tutularak, uyarım hatlarının erişimini kolaylaştırmak amacıyla, Şekil 36'da gösterilen köşeli merkezli yerleşim tercih edilmiştir.

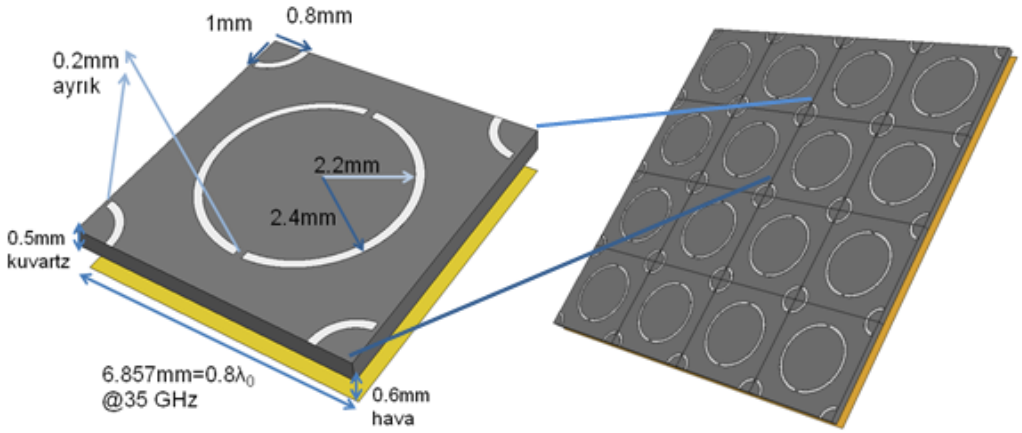

Şekil 36. Çift frekansta çalışan yansıtıcı dizi anten elemanının gösterimi

İki frekansta çalışan yansıtıcı dizi anten elemanı, MEMS anahtarlarla bütünleştirilmeden önce, elektriksel kısa devreye denk gelen anahtarlar tam metalizasyonlarla, açık devrelere denk gelen anahtarlar ise ayrıkların geldiği metalizasyonsuz bölgelerle modellenmiştir. Dizi tasarlanırken, halkaların birbirlerine göre farklı konumlarının frekans tepkisinde değişikliğe yol açabileceği göz önüne alınarak tasarım yapılmıştır. Aksi takdirde ayrık halkaların farklı açısal konumlarında, yansıyan çapraz polarizasyonun yeteri kadar bastırılamaması söz konusu olabilir. Farklı boyutlardaki ayrık halkaların birbirine göre farklı pozisyonda yer aldığı durumlar için EM benzetimler yapılmıştır. Şekil 37'de görüldüğü üzere, yapı iki farklı frekansta çapraz polarizasyonu bastırmıştır. Küçük halka yüksek frekans (35.5GHz), büyük halka ise düşük frekansta (24.4GHz) işlev görmektedir. Görüldüğü üzere, yansıma yanıtı, halkaların farklı göreli konumları için yaklaşık aynı frekanslarda işlev yeteneğini korumaktadır.

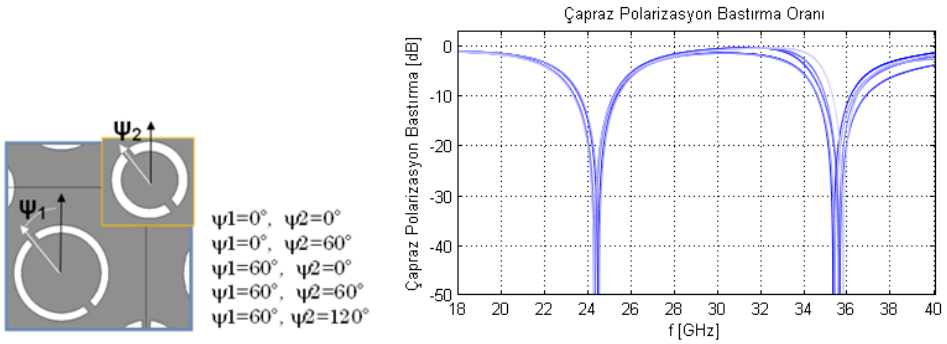

Şekil 37. Farklı göreli açısal konumdaki halkalar için yansıyan çapraz polarizasyon bileşeninin büyüklüğü

Şekil 38'de çift frekansta çalışan yapının (a) düşük frekansta, (b) yüksek frekanstaki çapraz polarizasyon bastırma ve eş polarizasyonun faz eğrileri verilmiştir. Beklendiği gibi eş polarizasyonun yansıma fazı doğrusal değişmektedir. Çapraz polarizasyon -20 dB'nin altında kalacak şekilde bastırılmıştır. Bu birim hücre tasarımının uygun bir şekilde yapıldığını göstermektedir.

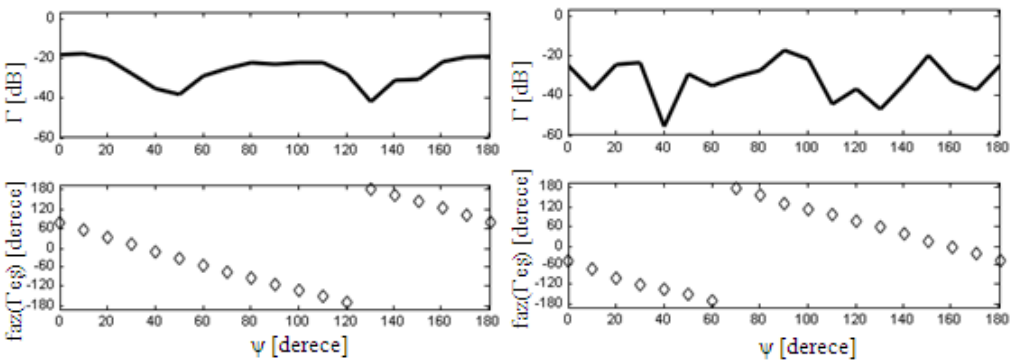

(a) (b)

Şekil 38. İki ayrı frekansta çalışan elemanın, çapraz polarizasyon bastırma ve faz kontrol yeteneği (a) 24.4 GHz (b) 35.5 GHz.

4.4 MEMS ile Bütünleşmiş Çift Frekansta Çalışan Eleman

Tasarlanan iki halkalı, çift frekansta çalışan elemanın yeniden şekillendirilebilir hale getirilmesi için MEMS anahtarlar kullanılması uygun görülmüştür. MEMS anahtarlar hem tümleşik bir şekilde antenle birlikte üretilebilmekte, hem de yarı-iletken anahtarlarla karşılaştırıldığında daha düşük araya girme kaybı, sıfıra yakın DC güç gereksinimi gibi daha iyi performans sağlamaktadır. Yapıda kullanılan MEMS anahtarlar, ODTÜ MEMS Merkezi bünyesinde geliştirilen üretim süreciyle üretilmektedir. Yansıtıcı dizi anten elemanında, Şekil

39’da görülen metal temaslı seri MEMS anahtarlar kullanılarak, halka üzerindeki ayrığın açısal konumunu 60° çözünürlükle değiştirmek ve 120° faz çözünürlüğü sağlamak mümkündür.

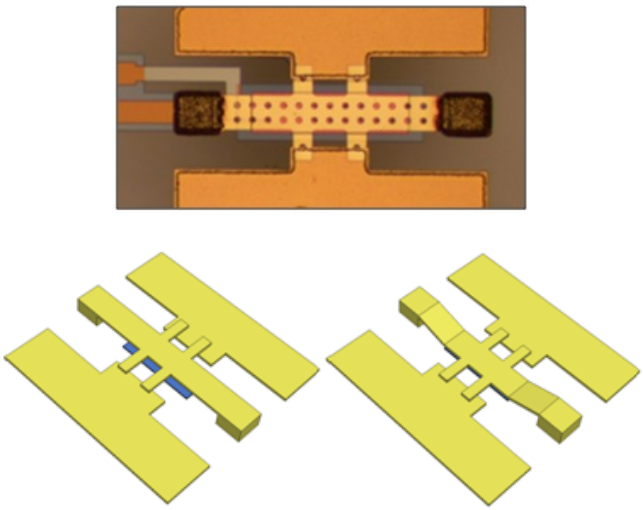

Şekil 39. Metal temaslı seri MEMS anahtar

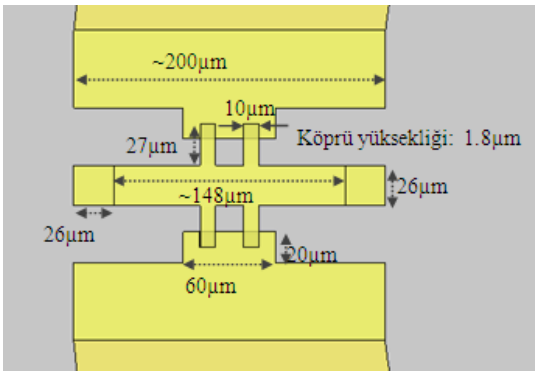

Şekil 40.Tasarlanan anahtarın boyutları

Tasarlanan MEMS anahtarın boyutları Şekil 40’da verilmektedir. Bu MEMS anahtar, statik elektrik alan ile uyarılmazken ortadaki köprü havada durduğu konumda elektriksel teması engellemektedir. DC gerilimle uyarıldığında ise köprü aşağı çökmekte ve iki kanat arasında elektriksel hat oluşmaktadır. Bu MEMS anahtar yapısı daha önce (BAYRAKTAR 2010)’da tasarlanan ve üretilen yansıtıcı dizi anteninde de kullanılmıştır. Tasarlanan iki ayrık halkalı eleman, MEMS anahtarlarla birleştirildiğinde frekans tepkisinde belli oranda değişiklik meydana gelmektedir. Bu değişiklik boyut ayarlamayla kolayca telafi edilebilir.

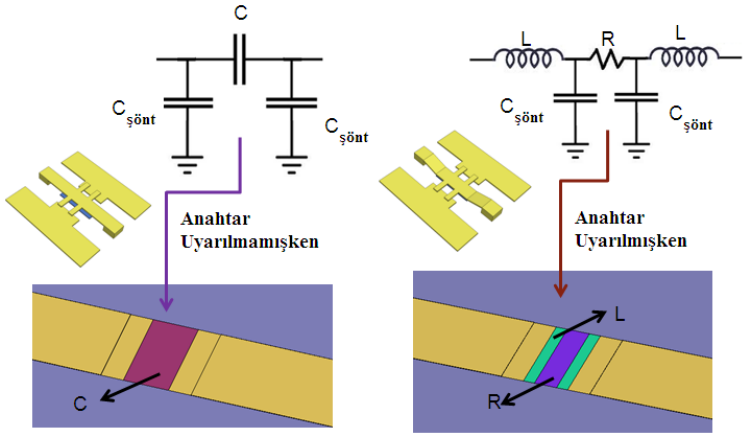

Şekil 41. MEMS anahtarın modellenmesi

MEMS anahtarların yerleştirildiği birim hücre elemanında, toplam 12 adet MEMS anahtar yer almaktadır. MEMS anahtarlar yüksek ayrıt oranlarına sahip elemanlar barındırdığı için, EM benzetimlerde gerekli göz sayısı ve buna bağlı olarak benzetim süreleri çok uzun olmaktadır. Tasarımın bu aşamasını hızlandırmak için bu anahtarların, yüzey direnci, indüktansı ve kapasitansı olarak modellenmesi yoluna gidilmiştir. Bu modelde, Şekil 41'de gösterildiği gibi, anahtarın açık-devre olduğu durum seri bir kapasitör, kapalı-devre olduğu durum ise seri bir direnç ve indüktörle modellenmiştir. Anahtarın toprak yüzeyine olan kapasitif bağı da şönt kapasitörlerle modellenmiştir. Anahtarın, modellerden elde edilen seri devre elemanı parametreleri, daha sonra HFSS yazılımındaki benzetimlerde anahtar yerine yüzey empedansı olarak koyularak tüm dalga benzetimleri yapılmıştır. Şönt kapasitif etkiler benzetimdeki metalizasyonlar arasında kendiliğinden bulunduğu için ek olarak bir yüzey empedansı tanımı gerektirmemiştir.

Şekil 42'de görülen frekans tepkisinde, 3 boyutlu tam MEMS yapısı içeren ve bu yapının yüzey empedansı ile modellenmiş haliyle yapılan benzetimler gösterilmiştir. Bu iki benzetimin sonuçları birbiriyle çok iyi uyuşmaktadır, bu da modelin uygunluğunu göstermektedir. Yüzey modellemesi, 8 saatlik benzetim süresini 10 dakikaya indirerek, çok değerli bir zaman tasarrufu sağlamakla kalmamış, daha yüksek kesinlikte benzetimlerin de koşulmasını mümkün kılmıştır. Bu teknik kullanılarak MEMS içeren yansıtıcı dizi anten elemanının yansıma fazı benzetimleri daha iyi kesinlikte ve yüksek sayıda göz içererek yapılabilmiştir. Görüldüğü üzere 22.7 GHz ve 34 GHz'te çalışma frekanslarında çapraz polarizasyon bastırılmıştır.

Şekil 43'de görüldüğü üzere MEMS anahtarlarla bütünleşik eleman, iki frekansta da çapraz polarizasyonu başarıyla bastırmakta ve doğrusal faz eğrisi sunmaktadır.

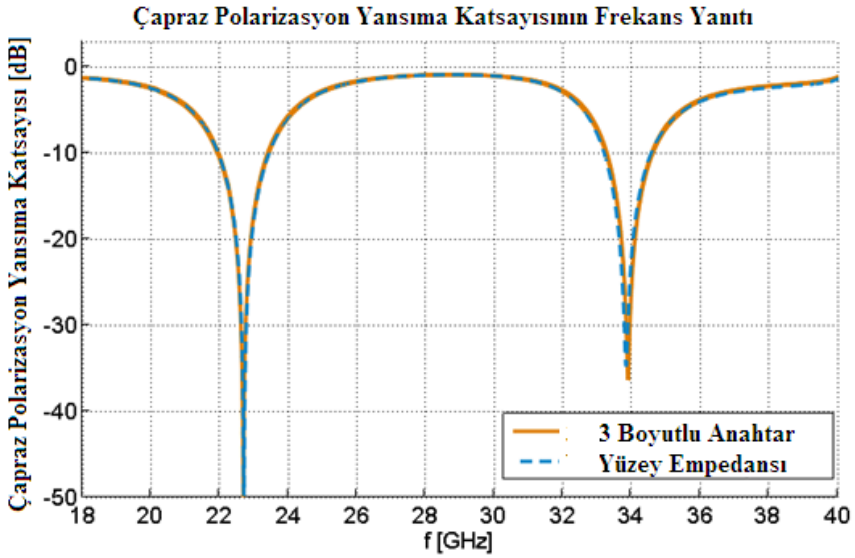

Şekil 42. İki frekanslı MEMS anahtarlı elemanın benzetim tekniklerinin kıyaslanması

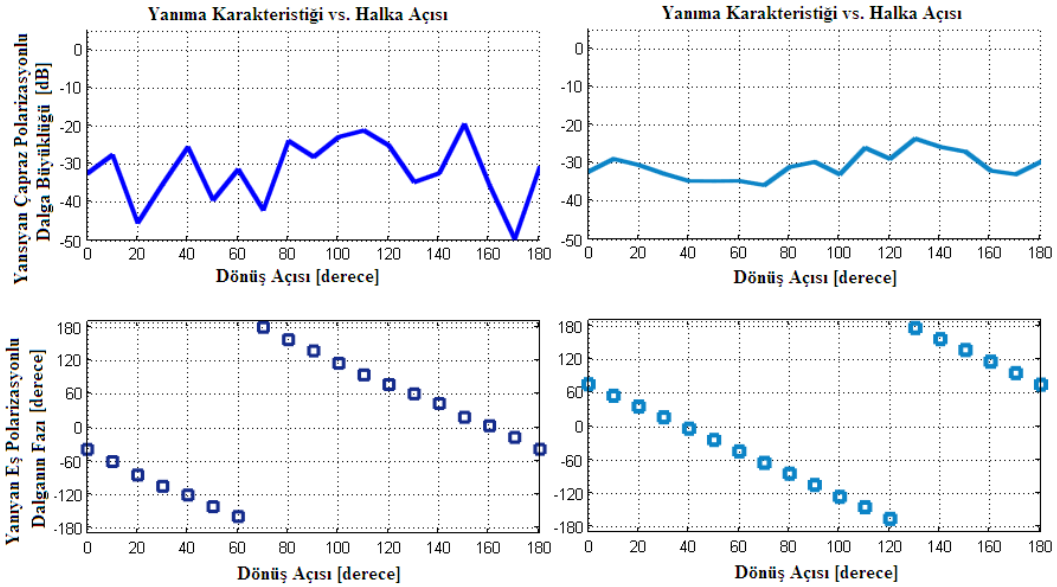

Şekil 43. İki ayrı frekansta çalışan MEMS'li elemanın, çapraz polarizasyon bastırma ve faz kontrol yeteneği (a) 22.65 GHz (b) 34 GHz

4.5 Yansıtıcı Dizi Anten Prototipi, Benzetim ve Ölçümler

Tasarlanan elemanlardan oluşan bir prototip yansıtıcı anten tasarlanmıştır. Bu prototip anten üzerindeki MEMS anahtarlar, ilk tasarım aşamasındaki gibi açık ve kapalı metalizasyonlar şeklinde modellenmiştir. Yansıtıcı dizi yüzeyi, 24.4 GHz'te çalışan 109 ve 35.5 GHz'te çalışan 112 halkadan oluşmaktadır. Tüm antenin HFSS ortamında benzetimleri yapılmıştır. Kuvartz taban üzerinde, dizi elemanlarının dağılımı Şekil 44'de görülmektedir.

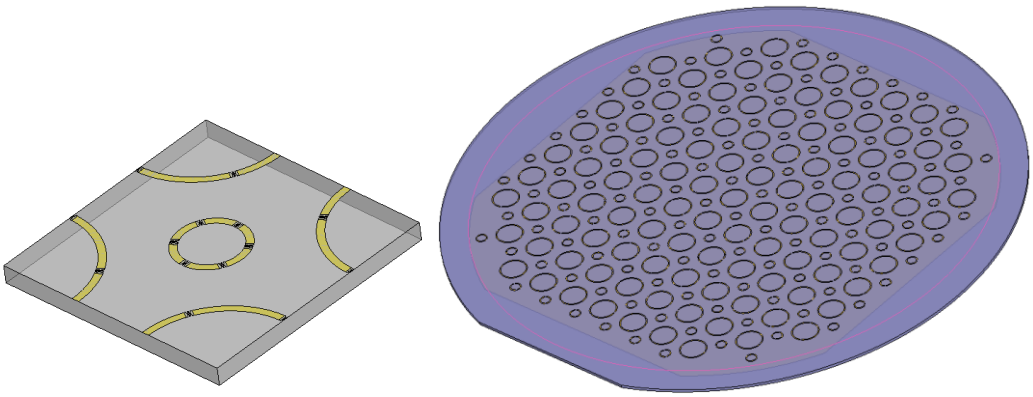

Şekil 44. Tasarlanan MEMS'li iki frekansta çalışan eleman ve 4 inçlik kuvartz taban üzerine yerleşimi

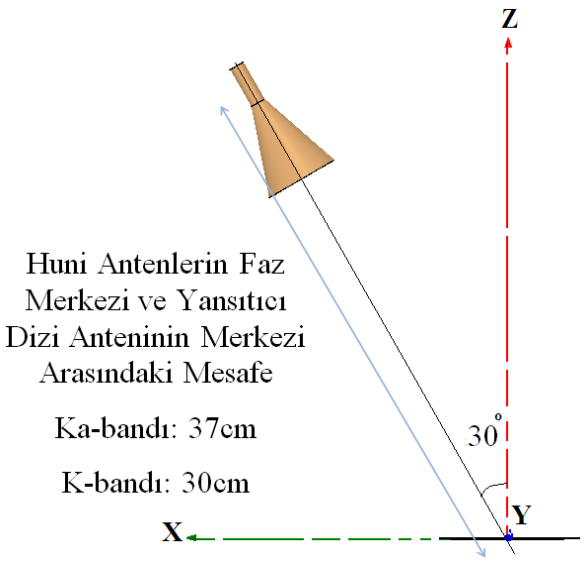

Şekil 45. Aydınlatma huni antenlerinin yerleşimi

Yansıtıcı dizi antenin yüzeyini aydınlatmakta, dairesel polarizasyonlu iki adet Ka ve K bantlarında huni anten kullanılmıştır. Bu antenler, yansıtıcı dizi anten uzak alanlarında kalacak şekilde, Şekil 45'de gösterildiği gibi yerleştirilmiştir ve antenin yayın yaptığı düzlemi kapatmaması için 30° eğim verilmiştir. Antenin tasarımında, huni aydınlatma antenlerinden gelen dalgaların yüzeye geliş açıları ayrık halkaların dönüşüyle telafi edilmiştir. Bu durumda,

tüm yüzeyin eş fazda yansıma sağladığı ve tek doğrultudaki ardışık elemanlar arasında 120° faz farkı olan iki prototip tasarlanmıştır. Ana huzmenin faz farkı olmayan durumda Z yönünde olacağı ve Y yönünde 120° ardışık faz farkı olan durumda YZ düzlemi üzerinde döneceği şekilde tasarım yapılmıştır. Yapılan benzetimler kısıtlı bilgisayar imkanları (8GB RAM ve 2.4GHz çift çekirdek işlemci) dahilinde 6 saatten uzun sürmüştür. Kullanılan benzetim tekniğinde, aydınlatma antenlerinin açıklığındaki eş akımların entegrasyonuyla bulunan uzak alanlar, yansıtıcı dizi antenin üzerine uygulanmıştır. Elde edilen ışıma örüntüleri Şekil 47 ve Şekil 48'de ölçüm sonuçlarıyla karşılaştırılmalı şekilde verilmiştir.

Tasarlanan diziler, ODTÜ MEMS merkezinde mikroişleme teknolojisiyle üretilmiştir. Antenin ışıma örüntüsü ölçümleri ODTÜ Elektrik-Elektronik Mühendisliğindeki Yankısız odada gerçekleştirilmiştir. Ölçüme alınan anten düzeneğinin anten dışında kalan kısımları tamamen EM soğurucularla kaplanmıştır ve bu sayede istenmeyen saçılmaların önüne geçilmiştir. Yankısız odaya yerleştirilmiş antenin fotğrafları Şekil 46'da görülmektedir. Yapılan ölçümlerde, yansıtıcı dizi yüzeyi ve bunu aydınlatan dairesel polarizasyonlu bir huni antenden oluşan yansıtıcı anten alıcı anten olarak, doğrusal polarizasyonlu geniş bandlı bir huni anten de verici anten olarak yerleştirilmiştir. Bu bakımdan yapılan ölçümlerde, doğrusal polarizasyonlu dalganın çapraz polarizasyon bileşeninin yansıdıktan sonra eş polarizasyona dönüşen bileşenini de içermektedir. Fakat, bu bileşen çok küçük olduğundan (yaklaşık 20 dB kadar bastırıldığı göz önüne alınırsa), antenin performansını etkilememiştir. Bu, ölçüm sonuçlarından da gözlenmektedir.

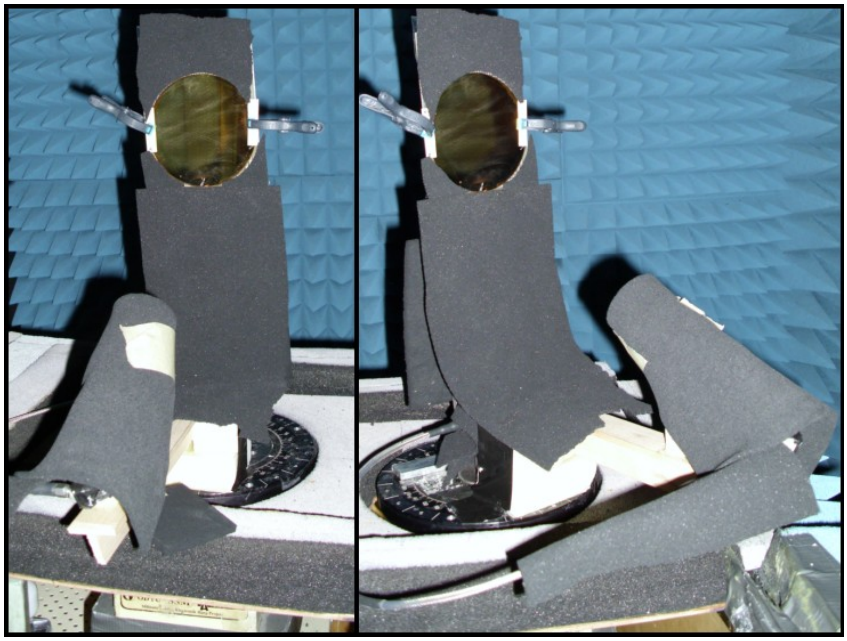

Şekil 46. Ölçüm düzeneğinin bir fotoğrafı

Antenin ışıma örüntüleri K ve Ka bandlarında Şekil 47 ve Şekil 48'de benzetim sonuçlarıyla karşılaştırılmalı olarak verilmektedir. Şekil 47'de görüldüğü gibi, ölçüm ve benzetim sonuçları büyük oranda örtüşmektedir. Işınımın 0°'ye baktığı durumda yan huzmelerin benzetime göre yükselmiş olduğu görülmektedir. Huzme beklendiği gibi 35°'ye dönmüş, ilk yan huzmelerde dahi uyum yakalanmıştır.

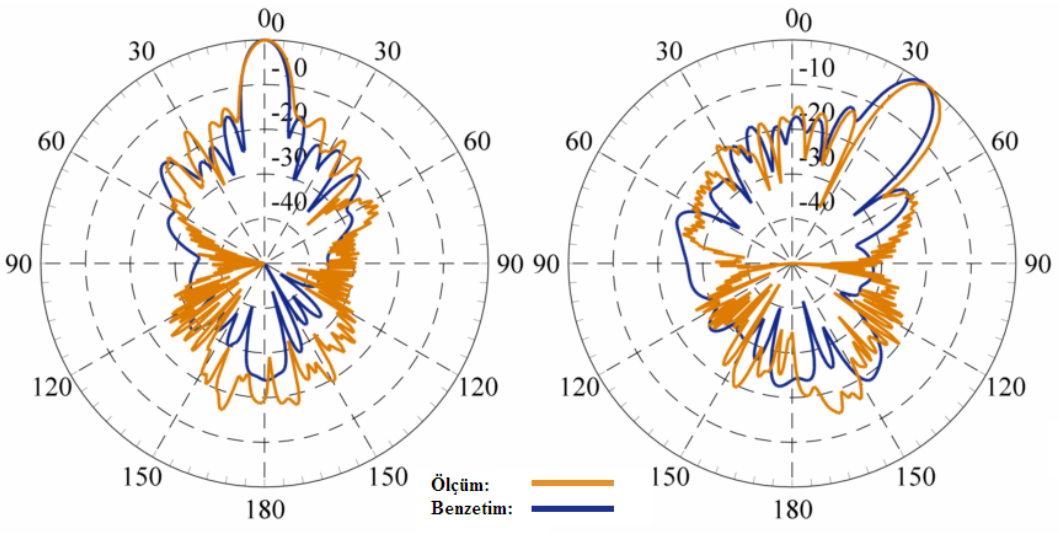

Şekil 47. 24.4 GHz'te ölçüm ve benzetim sonuçlarının iki durum için karşılaştırması

Şekil 48'de, 35.5 GHz'teki ışıma örüntülerinin benzetim ve ölçümde uyumlu olduğu görülmektedir. Huzme beklendiği gibi 24°'ye dönmüştür. Huzmenin döndüğü durumda, 50° dolaylarında bir ikinci huzme (grating lobe) görülmektedir. Bu durum, yüksek frekanstaki ayrık halka elemanları arasındanki uzaklığın $0.8\lambda_0$ (λ_0=dalgaboyu) olmasından kaynaklanmaktadır. Bundan kurtulmak için büyük halkaların ortasına birer küçük halka yerleştirilerek elemanlar arası uzaklığın bu tür ikincil huzmeler çıkmayacak büyüklüğe getirilmesi bir çözüm olabilir.

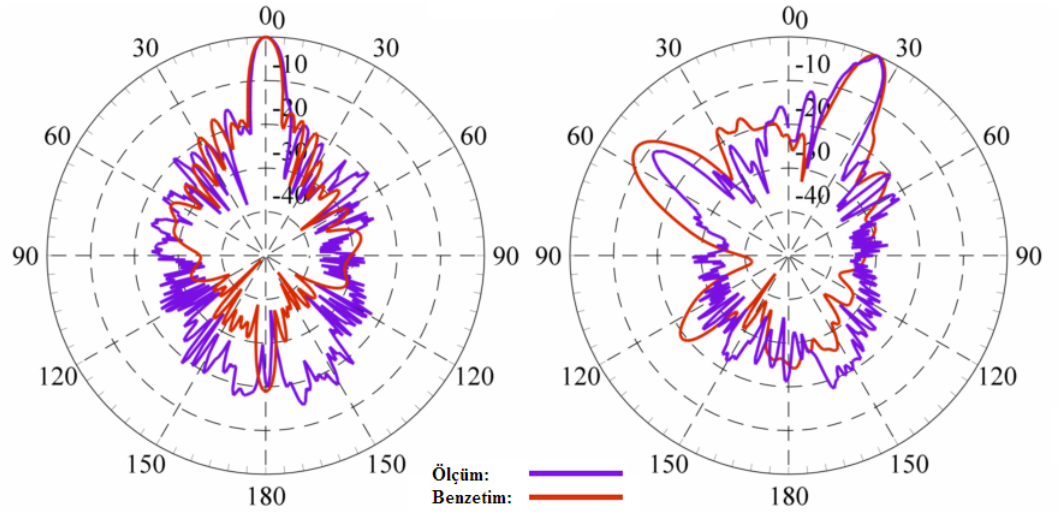

Şekil 48. 35.5 GHz'te ölçüm ve benzetim sonuçlarının iki durum için karşılaştırması

Yapılan bu çalışmada, iki farklı frekansta huzmenin birbirinden bağımsız olarak döndürülebildiği yeniden şekilendirilebilir bir yansıtıcı dizi anten tasarlanıp üretilmiş ve ölçümlerle antenin çalıştığı gösterilmiştir.

5. ODTÜ RF MEMS ÜRETİM SÜRECİ

ODTÜ RF MEMS grubu araştırmacıları tarafından yaklaşık 2000 yılından bu yana RF MEMS anahtarların ve diğer bileşenlerin üretiminde kullanılmak üzere yüzey mikro işleme yöntemlerine dayalı bir üretim süreci sürekli olarak geliştirilmektedir. Bu proje kapsamında da bu üretim sürecinin iyileştirilmesi için çalışmalar yapılmıştır. Bu Bölümde üretim sürecinin en son hali verilmektedir.

ODTÜ MEMS merkezi tesislerinde üretim yapmak üzere geliştirilen RF MEMS yüzey mikro işleme üretim süreçleri Şekil 49'da gösterilmiştir. RF anahtarlamada kullanılan RF MEMS köprü yapısının üretimi şu şekilde gerçekleştirilmektedir:

Şekil 49 (a): İlk olarak pul Piranha (H_2SO_4:H_2O_2 1:1.2) çözeltisine daldırılarak yüzey pürüzlülüğü arttırılır. 2000 Å kalınlığında silikon krom (Si-Cr) katmanı tozutma ile büyütülüp tampon hidro florik asit (buffered HF) ile şekillendirilir ve Si-Cr uyarım hatları oluşturulur.

Şekil 49 (b): 0.1/0.8 μm kalınlığında Ti/Au katmanının Si-Cr katmanı üzerinde tozutma yöntemi ile büyütülür. Au ve Ti aşındırıcı ile bu tabakanın şekillendirilmesi sonucu, iletim hatları ve uyarım tabakası oluşturulur. Köprü aşağı konuma geldiğinde, köprü ile uyarım tabakası arasındaki gerilim farkından dolayı kısa devre olmasını önlemek amacı ile 3000 Å kalınlığında Si_3N_4 katmanı PECVD (Plasma enchanced chemical vapor deposition) cihazı ile büyütülür ve RIE (Reactive Ion Etching) cihazı ile şekillendirilir.

Şekil 49 (c): Uyarım tabakası ve köprüler arasındaki boşluğu oluşturmak üzere 2 μm kalınlığında PI2737 cinsi poliimid ara katmanı serilip fotolitografi yöntemi ile şekillendirilir ve 220 °C' de fırınlanır.

Şekil 49 (d): 1 μm kalınlığında Au katmanı köprüleri oluşturmak üzere tozutma yöntemi ile büyütülür.

Şekil 49 (e): Köprünün pula olan bağlantı yerlerinin kuvvetlendirilmesi ve köprülerin düz bir biçimde oluşturulabilmesi amacı ile SPR 220-7 tipi fotorezist elektro kaplama yönteminde kullanılmak üzere serilip şekillendirilir. Şekillendirme sonrası boş kalan yerler elektro kaplama yöntemi kullanılarak Au ile doldurulur.

Şekil 49 (f): SPR 220-7 fotorezist, aseton kullanılarak kaldırılır. Köprü katmanı şekillendirilir. Poliimid ara katmanı pulun 24 saat boyunca EKC-265 kimyasalı içerisinde tutulması ile aşındırılır. Alkol banyosunun ardından pullar kritik nokta kurutucusu cihazında kurutulur ve havada duran hareketli köprüler elde edilir.

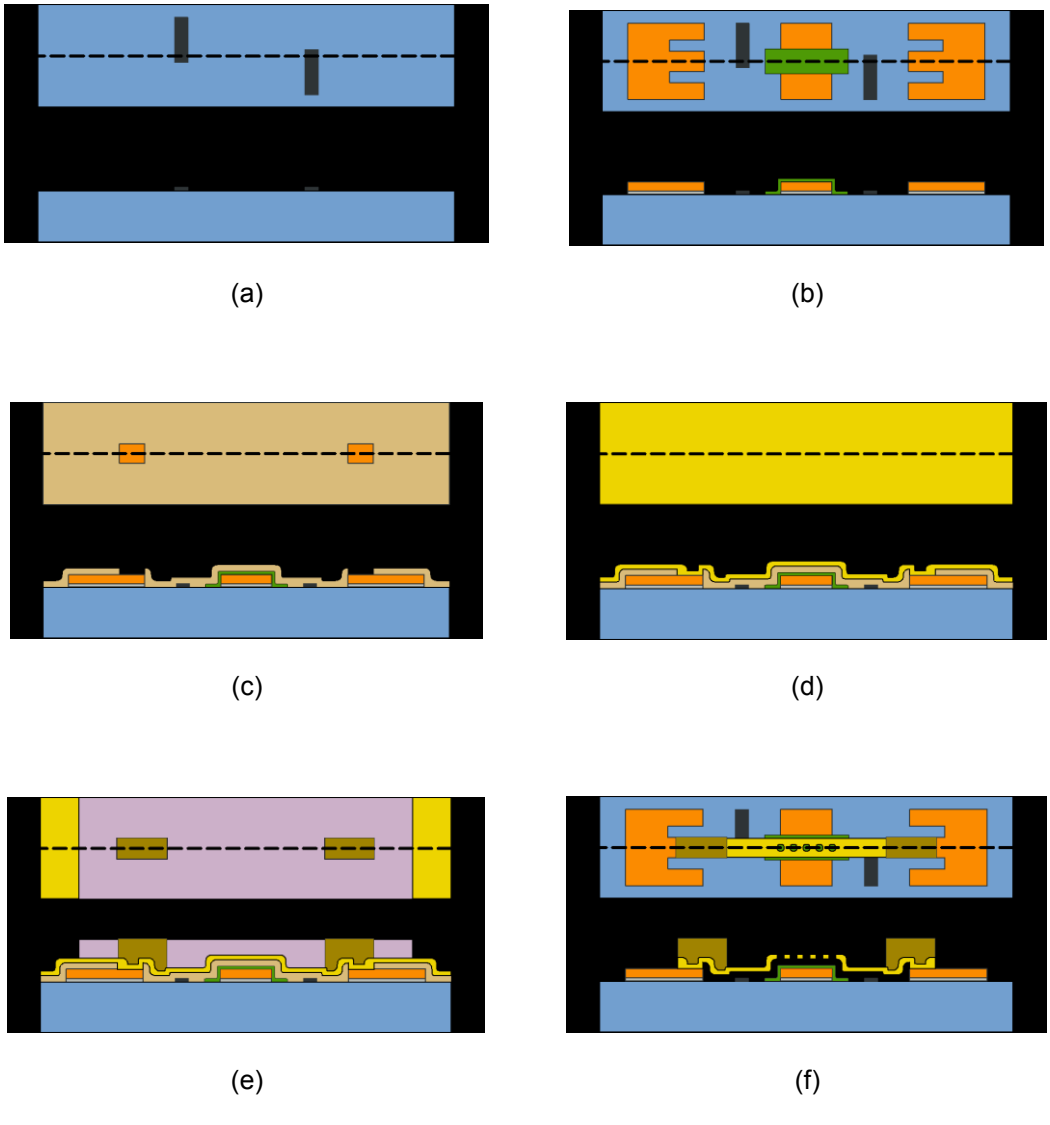

Şekil 49. ODTÜ-MEMS Tesislerinde geliştirilen (a) - (f) yüzey mikroişleme üretim sürecleri.

Yukarıda anlatılan ODTÜ RFMEMS Üretim Süreci, çeşitli projeler kapsamında geliştirilen, RF MEMS bileşenler ve bunları kullanan anten dizilerinin üretiminde başarıyla kullanılmış ve üretilen yapılar beklenildiği gibi yüksek performans ve düşük kayıplarla çalışmıştır,

(BAYRAKTAR 2010, ERDIL 2007, TOPALLI 2008, 2009, UNLU 2010). Bu üretim süreciyle üretilmiş faz kaydırıcı yapısının SEM ile çekilmiş yakın görüntüsü Şekil 50'de görülmektedir.

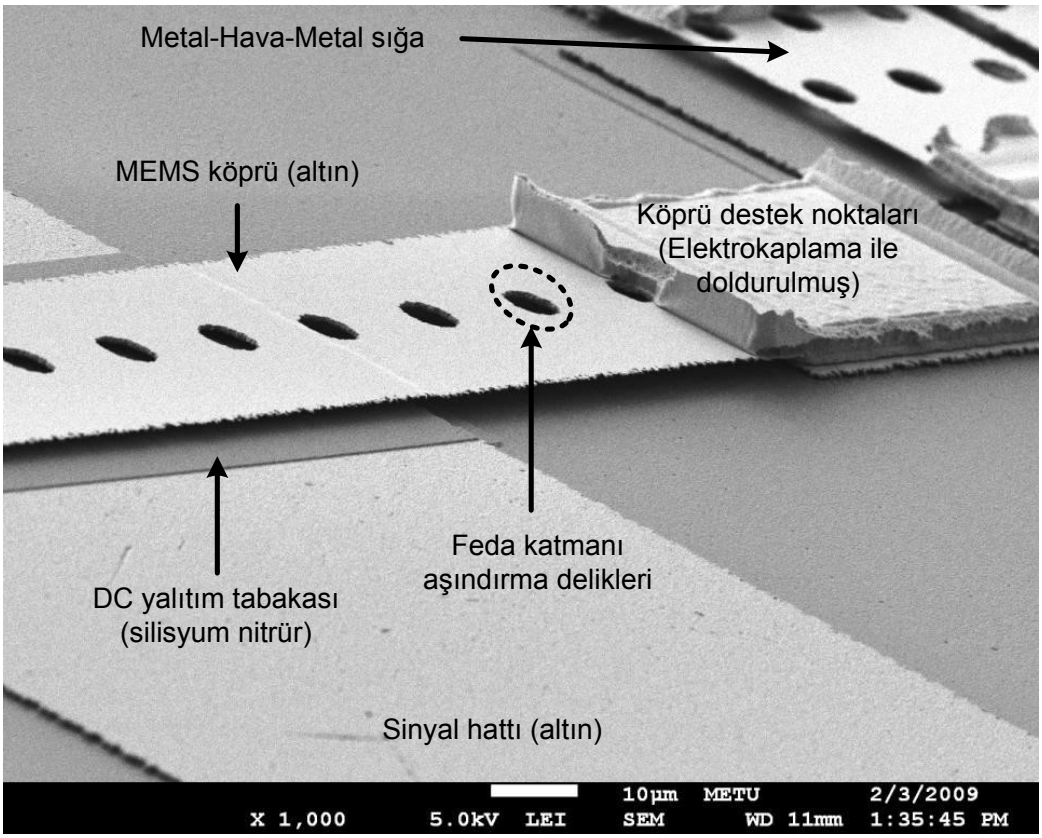

Şekil 50. ODTÜ'de geliştirilen RF MEMS üretim süreci ile üretilen RF MEMS faz kaydırıcı yapıları üzerindeki MEMS bölgelerinin SEM (Scanning electron microscope) ile elde edilen fotoğrafı.

6. SONUÇLAR

Bu proje kapsamında, özellikle milimetre-dalga frekanslarında çalışan yeniden şekillendirilebilir anten, elektronik taramalı dizi anten ve yansıtıcı dizi anten tasarımı, üretimi ve ölçümleri yapılmıştır. Yeniden şekillendirilebilirlik özelliği için farklı teknolojiler kullanılmıştır.

Huzmesi yönlendirilebilen sur biçimli mikroşerit yürüyen dalga anten dizisi X-bant uygulamalarında kullanılmak üzere tasarlamış, üretilmiş ve ölçülmüştür. Antenin ana huzmesinin istenilen yöne elektronik olarak döndürülebilmesini sağlayabilmek için mikroşerit hat üzerinde gerekli faz değişimini sağlayacak varaktör diyotlar kullanılmıştır. Yapılan EM benzetim ve ölçümler sonucu sur biçimli anten dizisinde, ana huzmenin diyot kontrolü ile tasarlandığı gibi 10° lik bir açı taraması yapabildiği gösterilmiştir. Bu, kavram kanıtlaması şeklinde bir çalışmadır; huzmenin daha büyük açı aralığında tarama yapabilmesi için tasarımda yapılması gereken değişiklikler belirtilmiştir.

MM-Dalga sabit genişlikli ve doğrusal sönümlenen yarık antenler tasarlanıp, üretilmiş ve antenin şeklinin, optik uyarımla bu iki yapı arasında değiştirilmesinin sağlanması durumunda ışıma örüntüsünün değiştirilebileceği gösterilmiştir.

Proje kapsamında gerçekleştirilen bir diğer çalışmada da, K ve Ka bantlarında bağımsız çalışabilen, RF MEMS anahtarlarla huzmesi elektronik olarak döndürülebilen dairesel polarizasyonlu yansıtıcı dizi anten tasarlanmış, üretilmiş ve ölçülmüştür. Çift frekanslı dizi iç içe geçmiş farklı boyutlarda iki ayrık-halka dizisi şeklinde tasarlanmıştır. Huzme döndürme amacıyla her bir ayrık halkanın açısal konumunu RF MEMS anahtarlarla ayarlayarak, yansıyan dairesel polarizasyonlu dalgaların fazları kontrol edilmektedir. Anten ODTÜ MEMS merkezinde geliştirilen yüzey mikro-işleme süreciyle üretilmiştir. Işıma örüntüleri ölçülmüş ve benzetim sonuçlarıyla karşılaştırılmıştır. Ölçümlerle, ana huzmenin, tasarlandığı gibi Ka bandında 35°'ye, K bandında 24°'ye döndürülebildiği gösterilmiştir. Bilgimiz dahilinde, bu anten, literatürdeki, çift frekansta huzmesi bağımsız kontrol edilebilen ilk yansıtıcı dizi antendir.

Proje çalışmalarından sur biçimli mikroşerit anten dizisiyle ilgili hazırlanan makale *Microwave and Optical Technology Letters* adlı dergide yayınlanmak üzere kabul edilmiştir. Yansıtıcı dizi antenle ilgili makale de hazırlık sürecindedir. Saygın konferanslarda yedi bildiri sunulmuştur. Ayrıca, proje kapsamında üç yüksek lisans tez çalışması tamamlanmıştır, (GÖKALP 2008, CİHANGİR 2010, GÜÇLÜ 2010).

Proje süresince COST IC0603 projesi toplantılarına, COST desteğiyle, Türkiye'yi temsilen proje yürütücüsü ve çalışanlarından bir kişi katılmış ve bu toplantılarda yapılan çalışmalarla

ilgili çeşitli sunuşlar yapılmıştır. Ayrıca, proje çalışanlarından Caner Güçlü, COST projesinin kısa süreli çalışma (Short Term Scientific Mission) desteği kapsamında Barselona'daki CTTC enstitüsünde Julien Perruisseau-Carrier ile yansıtıcı dizi antenler üzerine 2 hafta çalışmıştır.

7. REFERANSLAR

AYDIN CIVI, O., RF-MEMS Teknolojisi ile Faz Dizili Anten Yapımı 104E041 Sonuç Raporu, (2010).

BALANIS, C., *Antenna Theory: Analysis and Design,* John Wiley & Sons, Inc., New York, (1982).

BAYRAKTAR O.*,* Aydın Çivi Ö.*,* Akın T., Beam Switching Reflectarray with MEMS Controls, 2010 Proceedings of the Fourth European Conference on Antennas and Propagation *(EuCAP),* (2010), pp. 1-4.

BERRY D.*, et al.*, The Reflectarray Antenna*, IEEE Transactions on Antennas and Propagation,*11, pp. 645-651, (1963).

CHENG S., Öjefors E., Hallbjörner P., ve Rydberg A., Compact Reflective Microstrip Phase Shifter for Traveling Wave Antenna Applications, *IEEE Microwave and Wireless Components Letters*,16, 7, (2006).

CİHANGİR A., *Radiation Characteristic Analysis of Tapered Slot Antennas*, (Yüksek Lisans Tezi) Orta Doğu Teknik Üniversitesi, (2010).

DURAL,G., *Theory and Design of Microstrip Rampart Line Arrays*, (Yüksek Lisans Tezi), Orta Doğu Teknik Üniversitesi, (1983).

ERDİL E., Topalli K., Unlu M., Aydin Civi O., and Akin T, Frequency Tunable Microstrip Patch Antenna Using RF MEMS Technology, *IEEE Transactions on Antennas and Propagation*, 55, 4, pp.1193-1196, (2007).

GOKALP N., Aydin Civi, O, Millimeter-Wave Frequency Reconfigurable Slot Dipole Array with Packaged RF-MEMS Switches, 2009 European Conference on Antennas and Propagation EuCAP09, Berlin-Almanya, (2009), pp.1334 –6.

GÖKALP, N, *Beam Steerable Meanderline Antenna Using Varactor Diodes and Reconfigurable Antenna Designes by MEMS Switches*, (Yüksek Lisans Tezi) Orta Doğu Teknik Üniversitesi, (2008).

GÜÇLÜ C., *Dual Frequency Reconfigurable Reflectarray Antenna of Split Ring Elements with RF MEMS Switches*, (Yüksek Lisans Tezi) Orta Doğu Teknik Üniversitesi, (2010).

HAN C.*, et al.*, A C/Ka Dual Frequency Dual Layer Circularly Polarized Reflectarray Antenna with Microstrip Ring Elements, *IEEE Transactions on Antennas and Propagation,* 52, pp. 2871-6, (2004).

HUANG J. and Pogorzelski R. J., Microstrip Reflectarray with Elements Having Variable Rotation Angles, 1997 IEEE Antennas and Propagation Society International Symposium, (1997), pp. 1280-1283.

KÖKSAL, A., Characterization and Optimization of Linearly Tapered Slot Antenna Pattern, *International Journal of* Infrared and Millimeter-Waves, 18, 8, 1525-1537, (1997).

MALAGİSİ C., Microstrip disc element reflect array, Electronics and Aerospace Systems Convention, (1978), pp. 186-192.

MARTYNYUK A. E.*, et al.*, Spiraphase-type reflectarrays based on loaded ring slot resonators, *IEEE Transactions on Antennas and Propagation,* 52, pp. 142-153, (2004).

RATMON R., Oz I., Samson C. J., Comparision of Resonant and Travelling-Wave Meander-Line Antenna, 17th Convention of Electrical & Electronics Engineers in Israel,(1991) pp:149-151.

SCHÜPPERT, B., Microstrip/Slotline Transitions: Modelling and Experimental Investigation, *IEEE Trans. Microwave Theory Tech.,* 36, 8, (1988).

STRASSNER B.*, et al.*, Circularly polarized reflectarray with microstrip ring elements having variable rotation angles, *IEEE Transactions on Antennas and Propagation,* 52, pp. 1122-5, (2004).

SYEDA, K., *Design of a Wideband Vivaldi Antenna Array and Performance Enhancement of Small Vivaldi Arrays Using Baffles*, (Doktora Tezi), Electronics and Communication Engineering, Osmania University, (2003).

TİURİ M., Tallqvist S., Urpo S., Chain Antenna, Antennas and Propagation Society International *Symposium, (1974), pp:274 –7.*

TOPALLI K, Aydin Civi O., Demir S, Koc S, and Akin T, A Monolithic Phased Array using 3-bit Distributed RF MEMS Phase Shifters, *IEEE Transactions on Microwave Theory and Techniques*, 56, 2, pp. 270-277, (2008).

TOPALLI K, Unlu M., Atasoy H. I., Aydın Civi O., Demir S., and Akin T., Empirical Formulation of Bridge Inductance in Inductively Tuned RF MEMS Shunt Switches, *Progress In Electromagnetics Research, PIER 97*, pp. 343-356, (2009)

TOPALLI K, Erdil E, Aydin Civi O., Demir S, Koc S, Akin T, Tunable dual-frequency RF MEMS rectangular slot ring antenna, *Sensors And Actuators: A*, 156, 2, pp. 373-380, (2009)

UNLU M, Topalli K., Atasoy H. I., Demir S., Aydin Civi O., and Akin T., Hybrid Connection of RF MEMS and SMT Components in an Impedance Tuner*, Int J Electron Commun (AEU),* 64, 8, pp. 748-756, (2010)

YNGVESSON, S., Endfire Tapered Slot Antennas on Dielectric Substrates, *IEEE Transactions on Antennas and Propagation*, 33, 12, (1985).

EK1. MİKROŞERİT HAT VE YARIK İLETİM HATLARININ EMPEDANS HESABI

Yarık iletim hattının karakteeristik empedans denklemi aşağıda verilmiştir:

$$Z_0 = 60 + 3.69\sin\left[\frac{(\varepsilon_r - 2.22)\pi}{2.36}\right] + 133.5\ln(10\varepsilon_r)\sqrt{\frac{W}{\lambda_0}} +$$

$$2.81\left[1 - 0.011\varepsilon_r(4.48 + \ln\varepsilon_r)\right]\left(\frac{W}{h}\right)\ln\left(\frac{100h}{\lambda_0}\right) \qquad \text{(A1)}$$

$$+131.1(1.028 - \ln\varepsilon_r)\sqrt{\frac{h}{\lambda_0}} + 12.48(1 + 0.18\ln\varepsilon_r)\left(\frac{\left(\frac{W}{h}\right)}{\sqrt{\varepsilon_r - 2.06 + 0.85\left(\frac{W}{h}\right)^2}}\right)$$

Burada h dielektrik substratın kalınlığını, W ise yarık hat genişliğini ifade etmektedir.

Yarık hattaki kılavuzlu dalgaboyu ise aşağıdaki denklemle hesaplanır:

$$\frac{\lambda_g}{\lambda_0} = 1.045 - 0.365\ln\varepsilon_r + \frac{6.3\left(\frac{W}{h}\right)\varepsilon_r^{\,0.945}}{238.64 + 100\left(\frac{W}{h}\right)} - \left(0.148 - \frac{8.81(\varepsilon_r + 0.95)}{100\varepsilon_r}\right)\ln\left(\frac{h}{\lambda_0}\right) \qquad \text{(A2)}$$

Bir mikroşerit hattın etkili dielektrik sabiti ve karakteristik empedansı aşağıdaki formülle hesaplanabilir:

W/h<1 için:

$$\varepsilon_{eff} = \frac{\varepsilon_r + 1}{2} + \frac{\varepsilon_r - 1}{2}\left[\frac{1}{\sqrt{1 + \frac{12h}{W}}} + 0.04\left(1 - \frac{W}{h}\right)^2\right] \qquad \text{(A3)}$$

$$Z_c = \frac{60}{\sqrt{\varepsilon_{eff}}}.\ln\left(\frac{8h}{W} + \frac{W}{4h}\right) \qquad \text{(A4)}$$

W/h>1 için:

$$\varepsilon_{eff} = \frac{\varepsilon_r + 1}{2} + \frac{\varepsilon_r - 1}{2}\left(\frac{1}{\sqrt{1 + \frac{12h}{W}}}\right) \qquad \text{(A5)}$$

$$Z_c = \frac{120\pi}{\sqrt{\varepsilon_{eff}}} \cdot \frac{1}{\left[\frac{W}{h} + 1.393 + \left(0.677.\ln\left(\frac{W}{h} + 1.444\right)\right)\right]} \qquad \text{(A6)}$$

Denklemlerde W mikroşerit hattın genişliğini ifade etmektedir.

EK-2 CHEBYSHEV EMPEDANS DÖNÜŞTÜRÜCÜ TASARIMI

Üç bölümlü bir Chebyshev empedans dönüştürücünün her biriminin empedansı aşağıdaki formüllere gore hesaplanır:

$$\sec\theta_m = \cosh\left[\frac{1}{N}\cosh^{-1}\left(\frac{\ln(Z_L/Z_0)}{2\Gamma_m}\right)\right] = \cosh\left[\frac{1}{3}\cosh^{-1}\left(\frac{\ln(152.76/50)}{2\times 0.05}\right)\right] = 1.5849 \quad \text{(B1)}$$

$$2\Gamma_0 = A\sec^3\theta_m = 0.05\times(1.5849)^3 \Rightarrow \Gamma_0 = 0.0995 \quad \text{(B2)}$$

$$2\Gamma_1 = 3A\left(\sec^3\theta_m - \sec\theta_m\right) = 3\times 0.05\left(1.5849^3 - 1.5849\right) \Rightarrow \Gamma_1 = 0.1797 \quad \text{(B3)}$$

$$\ln Z_1 = \ln Z_0 + 2\Gamma_0 = \ln 50 + (2\times 0.1797) \Rightarrow Z_1 = 61.01\Omega \quad \text{(B4)}$$

$$\ln Z_2 = \ln Z_1 + 2\Gamma_1 = \ln 61.01 + (2\times 0.1797) \Rightarrow Z_2 = 87.39\Omega \quad \text{(B5)}$$

$$\ln Z_3 = \ln Z_2 + 2\Gamma_2 = \ln 87.39 + (2\times 0.1797) \Rightarrow Z_3 = 125.19\Omega \quad \text{(B6)}$$

Burada, $A=\Gamma_m=0.05$, simetriden dolayı $\Gamma_2=\Gamma_1$ ve N=3 alınmıştır.

EK 3. PROJE KAPSAMINDA YAPILAN YAYINLAR VE TEZLER

Tezler

1. Nihan Gökalp, *Beam Steerable Meanderline Antenna Using Varactor Diodes and Reconfigurable Antenna Designes by MEMS Switches*, Yüksek Lisans Tezi, Orta Doğu Teknik Üniversitesi, 2008. (Danışman: Özlem Aydın Çivi) (IEEE Microwave Theory and Techniques Society Lisansüstü bursuyla ödüllendirilmiştir)
2. Aykut Cihangir, *Radiation Characteristic Analysis of Tapered Slot Antennas*, Yüksek Lisans Tezi, Orta Doğu Teknik Üniversitesi, 2010 (Danışman: Lale Alatan, Eş-Danışman: Özlem Aydın Çivi)
3. Caner Güçlü, *Dual Frequency Reconfigurable Reflectarray Antenna of Split Ring Elements with RF MEMS Switches*, Yüksek Lisans Tezi, Orta Doğu Teknik Üniversitesi, 2010, (Danışman: Özlem Aydın Çivi, Eş-Danışman: Tayfun Akın).

Hakemli Dergilerde Yayınlanmış Makaleler

1. Nihan Gökalp, Ö.Aydın Çivi, "Beam Steerable Meanderline Antenna Using Varactor Diodes", *Microwave and Optical Technology Letters* dergisinde basılmak üzere kabul edildi, Aug, 2010.

Uluslararası Konferans Bildirileri

1. A. Cihangir, L. Alatan, " Reconfiguration in the Radiation Pattern of Tapered Slot Antennas," Proceedings of the 20th International Conference on Applied Electromagnetics and Communications (ICECOM) , Dubrovnik, Croatia, 20-23 Sept. 2010.

2. Caner Guclu, Julien Perruisseau-Carrier, and Ozlem Aydin Civi, "Dual Frequency Reflectarray Cell Using Split-ring Elements with RF MEMS Switches", 2010 IEEE AP-S International Symposium, Toronto, Canada, pp., 11-16 July 2010.

3. N. Gokalp, O. Aydin Civi, "Millimeter-Wave Frequency Reconfigurable Slot Dipole Array with Packaged RF-MEMS Switches", 2009 European Conference on Antennas and Propagation EuCAP09, Berlin, Almanya, Proceedings pp.1334 –1336 , 23-27 Mart 2009.

4. N. Gokalp, Ö. Aydin Civi, "Beam steerable traveling wave meander line antenna using varactor diode for X-band applications", IEEE 2008 Antennas and Propagation Society International Symposium, San Diego, ABD, pp.1 – 4, 5-11 July 2008.

5. K. Topalli, O. Bayraktar, M. Unlu, O. Aydin Civi, S. Demir, and T. Akin, "Reconfigurable antennas by RF MEMS technology," 30th ESA Antenna Workshop on Antennas for Earth Observation, Science, Telecommunications and Navigation Space Missions, pp.497-500, Noordwijk, The Netherlands, 27-30 May 2008.

Ulusal Konferans Bildirileri

1. Caner Guclu, Julien Perruisseau-Carrier, and Ozlem Aydin Civi, “Çift Frekansta Çalışan Yeniden Yapılandırılabilir Ayrık Halka Yansıtıcı Dizi Anten Birim Hücre Tasarımı”, URSI Türkiye 5. Bilimsel Kongresi, pp.128-131, ODTÜ-KKK, 25-27 Ağustos 2010.
2. Nihan Gökalp, Özlem Aydın Çivi , “Işınım Huzmesi Yönlendirilebilen Sur Biçimli Mikroşerit Anten Dizisi”, URSI 4.Bilimsel Kongresi, pp. 208-211, Antalya, 20-22 Ekim 2008

RADIATION CHARACTERISTIC ANALYSIS OF TAPERED SLOT ANTENNAS

A THESIS SUBMITTED TO
THE GRADUATE SCHOOL OF NATURAL AND APPLIED SCIENCES
OF
MIDDLE EAST TECHNICAL UNIVERSITY

BY

AYKUT CİHANGİR

IN PARTIAL FULFILLMENT OF THE REQUIREMENTS
FOR
THE DEGREE OF MASTER OF SCIENCE
IN
ELECTRICAL AND ELECTRONICS ENGINEERING

AUGUST 2010

Approval of the thesis:

RADIATION CHARACTERISTIC ANALYSIS OF TAPERED SLOT ANTENNAS

submitted by **AYKUT CİHANGİR** in partial fulfillment of the requirements for the degree of **Master of Science in Electrical and Electronics Engineering Department, Middle East Technical University** by,

Prof. Dr. Canan Özgen _____
Dean, Graduate School of **Natural and Applied Sciences**

Prof. Dr. İsmet Erkmen _____
Head of Department, **Electrical and Electronics Dept., METU**

Assist. Prof. Dr. Lale Alatan _____
Supervisor, **Electrical and Electronics Dept., METU**

Assoc. Prof. Dr. Özlem Aydın Çivi _____
Co-supervisor, **Electrical and Electronics Dept., METU**

Examining Committee Members:

Prof. Dr. Gülbin Dural _____
Electrical and Electronics Engineering Dept., METU

Assist. Prof. Dr. Lale Alatan _____
Electrical and Electronics Engineering Dept., METU

Assoc. Prof. Dr. Sencer Koç _____
Electrical and Electronics Engineering Dept., METU

Assoc. Prof. Dr. Şimşek Demir _____
Electrical and Electronics Engineering Dept., METU

M.Sc. Can Barış Top _____
ASELSAN

Date: **23/08/2010**

I hereby declare that all information in this document has been obtained and presented in accordance with academic rules and ethical conduct. I also declare that, as required by these rules and conduct, I have fully cited and referenced all material and results that are not original to this work.

Name Surname: Aykut Cihangir

Signature:

ABSTRACT

RADIATION CHARACTERISTIC ANALYSIS OF TAPERED SLOT ANTENNAS

Aykut Cihangir
M.Sc., Department of Electrical and Electronics Engineering
Supervisor: Assist. Prof. Dr. Lale Alatan
Co-Supervisor: Assoc. Prof. Dr. Özlem Aydın Çivi

August 2010, 87 pages

The aim of this study is to investigate the effects of changes in the physical parameters of tapered slot antennas (TSA) on their radiation characteristics and also to explore the possibility of reconfiguration in the radiation pattern of TSA by switching between two different types of tapering.

There are mainly three physical parameters that affect the radiation pattern of TSAs. These are antenna length, aperture width and the ground extension. After designing a wideband microstrip line to slot line transition, the effect of antenna parameter variations on the beamwidth and sidelobe level of the antenna are investigated through the use of a commercially available electromagnetic simulation software HFSS by ANSOFT. The radiation characteristics of constant width slot antennas (CWSA) and linearly tapered slot antennas (LTSA) are compared. It is observed that CWSAs exhibit narrower beamwidth and higher sidelobe level whereas linearly tapered slot antennas (LTSA) have wider beamwidth with lower sidelobe level compared to each other. A novel switching architecture between CWSA and LTSA is proposed to obtain a reconfigurable antenna.
Keywords: Tapered slot antennas, reconfigurable antennas, microstrip line to slotline transition.

ÖZ

SÖNÜMLENEN YARIK ANTENLERİN IŞIMA KARAKTERİSTİĞİ ANALİZİ

Aykut Cihangir
Yüksek Lisans, Elektrik ve Elektronik Mühendisliği Bölümü
Tez Yöneticisi: Yrd. Doç. Dr. Lale Alatan
Eş Tez Yöneticisi: Doç. Dr. Özlem Aydın Çivi

Ağustos 2010, 87 sayfa

Bu çalışma ile sönümlenen yarık antenlerin fiziksel özelliklerinin ışıma örüntüsüne etkilerini araştırmak ve iki farklı sönümlenme tipi arasında yapılacak geçişlerle ışıma örüntüsünde yeniden şekillendirilebilirlik elde edilebilme olasılığını araştırmak hedeflenmiştir.

Genel olarak bir sönümlenen yarık antenin ışıma örüntüsünü etkileyen üç fiziksel özellik vardır. Bunlar anten boyu, açıklık genişliği ve toprak uzantısı parametreleridir. Geniş bantlı bir mikroşerit hattan yarık hatta geçiş tasarımı sonrasında, ANSOFT firmasının ticari bir elektromanyetik benzetim yazılımı olan HFSS ile anten parametrelerinin yarım açı huzme genişliği ve yan lob seviyesi üzerine etkileri araştırılmıştır. Sabit Genişlikli ve Doğrusal Sönümlenen Yarık Antenlerin ışıma karakteristikleri karşılaştırılmıştır. Analiz sonucunda Doğrusal Sönümlenen Yarık Antenlerin daha dar huzme genişliği ve daha yüksek yan lob seviyesine, Doğrusal Sönümlenen Yarık Antenlerin ise daha geniş huzme genişliği ve daha düşük yan lob seviyesine sahip olduğu gözlemlenmiştir. Yeniden şekillendirilebilir bir anten elde etmek için Sabit Genişlikli ve Doğrusal Sönümlenen Yarık Antenler arasında bir geçiş mimarisi önerilmiştir.

Anahtar Kelimeler: Sönümlenen yarık antenler, yeniden şekillendirilebilirlik, mikroşerit hattan yarık hatta geçiş.

ACKNOWLEDGEMENTS

I would like to express my gratitude to my supervisor Assist. Prof. Dr. Lale Alatan, for her guidance, support, understanding and tolerance throughout this study.

I wish to thank my co-supervisor Assoc. Prof. Dr. Özlem Aydın Çivi, for her contribution and guidance in my study.

I would also want to thank Assoc. Prof. Dr. Sencer Koç, Ömer Bayraktar and Erdinç Yurdakul for their support in the antenna manufacturing and pattern measurement phase of the study.

Finally, I am indebted to my family and friends, who never let me lose my motivation and who never withheld their help from me, in all circumstances.

TABLE OF CONTENTS

LIST OF TABLES

LIST OF FIGURES

CHAPTER 1

INTRODUCTION

Electrical and Electronics Engineering Department of Middle East Technical University (METU) is a member of EU supported COST ASSIST project. The scope of this project is the design of reconfigurable antennas at millimeter-wave frequency band. Millimeter-wave band is considered in this project since the Personal Communication Systems (PCS) operate with high data rates that correspond to a large bandwidth requirement which can be easily satisfied in this frequency band. In millimeter-wave designs that are used in applications like PCS, automotive collision avoidance radars and local cellular radio networks, an integrated antenna that rests on a substrate and has ease to be integrated with other RF circuits on a common board or module is usually preferred. It is important for the antenna and rest of the system to be located on a single substrate to get a compact layout. Due to the easy integration and large bandwidth requirements, Tapered Slot Antenna (TSA) is chosen to be the antenna configuration that will be studied within the scope of this work. Different types of reconfigurable antennas are studied at METU. In those antennas generally reconfiguration is done either on the operating frequency of the antenna or on the polarization of the antenna. Since the bandwidth of TSA is already wide and excitation of different polarizations in TSA requires the design of complex structures, a different type of reconfiguration is searched for TSA. During the literature survey about TSA, it is found that the tapering profile of TSA significantly affects the radiation characteristics of the antenna. Consequently in this thesis, it is aimed to investigate the radiation characteristics of TSA and to explore the possibility of reconfiguring the radiation pattern of TSA by switching between different tapering profiles.

Tapered slot antennas (TSA) are travelling wave antennas. In general, all antennas whose voltage or current distribution can be modeled by one or more travelling waves are called travelling wave (nonresonant) antennas. Unlike standing wave (resonant) antennas, the phase distribution along a traveling wave antenna can not be assumed to be constant as stated in [1]. The reflected wave in resonant antennas is totally or partially minimized in the traveling wave antennas by proper termination. An example to this phenomenon is the long wire antenna which is actually a resonant dipole antenna terminated by a matched load.

There are two types of traveling wave antennas: slow wave antennas and fast wave antennas. Slow wave antennas are antennas whose phase velocities are equal to or smaller than the speed of light. For surface wave antennas, a type of slow wave antennas, the radiation takes place at the discontinuities, nonuniformities and curvatures where the bound wave on the antenna surface is interrupted. The travelling wave antennas of this class are endfire or near endfire radiators. Fast wave antennas on the other hand have phase velocities larger than the speed of light. Consequently, leaky wave antennas are considered as fast wave antennas. This type of antenna couples power discretely or continuously through its length. The result is a tilted main beam from the endfire direction.

A tapered slot antenna uses a slot line etched on a dielectric material, which is widening through its length to produce an endfire radiation [2]. An electromagnetic wave propagates through the surface of the antenna substrate with a velocity less than the speed of light which makes TSAs gain slow wave antenna properties. The EM wave moves along the increasingly separated metallization tapers until the separation is such that the wave detaches from the antenna structure and radiates into the free space from the substrate end. The E-plane of the antenna is the plane containing the electric field vectors of the radiated electromagnetic (EM) waves. For TSAs, this is parallel to the substrate since the electric field is established between two conductors that are separated by the tapered slot. The H plane, the plane containing the magnetic component of the radiated EM wave runs perpendicular to the substrate.

TSAs have moderately high directivity (on the order of 10-17 dB) and narrow beamwidth because of the traveling wave properties and almost symmetric E-plane and H-plane radiation patterns over a wide frequency band as long as antenna parameters like shape, total length, dielectric thickness and dielectric constant are chosen properly. Other important advantages of TSAs are that they exhibit broadband operation, low sidelobes, planar footprints and ease of fabrication. A TSA can have large bandwidth if it exhibits a good match both at the input side (transition from the feed line to slot line) and the radiation side (transition from the antenna to free space) of the antenna [3]. The gain of a TSA is proportional to the length of the antenna in terms of wavelength. Tapered slot antennas are also suitable to be used at high operating frequencies (greater than 10 GHz), where a long electrical length corresponds to a considerably short geometrical length. The main disadvantage of the TSA is that only linear polarization can be obtained with conventional geometries.

As shown in Figure 1, several TSA types exist according to the shape of tapering. Most common types are Linearly Tapered Slot Antenna (LTSA), Vivaldi or Exponentially Tapered Slot Antenna and Constant Width Slot Antenna (CWSA).

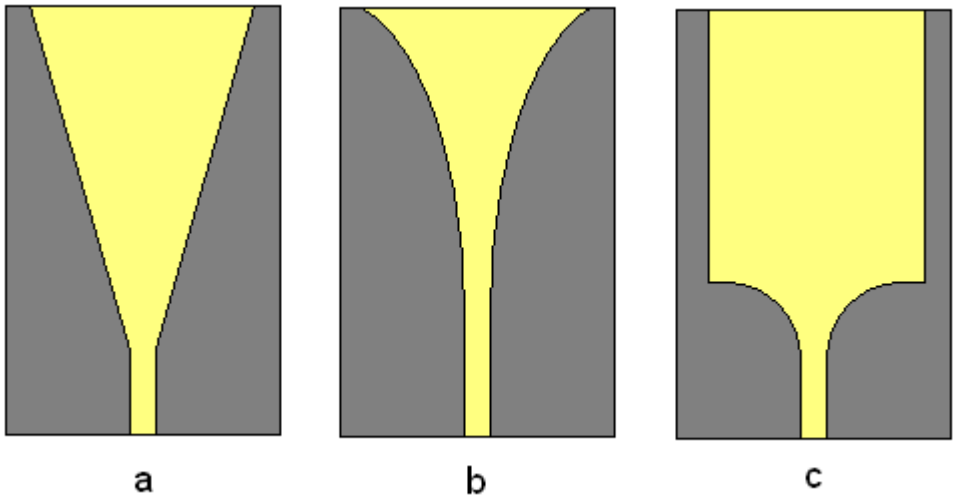

Figure 1 Tapered Slot Antenna Types

(a) Linearly Tapered Slot Antenna (b) Exponentially Tapered Slot Antenna (Vivaldi) (c) Constant Width Slot Antenna

These three main types of TSAs are compared in [4] in terms of beamwidths and side lobe levels. For a TSA with the same antenna length, aperture width and substrate parameters, CWSA has the narrowest beamwidth, followed by LTSA and then Vivaldi. The sidelobe levels are highest for CWSA, followed by LTSA and then Vivaldi. So a transition between the LTSA and CWSA structures could provide reconfigurability about antenna beamwidth and sidelobe levels. Within the scope of this thesis, the two configurations are studied separately and the changes in the radiation patterns of LTSA and CWSA are examined.

TSAs are first introduced in 1979 in the 9th European Microwave Conference by two independent presentations [5], [6]. In [5], an ETSA (Vivaldi) to be used in a 8-40 GHz video receiver module is proposed. The antenna had a usable bandwidth of 2-20 GHz with a gain of approximately 10dBi and -20dB sidelobe level. Exponential taper was chosen in this work in order to achieve a wideband performance with an aperiodic continuously scaled structure. It is stated that the energy in the travelling wave on the tapered slot becomes weaker as the separation between the arms of the slot line increases and at last the energy couples to the radiated field.

In [6], an X-band LTSA excited by a microstrip line on alumina substrate is proposed. The antenna was designed to be used in short range radar and phased array systems. The LTSA had a gain of 6dBi and a sidelobe level of -10dB. The antenna had a %5 bandwidth centered at 9 GHz. The slot width at the open end of the slot line was changed while keeping the antenna length constant and the change in the gain and sidelobe levels were observed.

In 1985, CWSA is proposed in [7]. In this study, the effective thickness value required for compliance with Zucker's curves for travelling wave antennas are stated. Effects of the parameters of the dielectric substrate and the dimensions of the antenna on the radiation characteristics of the antenna were investigated experimentally for LTSA, Vivaldi and CWSA geometries.

Until 1986, only experimental studies had been conducted for the analysis of TSAs. The numerical analysis of TSAs through the use of Method of Moments (MoM) is

first proposed by Janaswamy in his Ph.D. dissertation [8]. In 1989, Johansson also demonstrated the MoM analysis of LTSAs to determine the surface currents on the antenna [9]. In [10], analyses of TSAs are also performed by MoM and the dielectric constant profile of the substrate is optimized to achieve a required radiation pattern.

After the work of Yngvesson et al [4] that emphasizes the easy integration feature of TSAs, they started to be widely used in millimeter-wave and array applications. TSAs operating at millimeter-wave frequency band are designed and studied in [11]-[13]. In [11], two types of TSAs (LTSA and ETSA) operating at 23-80 GHz band are designed. According to simulation results the input return loss values of both of the antennas are below -10dB within the frequency band. However, when the radiation characteristics of the antennas are investigated, it is observed that the antenna starts to be more directive as the frequency increases. Therefore the gain of the antenna varies between 7-12 dBi for the LTSA and between 8-10 dBi for the ETSA. It is concluded that the radiation pattern bandwidth of the ETSA is wider compared to LTSA. In [12], a LTSA operating at 45-75 GHz band is designed on a low temperature cofired ceramic (LTCC) substrate. It is observed that the high dielectric constant of the LTCC substrate degrades the radiation characteristics of the antenna by lowering the gain and distorting the radiation pattern. Therefore an air cavity at the back of the antenna is introduced to lower the effective dielectric constant of the substrate. In this way, the distortions in the radiation pattern of the antenna are eliminated but still a variation of 4.9dBi to 5.9dBi is observed in the gain of the antenna within the frequency band. In [13], the effective dielectric constant of the substrate is reduced by selectively machining holes in the dielectric substrate. The radiation characteristics of the designed antenna are investigated at 24, 30 and 36 GHz both with and without holes. It is observed that the introduction of the holes lowers the sidelobe levels, significantly decreases 10dB beamwidths and increases the gain of the antenna. However, the dependency of the gain of the antenna on frequency is same as the examples discussed so far.

Arrays of TSAs can be used to obtain higher directivity and some demonstrative TSA antenna array examples can be found in [14]-[16].

Since the tapered slot antennas are extensions of a slot line, one should generally design a transition between a slot line and some other type of transmission line that feeds the antenna. These transitions can be classified into two groups as stated in [3]:

Electromagnetically coupled transitions:

The coupling is through EM fields rather than direct electrical contact as shown in Figure 2. The feed line is printed on one side of the substrate and the slot line is etched on the other side. This type of transitions may use microstrip line, coplanar waveguide (CPW) or stripline as the feed line.

Directly coupled transitions:

Coupling is through a direct current path like a wire or a solder connection. Transitions that use a coaxial line, bond wires or ribbons are directly coupled transitions. Coplanar waveguide type feed line can be directly coupled to the antenna as well. In that case, feed line is printed on the same side of the substrate with the antenna and one of the slots of CPW line is extended to be the slot line of the antenna whereas the other slot in the feed is properly terminated as illustrated in Figure 3.

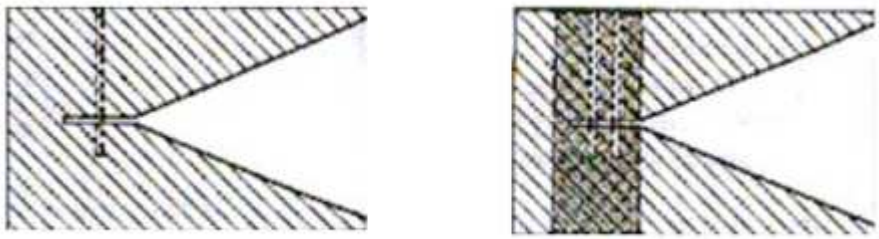

Figure 2 Examples of electromagnetically coupled transitions

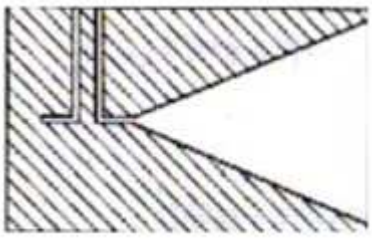

Figure 3 Directly coupled transition for CPW feed line

Many studies have been conducted on the design of transitions from various transmission line types to slot lines. Most popular of the input transmission line types are coplanar waveguide and microstrip line. In [17], different transition topologies between coplanar waveguide to slot line are studied. Wideband microstrip line to slot line transitions can be found in [18], with reference to the simplified circuit models of the transitions. The designs studied are orthogonal microstrip line to slotline transitions where two transmission lines intersect at a right angle on different faces of a dielectric substrate. Different topologies and transition models have been investigated with measurement results.

The second chapter of the thesis starts with the discussions about the proper choice of the dielectric substrate in the design of TSAs followed by the design of microstrip line to slot line transition used in this work. Next, the parametric study results for the LTSA and CWSA are presented in this chapter.

The third chapter includes the radiation characteristic and bandwidth comparisons between LTSAs and CWSAs having same physical dimensions. The reconfiguration method proposed for the switching between LTSA and CWSA configurations is also presented in this chapter.

In the fourth chapter, the radiation patterns obtained through measurement of LTSA and CWSA configurations will be evaluated. First, the measurement data will be compared to simulation data, then differences between the radiation patterns of LTSA and CWSA will be discussed and finally the variations in the radiation patterns with respect to frequency will be investigated.

The “Conclusion” chapter will sum up the general results deduced from this study.

CHAPTER 2

PARAMETRIC STUDY ON THE RADIATION CHARACTERISTICS OF TSA

In this section, how antenna substrate choice is made will be explained first. The design of microstrip line to slot line transition that will be used to feed the TSAs will be given next. The LTSA and CWSA design and the parametric study results for the LTSA and CWSA will be interpreted. This section will end with a bandwidth comparison of CWSA with linear and exponential taper profiles.

2.1.Substrate Choice

Tapered slot antennas are well-behaved travelling-wave antennas as long as a condition about the parameters of the substrate is satisfied. In order to state this condition, first the effective thickness of the dielectric substrate (t_{eff}) need to be defined as follows [19].

$$\frac{t_{eff}}{\lambda_0} = \left(\sqrt{\varepsilon_r} - 1\right)\frac{t}{\lambda_0} \tag{1}$$

where λ_0 is the free space wavelength at the center frequency, t is the thickness and ε_r is the dielectric constant of the substrate. The necessary condition for a TSA to possess travelling wave antenna characteristics is [19]:

$$0.005 \le \frac{t_{eff}}{\lambda_0} \le 0.03 \tag{2}$$

As stated in [13] and [16], for a t_{eff}/λ_0 value below 0.005, the antenna will have decreased directivity whereas for values larger than 0.03, unwanted substrate modes will develop that will deviate the antenna from travelling wave antenna characteristics and introduce grating lobes to the radiation pattern.

The dielectric materials that are available at METU are listed in Table 1 together with their parameters and effective thickness values at 35 GHz. Among the substrates considered, two dielectric materials, shown shaded in Table 1, with three different thickness values satisfy the condition given in Equation (2). 0.51mm thick RO5880 Duroid substrate is chosen to be used in this thesis study.

Table 1 Parameters of available dielectric materials

Material	ε_r	**tan δ**	**t(mm)**	t_{eff}/λ_0
TMM 10	9.2	0.0017	0.81	0.192
RO4003	3.38	0.0027	0.51	0.049
			0.81	0.079
			1.52	0.148
RO5880	2.2	0.0009	0.127	0.007
			0.51	0.028
			0.78	0.044
			1.57	0.088
R06006	6.15	-	1.27	0.219
RO6010	10.2	-	0.635	0.162
FR3	4	-	1.52	0.177
FR4	4.4	0.022	1.52	0.195
Cuflon	2.1	0.00045	0.127	0.006
			0.78	0.041

2.2. Design of microstrip line to slot line transition

The bandwidth goal for the LTSA and CWSAs to be designed is decided to be between 30-40 GHz centered at 35 GHz so a wideband transition between microstrip line and slot line is needed. Due to the simplicity in design and manufacturing, microstrip line is chosen as the feed line. The microstrip line to slot line transition proposed in [18] is considered. The geometry of the transition is shown in Figure 4. The transition is employing a microstrip line and a slot line crossing each other at a right angle. The microstrip extends about one quarter of a guided wavelength beyond the slot, and the slot extends about a quarter of a guided wavelength beyond the microstrip.

In order to obtain a transition that has low return loss over a wide frequency band, the impedances of the microstrip line and the slot line should be matched to each other to minimize the reflections. The slot line width shall be chosen not to have too large impedance values in order to be able to achieve impedance matching between microstrip line and slot line. The characteristic impedance of a slot line increases with increasing slot width, so the width of the slot should be chosen as small as possible to obtain an impedance value close to 50Ω. Because of the manufacturing limitations, a minimum slot width of 0.254 mm (10 mils) is chosen. To calculate the characteristic impedance and guided wavelength of the slot line, empirical formulas proposed in [20] and presented in Appendix A are used.

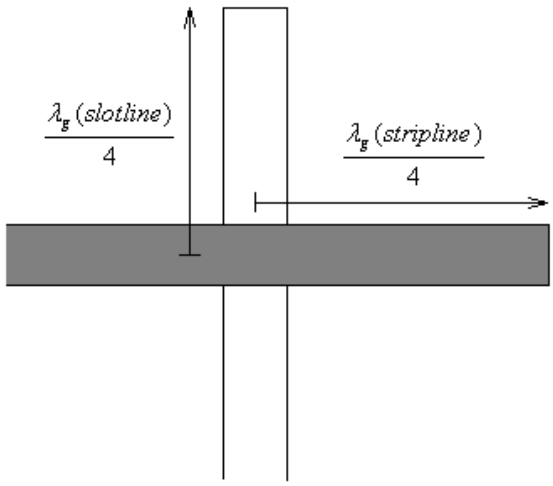

Figure 4 Orthogonal microstrip line to slot line transition

The characteristic impedance and the guided wavelength (at 35 GHz) of 0.254 mm wide slot line are calculated as 152.76Ω and 7.24 mm, respectively. A wideband impedance transformer needs to be designed in order to match the 50Ω microstrip line to 152Ω slot line. So, a Chebyshev impedance transformer circuit, studied in [21] and [22], is designed with three sections (N=3). As shown in Figure 5, the impedance transformer circuit consists of three microstrip segments of quarter guided wavelength long between the input microstrip line and the load. The input impedance (Z_0) of the Chebyshev Transformer will be the characteristic impedance

of the microstrip line and the load impedance will be the characteristic impedance of the slot line.

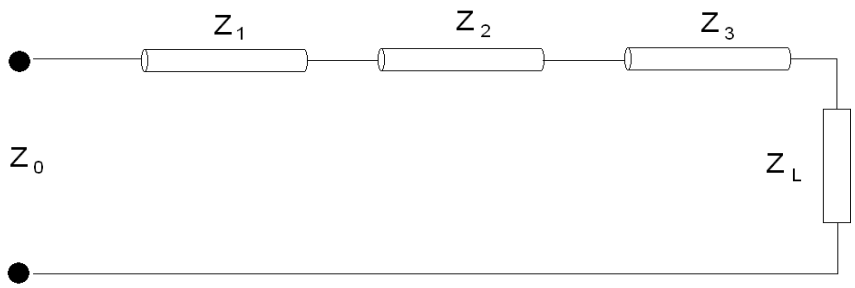

Figure 5 Chebyshev impedance transformer circuit

The characteristic impedance values of the three quarter wavelength long segments are calculated by using the equations given in Appendix B and listed as:

- $Z_1 = 61.01\ \Omega$
- $Z_2 = 87.39\ \Omega$
- $Z_3 = 125.19\ \Omega$

The line widths and effective dielectric constant (ε_{eff}) values corresponding to these impedances are determined by using the equations given in Appendix A. Guided wavelengths of microstrip segments are determined by Equation (3).

$$\lambda_g = \frac{\lambda_0}{\sqrt{\varepsilon_{eff}}} \tag{3}$$

The width and length values of each microstrip line segment are listed in Table 2.

Table 2 Calculated width and length values of microstrip line segments

	Strip Width	Quarter Guided Wavelength
Z_0=50 Ω	1.58 mm	1.56 mm
Z_1=61.01 Ω	1.16 mm	1.58 mm
Z_2=87.39 Ω	0.6 mm	1.61 mm
Z_4=125.19 Ω	0.26 mm	1.63 mm

In order to improve the accuracy of width and length values calculated from empirical formulas, simulations on HFSS are performed. Microstrip lines are modeled as two port networks with two wave ports at both ends. The characteristic impedance of the line is calculated from s_{11} results and the guided wavelength of the line is found from the phase of s_{12} parameter. A couple of simulations are performed to fine tune the width and length of the microstrip line such that the desired impedance and guided wavelength values are achieved. With the help of the simulation results, for 50Ω, 61.01 Ω, 87.39 Ω and 125.19 Ω transmission lines, the width and the quarter guided wavelength values are determined as given in Table 3.

Table 3 Microstrip Line Parameters

	Values Calculated		**Values obtained from HFSS**	
	strip width	$\lambda_g/4$	strip width	$\lambda_g/4$
Z_0=50 Ω	1.58 mm	1.56 mm	1.58 mm	1.54 mm
Z_1=61.01 Ω	1.16 mm	1.58 mm	1.08 mm	1.56 mm
Z_2=87.39 Ω	0.6 mm	1.61 mm	0.54 mm	1.60 mm
Z_4=125.19 Ω	0.26 mm	1.63 mm	0.2 mm	1.63 mm

To investigate the performance of the designed microstrip line to slot line transition, two structures are connected back to back as show in Figure 6. The simulation results

for the return loss and insertion loss of this structure from 20 to 50GHz are presented in Figure 8 and the dimensions of the final structure are given in Figure 7. It can be seen from the simulation results of the designed transition that, it exhibits return loss lower than -10dB and a good level of insertion loss (lower than 3 dB) over the frequency band of 27-40 GHz.

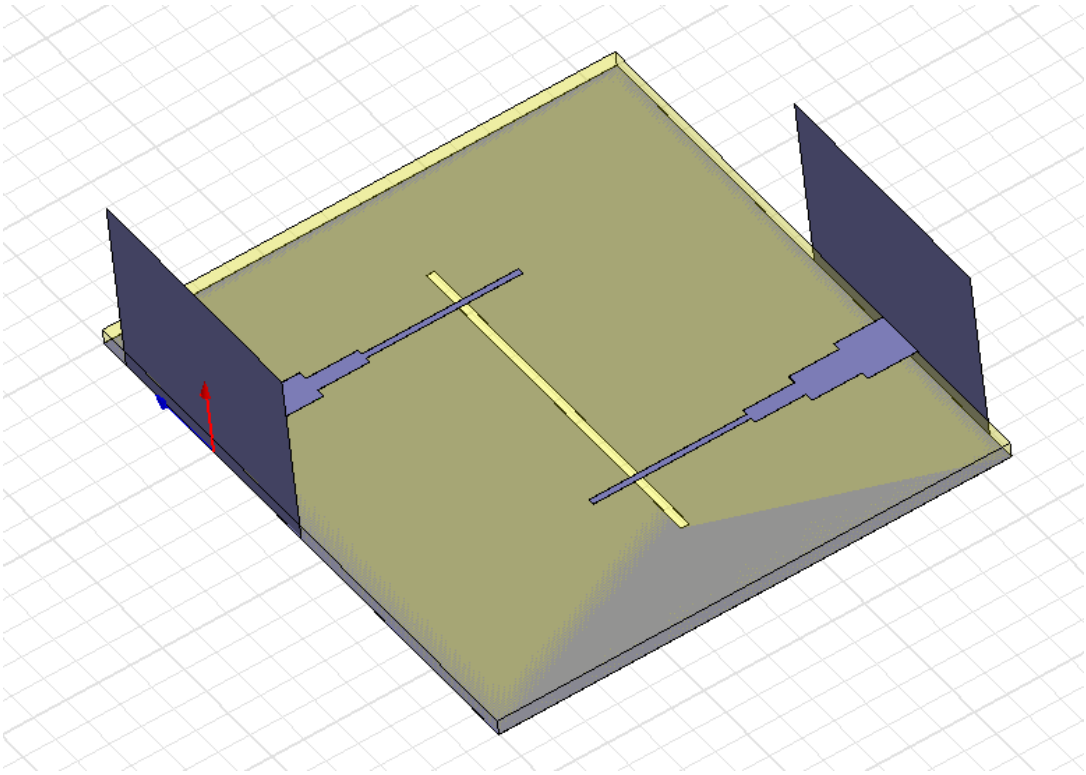

Figure 6 Back to back connected microstrip line to slot line transitions

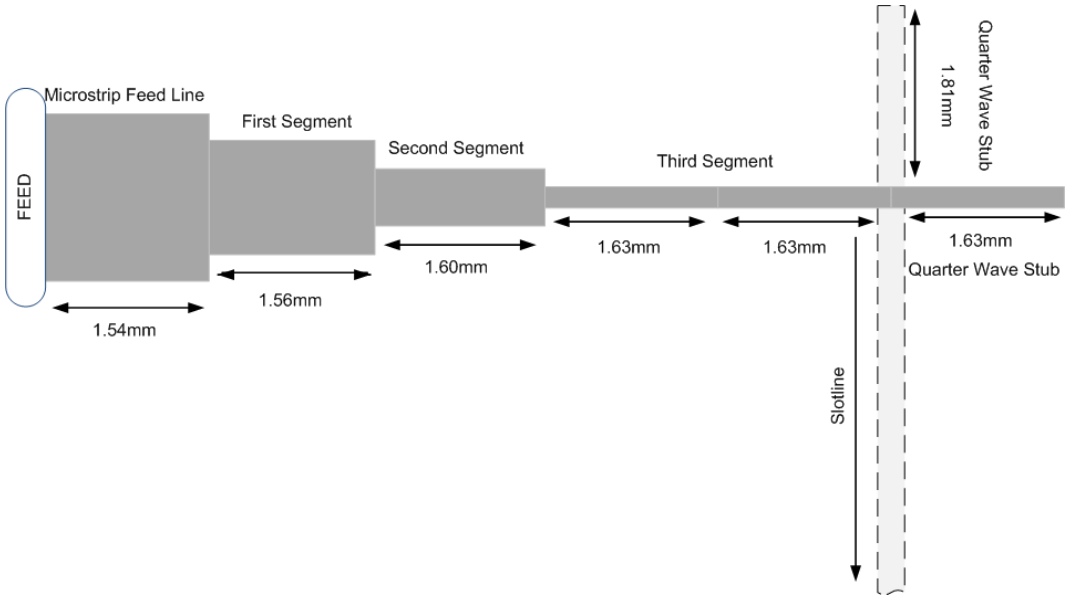

Figure 7 Final dimensions of the microstrip line to slot line transition

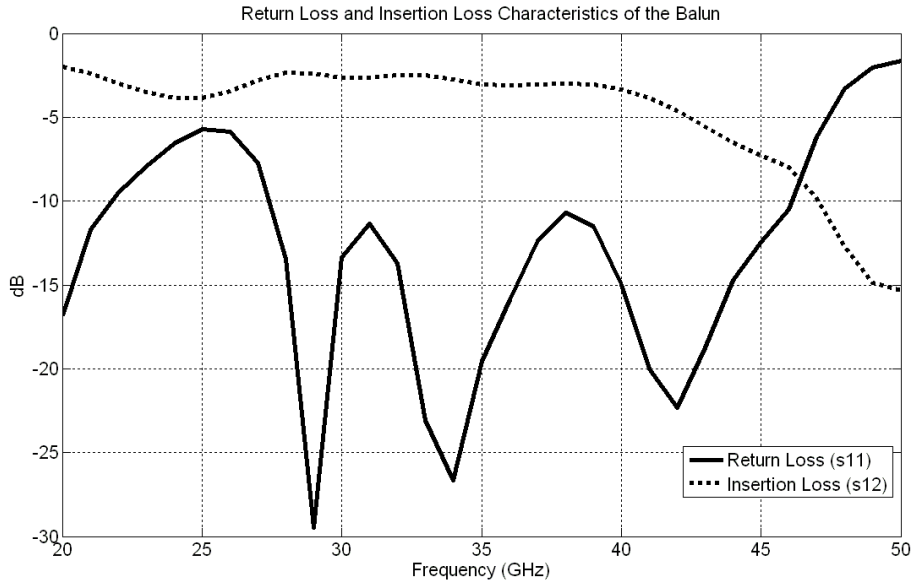

Figure 8 Simulation results of the microstrip line to slot line transition

2.3. Parametric Study of LTSA

A linearly tapered slot antenna (LTSA) consists of a slot line that gets wider linearly through the antenna length. As shown in Figure 9, there are basically three main parameters that determine the radiation characteristics of a LTSA. These are:

- Antenna length (L)
- Aperture width (W)
- Ground extension (H)

In order to determine the behavior of the radiation pattern with the changes in these three parameters, a parametric study has been carried out, where one of these parameters are changed and the other two are kept constant.

It is stated in [10] that for an LTSA to have endfire beam with no split in the beam, the antenna length should be longer than three wavelengths at the center frequency. Hence, for the antenna length four different values ($3\lambda_0$, $4\lambda_0$, $5\lambda_0$, $6\lambda_0$) are considered during the parametric study. According to [7], for an LTSA to radiate efficiently, the aperture width of the antenna should be larger than half wavelength at the center frequency. Two aperture width values are chosen as $\lambda_0/2$ and λ_0 for this purpose. Finally, three different values (λ_0, $3\lambda_0/2$, $2\lambda_0$) for the ground extension parameter are studied. In summary, LTSA configurations having totally 24 (4x2x3) different parameters are modeled and simulated at 35 GHz to observe the variations in the radiation characteristics of the antenna. Directivity, E-plane and H-plane half-power beamwidths and E-plane and H-plane first sidelobe levels are compared and the effects of antenna length, aperture width and ground extension on these antenna performance measures are observed. These parametric study results are also compared with the parametric study data of an air substrate LTSA presented in [10].

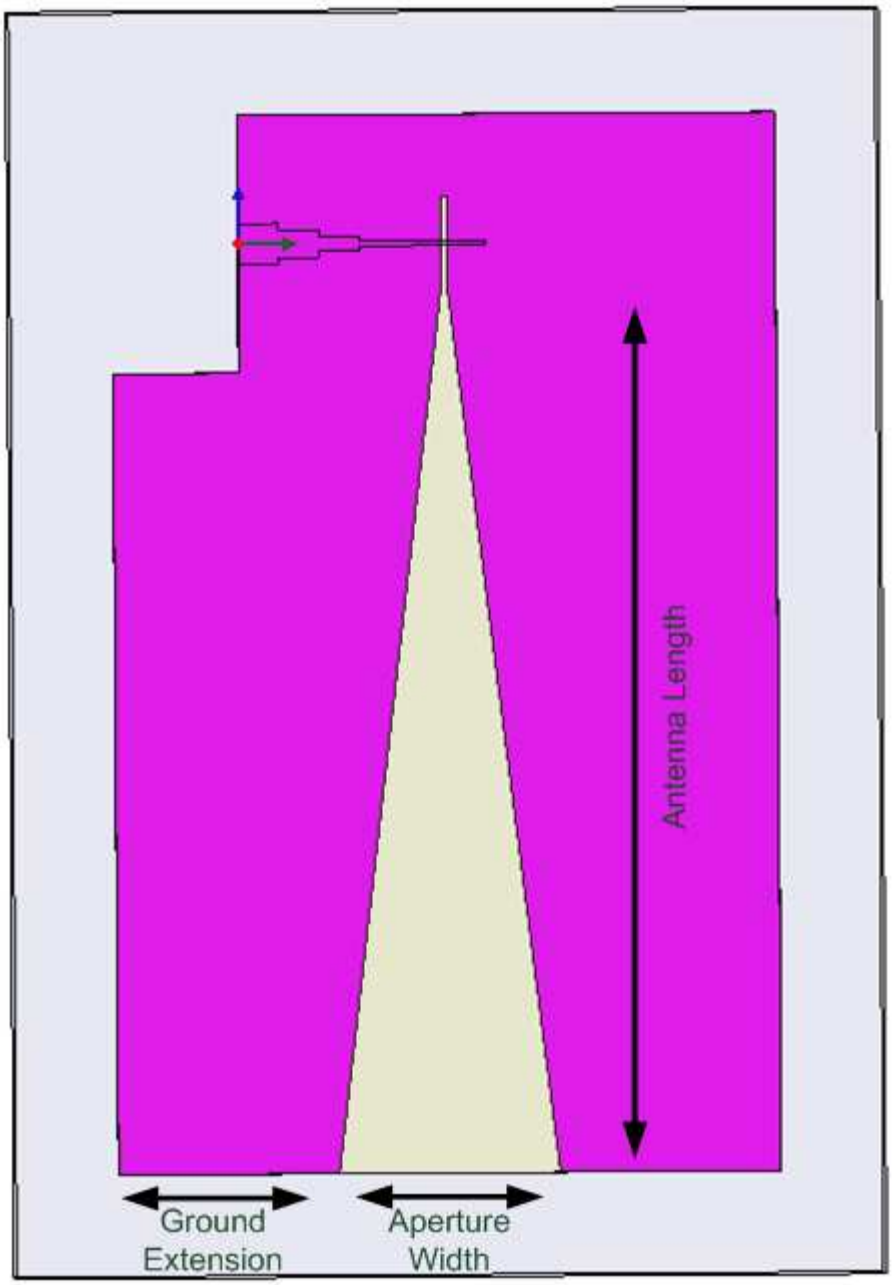

Figure 9 The geometry of LTSA

The simulation results are summarized in Table 4 in which the varying parameters of the antenna are given in terms of λ_0=8.57mm at 35GHz. The rows that are shown shaded in Table 4 correspond to configurations that deviate from the endfire antenna characteristics because of having tilted or split beams. When the aperture width is small and the antenna is long, the amount of tapering along the antenna becomes insufficient and the travelling wave can not properly detach from the antenna to

cause an endfire radiation. The flare angle, which is the angle between two arms of the LTSA is below 6^0 for these three configurations. The results in Table 4 are presented such that the effects of variations in the antenna length could be easily observed. When the antenna length is increased, the antenna is expected to be more directive. It is observed that the H-plane half power beamwidth decreases with increasing antenna length. This result stems from the fact that as the antenna length is increased with aperture width is kept constant, the flare angle decreases and the e-field distribution along the aperture approaches a uniform field distribution. The E-plane beamwidth also generally decreases with increasing antenna length, with some exceptions as in W=0.5 λ_0 and H=1 λ_0 case. Therefore these observations are consistent with initial expectations. When the effects on the sidelobe levels are studied, it is observed that H-plane sidelobe level slightly increase with increasing antenna length. The flare angle again is the reason of this increase in sidelobe level. As the flare angle decreases, the E-field along the aperture gets more uniform resulting in a higher sidelobe level. On the other hand, when the E-plane sidelobe levels are investigated it is observed that the sidelobe level in this plane depends also on the width of the aperture. For the case of W=0.5 λ_0, the E-plane sidelobe levels increase as the antenna length increases while for W=1 λ_0, the E-plane sidelobe level decreases with increasing length. Since the E-plane is parallel along the width of the aperture, a dependence on the width is expected for this plane. For narrow apertures, the flare angle will be the dominant parameter that affects the amount of tapering along the aperture. However for wider apertures, the increase in the amount of tapering due to the increase in the antenna length becomes more effective then the decrease in the amount of tapering due to decreasing flare angle.

Table 4 Parametric study results for the LTSA

W	H	L	Directivity (dB)	E-plane HPBW (degrees)	H-plane HPBW (degrees)	E-plane SLL (dB)	H-plane SLL (dB)
0.5	1	3	10,24	26	34	-4,19	-8,92
		4	10,03	37	27	-7,53	-8,54
		5	8,96	48	22	-5,38	-5,74
		6	8,13	44	21	-3,85	-1,35
	1.5	3	9,5	40	32	-7,41	-7,62
		4	10,2	30	27	-7,02	-7,82
		5	9,72	34	24	-6,92	-7,57
		6	8,06	45	21	-5,82	-5,52
	2	3	8,91	45	32	-6,85	-7,04
		4	10	33	28	-8	-6,02
		5	10,28	23	26	-4,74	-5,15
		6	9,13	25	23	-4,25	-3,59
1	1	3	11,72	26	34	-15,05	-9,16
		4	12,51	24	30	-12,15	-9,64
		5	12,83	23	26	-12,73	-9,82
		6	12,14	23	26	-12,56	-8,97
	1.5	3	10,94	38	33	-12,96	-8,13
		4	12,05	28	29	-13,04	-7,84
		5	12,65	24	26	-16,94	-7,63
		6	12,55	22	23	-15,77	-7,66
	2	3	10,94	40	34	-13,49	-8,95
		4	11,49	34	27	-14,49	-8,5
		5	12,31	29	26	-15,27	-7,02
		6	12,69	21	25	-16,55	-6,29

To demonstrate the changes in the radiation pattern of the antenna with respect to variations in the antenna length, E-plane and H-plane patterns for three different L values are plotted respectively in Figure 10 and Figure 11 for $W=\lambda_0$, $H=1.5\lambda_0$.

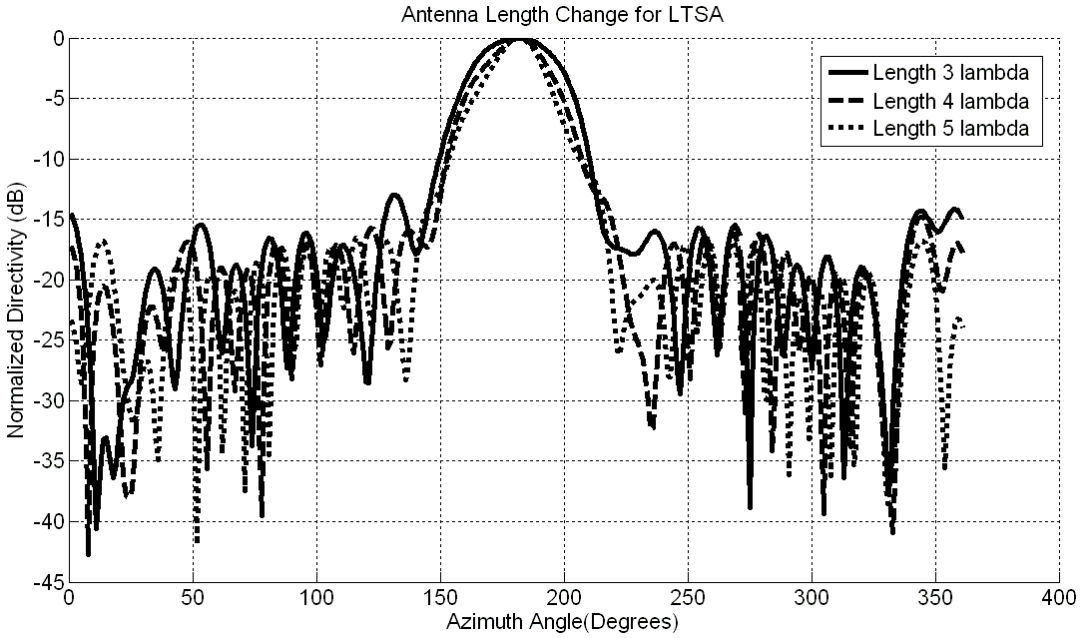

Figure 10 Effect of antenna length variations on E-Plane pattern for LTSA

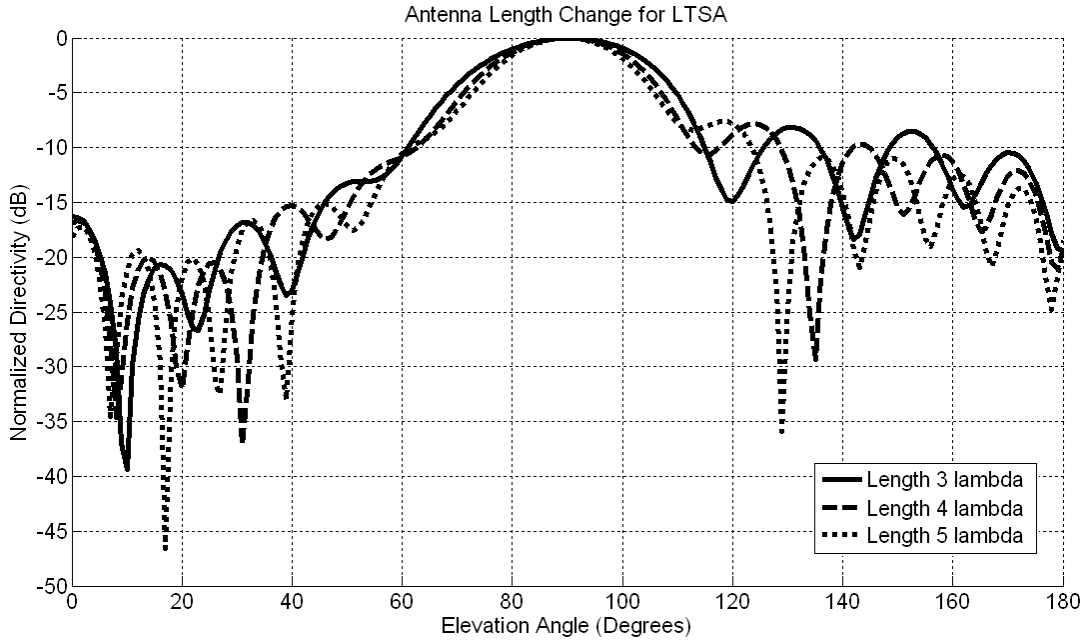

Figure 11 Effect of antenna length variations on H-Plane pattern for LTSA

In order to easily observe the effects of the aperture width parameter on E-plane and H-plane radiation patterns, Table 4 is rearranged as Table 5.

Table 5 Effects of the aperture width parameter variations for LTSA

L	H	W	Directivity (dB)	E-plane HPBW (degrees)	H-plane HPBW (degrees)	E-plane SLL (dB)	H-plane SLL (dB)
3	1	0.5	10,24	26	34	-4,19	-8,92
		1	11,72	26	34	-15,05	-9,16
	1.5	0.5	9,5	40	32	-7,41	-7,62
		1	10,94	38	33	-12,96	-8,13
	2	0.5	8,91	45	32	-6,85	-7,04
		1	10,94	40	34	-13,49	-8,95
4	1	0.5	10,03	37	27	-7,53	-8,54
		1	12,51	24	30	-12,15	-9,64
	1.5	0.5	10,2	30	27	-7,02	-7,82
		1	12,05	28	29	-13,04	-7,84
	2	0.5	10	33	28	-8	-6,02
		1	11,49	34	27	-14,49	-8,5
5	1	0.5	8,96	48	22	-5,38	-5,74
		1	12,83	23	26	-12,73	-9,82
	1.5	0.5	9,72	34	24	-6,92	-7,57
		1	12,65	24	26	-16,94	-7,63
	2	0.5	10,28	23	26	-4,74	-5,15
		1	12,31	29	26	-15,27	-7,02
6	1	0.5	8,13	44	21	-3,85	-1,35
		1	12,14	23	26	-12,56	-8,97
	1.5	0.5	8,06	45	21	-5,82	-5,52
		1	12,55	22	23	-15,77	-7,66
	2	0.5	9,13	25	23	-4,25	-3,59
		1	12,69	21	25	-16,55	-6,29

Increasing the aperture width of the antenna from $0.5\lambda_0$ to λ_0 decreases the E-plane beamwidth while increasing the H-plane beamwidth slightly. The E-plane sidelobe level is decreased significantly with an increase in aperture width. H-plane sidelobe level also decreases as aperture width increases although the decrease is not as significant as the decrease in the E-plane sidelobe level. As mentioned earlier, the variations on the aperture width is expected to cause significant changes in E-plane radiation pattern. A wider aperture results in a narrower beamwidth with lower sidelobe levels for the E-plane pattern. The effects of aperture width variations on the H-plane radiation pattern are again through the changes in the flare angle and the change in the E-field distribution that deviates from uniform field distribution. For a fixed antenna length, the flare angle increases with increasing aperture width. Therefore the amount of tapering increases with the aperture width that result in a wider beamwidth with lower sidelobe levels in the H-plane. According to [10], an increase in aperture width of the air LTSA decreases the E-plane beamwidth and E-plane sidelobe level for longer antennas as also seen here. For short antennas, with increasing aperture width, E-plane beamwidth remains the same and E-plane sidelobe level decreases which is also the case here for an antenna length of $3\lambda_0$. The H-plane beamwidth and H-plane sidelobe level are almost constant in [10] which is also not contradictory with the data here since the changes in H-plane beamwidth and sidelobe level are not significant.

The effects of aperture width variations on the E-plane and H-plane radiation patterns for $L=5\lambda_0$ and $H=1.5\lambda_0$ are given in Figure 12 and Figure 13, respectively.

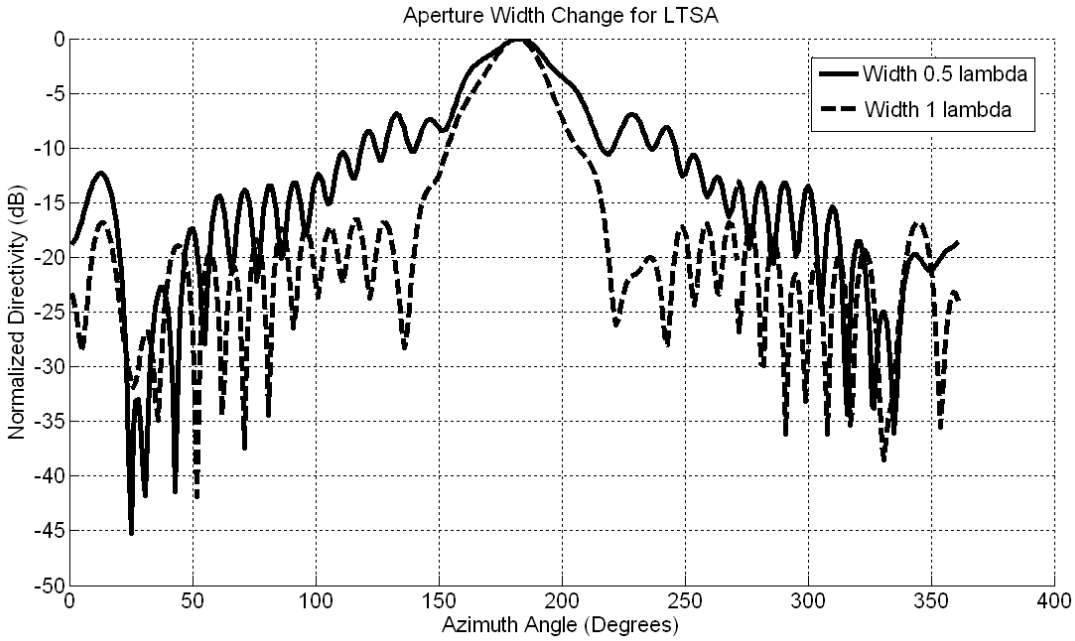

Figure 12 Effect of aperture width variations on E-Plane pattern for LTSA

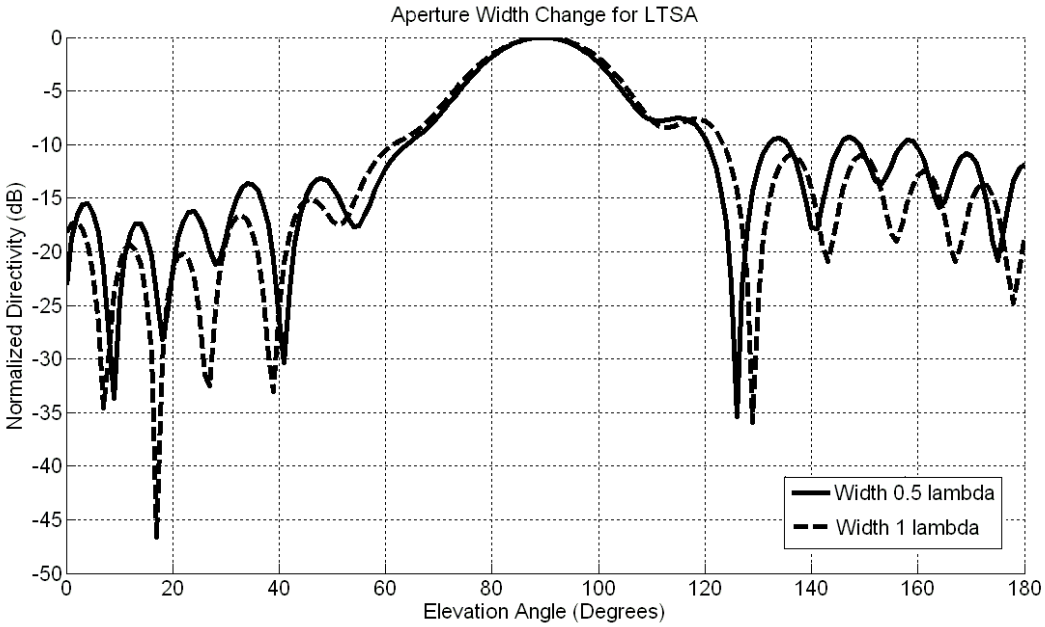

Figure 13 Effect of aperture width variations on H-Plane pattern for LTSA

Table 6 is utilized to analyze the radiation characteristics of the antenna with respect to ground extension (H) parameter. A consistent and regular impact of the ground extension parameter on the radiation pattern of the antenna could not be observed as

reported in [10]. However, it should be noted that the ground extension parameter needs to be properly chosen to meet the required specifications of an antenna to be designed.

Table 6 Effects of the ground extension parameter variations for LTSA

L	W	H	Directivity (dB)	E-plane HPBW (degrees)	H-plane HPBW (degrees)	E-plane SLL (dB)	H-plane SLL (dB)
		1	10,24	26	34	-4,19	-8,92
		1,5	9,5	40	32	-7,41	-7,62
	0,5	2	8,91	45	32	-6,85	-7,04
		1	11,72	26	34	-15,05	-9,16
		1,5	10,94	38	33	-12,96	-8,13
3	1	2	10,94	40	34	-13,49	-8,95
		1	10,03	37	27	-7,53	-8,54
		1,5	10,2	30	27	-7,02	-7,82
	0,5	2	10	33	28	-8	-6,02
		1	12,51	24	30	-12,15	-9,64
		1,5	12,05	28	29	-13,04	-7,84
4	1	2	11,49	34	27	-14,49	-8,5
		1	8,96	48	22	-5,38	-5,74
		1,5	9,72	34	24	-6,92	-7,57
	0,5	2	10,28	23	26	-4,74	-5,15
		1	12,83	23	26	-12,73	-9,82
		1,5	12,65	24	26	-16,94	-7,63
5	1	2	12,31	29	26	-15,27	-7,02
		1	8,13	44	21	-3,85	-1,35
		1,5	8,06	45	21	-5,82	-5,52
	0,5	2	9,13	25	23	-4,25	-3,59
		1	12,14	23	26	-12,56	-8,97
		1,5	12,55	22	23	-15,77	-7,66
6	1	2	12,69	21	25	-16,55	-6,29

For three different values of the ground extension parameter, the E-plane and H-plane radiation patterns for an antenna with W=0.5 λ_0 and L=4 λ_0 are presented in Figure 14 and Figure 15, respectively.

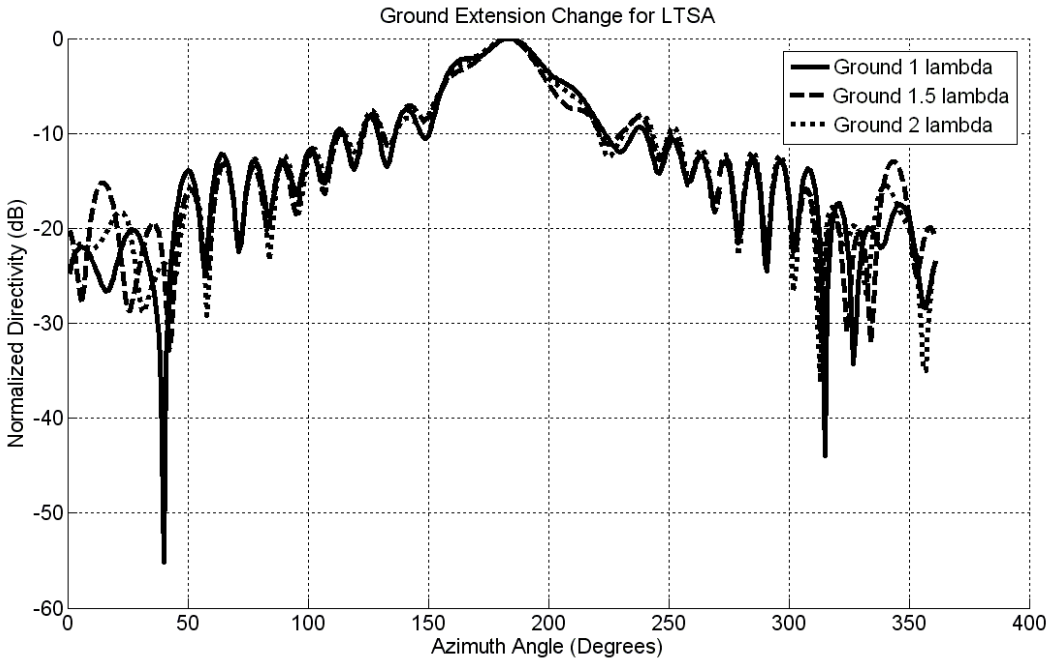

Figure 14 Effect of ground extension variations on E-Plane pattern for LTSA

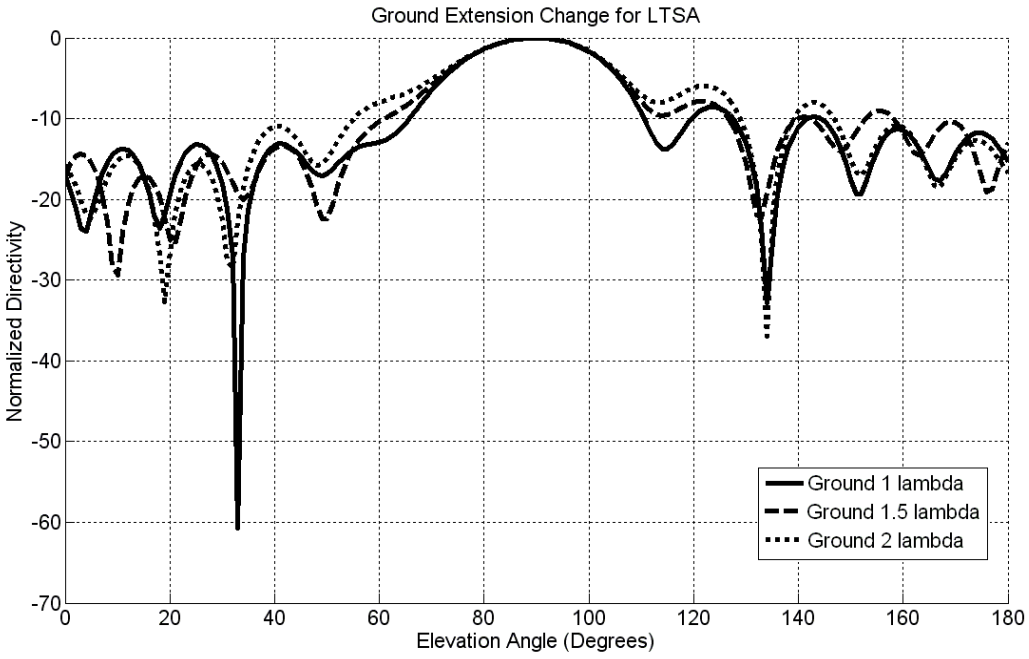

Figure 15 Effect of ground extension variations on H-Plane pattern for LTSA

2.4. Parametric Study of CWSA

The CWSA is a kind of tapered slot antenna for which the width of the radiating slot is constant over the antenna length. Since the slot line that feeds the antenna is generally narrow, there should be a tapering section between the feeding slot and the radiating slot in order to achieve better impedance matching. If such a transition is not used, there could be a high return loss due to the abrupt change in the characteristic impedance values. Two kinds of taper profiles for the CWSA are studied here, which are linear tapering and exponential tapering as shown in Figure 16. Although a wider bandwidth with the exponential taper profile is expected, the linear tapering alternative is also considered due to its simplicity in modeling and manufacturing.

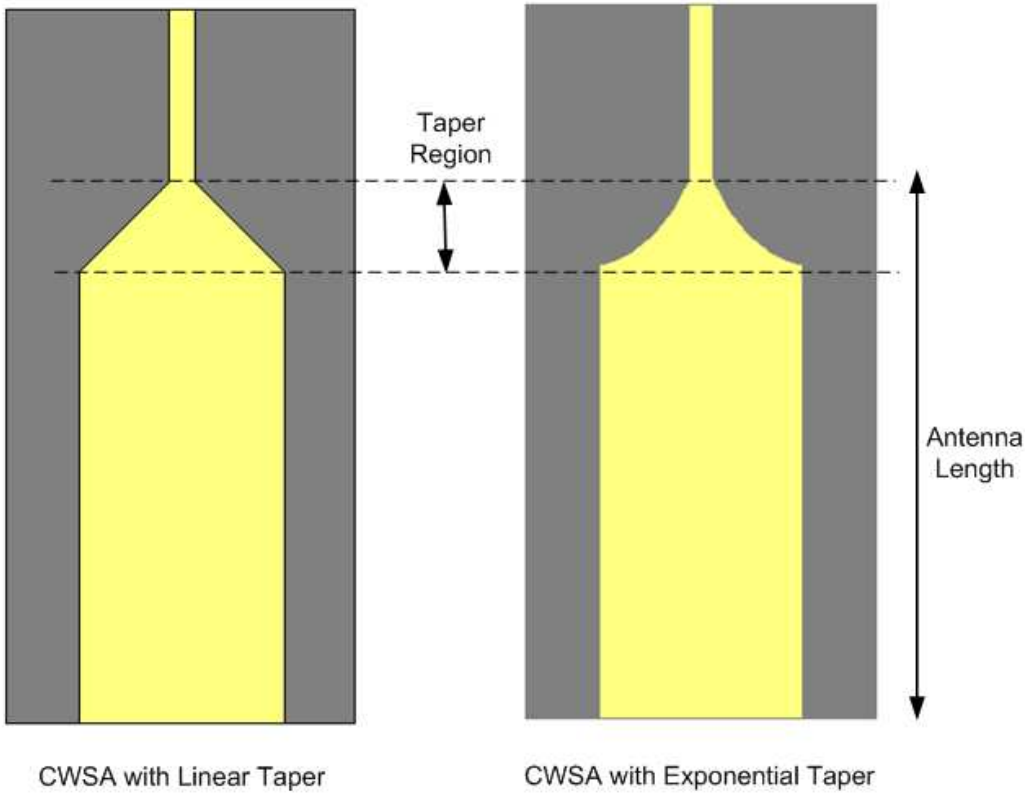

Figure 16 Tapering alternatives for CWSA

During the simulations, it was observed that the taper profile only affects the input return loss characteristics of the antenna and it does not exhibit any impact on the

radiation pattern of the antenna, as expected. Consequently, the parametric study about the radiation characteristics of the antenna was performed only for CWSA with exponential tapering and the layout of the antenna is shown in Figure 17, together with the parameters considered during the parametric analysis. The taper length was chosen to be λ_0 and the taper profile was determined according to the following formula.

$$y = a.e^{bx}$$

where a and b are constants deduced from the start and end points of the parabola and x, y are coordinate axes.

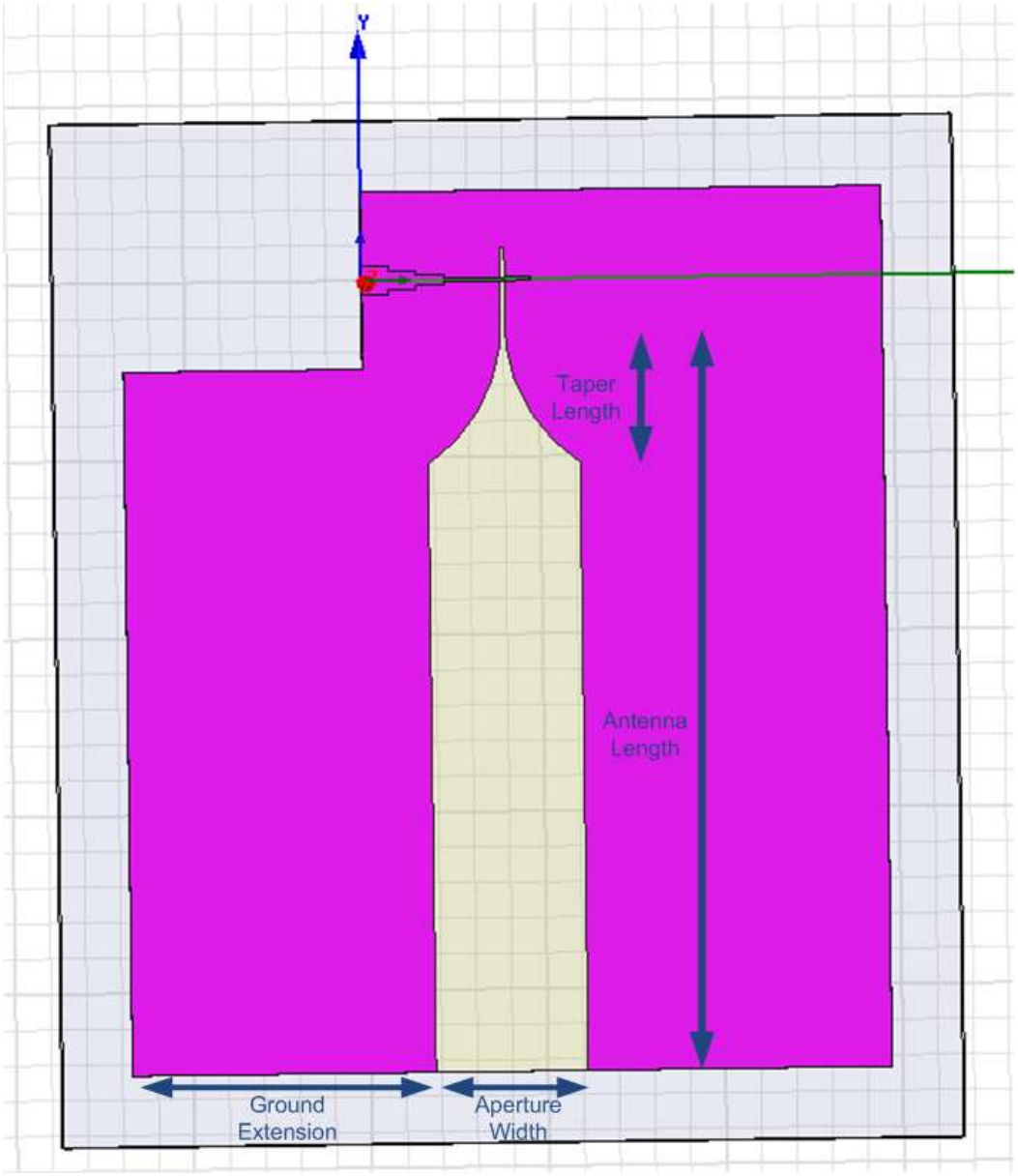

Figure 17 CWSA with Exponential Taper Geometry in HFSS

A parametric study was carried out for the CWSA by changing one of the antenna parameters while keeping the others constant. The parametric study results for CWSA with exponential taper are given in Table 7.

The row that is shaded in gray in Table 7 indicates that the antenna configuration with those parameters has a split beam characteristic so it was not taken into account in determining the effects of parameter changes.

Table 7 Parametric study results for the CWSA with exponential taper

W	H	L	Directivity (dB)	E-plane HPBW (degrees)	H-plane HPBW (degrees)	E-plane SLL (dB)	H-plane SLL (dB)
0.5	1	3	10,77	23	34	-8,12	-9,9
		4	11,06	22	28	-4,77	-11,23
		5	10,55	21	23	-3,31	-9,66
		6	9,08	48	18	-6,99	-5,21
	1.5	3	9,72	35	32	-8,63	-7,35
		4	10,49	22	26	-8,18	-7,77
		5	10,92	19	23	-8,18	-8,05
		6	10,6	19	20	-5,98	-8,76
	2	3	9,04	41	31	-7,57	-7,55
		4	9,71	32	25	-8,3	-5,73
		5	10,58	21	22	-6,29	-4,32
		6	11	15	21	-5,86	-4,38
1	1	3	9,71	20	32	-8,87	-6,85
		4	10,54	18	29	-8,09	-8
		5	11,14	16	25	-7,68	-9,88
		6	11,16	15	23	-4,78	-12,56
	1.5	3	8,55	32	29	-9,51	-5,62
		4	9,31	23	25	-7,27	-4,71
		5	10,05	17	23	-6,97	-4,72
		6	10,81	14	22	-5,34	-6,91
	2	3	8,66	30	30	-9,32	-7,08
		4	8,54	28	25	-7,82	-6
		5	9,06	26	21	-7,07	-4,05
		6	10,19	18	21	-5,88	-3,26

As the length of the antenna increases, the E-plane beamwidth becomes narrower and E-plane sidelobe level increases. The beamwidths in H-plane plane also decrease as the length of the antenna increases. However, a consistent behavior for sidelobe levels in the H-plane with changing antenna length is not observed.

For an antenna with aperture width of λ_0 and ground extension of $1.5\lambda_0$, the effect of antenna length variations on E-plane and H-plane radiation patterns can be seen in Figure 18 and Figure 19, respectively.

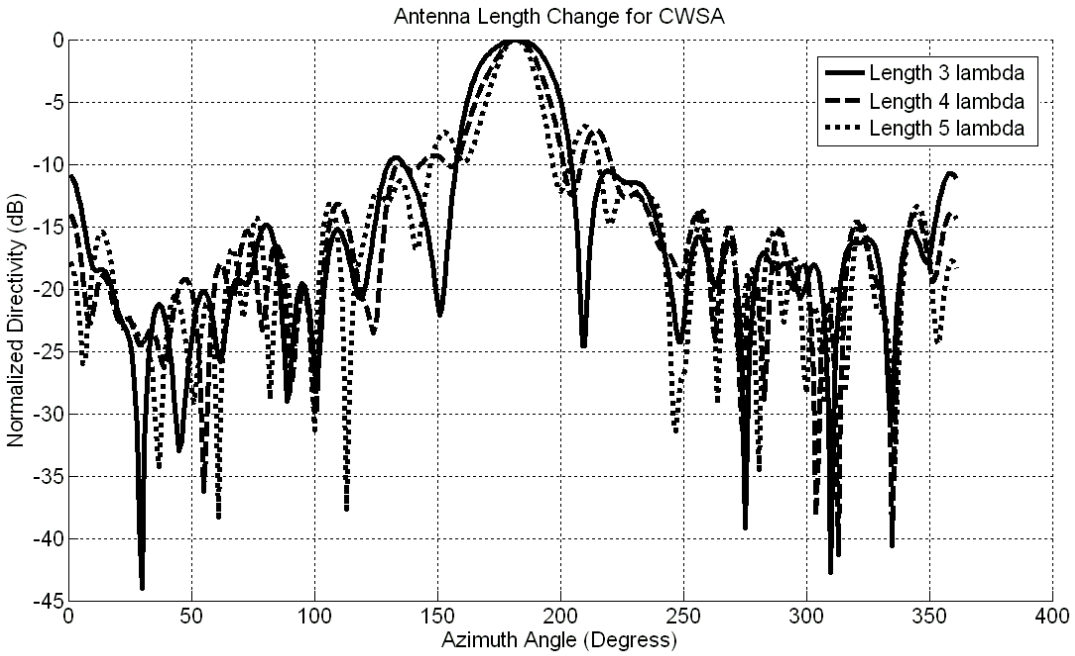

Figure 18 Effect of antenna length variations on E-Plane pattern for CWSA

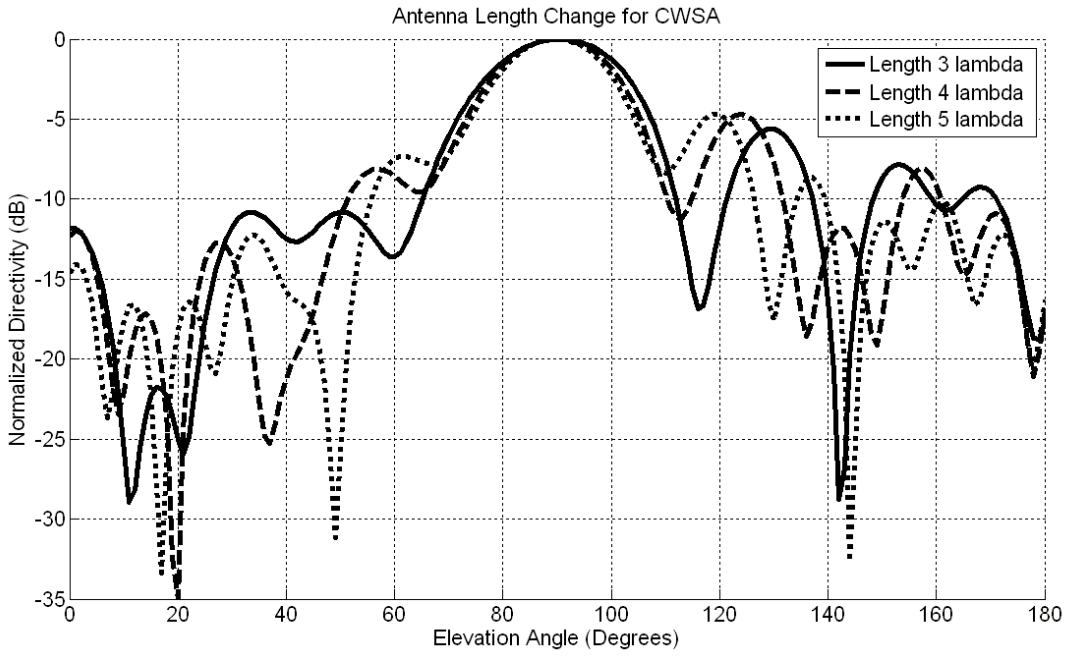

Figure 19 Effect of antenna length variations on H-Plane pattern for CWSA

In order to easily observe the effects of the aperture width parameter on E-plane and H-plane radiation patterns, Table 7 is rearranged as Table 8.

Table 8 Effects of the aperture width change for CWSA

L	H	W	Directivity (dB)	E-plane HPBW (degrees)	H-plane HPBW (degrees)	E-plane SLL (dB)	H-plane SLL (dB)
3	1	0.5	10,77	23	34	-8,12	-9,9
		1	9,71	20	32	-8,87	-6,85
	1.5	0.5	9,72	35	32	-8,63	-7,35
		1	8,55	32	29	-9,51	-5,62
	2	0.5	9,04	41	31	-7,57	-7,55
		1	8,66	30	30	-9,32	-7,08
4	1	0.5	11,06	22	28	-4,77	-11,23
		1	10,54	18	29	-8,09	-8
	1.5	0.5	10,49	22	26	-8,18	-7,77
		1	9,31	23	25	-7,27	-4,71
	2	0.5	9,71	32	25	-8,3	-5,73
		1	8,54	28	25	-7,82	-6
5	1	0.5	10,55	21	23	-3,31	-9,66
		1	11,14	16	25	-7,68	-9,88
	1.5	0.5	10,92	19	23	-8,18	-8,05
		1	10,05	17	23	-6,97	-4,72
	2	0.5	10,58	21	22	-6,29	-4,32
		1	9,06	26	21	-7,07	-4,05
6	1	0.5	9,08	48	18	-6,99	-5,21
		1	11,16	15	23	-4,78	-12,56
	1.5	0.5	10,6	19	20	-5,98	-8,76
		1	10,81	14	22	-5,34	-6,91
	2	0.5	11	15	21	-5,86	-4,38
		1	10,19	18	21	-5,88	-3,26

It is inferred from the parametric study results that an increase in the aperture width decreases the E-plane beamwidth except for long antennas with wide ground extension while it has no significant effect on H-plane beamwidth. The E-plane sidelobe level also decreases with an increase in aperture width for antennas with small length. As the antenna gets longer the E-plane sidelobe level is not much affected by a change in aperture width.

The antenna pattern changes for antenna length of $3\lambda_0$ and ground extension of $2\ \lambda_0$ in E and H-planes due to aperture width change can be seen in Figure 20 and Figure 21, respectively.

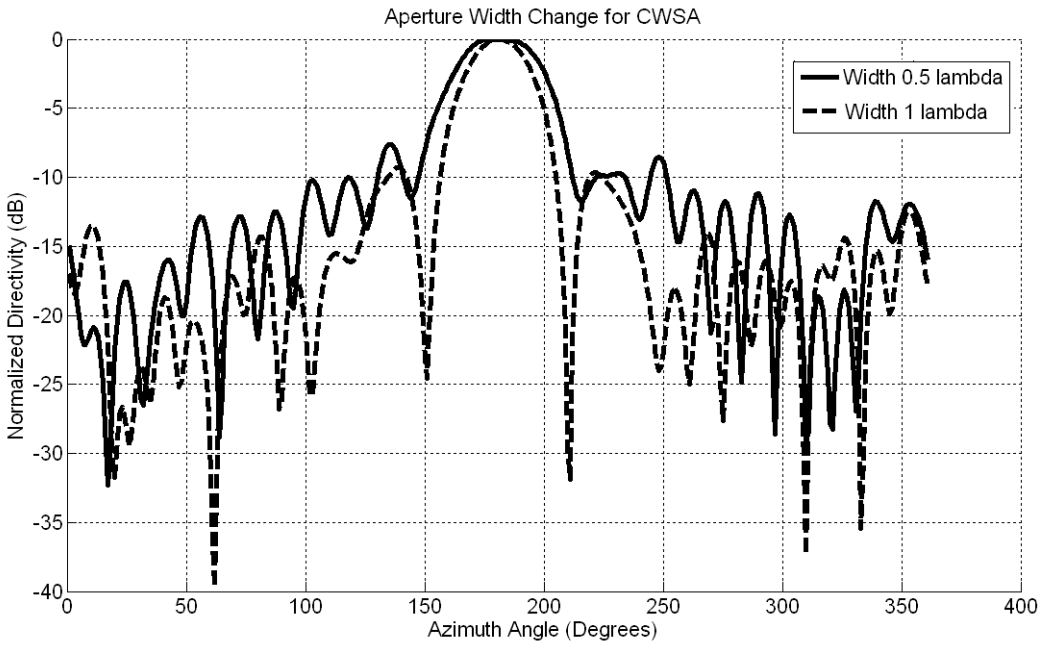

Figure 20 Effect of aperture width variations on E-Plane pattern for CWSA

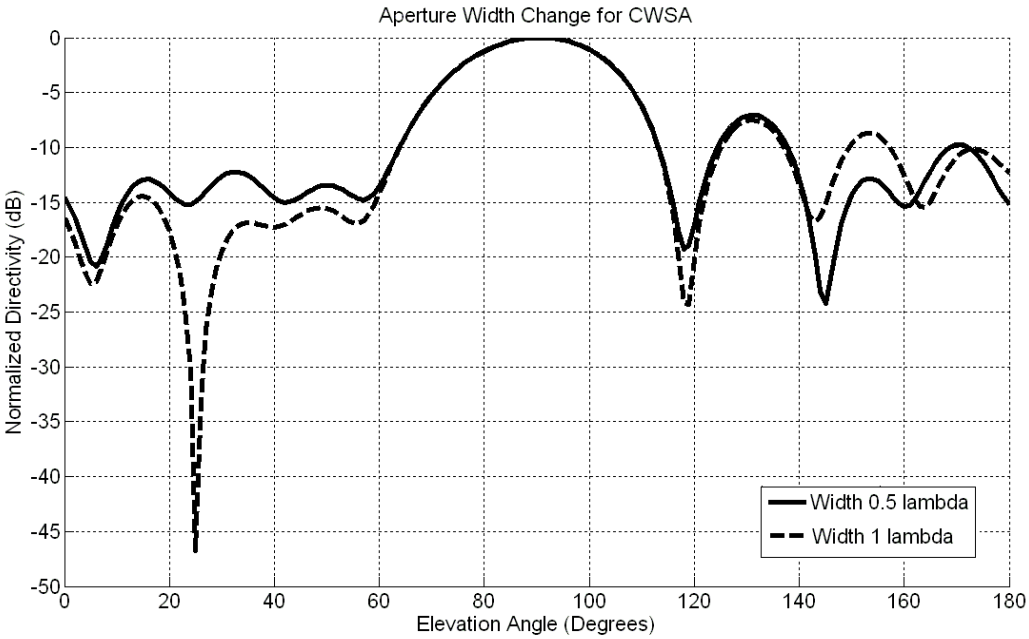

Figure 21 Effect of aperture width variations on H-Plane pattern for CWSA

Table 9 is utilized to interpret the parametric study results in terms of the ground extension parameter (H).

Table 9 Effects of the ground extension parameter for CWSA

L	W	H	Directivity (dB)	E-plane HPBW (degrees)	H-plane HPBW (degrees)	E-plane SLL (dB)	H-plane SLL (dB)
3	0,5	1	10,77	23	34	-8,12	-9,9
		1,5	9,72	35	32	-8,63	-7,35
		2	9,04	41	31	-7,57	-7,55
	1	1	9,71	20	32	-8,87	-6,85
		1,5	8,55	32	29	-9,51	-5,62
		2	8,66	30	30	-9,32	-7,08
4	0,5	1	11,06	22	28	-4,77	-11,23
		1,5	10,49	22	26	-8,18	-7,77
		2	9,71	32	25	-8,3	-5,73
	1	1	10,54	18	29	-8,09	-8
		1,5	9,31	23	25	-7,27	-4,71
		2	8,54	28	25	-7,82	-6
5	0,5	1	10,55	21	23	-3,31	-9,66
		1,5	10,92	19	23	-8,18	-8,05
		2	10,58	21	22	-6,29	-4,32
	1	1	11,14	16	25	-7,68	-9,88
		1,5	10,05	17	23	-6,97	-4,72
		2	9,06	26	21	-7,07	-4,05
6	0,5	1	9,08	48	18	-6,99	-5,21
		1,5	10,6	19	20	-5,98	-8,76
		2	11	15	21	-5,86	-4,38
	1	1	11,16	15	23	-4,78	-12,56
		1,5	10,81	14	22	-5,34	-6,91
		2	10,19	18	21	-5,88	-3,26

The change in the E-plane beamwidth due to ground extension is dependent also on the antenna length. For antenna lengths below 5 λ_0, increasing the ground extension also increases the E-plane beamwidth. However above 5 λ_0, the E-plane beamwidth is not affected considerably by a change in ground extension. H-plane beamwidth is

not also affected by ground extension changes. For the sidelobe level behavior, it can be said that the E-plane sidelobe level is not affected and the H-plane sidelobe level is increased with an increase in ground extension parameter.

The effect of the ground extension change on antenna pattern for antenna length of 6 λ_0 and aperture width of λ_0 can be observed in Figure 22 and Figure 23, respectively.

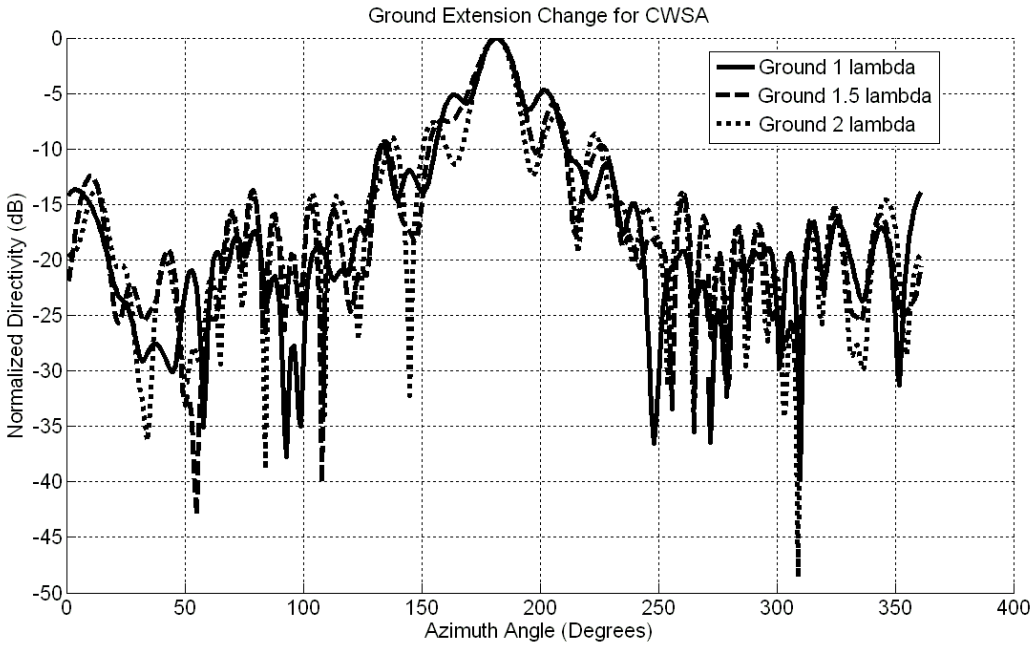

Figure 22 Effect of ground extension variations on E-Plane pattern for CWSA

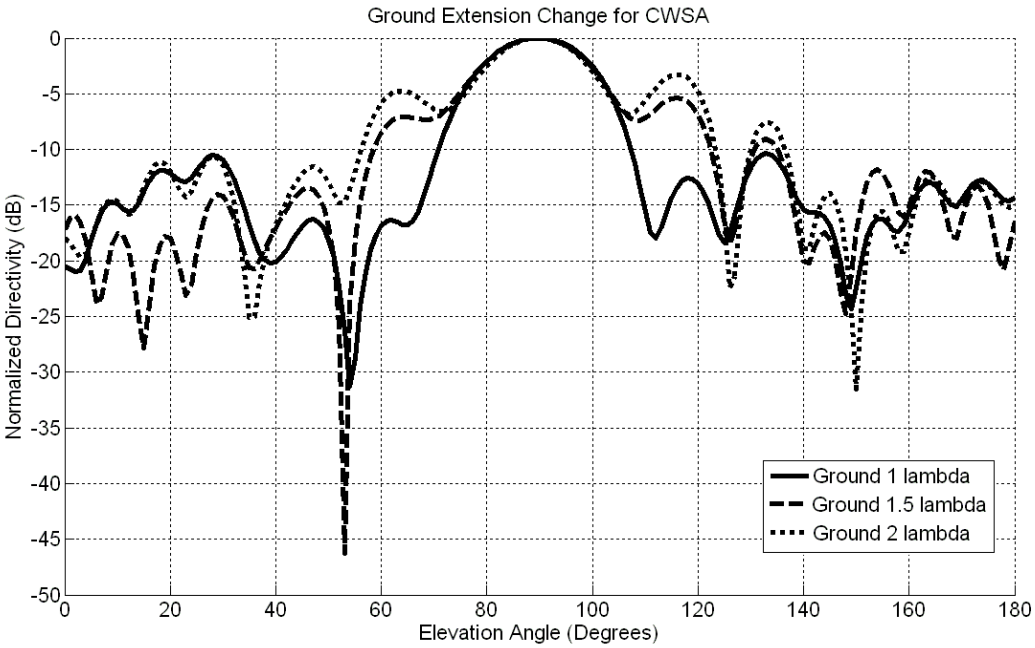

Figure 23 Effect of ground extension variations on H-Plane pattern for CWSA

2.5. Effect of Taper Profile on Bandwidth of CWSA

Since the general behavior of the antenna radiation characteristics with the parameter changes are the same for CWSA with exponential taper and with linear taper, only their bandwidth characteristics were compared. The first simulated configuration is a CWSA having an antenna length of $3\lambda_0$, aperture width of 1 λ_0 and ground extension of 1 λ_0. The return loss graphs of CWSA with linear taper and CWSA with exponential taper are given in Figure 24. As seen in Figure 24, the return loss value of the CWSA with exponential taper profile is below that of CWSA with linear taper profile in the whole band of 25-45 GHz except a narrow frequency region near 30 GHz. For frequencies near 35 GHz, the usable bandwidth that the return loss value is below -10dB is the same for both types of taper profiles of CWSA. The exponential taper configuration has also a usable bandwidth between below 25GHz to nearly 29 GHz and an acceptable return loss value between 37.5 GHz and 45 GHz.

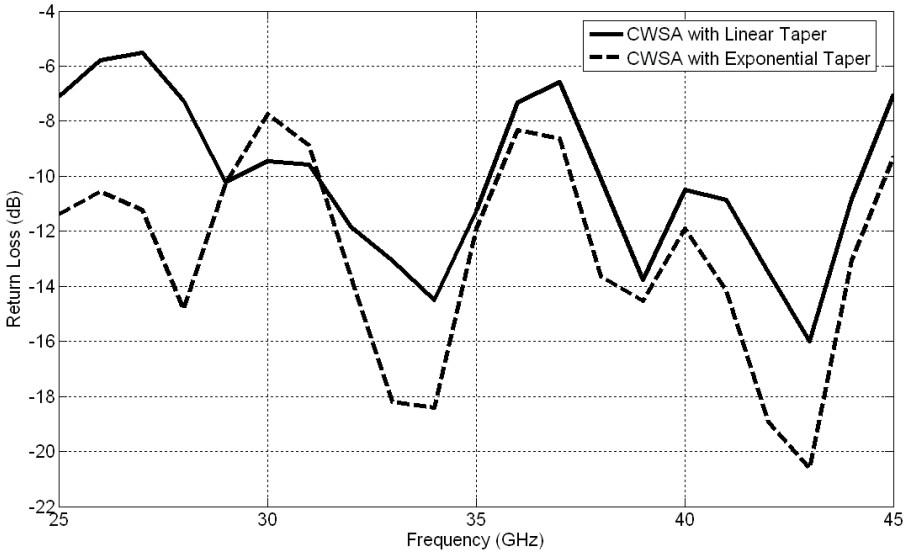

Figure 24 Bandwidth comparison of CWSAs with exponential and linear taper with L=3λ_0, W=1 λ_0, H=1 λ_0

Another antenna with antenna length of 5λ_0, aperture width of 0.5λ_0 and ground extension of λ_0 was considered to investigate an example with narrow aperture. As seen in Figure 25, the return loss behaviors of linearly and exponentially tapered antennas do not differ significantly over the 25-45 GHz band for the antenna with aperture width of 0.5λ_0. This is an expected result since linear and exponential taper profiles start to resemble each other as the width of the antenna becomes smaller.

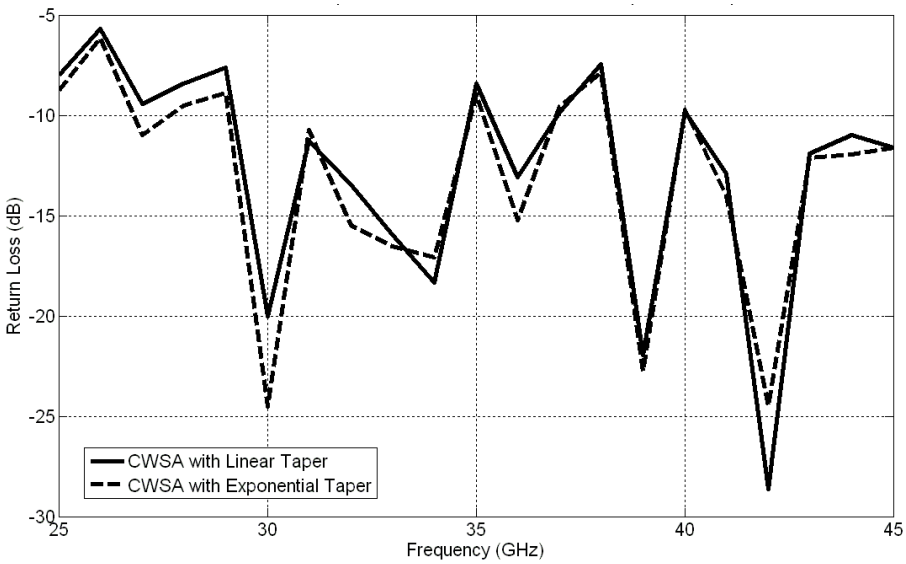

Figure 25 Bandwidth comparison of CWSAs with exponential and linear taper with L=5λ_0, W=0.5 λ_0, H=1 λ_0

To observe the effect of the taper on antenna bandwidth for longer antennas, another simulation was carried out for a CWSA with antenna length of $6\lambda_0$, aperture width of λ_0 and ground extension of $1.5\lambda_0$. As seen in Figure 26, again the exponentially tapered antenna has lower return loss values compared to the linearly tapered antenna. Only the exponentially tapered CWSA can be utilized for lower frequency bands like 25-29 GHz.

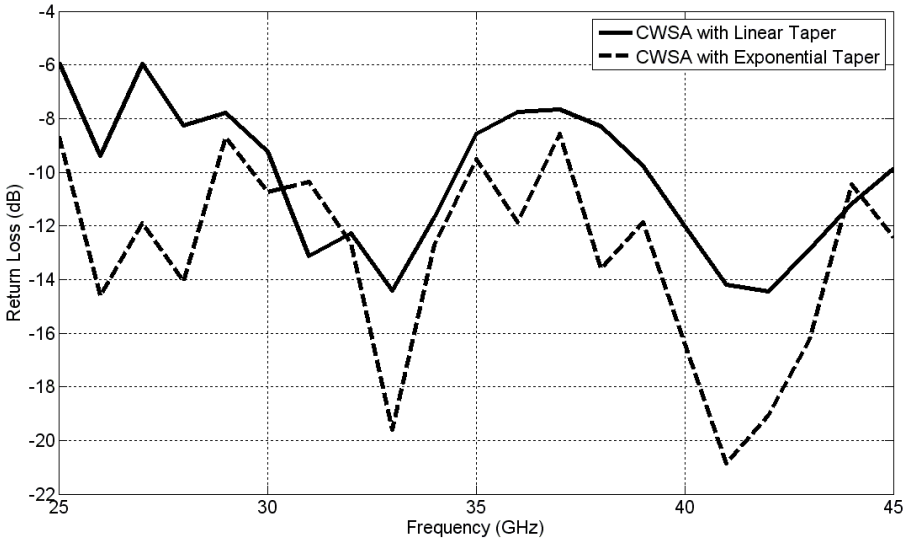

Figure 26 Bandwidth comparison of CWSAs with exponential and linear taper with L=6λ_0, W=1 λ_0, H=1.5 λ_0

CHAPTER 3

RECONFIGURABILITY IN THE RADIATION PATTERN OF TAPERED SLOT ANTENNAS

As mentioned in Chapter 1, one of the aims of this study is to provide pattern reconfigurability between an LTSA and a CWSA at 35 GHz. Up to now, the LTSA and CWSA designs and antenna patterns were studied with respect to variations in antenna parameters. These parametric study results were discussed and general conclusions about design of LTSA and CWSA were derived. In this chapter, the radiation patterns of LTSA and CWSAs will be compared to each other.

3.1. LTSA-CWSA Pattern Comparison and Reconfigurability

In the parametric study, LTSA simulation results were compared with other LTSA results, same is also true for CWSA. To obtain pattern reconfigurability between these two types of antennas, the antenna patterns of the two kinds, LTSA and CWSA, shall be compared.

The compared antenna configurations should have same antenna parameters like antenna length, aperture width and ground extension in order to achieve efficient switching between different antenna layouts. Both antennas will be fed by using the same microstrip line to slot line transition. Figure 27 illustrates the possible layout of the reconfigurable antenna.

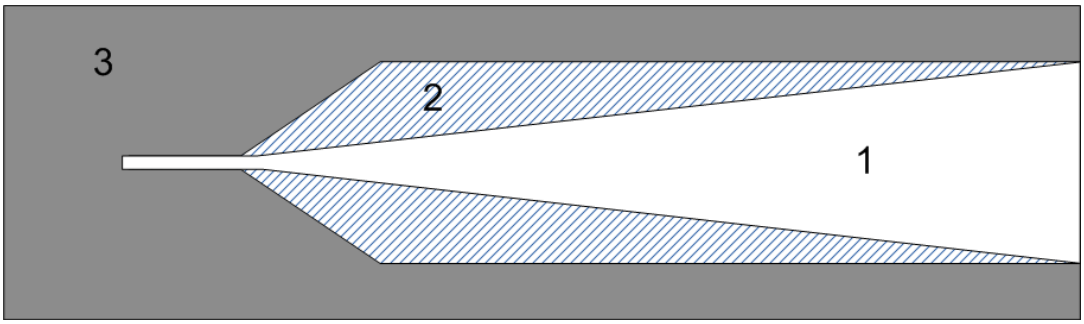

Figure 27 Reconfigurable antenna layout

The region numbered as 1 in Figure 27 contains no metalization so this region is directly the substrate. Region 2 will be formed by a special material that will behave like conductor when excited optically and like an insulator when excitation is not applied, and Region 3 is the metal layer. When Region 2 is not excited, the antenna will have the CWSA configuration. When Region 2 is excited, the antenna will have the LTSA geometry. Hence, excitation of Region 2 provides switching between LTSA and CWSA configurations. The taper region of Region 2 can be designed to be linear or exponential according to the intent of taper profile in CWSA. The CWSA configurations with exponential taper profile are used instead of linear taper since they provide wider frequency bands.

The special material proposed to be used in Region 2 could be a photosensitive dielectric material like photoconductive polymer or photo-induced plasma in silicon. Recently, these types of photosensitive materials started to be used in various reconfigurable antenna and array applications [23]-[26], since the optical excitation of these materials eliminate the use of bias lines required for the actuation of electronic control components utilized in conventional reconfigurable antenna structures.

The parametric study results for LTSA and CWSA with exponential taper can be seen in Table 10. For a transition from LTSA configuration to CWSA configuration, the reductions in the E-plane and H-plane beamwidths and the change in the E-plane and H-plane sidelobe levels are presented in the related columns of Table 10. Using the parametric study results, the LTSA configurations that show largest beamwidth

change when compared to CWSA with the same antenna parameters need to be determined.

Table 10 Pattern comparison between LTSA and CWSA

			LTSA				CWSA with Exponential Taper				Reduction in Beamwidth		Increase in SLL	
L	W	H	BW_E	BW_H	SLL_E	SLL_H	BW_E	BW_H	SLL_E	SLL_H	BW_E	BW_H	SLL_E	SLL_H
3	0,5	1	26	34	-4,19	-8,92	23	34	-8,12	-9,9	3	0	-3,93	-0,98
		1,5	40	32	-7,41	-7,62	35	32	-8,63	-7,35	5	0	-1,22	0,27
		2	45	32	-6,85	-7,04	41	31	-7,57	-7,55	4	1	-0,72	-0,51
	1	1	26	34	-15,0	-9,16	20	32	-8,87	-6,85	6	2	6,18	2,31
		1,5	38	33	-12,9	-8,13	32	29	-9,51	-5,62	6	4	3,45	2,51
		2	40	34	-13,4	-8,95	30	30	-9,32	-7,08	10	4	4,17	1,87
4	0,5	1	37	27	-7,53	-8,54	22	28	-4,77	-11,2	15	-1	2,76	-2,69
		1,5	30	27	-7,02	-7,82	22	26	-8,18	-7,77	8	1	-1,16	0,05
		2	33	28	-8	-6,02	32	25	-8,3	-5,73	1	3	-0,3	0,29
	1	1	24	30	-12,1	-9,64	18	29	-8,09	-8	6	1	4,06	1,64
		1,5	28	29	-13,0	-7,84	23	25	-7,27	-4,71	5	4	5,77	3,13
		2	34	27	-14,4	-8,5	28	25	-7,82	-6	6	2	6,67	2,5
5	0,5	1	48	22	-5,38	-5,74	21	23	-3,31	-9,66	27	-1	2,07	-3,92
		1,5	34	24	-6,92	-7,57	19	23	-8,18	-8,05	15	1	-1,26	-0,48
		2	23	26	-4,74	-5,15	21	22	-6,29	-4,32	2	4	-1,55	0,83
	1	1	23	26	-12,7	-9,82	16	25	-7,68	-9,88	7	1	5,05	-0,06
		1,5	24	26	-16,9	-7,63	17	23	-6,97	-4,72	7	3	9,97	2,91
		2	29	26	-15,2	-7,02	26	21	-7,07	-4,05	3	5	8,2	2,97
6	0,5	1	44	21	-3,85	-1,35	48	18	-6,99	-5,21	-4	3	-3,14	-3,86
		1,5	45	21	-5,82	-5,52	19	20	-5,98	-8,76	26	1	-0,16	-3,24
		2	25	23	-4,25	-3,59	15	21	-5,86	-4,38	10	2	-1,61	-0,79
	1	1	23	26	-12,5	-8,97	15	23	-4,78	-12,5	8	3	7,78	-3,59
		1,5	22	23	-15,7	-7,66	14	22	-5,34	-6,91	8	1	10,43	0,75
		2	21	25	-16,5	-6,29	18	21	-5,88	-3,26	3	4	10,67	3,03

When Table 10 is observed, it is seen that most of the configurations exhibit a change in sidelobe levels when a transition from LTSA to CWSA is applied. The

only configuration that has negligible sidelobe level change and a high beamwidth change with the transition is the configuration with antenna length 5λ0, aperture width of 0.5 λ0 and ground extension of 1.5 λ0. The radiation pattern of this configuration for LTSA and CWSA cases can be seen in Figure 28 and Figure 29.

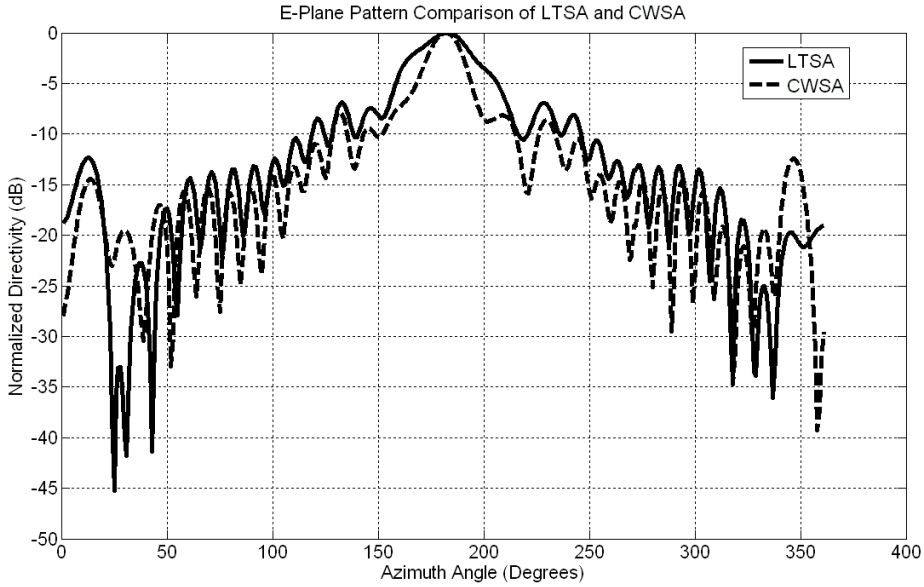

Figure 28 E-Plane pattern comparison for LTSA and CWSA with L=5λ_0, W=0.5λ_0, H=1.5 λ_0

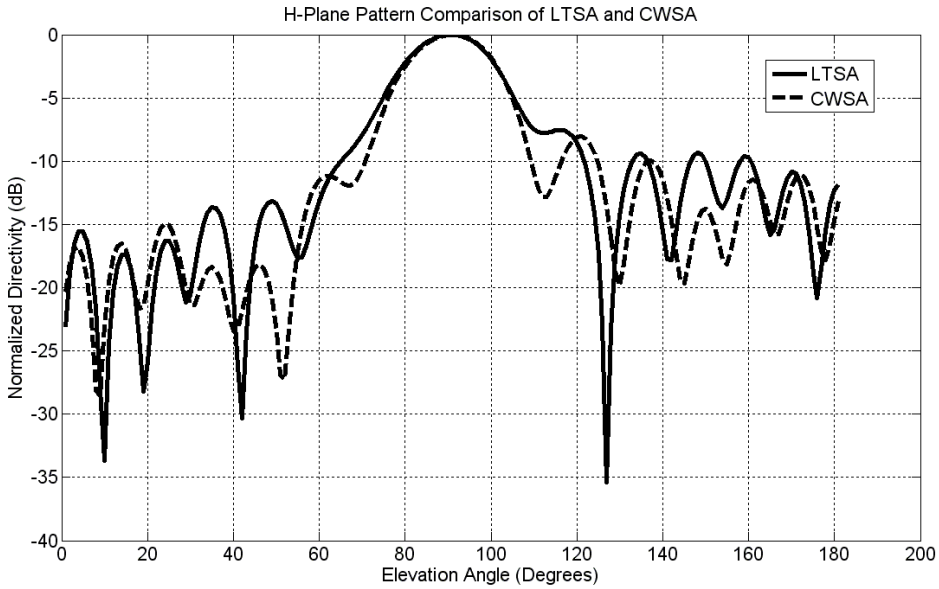

Figure 29 H-Plane pattern comparison for LTSA and CWSA with L=5λ_0, W=0.5 λ_0, H=1.5 λ_0

Since this configuration has high sidelobe levels for LTSA case, other configurations that show higher sidelobe level change were also considered.

It was seen in the parametric study that the sidelobe levels in both planes for an LTSA is highly dependent on aperture width value. Wider aperture width configurations will be utilized for pattern reconfigurability between LTSA and CWSA since LTSAs with wider aperture provide lower sidelobe levels.

One of the configurations that show a high beamwidth change also with sidelobe level change when a transition between LTSA and CWSA occurs is the antenna with antenna length of $3\lambda_0$, aperture width of λ_0 and a ground extension of $2\lambda_0$. The E-plane patterns of LTSA and CWSA having the physical parameters mentioned are plotted in Figure 30. As seen in Figure 30, the CWSA half power beamwidth is smaller than the LTSA case by approximately 10 degrees in E-plane. When the first sidelobe levels of the LTSA and CWSA configurations are compared, it is seen that the sidelobe level is higher as much as approximately 4 dB relative to LTSA configuration. So it can be concluded that when a transition from LTSA to CWSA is provided, the beam will be narrower with a tradeoff of an increased sidelobe level in E-plane.

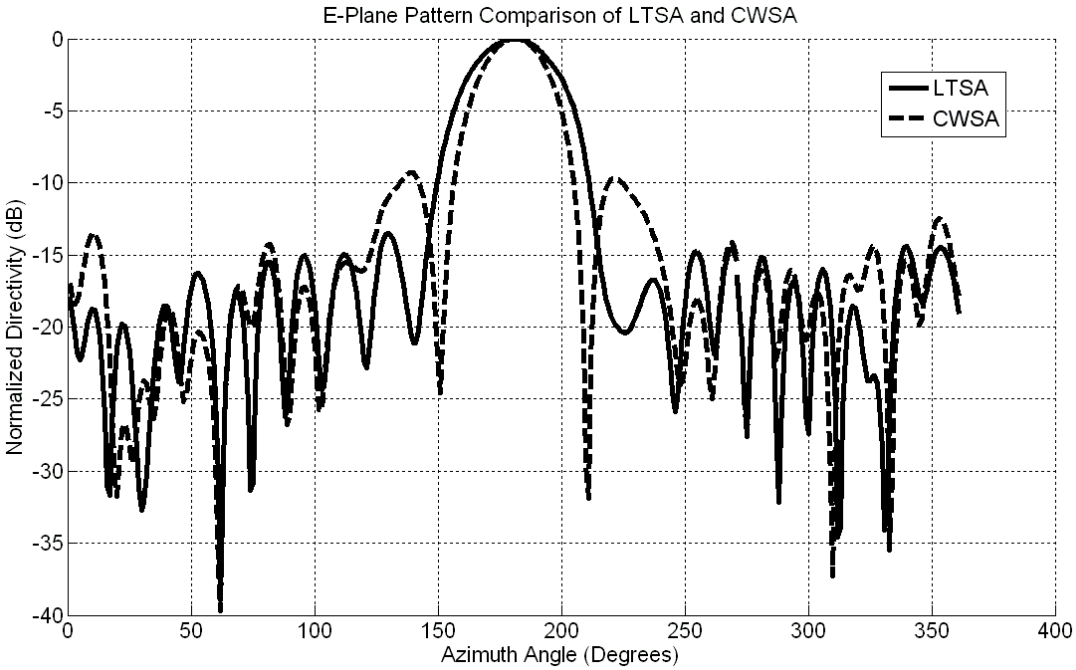

Figure 30 E-Plane pattern comparison for LTSA and CWSA with $L=3\lambda_0$, $W=1\lambda_0$, $H=2\ \lambda_0$

The H-plane pattern comparison for the same configurations is given in Figure 31. The conclusions obtained for the E-plane reconfigurability also holds for the H-plane case. The H-plane beamwidth of CWSA case is smaller as compared to the LTSA case although not as much as E-plane case. The beamwidth difference between two configurations is on the order of 4 degrees. The sidelobe level is slightly larger for CWSA.

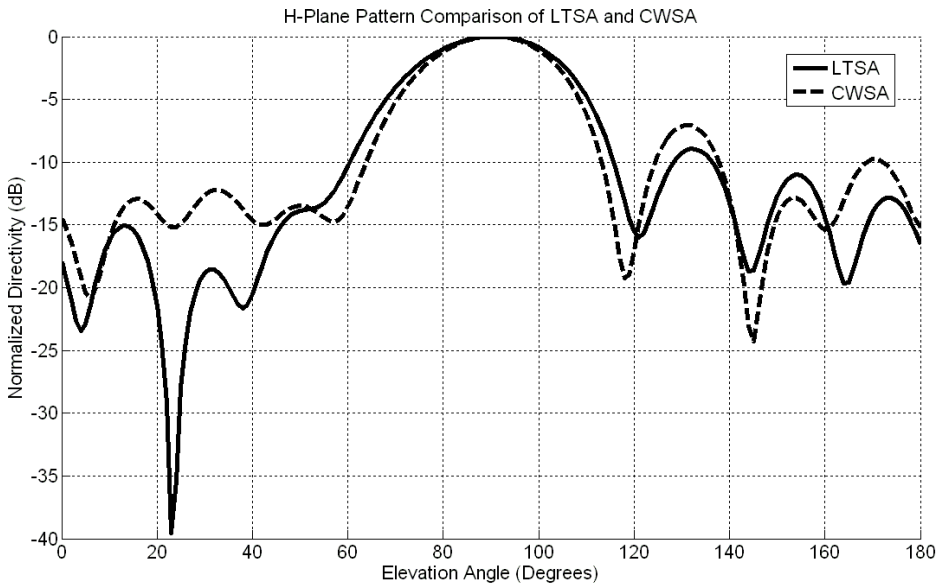

Figure 31 H-Plane Pattern Comparison for LTSA and CWSA for LTSA and CWSA with L=3λ_0, W=1λ_0, H=2 λ_0

Another antenna configuration that exhibits a good variation in pattern with a transition from LTSA to CWSA is the one having an antenna length of $4\lambda_0$, aperture width of $1\lambda_0$ and a ground extension of $1.5\lambda_0$. The E-plane pattern comparison of the LTSA and CWSA with these physical parameters can be seen in Figure 32. The main beam is narrower for the CWSA as compared with LTSA. The difference between the beamwidths of the two antenna types is approximately 5 degrees. If the sidelobe levels between the antennas are observed, it can be seen that the LTSA has a lower sidelobe level of as much as 6dB.

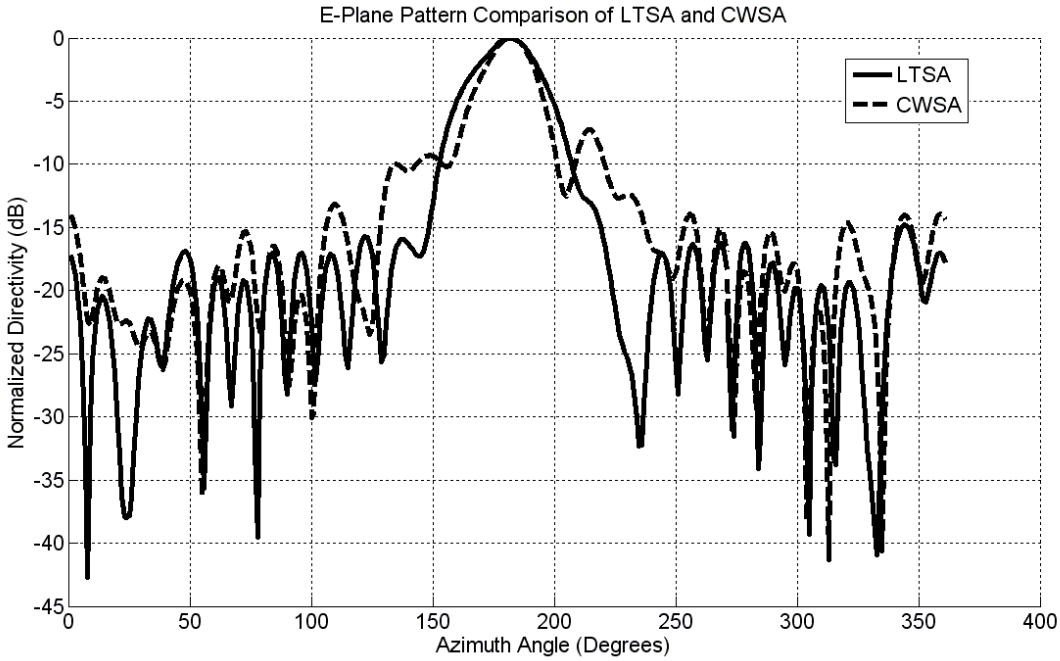

Figure 32 E-Plane Pattern Comparison for LTSA and CWSA for LTSA and CWSA with L=4λ_0, W=1λ_0, H=1.5 λ_0

The H-plane pattern comparison can be seen in Figure 33. A transition from LTSA to CWSA provides a beamwidth decrease of 4 degrees and a sidelobe level rise of 3 dB in H-plane.

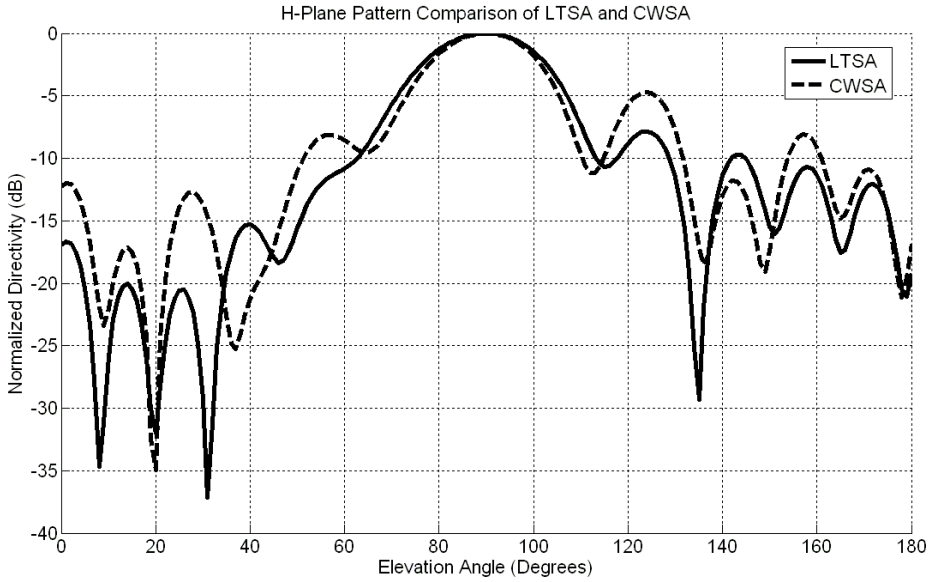

Figure 33 H-Plane Pattern Comparison for LTSA and CWSA for LTSA and CWSA with L=4λ_0, W=1λ_0, H=1.5 λ_0

Another example is the configuration with an antenna length of $5\lambda_0$, an aperture width of 1 λ_0 and a ground extension of 1.5 λ_0. The E-plane and H-plane patterns are shown in Figure 34 and Figure 35, respectively.

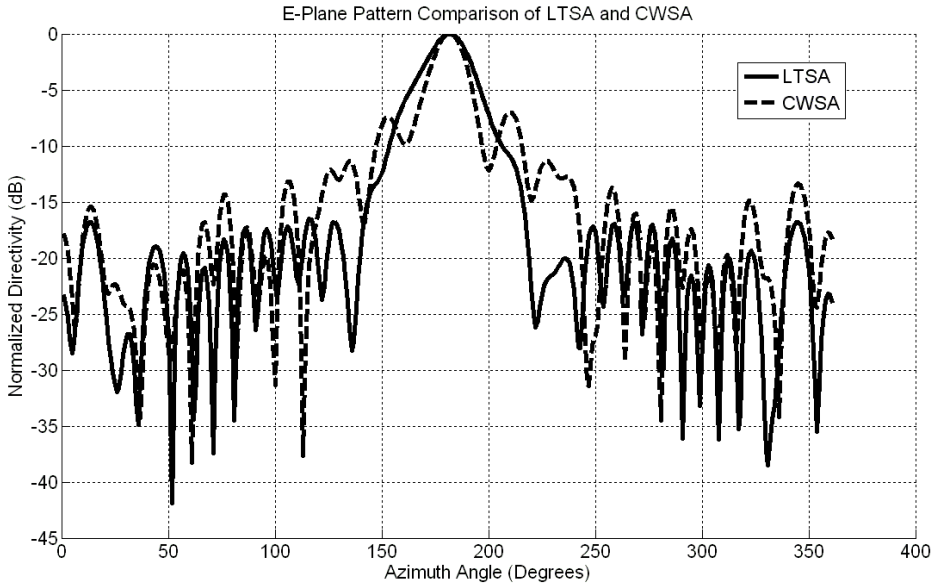

Figure 34 E-Plane Pattern Comparison for LTSA and CWSA with L=5λ_0, W=1λ_0, H=1.5 λ_0

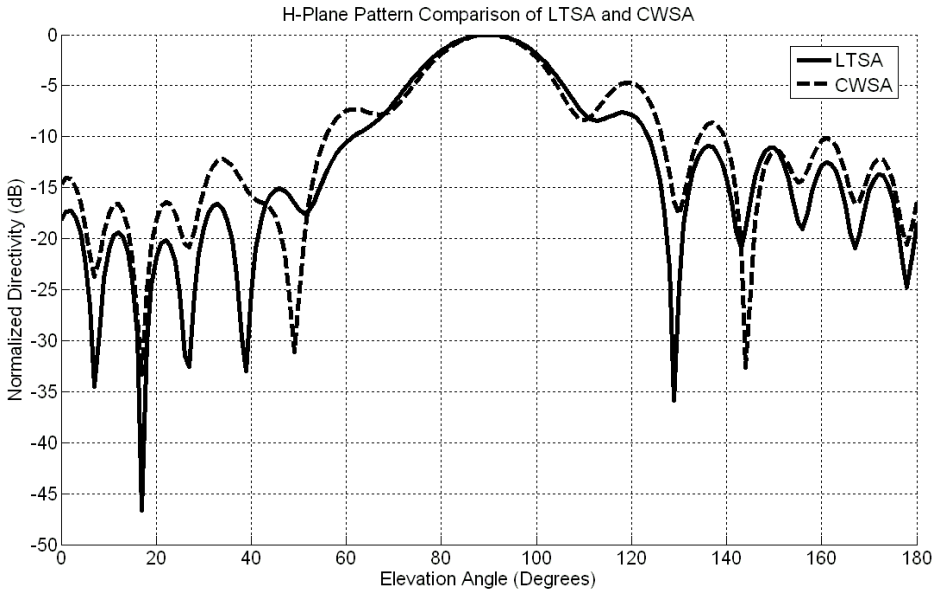

Figure 35 H-Plane Pattern Comparison for LTSA and CWSA with L=5λ_0, W=1λ_0, H=1.5 λ_0

Figure 36 shows the E-plane patterns of the antennas with an antenna length of $6\lambda_0$, an aperture width of $1\lambda_0$ and a ground extension of 1.5 λ_0. The reduction in the beamwidth is about 8 degrees in E-plane pattern. The sidelobe level is as much as 11 dB lower in LTSA case than CWSA. The H-plane patterns of the antennas having these physical properties do not show significant difference between LTSA and CWSA configurations as seen in Figure 37.

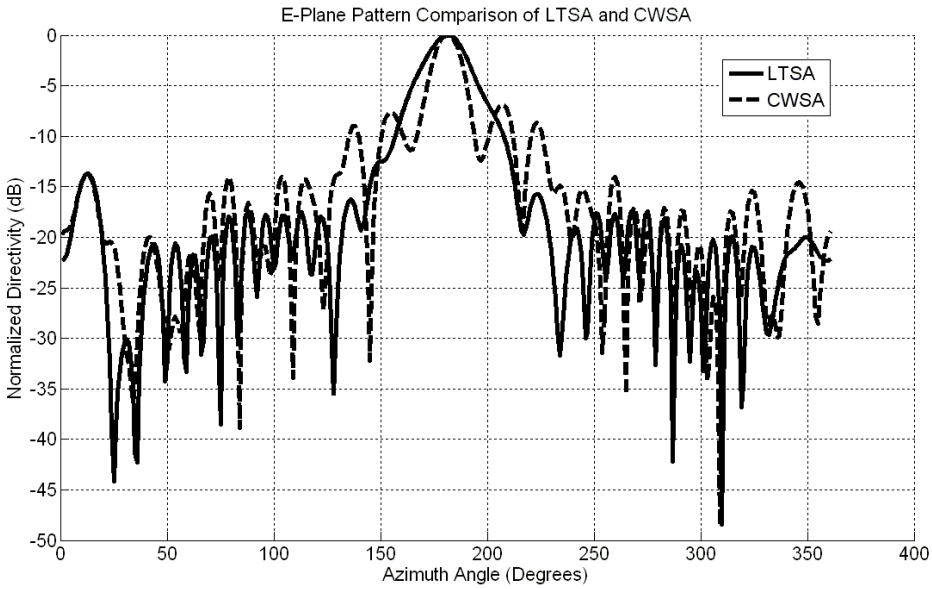

Figure 36 E-Plane Pattern Comparison for LTSA and CWSA with $L=6\lambda_0$, $W=1\lambda_0$, $H=1.5\ \lambda_0$

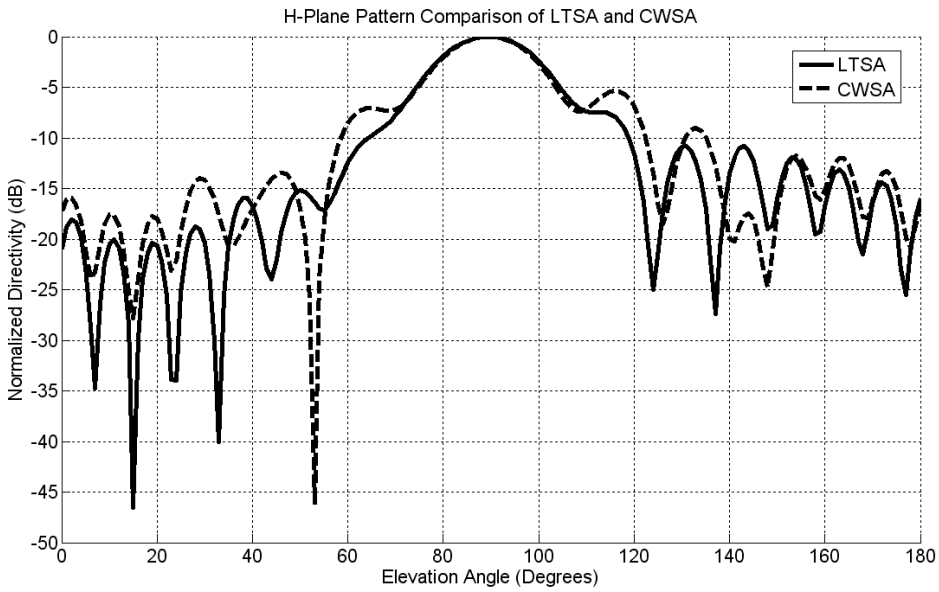

Figure 37 H-Plane Pattern Comparison for LTSA and CWSA with L=6λ_0, W=1λ_0, H=1.5 λ_0

3.2.LTSA-CWSA Bandwidth Comparison

The operating bandwidths of CWSA with exponential taper and LTSA were also compared in order to investigate if a degradation in input return loss characteristics of the antenna occurs when switching between two different antenna configurations. The return loss comparison of CWSA with exponential taper and LTSA for an antenna length of 3 λ_0, aperture width of 1 λ_0 and ground extension of 1 λ_0 can be seen in Figure 38. The return loss value on the band 25-45GHz generally follows the same trend for CWSA and LTSA. The return loss is below -10dB under 29GHz for CWSA so the CWSA is usable below 29GHz whereas LTSA is not. Likewise, the LTSA is usable for 29-32GHz however CWSA is not.

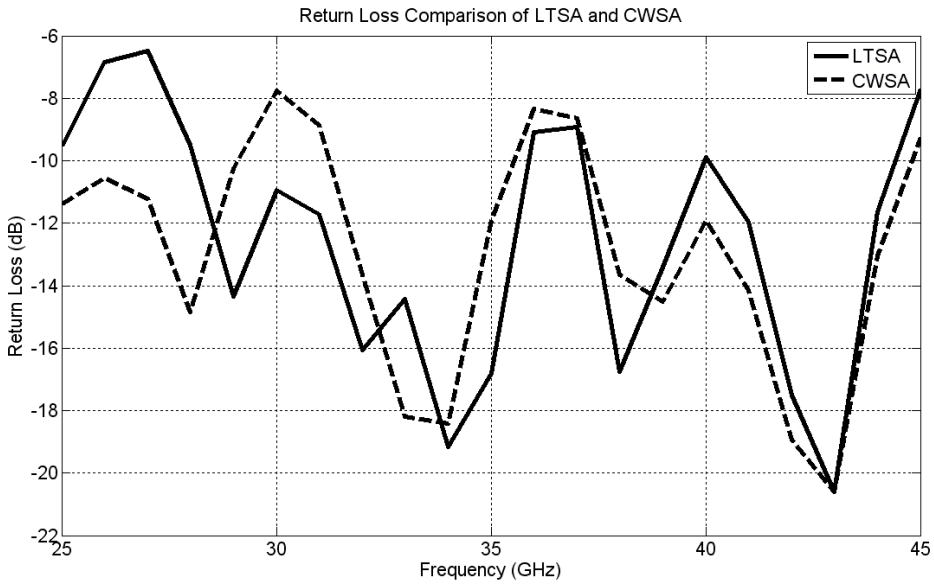

Figure 38 Bandwidth Comparison of CWSA with Exponential and LTSA with $L=3\lambda_0$, $W=1\lambda_0$, $H=1\lambda_0$

Figure 39 shows the return loss comparison for the case of 4 λ_0 antenna length, 0.5 λ_0 aperture width and 1.5 λ_0 ground extension. For narrow aperture width, there is no significant difference between the return loss characteristics of CWSA and LTSA.

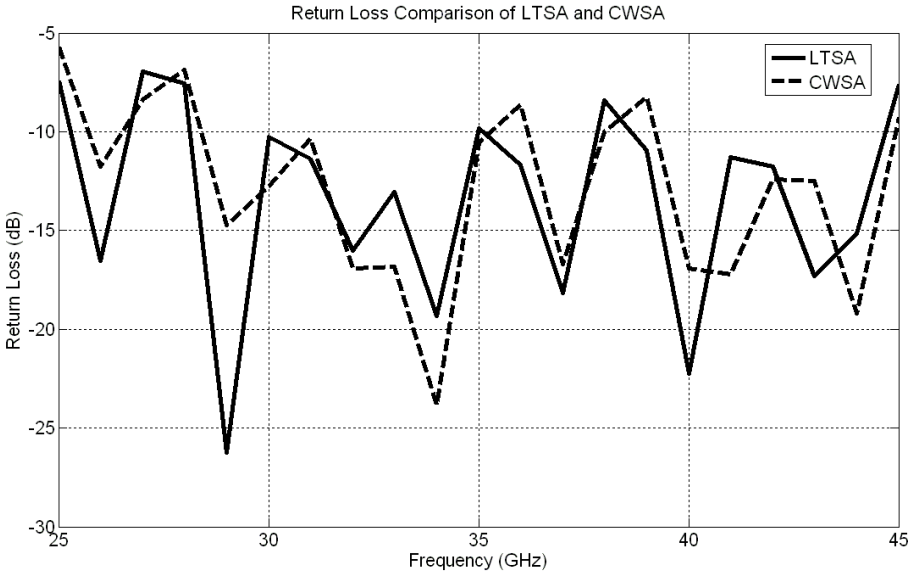

Figure 39 Bandwidth Comparison of CWSA with Exponential and LTSA with $L=4\lambda_0$, $W=0.5\lambda_0$, $H=1.5\lambda_0$

To observe the effect of aperture width on return loss another antenna with 5 λ_0 of antenna length, 0.5 λ_0 of aperture width and 1 λ_0 of ground extension is simulated. Figure 40 shows the results of bandwidth comparison of CWSA and LTSA for this antenna configuration. As seen in Figure 40, the return loss and the usable frequency bands again do not differ between CWSA and LTSA configurations with narrow aperture width.

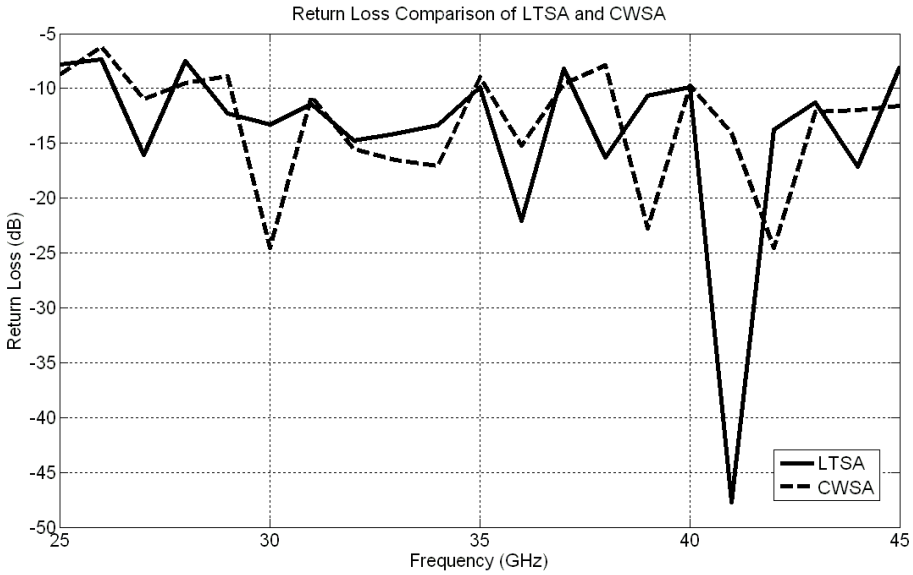

Figure 40 Bandwidth Comparison of CWSA with Exponential and LTSA with $L=5\lambda_0$, $W=0.5\lambda_0$, $H=1\lambda_0$

The return loss comparison of LTSA and CWSA with antenna length of 5 λ_0, aperture width of 1 λ_0 and ground extension of 2 λ_0 can be observed in Figure 41. The LTSA configuration shows better return loss for below 35GHz, whereas the return loss of CWSA is better for above 35GHz. However the usable bandwidth where the return loss is below -10dB do not show difference between LTSA and CWSA.

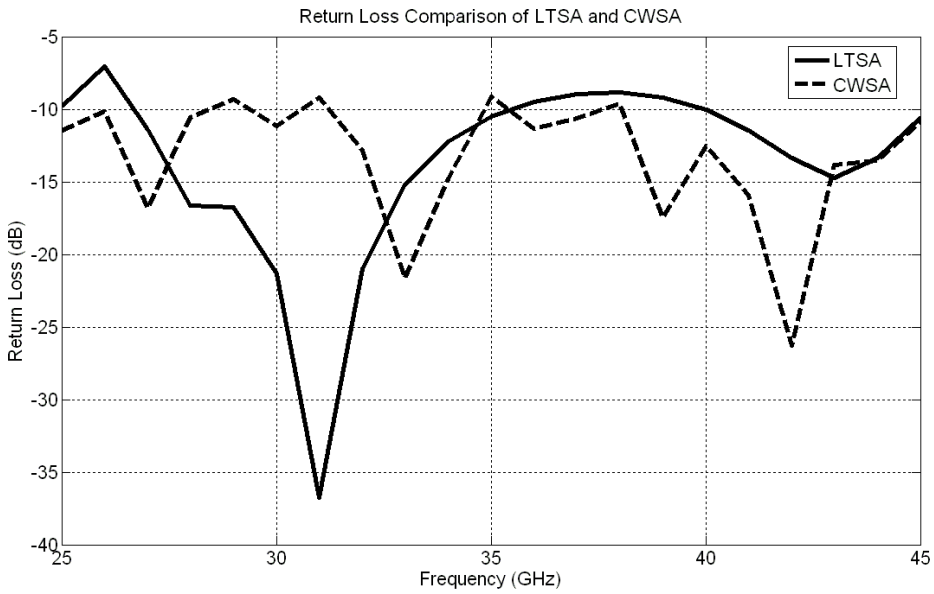

Figure 41 Bandwidth Comparison of CWSA with Exponential and LTSA with $L=5\lambda_0$, $W=1\lambda_0$, $H=2\lambda_0$

The final configuration used to compare the bandwidths of LTSA and CWSA is with an antenna length of 6 λ_0, aperture width of 1 λ_0 and ground extension of 1.5 λ_0. The LTSA again shows better return loss below 35GHz whereas CWSA's return loss is lower above 35GHz. As a result it can be concluded that, the usable bandwidth that has return loss below -10dB does not differ much for the LTSA and CWSA with exponential taper.

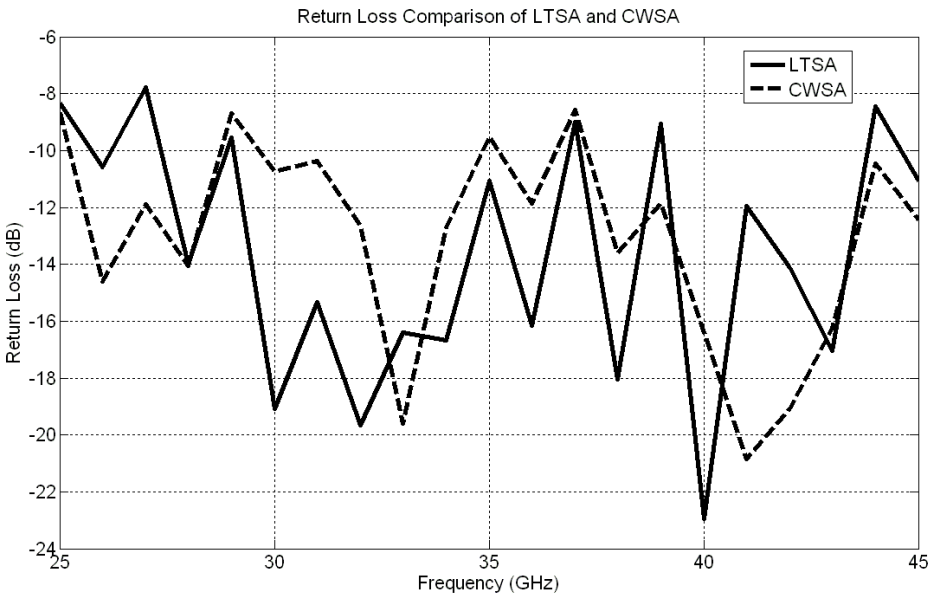

Figure 42 Bandwidth comparison of CWSA with exponential tapering and LTSA with L=6λ_0, W=1λ_0, H=1.5λ_0

It was stated in Chapter 2.2 that the designed antenna is aimed to operate at the frequency band of 30-40GHz centered at 35 GHz. The return loss characteristics previously mentioned proves that the bandwidth aim is met in terms of return loss. Next, the simulation results for the radiation patterns of LTSA and CWSA configurations were observed for 30GHz and 40GHz in order to see the radiation patterns at the frequency band boundaries.

3.3. Radiation Patterns of LTSA and CWSA With Respect to Frequency

The E-plane and H-plane radiation patterns for three different frequencies of the LTSA with an antenna length of 3λ_0, aperture width of 1 λ_0 and ground extension of 2 λ_0 can be seen in Figure 43 and Figure 44. The radiation patterns are not normalized in order to observe the variations in the directivity of the antenna with frequency. The maximum value in the radiation patterns indicates the directivity of the antenna. As seen from the radiation patterns, the antenna keeps its endfire radiating characteristics and exhibits similar directivity levels for frequencies between 30GHz and 40GHz which implies that the antenna has a pattern bandwidth

of at least 30-40GHz. It is also observed that as the frequency increases, half power beamwidths in both planes decrease which is expected as a result seen from the parametric study. Due to the decrease in beamwidths, the directivity of the antenna slight increases at higher frequencies. The E-plane SLL is almost the same and the H-plane SLL slightly increases.

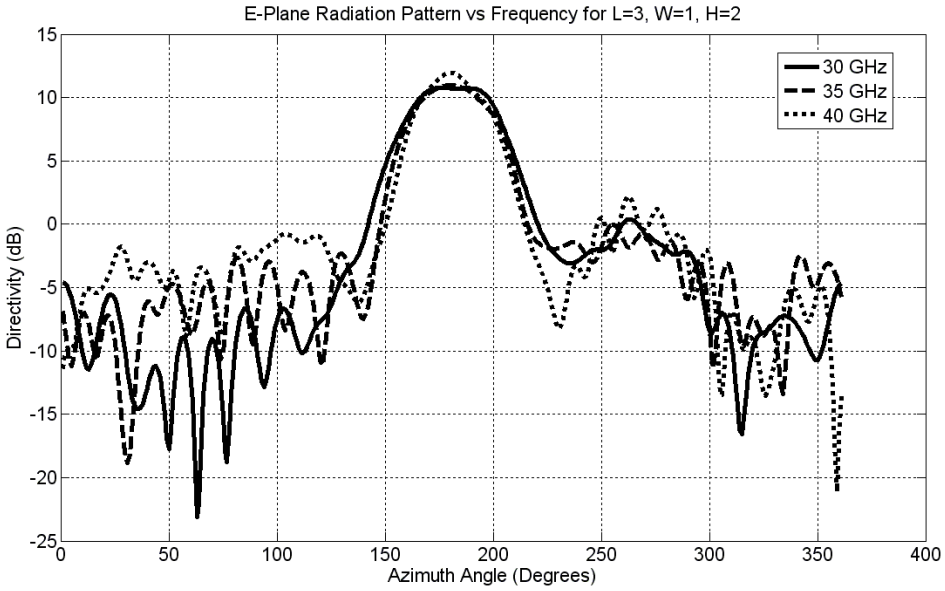

Figure 43 E-Plane Radiation Pattern of LTSA with L=3 λ_0, W=1 λ_0, H=2 λ_0 at different frequencies

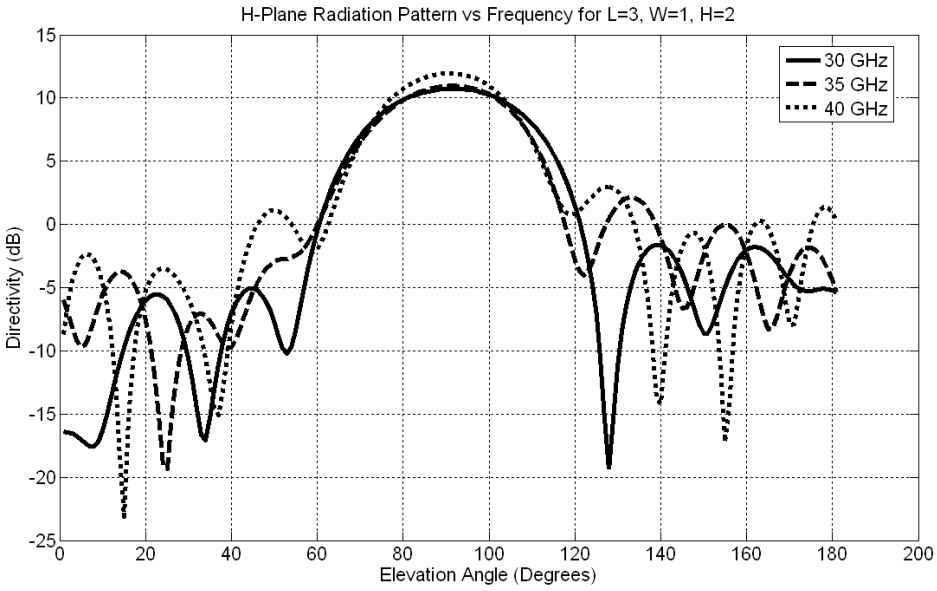

Figure 44 H-Plane Radiation Pattern of LTSA with L=3 λ_0, W=1 λ_0, H=2 λ_0 at different frequencies

The E-plane and H-plane radiation patterns for three different frequencies of the CWSA with an antenna length of $3\lambda_0$, aperture width of 1 λ_0 and ground extension of 2 λ_0 can be seen in Figure 45 and Figure 46.

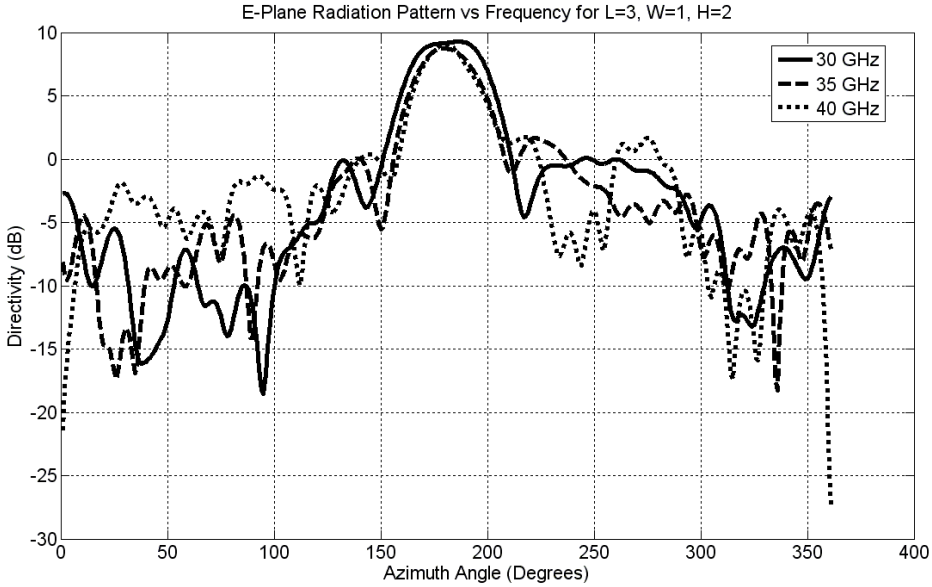

Figure 45 E-Plane Radiation Pattern of CWSA with L=3 λ_0, W=1 λ_0, H=2 λ_0 at different frequencies

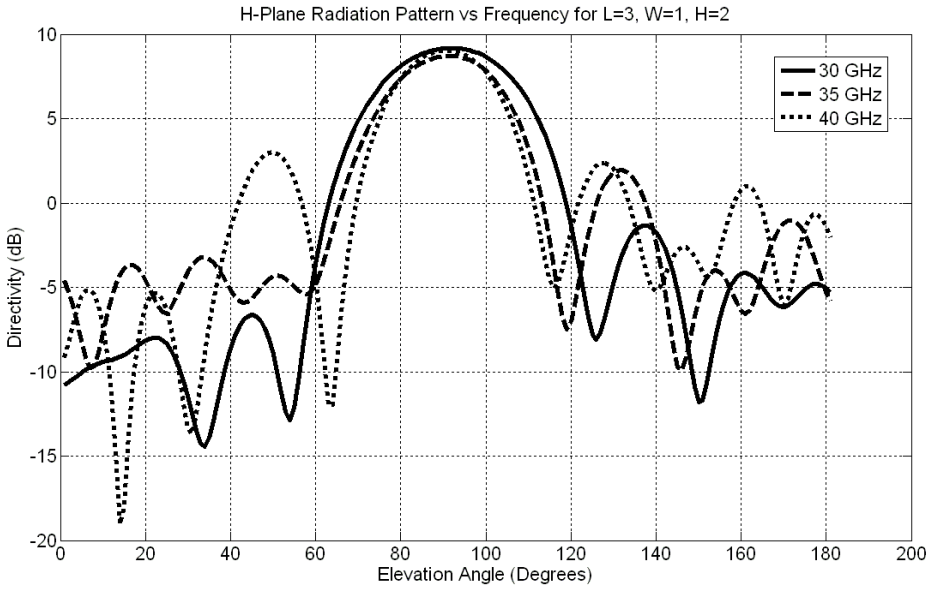

Figure 46 H-Plane Radiation Pattern of CWSA with L=3 λ_0, W=1 λ_0, H=2 λ_0 at different frequencies

The CWSA has a usable pattern bandwidth of 30-40GHz as well. An increase in frequency implies an increase in the electrical dimensions (physical dimensions normalized with respect to wavelength) of the antenna so the decrease in beamwidths and increase in H-plane SLL is compliant with the parametric study results of CWSA. It should be noted that the increase in sidelobe levels with increasing frequency is more dominant in CWSA compared to LTSA. Consequently, although the beamwidths become narrower with increasing frequency, an increase in the directivity of CWSA is not observed, since higher sidelobe levels reduce the directivity of the antenna.

The E-plane and H-plane radiation patterns are plotted for another configuration with antenna length of 6 λ_0, aperture width of 1 λ_0 and ground extension of 1.5 λ_0 for three different frequencies of the LTSA in Figure 47 and Figure 48. The radiation pattern again is suitable in the frequency band of 30-40 GHz for an endfire radiating antenna. It is observed that for shorter antenna (L=3λ_0), the directivity is almost constant with changing frequency, whereas for longer antenna (L=6 λ_0) the directivity change is higher. For L=6λ_0 case, the variation in the beamwidths (especially in E-plane) with frequency is not as significant as L=3λ_0 case. However, the increase in the H-plane side lobe levels with increasing frequency is more pronounced compared to L=3λ_0 case. Consequently, the directivity of the antenna decreases with increasing frequency.

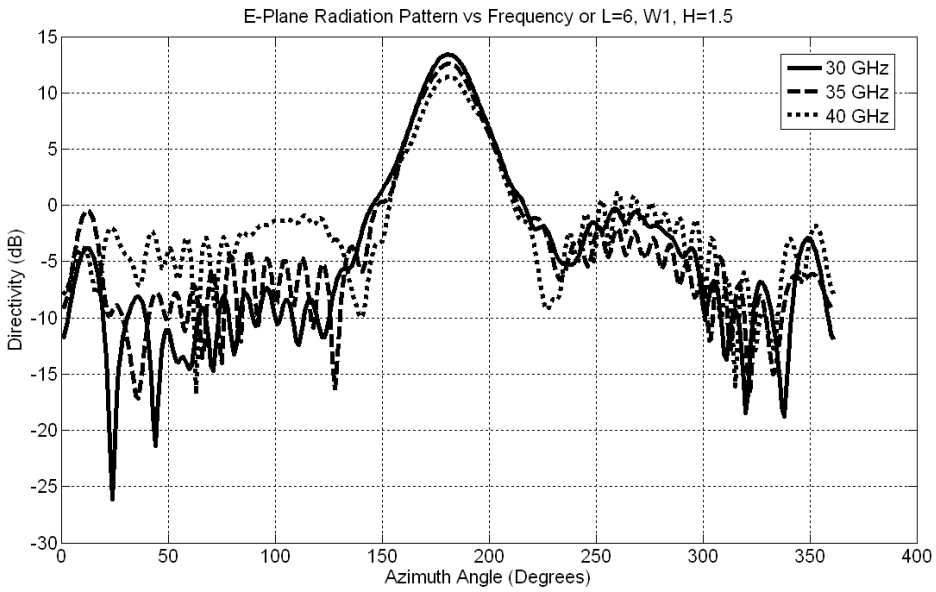

Figure 47 E-Plane Radiation Pattern of LTSA with L=6 λ_0, W=1 λ_0, H=1.5 λ_0 at different frequencies

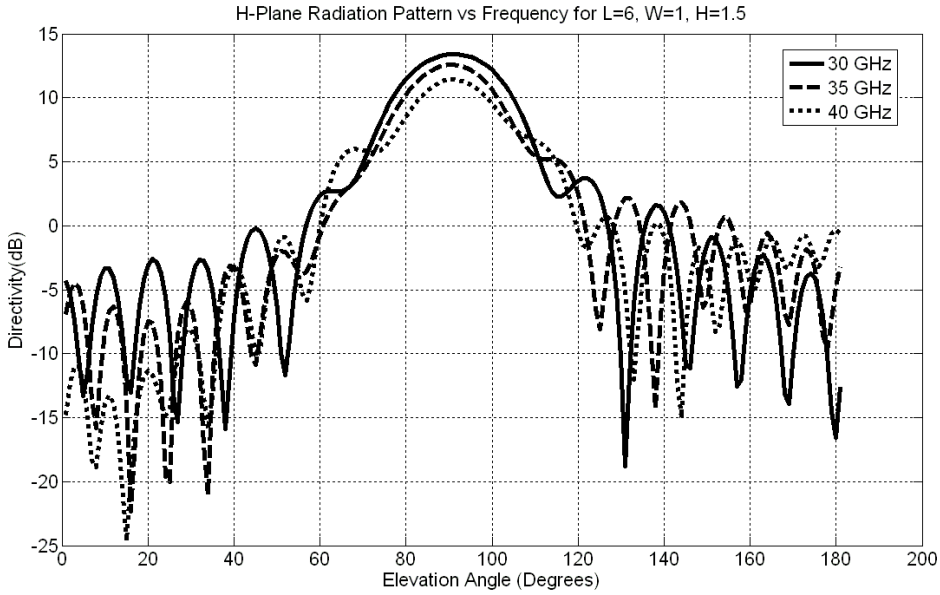

Figure 48 H-Plane Radiation Pattern of LTSA with L=6 λ_0, W=1 λ_0, H=1.5 λ_0 at different frequencies

The E-plane and H-plane radiation patterns for three different frequencies of the CWSA with an antenna length of $6\lambda_0$, aperture width of 1 λ_0 and ground extension of 1.5 λ_0 can be seen in Figure 49 and Figure 50.

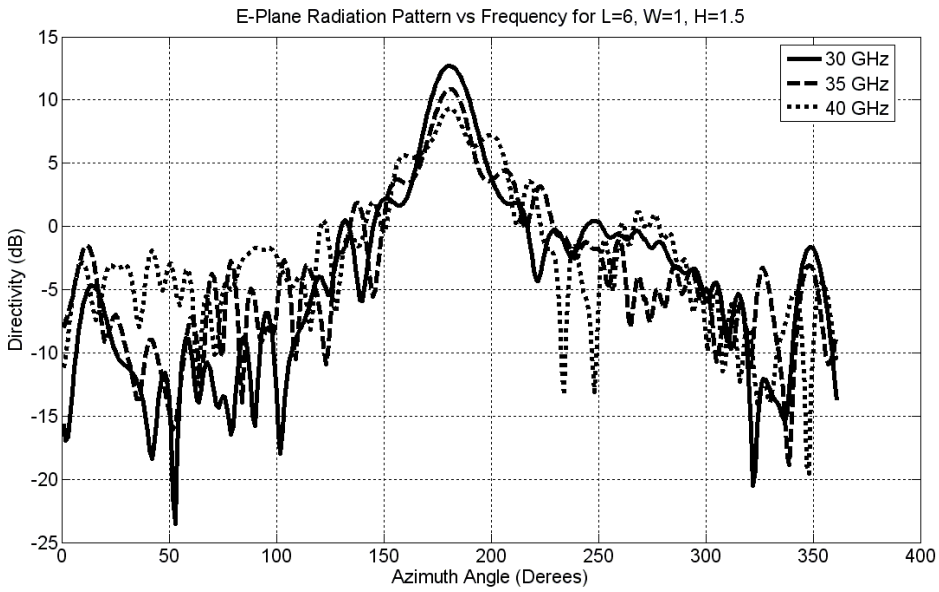

Figure 49 E-Plane Radiation Pattern of CWSA with L=6 λ_0, W=1 λ_0, H=1.5 λ_0 at different frequencies

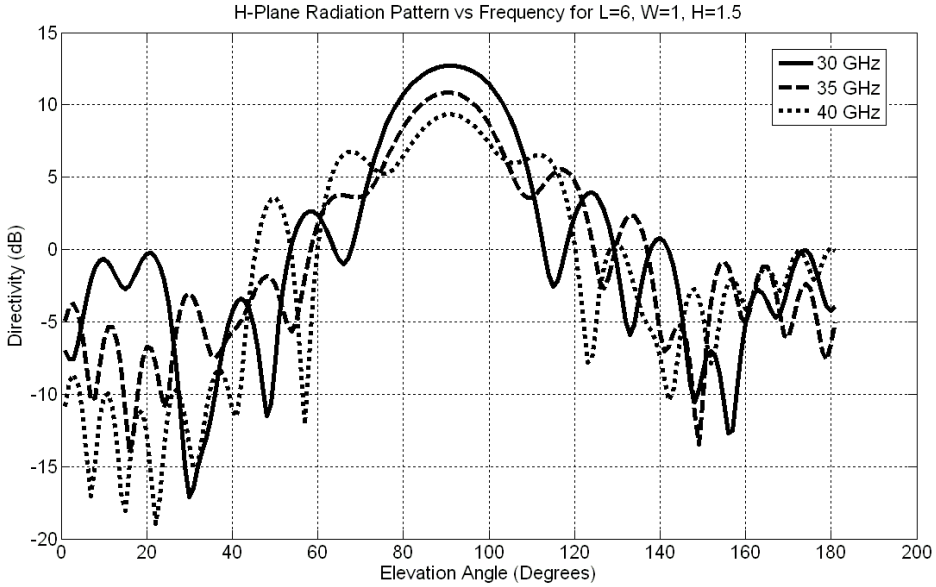

Figure 50 H-Plane Radiation Pattern of CWSA with L=6 λ_0, W=1 λ_0, H=1.5 λ_0 at different frequencies

As seen from Figure 49 and Figure 50, the decrease in the directivity of the antenna with increasing frequency is more effective compared to LTSA. Also the increase in the sidelobe levels is so significant that the sidelobes start to merge with the main

beam with increasing frequency. Hence, it can be concluded that the radiation pattern bandwidth of the LTSA is wider compared to CWSA as expected.

CHAPTER 4

MEASUREMENT RESULTS

In this chapter, the antenna manufacturing phase will be explained and the antenna measurement results will be given. First, the measurement results will be compared to the simulation results to investigate the accuracy of the simulation tool. Then, measured radiation patterns for LTSA and CWSA will be compared to explore the possibility of pattern reconfigurability.

4.1. Antenna Manufacturing Phase

Among the antenna geometries proposed in Chapter 3, two configurations for each of LTSA and CWSA have been manufactured. One of these configurations have the physical parameters of antenna length $3\lambda_0$, aperture width of 1 λ_0, ground extension of 2 λ_0 and the other configuration have the antenna length of 4 λ_0, aperture width of 1 λ_0 and ground extension of 1.5 λ_0.

For these four antennas, it was seen that the last microstrip segment of the impedance transformer of microstrip line to slot line transition was too narrow to be manufactured and also the substrate was not suitable for etching the metal layer above the substrate.

In order to obtain a design that can be manufactured, the substrate was changed to RO4003 and another microstrip line to slot line transition was designed on HFSS that does not have an impedance transformer and has a wider microstrip line width. The dielectric permittivity, thickness and loss tangent of RO4003 substrate are 3.38, 0.51mm and 0.0027 respectively. So the effective dielectric thickness is 0.049 as can also be seen in Table 1. Although the effective thickness value for this substrate is larger than the maximum recommended effective thickness value which is 0.03;

RO4003 was chosen due to the availability of the substrate and the ease of etching the metal layer.

In the new transition design, the microstrip line width was calculated to be 1.1mm that corresponds to an impedance of 50Ω on RO4003 substrate and a slotline width of 0.3mm was seen to be appropriate for manufacturing purposes.

An orthogonal transition was designed between microstrip line and slot line carrying out a parametric study on HFSS. The geometry of the new transition can be seen in Figure 51.

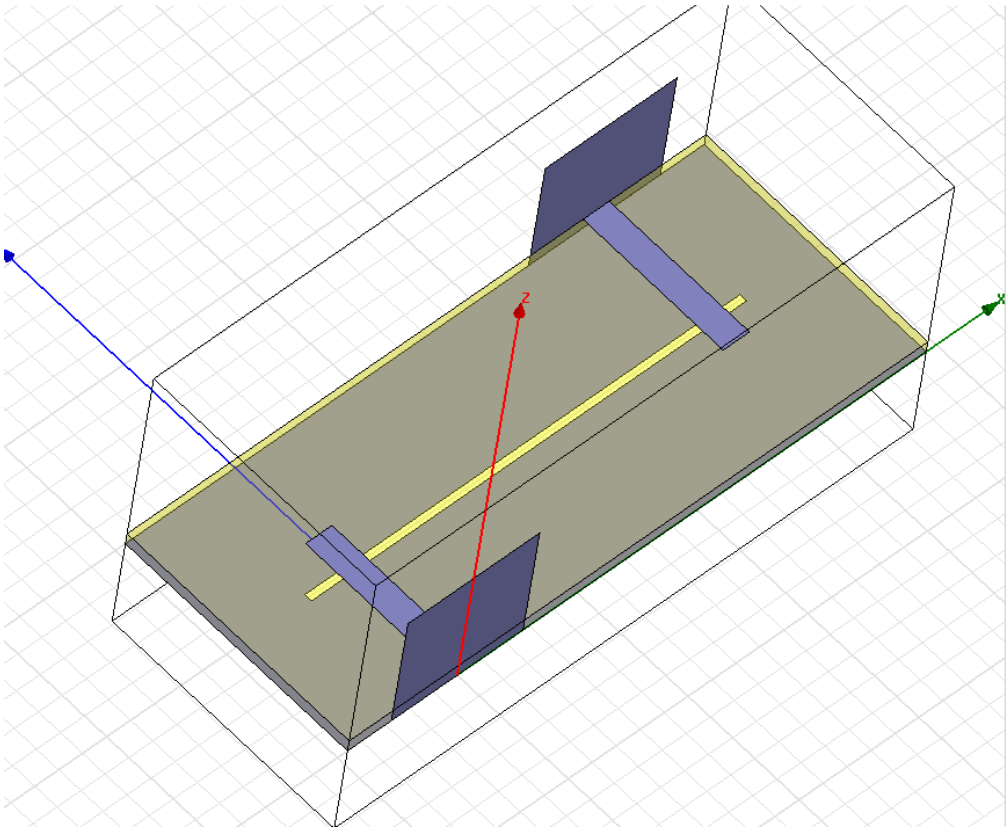

Figure 51 The Geometry of the New Microstrip Line to Slotline Transition

The transition contains no impedance transformer and is compliant with the w=v case given in detail in [18]. For the parametric study of the new transition, the microstrip line width was kept constant at 1.1mm and the slot line width was kept constant at 0.3mm. The parameters that were changed are the microstrip stub length and slot line stub length values as seen in Figure 52. These two parameters were

changed with 0.1mm increments and the return loss and insertion loss values of two transitions connected back to back through the slot line were evaluated to determine the optimum values of these parameters.

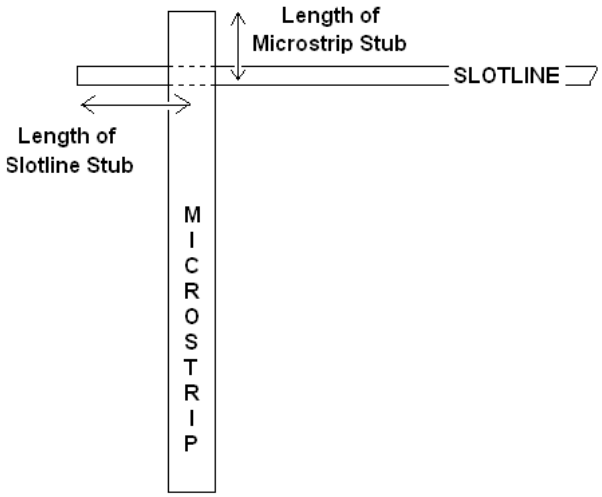

Figure 52 Parameters of the New Microstrip Line to Slot line Transition

As a result of the parametric study, the transition that has a microstrip line stub length and slot line stub length of 0.8mm each was found to exhibit the lowest return loss and the best insertion loss characteristics. The performance of the transition can be observed in Figure 53.

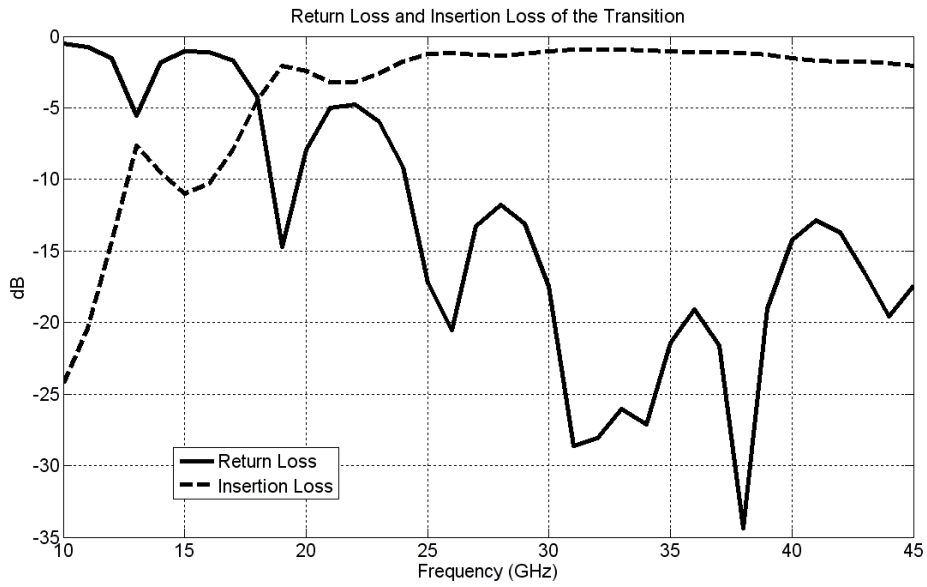

Figure 53 Return and Insertion Loss of the Transition

The return loss of the transition is seen to be below -10dB and insertion loss below 2 dB for the frequency band of 23-45GHz.

Using the designed transition, four antennas were manufactured:

[1] LTSA with L=3 λ_0, W=1 λ_0, H=2 λ_0

[2] CWSA with L=3 λ_0, W=1 λ_0, H=2 λ_0

[3] LTSA with L=4 λ_0, W=1 λ_0, H=1.5 λ_0

[4] CWSA with L=4 λ_0, W=1 λ_0, H=1.5 λ_0

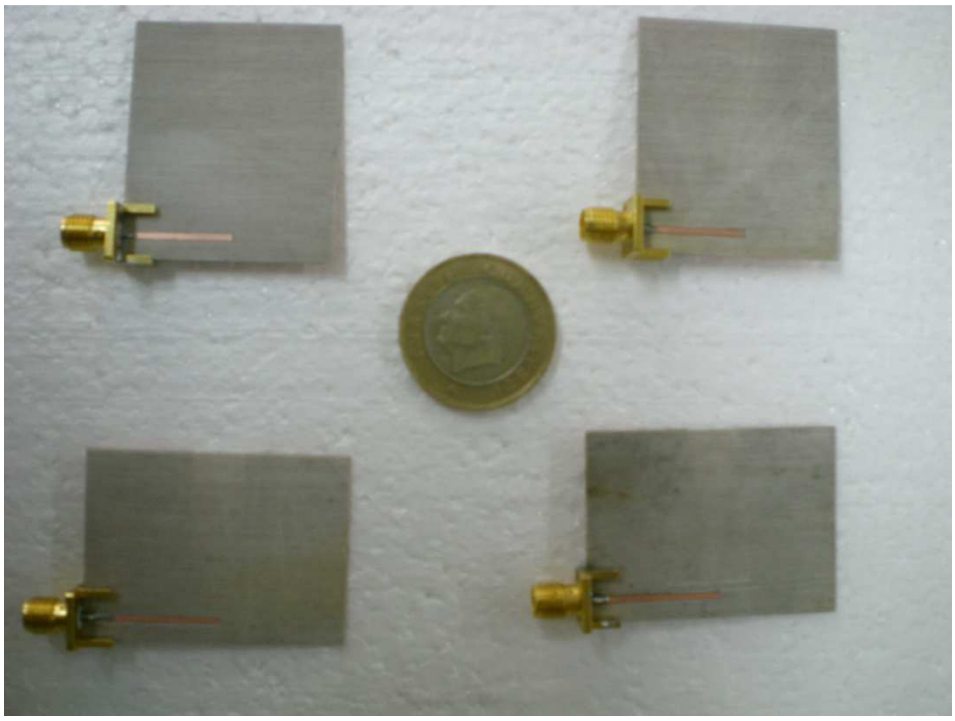

Figure 54 Manufactured Antennas-Top Side

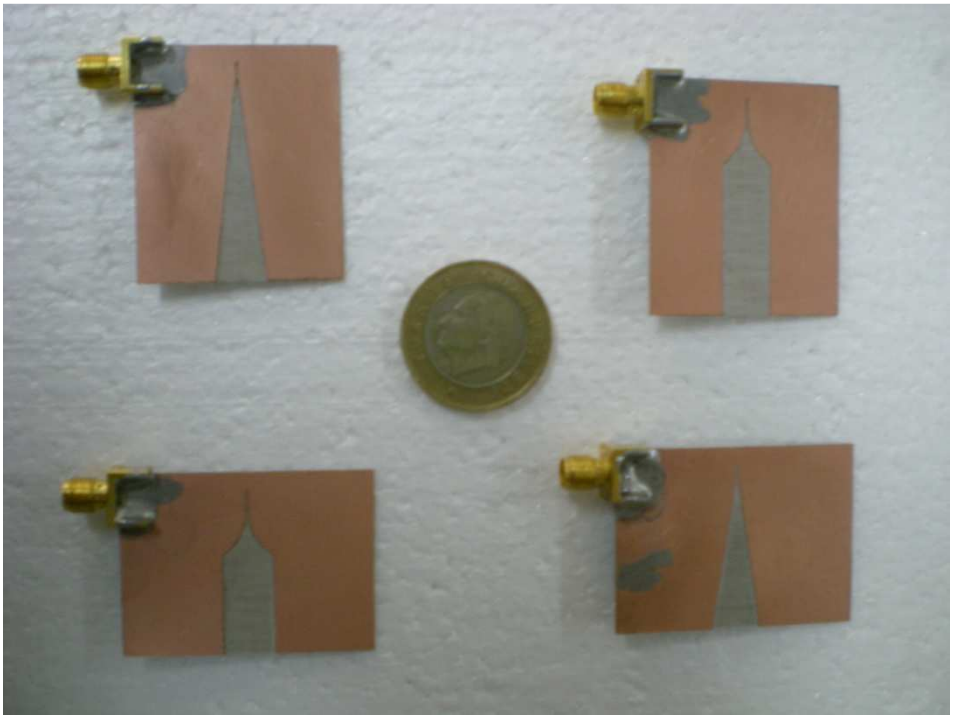

Figure 55 Manufactured Antennas-Bottom Side

4.2. Antenna Pattern Measurement Results

For each of the four antennas manufactured, two sets of pattern measurement (one for E-plane and one for H-plane) were performed which makes a total of eight sets of measurements. For each set of measurement, multiple frequency patterns were measured from 28 to 40 GHz. The set-up given in Figure 56 was used for the antenna pattern measurements in the anechoic chamber.

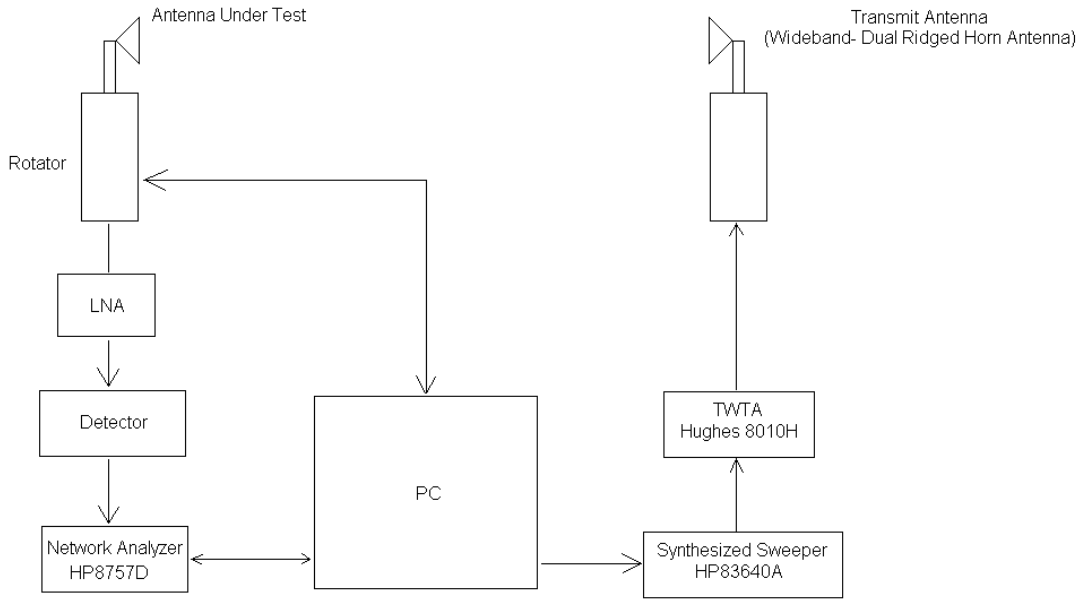

Figure 56 Antenna Measurement Set-Up

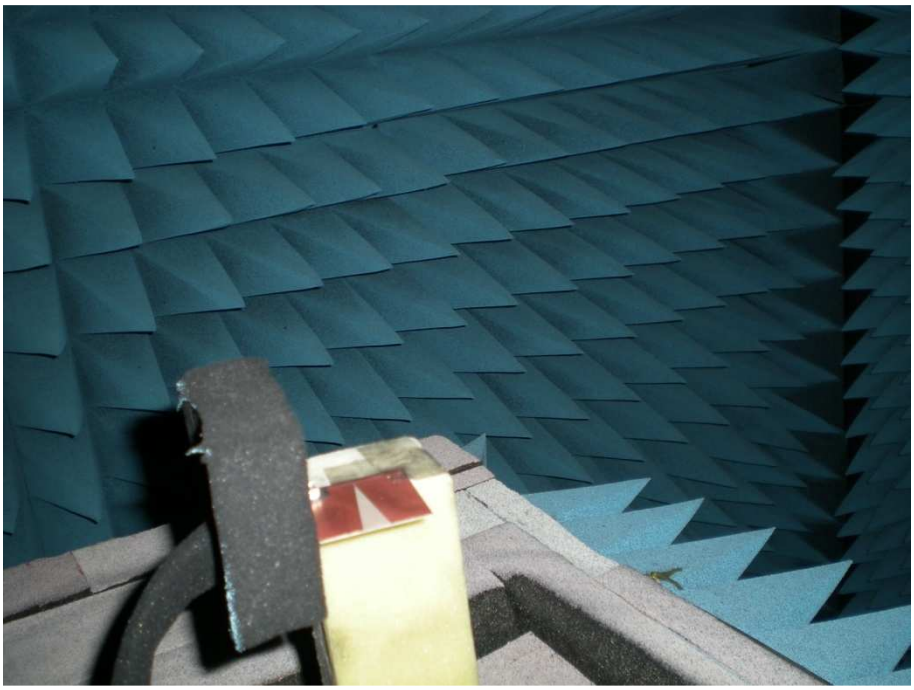

Figure 57 Antenna Under Test

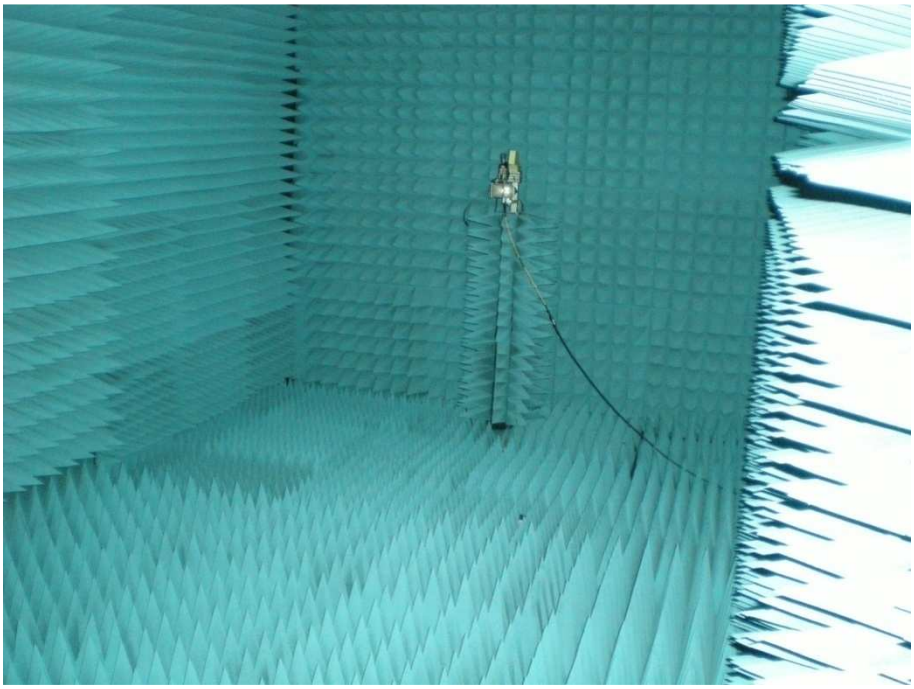

Figure 58 Anechoic Chamber and the Transmit Antenna

The four antenna configurations were also simulated in HFSS to see if there is consistency between the simulated and measured antenna patterns. The comparison between simulated and measured E-plane and H-plane radiation patterns of LTSA

with L=3λ_0 , W=1 λ_0 and H=2 λ_0 can be seen in Figure 59 and Figure 60, respectively at 35GHz.

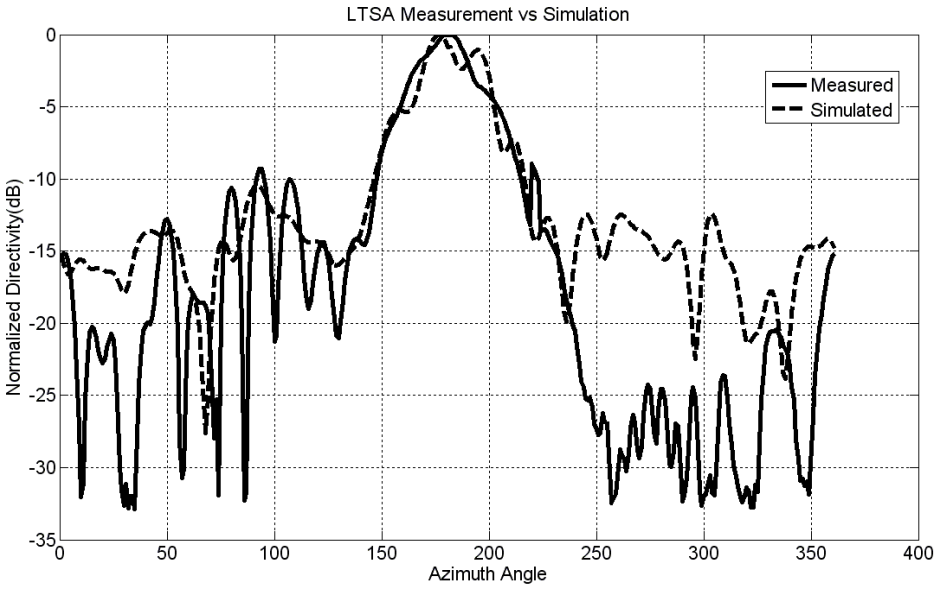

Figure 59 E-Plane Radiation Pattern of LTSA with L=3λ_0, W=1λ_0 and H=2λ_0

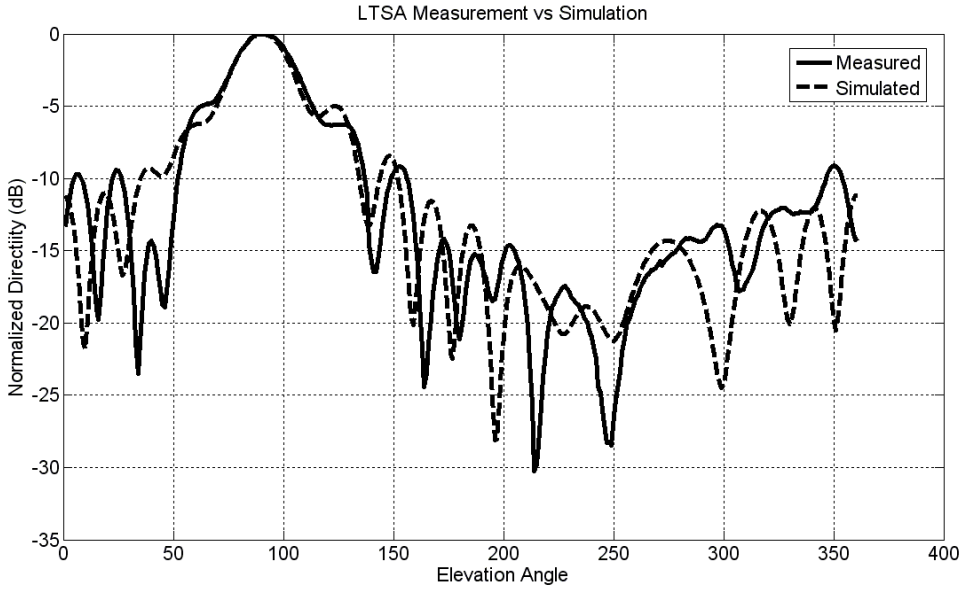

Figure 60 H-Plane Radiation Pattern of LTSA with L=3λ_0, W=1λ_0 and H=2λ_0

As seen from Figure 59 and Figure 60, there is a good agreement between the measured radiation pattern and simulated radiation pattern for both planes. The only difference in the patterns can be seen in the E-plane radiation pattern on the region through the direction of the microstrip feed line on top of the substrate. In this region, the simulation result predicts a higher radiation whereas in the measurement a lower radiation level is seen. The reason for this is believed to be due to the measurement set-up where the microstrip line lies between supporting foam and the substrate. So the feed radiation seen in simulations might have been absorbed by the supporting foam in the measurement.

The comparison between simulated and measured E-plane and H-plane radiation patterns of LTSA with L=4λ_0, W=1 λ_0 and H=1.5 λ_0 can be seen in Figure 61 and Figure 62, respectively at 35GHz.

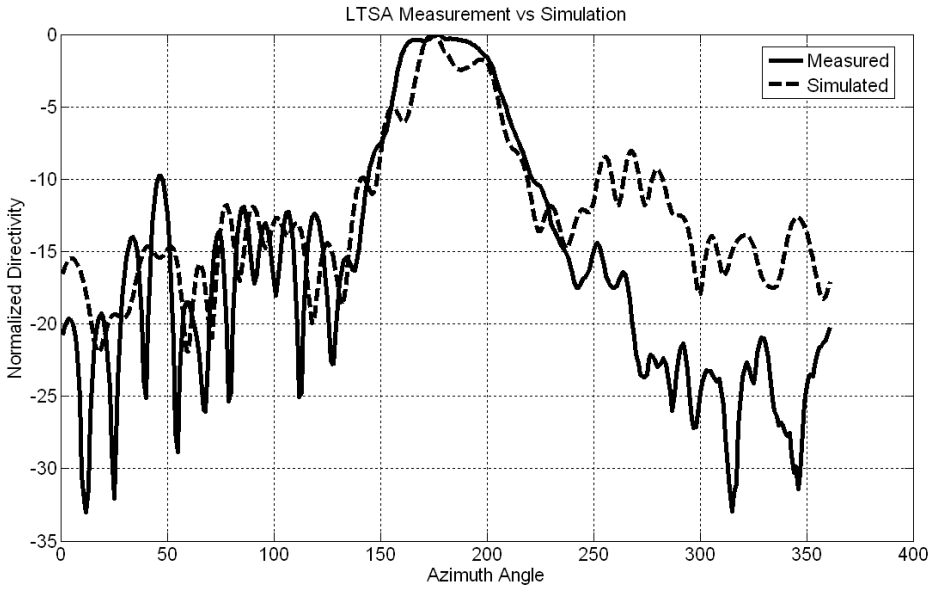

Figure 61 E-Plane Radiation Pattern of LTSA with L=4λ_0, W=1λ_0 and H=1.5λ_0

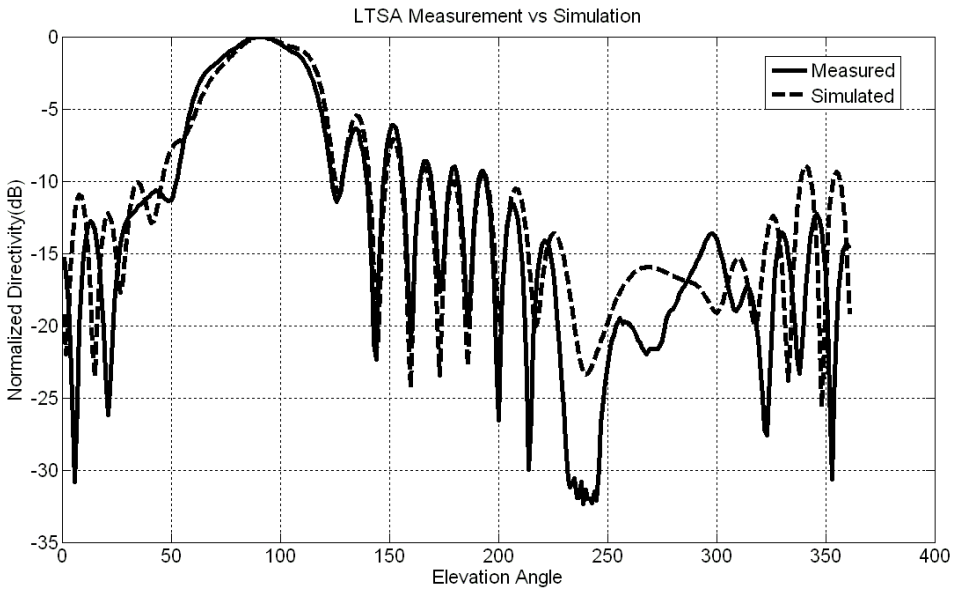

Figure 62 H-Plane Radiation Pattern of LTSA with L=4λ_0, W=1λ_0 and H=1.5λ_0

There is again a good agreement between simulation and measurement results except for the microstrip feed region in E-plane.

The comparison between simulated and measured E-plane and H-plane radiation patterns of CWSA with L=3λ_0, W=1 λ_0 and H=2 λ_0 can be seen in Figure 63 and Figure 64, respectively at 35GHz.

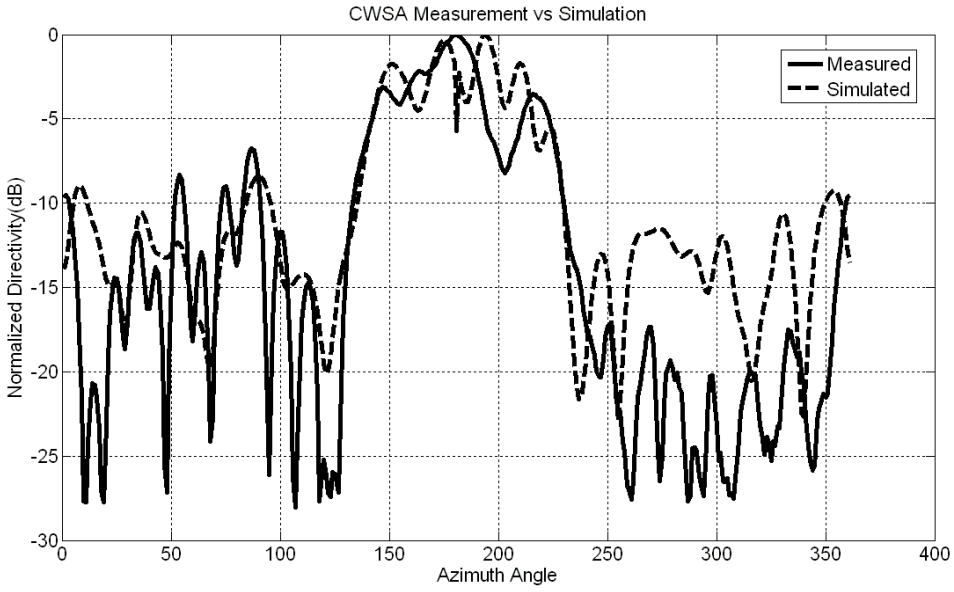

Figure 63 E-Plane Radiation Pattern of CWSA with L=3λ_0, W=1λ_0 and H=2λ_0

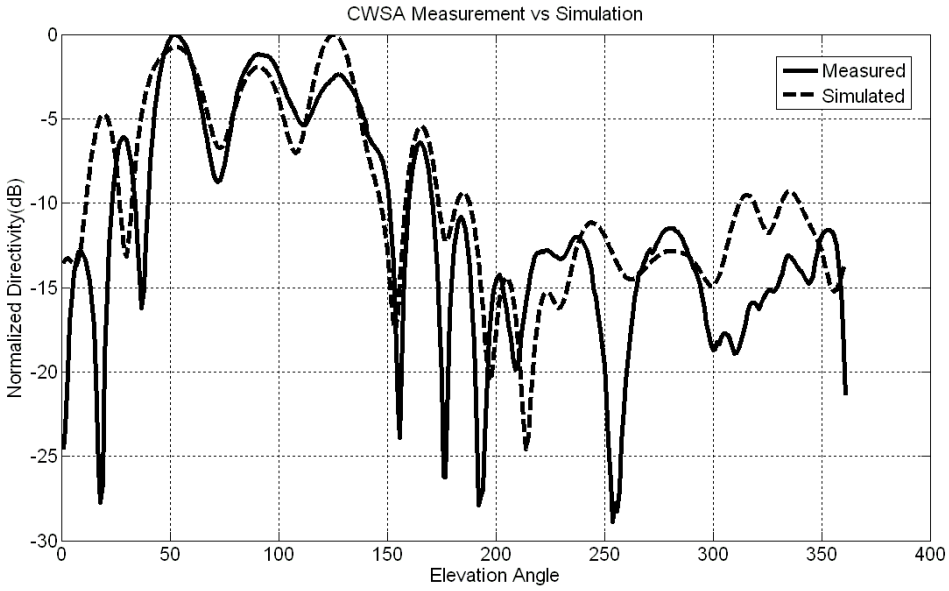

Figure 64 H-Plane Radiation Pattern of CWSA with L=3λ_0, W=1λ_0 and H=2λ_0

CWSA is seen to be deviating from the endfire radiation characteristics due to the split in the main beam and unsymmetrical pattern with respect to endfire direction. It was stated in section 4.1 that RO4003 substrate was used in manufactured antennas with a substrate thickness of 0.51mm which causes an effective thickness value larger than the value proposed in [19]. This fact is believed to be the reason for the deviation in antenna patterns from endfire radiation characteristics. It can be concluded that the manufactured antennas are not well-behaved endfire radiating antennas because of the high effective dielectric thickness.

The comparison between simulated and measured E-plane and H-plane radiation patterns of CWSA with L=4λ_0, W=1 λ_0 and H=1.5 λ_0 can be seen in Figure 65 and Figure 66, respectively at 35GHz.

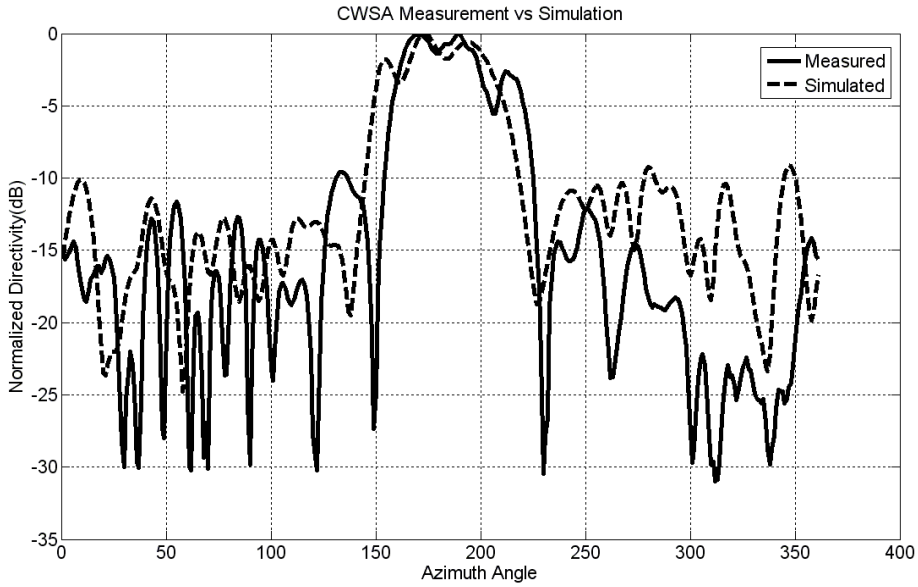

Figure 65 E-Plane Radiation Pattern of CWSA with L=4λ_0, W=1λ_0 and H=1.5λ_0

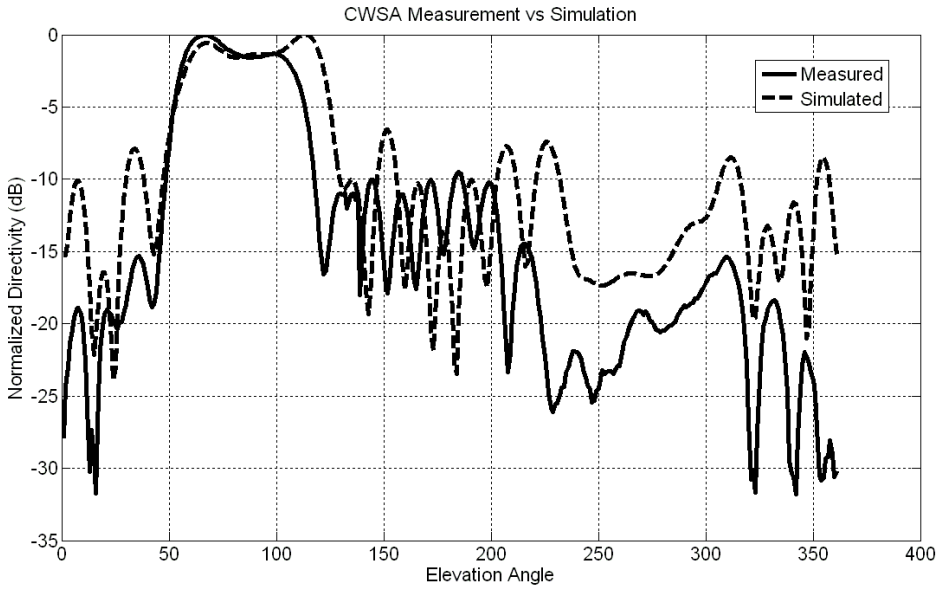

Figure 66 H-Plane Radiation Pattern of CWSA with L=4λ_0, W=1λ_0 and H=1.5λ_0

4.3. Radiation Pattern Comparison of LTSA and CWSA

The LTSA and CWSA pattern measurement results will be compared next. Figure 67 and Figure 68 show the E-plane and H-plane radiation pattern comparison between LTSA and CWSA with the same physical parameters as antenna length of 3λ_0, aperture width of 1 λ_0 and ground extension of 2 λ_0 for 35GHz.

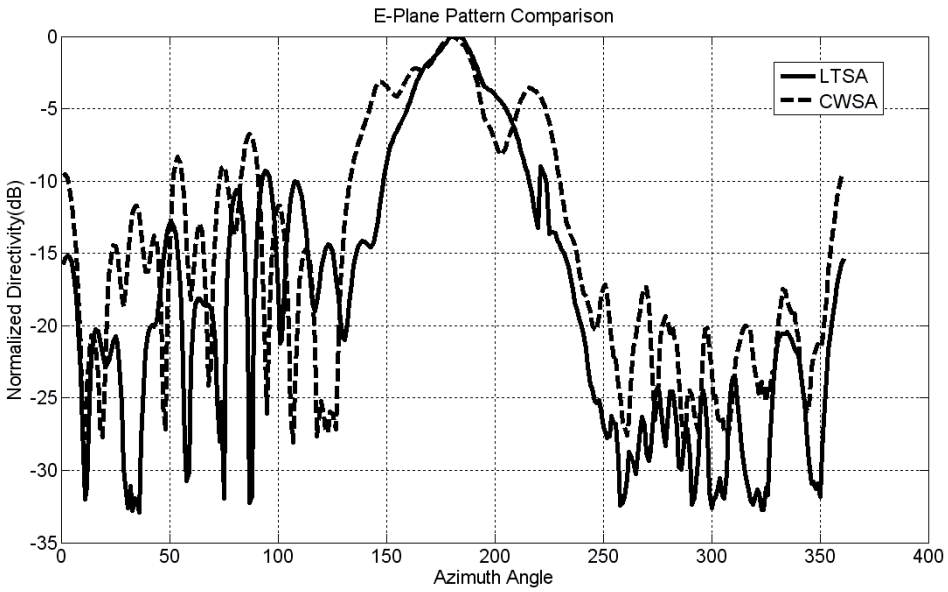

Figure 67 E-Plane Pattern Comparison of LTSA&CWSA with L=3λ_0, W=1λ_0 and H=2 λ_0

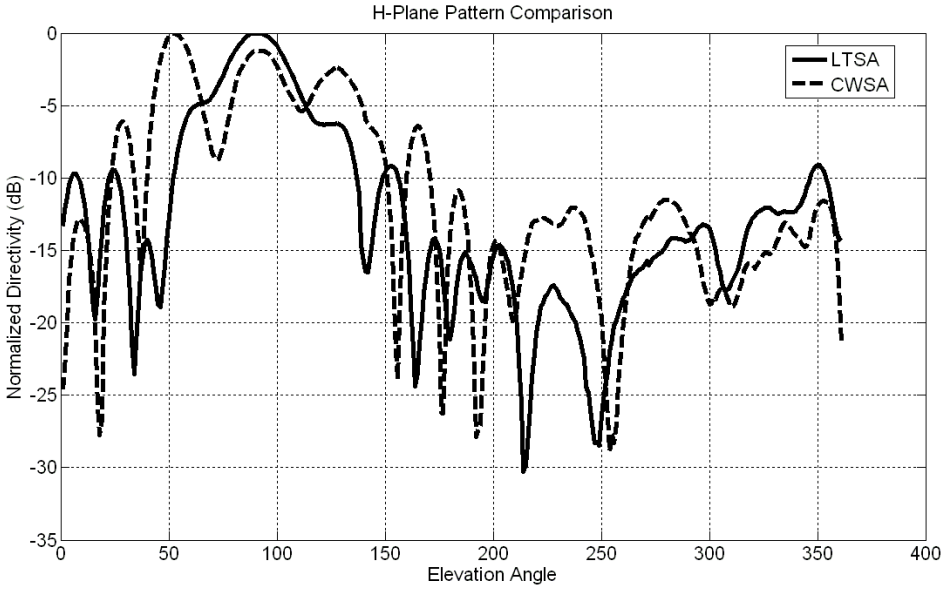

Figure 68 H-Plane Pattern Comparison of LTSA&CWSA with L=3λ_0, W=1λ_0 and H=2 λ_0

For LTSA and CWSA with antenna length of 4λ_0, aperture width of 1 λ_0 and ground extension of 1.5 λ_0, the E-plane and H-plane radiation pattern measurement result comparison can be seen in Figure 69 and Figure 70.

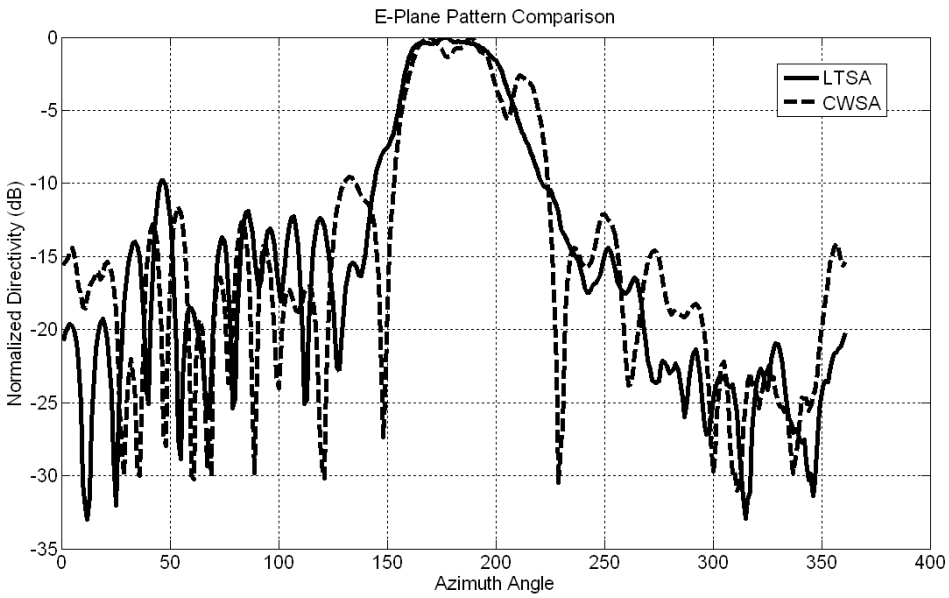

Figure 69 E-Plane Pattern Comparison of LTSA&CWSA with L=4λ_0, W=1λ_0 and H=1.5 λ_0

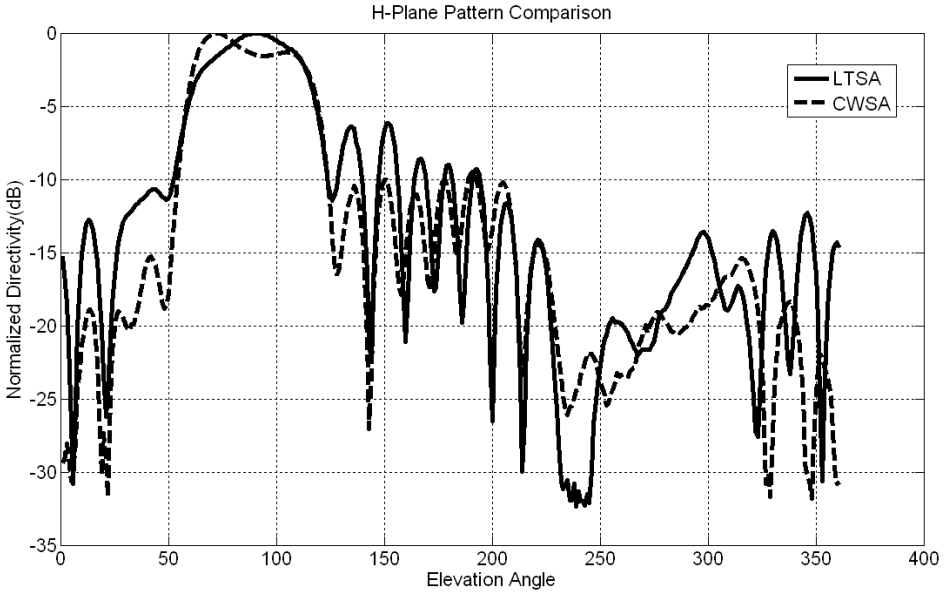

Figure 70 H-Plane Pattern Comparison of LTSA&CWSA with L=4λ_0, W=1λ_0 and H=1.5 λ_0

Since the radiation patterns for the CWSA are far from proper endfire radiation characteristics, it is not meaningful to make a comparison with LTSA.

4.4. Measured Radiation Patterns with Respect to Frequency

In order to be able to see the pattern bandwidth of the manufactured antennas, the radiation patterns are plotted for three different frequency values as 30GHz, 35GHz and 40GHz.

The E-plane radiation patterns of LTSA with L=3λ_0, W=1 λ_0 and H=2 λ_0 at three different frequencies are given in Figure 71.

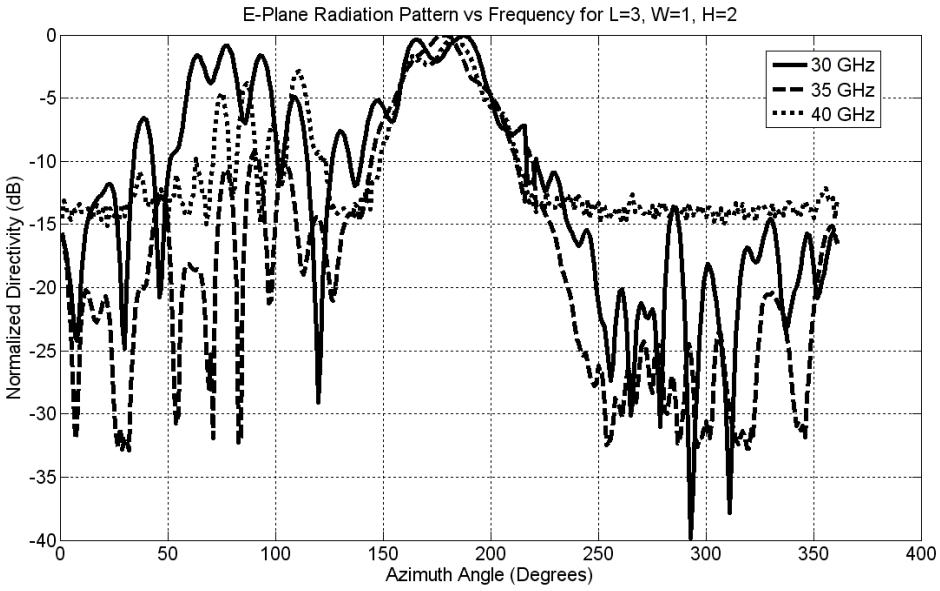

Figure 71 E-Plane Radiation Pattern vs Frequency for LTSA with L=3λ_0, W=1λ_0 and H=2 λ_0

It can be seen from Figure 71 that for 40GHz, the received power is almost constant for azimuth angles between 220^0 and 360^0. This might be due to the fact that the signal level on the antenna is too low to be measured by the detector in the set-up because of the fact that the maximum recommended usable frequency of the test set-up is 40 GHz and the SMA connectors used in the antennas have high loss values above 18 GHz.

Concerning the patterns for different frequencies, the antenna seems to keep its endfire radiation characteristics in the 30-40GHz band although the sidelobe level at 30 GHz is too high.

The H-plane radiation patterns of LTSA with L=3λ_0, W=1λ_0 and H=2λ_0 at three different frequencies are given in Figure 72. For the H-plane characteristics, the antenna has a tilted beam for 40GHz and the sidelobe level for 30GHz is higher than the main beam directivity.

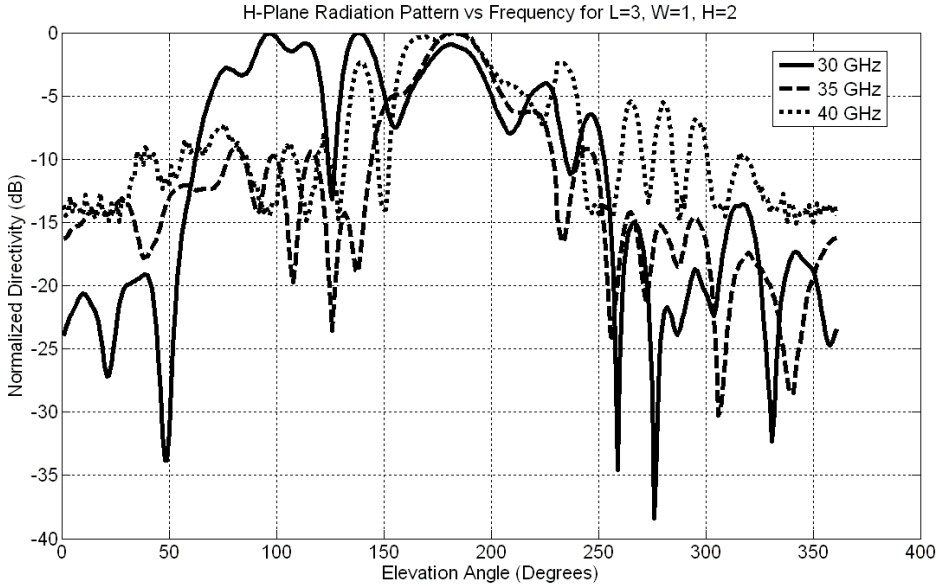

Figure 72 H-Plane Radiation Pattern vs Frequency for LTSA with L=3λ_0, W=1λ_0 and H=2 λ_0

The E-plane and H-plane radiation patterns of CWSA with L=3λ_0, W=1 λ_0 and H=2 λ_0 at three different frequencies are given in Figure 73 and Figure 74. The CWSA deviates from endfire characteristics at 40GHz with a tilted beam.

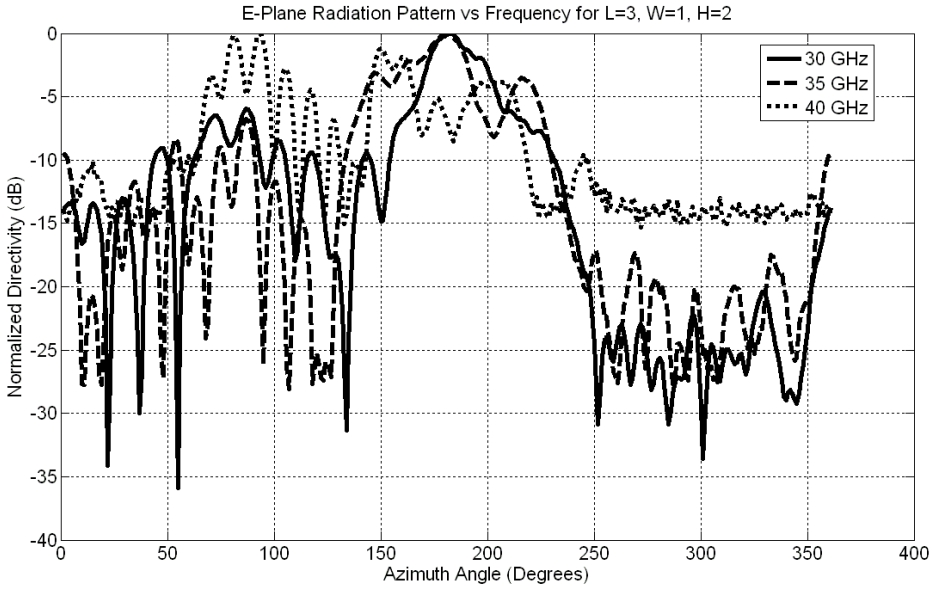

Figure 73 E-Plane Radiation Pattern vs Frequency for CWSA with L=3λ_0, W=1λ_0 and H=2 λ_0

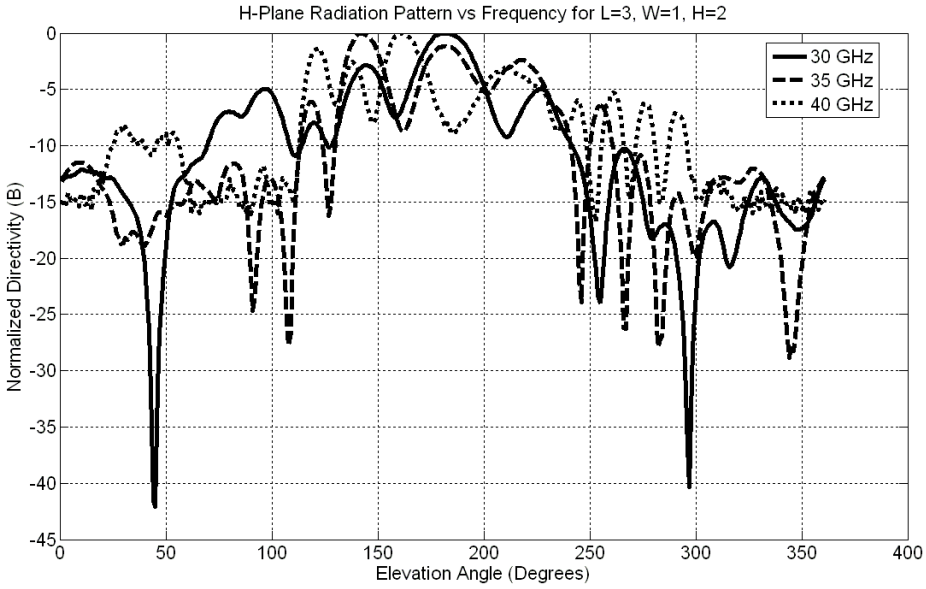

Figure 74 H-Plane Radiation Pattern vs Frequency for CWSA with L=3λ_0, W=1λ_0 and H=2 λ_0

The E-plane and H-plane radiation patterns of LTSA with L=4λ_0, W=1 λ_0 and H=1.5 λ_0 for different frequencies are given in Figure 75 and Figure 76. For this LTSA configuration, the antenna keeps its endfire characteristics for the frequency range of

30-40 GHz. The increase in the sidelobe level for 30GHz is again need to be noted. The H-plane beamwidth is narrower than 35GHz case for both 30GHz and 40GHz.

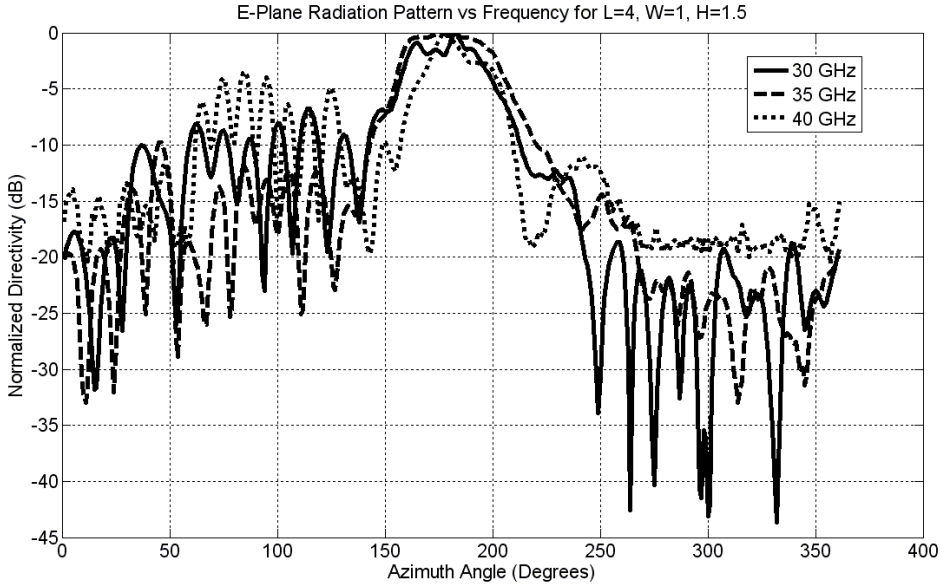

Figure 75 E-Plane Radiation Pattern vs Frequency for LTSA with L=4λ_0, W=1λ_0 and H=1.5 λ_0

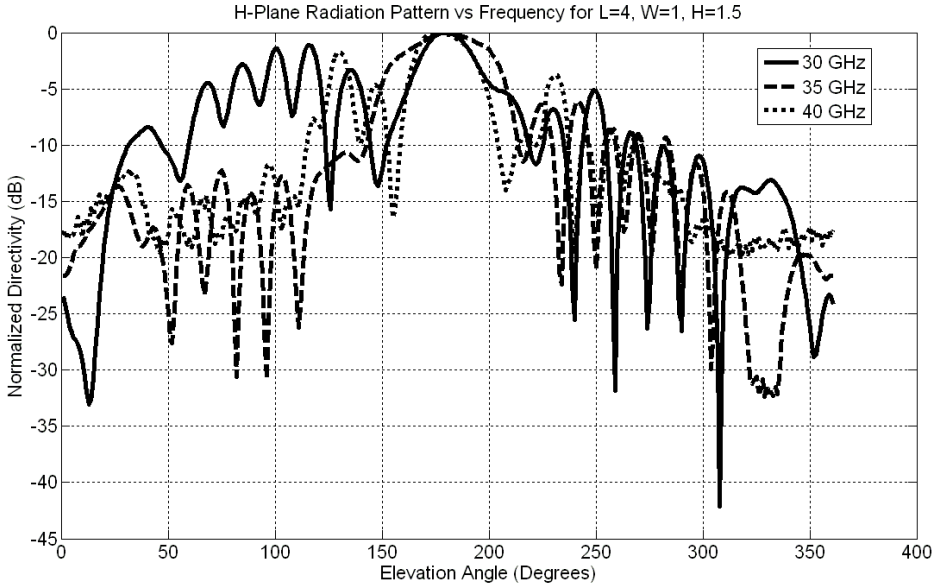

Figure 76 H-Plane Radiation Pattern vs Frequency for LTSA with L=4λ_0, W=1λ_0 and H=1.5 λ_0

The E-plane and H-plane radiation patterns of CWSA with L=4λ_0, W=1 λ_0 and H=1.5 λ_0 at three different frequencies are given in Figure 77 and Figure 78. The CWSA deviates from endfire characteristics for the frequency of 30GHz.

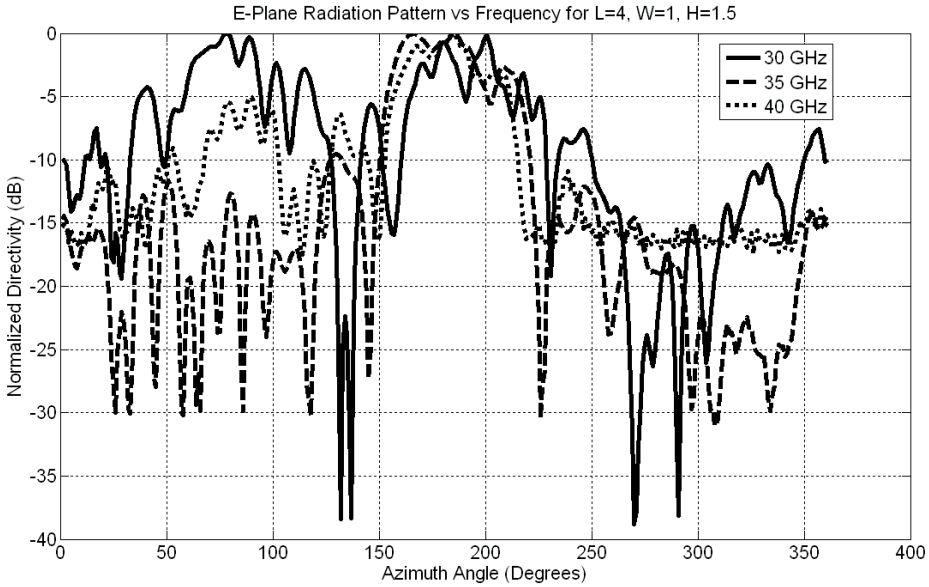

Figure 77 E-Plane Radiation Pattern vs Frequency for CWSA with L=4λ_0, W=1λ_0 and H=1.5 λ_0

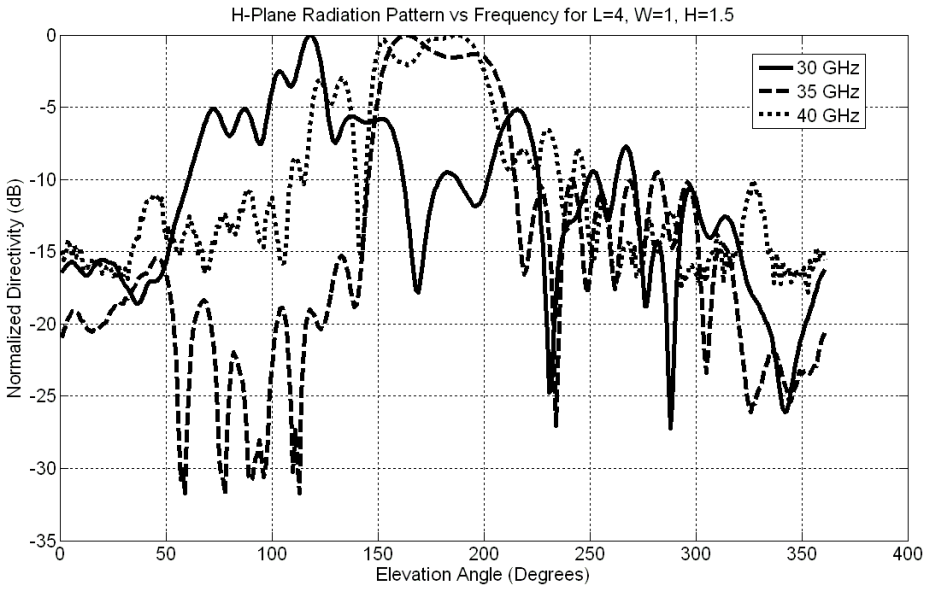

Figure 78 H-Plane Radiation Pattern vs Frequency for CWSA with L=4λ_0, W=1λ_0 and H=1.5 λ_0

Although for these configurations, some of the antennas have split or tilted beams for some different frequencies, it is mandatory to note that even at the center frequency, the effective thickness value of the substrate does not satisfy the condition required to achieve good travelling wave antenna characteristics.

CHAPTER 5

CONCLUSION

A parametric study on the radiation characteristics of LTSA and CWSA was performed. According to the results of this parametric study a reconfigurable antenna configuration operating at 35 GHz was proposed.

Since tapered slot antennas are a class of travelling wave antennas composed of a slot line that gets wider through the antenna until the wave detaches to air and microstrip line was chosen as the antenna feed, a microstrip line to slot line transition was needed to be designed. To obtain a wideband antenna, a wideband microstrip line to slot line transition was designed through the use of Chebyshev impedance transformer circuit. The designed microstrip line to slot line transition showed good return loss characteristics in the frequency band of 26-47 GHz according to the simulation results carried out in HFSS.

A parametric study about the relationship between physical antenna parameters (aperture width, antenna length and ground extension) and the radiation pattern was performed for both LTSA and CWSA. In this study, simulations in HFSS were carried out by changing one of the parameters of the antenna while keeping others constant. Then, the variations in the E-plane and H-plane beamwidths and sidelobe levels were observed and discussed. The results of this study were also compared with a similar study presented in [10], and a good agreement between these studies was observed.

The conclusions drawn from the parametric studies are summarized in Table 11.

Table 11 Summary of the Parametric Study Results

	LTSA				CWSA			
	E-BW	H-BW	E-SLL	H-SLL	E-BW	H-BW	E-SLL	H-SLL
Increasing Antenna Length	↓	↓	–	↑	↓	↓	↑	–
Increasing Aperture Width	↓	↑	↓	↓	↓	↔	↓	↑
Increasing Ground Extension	–	–	–	–	–	↔	↔	↑

The up-arrow in the table indicates that the pattern parameter is increasing with the increase in the antenna parameter, down-arrow indicates a decrease, the horizontal arrow indicates no change and a dash means that the pattern change is dependent on at least one more physical parameter so a generalization can not be done.

As seen in Table 11, the general effects of the physical parameter change on antenna pattern are similar for the LTSA and CWSA cases. Generally, increasing the length of the antenna decreases the half-power beamwidths in both planes. An increase in the aperture width acts as to decrease both the beamwidth and the sidelobe level in E-plane. The change in the ground extension has no significant effect on H-plane beamwidth or E-plane sidelobe level, but increasing the ground extension increases the H-plane sidelobe level.

The CWSA needs some kind of taper in order to get a reasonable return loss value from the antenna. Two different taper profiles as exponential and linear taper were considered and according to the results of the HFSS simulations, it was seen that there is not a significant difference in the antenna pattern for the linear taper and exponentially tapered CWSA cases. The exponential taper simulations were used in the parametric study. Although there is not a significant change in antenna pattern with taper profile, the usable antenna bandwidth depends on it. For narrow aperture width CWSAs, the return loss is not affected by the taper profile, however for an

aperture width of $1\lambda_0$, the CWSA with exponential taper exhibits lower return loss in comparison with linear taper.

The main aim of the thesis study was to get an understanding of the possible chance of using a transition between LTSA and CWSAs to obtain reconfigurability in the antenna radiation pattern. It was expected to get a narrower beam with a tradeoff of higher sidelobe level for a transition from LTSA to CWSA. As a result of the parametric study, it was seen that for most of the configurations, the desired pattern change could be obtained. The configurations that show more significant pattern change and the radiation pattern graphs for these configurations are given in Chapter 3. The amount of fall in the beamwidth is on the orders of 5-15 degrees and the rise in the sidelobe levels are on the order of 5-10 dB for a transition between LTSA and CWSA with same antenna parameters.

To prove the results of the parametric study obtained from simulations, antenna pattern measurements for four antennas were made. Due to the problems in manufacturing phase, the substrate (Duroid 5880) that was used in the parametric study simulations was not used in the manufactured antennas. So a new transition from microstrip line to slot line was designed. Four antennas were manufactured with the new transition design on the new substrate (RO4003). The pattern measurements of these antennas were performed in both planes and a good agreement between measurement and simulation results were observed. When the measured patterns of LTSAs and CWSAs having the same physical sizes were compared, it was seen that the desired reconfigurability was not achieved due to the split beam characteristics of CWSAs, also seen in simulations. This was due to the fact that the dielectric constant of the new substrate used in the manufactured antennas was too high and not suitable to be used in the design of TSAs. Therefore the conclusion drawn through the measurement results is the importance of the choice of the dielectric substrate for the design of TSAs. The dielectric constant of the substrate should be low for the proper radiation of the antenna. If a substrate with high dielectric constant is chosen as in this work, then the effective dielectric constant need to be lowered by introducing a cavity under the antenna or by drilling holes in the substrate as proposed in [12] and [13], respectively.

REFERENCES

[1] Balanis, Constantine A., *Antenna theory : analysis and design,* John Wiley & Sons, Inc., New York : 1982.

[2] Milligan, T. A., Traveling-Wave Antennas, Chapter 10 in *Modern Antenna Design,* Second Edition, John Wiley & Sons, Inc., NJ, USA. : 2005.

[3] Amena Kauser Syeda, "Design of a Wideband Vivaldi Antenna Array and Performance Enhancement of Small Vivaldi Arrays Using Baffles," B.E., Electronics and Communication Engineering, Osmania University, India, 2003.

[4] K.S. Yngvesson, T.L. Korzienowski, Y.S. Kim, "The Tapered Slot Antenna-A New Integrated Element for Millimeter-Wave Applications," *IEEE Trans. on Microwave Theory and Techniques*, vol. MTT-37, pp. 365-374, Feb. 1989.

[5] P. J. Gibson, "The Vivaldi Aerial," *Proc. 9th European Microwave Conf. Brighton, U.K,* pp. 101-105, *1979*.

[6] S.N. Prasad, S. Mahapatra, "A Novel MIC Slot-Line Antenna," *Proc. 9th European Microwave Conf. Brighton, U.K,* pp.120-124, 1979.

[7] K. Sigfrid Yngvesson, Daniel H. Schaubert, Thomas L. Korzienowski et al, "Endfire Tapered Slot Antennas on Dielectric Substrates," *IEEE Transactions on Antennas and Propagation*, Vol. AP-33, No. 12, December 1985.

[8] R. Janaswamy, "Radiation Pattern Analysis of the Tapered Slot Antenna," Ph.D. dissertation, Univ. Massachusetts, USA, 1986.

[9] J.F. Johansson, "A Moment Method Analysis of Linearly Tapered Slot Antennas," *IEEE Antennas and Propagation Society International Symposium,* pp. 383-386, 1989.

[10] Adnan Köksal, "Characterization and Optimization of Linearly Tapered Slot Antenna Pattern," *International Journal of Infrared and Millimeter-Waves,* Vol.18, No.8, pp. 1525-1537, 1997.

[11] Dong-Sik Woo; Young-Gon Kim; Kang Wook Kim; Young-Ki Cho; , "Ultra-wideband millimeter-wave tapered slot antennas," *IEEE Antennas and Propagation Society International Symposium,* pp.1969-1972, June 2007.

[12] I.K. Kim, N. Kidera, S. Pinel, J. Papapolymerou, J. Laskar, J.G. Yook, M.M. Tentzeris, "Linear Tapered Cavity-Backed Slot Antenna for Millimeter-Wave LTCC Modules," *IEEE Antennas and Wireless Propagation Letters,* Vol.5, No.1, pp.175-178, Dec. 2006.

[13] Jeremy B. Muldavin, Gabriel M. Rebeiz, "MM-Wave Tapered Slot Antennas on Synthesized Low Permittivity Substrates," *IEEE Transactions on Antennas and Propagation,* Vol.47, No.8, pp.1276-1280, August 1999.

[14] Y.S. Kim, K.S. Yngvesson, "Characterization of Tapered Slot Antenna Feeds and Feed Arrays," *IEEE Transactions on Antennas and Propagation,* Vol.38, No.10, pp.1559-1564, October 1990.

[15] J.H.G. Ender, A.R. Brenner, "PAMIR - a wideband phased array SAR/MTI system," *IEE Proceedings Radar, Sonar and Navigation*, Vol.150, No.3, pp.165 – 172, June 2003.

[16] Ian Wood, "Linear Tapered Slot Antenna for Imaging Arrays," Ph.D. dissertation, University of Victoria, USA, 2005.

[17] Simons, R. N. Coplanar Waveguide Transitions, Chapter 10 in *Coplanar Waveguide Circuits, Components, and Systems*, John Wiley & Sons, Inc., New York, USA. : 2002.

[18] Bernd Schüppert, "Microstrip/Slotline Transitions: Modelling and Experimental Investigation," *IEEE Trans. Microwave Theory Tech.* Vol.36, No.8, August 1988.

[19] Johnson, Richard C., *Antenna Engineering Handbook,* 3rd Edition, pp: 8.5-8.6, McGraw-Hill. : 1993.

[20] R. Janaswamy, D.H. Schaubert, "Characteristic Impedance of a Wide Slotline on Low-Permittivity Substrates," *IEEE Trans. Microwave Theory Tech.* Vol MTT-34, No 8, August 1986.

[21] J. Thaysen, K.B. Jakobsen, J. Appel-Hansen, "A Wideband Balun-How Does It Work?," *Applied Microwave&Wireless*, Vol.12, No.10, pp.40-50, October 2000.

[22] Nai-Biao Wang, Yang-Chang Jiao et al, "A Simple Low-Loss Broadband 1-14 GHz Microstrip-to-Slotline Transition," *Microwave and Optical Technology Letters,* Vol.51, No.9, September 2009.

[23] B. Boyer, J. Haidar, A. Vilcot, and M. Bouthinon, "Tunable microwave load based on photoinduced plasma in silicon," *IEEE Transaction on Microwave Theory and Techniques*, vol.45, issue 8, pp. 1362-1367, Aug. 1997.

[24] R.K. Shevgaonkar and S. Shevgaonkar, "Study of optically controlled microwave devices" *Proceedings of International Union of Radio Science (URSI): XXIX General Assembly*, August 7 - 16, 2008, Chicago, USA.

[25] M.R. Chaharmir, J. Shaker, M. Cuhaci and A. Sebak, "Novel photonically-controlled reflectarray antenna," *IEEE Transactions on Antennas and Propagation*, vol. 54, no. 4, pp. 1134-1142, April 2006.

[26] T. Morolari, "Characterization of Optically Sensitive Polymer and Application to Microwave Antenna," M.A.Sc. Thesis Dissertation, Carleton University, Ottawa, Canada, Dec. 2009.

APPENDIX A - Calculation of characteristic impedance of slot lines and microstrip lines

The characteristic impedance of a slot line can be calculated as:

$$Z_0 = 60 + 3.69\sin\left[\frac{(\varepsilon_r - 2.22)\pi}{2.36}\right] + 133.5\ln(10\varepsilon_r)\sqrt{\frac{W}{\lambda_0}} +$$

$$2.81\left[1 - 0.011\varepsilon_r(4.48 + \ln\varepsilon_r)\right]\left(\frac{W}{h}\right)\ln\left(\frac{100h}{\lambda_0}\right) \qquad \text{(A1)}$$

$$+131.1(1.028 - \ln\varepsilon_r)\sqrt{\frac{h}{\lambda_0}} + 12.48(1 + 0.18\ln\varepsilon_r)\left(\frac{\left(\frac{W}{h}\right)}{\sqrt{\varepsilon_r - 2.06 + 0.85\left(\frac{W}{h}\right)^2}}\right)$$

where h is the height of the dielectric substrate and W is the width of the slot line.

The guided wavelength of the slot line can be found as:

$$\frac{\lambda_g}{\lambda_0} = 1.045 - 0.365\ln\varepsilon_r + \frac{6.3\left(\frac{W}{h}\right)\varepsilon_r^{\,0.945}}{238.64 + 100\left(\frac{W}{h}\right)} - \left(0.148 - \frac{8.81(\varepsilon_r + 0.95)}{100\varepsilon_r}\right)\ln\left(\frac{h}{\lambda_0}\right) \qquad \text{(A2)}$$

The effective dielectric constant and characteristic impedance of a microstrip line can be calculated as:

For W/h<1:

$$\varepsilon_{eff} = \frac{\varepsilon_r + 1}{2} + \frac{\varepsilon_r - 1}{2}\left[\frac{1}{\sqrt{1 + \frac{12h}{W}}} + 0.04\left(1 - \frac{W}{h}\right)^2\right] \qquad \text{(A3)}$$

$$Z_c = \frac{60}{\sqrt{\varepsilon_{eff}}}.\ln\left(\frac{8h}{W} + \frac{W}{4h}\right) \qquad \text{(A4)}$$

For W/h>1:

$$\varepsilon_{eff} = \frac{\varepsilon_r + 1}{2} + \frac{\varepsilon_r - 1}{2}\left(\frac{1}{\sqrt{1 + \frac{12h}{W}}}\right) \tag{A5}$$

$$Z_c = \frac{120\pi}{\sqrt{\varepsilon_{eff}}} \cdot \frac{1}{\left[\frac{W}{h} + 1.393 + \left(0.677.\ln\left(\frac{W}{h} + 1.444\right)\right)\right]} \tag{A6}$$

where W is the width of the microstrip line.

APPENDIX B - Design of Chebyshev Impedance Transformer

The impedance calculation formulas for Chebyshev impedance transformer with three sections is presented here.

$$\sec\theta_m = \cosh\left[\frac{1}{N}\cosh^{-1}\left(\frac{\ln(Z_L/Z_0)}{2\Gamma_m}\right)\right] = \cosh\left[\frac{1}{3}\cosh^{-1}\left(\frac{\ln(152.76/50)}{2\times 0.05}\right)\right] = 1.5849 \quad \text{(B1)}$$

$$2\Gamma_0 = A\sec^3\theta_m = 0.05\times(1.5849)^3 \Rightarrow \Gamma_0 = 0.0995 \quad \text{(B2)}$$

$$2\Gamma_1 = 3A\left(\sec^3\theta_m - \sec\theta_m\right) = 3\times 0.05\left(1.5849^3 - 1.5849\right) \Rightarrow \Gamma_1 = 0.1797 \quad \text{(B3)}$$

$$\ln Z_1 = \ln Z_0 + 2\Gamma_0 = \ln 50 + (2\times 0.1797) \Rightarrow Z_1 = 61.01\Omega \quad \text{(B4)}$$

$$\ln Z_2 = \ln Z_1 + 2\Gamma_1 = \ln 61.01 + (2\times 0.1797) \Rightarrow Z_2 = 87.39\Omega \quad \text{(B5)}$$

$$\ln Z_3 = \ln Z_2 + 2\Gamma_2 = \ln 87.39 + (2\times 0.1797) \Rightarrow Z_3 = 125.19\Omega \quad \text{(B6)}$$

where, $A=\Gamma_m=0.05$, $\Gamma_2=\Gamma_1$ due to symmetry and N=3.

Beam Steerable Traveling Wave Meander Line Antenna Using Varactor Diode for X-Band Applications

Nihan Gokalp[(1)], Özlem Aydin Civi[(2)]
[(1)] Radar & Electronic Hardware Department, ASELSAN Inc., Ankara, Turkey
e-mail:ngokalp@aselsan.com.tr
[(2)] Dept. of Electrical-Electronics Eng., Middle East Technical Univ., Ankara, Turkey
e-mail:ozlem@metu.edu.tr

I. Introduction

In recent years, printed microstrip antennas are widely preferred in several commercial and military applications due to the characteristics such as light weight, low profile, low manufacturing cost, and easy integration with active devices and beam forming network. Besides these advantages, high directivity, low side lobe level and polarization agility characteristics of printed traveling wave antennas make these antennas as good candidates for radar applications. Especially, traveling wave meander line antennas have advantages over printed standing wave antennas, such as side lobe level control, low return loss and electronic beam-steering capability, [1-3]. In this paper, a novel beam-steering traveling wave meander line antenna has been introduced for X-band radar applications. Beam steering capability of the meander line antenna has been achieved by loading the antenna by varactor diodes. The design and characteristics of the varactor loaded meander line antenna are presented in the following sections.

II. Beam Steerable Meander Line Antenna

The beam steerable meander line antenna is composed of eight meander line elements and sixteen varactor diodes placed on the arms of the meander line as shown in Figure 1. The operation frequency of the meander line antenna is selected as 10 GHz, which is suitable for X band radar applications as well. Due to its low dielectric loss and high frequency operation capability, the antenna system is printed on 15 mil thick Rogers 5880 with ε_r=4.6. Meander line array is terminated with 50 ohm to prevent the reflection of the wave from the end of the array. Varactor diode is a voltage controllable device in which the capacitance varies with the bias voltage. Bias lines and DC bias pad are also shown in Figure 1.

The meander line antenna element (unit cell of the array) is a microstrip line formed by four right-angled bends. In order to reduce the right-angled discontinuity, right-angled bends are chamfered. Radiation of the meander line antenna mainly occurs from the right-angled bends, [1]. It is possible to model

978-1-4244-2042-1/08/$25.00 ©2008 IEEE

these right-angled bends as magnetic current elements as seen in Figure 2 (a), [1] At the bend there is an imbalance magnetic current since the current path on the inside edge is shorter than one on the outside edge. Thus, the four-corner meander line antenna cell can be modeled as an array of magnetic current elements fed in a phase progression for a wave-wave array. The properties of the meander line antenna radiation pattern are controlled by the *s*, *l* and *d* parameters of the unit meander line cell given in Figure 2 (b). For instance, when $s=\lambda/2$, $l=\lambda/4$ and $d=3\lambda/4$, the vertical and horizontal components of the radiated field have a phase difference of $\pi/2$ and thus produce circular polarization. In addition by varying the length *s,* it is possible to steer the beam towards the desired position. Furthermore, as the number of elements in the meander line array increases, gain increases, side lobe level decreases and power reached to the termination decreases, i.e. efficiency of the array increases as well.

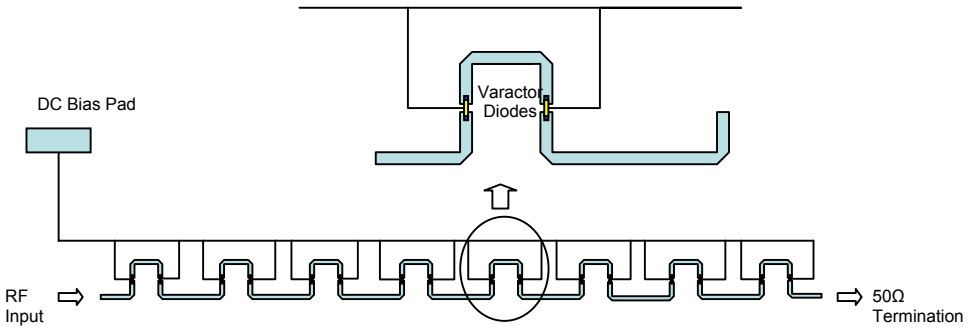

Figure 1. The Schematic view of Beam Steerable Meander line Antenna

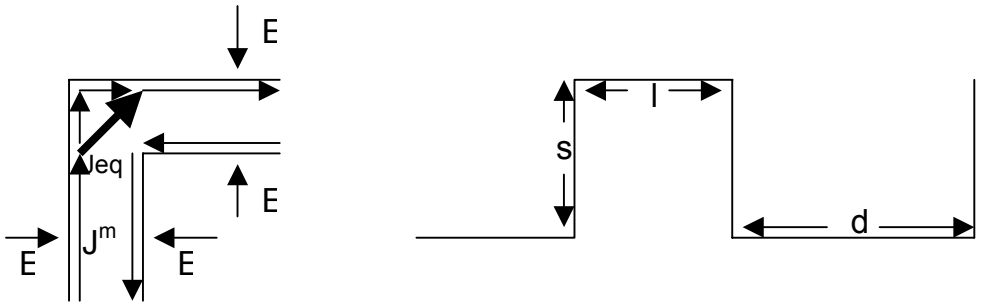

Figure 2. (a) Equivalent Current Distribution at the Right-Angled Bend
(b) Parameters of a Meander Line Cell

As mentioned above, in order to achieve beam steering at a fixed frequency, electrical dimensions of the antenna should be varied in some manner. In this work, beam steering has been achieved by loading the arms of the meander line by varactor diodes. This is equivalent to changing the length of *s*. Varactor diode used in this antenna is MICROSEMI MPV2100-206. Under 0 volt bias varactor diode capacitance equals to 3.25 pF and it decreases up to 0.25 pF when 20 volts bias voltage is applied to varactor.

Ansoft Designer v3, -a commercial computer software package based on the Method of Moment (MoM)-, is used to design the meander line antenna. S-parameters of the varactor are inserted into the electromagnetic model of the meander line antenna in Designer. Then, full wave electromagnetic simulation has been performed. The obtained S parameters of the antenna are shown in Figure 3.

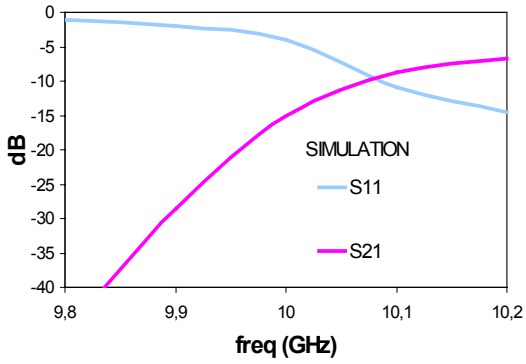

Figure 3. Simulated S-parameter results

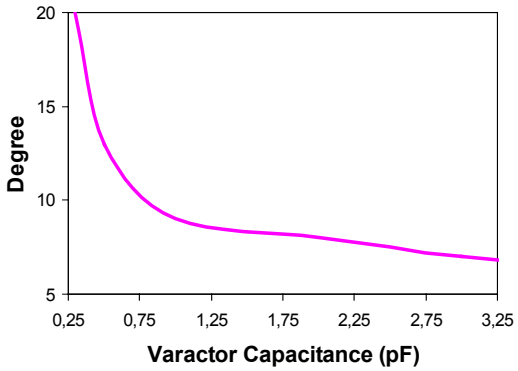

Figure 4. Beam direction versus varactor capacitance

EM simulations have been performed for different values of varactor capacitance. From the results of these simulations it is observed that main beam direction has been varied as shown in Figure 4.

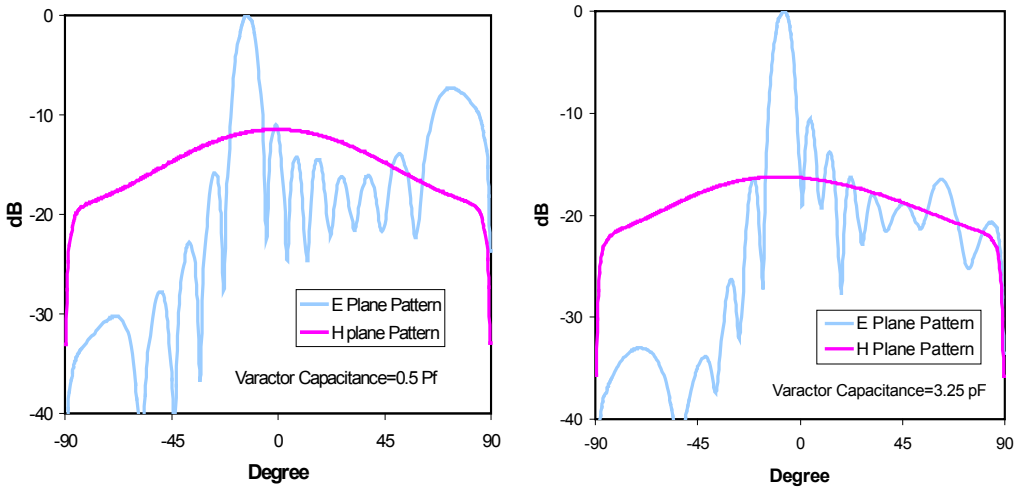

(a) (b)

Figure 5. Radiation patterns in E plane and H plane for (a) varactor capacitance of 0.5 pF and for (b) varactor capacitance of 3.25 pF.

Simulated radiation patterns in E and H planes of the meander line antenna for 0.5 pF and 3.25 pF capacitance values have been shown in Figure 5. It is observed

that when varactor capacitance is 0.5 pF the main beam is in the direction of 5°, whereas main beam is steered to 15° when the varactor capacitance is 3.25 pF.

A prototype antenna is currently in fabrication. The measurement results of the array will be presented at the conference.

III. Conclusions

This paper presents a novel beam steerable meander line antenna with varactor diode for X-band applications. Beam steering has been achieved by loading the arms of the meander line antenna with varactor diodes. The capacitances of the varactor diodes have been controlled by DC bias voltage. Instead of varactor diodes, RF-MEMS variable capacitances can be used [4] to scan the beam. Since the insertion loss of MEMS capacitances are small compared to loss of varactor diodes, use of MEMS capacitors will increase the overall efficiency of the antenna.

Acknowledgement

This work is partially supported by The Scientific and Technical Research Council of Turkey (TUBITAK-EEEAG-107E090) and COST IC0603 ASSIST.

References

[1] Dural,G., *Theory and Design of Microstrip Rampart Line Arrays*, Master Thesis, Middle East Technical University, Ankara, Turkey, 1983.

[2] R. Ratmon, I. Oz, C. J. Samson, "Comparison of Resonant and Wave-Wave Meander-Line Antenna" Electrical & Electronics Engineers in Israel,1991, *17th Convention,* pp.149-151, 5-7 March 1991.

[3] M. Tiuri, S. Tallqvist, S. Urpo, "Chain Antenna", *1974 Antennas and Propagation Society International Symposium*, vol. 12, pp.274 – 277, Jun 1974.

[4] E. Erdil, K. Topalli, M. Unlu, O. Aydin Civi, and Tayfun Akin, "Frequency Tunable Microstrip Patch Antenna Using RF MEMS Technology", *IEEE Transactions on Antennas and Propagation*, vol.55, no.4, pp.1193-1196, April 2007.

Dual Frequency Reflectarray Cell Using Split-ring Elements with RF MEMS Switches

Caner Guclu* [(1)], Julien Perruisseau-Carrier[(2)], and Ozlem Aydin Civi[(1)]
(1) Middle East Technical University (METU) - Department of Electrical and Electronics Engineering, Ankara, Turkey
(2) Centre Tecnològic de Telecomunicacions de Catalunya (CTTC), Barcelona, Spain
E-mail: cguclu@metu.edu.tr

Introduction

In this study, a dual frequency circularly polarized reconfigurable reflectarray (RA) cell with RF-MEMS switches is designed. RA combines the advantages of reflector-based and phased array antennas, providing a low-cost and high performance antenna array solution. In their reconfigurable implementations, RAs are capable of electronic beam scanning/forming with potential multiband operation, as discussed here. The design principles of RA are described in [1]. For beam forming/steering capability of a RA antenna, it is important that the RA cell's phase design curve is linear and has a phase coverage of 360° or more. For linearly polarized RAs, various methods for controlling the reflection phase of the RA cell are presented in [2], [3]. In case of circularly polarized RA antennas, identical reflective elements with different angular rotation can be used as an alternative to the element geometry modification [4]. When the element is rotated, a reflection phase that is linearly proportional to the rotation angle of the element is achieved, provided that the senses of polarization of incident and reflected waves are the same. In this work the RA element is a ground-backed split-ring on a quartz substrate with RF-MEMS switches located on the reflecting surface. The ring antenna is advantageous over patches for multi-frequency applications, since it geometrically allows placement of elements in various sizes [5]. In this design, dual-frequency operation is achieved by placing rings in two different sizes on the same substrate, with either concentric layout or interlaced arrays of unit cells. In the literature, there are a few examples of dual band reflectarrays, which are not reconfigurable [5]. In this work, reconfigurability is achieved by series RF-MEMS switches that are placed on the ring strips. Switches are used to change the orientation of the gaps to realize the rotation of the element. The RA antenna composed of these elements will be capable of beam-steering independently for the two operating frequencies. In the following section the RA unit cell geometry is presented, some simulation results are given, and the phase design curve is discussed.

Principles and Design of the RA Cell

The split-ring is chosen as a RA element. The control of the reflection phase by rotating the element is studied based on mathematical derivations given in [4] and [5]. The phase of the reflected co-polarized component is shifted by an additional phase which is twice the geometrical rotation angle as shown in Figure 1. The ground-backed split-ring used here is capable of suppressing the reflected cross-polarized CP wave in a specific band, allowing the control of the phase of the reflected wave. Note that any elliptically polarized wave can be decomposed into two waves of opposite senses of circular polarization, which correspond here to cross- and co-polarizations with respect to the sense of polarization of the incident CP wave.

978-1-4244-4968-2/10/$25.00 ©2010 IEEE

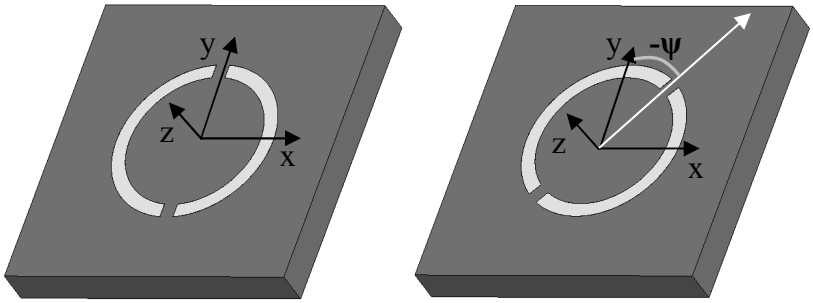

(a) (b)

Figure 1. Split-ring element as the RA cell.

Here, we briefly present the basic mathematics demonstrating the link between element rotation and phase shift. We assume a time harmonic E-field propagating in the z direction as the incident field to the structure:

$$\overrightarrow{E^i} = (\hat{a}_x + j\,\hat{a}_y)E^i\,e^{jz} \qquad (1)$$

If the reflection coefficients of the x and y components of the E-field are known as Γ_x, Γ_y for the reference element (Figure 1-a), then the reflected field for the ψ degree-rotated element (Figure 1-b), can be found as:

$$\overrightarrow{E^r} = 0.5E^i(\Gamma_x - \Gamma_y)(\hat{a}_x - j\,\hat{a}_y)e^{j2\psi}e^{-jz} + 0.5E^i(\Gamma_x + \Gamma_y)(\hat{a}_x + j\,\hat{a}_y)\,e^{-jz} \qquad (2)$$

This equation shows that phase control by element rotation is only applied to the reflected wave component in the same sense of circular polarization with the incident field, i.e. the co-polarized reflected wave. In general the reflected wave is an elliptically polarized wave, however provided that $\Gamma_x = -\Gamma_y$, the reflected wave is a circularly polarized wave whose phase can be controlled by angular rotation of the element. The cell designed to satisfy this condition is shown in Figure 2.

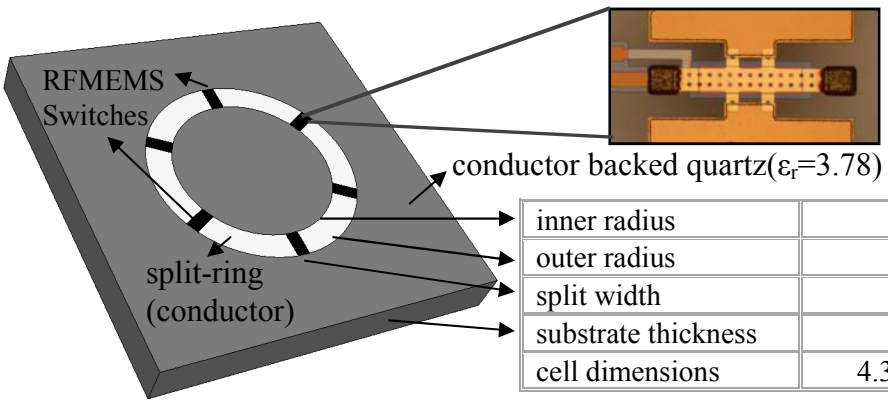

inner radius	1mm
outer radius	1.2mm
split width	0.2mm
substrate thickness	0.5mm
cell dimensions	4.3mm x4.3 mm

Figure 2. RA cell geometry with RF-MEMS switches produced in METU.

The split-ring in Figure 2 is designed to control the reflection phase at 27.15GHz. This split-ring is used in the dual-frequency RA together with another split-ring for 35GHz.

To avoid grating lobes at 35GHz, the cell dimensions are set as the half a free-space wavelength at 35GHz (λ_o=8.6mm).

There are pairs of RF MEMS switches, positioned on either side of the split-ring. These pairs have different angular orientations as shown in Figure 2. Proper actuation of the series switches corresponds to rotating the axis of the gaps (open switch pairs). The progressive angular difference between the axes of the pairs of switches determines the phase resolution.

EM modeling of the RA cell is performed in Ansoft HFSS. With HFSS's Floquet port simulation tool, periodic boundary conditions are used to simulate an infinite array environment. The Floquet port treats the simulated structure as a two port network as shown in Figure 3 and provides S-parameters that are used to calculate co- and cross-circularly polarized waves as in equations (3) and (4).

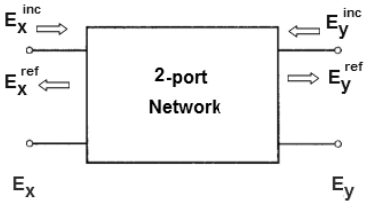

$$\begin{bmatrix} E_x^r \\ E_y^r \end{bmatrix} = \begin{bmatrix} s_{11} & s_{12} \\ s_{21} & s_{22} \end{bmatrix} \begin{bmatrix} E_x^i \\ E_y^i \end{bmatrix}$$

Figure 3. Floquet port S-parameters corresponding to E-field components.

$$\Gamma_{cross} = E_{cross}^r / E^i = \tfrac{1}{2}[(s_{11} + s_{22}) + j\,(s_{12} - s_{21})] \quad (3)$$

$$\Gamma_{co} = E_{co}^r / E^i = \tfrac{1}{2}[(s_{11} - s_{22}) + j\,(s_{12} + s_{21})] \quad (4)$$

In Figure 4, the magnitude of the reflection coefficient of co- and cross- pol. components are given and it is seen that the cross-polarization is suppressed around 27.15GHz. The simulation results of the co-/cross-pol. levels and reflected wave phase corresponding to sweeping ψ from 0° to 180° at 27.15GHz are given in Figure 5 and Figure 6. As expected, the reflection phase is linearly proportional to the rotation angle of the element and the cross-pol. suppression is better than 20dB for any rotation angle.

Dual Frequency Operation: Two split-rings of different sizes are placed on the substrate to achieve operation at two frequencies. The independent control of the states of RF-MEMS switches on the two rings provides independent beam scanning at both frequencies. These two split-rings are placed concentrically as shown in Figure 7. Another possible configuration is an interlaced array of two rings of different sizes. Both dual-frequency configurations are designed and simulated. If two operation frequencies are close, the concentric configuration is prone to more coupling since the two rings are located very closely. Interlaced array configuration allows relatively closer operating frequencies, for example 28GHz and 35GHz. After the completion of the optimized design of unit cell, a 10x10-element RA antenna will be designed and the first prototype will be produced with frozen MEMS switches to prove the concept. Measurement results in the form of radiation patterns will be presented in the conference.

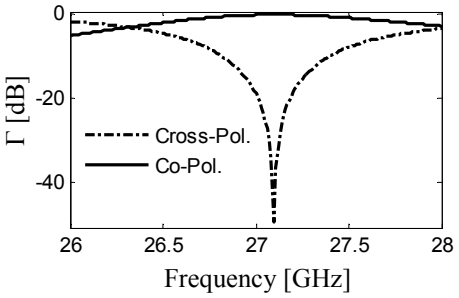

Figure 4. Co- and cross-pol. reflection magnitudes vs. frequency.

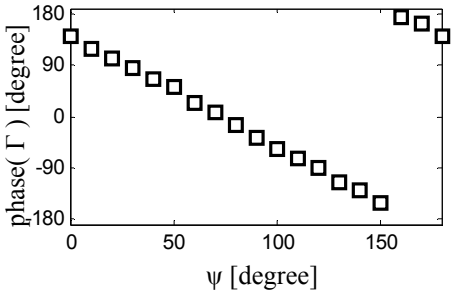

Figure 5. Phase of co-pol. reflected wave vs. ψ, phase design curve at 27.15GHz.

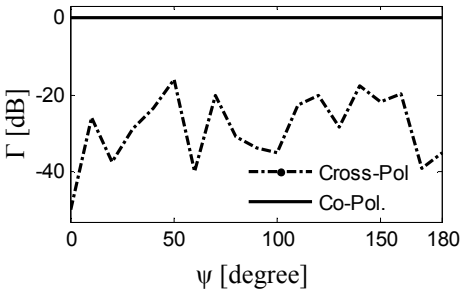

Figure 6. Co- and cross-pol. reflection magnitudes vs. ψ at 27.15GHz.

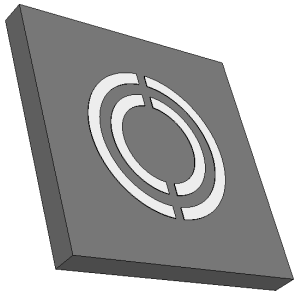

Figure 7. Concentrically placed split-ring for dual frequency operation.

Acknowledgments

This work is partially supported by The Scientific and Technical Research Council of Turkey (TUBITAK-EEEAG-107E090) and COST IC0603 ASSIST.

References

[1] Pozar, D.M.; Targonski, S.D.; Syrigos, H.D., "Design of millimeter wave microstrip reflectarrays," *Antennas and Propagation, IEEE Transactions on* , vol.45, no.2, pp.287-296, Feb 1997

[2] Javor, R.D.; Xiao-Dong Wu; Kai Chang, "Beam steering of a microstrip flat reflectarray antenna," *Antennas and Propagation Society International Symposium, 1994. AP-S. Digest* , vol.2, no., pp.956-959 vol.2, 20-24 Jun 1994

[3] Pozar, D.M.; Metzler, T.A., "Analysis of a reflectarray antenna using microstrip patches of variable size," *Electronics Letters* , vol.29, no.8, pp.657-658, 15 April 1993

[4] Huang, J.; Pogorzelski, R.J., "A Ka-band microstrip reflectarray with elements having variable rotation angles," *Antennas and Propagation, IEEE Transactions on* , vol.46, no.5, pp.650-656, May 1998

[5] Han, C.; Rodenbeck, C.; Huang, J.; Kai Chang, "A C/ka dual frequency dual Layer circularly polarized reflectarray antenna with microstrip ring elements," *Antennas and Propagation, IEEE Transactions on* , vol.52, no.11, pp. 2871-2876, Nov. 2004

RECONFIGURABLE ANTENNAS BY RF MEMS TECHNOLOGY

Kagan Topalli, Omer Bayraktar, Mehmet Unlu, Ozlem Aydin Civi, Simsek Demir, and Tayfun Akin

Middle East Technical University, Dept. of Electrical and Electronics Eng., Ankara, Turkey, kagan@metu.edu.tr

INTRODUCTION

MEMS technology is a powerful way of merging the functions of sensing and actuation with computation and communication to control physical parameters at the microscale. Present markets of MEMS technology are mainly in pressure and inertial sensors, inkjet print heads, and high-resolution digital displays. Future and emerging applications include tire pressure sensing, fiber optical components, fluid management and processing devices for chemical microanalysis, medical diagnostics, and drug delivery, and RF and wireless electronics, namely RF MEMS. The application of MEMS technology to RF systems enables production of components with low power consumption, high linearity, low insertion loss, and high isolation. RF MEMS components are particularly attractive for researchers due to their tunable properties. This technology is used to implement many tunable circuits and systems in a miniaturized way that has never been implemented before using any other technology [1].

With the development of advanced commercial and military microwave systems and applications, there is a growing need for a single antenna that can be operated at different frequencies, where each of these frequencies are tunable. For example, an antenna whose resonant frequency can be tuned continuously in a frequency range can be used in radar applications for frequency hopping. A tunable antenna can also be used in telecommunications to maintain different system frequencies. Another application area of such antennas is satellite communications systems, where one operating frequency is used for the transmitter and the other for the receiver. There is a need for monolithic implementation of such antennas to reduce the system size, parasitic coupling between radiators, system complexity, and cost.

Monolithic implementation of various antennas and components has become possible with the MEMS technology. The MEMS technology and its application to RF systems enable production of tunable components such as switches, capacitors, and matching networks with low power consumption, high linearity, and high performance [1]. RF MEMS tunable circuit elements make the realization of reconfigurable antenna structures more efficiently in terms of lower insertion losses and lower volumes. Also, the monolithic fabrication of the antenna together with these tunable components reduces the power losses and parasitic effects compared to hybrid integration of antennas with discrete components. It has been shown in literature that MEMS switches and MEMS tunable capacitors are used in reconfigurable antennas to control the resonant frequency, bandwidth, polarization, and radiation pattern [2], [3].

This paper presents the RF MEMS reconfigurable antennas designed and produced in METU using the in-house fabrication process developed at the Microelectronics Facilities. The next sections presents the frequency tunable slot antenna, frequency tunable patch antenna, the monolithic phased array, and the RF MEMS fabrication flow developed at METU.

FREQUENCY TUNABLE PATCH ANTENNA

Fig. 1 shows the frequency tunable patch antenna designed and fabricated at METU. The structure consists of a patch antenna loaded with a coplanar waveguide (CPW) loading section attached to the antenna via microstrip to CPW transition. The reconfigurability in the resonant frequency of the antenna is provided with the aid of the MEMS bridges acting as a variable capacitor placed on the CPW stub [3]. MEMS capacitors are electrostatically actuated with a low tuning voltage in the range of 0-11.9 V. The antenna resonant frequency can continuously be shifted from 16.05 GHz down to 15.75 GHz as the actuation voltage is increased from 0 to 11.9 V. These measurement results are in good agreement with the simulation results obtained with Ansoft HFSS as given in Fig. 1 (b).

DUAL-FREQUENCY RECONFIGURABLE SLOT DIPOLE ARRAY

This section of the paper presents a 4-element linear array of dual-frequency slot dipole antennas whose resonant frequencies are controlled via MEMS switches placed on the slots. Fig. 2 shows the schematic view of the dual-frequency array. The operation frequencies are selected as 10 and 16 GHz so that the system can be fitted into a 500 µm-thick 4” glass substrate. The distance between phase centers of antennas are 1.8 cm to avoid grating lobe for

both frequencies. The slot dipole antennas can either be operated at 10 GHz or 16 GHz with the aid of RF MEMS switches located on the slot arms. The feed network includes 50 Ω-100 Ω dual-frequency transformers, chamfered CPW right-angle bends and T-junctions. Fig. 3 (a) and (b) shows the fabricated prototypes of the slot antennas on a duroid substrate , where metallic strips are employed in order to model the switches in the up and downstate. Fig. 3 (c) gives the measured and simulated reflection coefficients values of the prototype antennas.

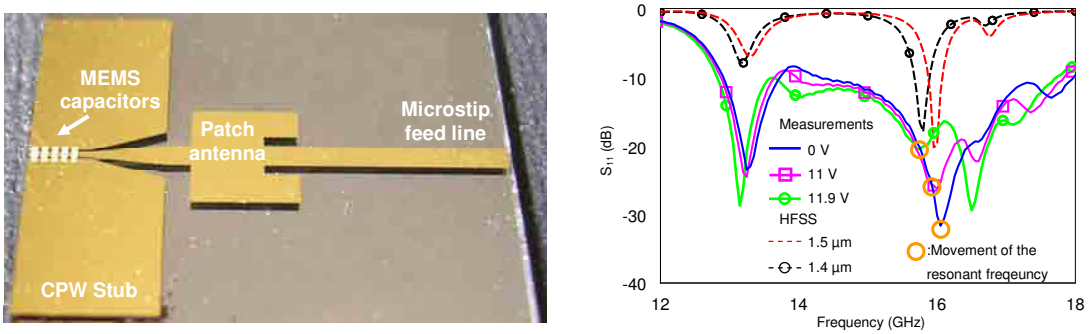

(a) (b)

Fig. 1. (a) The photograph of the patch antenna loaded with MEMS capacitors. (b) The measurement results of the patch antenna for different actuation voltages.

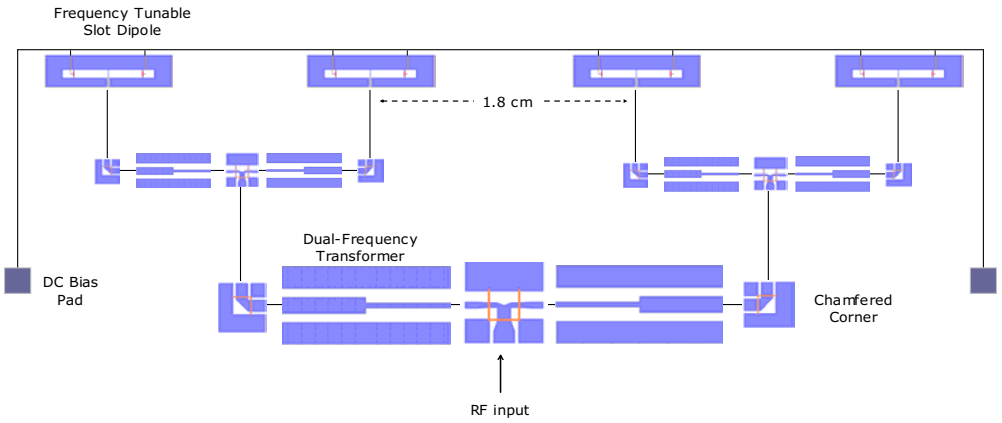

Fig. 2. The schematic view of the dual-frequency array.

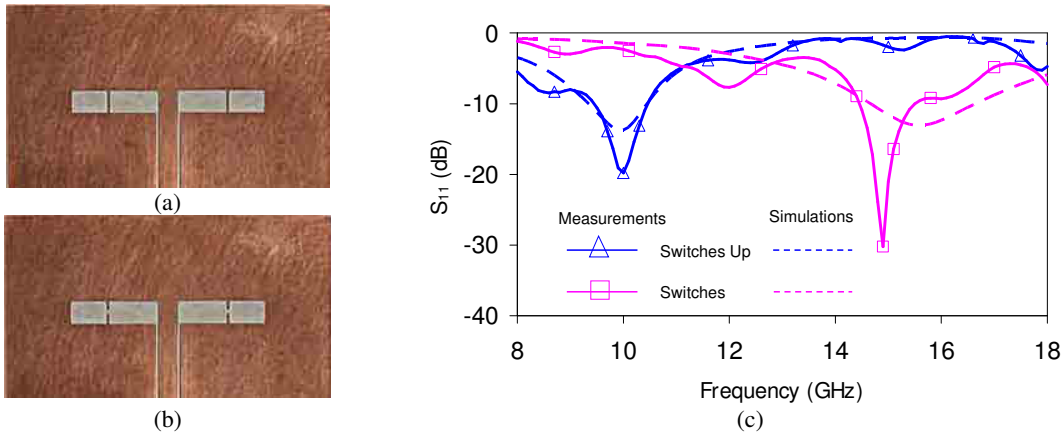

(a) (b) (c)

Fig. 3. Fabricated prototypes of the slot antennas and measurement results: (a) switches up, (b) switches down, and (c) measured and simulated performances of the prototype antennas.

MONOLITHIC PHASED ARRAY

This section presents the phased array system designed at 15 GHz employing 3-bit Distributed MEMS transmission line (DMTL) type phase shifters which are monolithically integrated with the feed network of the system and the radiating elements on the same substrate [7]. The phase shifters of the phased array include a total of 128 switches. The phase shifter can give 0°-360° phase shift with 45° steps at 15 GHz which is used to obtain various combinations of progressive phase shift in the excitation of radiating elements. The phased array is composed of four linearly placed microstrip patch antennas. Fig. 4 shows the photograph of the phased array fabricated on a glass substrate. The digital phase shifter used in the system is composed of a periodically loaded high-impedance transmission line (> 50 Ω) with MEMS bridges in series with lumped capacitors, forming a DMTL. Fig. 5 (a) shows the measured inserted phase shifts for different state. Fig. 5 (b) shows the measured radiation pattern results for different progressive phase shift. The main beam can be steered by 4°, 14° as the phase shifter states are adjusted accordingly. To the authors' knowledge this work is one of the first few monolithically fabricated electronically scanning phased array systems employing large amount of RF MEMS components, reported in the literature.

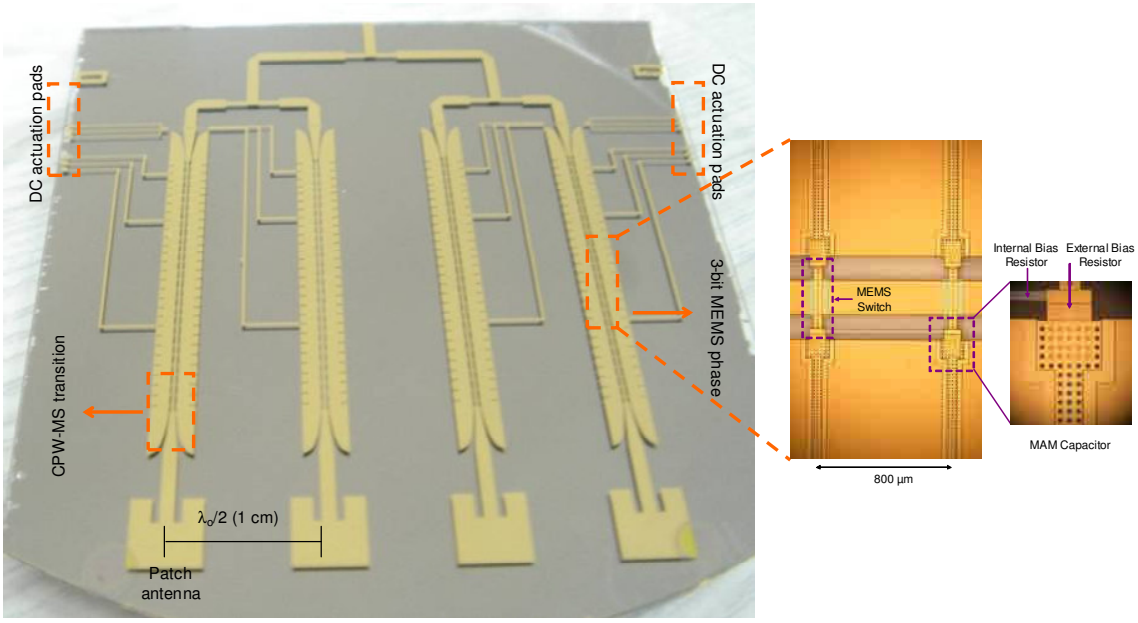

Fig. 4. (a) Photograph of the fabricated phased array. Total chip size is about 6 cm × 5 cm.

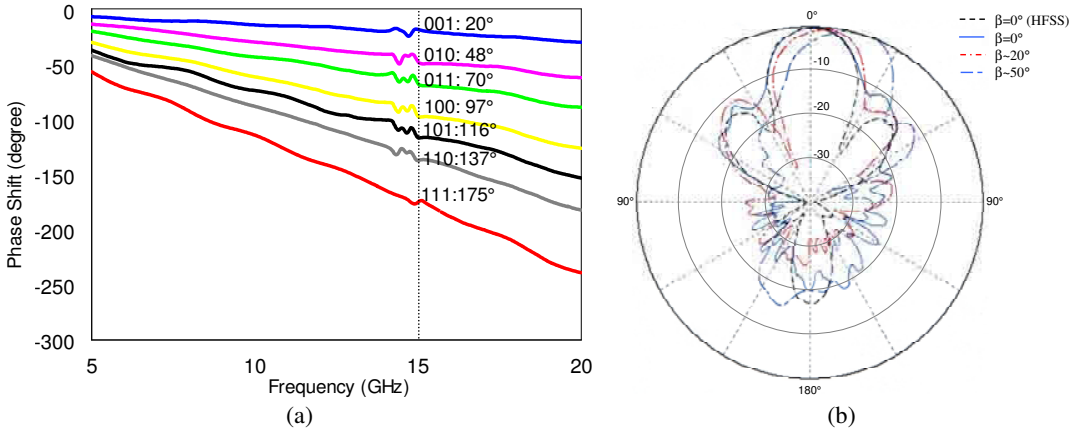

(a) (b)

Fig. 5. (a) Measured phase shift vs. frequency plot obtained for 8 states of the 3-bit RF MEMS phase shifter, (b) Measured radiation pattern of the monolithic phased array for different settings of the phase shifters.

FABRICATION PROCESS

Fig. 6 shows the fabrication process developed at METU Microelectronics Facilities. The process starts with sputtering of a 100/3000-Å thick Ti/Au layer, which is required as the seed layer for electroplating of the base metallization. The base metallization layer is formed using a 2-µm thick gold layer, which is electroplated inside the regions defined by the mold photoresist. The remaining Ti/Au seed layer is etched using wet etchants. A 3000 Å-thick Si_3N_4 layer is coated as the DC isolation layer using plasma enhanced chemical vapor deposition technique (PECVD) and patterned using the reactive ion etching (RIE) technique. The next step is the spin-coating of the photodefinable polyimide, PI 2737, as the 2-µm thick sacrificial layer. Then, a 1-µm thick gold layer is sputter-deposited and patterned. The sacrificial layer is wet etched, rinsed, and dried in a critical point dryer.

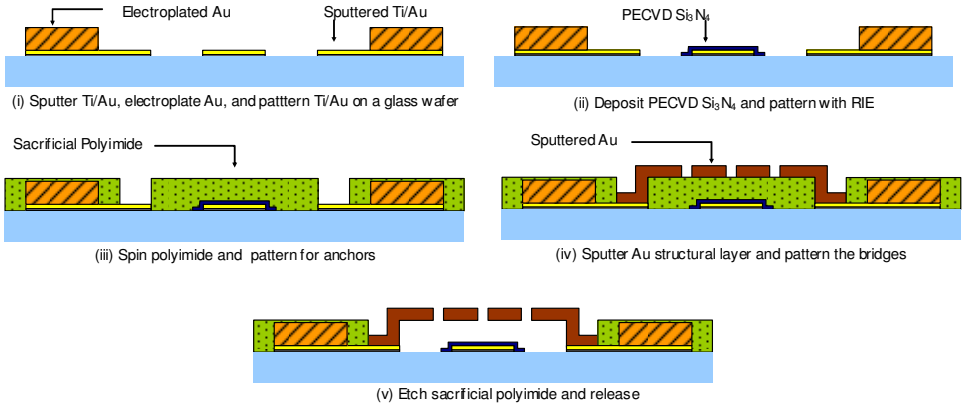

Fig. 6. The process flow used in the fabrication of the reconfigurable antenna structures.

CONCLUSIONS

This paper reviews some examples of reconfigurable antennas designed and fabricated using RF MEMS technology developed at METU. It is shown by the measurement results that the fabricated antennas satisfy the design specifications. More components, as well as production, modeling and packaging studies will be presented and discussed during the presentation in the conference.

ACKNOWLEDGMENT

This research is supported by The Scientific and Technical Research Council of Turkey (TUBITAK-COST IC 0603-107E090, TUBITAK-COST284-102E036, TUBITAK-104E041), Turkish State Planning Organization (DPT), and AMICOM (Advanced MEMS For RF and Millimeter Wave Communications) Network of Excellence under 6th Framework Program of European Union.

REFERENCES

[1] G. M. Rebeiz, "RF MEMS theory, design, and technology", *Hoboken, NJ: John Wiley & Sons*, 2003.
[2] J. C. Chiao, S. –Y. Cheng, J. L. Chang, I. M. Chio, Y. Kang, and J. Hayasaka, "MEMS reconfigurable antennas," *Int. J. RF Microwave CAE*, vol.11, pp. 301-309, 2001.
[3] E. Erdil, K. Topalli, M. Unlu, O. A. Civi, and T. Akin, "Frequency tunable microstrip patch antenna using RF MEMS technology," *IEEE Transactions on Antennas and Propagation*, vol. 55, pp.1193-1196, April 2007.
[4] Daniel Llorens, Pablo Otero, and Carlos Camacho-Peñalosa, "Dual-band, single CPW port, planar-slot antenna," *IEEE Trans. on Antennas and Propagation*, vol. 51, pp.137-139, Jan. 2003.
[5] A.A. Eldek, A.Z. Elsherbeni, C. E. Smith, and K. Lee, "Wideband Rectangular Slot Antenna for Personal Wireless Communication Systems," *IEEE Antennas and Propagation Magazine*, vol. 44, pp.146-155, October 2002.
[6] E. Erdil, K. Topalli, M. Unlu, I. Istanbulluoglu, E. U. Temocin, H. I. Atasoy, O. Bayraktar, O. A. Civi, S. Demir, S. Koc, and T. Akin, "Reconfigurable slot antenna with fixed-fixed beam type RF MEMS capacitors," in *Proc. Eur. Conf. on Antennas and Propagation*, Nov. 6–10, 2006, on CD.
[7] K. Topalli, O. Aydin Civi, S. Demir, S. Koc, and T. Akin, "A Monolithic Phased Array using 3-bit DMTL RF MEMS Phase Shifters," *IEEE Trans. Microwave Theory and Tech.,* vol.56, pp. 270-277, February 2008.

Millimeter-Wave Frequency Reconfigurable Slot Dipole Array with Packaged RF-MEMS Switches

Nihan Gökalp[#*1], Özlem Aydin Çivi[#2]

[#] *Electrical and Electronics Engineering Department, Middle East Technical University*
Ankara Turkey
[2]ozlem@metu.edu.tr

[*] *ASELSAN Inc. Radar Electronic Warfare and Intelligence Systems Department*
Ankara Turkey
[1]ngokalp@aselsan.com.tr

***Abstract*— This paper presents a frequency reconfigurable slot dipole array operating at millimeter-wave frequency band. Dual frequency operation of the array is achieved by using commercial packaged RF-MEMS switches. RF-MEMS switches located on the dipole arms control the electrical length of the slot and enable dual frequency operation.**

I. Introduction

Recently, reconfigurable antennas have attracted significant interest due to their high adaptation with changing system requirements. Specifically, dual frequency operation capability of an antenna decreases system size significantly, since use of one antenna unit is sufficient instead of two different antenna units for different frequencies. Various methods are reported in the literature to achieve frequency reconfiguration ([1]-[4]). In millimeter-wave applications, MEMS (Micro Electro Mechanical Systems) devices have proven their usefulness with their small size, low insertion loss and improved performance compared to their semiconductor counterparts. In addition, packaged RF-MEMS switches makes possible the hybrid integration of switches on the antennas and decreases the fabrication cost and burden.

This paper presents a dual-frequency reconfigurable antenna array operating at millimeter-wave band. Array of coplanar waveguide (CPW) fed slot dipole elements monolithically integrated by MEMS switches has been designed at X- and K-band in [5] but not manufactured yet. Furthermore, in this study hybrid integration of MEMS switches with the antenna will be performed. The packaged RF-MEMS switches integrated with a slot dipole antenna provide dual frequency operation. In the following sections, the array structure, operation of the antenna and EM simulation results in the form of input return loss, current distribution and radiation patterns are presented.

II. Antenna Design

The dual frequency array is composed of 2 linearly placed frequency-tunable slot dipole elements and a CPW-based feed network. CPW transmission lines are used in the corporate feed network of 2-element linear array due to its advantages over a microstrip feeding network, such as less dispersion, easier combination with MEMS and active devices [6]. Fig. 1 shows the schematic view of the dual-frequency array.

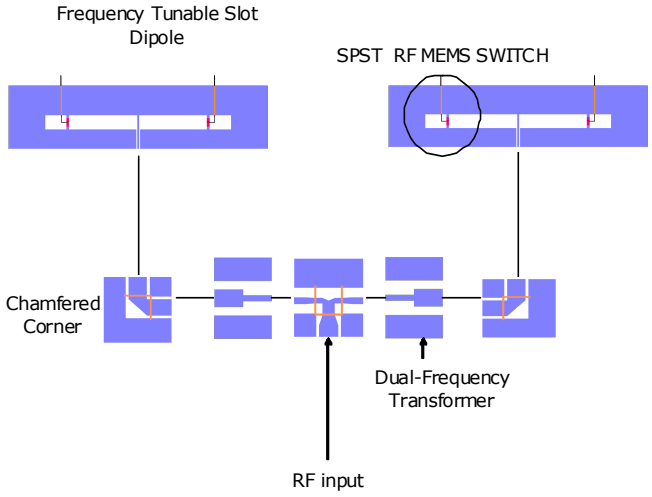

Fig. 1 The schematic view of 2-element reconfigurable slot dipole antenna array structure with MEMS switches

A. Slot Dipole Antenna

Coplanar patch antennas have advantages over microstrip patch antennas, such as easy integration with MEMS components and other active components. Due to this feature, these antenna structures are more preferable for reconfigurable antenna applications. Fig. 2 shows the CPW fed slot dipole antenna structure with RF-MEMS switches used in the array. For the antenna, a 10 mil-thick Rogers 6002 Duroid (ε_r=2.94) substrate with 0.5 Oz Copper has been used. The operation frequency of the slot antenna is determined by the length of the slot. Also, it is stated in [7] that, in addition to the length of the slots, height of the dielectric substrate controls the resonance frequency. Slot width and feed line parameters control the return loss level. In fact, slot dipole antennas exhibit 40-70Ω input impedance when the total

length is about 0.8-0.9λ_g at the frequency of interest. Dual frequency operation of the slot dipole antenna is achieved by using packaged RF-MEMS switches. SPST MEMS switches operating up to 40 GHz produced by RADANT are used in the array. The functional block diagram of this switch is shown in [8]. These RF MEMS switches are located on the arms of the CPW slot dipole antenna as shown in Fig. 2 by using bonding techniques. DC bias pads of the switches are placed under the substrate. Common DC bias is applied by using vias to the gate terminals of the switches. When the switches are in the up state, the total length of the dipole is equal to 0.85λ_g (L1), and it resonates at 25 GHz. The length of the dipole is equal to 0.7λ_g (L2) when the switches are in down state (DC voltage (~70 volt) is applied between the gate and source electrodes) and it resonates at 35 GHz.

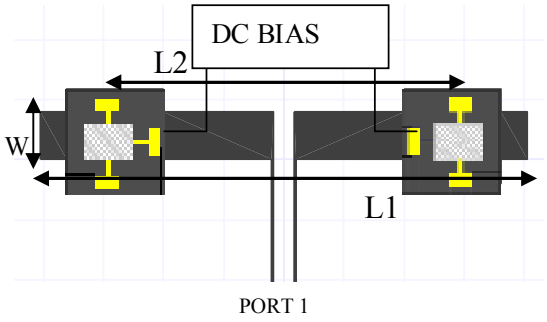

Fig. 2 The schematic view of reconfigurable slot dipole antenna with MEMS switches located on the arms to control resonant frequency with DC bias pad.

B. Reconfigurable Slot Dipole Antenna Design

CPW fed slot dipole antenna at two different lengths operating at 25 and 35 GHz has been designed by using ANSOFT Designer V2. The schematics and dimensions of the antennas are given in Fig. 3 (a) and (b) for the operation at 25 GHz and 35 GHz, respectively.

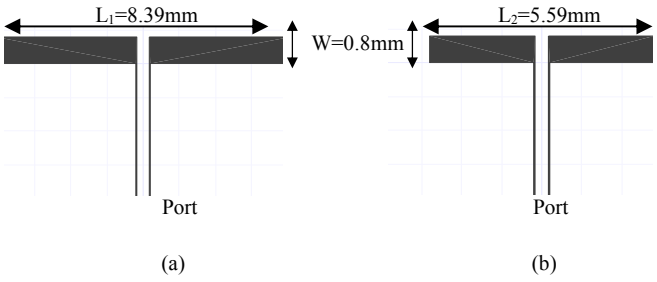

Fig. 3 Ansoft Designer schematic models of slot dipole antennas operating at (a) 25 GHz (b) 35 GHz

Radiation of the CPW slot antenna is caused by the fields in slot arms. In order to observe the radiation mechanism on the slot arms, equivalent current distribution on the slots is obtained using Ansoft Designer V2. Fig. 4 shows the equivalent current distribution of the antenna operating at 35 GHz.

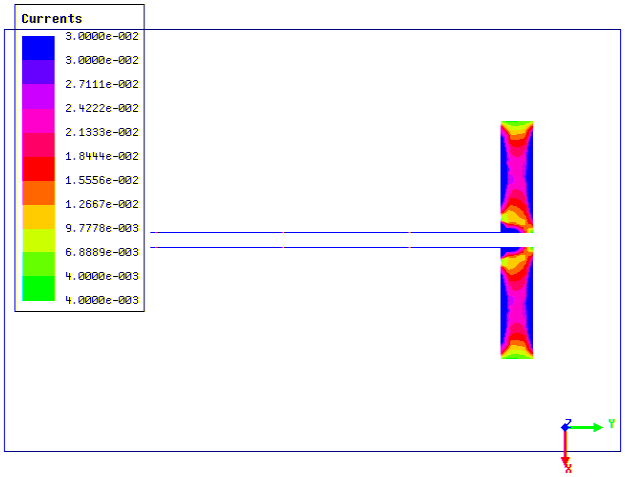

Fig. 4 Current distribution of slot dipole antenna at 35 GHz

Input return loss graphs of the antennas operating at 25 GHz and 35 GHz obtained by simulations are plotted in Fig. 5. As seen from the figure, antennas resonate at the design frequencies.

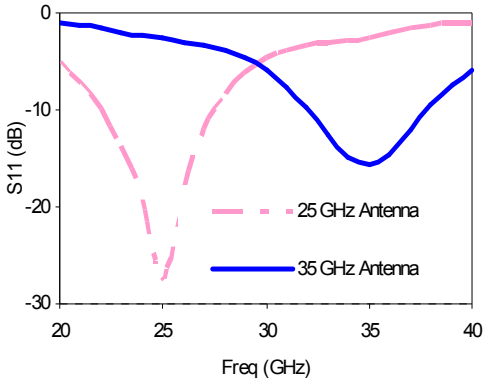

Fig. 5 S-Parameter simulation results of slot dipole antennas operating at 25 GHz and 35 GHz.

Far field simulations of the prototype structures have been performed and shown in Fig. 6 and Fig. 7. E-plane simulations of the antennas operating at 25 GHz and 35 GHz shows that antenna patterns do not change with respect to frequency variation, as expected.

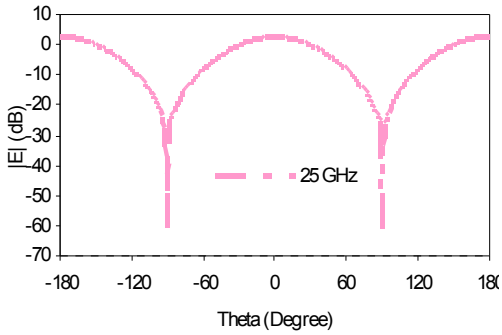

Fig. 6 E-Plane electric field patterns of single dipole antennas at 25 GHz.

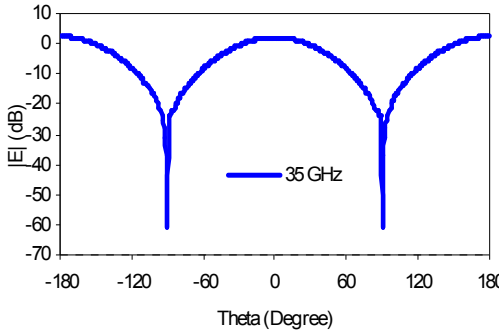

Fig. 7 E-Plane electric field patterns of single dipole antennas at 35 GHz.

C. Feed Network

The CPW-based feed network includes T-junctions, chamfered corners, and dual frequency transformers to match the input impedance at both resonant frequencies (25 GHz and 35 GHz) of the antennas. The dual frequency transformer presented in this study is used to transform 50-Ω input impedance of the antennas to 100-Ω impedance at the two ports of the T-junction [9]. The circuit schematic and parameters of the designed transformer are given in Fig. 8.

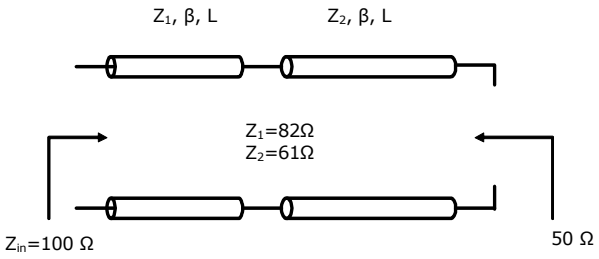

Fig. 8 The circuit schematic view of the dual-frequency transformer

III. CONCLUSION

In conclusion, a reconfigurable dual frequency slot dipole array operating at millimeter-wave band has been presented. Reconfigurable dual frequency operation is provided by RF-MEMS switches integrated on CPW fed slot antenna produced on Duroid substrate in a hybrid fashion. Measurement results will be presented in the conference. It is possible to increase the number of elements in the array structure to enhance the directivity of the antenna array.

ACKNOWLEDGMENT

This work is partially supported by The Scientific and Technical Research Council of Turkey (TUBITAK-EEEAG-104E041 and 107E090) and COST IC0603 ASSIST.

REFERENCES

[1] B. Markus, K. Mikko, S. Erkki, and J. Heli, "Frequency Reconfigurable Microstrip-Fed Annular Slot Antenna," *Antennas and Propagation EuCAP 2006 First European Conference* Page(s):1 – 6 Nov. 2006.

[2] S.L.S. Yang, A.A. Kishk, K.F. Lee, "Frequency Reconfigurable U-Slot Microstrip Patch Antenna" *Antennas and Wireless Propagation Letters, IEEE* Volume 7, 2008 Page(s):127 – 129

[3] G.H. Huff, J. Feng, S. Zhang, J.T. Bernhard, "A novel radiation pattern and frequency reconfigurable single turn square spiral microstrip antenna" *Microwave and Wireless Components Letters, IEEE* Volume 13, Issue 2, Feb. 2003 Page(s):57 – 59

[4] D. L. Sengupta, "Resonant Frequency of a Tunable Rectangular Patch Antenna," *Electronics Letters,* vol. 20, pp.614-615, 1984

[5] Kagan Topalli, Ozlem Aydin Civi, Simsek Demir, Sencer Koc, and Tayfun Akin, "Dual-Frequency Reconfigurable Slot Dipole Array with a CPW-Based Feed Network using RF MEMS Technology for X- and Ku-Band Applications," *Antennas and Propagation Society International Symposium, 2007 IEEE* Volume , Issue , 9-15 June 2007 Page(s):825 - 828

[6] M. Riaziat, R. Majidi-Ahy, and I. Feng, "Propagation modes and dispersion characteristics of coplanar waveguides," *IEEE Trans. Microwave Theory Tech.*, vol. 38, pp. 245–251, Mar. 1990.

[7] A. A. Eldek, A. Z. Elsherbeni, C. E. Smith and K-F Lee, "Wideband slot antennas for radar applications," *Proc. IEEE Radar Conf,* Huntsville, AL, May 2003, pp. 79-84.

[8] RADANT SPST, Broadband (0-40 GHz) RF-MEMS Switch Datasheet. <http://www.radantmems.com/radantmems.data/Library/Radant-Datasheet200_1.5.pdf>

[9] C. Monzon, "A Small Dual-Frequency Transformer in Two Sections," *IEEE Trans. Microwave Theory & Tech.,* vol.51, pp.1157-1161, April 2003.

Reconfiguration in the Radiation Pattern of Tapered Slot Antennas

Aykut Cihangir[1] **Lale Alatan**[2]
[1]Turkish Aerospace Industry, Havacılık Bulvarı No:17, 06980 Ankara, TURKEY
[2]Middle East Technical University, Dept. of Elect. and Electronics Eng., 06531 Ankara, TURKEY
lalatan@metu.edu.tr

Abstract

The aim of this work is to reconfigure the radiation pattern of tapered slot antennas (TSA) by switching between two different types of tapering. Constant width slot antennas (CWSA) are known to have narrower beamwidth and higher sidelobe level whereas linearly tapered slot antennas (LTSA) have wider beamwidth with lower sidelobe level compared to each other. A CWSA and a LTSA operating at millimeterwave band are designed together with their feed structures. EM simulations of these two antennas are performed and their radiation characteristics are compared to explore the potential of TSA for radiation pattern reconfigurability.

1. INTRODUCTION*

A Tapered Slot Antenna (TSA) uses a slotline etched on a dielectric material, which is widening through its length to produce an endfire radiation. The EM wave moves along the increasingly separated metallization tapers until the separation is such that the wave detaches from the antenna structure and radiates into the free space from the substrate end. Most commonly used tapering profiles are linear tapering (LTSA) and exponential tapering (Vivaldi). In some applications, tapering is not applied and the width of the slot antenna is kept constant (CWSA). These three types of TSAs are compared in [1], in terms of their beamwidths and sidelobe levels. For TSAs with the same antenna length and aperture width, CWSA has the narrowest beamwidth, followed by LTSA and then Vivaldi. The sidelobe levels are highest for CWSA, followed by LTSA and then Vivaldi. From this comparison, it is concluded that a transition between the LTSA and CWSA structures could provide reconfigurability about antenna beamwidth and sidelobe levels. The transition between these two structures could be achieved by changing the conductivity of a semiconductor material (shown by region 2) through optical excitation as shown in Figure 1.

The scope of this paper is to compare the radiation characteristics of LTSA and CWSAs operating at millimeter frequency bands and to explore the potential of TSA for radiation pattern reconfigurability.

The design of CWSA and LTSA operating in the frequency band of almost 25-45 GHz is summarized in Section 2. The simulation results obtained via HFSS by Ansoft are presented and compared in Section 3. Finally, conclusions and discussions together with future plans are given in Section 4.

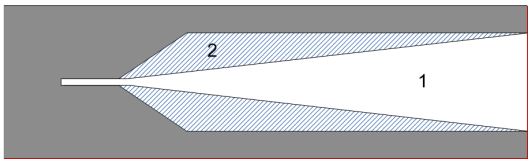

Figure 1 Transition between LTSA and CWSA

2. DESIGN PROCEDURE

The TSAs studied in this work are fed by a microstrip line. Therefore, a "balun" design is required to achieve the transition between the balanced slot line and the unbalanced microstrip line. As shown in Figure 2, an orthogonal microstrip line to slotline transition, proposed in [2], is utilized. The microstrip extends about one quarter of a guided wavelength beyond the slot, and the slot extends about a quarter of a guided wavelength beyond the microstrip.

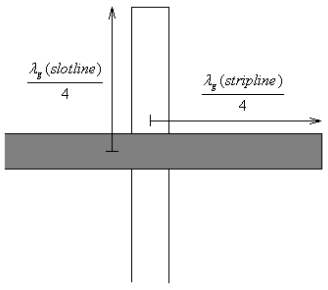

Figure 2 Orthogonal microstrip line to slotline transition

* This work is partially supported by The Scientific and Technical Research Council of Turkey (TUBITAK-EEEAG-107E090) and COST IC0603 ASSIST.

RO5880 substrate with a thickness of 0.51mm and dielectric constant of 2.2 is chosen to satisfy the effective height condition required to obtain a well-behaved traveling wave antenna. It should also be noted that RO5880 is a low loss substrate with a loss tangent of 0.0009. Because of the manufacturing limitations, a minimum slot width of 0.254 mm (10 mils) is chosen. The characteristic impedance of the slot line is calculated to be 152Ω with a quarter wavelength of 1.81 mm at 35 GHz [4].

To obtain a wideband transition between 50Ω microstrip line and 152Ω slot line, a Chebyshev impedance transformer circuit is designed with three sections (N=3) and with Γ_m=0.05, [3]. First, the characteristic impedance values of each section are calculated, then the corresponding width and length values of each line is estimated by using empirical formulas, and finally these initial estimates are optimized by using an EM simulation software (HFSS by Ansoft). The parameters of the Chebyshev impedance transformer circuit are summarized in Table1.

Table 1 Parameters of the Chebyshev impedance transformer

	Initial estimates		**Optimized by HFSS**	
	Width (mm)	$\lambda_g/4$ (mm)	Width (mm)	$\lambda_g/4$ (mm)
Z_0=50Ω	1.58	1.56	1.58	1.54
Z_1=61Ω	1.16	1.58	1.08	1.56
Z_2=87Ω	0.6	1.61	0.54	1.60
Z_3=125 Ω	0.26	1.63	0.2	1.63

The return loss and insertion loss simulation results of two back-to-back connected balun structures are given in Figure 3.

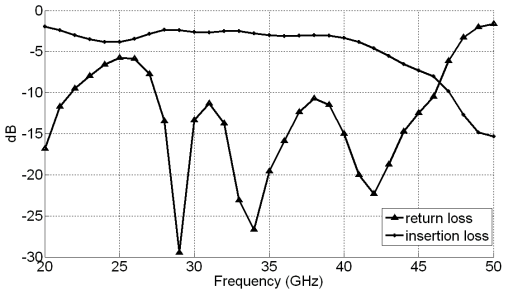

Figure 3 Return loss and insertion loss results of two back-to-back connected balun structures

There are three important parameters that determine the radiation characteristics of an LTSA; these are antenna length (L), aperture width (W) and ground extension (H) as shown in Figure 4. In order to investigate the effects of each parameter on the performance of the antenna, a parametric study is carried out. The change of the antenna characteristics related to the change in antenna parameters can be observed in Table 2. The antenna parameters (L, W and H) are given in terms of free space wavelength which is 8.57mm at frequency of 35 GHz.

Table 2 LTSA Parametric Study Results

L	W	H	Directivity	E- plane		H-plane	
				BW	SLL	BW	SLL
		1	10,24	26	-4,19	34	-8,92
		1,5	9,5	40	-7,41	32	-7,62
	0,5	2	8,91	45	-6,85	32	-7,04
		1	11,72	26	-15,1	34	-9,16
		1,5	10,94	38	-13	33	-8,13
3	1	2	10,94	40	-13,5	34	-8,95
		1	10,03	37	-7,53	27	-8,54
		1,5	10,2	30	-7,02	27	-7,82
	0,5	2	10	33	-8	28	-6,02
		1	12,51	24	-12,2	30	-9,64
		1,5	12,05	28	-13	29	-7,84
4	1	2	11,49	34	-14,5	27	-8,5
		1	8,96	48	-5,38	22	-5,74
		1,5	9,72	34	-6,92	24	-7,57
	0,5	2	10,28	23	-4,74	26	-5,15
		1	12,83	23	-12,7	26	-9,82
		1,5	12,65	24	-16,9	26	-7,63
5	1	2	12,31	29	-15,3	26	-7,02
		1	8,13	44	-3,85	21	-1,35
		1,5	8,06	45	-5,82	21	-5,52
	0,5	2	9,13	25	-4,25	23	-3,59
		1	12,14	23	-12,6	26	-8,97
		1,5	12,55	22	-15,8	23	-7,66
6	1	2	12,69	21	-16,6	25	-6,29

The LTSA configurations shown shaded in Table 2 have a tilted and split beam characteristic so these are not taken into consideration when deciding the relationship between parameters and antenna specifications.

It can be inferred from Table 2 that an increase in ground extension decreases E-plane beamwidth for larger aperture width and increases E-plane beamwidth for narrower aperture width. The H-plane beamwidth is not affected by the change in ground extension considerably. The E-plane sidelobe level changes inverse proportionally with ground extension whereas H-plane sidelobe level changes directly proportionally.

Increasing the aperture width of the antenna is seen to increase the directivity of the antenna. Except the large ground extension case, E-plane beamwidth generally decreases with an increase in aperture width and E-plane sidelobe level decreases significantly with larger aperture width.

An increase in the antenna length causes both E and H-plane beamwidths to decrease and H-plane sidelobe level to increase.

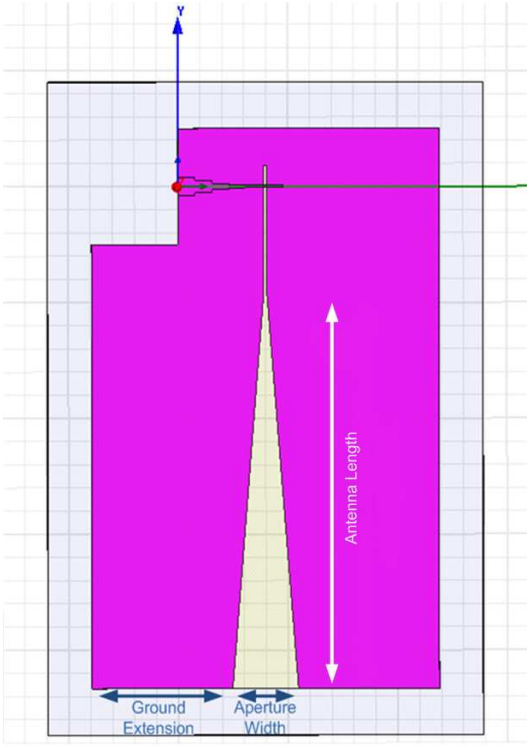

Figure 4 Parameters of LTSA

During the simulations, it is observed that without a taper, CWSA shows high return loss due to the abrupt change in the slotline width and thus the characteristic impedance of slotline. Therefore, this transition region needs to be smooth out by introducing a tapered region as shown in Figure 5. Consequently an additional parameter, the taper length, should also be considered during the design of CWSA. Two kinds of taper profile (linear and exponential) were simulated and among the two, exponential taper was seen to provide wider frequency bandwidth. So, exponential taper with a length of 1 free space wavelength was used for the pattern simulations with CWSA.

A parametric study concerning the antenna length, ground extension and aperture width is carried out also for CWSA with exponential taper case. The antenna characteristics for different parameters can be observed in Table 3.

It can be observed in Table 3 that, increasing the ground extension of a CWSA increases the H-plane sidelobe level considerably. Aperture width also has an important effect on sidelobe levels. An increase in the aperture width increases the H-plane sidelobe level while decreasing E-plane sidelobe level. Increasing the antenna length decreases the E and H-plane beamwidth while increasing the sidelobe level on both planes.

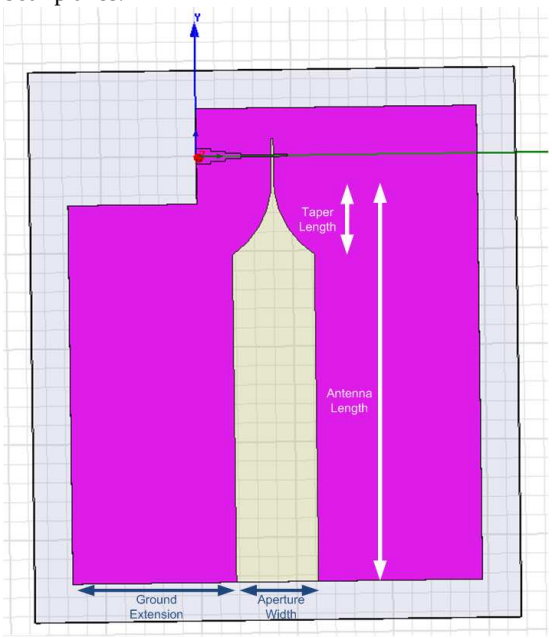

Figure 5 Parameters of CWSA

Table 3 CWSA Parametric Study Results

L	W	H	Directivity	E-plane		H-plane	
				BW	SLL	BW	SLL
3	0,5	1	10,77	23	-8,12	34	-9,9
		1,5	9,72	28	-8,63	32	-7,35
		2	9,04	41	-7,57	31	-7,55
	1	1	9,71	20	-8,87	32	-6,85
		1,5	8,55	32	-9,51	29	-5,62
		2	8,66	30	-9,32	30	-7,08
4	0,5	1	11,06	22	-4,77	28	-11,2
		1,5	10,49	22	-8,18	26	-7,77
		2	9,71	32	-8,3	25	-5,73
	1	1	10,54	18	-8,09	29	-8
		1,5	9,31	23	-7,27	25	-4,71
		2	8,54	28	-7,82	25	-6
5	0,5	1	10,55	21	-3,31	23	-9,66
		1,5	10,92	19	-8,18	23	-8,05
		2	10,58	21	-6,29	22	-4,32
	1	1	11,14	16	-7,68	25	-9,88
		1,5	10,05	17	-6,97	23	-4,72
		2	9,06	26	-7,07	21	-4,05
6	0,5	1	9,08	48	-6,99	18	-5,21
		1,5	10,6	19	-5,98	20	-8,76
		2	11	15	-5,86	21	-4,38
	1	1	11,16	15	-4,78	23	-12,6
		1,5	10,81	14	-5,34	22	-6,91
		2	10,19	18	-5,88	21	-3,26

3. SIMULATION RESULTS

The input return loss results obtained with the optimized parameters of LTSA and CWSA are plotted in Figure 6. Using the results of the parametric study, the antenna configurations that are decided to be used for the reconfigurability have the physical lengths of 5 wavelengths for antenna length, 1 wavelength for the aperture width and 1.5 wavelengths for ground extension. It is observed that an ultra wide frequency band can be covered with both types of antennas. LTSA antenna has a return loss below -10 dB from approximately 26.5 GHz to 45 GHz and CWSA has a return loss below -10 dB in all the frequencies between 25-45 GHz.

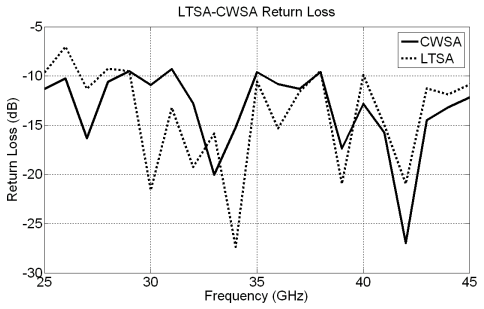

Figure 6 Input return loss for LTSA and CWSA

The E-plane and H-plane radiation patterns for the LTSA and CWSA are presented in Figure 7 and Figure 8, respectively.

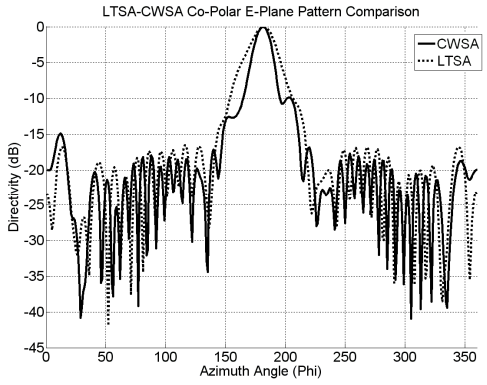

Figure 7 E-plane radiation patterns

As can also be seen from Table 2 and Table 3 with L=5, W=1 and H=1.5, the directivity of the LTSA is almost 2.5 dB more than that of CWSA. When the beamwidth in both planes are compared, it can be seen that the E-plane half power beamwidth of CWSA is 7 degrees narrower and H-plane beamwidth is 3 degrees narrower than LTSA. If the first sidelobe levels for the two cases of LTSA and CWSA are observed, it is seen that the E-plane first sidelobe level is approximately 10 dB greater and H-plane sidelobe level is 3 dB greater for CWSA case in comparison to LTSA case. The large increase in the E-plane sidelobe level for CWSA can be explained according to the radiation pattern in Figure 7. The beamwidth is narrower for the CWSA case, although sidelobes comprises from the main lobe with a transition to CWSA from LTSA.

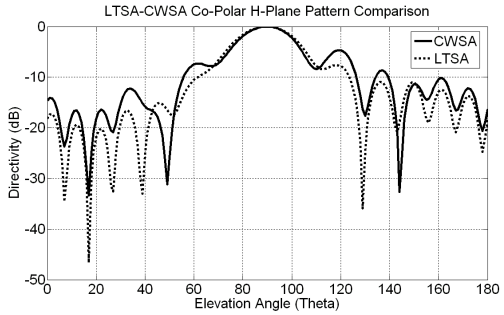

Figure 8 H-plane radiation patterns

4. CONCLUSION

Two antenna configurations (LTSA and CWSA) of the same basic antenna parameters like length and aperture width were proposed. The configurations were of the same size in order to make them reconfigurable in the future. It was shown by the simulations that a transition between these two antennas result in two pattern configurations, one is a narrower beam (by 10^o) and higher sidelobe level (by 13 dB) case and the other is a wider beam and lower sidelobe level case.

REFERENCES

[1] K. Sigfrid Yngvesson, T.L. Korzeniowski, et. al. "The Tapered Slot Antenna, A New Integrated Element For Millimeter-Wave Applications", IEEE Transactions on Microwave Theory and Techniques, Vol. 37, No. 2 February 1989

[2] Bernd Schüppert, "Microstrip/Slotline Transitions: Modelling and Experimental Investigation", IEEE Trans. Microwave Theory Tech., Vol. 36, No. 8, August 1988.

[3] J. Thaysen, K. B. Jakobsen and J. Appel-Hansen, "A Wideband Balun-How Does It Work?", Applied Microwave&Wireless, Technical Feature

[4] R. Janaswamy, D. H. Schaubert, "Characteristic Impedance of a Wide Slotline on Low-Permittivity Substrates", IEEE Trans. Microwave Theory Tech., Vol. MTT-34, No 8, August 1986.

Işınım Huzmesi Yönlendirilebilen Sur Biçimli Mikroşerit Anten Dizisi

Nihan Gökalp[1,2], Özlem Aydın Çivi[2]
[1]Radar, Elektronik Harp ve İstihbarat Teknolojileri Grubu, ASELSAN
Ankara
ngokalp@aselsan.com.tr

[2]Orta Doğu Teknik Üniversitesi
Elektrik Elektronik Mühendisliği Bölümü
Ankara
ozlem@metu.edu.tr

Özet: *Bu çalışmada, ışınım huzmesi yönlendirilebilen sur biçimli mikroşerit yürüyen dalga anten dizisi X-bant uygulamalarında kullanılmak üzere tasarlamış, üretilmiş ve ölçülmüştür. Anten Işınım huzmesinde istenilen yönlenmeyi sağlayabilmek için mikroşerit hat üzerinde faz değişimini sağlayacak varaktör diyotlar kullanılmıştır. Yapılan EM benzetim ve ölçümler sonucu sur biçimli anten dizisinde ışınım huzmesinin diyot kontrolü ile istenilen doğrultulara yönlendirilebildiği gösterilmiştir.*

1. Giriş

Günümüzde mikroşerit antenler düşük üretim maliyetleri, sisteme kolay entegre edilmeleri, hafif ve yüzeysel olmaları, huzme şekillendirici sistemlerle beraber kullanılabilmeleri nedeniyle askeri ve endüstriyel alanlarda sıkça tercih edilmektedir. Bu avantajlarının yanı sıra yürüyen anten dizileri yüksek kazançları, düşük yan huzme değerleri ve ayarlanabilen ışınım polarizasyon özellikleri ile radar uygulamaları için uygun anten tipleri arasındadır [1-4]. Bu bildiride radar uygulamalarında kullanılabilecek ışınım huzmesi yönlendirilebilen sur biçimli yürüyen dalga anten dizisinin tasarım, üretim ve ölçüm aşamaları anlatılmıştır. Anten dizisinin ışınım huzmesinin yönlendirilmesi mikroşerit hattın üzerine varaktör diyot yerleştirilerek sağlanmıştır. Tasarlanan ve üretilen anten dizisinin fiziksel ve elektriksel özellikleri aşağıdaki bölümlerde anlatılmıştır.

2. Sur Biçimli Mikroşerit Anten Dizisi

Işınım huzmesi yönlendirilebilen yürüyen dalga anten dizisi sekiz adet sur biçimli yapıdan oluşmaktadır, sekiz adet varaktör diyot Şekil 1'de görüldüğü gibi sur dizilerinin üzerine bulunmaktadır. Anten dizisinin çalışma frekansı X-bant radar uygulamalarına uygun olacak biçimde 10 GHz seçilmiştir. Anten taban malzemesi olarak yüksek frekansta çalışan, düşük kayıplı 15 mil kalınlığında dielektrik sabiti 2.2 olan Rogers 5880 Duroid kullanılmıştır. Yürüyen anten dalga dizisi 50-Ω yükle sonlandırılarak anten sonuna ulaşan dalganın geri yansıması engellenmektedir. Anten dizisinde kullanılan varaktör diyotlar voltaj ile kontrol edilebilen ve kapasitansları uygulanan voltaj ile orantılı olarak değişebilen yapılardır. Mikroşerit anten dizisi varaktör diyotlarla yüklenerek ışınım huzmesinin istenilen doğrultuya yönlendirilmesi sağlanmıştır.

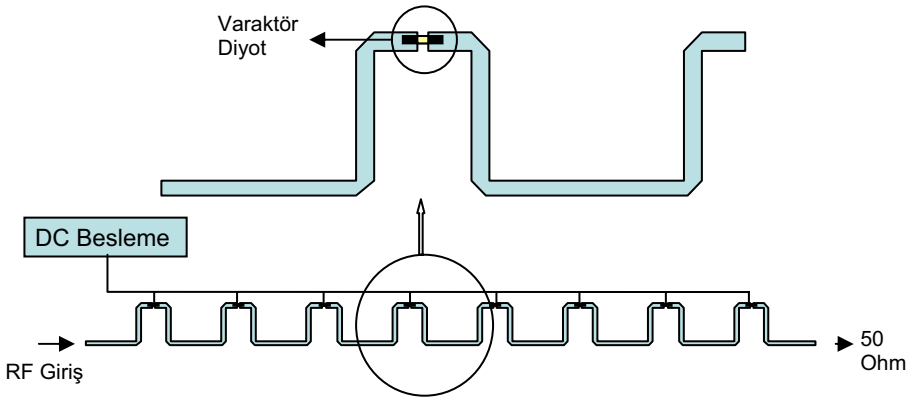

Şekil 1 Işınım huzmesi yönlendirilebilen, varaktörlü mikroşerit anten dizisinin şematik gösterimi

Sur biçimli mikroşerit anten dizilerinin birim elemanı dört köşeli sur biçimli yapıdan oluşur. Köşelerdeki keskin geçiş geri dönüş kaybını artırmaktadır, [1]. Bu kaybı azaltmak amacıyla köşeler kesikli yapılandırılmıştır. Sur biçimli mikroşerit anten dizisinde ışıma bu köşelerden kaynaklanmaktadır [1]. Mikroşerit üzerindeki manyetik akımın

köşenin iç ve dış kenarlarında ilerlerken aldığı yol farklıdır. Bu farklılık Şekil 2'de görüleceği gibi manyetik akım vektörleri olarak modellenebilir. Sur biçimli mikroşerit antenin ışıma özellikleri, polarizasyonu Şekil 2-b' de gösterilen birim elemanın s,l ve d değerleri ile belirlenebilmektedir. Örneğin, s=λ/2, l= λ/4 ve d=3λ/4 değerleri için yayılan manyetik alanın yatay ve dikey bileşenleri arasında doksan derecelik bir faz farkı oluşur ve dairesel polarizasyon elde edilir. Bu çalışmada tasarlanan anten dikey polarizasyondadır.

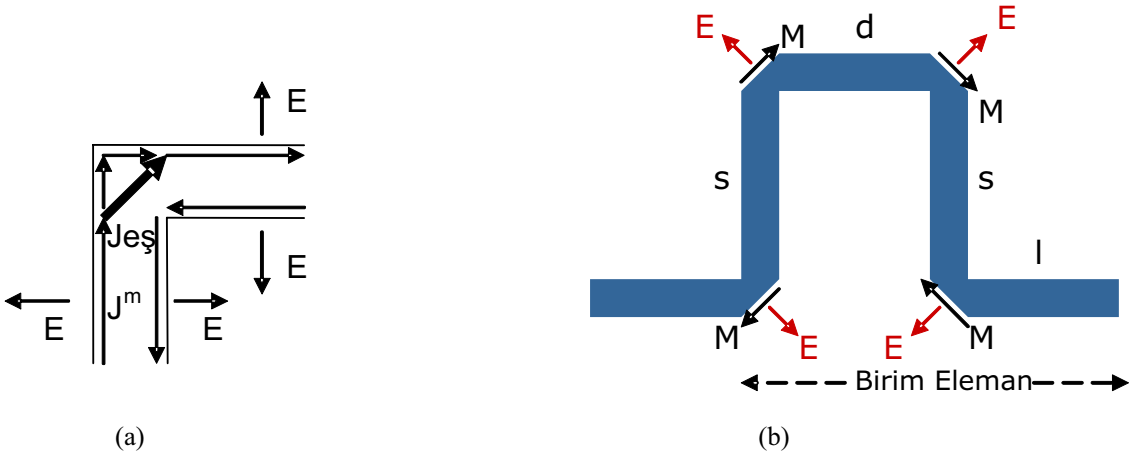

(a) (b)

Şekil 2 (a) Sur biçimli anten dizisindeki köşe yapısında eşlenik akım dağılımı (b) Dört köşeli sur biçimli anten dizisinin birim elemanı

Antenin d uzunluğunu değiştirerek ışınım huzmesini istenilen yöne yönlendirmek mümkündür. Anten dizisindeki birim eleman sayısı arttıkça anten dizisinin kazancı artar, yan huzmeleri küçülür ve anten dizisinin sonundaki 50-Ω yüke ulaşan sinyal seviyesi de azalır.

Bu çalışmada anten elemanının elektriksel boyu, üzerine takılan varaktör diyotlar ile ayarlanmaktadır. Bu anten dizisinde kullanılan varaktör diyotlar kapasitans değerleri 0.3 pF'tan 2.4 pF'a kadar değişebilen MICROSEMI MPV2100-206'dır. 0 volt besleme voltajı altında 2.4 pF, 20 volt besleme voltajı altında 0.3 pF kapasitans değerini sağlayabilmektedir.

Anten dizisinin tasarımında Momentler metoduyla (MoM) çalışan Ansoft Designer v3, bilgisayar yazılımı kullanılmıştır. Varaktör diyotların S-parametreleri mikroşerit hattın üzerine yerleştirilerek tüm yapının EM benzetimi yapılmıştır.

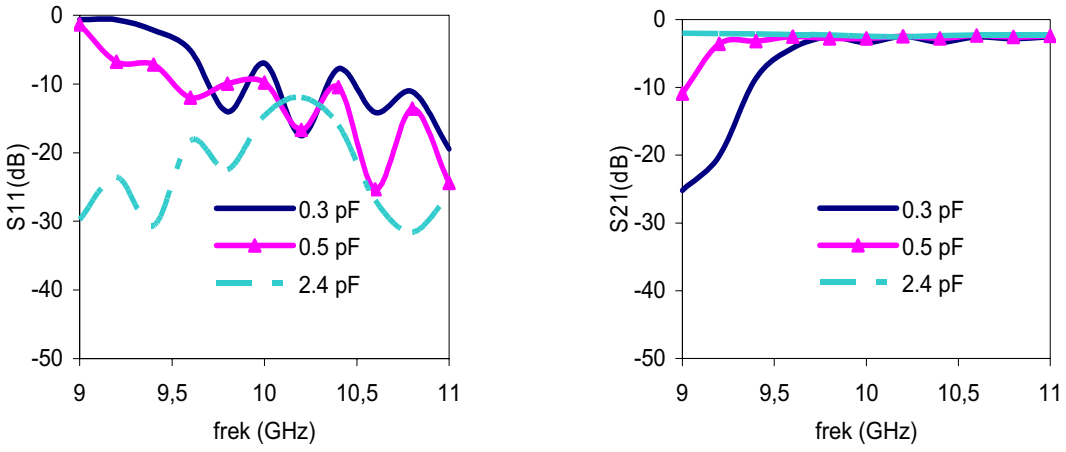

Şekil 3 EM benzetimlerle elde edilen S11 ve S21 değerleri

Farklı kapasitans değerleri için anten dizisinin S-parametresi değerleri Şekil 3'te gösterilmiştir. Bu sonuçlara göre 10 GHz'de anten dizisinin S11 değeri -10 dB'nin altındadır. S21 değeri ise -3 dB civarındadır.

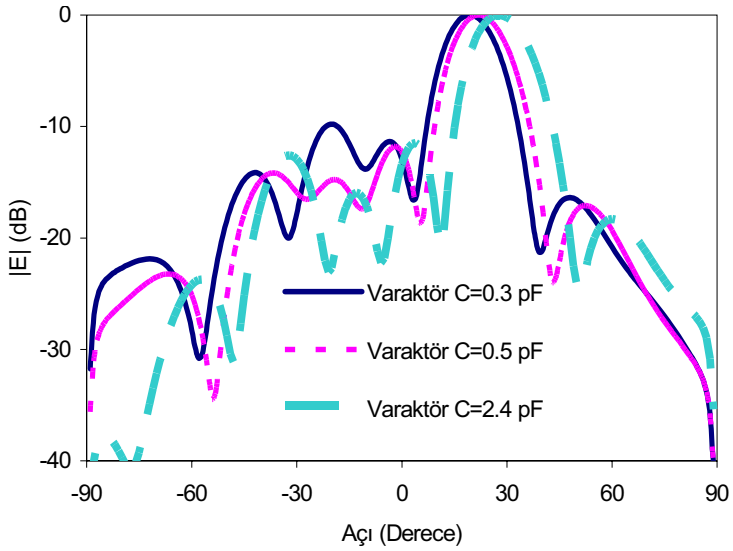

Şekil 4 Varaktör kapasitans değeri 0.3 pF, 0.5 pF ve 2.4 pF kapasitans değerleri için E düzlemi ışınım örüntüsü

Farklı kapasitans değerleri için ışınım huzmesinin döndüğü elektromanyetik benzetimlerle gösterilmiştir. Bu simülasyon sonuçlarına göre varaktör diyot'un kapasitans değeri 0.3 - 2.4 pF arasında değişirken ışınım huzmesi 30°'den 19°'ye dönmektedir. Işınım örüntülerinin farklı kapasitans değerleri için dönüşü Şekil 4'te gösterilmiştir.

Prototip anten dizisi üretilmiş ve elektriksel parametreleri ölçülmüştür. Şekil 5'de üretilen varaktör diyotlu anten dizisi görülmektedir.

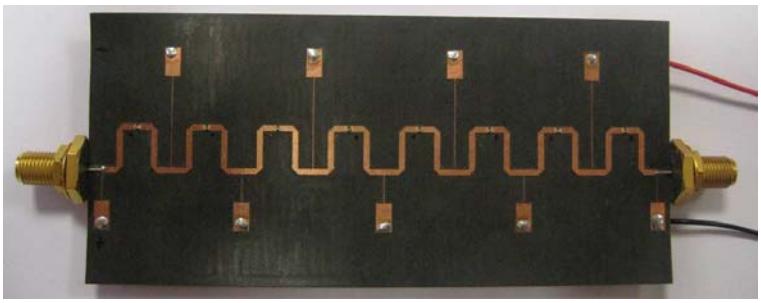

Şekil 5 Prototip olarak üretilen ışınım huzmesi yönlendirilebilen anten dizisi

Üretilen anten dizisindeki varaktör diyotların kapasitans değişimleri varaktörlerin iki kolları arasına farklı voltaj değerleri uygulanarak sağlanmıştır. Anten dizisinin S-parametreleri farklı voltaj değerleri için ölçüm sonuçları Şekil 6'de sunulmuştur. S-parametresi ölçüm sonuçları 10 GHz'de antenin geri dönüş kaybının -10 dB'nin altında olduğunu ve varaktör diyotların araya girme kayıplarının toplam 7 dB civarında olduğunu göstermektedir.

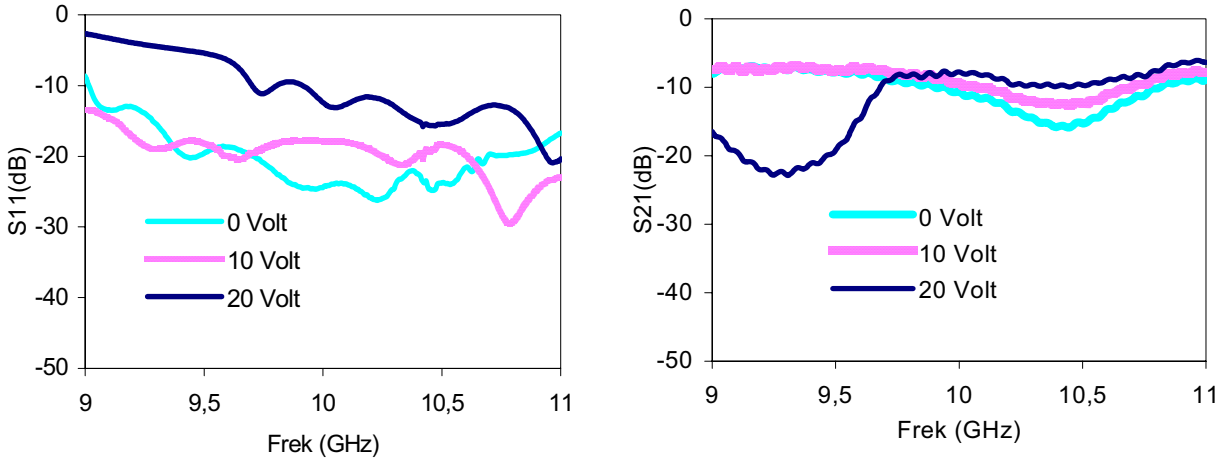

Şekil 6 Ölçülen S11 ve S21 değerleri

Anten dizisinin E-düzleminde ışınım örüntüleri farklı voltaj değerleri için 10 GHz'de ölçülmüştür ve Şekil 7'de verilmiştir. Simülasyonlarda olduğu gibi ölçümde de antenin ışınım huzmesi 10°'den fazla dönmektedir. Simülasyon sonuçları ile ölçüm sonuçları benzerlik göstermektedir. Elektriksel alan ölçümlerinden antenin çapraz polarizasyonun -15 dB'den düşük olduğu gözlenmiştir.

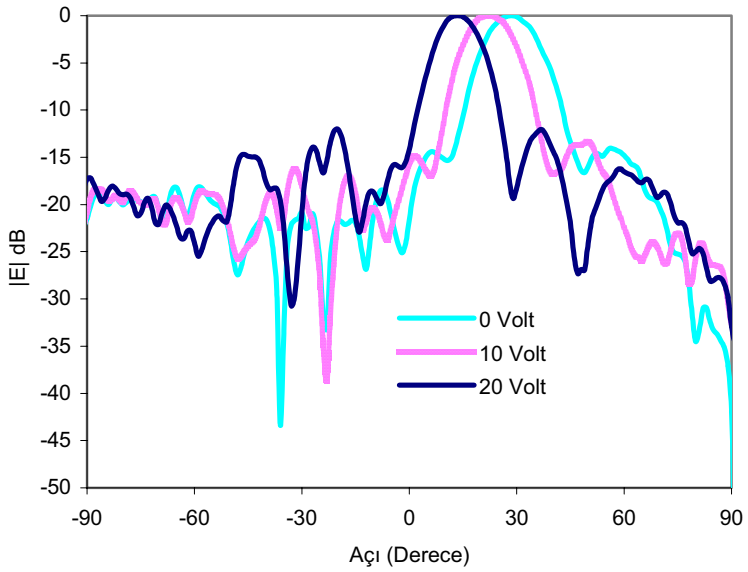

Şekil 7 Farklı voltaj değerleri için anten dizisinin elektrik alan ölçümü

3. Sonuç

Bu makalede ışınım huzmesi yönlendirilebilen sur biçimli mikroşerit yürüyen dalga anten dizisi anlatılmıştır. Anten dizisinde istenilen ışınım huzmesi yönlendirilmesi mikroşerit hat üzerine yerleştirilen varaktör diyotlarla sağlanmıştır. Varaktör diyotların kapasitans değişimleri DC besleme yapısı ile kontrol edilmektedir. Anten dizisinde kapasitansları değişebilen varaktör diyotlar yerine kapasitansları değişebilen RF-MEMS yapılar da kullanılabilir [4]. Varaktör diyotlara göre çok düşük araya girme kaybına sahip olmaları nedeniyle MEMS kapasitörlerin kullanımı antenin toplam kazancını da yükseltecektir.

Bilgi

Bu çalışma TUBITAK-107E090 - COST-ASSIST (Antenna Systems & Sensors for Information Society Technologies -IC 0603) tarafından kısmen desteklenmiştir.

Kaynaklar

[1] . Dural,G., Theory and Design of Microstrip Rampart Line Arrays, Yüksek Lisans Tezi, ODTÜ, 1983
[2] . R. Ratmon, I. Oz, C. J. Samson, "Comparision of Resonant and Travelling-Wave Meander-Line Antenna" Electrical & Electronics Engineers in Israel,1991, 17th Convebtion of. 5-7 Mart 1991 s:149-151
[3] . M. Tiuri, S. Tallqvist, S. Urpo, "Chain Antenna" 1974 Antennas and Propagation Society International Symposium, vol. 12, Haziran 1974 s:274 – 277
[4] . E. Erdil, K. Topalli, M. Unlu, O. Aydin Civi, ve Tayfun Akin, "Frequency Tunable Microstrip Patch Antenna Using RF MEMS Technology", IEEE Transactions on Antennas and Propagation, vol.55, no.4, s.1193–1196, Nisan 2007

Çift Frekansta Çalışan Yeniden Yapılandırılabilir Ayrık Halka Yansıtıcı Dizi Anten Birim Hücre Tasarımı

Caner Güçlü[1], Julien Perruissau-Carrier[2], Özlem Aydın Çivi[1]
[1] Orta Doğu Teknik Üniversitesi, Elektronik-Elektronik Mühendisliği Bölümü, Ankara
cguclu@metu.edu.tr, ozlem@metu.edu.tr,

[2]Centre Tecnològic de Telecomunicacions de Catalunya (CTTC), Barselona, İspanya
julien.perruisseau@cttc.cat

Özet: *Bu çalışmada K ve Ka bantlarında bağımsız çalışabilen, RF MEMS anahtarlarla yeniden yapılandırılabilir özellik kazandırılmış, ayrık halka elemanlı yansıtıcı dizi anten birim hücresi tasarlanmıştır. Tasarlanan birim hücre, dairesel polarizasyonlu dalgaların polarizasyon yönlerini koruyarak yansıtmakta ve faz kontrolünü sağlamaktadır. Ayrı halka elemanı, iletken tabaka ile sonlandırılmış 0.5mm kuvartz taban üzerinde RF MEMS anahtarlarla birlikte üretilecektir. Çift frekanslı dizi iç içe geçmiş farklı boyutlarda iki ayrık-halka dizisi şeklinde tasarlanmıştır.*

1. Giriş

Bu çalışmada, dairesel polarizasyonda çift frekansta çalışan, yeniden yapılandırılabilir yansıtıcı dizi anten için birim eleman tasarımı yapılmıştır. Yeniden yapılandırma, RF MEMS anahtarların birim eleman tasarımıyla bütünleştirilmesi ile sağlanmıştır. Yansıtıcı dizi antenler, yansıtıcı antenlerin ve dizi antenlerin avantajlarını bir araya getirerek, düşük maliyet ve yüksek performans sağlamaktadır. Yeniden yapılandırılabilir uygulamalarda ise, çoklu bant uygulamaları, örüntü şekillendirme ve elektronik tarama yetenekleri kazanırlar. Bu nitelikleri gerçekleyebilmek bakımından seçilen yansıtıcı elemandan elde edilen faz eğrisinin, doğrusal ve 360° kapsamlı olması önemlidir [1]. Doğrusal polarizasyonlu yansıtıcı dizi antenlerde elemanın fazını kontrol etmek için, eleman büyüklüğünü değiştirmek, kapasitif yükleme, çıkıntılar ekleyerek faz denetleme gibi birçok yöntem vardır [2], [3]. Dairesel polarizasyonlu yansıtıcı dizi antenlerde ise, bu geometri değiştirme yöntemlerine ek olarak farklı fiziksel açılarda konumlandırılmış özdeş elemanlar da kullanılabilir [4]. Birim elemandan yansıyan dalganın, gelen dalgayla aynı yönde dairesel polarizasyona sahip bileşeni, elemanın fiziksel dönüş açısıyla doğru orantılı bir faz kaymasına uğrar.

Bu çalışmada, yansıtıcı dizi birim elemanı olarak, arka tarafı iletken kaplı kuvartz taban malzemesi üzerine basılmış ayrık halka kullanılmıştır. Ayrık halka belli frekans aralıklarında, yüzeye dik gelen dairesel polarizasyonlu dalgaları, dönüş yönlerini koruyarak yansıtma niteliğine sahiptir. Ayrıca, ayrık halka, geometrisi bakımından farklı boyutlarda biraraya getirilerek çoklu frekans uygulamalarında kullanılmaya uygundur. Ayrık halkanın simetrik geometrisi, RF MEMS anahtar ile anahtarlanarak fiziksel dönüşü sağlayacak biçimde ayrığın açısal konumunu değiştirmeye elverişlidir.

Şekil 2'te görüldüğü gibi 3 çift karşılıklı anahtar yoluyla, her seferinde açıklıkları oluştumak üzere karşılıklı iki anahtar açık ve diğerleri kapalı olmak üzere 3 farklı açısal konumda ayrık halka oluşturulabilmektedir. Bu çalışmada, iki farklı frekansta çalışan ayrık halka dizilerinin birbirinin içine geçecek şekilde Şekil 4'te görüldüğü gibi yerleştirildiği, dairesel polarizasyonlu, çift frekansta çalışan yeniden yapılandırılabilir yansıtıcı dizi anten için birim eleman tasarımı ve elektromanyetik benzetimi yapılmıştır

2. Teori ve Tasarım İlkeleri

Dairesel polarizasyonlu dalgaların fazının, yansıtıcı elemanın fiziksel açısına bağımlılığının matematiksel ifadesine erişmek tasarımın temel ilkelerini belirlemek açısından önemlidir. Hedeflenen ifadenin türetilmesi için gerekli tanımların yapılması yansıtıcı elemanın işlevsel niteliklerini belirlemek kadar, dairesel polarizasyonlu dalgaların ifadelerinin anlamlanmasını sağlayacaktır. Bu matematiksel işlemlerin ayrıntıları [4]ve [5]'te verilmiştir.

Dairesel polarizayonlu dalganın, ayrık halka birim hücresinden yansımasının, halkadaki ayrığın dönüş açısıyla olan ilişkisini incelerken Şekil 1'deki üslü ve üssüz koordinat sistemleri arasında ileri ve geri dönüşümler yaparak temel ifadeye erişebiliriz.

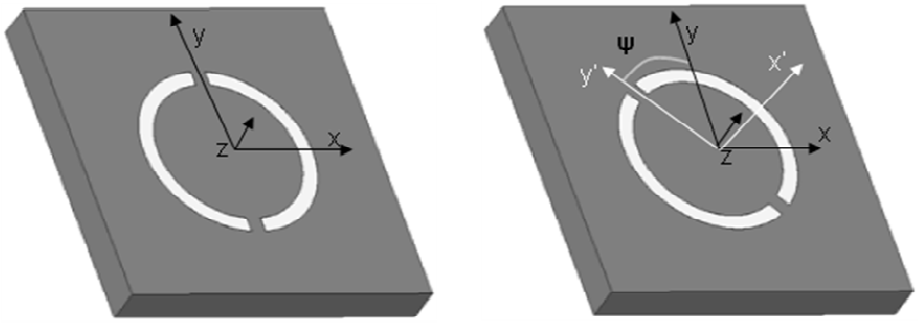

(a) (b)

Şekil 1. Yansıtıcı elemanla birlikte dönen üslü koordinat sistemi ve temel koordinat sistemi.

Şekil 1-(b)'deki birim hücreye, denklem (1)'deki gibi bir dairesel polarizasyonlu dalga gönderidiğimizde, yansıyan dalganın ifadesi denklem (2)'deki gibi olacaktır:

$$\overrightarrow{E^{gelen}} = (\hat{a}_x \pm j\,\hat{a}_y)E^{gelen}\,e^{jz} \tag{1}$$

$$\overrightarrow{E^{yansıyan}} = 0.5E^{gelen}\Gamma_{eş-pol.}(\hat{a}_x \mp j\,\hat{a}_y)e^{\pm j2\psi}e^{-jz} + 0.5E^{i}\Gamma_{çapraz-pol.}(\hat{a}_x \pm j\,\hat{a}_y)\,e^{-jz} \tag{2}$$

Denklem (1) ve (2)'den yola çıkarak, yansıyan dalgada eş polarizasyonlu ve çapraz polarizasyonlu iki bileşen oluştuğu görülür. Yansıyan dalganın içindeki eş polarizasyonlu bileşenin fiziksel dönüş açısıyla doğru orantılı bir faz kazandığı, buna karşılık yansıyan dalganın çapraz polarizasyonlu bileşeninde böyle bir değişikliğin bulunmadığı görülmektedir. Ayrıca dikkat edilmesi gereken başka bir nokta, eş polarizasyonlu yansıyan bileşenin fazındaki katkının, polarizasyonun sağ veya sol dairesel polarizasyona göre işaret değiştirmiş olmasıdır. Son olarak üzerinde durulması gereken önemli bir nokta da bu faz katkısının frekanstan ve eş polarizasyonlu dalganın yansıma seviyesinden bağımsız oluşudur.

Bu bilgiler ışığında elimizdeki yansıtıcı eleman hakkında sağlamamız gereken bir koşul, çalışma frekansında yansıma esnasında çapraz polarizasyonu kabul edilebilir ölçülerde bastırmasıdır. Bu çalışmada seçilen birim elemanın dairesel polarizasyonlu aydınlatma altındaki bir yansıtıcı dizi anten elemanında fiziksel dönüşle faz kontrolü prensiplerini uygulamaya uygun olması gerekmektedir.

3. Yansıtıcı Birim Eleman Olarak Ayrık-halka

Ayrık-halka bu çalışma kapsamında yansıtıcı dizi anten birim elemanı olarak seçilmiştir, çünkü toprak düzlem üzerinde kuvartz tabanda tasarlanan ayrık halka elemanı, üzerine dik olarak düşen dairesel polarizasyonlu bir dalgayı eş polarizasyonlu olarak yansıtabilir. Yapının simetrik olması nedeniyle, fiziksel dönüş etkisini uygulamak yalnızca ayrığın konumunu değiştirerek kolayca halledilir. Üzerindeki ayrığın açısal konumunun değişmesi sonucu dairesel polarizasyonlu dalgaların fazı kontrol edilir.

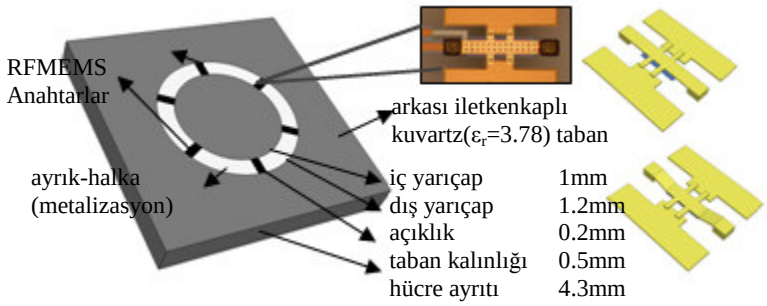

Şekil 2. Benzetimi gerçekleştirilen tek frekanstaki ayrık-halkalı birim hücre ve RF MEMS anahtarlar.

Ansoft HFSS mikrodalga benzetimi kullanılarak tasarlanan örnek ayrık-halka birim elemanın faz kontrol eğrisi ve frekans tepkisi elde edilmiştir. Şekil 3-a'da görüldüğü üzere, tasarlanmış eleman 27.15GHz'de çapraz polarizasyonu bastırmıştır. Bu frekansta, ayrık halka yapısı fiziksel olarak çevrildiğinde doğrusal ve 360° kapsamlı bir faz eğrisi elde edilmiştir ve çapraz polarizasyon tüm açılar için iyi bastırılmıştır (Şekil 3 (b) ve (c)).

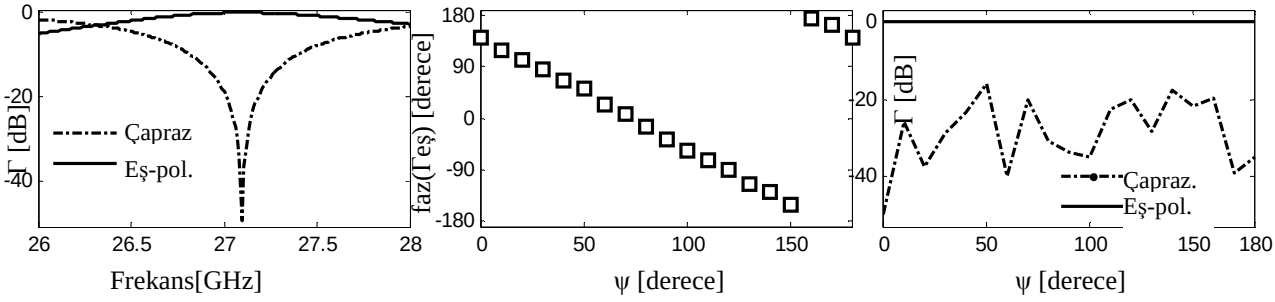

(a) (b) (c)

Şekil 3. Tek ayrık-halkadan oluşan yansıtıcı dizi elemanın karakteristiği, (a) frekans tepkisi, (b) faz eğrisi, (c) farklı açılar için yansıyan eş ve çapraz polarizasyon seviyeleri.

Elemanının yeniden yapılandırılabilir hale getirilmesi, üzerinde koyulan RF MEMS anahtar çiftleriyle gerçekleştirilmiştir (Şekil 2). Toplam 6 adet olmak üzere, 60° fiziksel açı aralığıyla yerleştirilen anahtarların, halka üzerinde karşılıklı olarak eşleştirilmesi ile 3 anahtar çifti oluşturulur. Bu çiftlerden 2 tanesi uyarılmış, 1 tanesi uyarılmamış olduğunda ayrık-halka yapısı elde edilir. Böylece 60° fiziksel arayla yerleşmiş RF MEMS anahtar çiftleri, 120°'lik faz çözünürlüğü sağlar.

3- Çift Frekansta Çalışan Birim Hücre

Çift frekansta çalışan bir hücre oluşturmak için iki ayrı boyutta ayrık-halka tasarlamak ve bunları bir arada kuvartz tabana yerleştirmek gereklidir. Alternatifler, bu halkaları eş merkezli olarak yerleştirmek ya da iki ayrı boyutta halka içeren birim hücre dizilerini köşeli/merkezli iç içe geçirmektir. Amaç oluşturulan çift frekanslı bu yeni birim elemanın iki frekansta bağımsız faz kontrol yeteneğine sahip olmasıdır. Bu yönde yapılan tasarımlar eş merkezli halkaların, eşlenim bakımından büyük dezavantaja olduğunu ortaya çıkarmıştır ve tasarımın Şekil 4'te gösterilen hali tercih edilmiştir. Sonuçta, tasarlanan birim eleman K ve Ka bantlarında faz kontrol yeteneğine sahiptir.

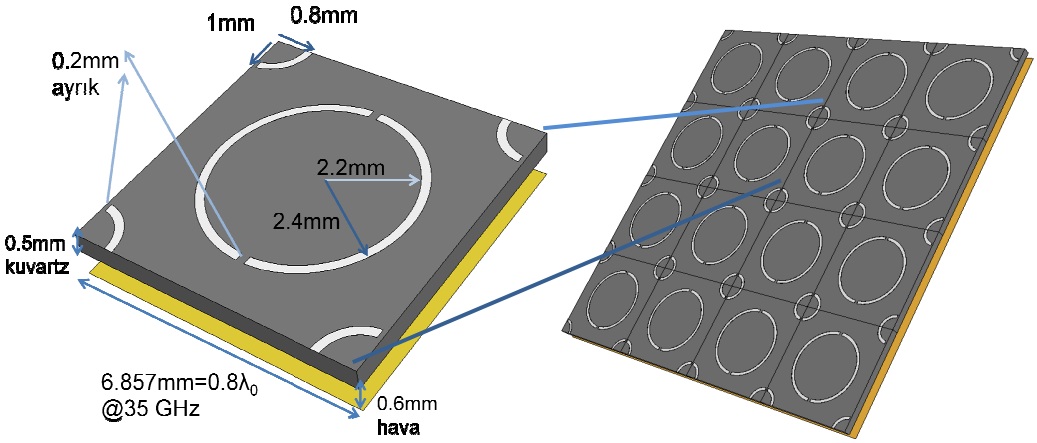

Şekil 4. Çift frekansta çalışan, yansıtıcı birim eleman yapısı.

EM benzetimler, Ansoft HFSS yazılımında periyodik sınır koşulları ve sonsuz düzlemsel dizi kabulü kullanılarak yapılmıştır. Beklendiği gibi ODTÜ RF MEMS grubunun geliştirdiği RF MEMS anahtar ayrık halkayla bütünleştirildiğinde frekans tepkisinde kayma olmakla beraber bu beklenen ve telafi edilebilecek bir durumdur. Şekil 5'te görüldüğü üzere 24.4GHz ve 35GHz olmak üzere, K ve Ka bantlarında çapraz polarizasyon bastırılmıştır.

Büyük ayrık-halka düşük bantta ve küçük ayrık-halka da yüksek bantta fazı kontrol etmektedir. İlgili bantlarda, faz kontrolünde görevli ayrık-halka döndürüldüğü ve diğeri statik tutulduğu durumlarda benzetimler yapılmıştır. Şekil 6'da açıkça görüldüğü gibi, tasarlanan yansıtıcı dizi anten birim hücresi K ve Ka bantlarında işlevini beklendiği gibi yerine getirmektedir, faz eğrisi doğrusal ve 360° kapsamlı, çapraz polarizasyon ise tüm açısal konumlar için kabul edilebilir derecede düşük seviyelerdedir.

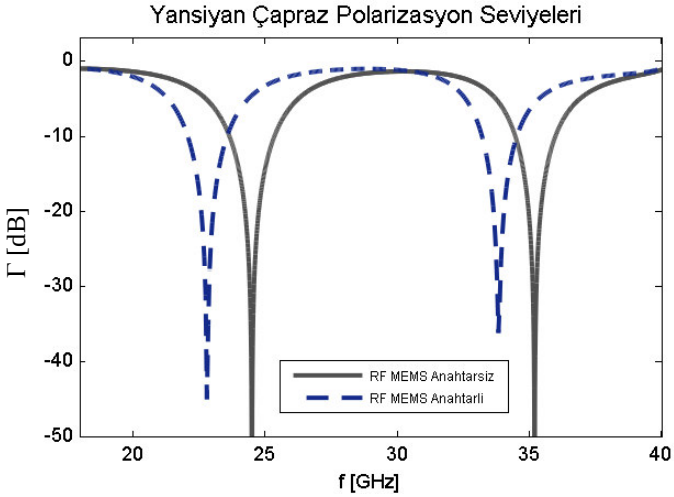

Şekil 5. Çift frekansta çalışan birim hücrenin frekans tepkisi (RF MEMS anahtarları benzetime dahilken ve dahil değilken).

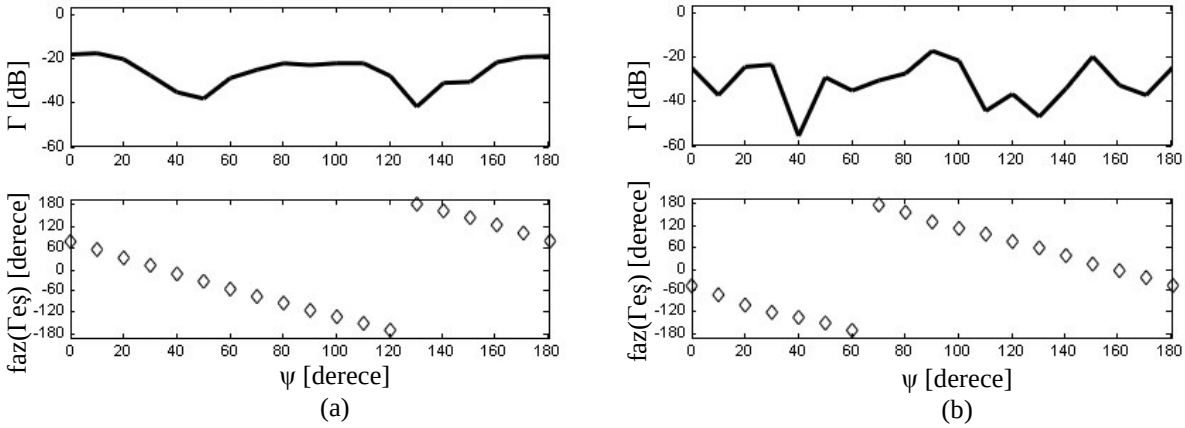

Şekil 6. Çift frekansta çalışan birim hücrenin (a) K bantında, (b) Ka bantında çapraz polarizasyon bastırma ve faz eğrisi.

3. Sonuç

0.5mm kuvartz taban üzerinde, K ve Ka bantlarında dairesel polarizasyonlu dalgaların fazını kontrol edebilen yansıtıcı dizi anten birim hücresi tasarlanmıştır. Birim hücre yansıtıcı dizi antenlerin temel beklentilerini karşılayacak faz aralığına ve doğrusallığa sahiptir. Kullanılan anahtar teknolojisi ODTÜ RF MEMS grubu tarafından geliştirilmiştir ve tasarım ODTÜ RFMEMS üretim süreci kullanılarak ODTÜ MEMS Merkezinde üretilecektir .

Teşekkür

Bu çalışma TÜBİTAK-EEEAG-107E090 ve COST-IC0603-ASSIST tarafından kısmen desteklenmiştir.

Kaynaklar

[1] Pozar, D.M.; Targonski, S.D.; Syrigos, H.D., "Design of millimeter wave microstrip reflectarrays," *Antennas and Propagation, IEEE Transactions on* , vol.45, no.2, pp.287-296, Şubat 1997

[2] Javor, R.D.; Xiao-Dong Wu; Kai Chang, "Beam steering of a microstrip flat reflectarray antenna," *Antennas and Propagation Society International Symposium, 1994. AP-S. Digest* , vol.2, no., pp.956-959 vol.2, 20-24 Haziran 1994

[3] Pozar, D.M.; Metzler, T.A., "Analysis of a reflectarray antenna using microstrip patches of variable size," *Electronics Letters* , vol.29, no.8, pp.657-658, 15 Nisan1993

[4] Huang, J.; Pogorzelski, R.J., "A Ka-band microstrip reflectarray with elements having variable rotation angles," *Antennas and Propagation, IEEE Transactions on* , vol.46, no.5, pp.650-656, Mayıs 1998

[5] Han, C.; Rodenbeck, C.; Huang, J.; Kai Chang, "A C/ka dual frequency dual Layer circularly polarized reflectarray antenna with microstrip ring elements," *Antennas and Propagation, IEEE Transactions on* , sayı.52, no.11, pp. 2871-2876,Kasım 2004

added to complete the CWR circuit structure as shown in Figure 1.

Figure 6 shows the waveform at the receiver input for a 16-dBm carrier with a QPSK modulation at a rate of 20 Mbps. Figure 7 shows the measured sinusoid interference signal when a 16-dBm microwave carrier with a QPSK modulation at 20 Mbps and an AM interference with 7 dBm carrier level are added at the receiver input port. The amplitude modulating frequency of this interference is 1 MHz, and its carrier frequency is the same as the carrier frequency of the useful QPSK signal.

Figure 8 shows the measured noise interference signal when a 16-dBm microwave carrier with QPSK modulation at 20 Mbps and a wideband noise interference signal are added at the receiver input port.

5. CONCLUSION

An approach to perform an active cancellation of a QPSK digital signal using four outputs of the WR receiver is proposed and exposed. Simulation and measurement results validate the proposed active cancellation approach with an interference signal spectrum sensing in the ZSTI of the CWR receiver. More digital modulation possibilities may be achieved by using the CWR-based structure on existing WR receivers. Significant methodical signal processing is still required to reach to an operational CWR system.

ACKNOWLEDGMENTS

Funding by NSERC of Canada is gratefully acknowledged. Authors also acknowledge Jules Gauthier, Steve Dubé, and Jean-Sébastien Décarie for technical assistance.

REFERENCES

1. J. Li, R.G. Bosisio, and K. Wu, Computer and measurement simulation of a new digital receiver operating directly at millimeter-wave frequencies, IEEE Trans Microwave Theory Techniques 43 (1995), 2766–2772.
2. R.G. Bosisio, Y.Y. Zhao, X.Y. Xu, S. Abielmona, E. Moldovan, Y.S Xu, M. Bozzi, S.O. Tatu, C. Nerguizian, J.F. Frigon, C. Caloz, and K. Wu. New wave radio, IEEE Microwave Magazine 9 (2008), 89–100.
3. J. Hyrylainen, L. Bogod, S. Kangasmaa, H.O. Scheck, and T. Ylamurto, Six-port direct conversion receiver, In: Proceedings of 27th European Microwave Conference, 1997, pp. 341–346.
4. M. Abe, N. Sasho, V. Brankovic, and D. Krupezevic, Direct conversion receiver MMIC based on six-port technology, In: Proceedings of European Wireless Technology Conference, 2000, pp. 139–142.
5. Y. Xu, J. Gauthier, and R.G. Bosisio, Six-port digital receivers (SPDRs): A new design approach, Microwave Opt Technol Lett 25 (2000), 356–360.
6. S.O. Tatu, E. Moldovan, K. Wu, and R.G. Bosisio, A new direct millimeter-wave six-port receiver, IEEE Trans Microwave Theory Techniques 49 (2001), 2517–2522.
7. C.A. Hoer and K.C. Roe, Using an arbitrary six-port junction to measure complex voltage ratios, IEEE Trans Microwave Theory Techniques 23 (1975), 978–984.
8. G.F. Engen, The six-port reflectometer: An alternative network analyzer, IEEE Trans Microwave Theory Techniques 25 (1977), 1075–1080.
9. R. Halir, A. Ortega-Moñux, Í. Molina-Fernández, J.G. Wangüemert-Pérez, P. Cheben, D.-X. Xu, B. Lamontagne, and S. Janz, Integrated optical six-port reflectometer in integrated silicon-on-insulator, IEEE J Lightwave Technol, in press.
10. H.-J. Chou and J.-M. Wu, MIMO active interference cancellation for stealth cognitive radio in MB-OFDM UWB, In: Proceedings of the Third International Conference on Communication and Networking in China 2008, China Com 2008, August 25–27, 2008, pp. 173–177.
11. J. Mitola and G.Q. Maguire, Cognitive radio: Making software radio more personal, IEEE Personal Commun 6 (1999), 13–18.
12. D. Cabric, S.M. Mishra, and R.W. Broderson, Implementation issues in spectrum sensing for cognitive radios, Presented at the 38th Annual Asilomar Conference on Signals, Systems and Computers, Pacific Grove, CA, November 2004.
13. D. Cabric, M.S.W. Chen, D.A. Sobel, J. Yang, and R.W. Brodersen, Future wireless systems: UWB, 60 GHz, and cognitive radios, In: Proceedings of the IEEE 2005 Custom Integrated Circuits Conference, September 21, 2005, pp. 793–796.
14. E. Marsan, J.C. Schiel, K. Wu, and R.G. Bosisio, High speed carrier recovery in QPSK wireless communications, In: Proceedings of the Radio Wireless Conference (RAWCON '02), Boston, MA, 2002, pp. 103–106.

BEAM-STEERABLE MEANDERLINE ANTENNA USING VARACTOR DIODES

Nihan Gökalp,[1,2] and Özlem Aydin Civi[1]

[1] Department of Electrical and Electronics Engineering, Middle East Technical University, Ankara, Turkey; Corresponding author: ozlem@metu.edu.tr

[2] Radar Electronic Warfare and Intelligence Systems Department, ASELSAN Inc., Ankara, Turkey

Received 12 April 2010

ABSTRACT: *This study presents a beam-steerable traveling wave meanderline array at X-band. Beam steering is achieved by the varactor diodes mounted on the meanderline that provide progressive phase shift between array elements. It is demonstrated that the radiation direction of the eight-section meanderline array containing eight varactors can be rotated 10° by changing the varactor diode's bias voltage.* © 2010 Wiley Periodicals, Inc. Microwave Opt Technol Lett 53:200–204, 2011; View this article online at wileyonlinelibrary.com.
DOI 10.1002/mop.25634

Key words: *reconfigurable antennas; electronically scanning antennas; meanderline antennas; traveling wave antennas*

1. INTRODUCTION

Recently, reconfigurable antennas have attracted significant interest to implement several operating characteristics by using a single antenna [1]. Various methods are reported in the literature to achieve reconfigurability in frequency, polarization, and radiation pattern [2–4]. Printed microstrip antennas are widely preferred in reconfigurable antenna applications because of their low profile and easy integration with active devices [5–8]. Meanderline antenna has been proposed for some applications that require compact antenna [9, 10]. Especially, traveling wave meanderline antennas have advantages over printed standing wave antennas, such as side lobe level control, low return loss, and electronic beam-steering capability [11]. In this study, a novel beam scanning traveling wave meanderline antenna is proposed for X-band applications. Beam steering capability of the proposed antenna is achieved by loading each section of the meanderline by varactor diodes. By changing the bias voltage of varactors, the phase shift between the array elements can be controlled to steer the main beam. The proposed varactor-controlled meanderline antenna and its characteristics are presented and discussed in the following sections.

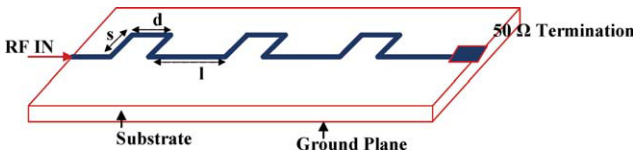

Figure 1 The schematic view of meanderline antenna. [Color figure can be viewed in the online issue, which is available at wileyonlinelibrary.com]

2. ANTENNA DESIGN AND RESULTS

Meanderline arrays consist of a meandering microstrip line with a matched load at the end as shown in Figure 1. They have some advantages compared with other types of printed antennas; for instance, their polarization and beam direction can be controlled by simply adjusting the spacing between the bends [12, 13]. A meanderline antenna can be considered as a linear array of unit cells shown in Figure 2(b). The linear spacing between the successive elements is $d + l$. Each unit cell has four corners as shown in Figure 2(b). According to Ref. 14, radiation of the meanderline antenna mainly occurs from the right-angle bends. These right-angled bends can be modeled as magnetic current elements as seen in Figure 2(a). Because the current on the meanderline antenna travels a shorter path at inside edge compared with the one at the outside edge, it creates an imbalanced magnetic current [14]. Thus, the four-cornered meanderline antenna cell can be modeled as an array of magnetic current elements, which are fed in a phase progression [15]. To reduce the right-angled discontinuity susceptance and return loss, right-angled bends are chamfered. By using array theory, direction of the maximum radiation of the meanderline array, ϕ, can be found from the following relation

$$k_0(d+l)\mathrm{Cos}\phi - (2s+d+l)\beta = 2n\pi, \qquad n = 0, 1, 2\ldots \quad (1)$$

where k_0 is the free space wave number, β is the propagation constant of microstrip line, ϕ is measured from the array axis, and $\phi = 90^\circ$ corresponds to broadside of the antenna array.

In the case of four-cornered meander cell, polarization of the wave radiated by the cell is controlled by two lengths s and d, and the third length l is used to control the required array scan angle [10]. In this study, the polarization of the meanderline array is set vertically polarized, and the main beam direction of the meanderline array consisting of eight sections is set to 30° at the operating frequency of 10 GHz for the array without varactors. To provide these requirements, s, d, and l are calculated as 6.687, 5.452, and 5.522 mm, respectively.

To rotate the main beam at the operating frequency, eight varactor diodes are placed on the arms of the meanderline sections as shown in Figure 3. Varactor diode used in the design is a voltage-controllable device, and the capacitance of the diode varies with the bias voltage. This capacitance variation is used to control the progressive phase difference, ψ, between successive elements of the meanderline array. Thus, Eq. (1) can be modified as follows to determine maximum radiation direction, ϕ,

$$k_0(d+l)\mathrm{Cos}\phi - \{(2s+d+l)\beta + \psi\} = 2n\pi \quad (2)$$

By changing ψ, one can steer the beam to the desired direction.

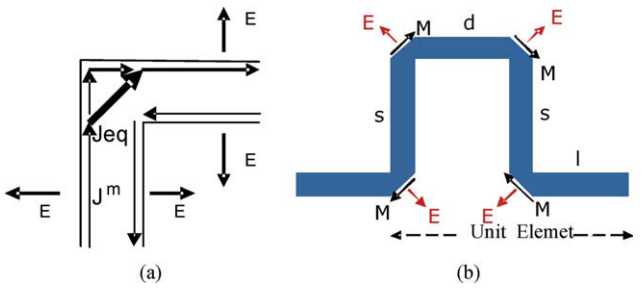

Figure 2 (a) Equivalent current distribution at the right angle bend. (b) Equivalent model of the four-cornered meanderline cell. [Color figure can be viewed in the online issue, which is available at wileyonlinelibrary.com]

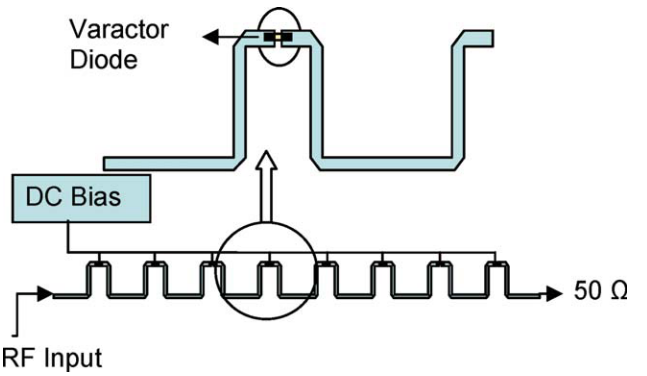

Figure 3 The schematic view of beam-steerable meanderline antenna. [Color figure can be viewed in the online issue, which is available at wileyonlinelibrary.com]

2.1. Varactor Diode Phase Shifting Mechanism

Microsemi MPV2100 type varactors used in this design provides very wide capacitance range (0.3–2.4 pF) under different bias voltages. To measure the phase shift provided by the varactor, varactor diode is mounted on a microstrip line fabricated on ROGERS 6010 Duroid of dielectric constant $\varepsilon_r = 10.2$ and dielectric loss tangent $\delta = 0.0023$. Soldering pads of the varactor diodes are placed on the back side; therefore, silver epoxy has been used to mount the diode on the circuit board as shown in Figure 4.

For different bias voltages, S_{21} phase values have been recorded and phase variation with respect to the bias voltage curve has been obtained and given in Figure 5. It is observed from the measurements that more than 25° phase shift is achieved. In addition, phase variation with the bias voltage is linear, which results in ease in the design of the array.

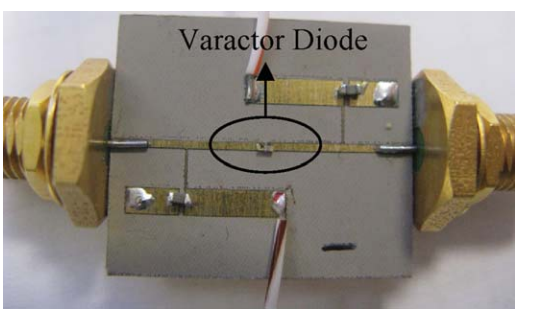

Figure 4 Bias circuit of the Microsemi MPV2100 varactor diode mounted on the 50-Ω microstrip line. [Color figure can be viewed in the online issue, which is available at wileyonlinelibrary.com]

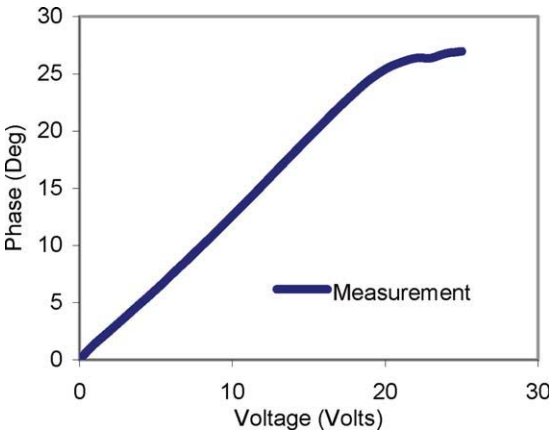

Figure 5 Measured phase variation provided by varactor for different DC bias voltages. [Color figure can be viewed in the online issue, which is available at wileyonlinelibrary.com]

2.2. EM Simulation Results

Simulations of the beam-steerable meanderline array have been performed using a full-wave EM simulator Ansoft Designer based on method of moment. In Ansoft Designer, *S*-parameters of N-port devices obtained from linear simulations or measurements can be inserted in electromagnetic modeling. Therefore, during the simulations of the beam-steerable meanderline array, instead of varactor diodes, *S*-parameters of different capacitance values are inserted into two-port boxes, and these boxes are connected to meanderline sections.

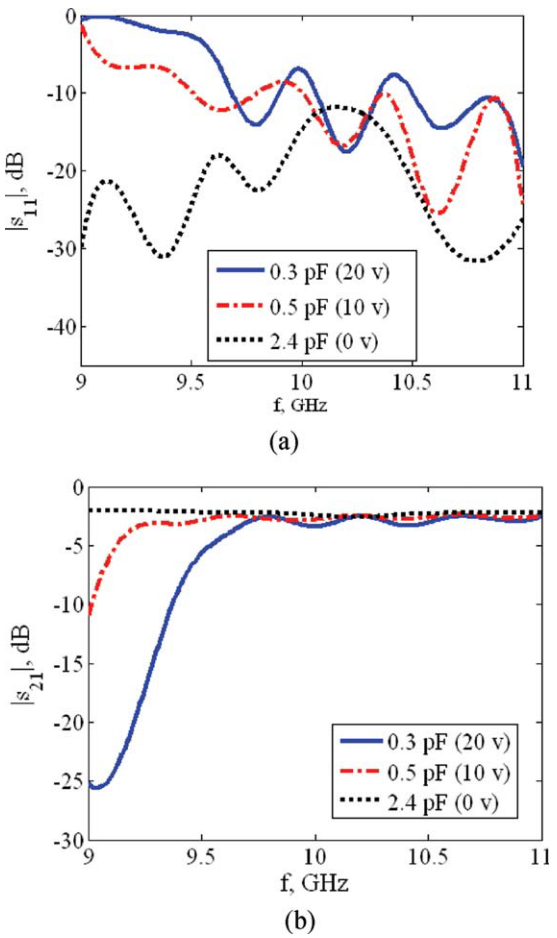

Figure 6 Simulated (a) S_{11} and (b) S_{21}values of the array for various capacitance values. [Color figure can be viewed in the online issue, which is available at wileyonlinelibrary.com]

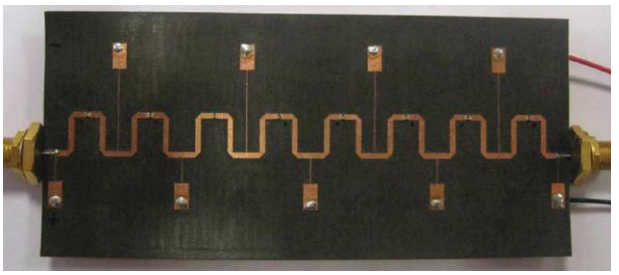

Figure 7 Fabricated meanderline array with varactor diodes. [Color figure can be viewed in the online issue, which is available at wileyonlinelibrary.com]

Simulated return loss values of the antenna are given in Figure 6(a). As observed from the plots, for different values of varactor capacitance, return loss of the beam-steerable array changes because of the impedance variation of the varactor. It is noted that, at 10 GHz, S_{11} value is well below -10 dB. In Figure 6(b), S_{21} values for different capacitance values are given. S_{21} is about -3 dB at 10 GHz.

Radiation patterns in the E-plane of the antenna obtained by simulations at 10 GHz are given in Figure 10 for different values of varactor capacitances. The direction of the beam for 2.4-pF capacitance is 30°, and beam steers up to 19° for 0.3-pF capacitance. It is observed that beam steers more that 10° with corresponding varactor capacitance variation.

2.3. Fabrication and Measurement of Beam-Steerable Antenna

Because of its low dielectric loss and high-frequency operation capability, the beam-steerable meanderline array has been manufactured on 15-mil thick ROGERS 5880 Duroid of dielectric constant $\varepsilon_r = 2.2$ as shown in Figure 7. Tyco/AMP SMA connectors operating from DC to 18 GHz have been used at the input and termination ports.

To bias varactors, two-section microstrip line is used on the antenna side as shown in Figure 7. To reduce the effect of the

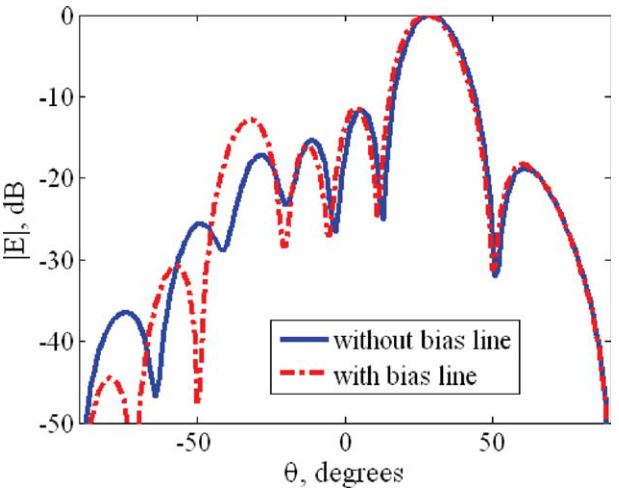

Figure 8 The effect of bias lines on the simulated electric field patterns in the E-plane of the array (θ is measured from broadside). [Color figure can be viewed in the online issue, which is available at wileyonlinelibrary.com]

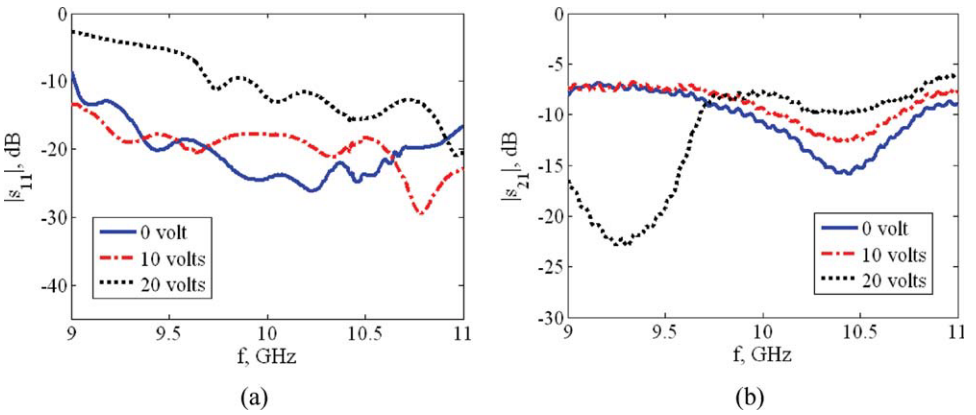

Figure 9 Measured (a) S_{11} and (b) S_{21} values of the array under different bias voltages. [Color figure can be viewed in the online issue, which is available at wileyonlinelibrary.com]

bias line on the array performance, 100 Ω quarter-wavelength long line is used to provide connection to the array. Then, 50 Ω odd multiple of quarter-wavelength long line section is used. Bias wires are soldered to the end of these 50-Ω lines through vias from the back side of the antenna. The effect of bias lines are investigated by comparing the simulated E-plane radiation patterns of the antenna with and without bias lines. Figure 8 shows that bias lines results in a slight shift ($\sim 1^\circ$) in the pattern and an increase in the far side lobe levels. This slight shift in the beam can be compensated by adjusting varactor capacitances accordingly.

S-parameter measurements of the beam-steerable meanderline array have been performed by using Agilent E8364C PNA, 10 MHz to 50 GHz Vector Network Analyzer. Return loss of the beam-steerable meanderline array under different bias voltages has been measured to see the effect of capacitance variation to the *S*-parameters of the antenna. S_{11} measurement results are given in Figure 9(a). As it is seen, measured return loss of the array is well below −10 dB for different values of bias voltages. Figure 9(b) shows measured S_{21} values of the array. As it is observed, S_{21}'s of the array are between −10 and −15 dB. Actually, S_{21} includes mainly varactor diodes' insertion losses in addition to dielectric, conductor, and radiation losses. Because the capacitance of the varactor decreases by the increase in the applied voltage, return loss increases, but it is still below −10 dB in the region of interest, which can be considered as acceptable for such arrays.

Radiation patterns of the beam-steerable meanderline array have been measured for different values of varactor diode bias voltage in the tapered anechoic chamber. The capacitances of the varactor diodes for the corresponding bias voltages could not be measured in our facilities. To obtain corresponding capacitance for the applied voltage values, measured values of phase of S_{21} versus voltage and simulated values of phase of S_{21} versus capacitance are compared. It is determined that 0, 10, and 20 volts correspond to 2.4, 0.5, and 0.3 pF's, respectively. Figure 10 illustrates the measured and the simulated radiation patterns in the E-plane at 10 GHz. It is observed that the measured radiation patterns agree well with the simulated ones. The direction of the radiated beam steers linearly with the applied DC bias voltage. On the other hand, while the beam is steering, side lobes of the beam-steerable meanderline array also increase up to −15 dB. It is demonstrated by the measurements that beam steering of more than 10° is achieved by varactor-loaded meanderline array antenna. In surveillance and tracking radars, although antenna is rotating mechanically, there may be a need to rotate the main beam electronically few degrees for verification beams. The proposed antenna with a limited scan range can be used in such applications.

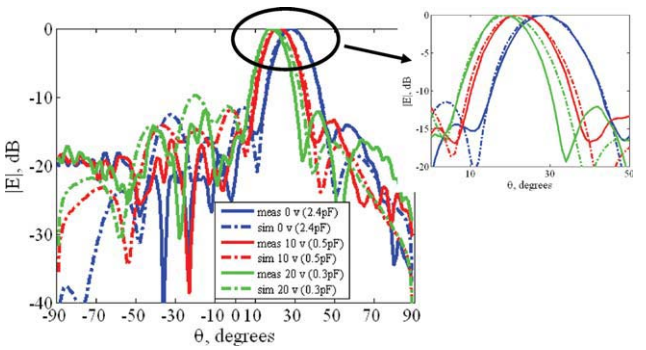

Figure 10 Measured and simulated electric field patterns in the E-plane of the array at 10 GHz under different values of bias voltages (θ is measured from broadside). [Color figure can be viewed in the online issue, which is available at wileyonlinelibrary.com]

3. CONCLUSION

A 10-GHz beam-steerable meanderline array of eight sections is designed, manufactured, and measured. The 10° beam scanning range is achieved by loading the array elements by reverse-biased varactor diodes. This study proves the concept of varactor-controlled beam steering for the meanderline antenna applications that especially require limited scan range, low cost, and easy implementation. To achieve beam steering more than 10°, different phase shifting mechanisms using varactors can be used such as 90° hybrid loaded by the varactor diodes [16]. Furthermore, the use of MEMS capacitors will increase the overall efficiency of the antenna because the insertion loss of MEMS capacitances is small compared with varactor diodes [6].

ACKNOWLEDGMENTS

This work is partially supported by The Scientific and Technological Research Council of Turkey (TUBITAK-EEEAG-107E090) and COST IC0603 ASSIST.

REFERENCES

1. J.T. Bernhard, Reconfigurable antennas, Morgan & Claypool Publishers Series, San Rafael, CA, 2007.
2. X.-S. Yang, B.-Z. Wang, W. Wu, and S. Xiao, Yagi patch antenna with dual-band and pattern reconfigurable, IEEE Antenn Wireless Propag Lett 6 (2007), 168–171.

3. J.-C. Chiao, F. Yiton, M.C. Iao, M. DeLisio, and L.-Y. Lin, MEMS reconfigurable Vee antenna, IEEE MTT-S Int Microwave Symp Digest 4 (1999), 1515–1518.
4. C.W. Jung, M.-J. Lee, G.P. Li, and F. De Flaviis, Reconfigurable scan-beam single-arm spiral antenna integrated with RF-MEMS switches, IEEE Trans Antenn Propag 54 (2006), 455–463.
5. S. Liu, M.-J. Lee, C. Jung, G.-P. Li, and F. De Flaviis, A frequency-reconfigurable circularly polarized patch antenna by integrating MEMS switches, In: Proceedings of the IEEE/URSI International Symposium on Antennas and Propagation, Vol. 2A, 2005, pp.413–416.
6. K. Topalli, E. Erdil, O. Aydin Civi, S. Demir, S. Koc, and T. Akin, Tunable dual-frequency RF MEMS rectangular slot ring antenna, Sensors Actuators: A 156 (2009), 373–380.
7. R.N. Simons, D. Chun, and L.P.B. Katehi, Polarization reconfigurable patch antenna using microelectromechanical systems (MEMS) actuators, Proc IEEE/URSI Int Symp Antenn Propag 1 (2002), 6–9.
8. K. Topalli, O. Aydin Civi, S. Demir, S. Koc, and T. Akin, A monolithic phased array using 3-bit distributed RF MEMS phase shifters, IEEE Trans Microwave Theory Techniques 56 (2007), 270–277.
9. K. Asakura, et al., Meanderline antenna, US Patent 5892490, April 1992.
10. G. Dural, Theory and design of microstrip rampart line arrays, Master Thesis, METU, Ankara, Turkey, 1983.
11. R. Ratmon, I. Oz, and C.J. Samson, Comparison of resonant and travelling-wave meander-line antenna, In: Proceedings of the 17th Convention of Electrical & Electronics Engineers in Israel, March 5–7, 1991, pp.149–151.
12. P. Bhartia and I.J. Bahl, Frequency agile microstrip antennas, Microwave J 25 (1982), 67–70.
13. M. Tiuri, S. Tallqvist, and S. Urpo, Chain antenna, In: Proceedings of the 1974 Antennas and Propagation Society International Symposium, Vol. 12, 1974, pp.274–277.
14. I.J. Bahl and P. Bhartia,Microstrip antennas,Artech House, Inc.,Norwood, MA,1980.
15. J.R. James, P.S. Hall, and C. Wood,Microstrip antenna theory and design, IEE electromagnetic waves series 12,Peter Peregrisnus Ltd.,London,1981.
16. S. Cheng, E. Öjefors, P. Hallbjörner, and A. Rydberg, Compact reflective microstrip phase shifter for traveling wave antenna applications, IEEE Microwave Wireless Compon Lett 16 (2006), 431–433.

A NOVEL PIFA ANTENNA FOR BROADBAND CIRCULAR POLARIZATION

Lehu Wen, Yingzeng Yin, Yan Wang, Jingxiu Huang, Xueshi Ren, and Shaoli Zuo
National Key Laboratory of Antennas and Microwave Technology, Xidian University, Xi'an, Shaanxi 710071, China; Corresponding author: wlh66@163.com

Received 13 April 2010

ABSTRACT: *A novel broadband circularly polarized antenna is proposed, designed, and measured. Basically, the antenna consists of a PIFA and a square ground with an arrow-like branch at its corner, which permit the antenna both broadband and circular polarization characteristics. For ease integration with active devices and design facilitation, the radiating element and ground are etched on the same layer of the substrate. Prototypes of the proposed antenna are fabricated and tested. The obtained −10-dB return loss bandwidth and 2-dB axial ratio (AR) bandwidth reach as large as 39.8 and 41.7%, respectively.*
 Microwave Opt Technol Lett 53:204–208, 2011; View this article online at wileyonlinelibrary.com. DOI 10.1002/mop.25633

Key words: *broadband; circular polarization (CP); PIFA antenna*

1. INTRODUCTION

Circular polarization (CP) is particularly useful for applications in global position, satellites, radio frequency identification systems, and mobile communications for its better mobility and weather penetration [1]. Amount of circularly polarized antennas have been developed. Normally, single-fed microstrip patch antennas are of good performance in directive radiation patterns [2–5], but not in impedance and axial ratio (AR) bandwidths for the existence of back grounds. To enhance the bandwidth performance, multifeed methods are used [3–4]. However, it is necessary to comprise an external feed network such as a Wilkinson power divider, which might complicate the design of array antennas. To avoid the disadvantages stated above, [6–13] put forward other types of slot broadband circularly polarized antenna, but the published literatures show there are not enough in AR bandwidth comparing with the voltage standing wave ratio (VSWR) bandwidth. Recently, PIFA antennas [14–16] have been dawn much attention in antenna design with wideband characteristic, good radiation patterns, simple structure, and easy integration with other active devices, but they usually generate linear polarization. It is rarely scarce to design CP antennas using PIFA structure.

In this article, a novel printed single-layer antenna with a broad AR bandwidth is put forward. The design comprises a PIFA and an arrow-branch loaded ground, which are applied to widen both the impedance bandwidth and the AR bandwidth. The impedance matching mainly depends on the length of the PIFA, and the major factor of the AR bandwidth is the arrow branch. Details of the antenna design are presented, and measured results are given to demonstrate the performance of the proposed antenna.

2. ANTENNA DESIGN

Figure 1 shows the configuration and photograph of the proposed CP antenna with the coordinate system and design parameters. As shown in the figure, all the metallic components of the antenna are printed on the same side of an inexpensive FR4 substrate with thickness of 0.8 mm, relative permittivity $\varepsilon_r = 4.4$, and total size of 80×80 mm^2. The antenna consists of a PIFA structure and a square ground with an arrow-shaped branch at its corner. The square ground is placed in the center of the substrate with length of 40 mm. The outer surface of the coaxial feeding line is in full conjunction with the square ground, and the inner copper is connected to the PIFA to excite the antenna.

The incorporated PIFA structure is of great effect on the impedance bandwidth so that the length of which is carefully selected to realize a wideband performance. The arrow-shaped branch, which is symmetric with respect to $\phi = -45^\circ$ diagonal axis, is introduced and optimized to create a broadband CP. Simulator Ansoft HFSS v.11 is used in this study to perform the design and optimization process. The finally chosen dimensions of the proposed antenna are as illustrated in Figure 1, where l_mono = 30 mm, l_prot = 8.3 mm, and sl = 12 mm.

3. EXPERIMENTAL RESULTS

To verify the proposed design, an experimental prototype is fabricated and tested. The measurement of the return loss for the presented antenna is accomplished with the assistance of a WILTRON-37269A Vector Network Analyzer. The measured and simulated return losses against frequency for the proposed antenna are depicted in Figure 2. As can be seen, the measured result is in good agreement with the simulated, obtaining an impedance bandwidth of around 980 MHz from 1.97 to 2.95 GHz for $s11 \leq -10$ dB.

DUAL FREQUENCY RECONFIGURABLE REFLECTARRAY ANTENNA OF SPLIT RING ELEMENTS WITH RF MEMS SWITCHES

A THESIS SUBMITTED TO
THE GRADUATE SCHOOL OF NATURAL AND APPLIED SCIENCES
OF
MIDDLE EAST TECHNICAL UNIVERSITY

BY

CANER GÜÇLÜ

IN PARTIAL FULFILLMENT OF THE REQUIREMENTS
FOR
THE DEGREE OF MASTER OF SCIENCE
IN
ELECTRICAL AND ELECTRONICS ENGINEERING

SEPTEMBER 2010

Approval of the Thesis:

DUAL FREQUENCY RECONFIGURABLE REFLECTARRAY ANTENNA OF SPLIT RING ELEMENTS WITH RF MEMS SWITCHES

submitted by **CANER GÜÇLÜ** in partial fulfillment of the requirements for the degree of **Master of Science in Electrical and Electronics Engineering Department, Middle East Technical University** by,

Prof. Dr. Canan Özgen
Dean, Graduate School of **Natural and Applied Sciences** _____

Prof. Dr. İsmet Erkmen
Head of Department, **Electrical and Electronics Engineering** _____

Assoc. Prof. Dr. Özlem Aydın Çivi
Supervisor, **Electrical and Electronics Engineering Dept., METU** _____

Prof. Dr. Tayfun Akın
Co-Supervisor, **Electrical and Electronics Engineering Dept., METU** _____

Examining Committee Members:

Assoc. Prof. Dr. S. Sencer Koç
Electrical and Electronics Engineering Dept., METU _____

Assoc. Prof. Dr. Özlem Aydın Çivi
Electrical and Electronics Engineering Dept., METU _____

Assist. Prof. Dr. Lale Alatan
Electrical and Electronics Engineering Dept., METU _____

Dr. Julien Perruisseau-Carrier
Centre Tecnològic de Telecomunicacions de Catalunya _____

Engineer, MSc. Erim İnal
Aselsan A.Ş. _____

Date: September 2, 2010

I hereby declare that all information in this document has been obtained and presented in accordance with academic rules and ethical conduct. I also declare that, as required by these rules and conduct, I have fully cited and referenced all material and results that are not original to this work.

Name, Last name: Caner Güçlü

Signature:

ABSTRACT

DUAL FREQUENCY RECONFIGURABLE REFLECTARRAY ANTENNA OF SPLIT RING ELEMENTS WITH RF MEMS SWITCHES

Güçlü, Caner

MSc., Department of Electrical and Electronics Engineering

Supervisor : Assoc. Prof. Dr. Özlem Aydın Çivi

Co-Supervisor : Prof. Dr. Tayfun Akın

September 2010, 106 pages

Dual band (K and Ka) electronically scanning reflectarray with RF MEMS switches is designed, implemented and measured. Unit cell of the reflect array is composed of conductor backed split-ring elements. In order to steer the beam, the phase of the incident circularly polarized wave is controlled by RF MEMS switches that modify the angular orientation of split-rings individually. Reflectarray is designed using unit cell approach with periodic boundary conditions. The antenna is fabricated by using surface micromachining process developed in METU MEMS Center. Radiation patterns of the antenna are measured and compared with the simulations. It has been shown that the reflectarray is capable of beam switching to 35° in Ka band, 24° in K band.

Keywords: Reflectarray, RF MEMS switches, Reconfigurable antennas, Split-ring, Dual band antennas.

ÖZ

ÇİFT FREKANSTA ÇALIŞAN YENİDEN YAPILANDIRILABİLİR RF MEMS ANAHTARLI AYRIK HALKA YANSITICI DİZİ ANTENİ

Güçlü, Caner

Yüksek Lisans, Elektrik ve Elektronik Mühendisliği Bölümü

Tez Yöneticisi : Doç. Dr. Özlem Aydın Çivi

Ortak Tez Yöneticisi : Prof. Dr. Tayfun Akın

Eylül 2010, 106 sayfa

Çift bantlı (K ve Ka) elektronik tarama yeteneğine sahip RF MEMS anahtarlı yansıtıcı dizi anten tasarlandı, üretildi ve ölçüldü. Yansıtıcı dizi antenin birim hücresi iletken katmanla sonlandırılmış ayrık halkalardan oluşmaktadır. Hüzme döndürme amacıyla her bir ayrık halkanın açısal konumunu RF MEMS anahtarlarla ayarlayarak, dairesel polarizasyonlu dalgaların fazları kontrol edilmektedir. Yansıtıcı dizi anten, periyodik sınır koşulları yaklaşımından yararlanarak birim hücreler şeklinde tasarlanmıştır. Anten ODTÜ MEMS merkezinde geliştirilen yüzey mikro-işleme süreciyle üretilmiştir. Işıma örüntüleri ölçülmüş ve benzetim sonuçlarıyla karşılaştırılmıştır. Ana hüzmenin Ka bandında 35°'ye K bandında 24°'ye döndürülebildiği gösterilmiştir.

Anahtar Kelimeler: Yansıtıcı dizi anteni, RF MEMS anahtarlar, Yeniden yapılandırılabilir antenler, Ayrık halka, Çift bantlı antenler.

“A taste for truth at any cost is a passion which spares nothing.”

Albert Camus

ACKNOWLEDGMENTS

I would like to thank Assoc. Prof. Dr. Özlem Aydın Çivi for her endless guidance, encouragement, and support. Her advices and the research opportunities that she created helped me gain a vision as a young scientist and paved my road to the future as a better researcher. I would like to present my deepest gratitude to Dr. Julien Perruisseau-Carrier for his continuous support, care and the ideas and approaches which made this study successful in such a short term. Also the important contributions of Prof. Dr. Tayfun Akın are a great chance for a new researcher and the research opportunities that he provided are of great importance for me. I would like to thank him for all his guidance.

I would like to thank to Prof. Dr. Altunkan Hızal, Assoc. Prof. Dr. Şimşek Demir, and Assoc. Prof. Dr. Seyit Sencer Koç for being close and helpful to me whenever I need their valuable ideas.

I would like to express my dearest appreciations to Dr. Kağan Topallı and Dr. Mehmet Ünlü. Their patience and mentoring skills, that I always admired, provided me a perfect environment to start as a new researcher. I would not have developed my skills and aspects as a real engineer without their supervision. I thank them very much for not only being perfect technical mentors, but standing always next to me as older brothers, sharing their experiences.

I declare my gratitutes to METU RF MEMS Group members. I would like to thank Ömer Bayraklı for sharing his technical background and helping me as an antenna engineer. Ozan Doğan Gürbüz, Özgehan (Şahin) Kılıç, Çağrı Çetintepe, İlker

Comart, Ramazan Çetin, and Korkut Kaan Tokgöz are not just colleagues to me, they are my friends. Their endless help and support always made me feel secure and confident while dealing with difficulties. They have always kept our office as a friendly ambience and a safe haven.

I appreciate the efforts of METU MEMS Facility personnel, especially Orhan Akar for his kind support and Evrim Özçakır for her contributions in fabrication. Also I wish to acknowledge that this thesis is partially supported by the Scientific and Technical Research Council of Turkey (TUBITAK-EEEAG-107E090) and COST IC0603 ASSIST.

I always think that man in life can have three families: the one he is born into, the one that is born to his hands and the one he acquires throughout his life- friends. I would like to thank my friends Emre Yılmaz, Emre Tatlı, Çiğdem Okuyucu, and Dilara Çalık, Gürkan Yılmaz who have always been close and supportive. Their continuous company has always made me a stronger person against the hardships.

I would like to express my deepest thanks to my girl friend Ayça Çavcı who has been family to me, the best friend and the owner of the warmest embrace in which I found the strength and the joy of living. The whole course of this study would not be as easy without her presence.

I particularly kept the last words for my family: my father Bülent Hilmi Güçlü, my mother Ayhan Güçlü, and my brother Tansel Güçlü. I cannot even think of how life would turn out without their unconditional love and selfless care.

To my family and friends, I dedicate this thesis.

TABLE OF CONTENTS

LIST OF TABLES

TABLES

LIST OF FIGURES

FIGURES

CHAPTER 1

INTRODUCTION

Recently smart antenna applications, electronic beam shaping technologies are emerging research topics. Their area of application varies from telecommunication technologies to radar applications, from data links to automated systems in daily use. Reconfigurable reflectarray antennas constitute a highly advantageous type for these applications. The advantages of the simple reflector type antennas and the phased arrays are combined in reflectarray antennas. In this study RF MEMS technology is integrated with the reflectarray antenna type to provide reconfigurability.

In this thesis a circularly polarized reconfigurable dual frequency reflectarray antenna element with RF MEMS switches operating at 22.65 GHz and 34 GHz is designed. The reflectarray element is composed of split rings in two different sizes integrated with RF MEMS switches to obtain dual frequency operation. The phase shift principle is applied with the rotation of split-rings that the location of splits are controlled by turning on and off the RF MEMS switches that are placed with 60° spacing. The rotational phase shift principle is applied, by switching properly and rotating the 'split' of the ring. In Figure 1.1, the element and the antenna are illustrated. A prototype on which the on and off-state switches are modeled by perfect shorts and opens is designed and fabricated. The reflectarray antenna is capable of 35°and 24° beam steering in Ka and K bands respectively. There are a total of 109 Ka band and 124 K band split-rings employed. This reflectarray antenna is the first reconfigurable reflectarray antenna capable of phase control in dual bands in literature to the author's knowledge.

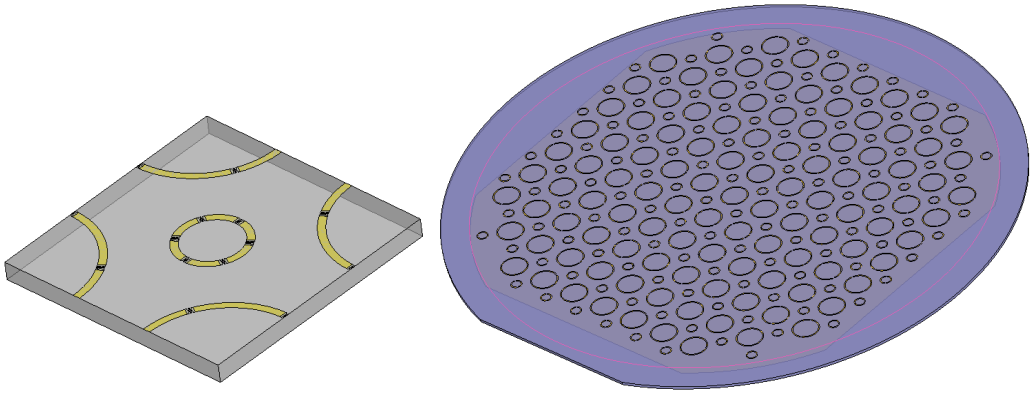

Figure 1.1 Overview of the reflectarray element and the antenna.

This introductory chapter gives the principles of reflectarray design with an overview of various reflectarray antenna applications. Then the objectives of the thesis are explained, and the organization of the thesis is presented to the reader.

1.1 Reflectarray Antennas

In this section the reflectarray antenna concept is explained and various important works in the literature are mentioned.

1.1.1 Definition and Historical Development

The reflectarray antenna is a well known antenna type whose history can be traced back to '70s [1]. The reflectarray antenna combines the advantages of the simple reflector type antennas and the phased arrays. While designing reflector type antennas, the phase front tailoring is done by making use of the different path lengths over the reflector surface. They are mostly preferred since there is no need for complex feed systems. As another common type, the phased arrays are well known and highly utilized antennas that make use of phase shifter technologies to create the desired phasing of the elements to shape the beam according to the requirements. Since their direction of radiation is determined by proper phasing, they provide freedom of physical positioning and can be mounted as desired. Reflectarray

antennas are composed of reflective elements that are especially designed to achieve phase control. Thus they are the synthesis of the phased array concept in 2D and the space feeding systems from reflector antennas. They transform the incident wave's phase front upon reflection to achieve the formation of the desired beam. It solves the complex feed-network problems of phased arrays via space-feed and volume occupation problem of reflector antennas via its planar shape.

In Figure 1.2, the reflectarray principle is depicted. The incident field on the reflectarray elements is tuned accurately to provide the phase shift upon reflection. The reflected wave front is formed by the reflected waves with the desired phase distribution, so that the phase front is adjusted to obtain the desired beam.

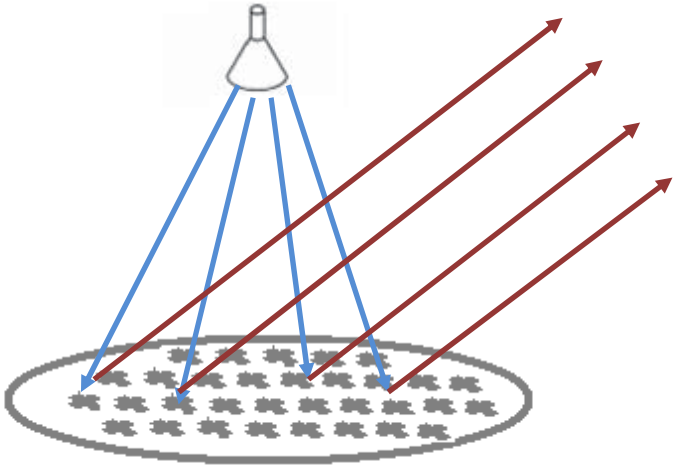

Figure 1.2 The reflectarray antenna, formation of the desired beam upon reflection.

The reflectarray antenna design is based on element design. The element design is done in various states corresponding to various reflection angles, according to the phase control principles. The phase design curve is the graph where the reflection phase is plotted against the element states. This curve is a convenient graph that shows the phase coverage, resolution and the linearity of a reflectarray element. Also the reflection magnitude versus element states can be another helpful plot.

The reflectarrays can be configured to provide pencil-beam radiation patterns, as well as multi-contoured beams. Reconfigurability can be brought in reflectarray concept to achieve electronic beam scanning.

The reflectarray antenna capabilities depend on the element properties. Reflection phase and reflection magnitude on a single element should be characterized to better analyze the behavior. Most important property of an element is the phase coverage, i.e. the phase shift contributed upon reflection. It is a fact that the magnitude of the reflected field from an element is primarily dependent on the free-space propagation loss from feed to reflectarray surface. In addition, the dielectric losses occurring in the reflective element; as well, the integrated phase shifting circuitry contributes to the losses.

The first reflectarray was proposed by Berry, Malech and Kennedy in [2]. The design was composed of short ended waveguides with variable lengths. The required phasing was formed by the delays in the waveguides where the incident field is coupled, traveled, reflected at the short end and radiated back into the sky.

In 1977 the spiraphase reflectarray was developed by Phelan [1]. This structure was implementing the rotational phase-shift principle which constitutes the basic principle in this thesis. This design employed switching diodes in a 4-arm spiral antenna. Also in '70s the microstrip antennas were developing, however the application of microstrip antennas in reflectarray concept was first done by Malagisi in 1978, [3]. Unfortunately the combination of reflectarrays with microstrip technology was no further studied until the late '80s when the necessity of low profile and low mass antennas emerged.

1.1.2 Notable Reflectarray Antennas in Literature

In reflectarrays, phase control is achieved by using several methods. One of the most favorable methods is to use variable-size patches [4], rings [5], and dipoles [6]. Also the bandwidth problem in the variable-size patch applications are solved by stacking double and triple layers of patches of different sizes, [7, 8]. The idea of loading the rectangular patches with stubs is another way of phase control. The incident field coupled to the rectangular patch travels along the stubs of different lengths reflects back and re-radiates. This method is demonstrated in [9].

The aperture coupled microstrip patch antenna is very suitable for designing a reflectarray element. The line coupled to the patch can be altered to control the phase. This type of element is suitable for single or dual polarization or circular polarization. The variable length transmission line coupled through the slot to the patch is implemented in [10]. Achieving wide phase range to solve the bandwidth problem by loading stubs is demonstrated in [11]. In addition, this element can be integrated with switches and active structures to introduce reconfigurability. A sample with Metal Semiconductor Field Effect Transistor to amplify and adjust the phase is shown in [12]. Also the linearly polarized ACMP (Aperture Coupled Microstrip Patch) antenna using RF MEMS switches to provide reconfigurability is studied [13-15].

The rotational phase shift principle which was first put forward by Phelan [1], is used in various applications to design circularly polarized reflectarrays. This principle states that the phase of the co-polarized wave upon circularly polarized wave incidence is linearly dependent on the elements rotation angle. Rotating patches are designed to utilize this principle in [16]; as well, multiple dipoles are employed with the same principle [17]. The most important applications of this phase control method in the context of this thesis are the ones using split-ring elements in single and dual frequency reflectarrays [18-21]. The work presented in this thesis also is a

dual frequency reflectarray with split-rings. In addition, this reflectarray unit cell element is the capable of phase control in two frequencies independently; at this aspect it is the only reconfigurable dual frequency ever presented to the author's knowledge.

The reconfigurable reflectarray configurations employ several techniques as tunable dielectrics, varactor diodes, PIN diodes and MEMS implementations including micro-motors and RF MEMS.

Varactor diodes affect on the radiation susceptance of antennas by capacitive loading. In [22] , the 2D rectangular patches are biased at their centers with vias through the substrate and ground plane. Then each patch is connected to the neighboring patches with varactors. By properly adjusting the voltage distribution, the surface turns in to a tunable impedance surface making it possible to steer beams. In [23], PIN and varactor diodes are put into a cross-shaped microstrip loop for a dual polarized, polarization flexible reflective cell whose phase can be dynamically controlled.

The tunable dielectrics may be used as substrates, or to fill cavities. Then the frequency/phase response of the reflective element is controlled by biasing these structures electrically. The examples for these applications are ferroelectric thin film, liquid crystals (LC) [24-28].

1.1.3 MEMS in Reflectarray Antennas

MEMS (Micro Electro-Mechanical Systems) is an enabling technology in microwave and antenna engineering field, for being suitable for monolithic fabrication, enabling miniaturization of the transceivers.

In [29], a pseudo-ring structure as the reflectarray element loaded with 5 pairs of switches is shown. The element has 360° phase coverage. The design is experimentally validated by testing in rectangular waveguide simulator. In another study [30], a suspended patch is designed and fabricated by micromachining. As the suspending patch is pulled down by electrostatic actuation, the phase is tuned. But the reflection phase characteristic is poor and limited to 200° coverage. In [31], a patch-slot element is utilized as the reflectarray cell. The slot of the element is loaded with RF MEMS shunt switches; approximately 120° phase coverage is demonstrated.

Most of the reflectarrays with MEMS are implemented only in unit cells and characterized by waveguide simulators. There a few examples of full reflectarrays with MEMS [13, 30, 32-34] and only one with measurement results, [13]. The reflectarray presented in this thesis also provides full reflectarray design.

1.2 Thesis Objective and Organization

The goal of this thesis is to design a reconfigurable circularly polarized dual band reflectarray antenna composing of split-ring elements integrated with RF MEMS switches. Rotational phase shift principle is implemented as the phase control principle. The RF MEMS fabrication process developed in Middle East Technical University is utilized in design. The objectives are stated as follows:

- Rotational phase shift principle,
    - is studied to reach a mathematical expression and a better comprehension of the phenomenon.
    - is implemented using a split-ring element.

- A reflectarray element,
    - capable of controlling the phase of the co-polarized reflected wave

upon a circularly polarized incident wave
    - having a linear phase design curve and 360° phase coverage in two frequency bands
    - achieving phase control in two frequency bands simultaneously, i.e. independent operation in both bands
    - integrated with RF MEMS switches, to provide 120° phase resolution in both bands

  is designed.

- A reflectarray antenna prototype,
    - composed of the aforementioned element
    - capable of beam switching between broad side and 24° at 24.4 GHz and 35° at 35.5 GHz.
    - that is aimed to verify the dual frequency split-ring element operation
    - composed of split-rings with short/open modeling of the MEMS switches instead of fully operational RF MEMS implementation.

  is designed, fabricated and measured.

This thesis constitutes a collection of the studies in the frame of the mentioned objectives. The studies and accomplishments up to date are bundled together in the course of five chapters. Beyond this introductory Chapter 1, which gives a summary of the reflectarray concept with historical background and provides the reader with organizational details of this thesis, the contents of the chapters are explained as follows:

Chapter 2: The rotational phase shift principle is defined. The mathematical expressions are derived to have an insight view to the phenomenon. The conditions on the reflective element and the illumination of the reflectarray antenna for the realization of the principle are given.

Chapter 3: The split-ring element is studied by means of simulation tools.

The element is subject to a parametric analysis. The essential information to tune the reflective characteristics is investigated in order to implement the rotational phase shift principle. In addition the characteristics of a reflectarray element operating at a single frequency composed of a split-ring is designed and characterized.

Chapter 4: A dual band reflectarray element of split-rings is designed and characterized. RF MEMS switch topology is given and the dual band reflectarray element with integrated switches is presented. A prototype reflectarray antenna design with radiation pattern simulation results is provided. Then these results are compared with the measurement results of the fabricated prototype.

Chapter 5: The conclusions and future works are explained. The discussion of the goals and achievements are made.

CHAPTER 2

THEORY OF THE ROTATIONAL PHASE SHIFT PRINCIPLE

2.1 Introduction

The reflectarray antenna design is basically dependent on the capabilities and characteristics of the reflective element. Along many techniques concerning the linearly polarized waves, some of which can be also applied to circularly polarized waves, there is the rotational phase shift principle special to circularly polarized waves. This chapter presents the theoretical derivations, and meanings of the final form of the reflection equation.

2.2 The Rotational Phase Shift Principle

In case of the circularly polarized wave incident on a reflective element, when the element is rotated the phase of the reflected wave is linearly dependent on the relative angular position of the reflective topology. This type of dependence requires some conditions on the incident and reflected waves, and derivation is hence important for the design process of the reflective element. The same principle was previously demonstrated in [1], [35] and a mathematical derivation is briefly given in [16] with a specific application.

Throughout this thesis, the electromagnetic waves of interest are circularly polarized. This is the reason for denoting a common convention. Since the circularly polarized waves with opposite senses constitute an independent orthogonal basis set for the

electromagnetic plane waves, any plane wave can be expressed as a sum of two circularly polarized plane waves with opposite senses. The co- and cross-polarization terms in the context of circularly polarized waves refer to the sense of interest and the latter sense respectively.

The rotational phase shift principle is explained as follows. Upon incidence of a circularly polarized wave onto a reflective surface, the phase of the reflected co-polarized circularly wave is linearly proportional to the angular position of the reflective element. That is, the phase of reflection may be controlled by the relative angular orientation of the reflective element. The phase shift is totally dependent on the geometry, and it is independent of the frequency of operation as well as the reflection coefficient of co-polarized wave.

2.3 Derivation of the Linear Proportionality

In this section the mathematical derivation of the rotational phase shift principle is given. The derivation provides an in-depth view for the design.

The aim is mathematically to reach an expression relating the reflection characteristics of an element and the reflection characteristics of its physically rotated version. The starting point of the derivation is deducing the reflection parameters of the rotated version by mathematical elaboration using coordinate transformations. In Figure 2.1, the reflective element (which is backed by a ground plane) and the physical rotation angle is demonstrated. Although the figure depicts a split-ring element on the plane, the derivation is valid for any arbitrary reflective surface.

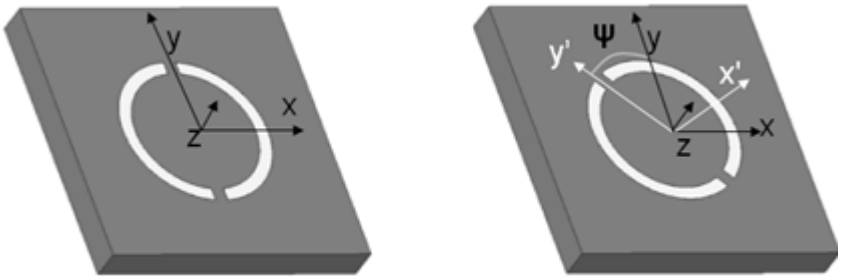

Figure 2.1 The illustration of a reflective element and rotation about z-axis.

Regarding Figure 2.1, there are two distinct coordinate systems. The primed coordinate system and the basic coordinate system have the common z/z' axes. The primed coordinate system is defined to have rotated about the common z axis, by an arbitrary angle ψ. In other words the primed and basic coordinate systems share the common XY plane, and the origin, but there is a rotational offset about z axis. For the initial state of the reflective element, say ψ=0°, the two coordinate systems are the same. It is assumed that the reflection coefficients for the element are known. From this point on, for the primed coordinate systems, the reflection coefficients for the reflective element is always the same and known, but the reflection coefficients with regard to the basic coordinate system is easy to derive applying rotational transformation matrices forth and back.

For conventional purposes, the incident and reflected fields in general are expressed as follows:

$$E^{inc} = (E_{x'}^{inc}\hat{a}_{x'} + E_{y'}^{inc}\hat{a}_{y'})e^{jz'} = (E_x^{inc}\hat{a}_x + E_y^{inc}\hat{a}_y)e^{jz} \tag{2.1}$$

$$E^{ref} = (E_{x'}^{ref}\hat{a}_{x'} + E_{y'}^{ref}\hat{a}_{y'})e^{-jz'} = (E_x^{ref}\hat{a}_x + E_y^{ref}\hat{a}_y)e^{-jz} \tag{2.2}$$

Note that e^{jz} and e^{-jz} are used for the incident and reflected field expressions respectively. From this point on, the derivations are assumed to be carried on at z=z'=0, on the surface where the reflection takes place. That is why the exponential terms are not represented.

The reflection characteristics are handled as an S-matrix, relating the reflection and cross-coupling of the x and y components of the incident and reflected fields. For example, the reflection characteristics for primed coordinate system correspond to:

$$\begin{pmatrix} E_{x'}^{ref} \\ E_{y'}^{ref} \end{pmatrix} = [S'] \begin{pmatrix} E_{x'}^{inc} \\ E_{y'}^{inc} \end{pmatrix} = \begin{pmatrix} s'_{11} & s'_{12} \\ s'_{21} & s'_{22} \end{pmatrix} \begin{pmatrix} E_{x'}^{inc} \\ E_{y'}^{inc} \end{pmatrix} \tag{2.3}$$

The Equation (2.3) shows the reflected and incident electric field quantities, the reflections and the cross-coupling between x and y components. The assumption is that this matrix is at hand. The goal is to achieve a similar matrix equation for the non-primed coordinate system:

$$\begin{pmatrix} E_{x}^{ref} \\ E_{y}^{ref} \end{pmatrix} = [S] \begin{pmatrix} E_{x}^{inc} \\ E_{y}^{inc} \end{pmatrix} = \begin{pmatrix} s_{11} & s_{12} \\ s_{21} & s_{22} \end{pmatrix} \begin{pmatrix} E_{x}^{inc} \\ E_{y}^{inc} \end{pmatrix} \tag{2.4}$$

To reach the s-matrix, the transformations between basic and the primed coordinate system is to be applied. These transformation matrices are as follows:

$$\begin{pmatrix} x \\ y \end{pmatrix} = \begin{pmatrix} \cos(\Psi) & -\sin(\Psi) \\ \sin(\Psi) & \cos(\Psi) \end{pmatrix} \begin{pmatrix} x' \\ y' \end{pmatrix} \tag{2.5}$$

$$\begin{pmatrix} x' \\ y' \end{pmatrix} = \begin{pmatrix} \cos(\Psi) & \sin(\Psi) \\ -\sin(\Psi) & \cos(\Psi) \end{pmatrix} \begin{pmatrix} x \\ y \end{pmatrix} \tag{2.6}$$

When the primed incident field is expressed with respect to the basic coordinate system:

$$\begin{pmatrix} E_{x'}^{inc} \\ E_{y'}^{inc} \end{pmatrix} = \begin{pmatrix} \cos(\Psi) & \sin(\Psi) \\ -\sin(\Psi) & \cos(\Psi) \end{pmatrix} \begin{pmatrix} E_{x}^{inc} \\ E_{y}^{inc} \end{pmatrix} \tag{2.7}$$

Then the reflected field expression in primed coordinate system is reached by combining Equations (2.3) and (2.7):

$$\begin{pmatrix} E_{x'}^{ref} \\ E_{y'}^{ref} \end{pmatrix} = \begin{pmatrix} s'_{11} & s'_{12} \\ s'_{21} & s'_{22} \end{pmatrix} \begin{pmatrix} \cos(\Psi) & \sin(\Psi) \\ -\sin(\Psi) & \cos(\Psi) \end{pmatrix} \begin{pmatrix} E_{x}^{inc} \\ E_{y}^{inc} \end{pmatrix} \tag{2.8}$$

The reflected field components in the basic coordinate system in terms of the primed coordinate system component are as follows:

$$\begin{pmatrix} E_x^{ref} \\ E_y^{ref} \end{pmatrix} = \begin{pmatrix} \cos(\Psi) & -\sin(\Psi) \\ \sin(\Psi) & \cos(\Psi) \end{pmatrix} \begin{pmatrix} E_{x'}^{ref} \\ E_{y'}^{ref} \end{pmatrix} \tag{2.9}$$

Combining the Equations (2.8) and (2.9):

$$\begin{pmatrix} E_x^{ref} \\ E_y^{ref} \end{pmatrix} = \begin{pmatrix} \cos(\Psi) & -\sin(\Psi) \\ \sin(\Psi) & \cos(\Psi) \end{pmatrix} \begin{pmatrix} s'_{11} & s'_{12} \\ s'_{21} & s'_{22} \end{pmatrix} \begin{pmatrix} \cos(\Psi) & \sin(\Psi) \\ -\sin(\Psi) & \cos(\Psi) \end{pmatrix} \begin{pmatrix} E_x^{inc} \\ E_y^{inc} \end{pmatrix} \tag{2.10}$$

The Equation (2.10) is a very important step because:

1. This is the first fundamental result, since it gives the reflected wave properties for any normally incident wave as a function of:
    a. A single characteristic S-matrix which is pertaining to a specific angular orientation of the reflective element,
    b. The angle of rotation of the reflective element.
2. This is a big advantage over characterizing the different angular orientations of the element to be regarded as simple angular rotations.

The reflective element is assumed to be composing of reciprocal materials, this makes the off-diagonal terms equal; $s'_{12} = s'_{21}$. With this contribution, after the necessary matrix multiplication operations the incident and reflected field relations in terms of physical rotation angle and the reflection characteristics at hand (which pertain to the primed coordinate system) the final form is:

$$\begin{aligned} \begin{pmatrix} E_x^{ref} \\ E_y^{ref} \end{pmatrix} &= [S] \begin{pmatrix} E_x^{inc} \\ E_y^{inc} \end{pmatrix} \\ &= \begin{pmatrix} [s'_{11}\cos^2(\Psi) + s'_{22}\sin^2(\Psi) & [(s'_{11} - s'_{22})\sin(\Psi)\cos(\Psi) \\ -2s'_{12}\sin(\Psi)\cos(\Psi)] & +s'_{12}(\cos^2(\Psi) - \sin^2(\Psi))] \\ [(s'_{11} - s'_{22})\sin(\Psi)\cos(\Psi) & [s'_{11}\sin^2(\Psi) + s'_{22}\cos^2(\Psi) \\ +s'_{12}(\cos^2(\Psi) - \sin^2(\Psi))] & +2s'_{12}\sin(\Psi)\cos(\Psi)] \end{pmatrix} \begin{pmatrix} E_x^{inc} \\ E_y^{inc} \end{pmatrix} \end{aligned} \tag{2.11}$$

To better analyze the matrix relation in (2.11), decomposing [S'] is a very helpful

method. [S'] can be expressed as a sum as shown:

$$[S'] = [S']_A + [S']_B + [S']_C \tag{2.12}$$

$$\begin{pmatrix} s'_{11} & s'_{12} \\ s'_{21} & s'_{22} \end{pmatrix} = \begin{pmatrix} A & 0 \\ 0 & A \end{pmatrix} + \begin{pmatrix} B & 0 \\ 0 & -B \end{pmatrix} + \begin{pmatrix} 0 & -jC \\ -jC & 0 \end{pmatrix} \tag{2.13}$$

Where:

$$A = \frac{1}{2}(s'_{11} + s'_{22}) \tag{2.14}$$

$$B = \frac{1}{2}(s'_{11} - s'_{22}) \tag{2.15}$$

$$C = js'_{12} \tag{2.16}$$

Simply using the distribution of multiplication over summation, the final expression can be meaningfully derived. It can be seen that any matrix [S'] can be decomposed into the three matrices in Equation (2.13). Moreover, as previously mentioned any incident wave can be expressed in terms of two circularly polarized waves of opposite senses. This is the reason that the reflected field will be examined upon incident circularly polarized fields. The reflected field expressions for the circularly polarized incident field are examined for each part (namely: $[S']_A$, $[S']_B$ and $[S']_C$) of the matrix [S'] to build up the final expression of the reflected field.

$$\text{Let } \begin{pmatrix} E_x^{inc} \\ E_y^{inc} \end{pmatrix} = \begin{pmatrix} 1 \\ \pm j \end{pmatrix} E_0^{inc} \tag{2.17}$$

- For the partial solution of $\begin{pmatrix} s'_{11} & s'_{12} \\ s'_{21} & s'_{22} \end{pmatrix}_A = \begin{pmatrix} A & 0 \\ 0 & A \end{pmatrix}$, the Equation (2.11) turns into:

$$\begin{pmatrix} E_x^{ref} \\ E_y^{ref} \end{pmatrix}_A = \begin{pmatrix} [A\cos^2(\Psi) + A\sin^2(\Psi) & [(A-A)\sin(\Psi)\cos(\Psi) \\ -2\cdot 0\cdot\sin(\Psi)\cos(\Psi)] & +0\cdot(\cos^2(\Psi) - \sin^2(\Psi))] \\ [(A-A)\sin(\Psi)\cos(\Psi) & [A\sin^2(\Psi) + A\cos^2(\Psi) \\ +0\cdot(\cos^2(\Psi) - \sin^2(\Psi))] & +2\cdot 0\cdot\sin(\Psi)\cos(\Psi)] \end{pmatrix} \begin{pmatrix} E_x^{inc} \\ E_y^{inc} \end{pmatrix} \tag{2.18}$$

$$= \begin{pmatrix} A & 0 \\ 0 & A \end{pmatrix} \begin{pmatrix} E_x^{inc} \\ E_y^{inc} \end{pmatrix} \tag{2.19}$$

After taking into account the incident field expressed as in Equation (2.17):

$$\begin{pmatrix} E_x^{ref} \\ E_y^{ref} \end{pmatrix}_A = \begin{pmatrix} A & 0 \\ 0 & A \end{pmatrix} \begin{pmatrix} 1 \\ \pm j \end{pmatrix} E_0^{inc} \tag{2.20}$$

$$\begin{pmatrix} E_x^{ref} \\ E_y^{ref} \end{pmatrix}_A = A \begin{pmatrix} 1 \\ \pm j \end{pmatrix} E_0^{inc} \tag{2.21}$$

The reflected field in Equation (2.21) is the cross polarized wave upon reflection. One should note that the direction of propagation reversed while the electric field vector is scaled by A.

- For the partial solution of $\begin{pmatrix} s'_{11} & s'_{12} \\ s'_{21} & s'_{22} \end{pmatrix}_B = \begin{pmatrix} B & 0 \\ 0 & -B \end{pmatrix}$, the Equation (2.11) turns into:

$$\begin{pmatrix} E_x^{ref} \\ E_y^{ref} \end{pmatrix}_B = \begin{pmatrix} [B\cos^2(\Psi) - B\sin^2(\Psi) & [(B+B)\sin(\Psi)\cos(\Psi) \\ -2\cdot 0\cdot\sin(\Psi)\cos(\Psi)] & +0\cdot(\cos^2(\Psi)-\sin^2(\Psi))] \\ [(B+B)\sin(\Psi)\cos(\Psi) & [B\sin^2(\Psi) - B\cos^2(\Psi) \\ +0\cdot(\cos^2(\Psi)-\sin^2(\Psi))] & +2\cdot 0\cdot\sin(\Psi)\cos(\Psi)] \end{pmatrix} \begin{pmatrix} E_x^{inc} \\ E_y^{inc} \end{pmatrix} \tag{2.22}$$

$$= \begin{pmatrix} B(\cos^2(\Psi)-\sin^2(\Psi)) & 2B\sin(\Psi)\cos(\Psi) \\ 2B\sin(\Psi)\cos(\Psi) & -B(\cos^2(\Psi)-\sin^2(\Psi)) \end{pmatrix} \begin{pmatrix} E_x^{inc} \\ E_y^{inc} \end{pmatrix} \tag{2.23}$$

$$= B \begin{pmatrix} \cos(2\Psi) & \sin(2\Psi) \\ \sin(2\Psi) & -\cos(2\Psi) \end{pmatrix} \begin{pmatrix} E_x^{inc} \\ E_y^{inc} \end{pmatrix} \tag{2.24}$$

After taking into account the incident field expressed as in Equation (2.17):

$$\begin{pmatrix} E_x^{ref} \\ E_y^{ref} \end{pmatrix}_B = B \begin{pmatrix} \cos(2\Psi) & \sin(2\Psi) \\ \sin(2\Psi) & -\cos(2\Psi) \end{pmatrix} \begin{pmatrix} 1 \\ \pm j \end{pmatrix} E_0^{inc} \tag{2.25}$$

$$= B\begin{pmatrix} \cos(2\Psi) \pm j\sin(2\Psi) \\ \sin(2\Psi) \pm j\cos(2\Psi) \end{pmatrix} E_0^{inc} \tag{2.26}$$

$$= B\begin{pmatrix} \cos(2\Psi) \pm j\sin(2\Psi) \\ \mp j(\cos(2\Psi) \pm j\sin(2\Psi)) \end{pmatrix} E_0^{inc} \tag{2.27}$$

$$= B\begin{pmatrix} e^{\pm j2\Psi} \\ \mp j e^{\pm j2\Psi} \end{pmatrix} E_0^{inc} \tag{2.28}$$

$$\begin{pmatrix} E_x^{ref} \\ E_y^{ref} \end{pmatrix}_B = Be^{\pm j2\Psi} \begin{pmatrix} 1 \\ \mp j \end{pmatrix} E_0^{inc} \tag{2.29}$$

The reflected field in Equation (2.29) is co-polarized with the incident wave. Note the y-component is reversed as the x-component is the same and the direction of propagation is reversed upon reflection. It is easily seen that a phase multiplication is present while the vector is scaled by B. This is a reflected co-polarized wave whose phase is in advance or delayed - depending on the circular polarization sense- twice the physical rotation angle of the reflective element.

- For the partial solution of $\begin{pmatrix} s'_{11} & s'_{12} \\ s'_{21} & s'_{22} \end{pmatrix}_C = \begin{pmatrix} 0 & -jC \\ -jC & 0 \end{pmatrix}$, the Equation (2.11) turns into:

$$\begin{pmatrix} E_x^{ref} \\ E_y^{ref} \end{pmatrix}_C = \begin{pmatrix} [0\cdot\cos^2(\Psi) + 0\cdot\sin^2(\Psi) & [(0-0)\sin(\Psi)\cos(\Psi) \\ -2\cdot(-jC)\cdot\sin(\Psi)\cos(\Psi)] & +(-jC)\cdot(\cos^2(\Psi) - \sin^2(\Psi))] \\ [(0-0)\sin(\Psi)\cos(\Psi) & [0\cdot\sin^2(\Psi) + 0\cdot\cos^2(\Psi) \\ +(-jC)\cdot(\cos^2(\Psi) - \sin^2(\Psi))] & +2\cdot(-jC)\cdot\sin(\Psi)\cos(\Psi)] \end{pmatrix} \begin{pmatrix} E_x^{inc} \\ E_y^{inc} \end{pmatrix} \tag{2.30}$$

$$= \begin{pmatrix} j2C\sin(\Psi)\cos(\Psi) & -jC(\cos^2(\Psi) - \sin^2(\Psi)) \\ -jC(\cos^2(\Psi) - \sin^2(\Psi)) & -j2C\sin(\Psi)\cos(\Psi) \end{pmatrix} \begin{pmatrix} E_x^{inc} \\ E_y^{inc} \end{pmatrix} \tag{2.31}$$

$$= -jC\begin{pmatrix} -\sin(2\Psi) & \cos(2\Psi) \\ \cos(2\Psi) & \sin(2\Psi) \end{pmatrix} \begin{pmatrix} E_x^{inc} \\ E_y^{inc} \end{pmatrix} \tag{2.32}$$

After taking into account the incident field expressed as in Equation (2.17):

$$\begin{pmatrix} E_x^{ref} \\ E_y^{ref} \end{pmatrix}_C = -jC \begin{pmatrix} -\sin(2\Psi) & \cos(2\Psi) \\ \cos(2\Psi) & \sin(2\Psi) \end{pmatrix} \begin{pmatrix} 1 \\ \pm j \end{pmatrix} E_0^{inc} \tag{2.33}$$

$$= C \begin{pmatrix} -\sin(2\Psi) & \cos(2\Psi) \\ \cos(2\Psi) & \sin(2\Psi) \end{pmatrix} \begin{pmatrix} -j \\ \pm 1 \end{pmatrix} E_0^{inc} \tag{2.34}$$

$$= C \begin{pmatrix} j\sin(2\Psi) \pm \cos(2\Psi) \\ -j\cos(2\Psi) \pm \sin(2\Psi) \end{pmatrix} E_0^{inc} \tag{2.35}$$

$$= C \begin{pmatrix} \pm(\cos(2\Psi) \pm j\sin(2\Psi)) \\ -j(\cos(2\Psi) \pm j\sin(2\Psi)) \end{pmatrix} E_0^{inc} \tag{2.36}$$

$$= C \begin{pmatrix} \pm e^{\pm j2\Psi} \\ -je^{\pm j2\Psi} \end{pmatrix} E_0^{inc} \tag{2.37}$$

$$= \pm C \begin{pmatrix} e^{\pm j2\Psi} \\ \mp je^{\pm j2\Psi} \end{pmatrix} E_0^{inc} \tag{2.38}$$

$$\begin{pmatrix} E_x^{ref} \\ E_y^{ref} \end{pmatrix}_C = \pm Ce^{\pm j2\Psi} \begin{pmatrix} 1 \\ \mp j \end{pmatrix} E_0^{inc} \tag{2.39}$$

The reflected field in Equation (2.39) is co-polarized with the incident wave. Note the y-component is reversed as the x-component is the same and the direction of propagation is reversed upon reflection. It is easily seen that a phase multiplication is present while the vector is scaled by C. This is also a reflected co-polarized wave whose phase is in advance or delayed -depending on the circular polarization sense- twice the physical rotation angle of the reflective element.

Then the total resultant reflected field expression for the reflective element having the reflection matrix [S'] with a ψ° angular offset is upon incident field mentioned in (2.17) can be found as:

$$\begin{pmatrix} E_x^{ref} \\ E_y^{ref} \end{pmatrix} = \begin{pmatrix} E_x^{ref} \\ E_y^{ref} \end{pmatrix}_A + \begin{pmatrix} E_x^{ref} \\ E_y^{ref} \end{pmatrix}_B + \begin{pmatrix} E_x^{ref} \\ E_y^{ref} \end{pmatrix}_C \tag{2.40}$$

$$\begin{pmatrix} E_x^{ref} \\ E_y^{ref} \end{pmatrix} = (B \pm C) e^{\pm j2\Psi} \begin{pmatrix} 1 \\ \mp j \end{pmatrix} E_0^{inc} + A \begin{pmatrix} 1 \\ \pm j \end{pmatrix} E_0^{inc} \tag{2.41}$$

Finally the phasor expressions of the incident and reflected fields in terms of the entries of [S'] and physical rotation angle ψ° are stated as follows:

$$E^{inc} = E_0^{inc} (\hat{a}_x \pm j\hat{a}_y) e^{jz} \tag{2.42}$$

$$\begin{aligned} E^{ref} = & \\ & E_0^{inc} [\frac{1}{2}(s'_{11} - s'_{22}) \pm j s'_{12}] (\hat{a}_x \mp j\hat{a}_y) e^{\pm j2\Psi} e^{-jz} \\ & + E_0^{inc} [\frac{1}{2}(s'_{11} + s'_{22})] (\hat{a}_x \pm j\hat{a}_y) e^{-jz} \end{aligned} \tag{2.43}$$

The interpretation of the reflected field expression is the key points of the reflective element design:

- Since the initial state, i.e. the matrix [S'] may be arbitrarily chosen; the simulation results for any angular position of the reflective element can provide the reflection levels of co- and cross-polarized reflected field levels. Referring to Equations (2.11) and (2.43) :

$$\Gamma_{co-pol.} = \frac{1}{2}(s'_{11} - s'_{22}) \pm j s'_{12} \tag{2.44}$$

$$\left| \frac{1}{2}(s'_{11} - s'_{22}) \pm j s'_{12} \right| = \left| \frac{1}{2}(s_{11} - s_{22}) \pm j s_{12} \right| \tag{2.45}$$

$$\Gamma_{cross-pol.} = \frac{1}{2}(s'_{11} + s'_{22}) \tag{2.46}$$

$$\frac{1}{2}(s'_{11} + s'_{22}) = \frac{1}{2}(s_{11} + s_{22}) \tag{2.47}$$

The magnitude of the reflected co-polarization level is constant with ψ -as expected the phase is not-, while the reflection magnitude and phase of the cross-

polarized component are constant, i.e. $\Gamma_{cross-pol.}$ is constant.

- The linear dependence of the phase of the reflected co-polarized wave on the rotation angle is independent of the reflection level.

- The sign of phase contribution by the rotational phase control principle depends on the sense of circular polarization.

- When the incident field is not a perfect circularly polarized wave (Regarding (2.48), $N \neq 0$), i.e. includes a cross-polarized wave; the element will not be capable of totally controlling the phase of the reflected co-polarized wave (Equation (2.49)).

  Moreover if the reflected field is required to be a perfect circularly polarized wave whose phase can be controlled by rotation, the cross-polarization should be suppressed by the reflective element ($\Gamma_{cross-pol.} = 0$) along with a perfect circularly polarized incident wave (N=0).

$$E^{inc} = M(\hat{a}_x + j\hat{a}_y)e^{jz} + N(\hat{a}_x - j\hat{a}_y)e^{jz} \tag{2.48}$$

$$\begin{aligned} E^{ref} = & \\ & [\Gamma_{co-pol.}Me^{+j2\Psi} + \Gamma_{cross-pol.}N](\hat{a}_x - j\hat{a}_y)e^{-jz} \\ & +[\Gamma_{co-pol.}Ne^{-j2\Psi} + \Gamma_{cross-pol.}M](\hat{a}_x + j\hat{a}_y)e^{-jz} \end{aligned} \tag{2.49}$$

2.4 Conclusion

Explanation of rotational phase control principle has been the main concern of this chapter. An in-depth aspect is acquired through the mathematical basis. The conditions to guarantee successful implementation of the principle are examined and well derived. It is evident that the most important factor is to provide an almost perfect circularly polarized incident wave. Also to increase the gain the reflective

element should well suppress the cross-polarized reflected component. Under these conditions the normally incident wave can be reflected as a totally phase-controllable co-polarized wave. As the incidence angle varies from normal, the characteristics are due investigations and these are strongly prone to the element type.

To utilize this principle in the reflectarray design, extensive comprehension of the principle should be figured out. In the beginning of the derivation, the coordinate systems are relatively rotated. This means that the whole plane is rotated actually, not the element. In reflectarray implementation, all the elements can independently rotate on the plane locally, that is, the principle is applied locally to each element. The assumption is that the unit cell of the reflectarray antenna exhibits the similar behavior over its own course, which is the each individual cell can control the phase by rotation independently.

CHAPTER 3

DESIGN OF SINGLE BAND REFLECTARRAY ELEMENT

3.1 Introduction

In this chapter, the element design of a reflectarray is explained. There are various methods used for the design such as designing the reflectarray elements as a unit cell in a periodic environment, or an element-based design using phase-shifters. The preference of these methods depends on the phase control principle employed as well as the design tools at hand. In this chapter, the reflectarray element designed as a unit cell of a periodic structure is studied, the necessary simulation tools, parametrical analysis of the reflective element and the phase design curves achieved by a single frequency split-ring reflectarray element are demonstrated.

The mathematical derivations for canonical structures and application of a theoretical principle to realizable structure to obtain an initial design should always be verified. The design procedure necessarily includes cycles of tests and re-designs. Even if there are available strong mathematical tools; each proposed structure cannot have analytical models, and these analytical models do not lack the requirement of tests. To quicken this design and verification cycle, fast and accurate simulation tools are of great importance.

Upon developing various efficient numerical methods and the capacitance of today's computers; full wave electromagnetic simulation software package programs are in

common use and provide a reliable design environment for the antenna engineers. These package software utilize various numerical methods to solve the integro-differential equations governing the electromagnetic phenomena. Among various numerical methods followings are the most used ones: method of moments (MoM), finite difference-time domain method (FDTD), and finite element method (FEM), fast multipole method (FMM). These methods are compared in [36]. Moreover, commercial software based on these numerical methods are also capable of implementation of various analytical techniques integrated with the numerical methods such as various boundary conditions, periodic arrays.

3.2 Characterization of a Reflectarray Element

The expectations from a reflect array element depend on mainly the system requirements aimed at the beginning of the study. The most general condition is a linear phase curve capable of minimum 360° phase range. Another one is the reflection levels of co- and cross-polarization as well as loss contributed by the unit cell upon reflection. The array theory implies that the beam steering properties of an array is sensitive to proper phasing than the magnitude, the magnitude distribution is effective on side-lobe levels and the beam-width. Thus it can be said that the aforementioned two quantities are to maintain the phase distribution and magnitude levels as desired. Also the frequency response of the reflectarray element is effective both on magnitude and phase. Moreover there may be additional requirements for the unit cell depending on the phase control mechanism. The Chapter 2 is on the requirements of reflectarray and the acquirements from the rotational phase shift principle. For example to use this principle with high gain the cross polarization should be suppressed in the operation frequency. That is why the frequency characteristics should also be set first. Then the rest will be to verify the rotational phase shift principle in a periodic planar array by rotating the element individually.

The reflectarray antennas intrinsically have the elements under illumination with different incident angles that span a solid angle. Figure 3.1 depicts the angle between the surface normal and the incident waves from the illumination horn. It is important

that the designer should consider the phase design curve and magnitude curve should also be examined for various incidence angles. The various incidence angles form the illumination solid angle span and the numerous element states constitute a great number of cases to simulate, and time needed for simulations can also rise drastically. That is why the simulations are also to be carried out for meaningfully sampled states from which the characteristics of the element can be well extracted.

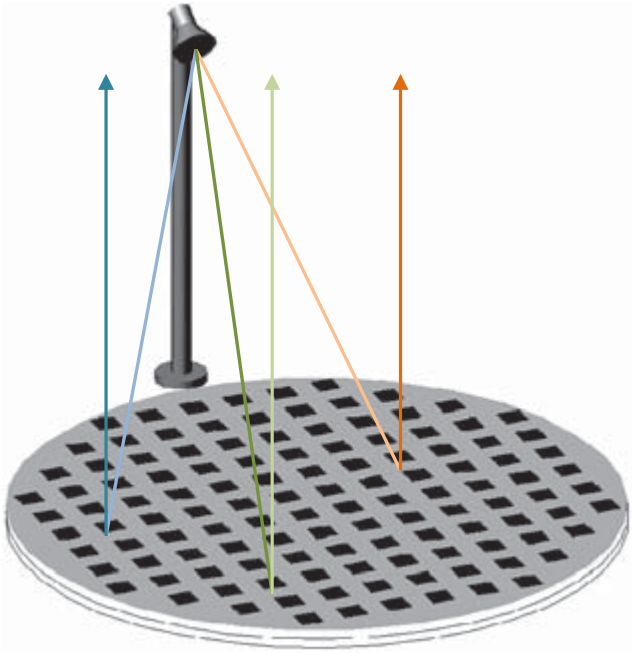

Figure 3.1 The illustration of incidence angle variation on the surface of the reflectarray antenna.

The elements of the reflectarray antenna lie on a surface surrounded by numerous similar elements. The element design procedure should integrate the coupling effects of the surrounding numerous elements. It is obvious that in fact most elements of a reflectarray are surrounded by slightly modified structures to maintain the phase distribution. The reflectarray element is thus designed and characterized in an

infinite planar array while designing in a simulation environment. The unit cell of the infinite array is simulated as a part of an infinite planar array composing of identical elements, as shown in Figure 3.2. The assumption of periodicity is widely accepted in reflectarray element design, although the results are not strictly valid for the elements placed close to the boundary of the array. This is the inevitable result of use of the software environments and the requirement of fast computation, since the cost of computational requirements for characterizing a finite array -if possible- is very high. The infinite array assumption enables the designer to use periodic boundary conditions in FEM, which in turn reduce the computational time.

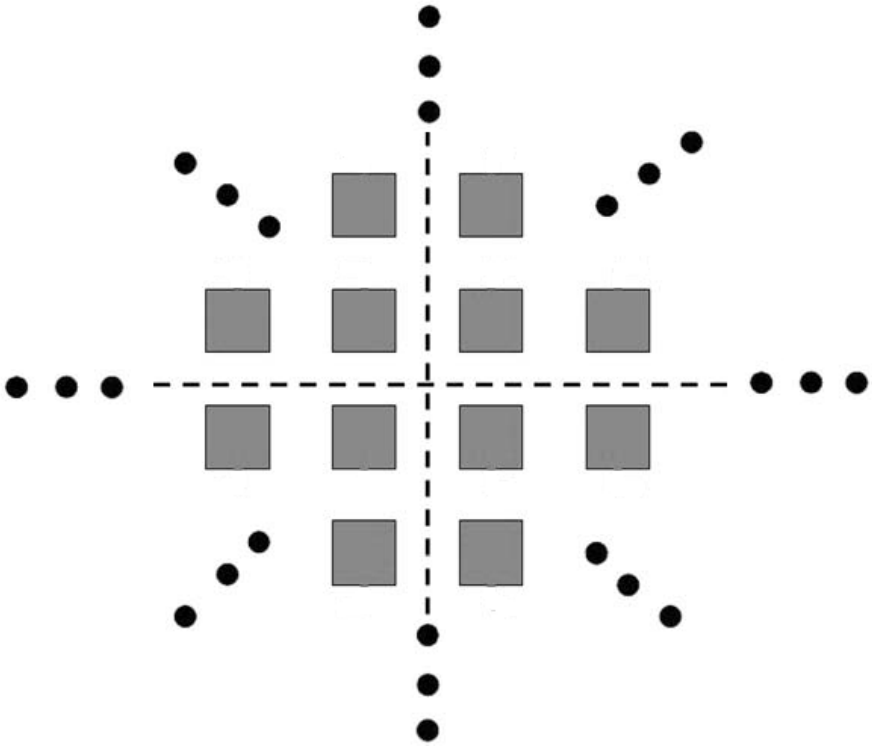

Figure 3.2 Infinite planar array.

To sum up the simulation requirements, the software should handle the following:

- ✓ Simulation of infinite periodic arrays.
- ✓ Ease of use to deduce the incident and reflected field characteristics.
- ✓ The incident wave can be applied at angles other than normal.

3.3 Simulation Environment

HFSS is a commercial full wave electromagnetic field solver. It is implemented based on the finite element method. HFSS solver provides the solutions of E- and H-fields, currents, S-parameters, near and far fields. The 3D structures are meshed automatically, and meshes are refined adaptively. This software is chosen for it includes the tools implemented for simulation of periodic structures, the Floquet port to easily calculate the reflection characteristics for the unit cell. The important parameters for simulations to be reliable are the implemented boundary conditions to the FEM and the meshing quality. First of all meshing is very important; it is no surprise that as the number of meshes increase the simulation results will converge to reality. This has a high cost of memory space and computational capacity of a computer. In this manner the implemented meshing algorithm of HFSS applies an adaptive meshing to increase the mesh number. However, the designer is also able to determine the meshing of any arbitrary element on the design.

HFSS can simulate unit cells and allow various types of periodic structures. This tool can be used to analyze planar or linear infinite arrays. The fields on the periodic boundaries are forced to have the same magnitude and direction with different phases depending on the required incidence angle and/or progressive phasing. The implementation of the periodic array is done by imposing periodic boundary conditions on the couples of surfaces named master and slave attributions. The master and slave boundaries are aligned using vector $\vec{v}$ and $\vec{u}$ in Figure 3.3. The unit cell simulation of a reflectarray cell is carried out by imposing the boundary condition in both dimensions to realize the planar infinite array conditions of the simulation. The implementation of these software tools are shown, because they also make it easier to comprehend the unit cell approach.

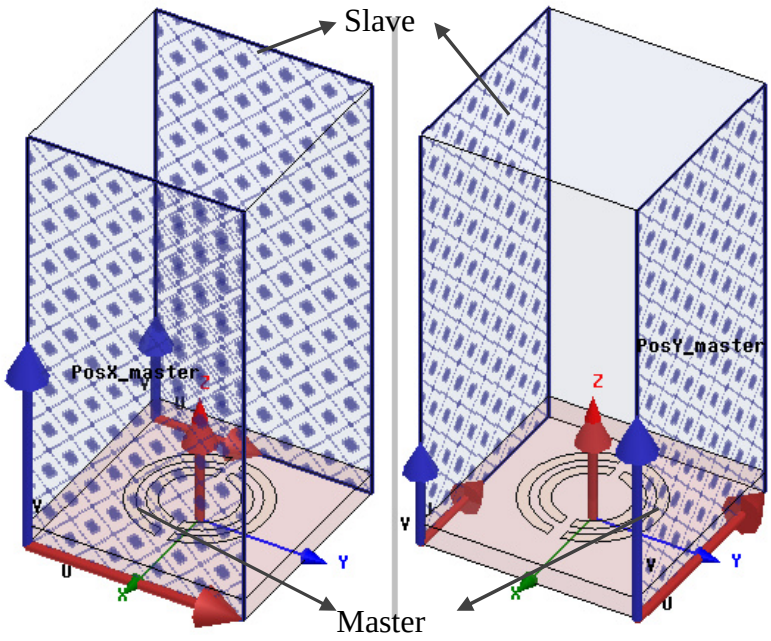

Figure 3.3 Implementation of the master and slave boundaries for periodicity

.

After imposing the periodicity, it is necessary the set-up of the simulation accordingly with proper excitation. Simulations of the unit cell require an incident and reflected plane wave relation. The most suitable tool for this purpose is the Floquet port available in HFSS. The Floquet port implements the Floquet mode spectrum. Floquet mode spectrum expansion is the Fourier domain expansion of the periodic solutions to a wave equation. That is the reason why the Floquet modes can be applied to planar periodic infinite arrays. This approach is valuable since the infinite array assumption is also advantageous in computational costs enabling the use of the Floquet expansion method. The Floquet modes needed to represent the plane wave incidence are automatically calculated by the calculator implemented in HFSS. The number of modes and the propagation and attenuation constants depend on the periodicity in two dimensions and the incidence angle of the wave. When the periodicity of the array is around half a wavelength there is one propagating Floquet mode that can be decomposed as two orthogonal components, and these are sufficient to characterize the plane wave incidence. These modes are named according to the grid system defined by the user and applied at the Floquet port

which are shown in Figure 3.4 as **a** and **b**. For the square unit cell structures like the one investigated in this thesis, the assignment is applied to coincide the **a** vector with x-axis, and **b** vector with y-axis, so that these correspond to the waves propagating in the same direction but having E-fields orthogonal to each other.

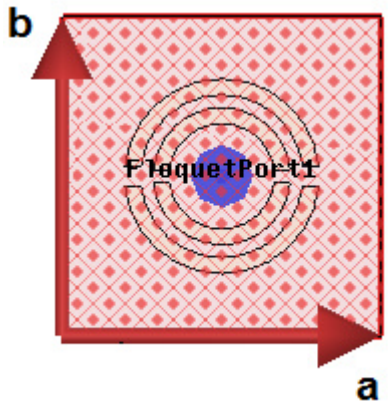

Figure 3.4 Imposing the Floquet port grid guide lines.

The results are easily de-embedded, that is the reference plane of the solutions is transferred to the surface of the reflective element as needed. The screen capture of the 3D modeler of HFSS is shown in Figure 3.5, the de-embedding vector points to the point on the reference plane.

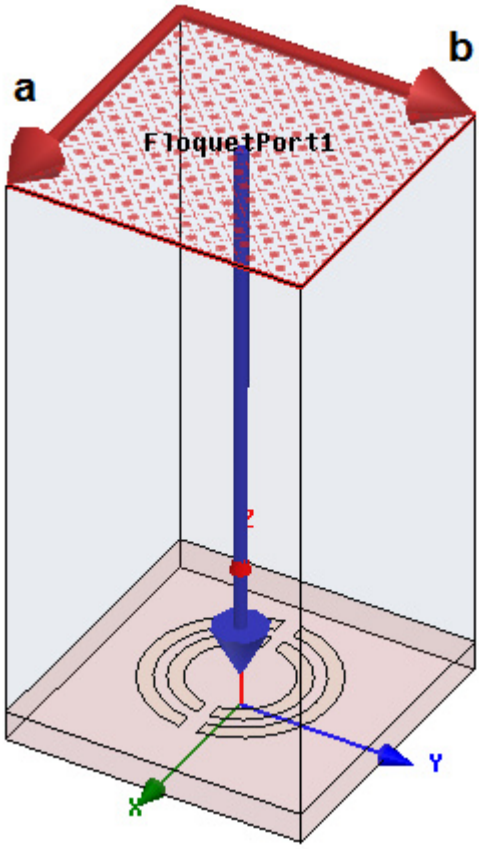

Figure 3.5 De-embedding vector shown, the result is referred to the end point of the blue de-embedding vector.

The simulation results of a Floquet port simulation of a unit cell in infinite planar array yields a 2-port network S-matrix, where the 1st and 2nd ports are aligned with the x- and y-axes respectively. By this means, as indicated in the Chapter 2, the unit cell can be characterized. Then this two-port network can be illustrated as in Figure 3.6.

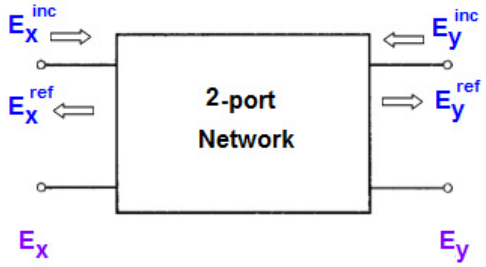

Figure 3.6 2-port representation of the Floquet port.

Recalling the incident and reflected field relation expression which was used in Chapter 2:

$$\begin{pmatrix} E_x^{ref} \\ E_y^{ref} \end{pmatrix} = [S] \begin{pmatrix} E_x^{inc} \\ E_y^{inc} \end{pmatrix} = \begin{pmatrix} s_{11} & s_{12} \\ s_{21} & s_{22} \end{pmatrix} \begin{pmatrix} E_x^{inc} \\ E_y^{inc} \end{pmatrix} \tag{3.1}$$

The simulation result of the Floquet port with two orthogonal modes is the [S] matrix in Equation (3.1). When the incident field is assumed to be the perfect circularly polarized wave:

$$\begin{pmatrix} E_x^{inc} \\ E_y^{inc} \end{pmatrix} = \begin{pmatrix} 1 \\ \pm j \end{pmatrix} E_0^{inc} \tag{3.2}$$

The total reflected field is:

$$E^{ref} = \{(s_{11} \pm j s_{12})\hat{a}_x + (s_{21} \pm j s_{22})\hat{a}_y\} E_0^{inc} \tag{3.3}$$

The reflected co- and cross-polarized waves are:

$$E_{co-pol.}^{ref} = (\hat{a}_x \mp j\hat{a}_y) E_0^{ref,co} \tag{3.4}$$

$$E_{cross-pol.}^{ref} = (\hat{a}_x \pm j\hat{a}_y) E_0^{ref,cross} \tag{3.5}$$

$$E^{ref} = E_{co-pol.}^{ref} + E_{cross-pol.}^{ref} \tag{3.6}$$

Then to find the reflected co- and cross-polarization coefficients, the solution of Equations (3.3) and (3.6) should be calculated.

$$\{(s_{11} \pm js_{12})\hat{a}_x + (s_{21} \pm js_{22})\hat{a}_y\}E_0^{inc} = (\hat{a}_x \mp j\hat{a}_y)E_0^{ref,co} + (\hat{a}_x \pm j\hat{a}_y)E_0^{ref,cross}$$
$$(s_{11} \pm js_{12})\hat{a}_x E_0^{inc} + (s_{21} \pm js_{22})\hat{a}_y E_0^{inc} = \hat{a}_x(E_0^{ref,co} + E_0^{ref,cross}) \mp j\hat{a}_y(E_0^{ref,co} - E_0^{ref,cross}) \quad (3.7)$$

Equalizing the x- and y-components independently:

$$(E_0^{ref,co} + E_0^{ref,cross}) = (s_{11} \pm js_{12})E_0^{inc} \quad (3.8)$$

$$(E_0^{ref,co} - E_0^{ref,cross}) = -(s_{22} \mp js_{21})E_0^{inc} \quad (3.9)$$

The reflection coefficients of the co- and cross-polarized waves upon incidence of a circularly polarized wave:

$$\Gamma_{co} = \frac{E_0^{ref,co}}{E_0^{inc}} = \frac{1}{2}[(s_{11} \pm js_{12}) - (s_{22} \mp js_{21})] = \frac{1}{2}[(s_{11} - s_{22}) \pm j(s_{12} + s_{21})] \quad (3.10)$$

$$\Gamma_{cross} = \frac{E_0^{ref,cross}}{E_0^{inc}} = \frac{1}{2}[(s_{11} \pm js_{12}) + (s_{22} \mp js_{21})] = \frac{1}{2}[(s_{11} + s_{22}) \pm j(s_{12} - s_{21})] \quad (3.11)$$

The Equations (3.10) and (3.11) are important because they constitute the basis to extract the characteristics of the unit cell upon circularly polarized incident wave. The co- and cross-polarized reflection levels are easily extracted from the simulation results via simple algebra.

In this section, the simulation configurations and the utilization of the simulation results is explained. The characterization of the split-ring structure as a phase control element in the unit cell of a reflectarray can be carried out using these methods in the following sections.

3.4 The Split-Ring as a Reflectarray Element

The split-ring element is advantageous for it is capable of reflecting an incident circularly polarized wave as a wave conserving the sense of polarization. Moreover its symmetrical form allows easy implementation of the rotation effect by integrating with RF MEMS switches. The split-ring does not have analytical formulas governing its operation bands. It is important to investigate the effects of parameters on the operation frequencies of a split-ring. Thus, the parametric analysis of the split-ring geometry and the unit cell have been performed and presented in the following sections.

3.4.1. Parametric Study

The unit-cell composing of a single split-ring on a ground backed substrate is studied parametrically to extract valuable information relating these parameters with the frequency and the bandwidth of co-pol. reflection. Then, it is shown that the split-ring can control the phase of the reflected co-pol. wave using the rotational phase shift principle. The response of unit cell is also studied for the oblique incidence cases. The parameters of the split-ring geometry that are changed in the parametric analysis are shown in Figure 3.7.

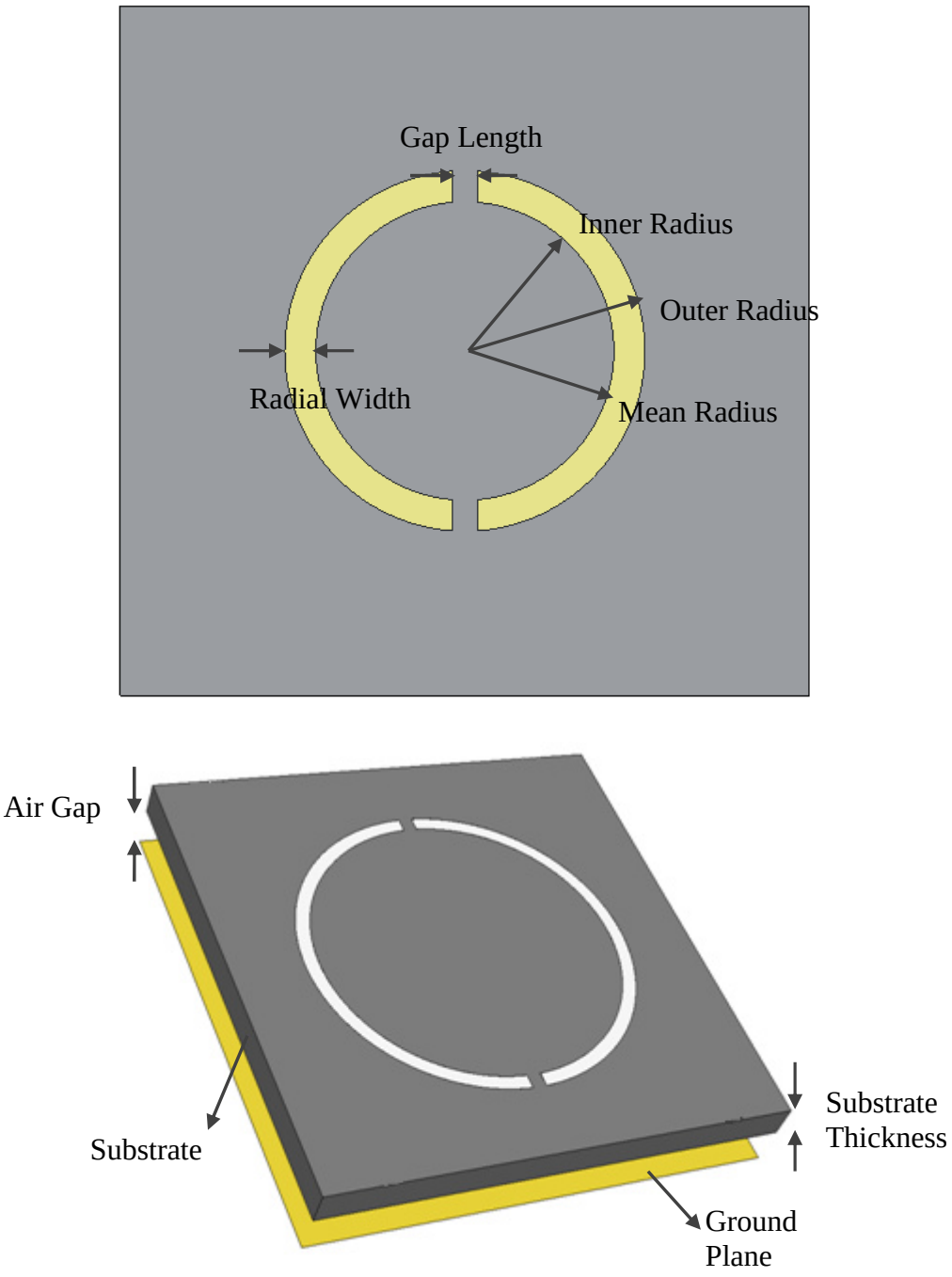

Figure 3.7 The parameters of the split-ring geometry.

Table 3.1 The unit cell and reflective element dimensions.

Initial Design Parameters Used as a Reference	
Inner Radius	0.98mm
Outer Radius	1.18mm
Radial Width	0.20mm
Gap Length	0.20mm
Substrate Thickness	0.50mm
Relative Substrate Permittivity	3.78 (Quartz)
Air Gap	0mm
Unit Cell Dimensions	5.55mm x 5.55mm (0.5λ @ 27 GHz)

In Table 3.1, all the parameter values are given. These values are a basis for the parametrical analysis. The following sections are including simulation results to obtain the effect of these parameters. The variations are carried out around the initial design values given in Table 3.1, this is an easing way of examining the effects. Note that in the initial design air gap thickness is 0mm, i.e. there is no air layer. Air gap thickness parameter is given, since it is used further in this section.

In the following sections this design is examined in terms of frequency response of the cross-pol. reflection coefficient. Recall that the aim was to suppress the cross-pol. reflected component, since the phase control principle employed is only applicable for the co-pol. reflected component. In this context, the operation frequency of a unit cell is defined as the frequency at which the cross-pol. reflection is at minimum. For example in Figure 3.8, the operation frequency is 27.15 GHz. Also the bandwidth is defined as the frequency interval including the operation frequency, in which the cross-pol. reflection coefficient is below -20dB. The bandwidth of the reference design of Table 3.1 as plotted in Figure 3.8 is 0.1 GHz between 27.1 GHz and 27.2 GHz. In the parametric study, these definitions constitute a basis in characterizing the unit cell.

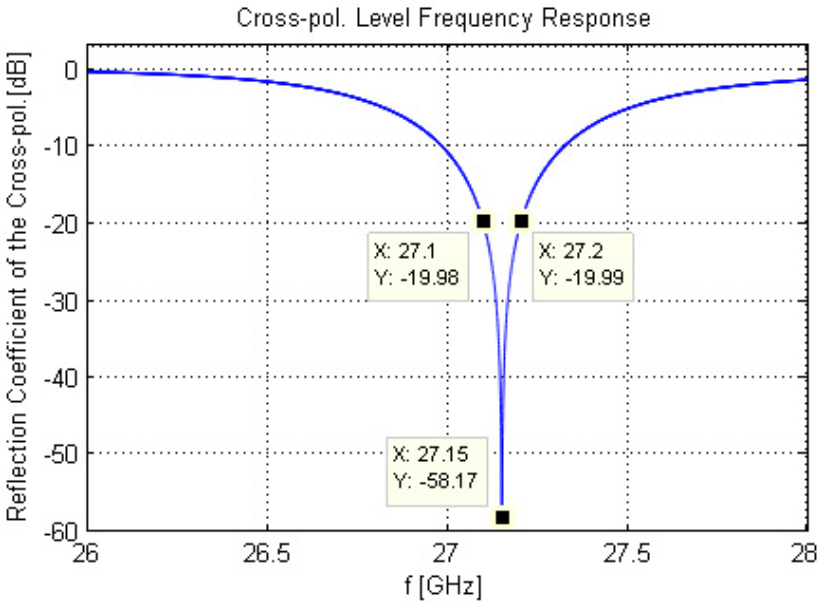

Figure 3.8 The frequency response of the reflection coefficient of the cross-pol.

3.4.1.1 Effect of the Mean Radius

The size of any microwave structure is surely governing its frequency response. Note that in the unit cell design, the size of the split-ring metallization cannot scale the

frequency response since the unit cell dimensions and the substrate height are kept constant. But the metallization is strictly related to the resonant characteristics due to the currents flowing on the split-ring. The simulations with the mean radius values listed in Table 3.2 show that the result is shown in Figure 3.9. As the mean radius increases, the operation frequency is shifted to lower frequencies. This is the expected result of the electrical length relationship. The bandwidth of co-polarized reflection is not affected obviously.

Table 3.2 Mean radius values used in parametrical sweep.

Swept Parameter	
Arithmetic Mean of The Radii	1.075mm 1.080mm 1.085mm 1.090mm 1.095mm 1.100mm
Other parameters set constant	

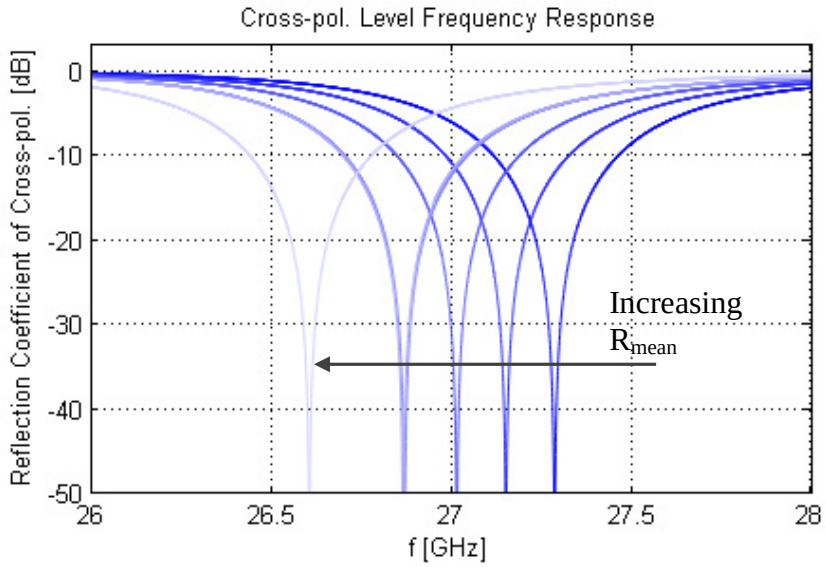

Figure 3.9 Cross-pol. Reflection Coefficient vs. Frequency for varying mean radius.

3.4.1.2 Effect of the Radial Width

The inner and outer radii of the split-ring are subject to testing. The frequency response may not be related to the radii with a mathematical dependence. To investigate the effect of width variance to the frequency response at least the constant parameters should be declared. There should be some initial point such as keeping the arithmetic mean or geometric mean of the inner and outer radii constant. Lacking the analytical expression for the frequency response, any of these assumptions are arbitrary. The results are the comparisons of the constant arithmetic mean radius. In Table 3.3, one can find the radial width values used in parametric sweep. The effect is obviously ineffective on the bandwidth; however the operation frequency is shifted to lower bands, as shown in Figure 3.10. The interpretation is that, the outer radius is more effective in defining the operation frequency.

Table 3.3 Radial width values used in parametrical sweep.

Swept Parameter	
Radial Width	0.180mm 0.190mm 0.200mm 0.210mm 0.220mm
Other parameters set constant *(Arithmetic mean of the radii is kept constant)*	

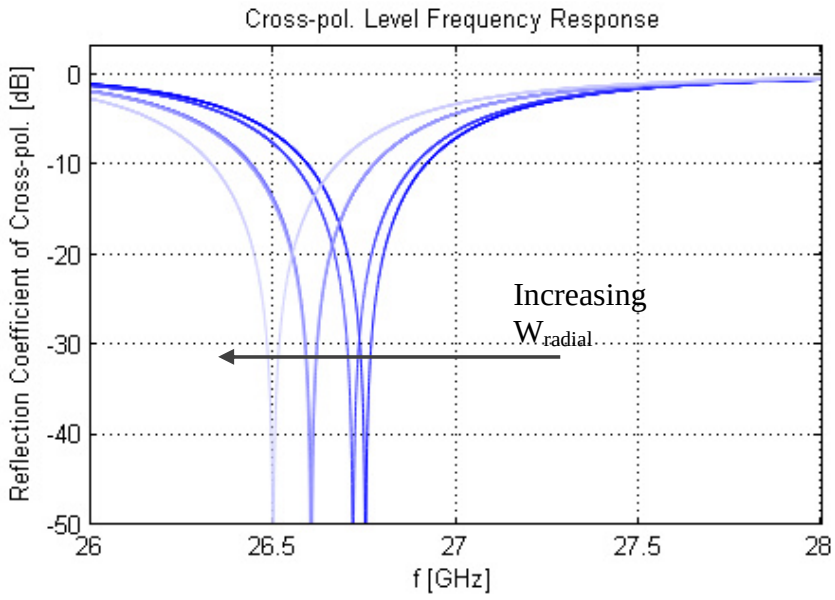

Figure 3.10 Cross-pol. Reflection Coefficient vs. Frequency for varying radial width.

3.4.1.3 Effect of the Gap Length

For the gap length values shown in Table 3.4, the results are illustrated in Figure 3.11. As the gap length is increased; the operation frequency shift to higher frequencies. However, no clear effect on the bandwidth is observed. It should be noted that the gap modifications were carried out in small dimensions that the ring geometry is preserved. This modification shows that the capacitive interaction through the gap is also a very important parameter in determining the operation frequency. The switches are to be implemented on the gaps for the further integration steps. This is an early estimation of the RF MEMS switches' effects on the gap.

Table 3.4 Gap length values used in parametrical sweep.

Swept Parameter	
Gap Length	0.200mm 0.250mm 0.300mm
Other parameters set constant	

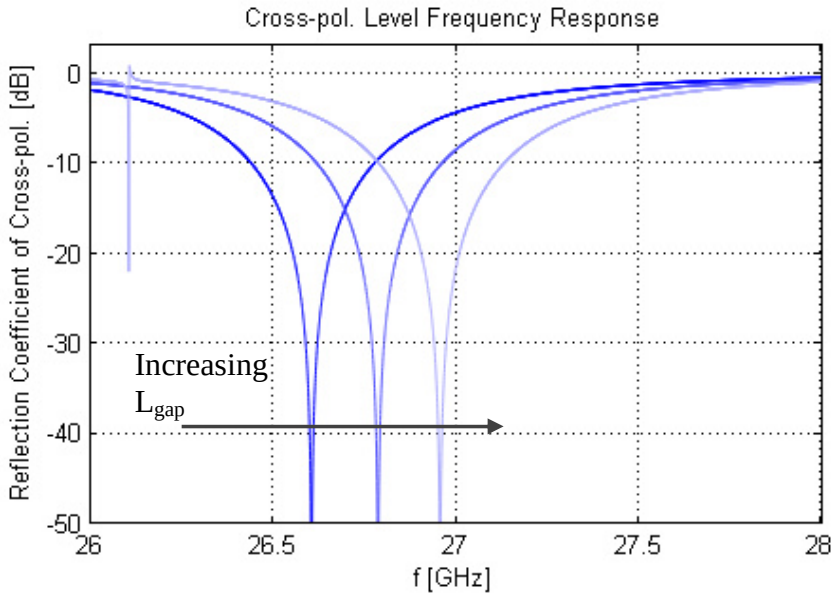

Figure 3.11 Cross-pol. Reflection Coefficient vs. Frequency for varying gap length.

3.4.1.4 Effect of the Unit Cell Dimension

The proposition that the unit cell dimension should affect the frequency response is logical; because the coupling of the elements depends on their separation from each other. In this section the following simulations demonstrates this phenomenon. Table 3.5 shows the unit cell dimensions for which the simulations have been performed, and the corresponding results are given in Figure 3.12. It is evident that the unit cell dimension affects the operation frequency. However, no rule that defines the relation between frequency and unit cell size can be obtained from these simulations. Thus, the unit cell dimension should be optimized with thorough trials.

Table 3.5 Unit cell dimensions used in parametrical sweep.

Swept Parameter	
Unit Cell Dimensions	0.40λ 0.50λ 0.55λ @27 GHz
Other parameters set constant	

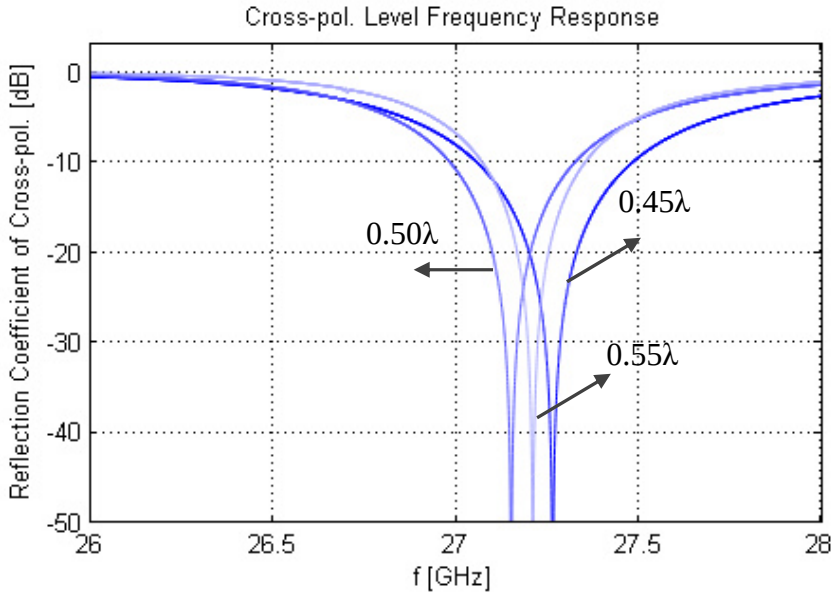

Figure 3.12 Cross-pol. Reflection Coefficient vs. Frequency for varying unit cell dimension.

3.4.1.5 Effect of the Substrate Thickness and Permittivity

Although the substrate selection is mainly dependent on the fabrication process, technology and material availability; it is valuable information to know the effect

osubstrate permittivity and thickness.

Table 3.6 Substrate thickness values used in parametrical sweep.

Swept Parameter	
Substrate Thickness	0.450mm 0.500mm 0.550mm
Other parameters set constant	

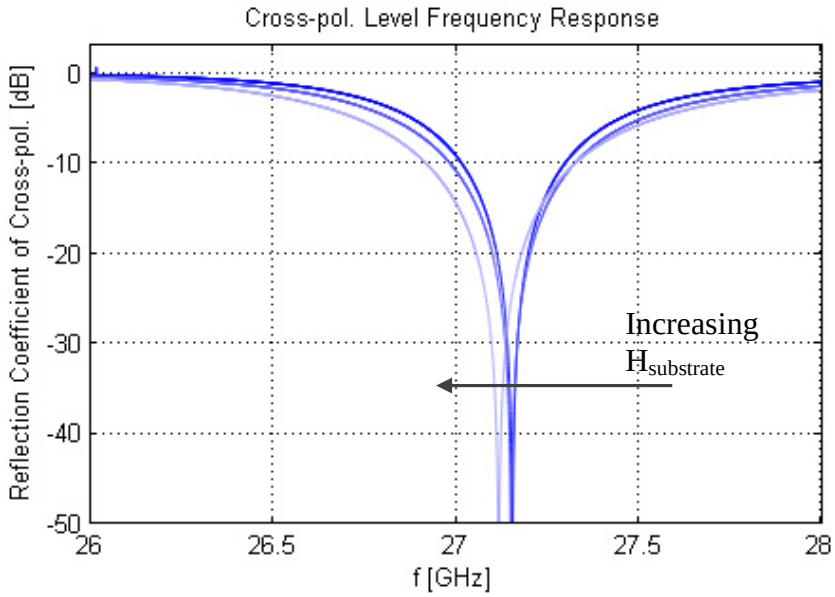

Figure 3.13 Cross-pol. Reflection Coefficient vs. Frequency for varying substrate thickness value.

In Table 3.6, the thickness values of the substrate used in the simulations presented

in Figure 3.13 are listed. It is observed that, the substrate thickness has a slight effect on the bandwidth of the suppression of cross polarized component. The operation frequency is slightly shifted and the bandwidth is slightly increased with the increasing substrate height

Table 3.7 Relative permittivity of substrate values used in parametrical sweep.

Swept Parameter	
Relative Permittivity of the Substrate	3.68 3.78 3.88
Other parameters set constant	

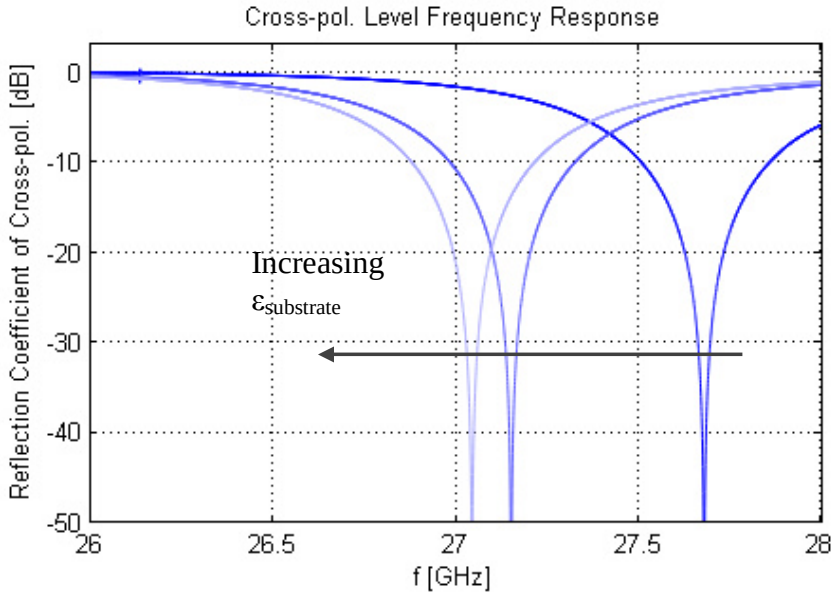

Figure 3.14 Cross-pol. Reflection Coefficient vs. Frequency for varying relative permittivity of the substrate.

The substrate material properties are certainly effective. Therefore permittivity values of the substrate are slightly varied to see the outcome. For the relative permittivity values stated in Table 3.7, the results given in Figure 3.14 show that the operation frequency is highly dependent on the permittivity. The bandwidth is not seriously changed, while the operation frequency is shifted to lower frequencies with increasing substrate permittivity as plotted in Figure 3.14.

The substrate thicknesses of the available materials are standardized, i.e. an arbitrary thickness for custom design is not always available and may cost more time and money. However the positive effect of the substrate thickness in increasing the bandwidth of cross-pol. suppression has to be utilized. On the other hand, it should be also taken into account that the permittivity affects the operation frequency. In Figure 3.14, it is seen that decreasing substrate permittivity is more effective than increasing it. Then it can be understood that adding an intermediate air layer between the ground plane and the bottom of the substrate can be used to increase the bandwidth. Since air has the lowest relative permittivity, the frequency of the operation will be shifted dominantly by its contribution, which can be compensated by adjusting the split-ring dimensions properly and the freedom to modify the air gap height is an advantage.

In Table 3.8, the air gap values are listed. The simulation results with the aforementioned air gap height values are plotted in Figure 3.15. Not that the air gap thickness is indeed very small, but this is only to show the effect with respect to no air gap case. The comparison in Figure 3.15, shows that the bandwidth is increased with increasing air gap height; as well, the frequency is shifted. This is an easy way to adjust the bandwidth.

Table 3.8 Air gap height values used in parametrical sweep.

Swept Parameter	
Air Gap	0.000mm 0.010mm 0.020mm 0.030mm 0.040mm
Other parameters set constant	

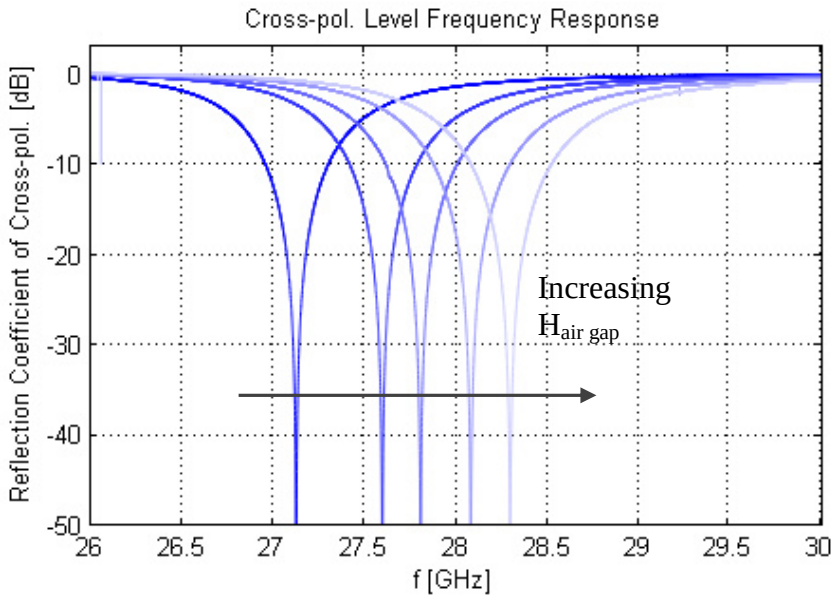

Figure 3.15 Cross-pol. Reflection Coefficient vs. Frequency for varying air gap height between ground plane and the bottom of the substrate.

.

3.4.2 The Reflectarray Unit Cell with Split-ring

The split-ring element is simulated and characterized with its frequency response in an infinite array. The parametric study presented in the previous section shows the important dimensions and how to tune the split-ring. In this section, the phase design curve is obtained by rotating the split ring.

To understand the application of the rotational phase shift principle in an array, it is logical that locally each element will be controlling phase independently over its own course. While using this characteristic in an array configuration, some of the conditions on the application of the phase control principle may be overridden. The most important statement was that only phase control of the reflected co-polarized wave is possible. Then the cross-pol. suppression should be guaranteed at the desired operation frequency for any state of the element.

Comparing the Figure 3.16 and Figure 3.17, these two arrays may have different frequency responses with regard to cross-pol. suppression. While determining the frequency interval in which the cross-pol. suppression is achieved; the approach should also include the comparison of the frequency responses of the infinite arrays for various cases that split-rings are rotated. None of the simulated unit cells can provide the exact frequency response for a reflectarray element, since this response is dependent on interaction with the neighboring elements.

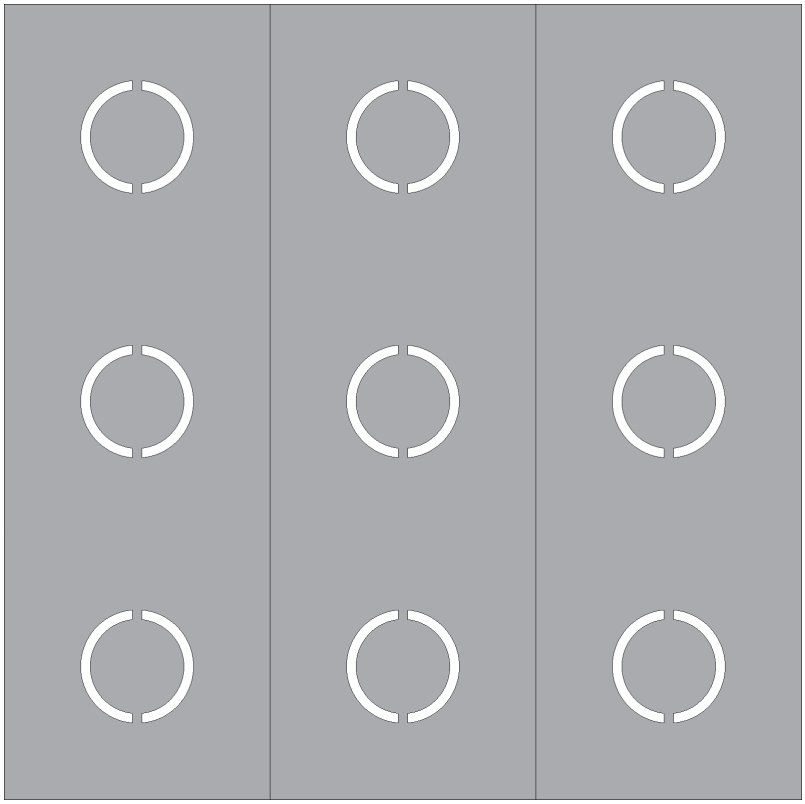

Figure 3.16 A part of an infinite array of unit cells with split-rings in initial state.

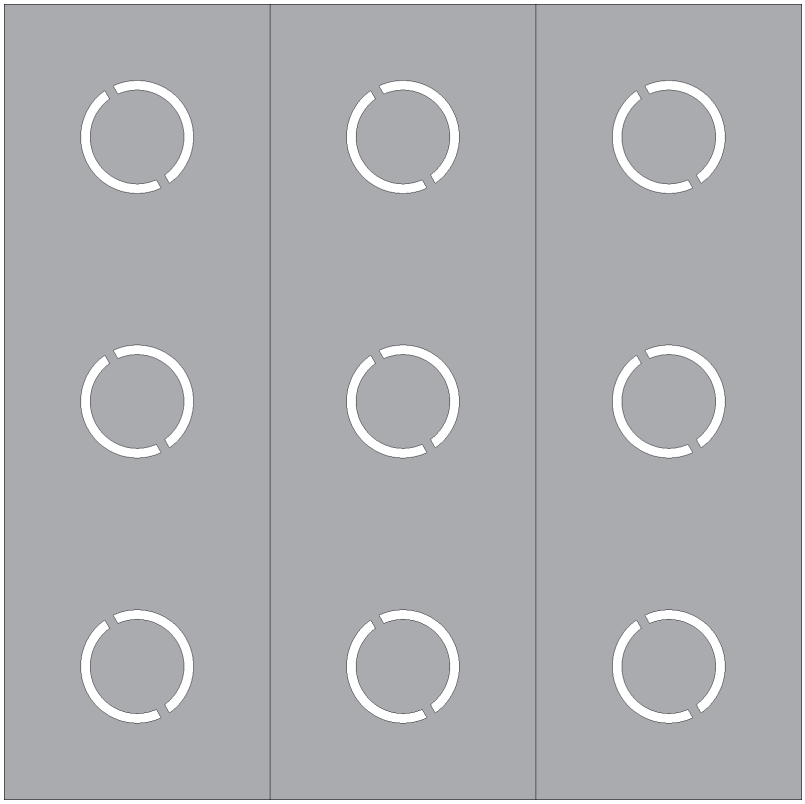

Figure 3.17 A part of an infinite array of unit cells with 30°-rotated split-rings relative to the initial state.

For the same reason, each element will have slight differences in the frequency responses. While utilizing the unit cell approach these simulated cases constitute the most regular form of the array. In actual utilization, the unit cells may have almost random states independently Figure 3.18. The approach should include the comparison of the frequency responses of unit cells with different rotations angles. Finally the operation frequency should be determined by comparing the frequency responses of unit cells in different states.

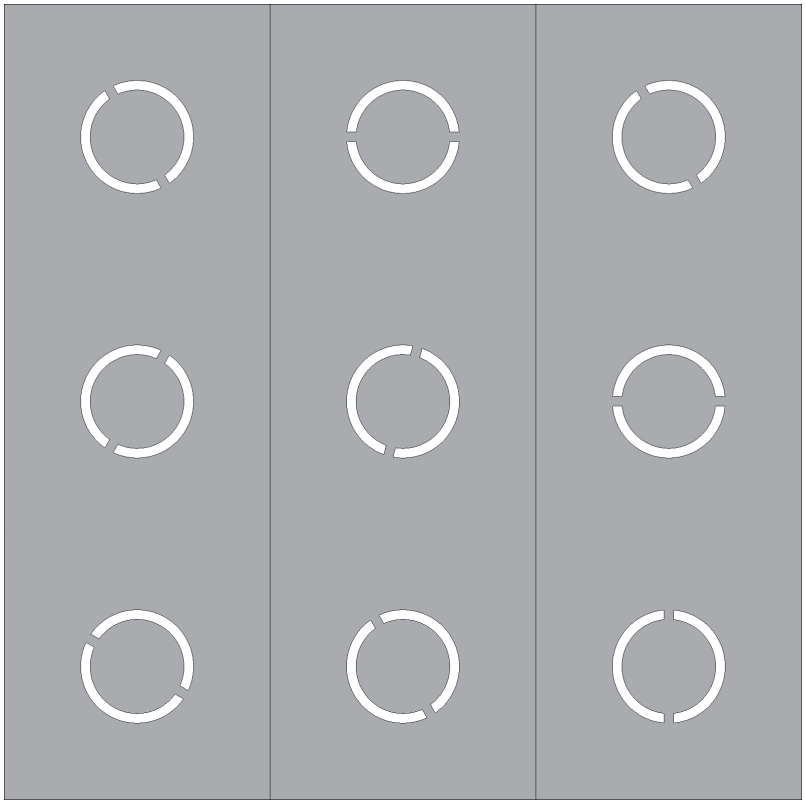

Figure 3.18 A part of an array of elements with random states.

Due to symmetry and the square shape of the unit cell, the angular states of the split-ring between 0° and 45° are enough to extract the necessary information. The result for angles 0°, 15°, 30°, 45° are shown for the reference design of the parametrical study.

As seen in Figure 3.19, as the rotation angle of the split-ring changes the frequency response is affected. This is apparently an unwanted situation, since the cross-pol. increases as the split-ring is rotated to control the phase. This is an important point the designer should avoid. The first thing to avoid this phenomenon is to increase the bandwidth of the element, so that the shifts in the frequency response due to rotation of the element would not result in higher cross-pol. levels. Given the bandwidth is optimized and kept intact; another parameter to prevent this phenomenon from happening is to change the unit cell size. For example in Figure 3.20, the same simulation results are shown for another unit cell size. As seen the minima of the

cross-pol. levels get closer to each other. For the previous case, the operation frequency for the best cross-pol. suppression constraint would be at 27.31 GHz / -11dB (Figure 3.19), for the second case it would be at 27.34 GHz / -20dB (Figure 3.20) which is a far better design. For the sake of better characteristics the dimensions of the unit cell would eventually be modified to 0.44mm.

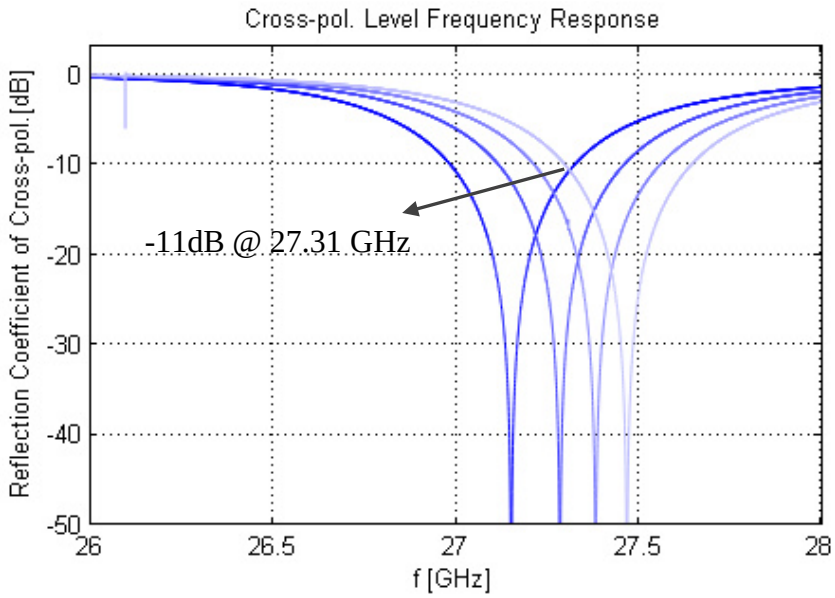

Figure 3.19 Frequency Response of the cross-pol. reflection, for various physical rotation angles of the split-ring. Unit cell dimension: 0.55mm.

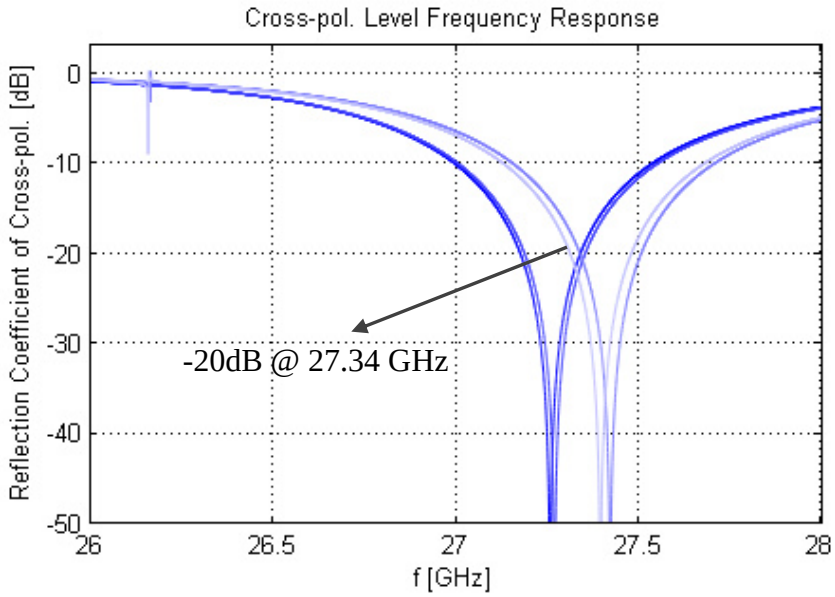

Figure 3.20 Frequency Response of the cross-pol. reflection, for various physical rotation angles of the split-ring. Unit cell dimension: 0.44mm.

The results of the simulations are given in the rest of this section to verify the application of the rotational phase shift principle with a single frequency split-ring element. The phase of the co-polarized wave plotted versus the physical rotation angle of split-ring is the phase design curve of this unit cell. Similarly the cross-pol. reflection coefficient by the rotation angle is demonstrated. Also these properties are investigated under oblique incidence.

In Figure 3.21, the phase of the reflected co-pol. component is plotted versus the rotation angle of the split-ring. The phase design curve has 360° coverage and almost a linear form. This is a simulated verification of the rotational phase shift principle applied to the split-ring reflectarray element via unit cell approach.

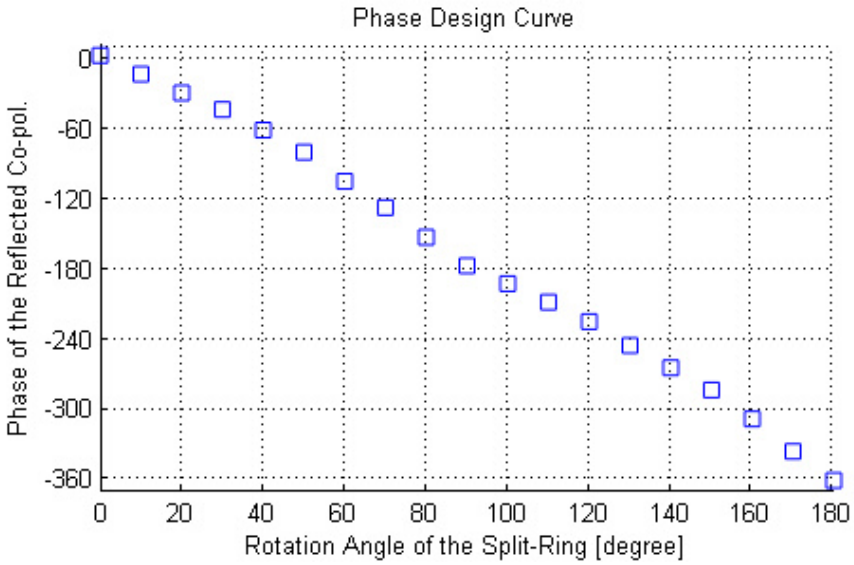

Figure 3.21 Phase design curve of the split-ring unit cell @ 27.34 GHz.

In Figure 3.22, magnitude of the reflection coefficient of e cross-pol. Component is plotted versus the rotation angle of the split-ring. The variation in the levels is due to the change in frequency response of reflection with varying rotation angle of the split-ring as previously mentioned. The suppression is preserved as low as -15dB, although the target was -20dB. This is because of the simulation technique employed during the frequency response simulations was interpolating sweep and phase-curve simulations was simulated with discrete sweeping. However this can also be tuned with further simulation trials with discrete sweeps. Since the aim was to prove the phase control technique, the tuning effort will be put forward in the final design of the dual band reflectarray element.

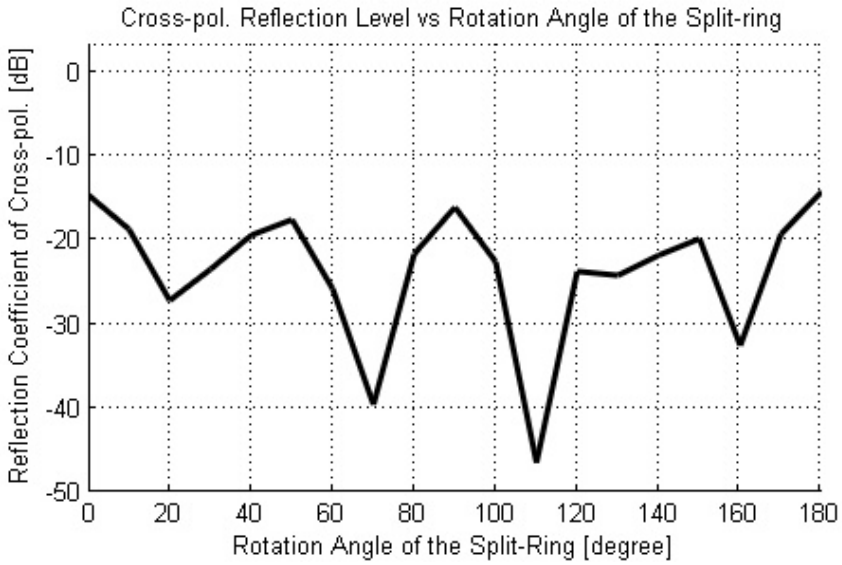

Figure 3.22 Magnitude curve of the split-ring unit cell @ 27.34 GHz.

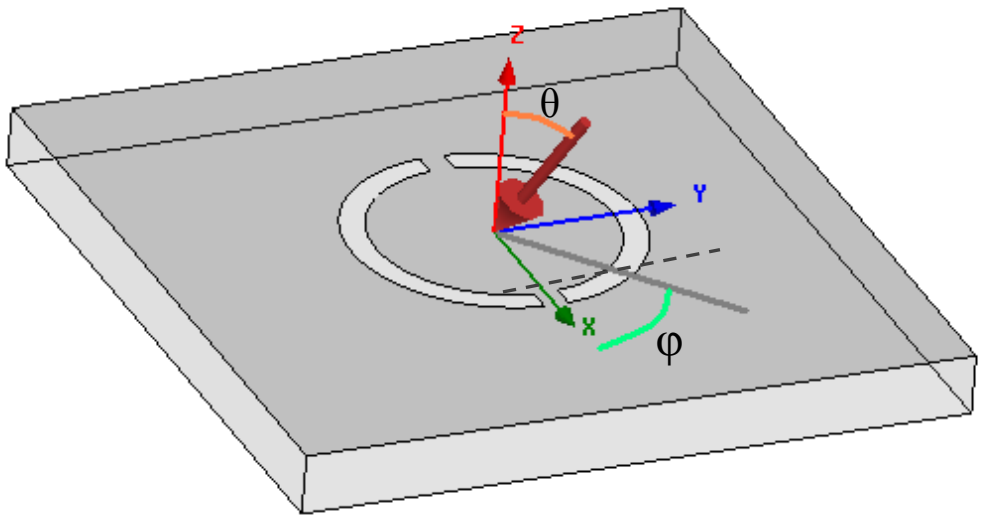

Figure 3.23 The oblique incidence angles with respect to spherical coordinates.

The oblique incidence cases to be simulated are quite narrow. Because of the symmetry of the unit cell, a simple case can be the set of φ=0° and θ={0°,10°,20°,30°,40°}. The simulations of oblique incidence are done and

compared.

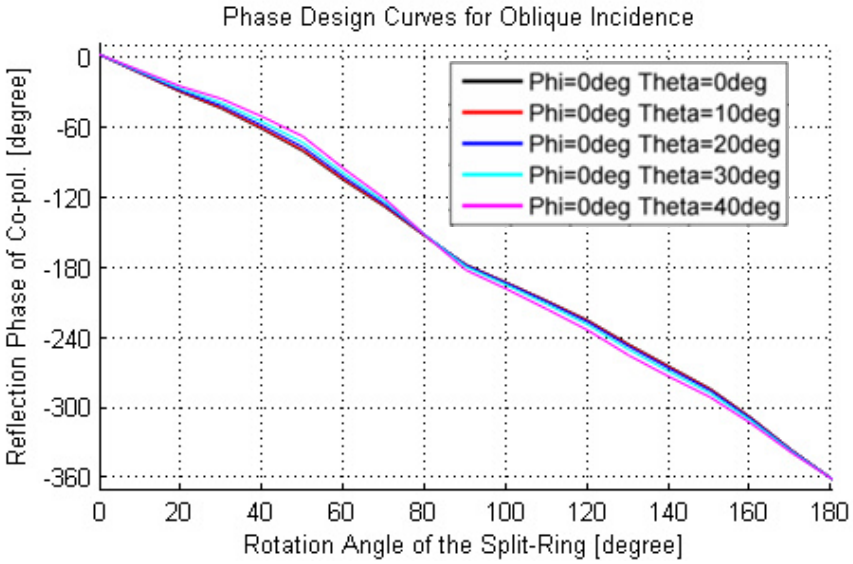

Figure 3.24 Phase design curve of the split-ring unit cell @ 27.34 GHz for various oblique incidence angles.

Figure 3.24 shows the phase design curves of the reflect array element under various oblique incident illumination. The phase curves are quite limited, although the slight deviations are observable as the angle of incidence increases. In Figure 3.25, it is apparent that the cross-pol. suppression is worsened with increasing incidence angle. This is an expected result. Moreover it can be integrated into the design of a reflectarray antenna composing of this element.

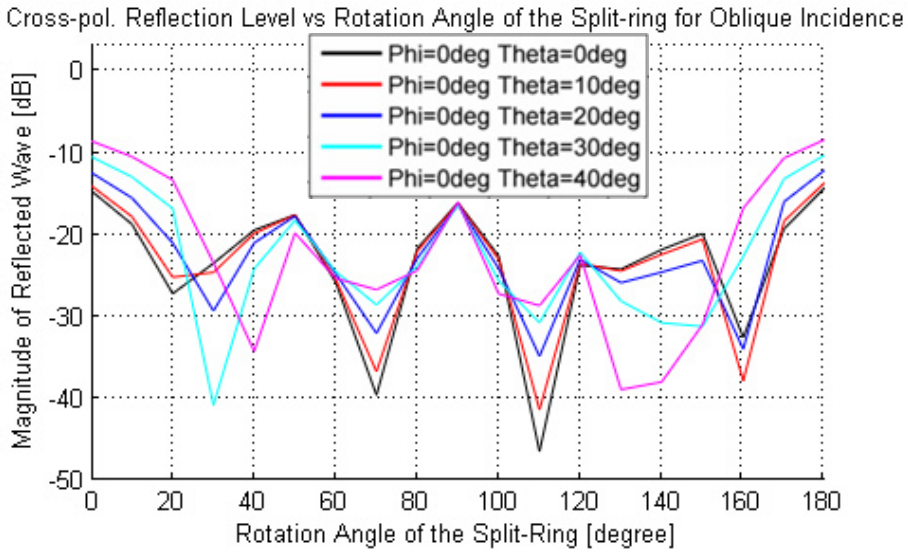

Figure 3.25 Magnitude curve of the split-ring unit cell @ 27.34 GHz for various oblique incidence angles.

3.5 Conclusion

The unit cell approach to characterize the reflectarray element with split-ring is explained and applied, yielding a single frequency split-ring element. The results of parametrical study are presented and discussed. The phase design curve based on rotation of split ring and the frequency response of the cross pol. component are obtained. This characterization procedure is utilized to design the dual band reflectarray element of split-rings in the following Chapter.

CHAPTER 4

DUAL BAND REFLECTARRAY ELEMENT AND REFLECTARRAY ANTENNA DESIGN

4.1 Introduction

The rotational phase shift principle is mathematically derived and simulations are completed to show that the split-ring element is suitable for phase control as a reflectarray element. The author's aim is to propose a simple topology for dual frequency operation employing the rotational phase shift principle. The dual frequency unit cell with split-rings is presented in this chapter. The possible configurations with split-ring are mentioned for dual frequency operation. The final choice of the reflectarray element is demonstrated. The reflectarray antenna formed by combining the dual band reflectarray element is designed, fabricated and measured. The comparison of measured patterns with simulated ones is discussed. The reflectarray element is integrated with RF MEMS switches, the result is put forward. After the element design, the dual frequency elements are combined to build a reflectarray antenna, the design principles and simulation results are given.

4.2 Dual Band Element Design

The goal is to achieve a dual band reflectarray element design using the aforementioned techniques and approaches to combine the split-rings in an appropriate form. This section is dedicated to the choice of the dual frequency configuration, determining the dimensions of the split-rings and characterization of

the final design.

4.2.1 Choice of the Dual Frequency Configuration

Among several split-ring structures to build up a reflectarray element operating at dual frequency, the set of choice is narrowed down by the fabrication methods and technology.

The fabrication technology in Middle East Technical University MEMS Center is to be utilized for the realization of the design. Thus the reconfigurability of the antenna will be provided by integrating RF MEMS switches. The capabilities of the RF MEMS process developed previously by the RF MEMS Group were demonstrated in [37], [14]. The demonstration of a switch similar to use in this design is given in [13]. The aim was to design a low profile and low volume antenna. Thus, single layer implementation of dual frequency rings is preferred.

Figure 4.1 Concentric configuration of two split-rings.

The operation frequency of the split-ring is directly related to the size of the rings. Using two split-rings in different sizes with possible configurations are studied to check if the configurations can satisfy the conditions to guarantee that the unit cell can operate in dual band and control the phase in the two bands independently. The characterizations of the elements are compared accordingly.

One possible configuration of the split-rings to obtain double frequency operation is concentric placement as in Figure 4.1. Before determining the dual frequency configuration, there are some constraints to keep in mind. The final design should be suitable for bias lines of the switches. The process flow to fabricate the element with surface micromachining is a well defined one whose most problems solved. Using the concentric configuration poses problems of reach for the bias lines of the switches on the inner ring. Then the process flow should be modified and optimized to build the necessary insulated transitions through the split-ring metallization. Furthermore, the bias lines that pass through the split-ring metallization can increase the microwave simulation efforts needed. Then another configuration is put forward and accepted as the dual frequency element after essential studies, the interleaved manner as in Figure 4.2. The latter configuration can overcome the problems of the concentric configuration.

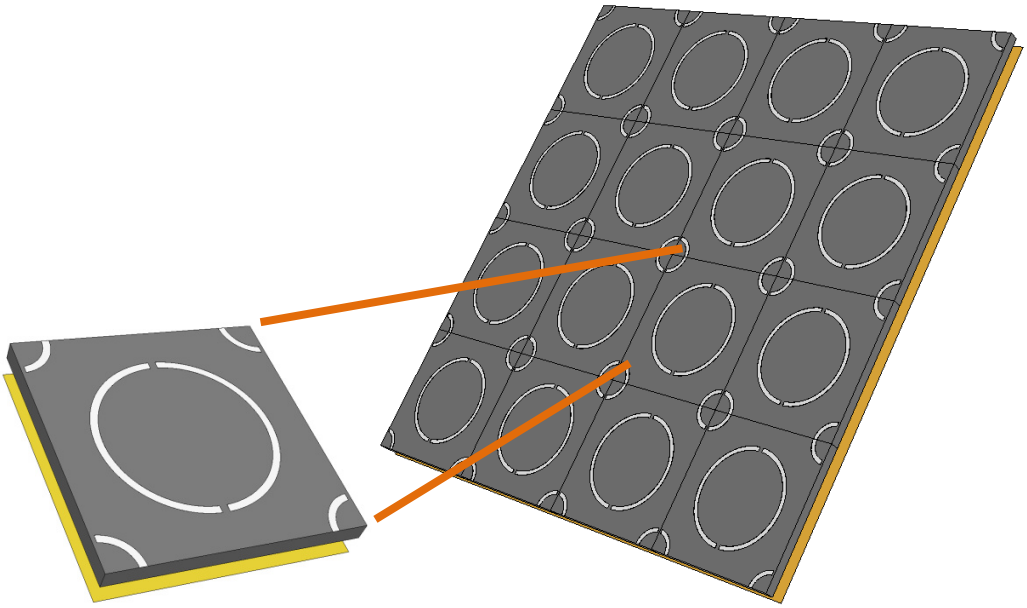

Figure 4.2 Interleaved configuration of two split-rings.

4.2.2 The Dual Frequency Reflectarray Element Design

The reflectarray element design with one split-ring is examined in the previous chapter. The similar procedure should be handled carefully to combine the two split-rings such that the phase control principle is still valid and applicable as well as the desired frequency response is achieved.

The dual-frequency configuration as a unit cell pertaining to an interleaved array of split-rings of two sizes is shown in Figure 4.3. Briefly, the larger ring operates at the lower frequency and the smaller ring operates at the higher frequency. The element's split-rings are first designed, and the element dimensions are optimized for a frequency response fairly independent of split ring position. And finally the operation in dual band is investigated and phase curve is verified. The element is further studied for its capabilities and then is to be integrated with RF MEMS switches.

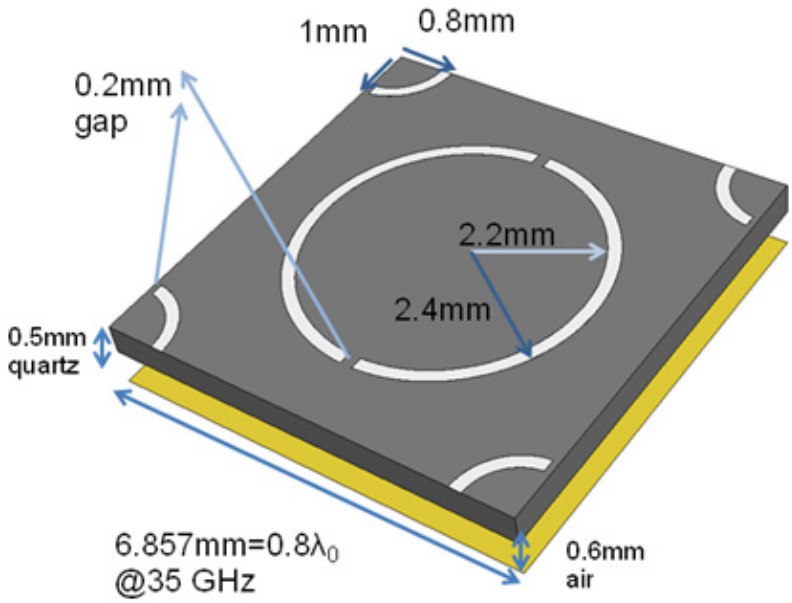

Figure 4.3 The tuned interleaved design of the dual frequency reflectarray element.

4.2.2.1 Optimizing the Frequency Response

As previously mentioned, the frequency response is prone to shifts with respect to the rotational states of the split-rings. That is why studying the frequency responses for various angular positions of the split-rings are necessary in order to achieve a rather unvarying frequency response. The unit cell dimension may be modified, all others being constant, to see if it is possible to reach an element design with an unvarying frequency response. Various angular positions of the two split-rings are chosen as a representative set, as in Figure 4.4. And these rings in many cells of different sizes are simulated to achieve the frequency response.

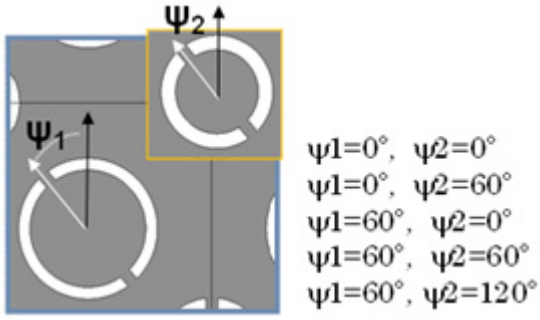

Figure 4.4 The set of angular position for the split-rings used to test if the frequency response is stable

The comparison of Figure 4.5, Figure 4.6, and Figure 4.7 clearly puts forward that the unit cell dimension should be set to 0.8λ @35 GHz in order to maintain a stable frequency response for various angular position of the two split-rings. The lower operating frequency can be determined as 24.4 GHz and the higher operating frequency as 35.5 GHz.

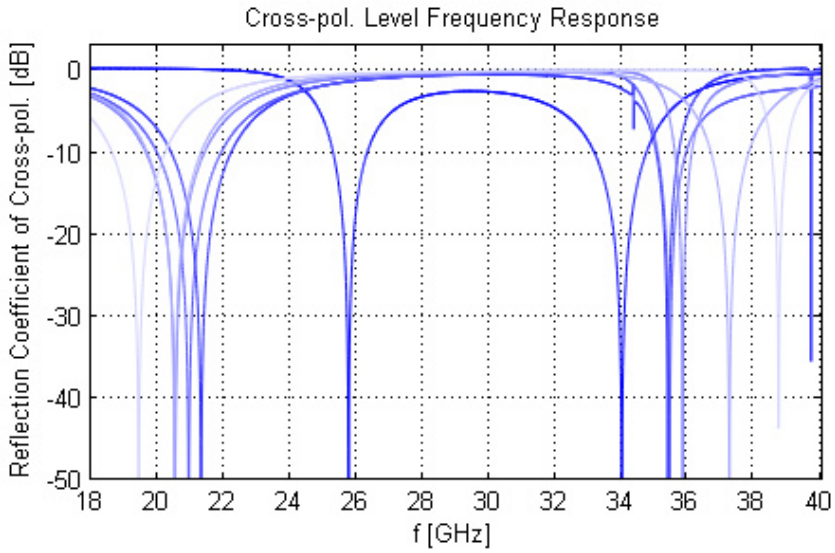

Figure 4.5 Frequency Response of the cross-pol. reflection, for various physical rotation angles of the split-ring. Unit cell dimension: 0.6λ @35 GHz.

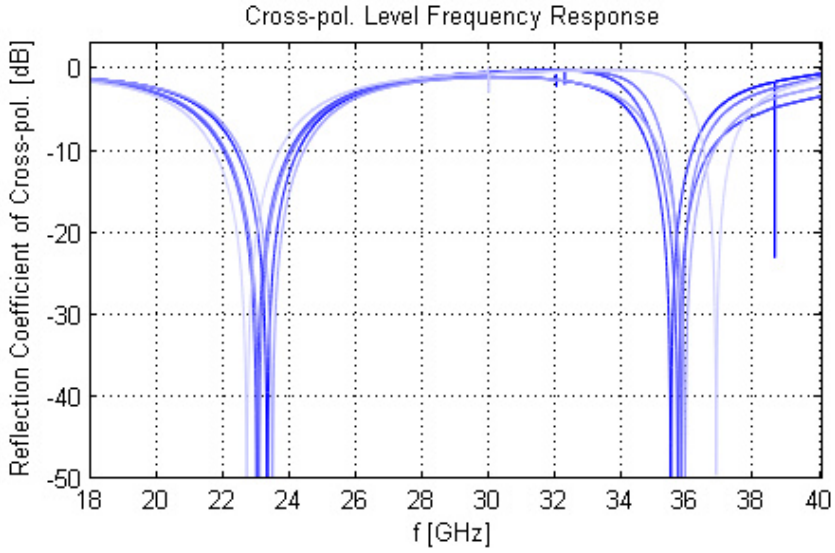

Figure 4.6 Frequency Response of the cross-pol. reflection, for various physical rotation angles of the split-rings. Unit cell dimension: 0.7λ @35 GHz.

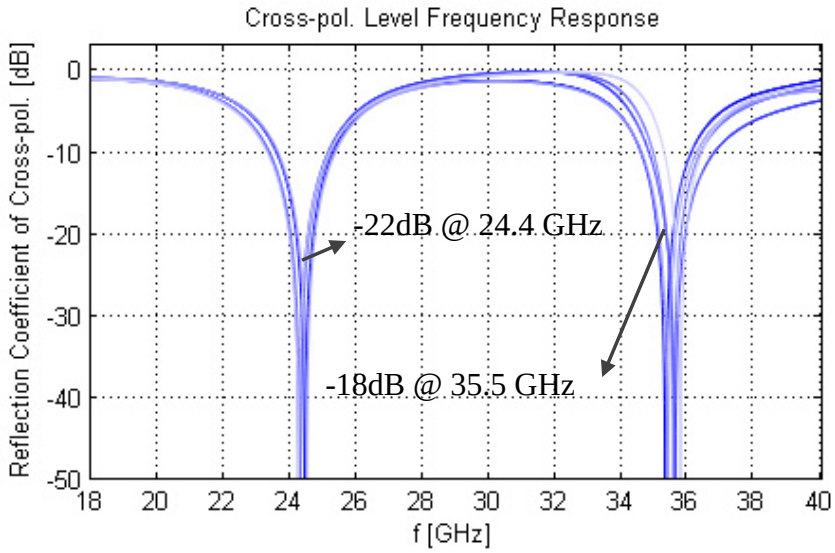

Figure 4.7 Frequency Response of the cross-pol. reflection, for various physical rotation angles of the split-rings. Unit cell dimension: 0.8λ @35 GHz.

4.2.2.2 The Combination of the Split-Rings in Two Sizes

To design the split-rings of different frequencies independently may be the starting point before combining them and achieving the dual frequency operation. It is obvious that the operation frequencies are prone to shifts related to the parasitic effects that they apply on each other. That is a reason to check their re-radiating currents at operation frequency after obtaining an unvarying frequency response. The mechanism that changes the operation frequencies of the split-rings when they are put together may also affect the phase control mechanism. It is thus worth examining.

In Figure 4.8, the frequency response of the larger ring alone is given, with the same air gap layer, substrate thickness, and unit cell dimensions as the final design given in Figure 4.3. The same simulation set-up is also used to simulate the smaller ring alone Figure 4.9. The design of the two split-ring elements does not mean that they will operate as expected after combining them in the interleaved array manner.

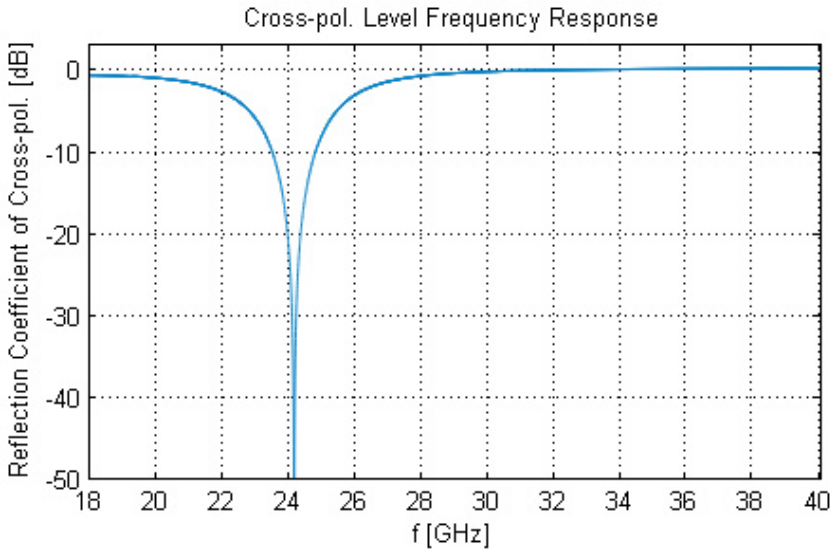

Figure 4.8 The reflection coefficient of cross-pol. vs. frequency for the larger ring alone.

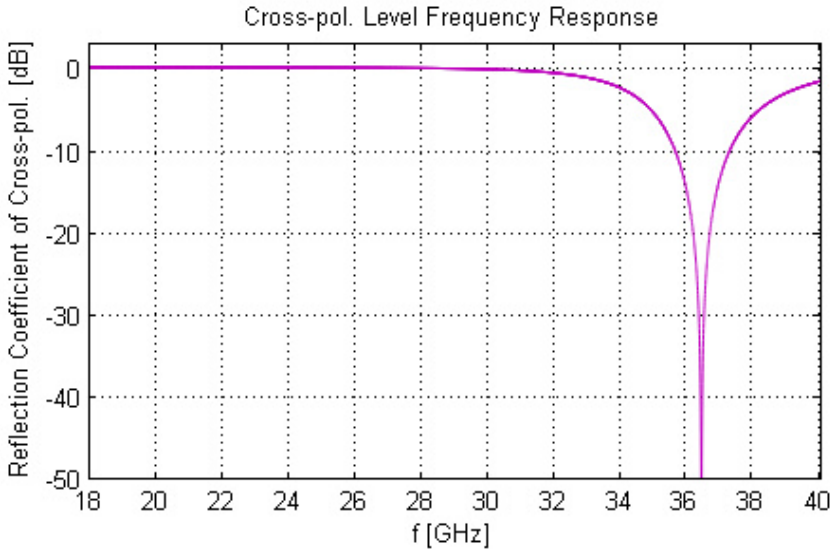

Figure 4.9 The reflection coefficient of cross-pol. vs. frequency for the smaller ring alone.

In Figure 4.10, it is seen that the both higher and lower operating frequencies are shifted. This is an expected result since the surrounding metallization can affect the frequency response and also yields to the interpretation that there is sure an interaction between the split-rings of two sizes. That is why the dual frequency element is further due to a question: Are they able to control the phase as expected and demonstrated in for single frequency?

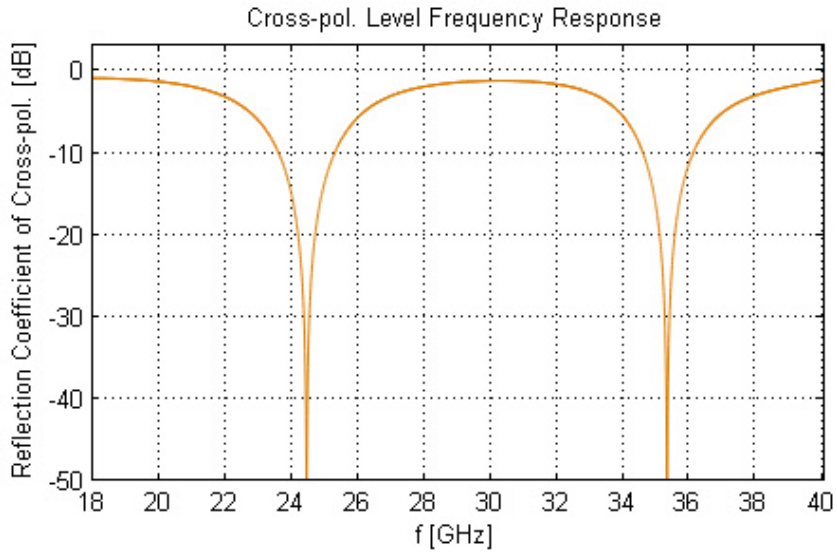

Figure 4.10 The reflection coefficient of cross-pol. vs. frequency when the two split-rings are put together.

There is also another aspect that may be helpful to check before passing to the simulations for the phase control capabilities of the array. The rotational phase control principle states that the phase of the reflected co-pol. component is linearly proportional to the rotation angle of the element. Then, combining this idea with the fact that the reflection is occurring by the currents on the metallization that re-radiate; the split-rings are required to control the phase at different frequencies independently. It is necessary that the currents should concentrate in the larger ring at the lower operation frequency and in the smaller ring for the higher operation

frequency, in order to guarantee that the application of the phase control principle.

In Figure 4.11 and Figure 4.12 the surface current density on split-rings are depicted respectively at lower and higher operating frequencies. The illustrations are put in a 10-to-1 magnitude ratio with logarithmic scaling. It is obvious that, the currents flow dominantly on the smaller split-ring for higher frequency, on the larger ring for the lower frequency. The fact that the reflected fields are formed via the surface currents, these rings are meant to dominate the reflection mechanism and the most of power is coupled to the currents on them at their specific frequencies dominantly. That is the reason why the rotational phase shift principle can be employed for the split-rings in two sizes to control the phase at different frequencies independently.

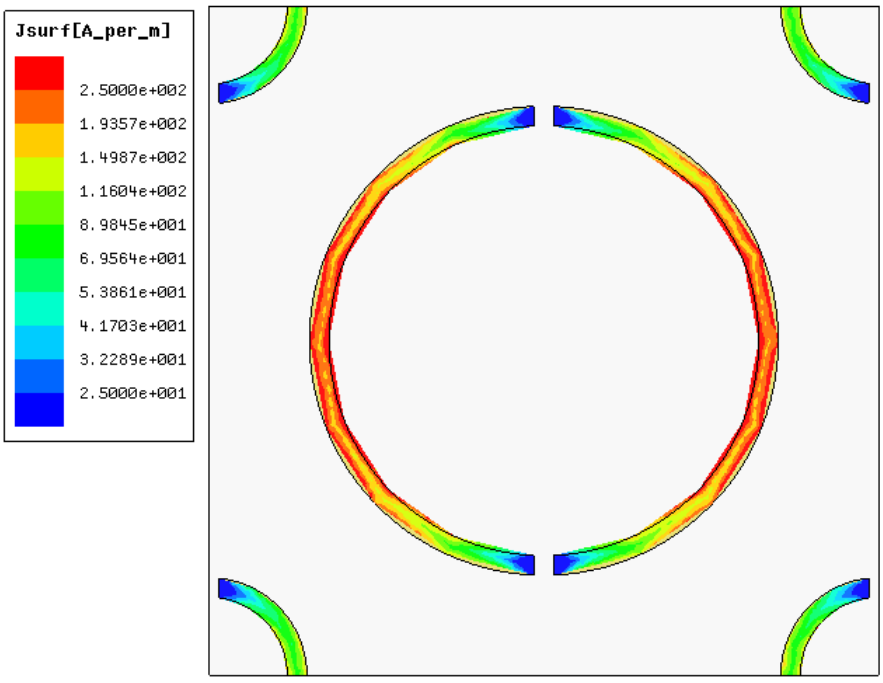

Figure 4.11 The surface current density on the dual frequency element metallization, at 27.4 GHz.

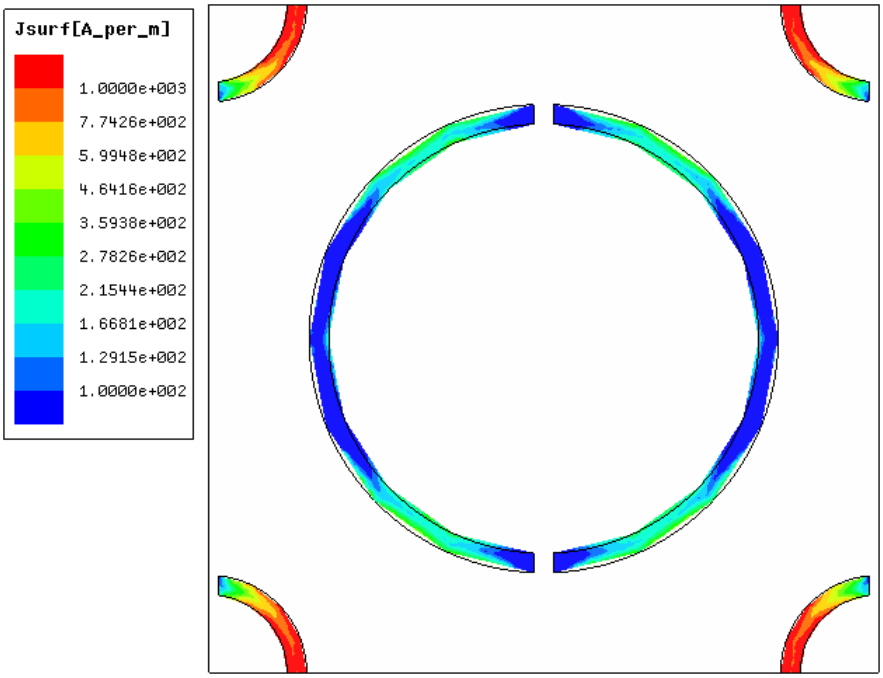

Figure 4.12 The surface current density on the dual frequency element metallization, at 35.3 GHz.

4.2.2.3 Characterization of the Dual Frequency Element

The element design steps are explained previously in this section. The results show that the phase control is realizable. The next step is to verify the phase design curve. This section includes the characterization of the final design and the specifications are shown to match the desired quality. The phase design curve and cross-pol. level plots are given to examine the performance.

In Figure 4.13, the phase design curve at lower band is given. The phase is linearly changing with respect to the rotation angle of the larger ring, this is the expected result. Moreover it can be seen in Figure 4.14 that the cross-pol. is suppressed for all states of the larger split-rings.

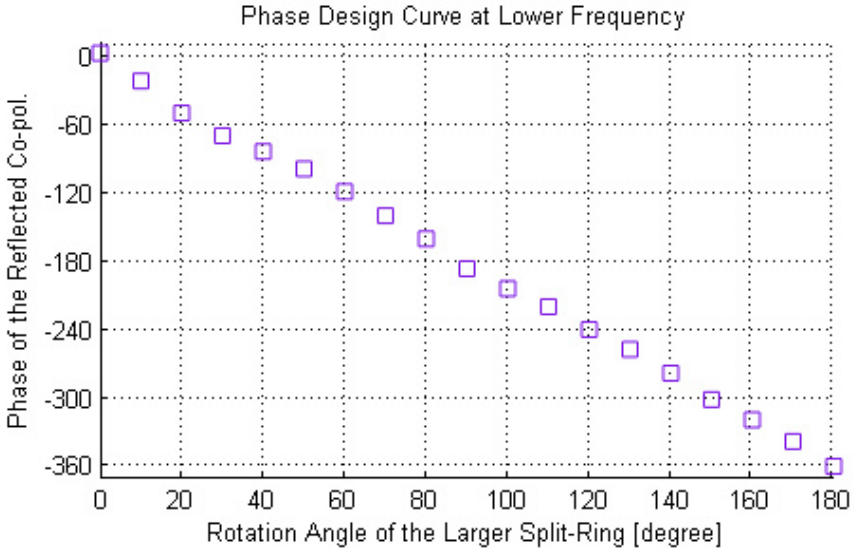

Figure 4.13 Phase Design Curve at 24.4 GHz.

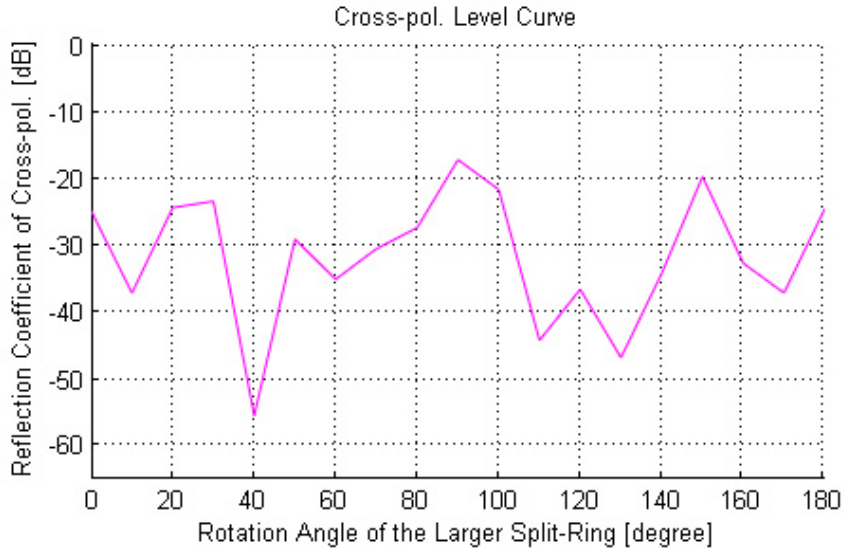

Figure 4.14 Magnitude of Reflection Coefficient of Cross-pol. vs ψ_{larger} at 24.4 GHz.

Then it should also be clear whether rotation of the larger split-ring affects the phase of the co-pol. wave at the higher band - it is required that it does not affect. To check

this, also the phase of the co-pol. wave and cross-pol. level at the higher frequency is plotted. In Figure 4.15, it is apparent that the phase is affected but the effect is very limited and acceptable. And Figure 4.16 shows that the cross-pol. suppression is not affected, either. Then the rotation of the larger split-ring behaves as desired, not disturbing the irrelevant band and controlling the phase at the lower band.

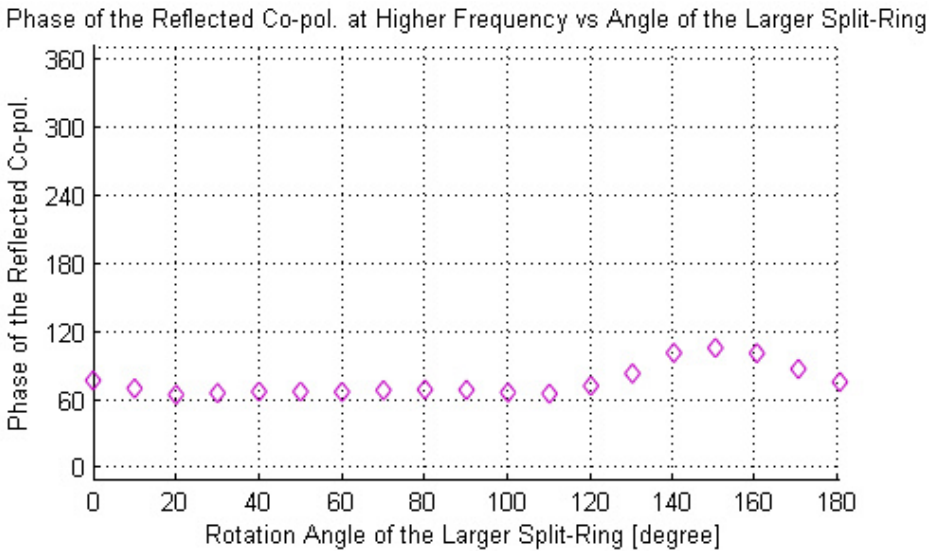

Figure 4.15 Phase of the Co-pol. vs ψ_{larger} at 35.5 GHz.

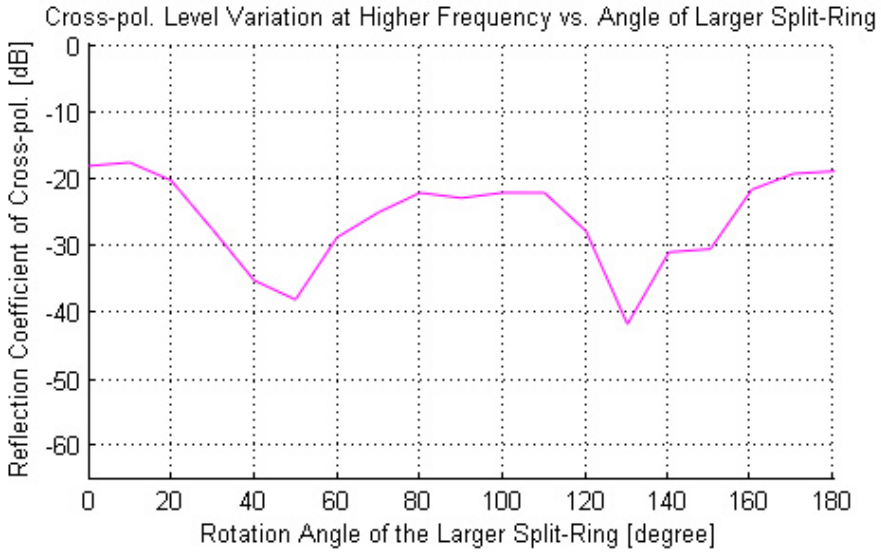

Figure 4.16 Reflection Coefficient of Cross-pol. vs. ψ_{larger} at 35.5 GHz.

Similarly Figure 4.17 and Figure 4.18 shows that the smaller ring controls the phase of the co-pol. component in the reflection linearly with the rotation angle while preserving the cross-pol. levels acceptably low. And in the lower band which it has no effect, it does not disturb the operation. The phase of the co-pol. and the cross-pol. suppression is affected at minimum, as seen in Figure 4.19 and Figure 4.20.

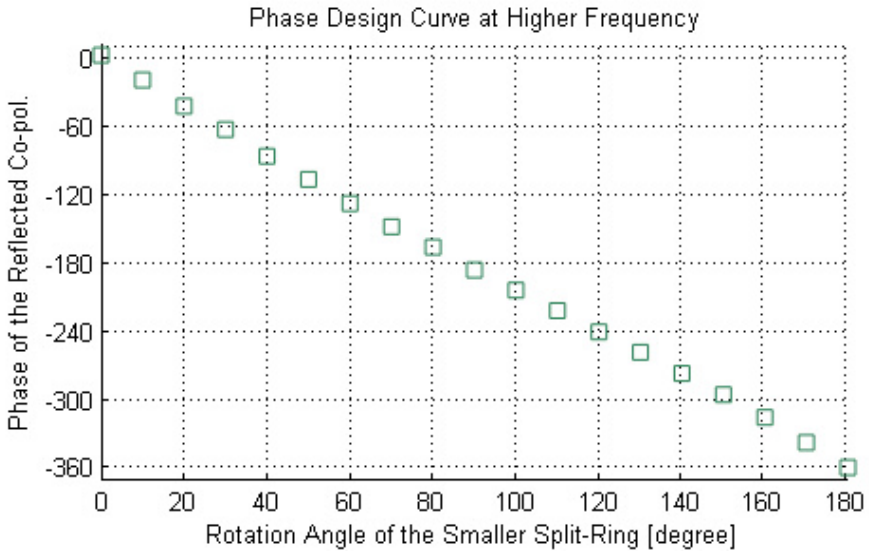

Figure 4.17 Phase Design Curve at 35.5 GHz.

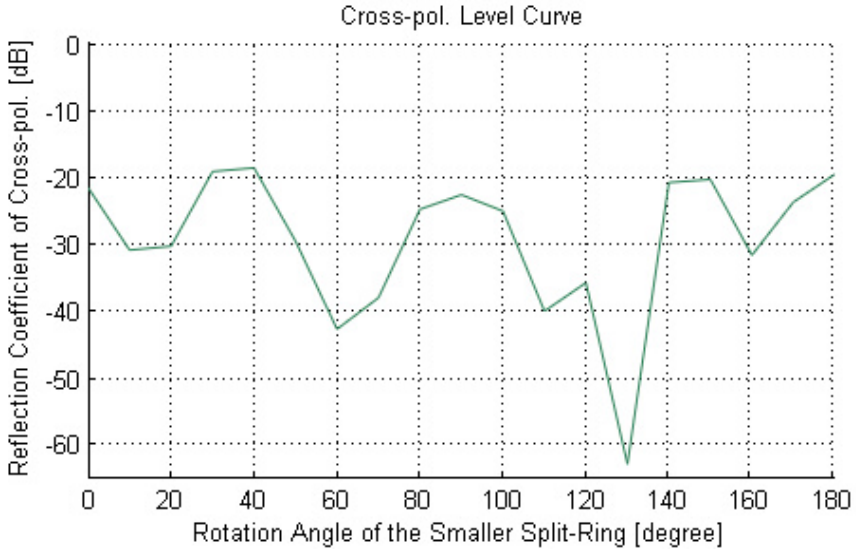

Figure 4.18 Magnitude of Reflection Coefficient of Cross-pol. vs $\psi_{smaller}$ at 35.5 GHz.

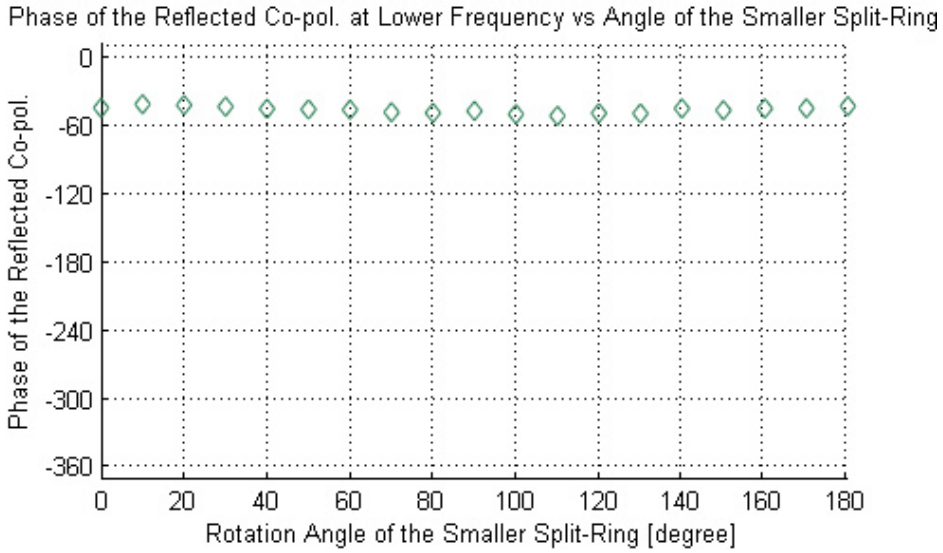

Figure 4.19 Phase of the Co-pol. vs $\psi_{smaller}$ at 24.4 GHz.

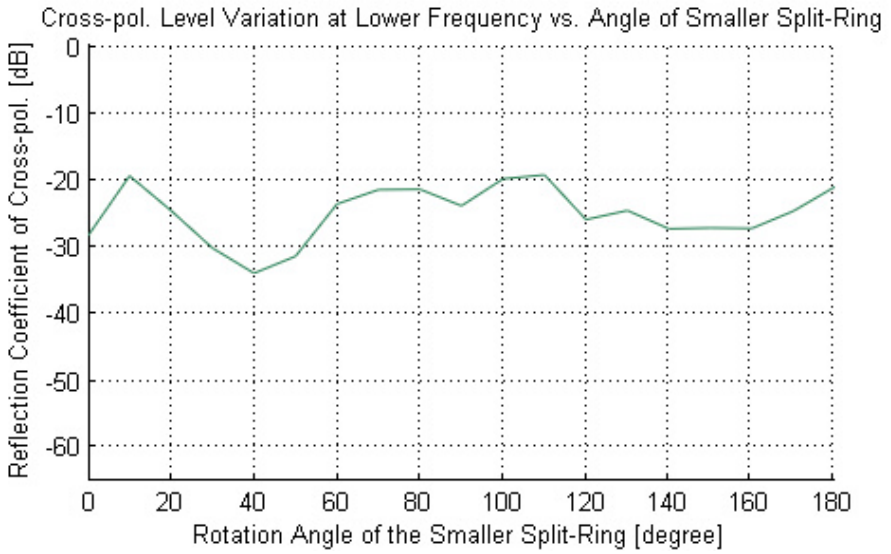

Figure 4.20 Magnitude of Reflection Coefficient of Cross-pol. vs $\psi_{smaller}$ at 24.4 GHz.

The phase curve and the cross-pol. suppression characteristics are all in desired quality. But the previous cases are simulated for the normal incidence. For a better understanding of the response of the reflectarray element, the oblique incidence should be checked. However the total number of cases to be simulated can increase

drastically, it would be sufficient and helpful to see what happens by giving the results for the lower frequency operation under oblique incidence. The case is only simulated at 24.4GHz, since oblique incident wave may lead to new propagating Floquet modes in higher frequency due to the unit cell size.

Regarding Figure 4.221 and Figure 4.22, variation in phase is limited to 40° which is very acceptable and the cross-pol. reflection level is limited to -10dB for up to θ=30°. The cross-pol. levels should be better than -20dB. But when the reflectarray design is examined, it is obvious that while the co-pol. is controlled to have a high directivity, the constant phase of the cross-pol. causes it to contribute into the specular reflection. That is the reason for element level thinking the -10dB cross-pol. reflection may be undesirable but the bigger picture seems to be more optimistic. In the frame of the reflectarray antenna, cross-pol. may not be as high.

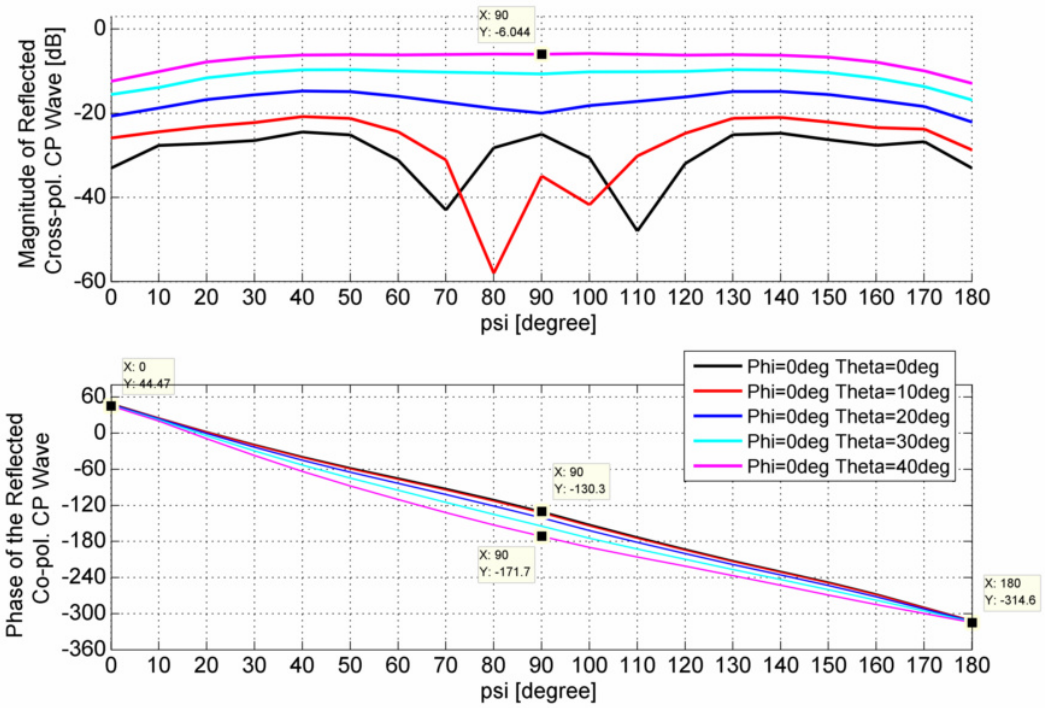

Figure 4.21 Magnitude of the reflected cross pol. and the phase design curve with respect to various oblique incidence angles, at 24.4GHz.

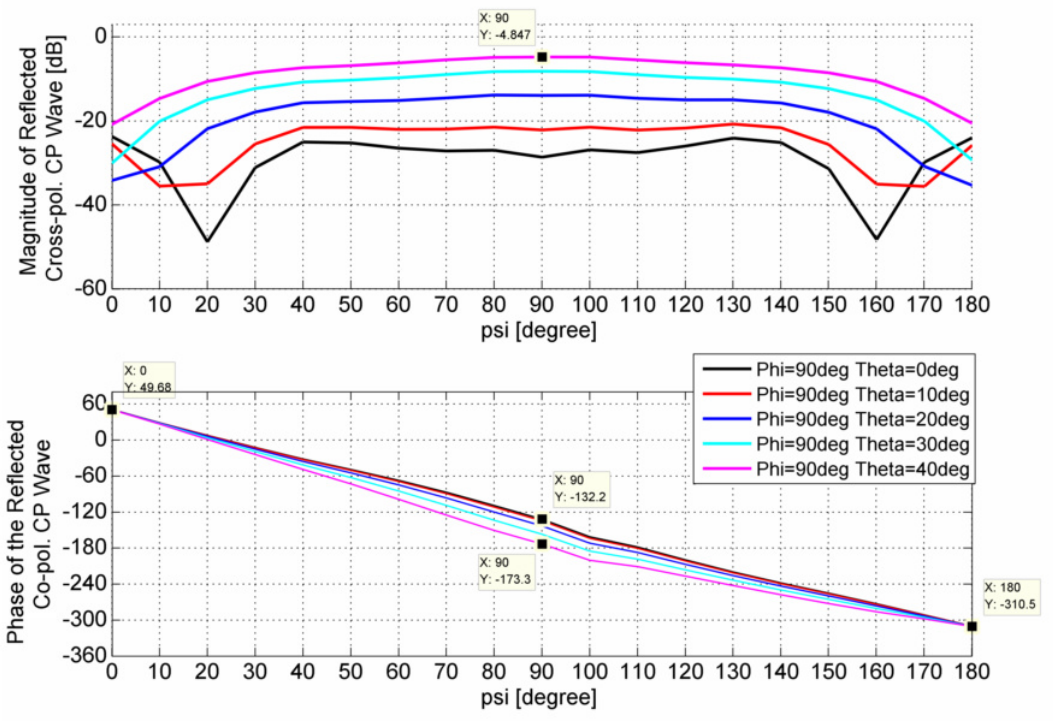

Figure 4.22 Magnitude of the reflected cross pol. and the Phase design with respect to various oblique incidence angles, for φ=90° plane at 24.4GHz.

To conclude this section, it can be stated that the designed dual band reflectarray element is matching the requirements.

4.2.3 Integration of the Element with RF MEMS Switches

The implementation of the rotational phase control principle with split-rings is done using the RF MEMS switches to change the orientation of the splits. By this way, reconfigurability is achieved. For the dual frequency element, the total number of switches is 12. 6 RF MEMS switches per ring are placed with 60° angular spacing about the center of the ring. These 6 switches on one ring are grouped into 3 pairs, where two switches lying on the same diameter constitute a pair. These 3 pairs of switches are biased accordingly to provide 60° rotation effect for the split-ring. Each state corresponds to 2 pairs of switches in on-state and 1 pair in off-state. In this

work, the state numbers are 3 for each frequency, corresponding to 120° phase resolution.

In fact, using a high number of MEMS switches is required to enjoy the reconfigurability with high resolution. However the problems of yield and bias line routing emerge, as the number of MEMS devices increase. Also the increase in phase resolution does not linearly contribute to the beam steering capabilities of an array. The designer should weigh the trade off. Thus a reasonable number of MEMS switches are decided by the designer.

Ohmic contact series switch, capacitive series and shunt switches are available for in house fabrication in METU MEMS Center. Since the design is based on the split-ring structures, the switch based design is also implemented on the previously investigated structure. The previously investigated structure constitutes a basis for the design with switches where the on and off switches correspond to short and open metallization. To achieve this goal capacitance ratio at a degree of 100 is necessary for RF short and open to be in accordance with the previous split-ring designs. This capacitance ratio is typically not achieved with capacitive MEMS switches in which the down state composes of two metal layers separated by a dielectric film, [38]. Thus the ohmic contact series MEMS switch shown in Figure 4.23, which constitutes a contacting metal path between two separated conductor lines in down state, is chosen. This topology is suitable to be modeled with open and short metallization on the split-ring. The design is based on the switch in [13] whose photograph is given in Figure 4.24 after fabrication steps given in [13]. The dimensions are modified with slight changes keeping the topology intact in order to fit into the gaps of the ring; the final dimensions are given in Figure 4.26. The view of the reflectarray element with RF MEMS switches is given in Figure 4.27. The fabrication layers whose final form is represented in Figure 4.25, a complete flow of process is found in [39].

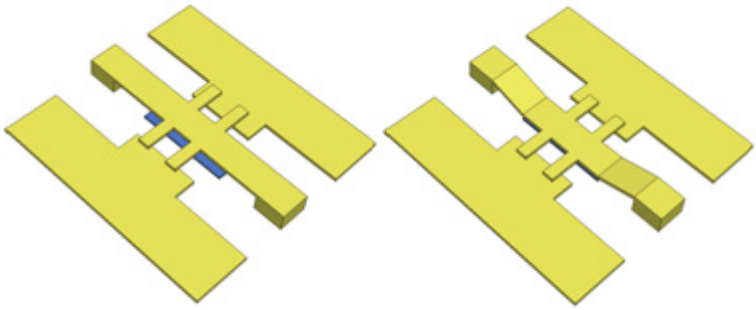

Figure 4.23 The overview of the designed RF MEMS switch.

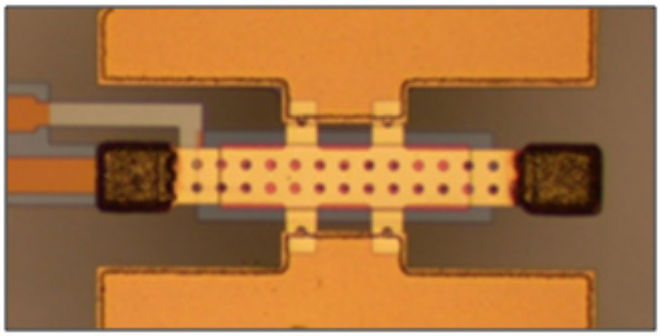

Figure 4.24 Ohmic contact series MEMS switch fabricated in METU.

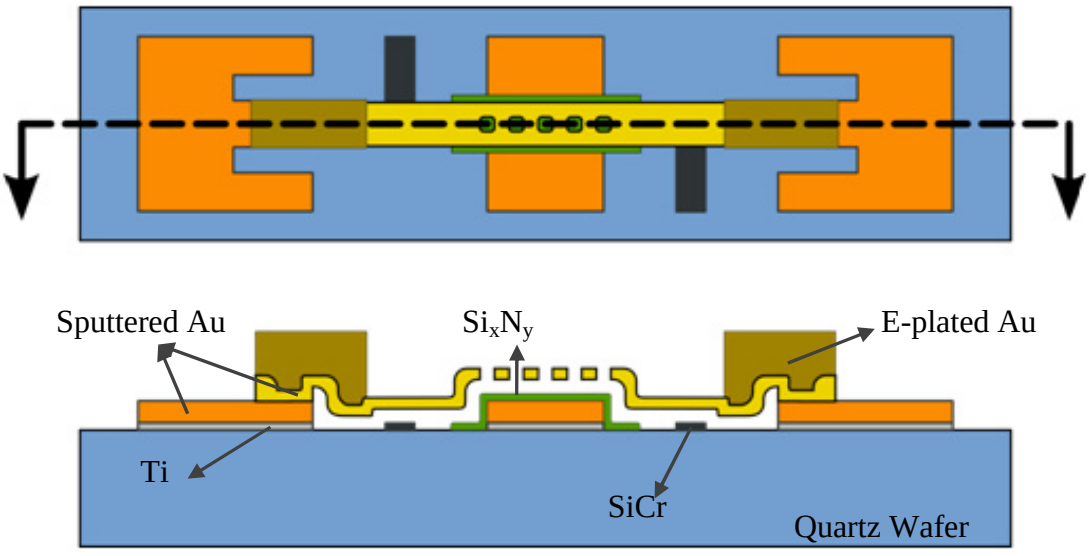

Figure 4.25 RF MEMS switch structure (Courtesy of Çağrı Çetintepe).

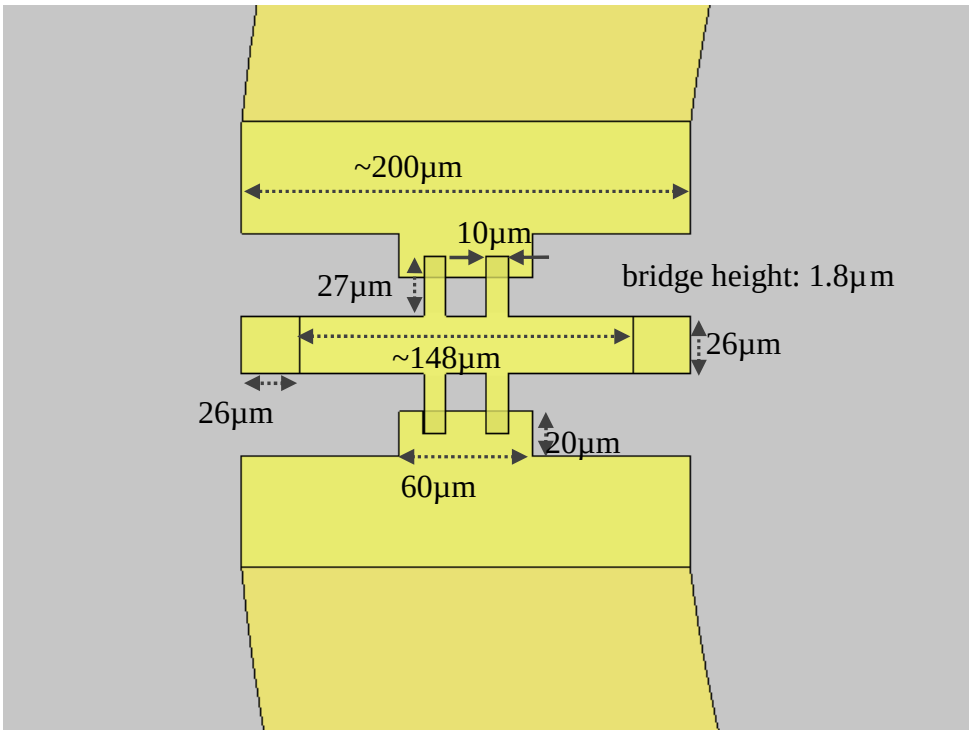

Figure 4.26 Dimensions of the ohmic contact series MEMS switch is illustrated.

Throughout the simulation of the reflectarray element with RF MEMS switches, the bias lines are not contributed into the topology. Furthermore, the 3D full wave simulation takes too much time and needs high memory space, when the accurate 3D MEMS switches are implemented in the simulation environment. Therefore the full 3D model of the reflectarray element, as seen in Figure 4.27, is only simulated once to yield the frequency response of the cross-pol. suppression. Then it is used for validation of modeling the switches.

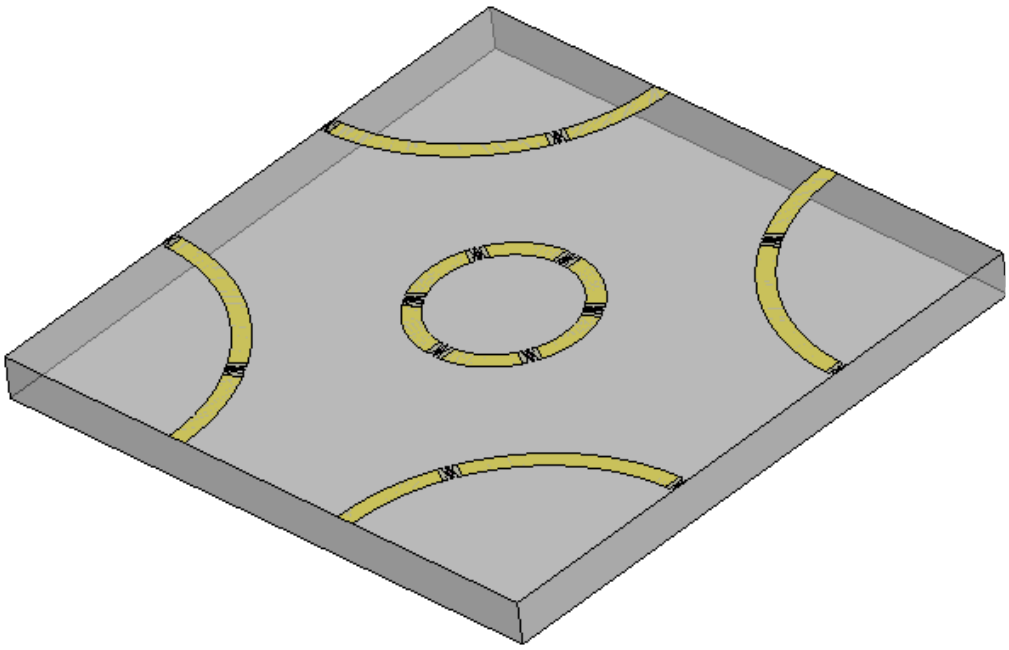

Figure 4.27 Overview of the reflectarray element with RF MEMS switches.

In Figure 4.28, it is seen that the integration of switches caused a shift in the frequency response. The radii of the rings in the element with RF MEMS switches are not tuned to the same operation frequencies not to waste time. These parameters can be tuned to operate in desired frequencies for a final design. Simply the dual band reflectarray element without the switches is a model of this final form where switches in on and off states are modeled simply by perfect shorts and opens respectively. To verify the phase controlling capability of the reflectarray element with 12 RF MEMS switches, the element has to be simulated with unit cell approach with numerous states and frequencies. However the fact that the 3D switch structures in the simulation environment causes drastically high numbers of meshes. The reason is that the edges of the switch topology are in high aspect ratio. To overcome this increased time of computation and memory usage, the switch is modeled using impedance boundary implemented in HFSS.

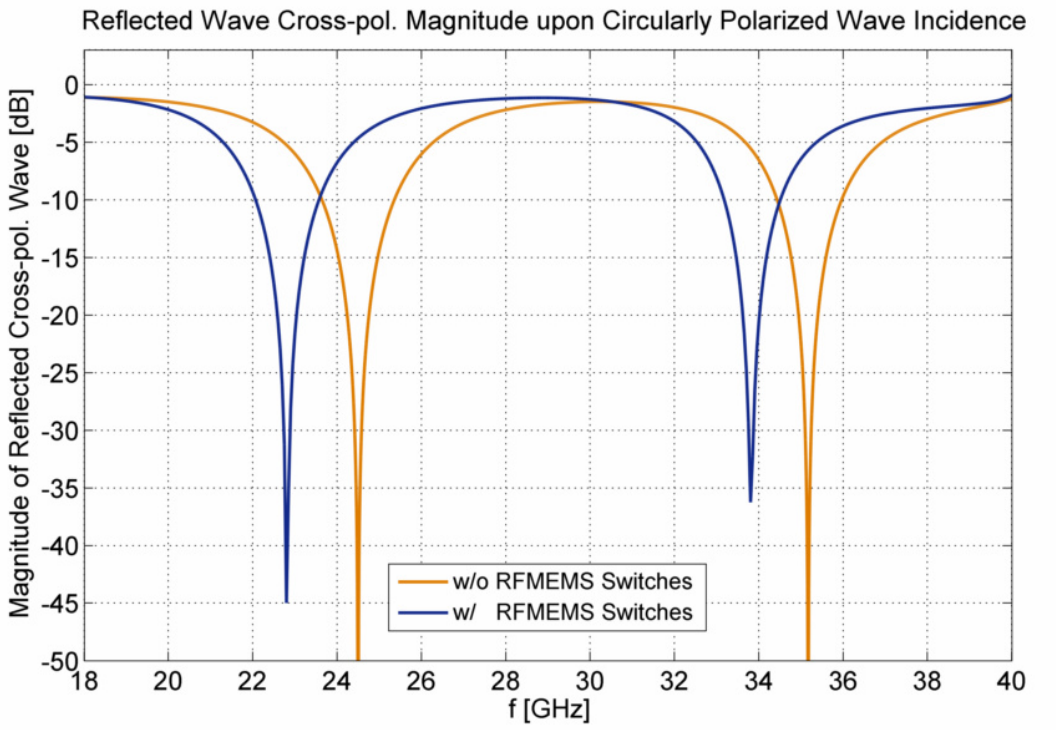

Figure 4.28 Frequency response of the reflectarray element compared before and after the integration of RF MEMS switches.

The aim of impedance boundary modeling of the RF MEMS switch is to verify that the dual band reflectarray element integrated with RF MEMS switches is capable of controlling phase as desired. Thus the high simulation time need for a successful simulation of the high-aspect-ratio switches is avoided, while numerous cases are simulated. Impedance boundaries are also supported by Ansoft HFSS. The impedance boundaries are implemented with 2D surfaces having resistance, inductance and capacitance in parallel. The R, L, C are given with respect to the lumped model together with the current direction. Then any lumped RLC circuit can be formed with necessary compositions of these surfaces in series and parallel.

The models are capable of successfully governing the series ohmic MEMS switch. Down state of the switch can be modeled with an inductor and a resistor in series and a shunt capacitor; and up state of the switch can be modeled with a series capacitor

and a shunt one [40]. The values of the components in the circuit model are optimized by the microwave circuit simulator software AWR using the simulations of the switch in a two port configuration. Thus the necessary lumped R, L, C values are obtained for both on and off states of the switch.

The lumped impedance values to be applied to the impedance boundaries in the simulation environment are to be investigated separately. The reason is that these impedance boundaries are imposed on the electric and magnetic fields by the simulation software. But these boundaries are present in the geometry. In addition to their imposed lumped relations, they intrinsically have inductive and capacitive effects due to their shape and interaction with the physical environment. This is the reason why the optimized lumped circuit parameters cannot be applied directly for the impedance boundaries. The designer should relate the impedance boundary parameters imposed with its corresponding circuit parameters. In this design the imposed values and their circuit parameters are related by curve fitting. Then the desired circuit model of the switch is realized with impedance boundary implementation. Thus the same characteristics for the accurate 3D switch model and impedance boundary model are found.

The aforementioned relation is applied for the shunt capacitors. The simulation results and previous studies [41] show that the shunt capacitor between the switch topology (which is coplanar with the signal trace) and the ground plane is already present in the simulation environment. There is no need to implement it with impedance boundaries.

In Figure 4.29 and Figure 4.30, the implementation of the RLC lumped impedance boundary for the on and off states of the RF MEMS ohmic contact switch. The RLC boundaries are implemented symmetrically to be consistent physically.

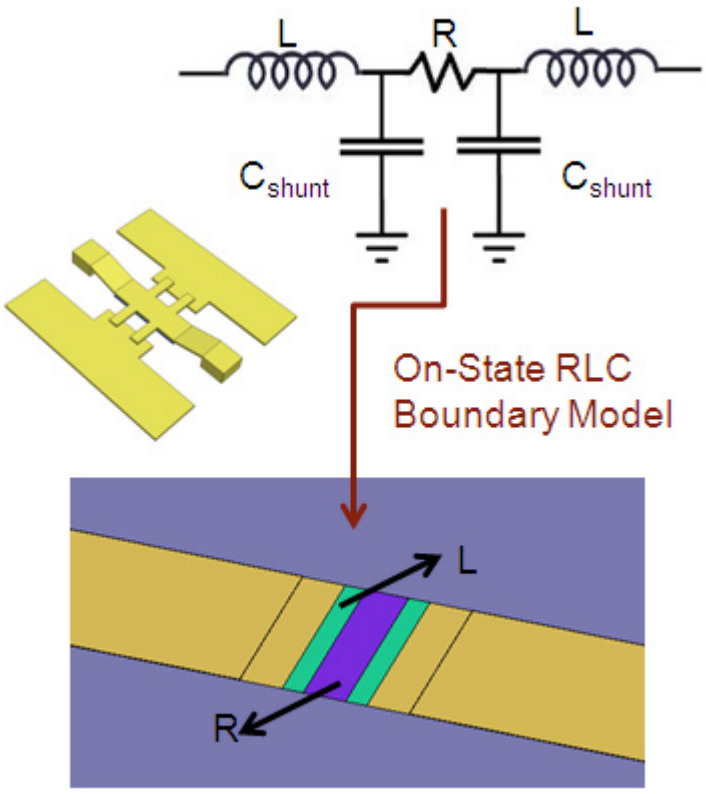

Figure 4.29 Impedance boundary modeling of the switch in on-state (bridge is down).

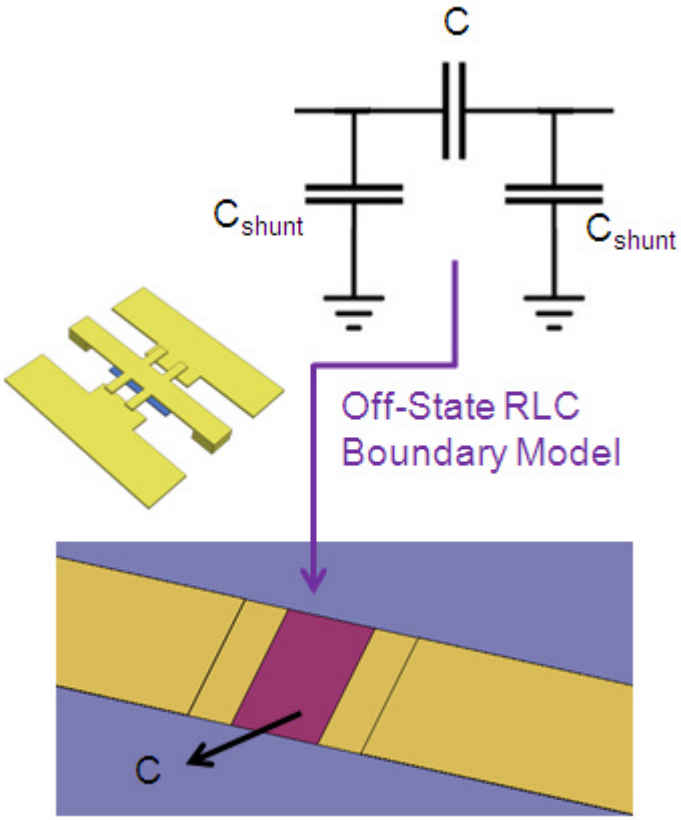

Figure 4.30 Impedance boundary modeling of the switch in off-state (bridge is up).

In Figure 4.31, the frequency responses of the dual frequency reflectarray element with switches as 3D drawing, and with the RLC model of the switch are compared. The graph shows a perfect agreement, proving that the RLC boundary model is successful in modeling the switches. Moreover the impedance boundary modeling method reduced the computation time to 10 minutes, from 8 hours. The simulations are carried out using a 2.5GHz Core2 Quad© processor, 8GB RAM computer with the highest number of mesh available and identical settings.

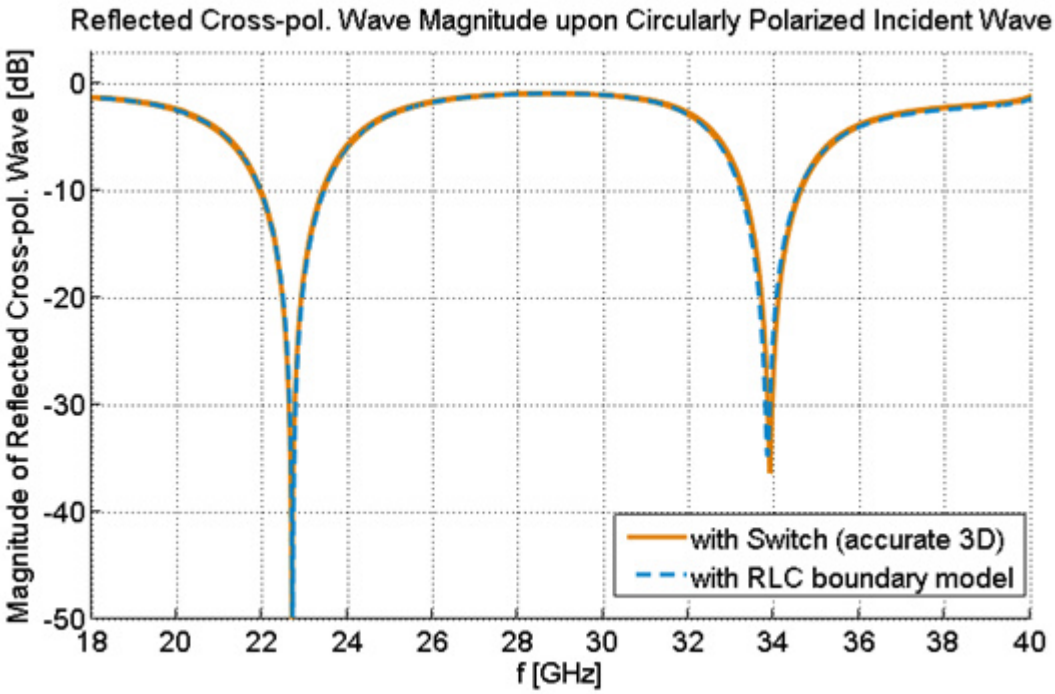

Figure 4.31 Comparison of the unit cell simulation results with 3D switch and its RLC model.

By the help of impedance boundary modeling, there is a sharp decrease in simulation time while preserving the accuracy. This makes the simulation of the reflectarray element integrated with MEMS switches for various cases available. The results of the simulations with modeled switches to verify the phase controlling capability are shown in Figure 4.32 and Figure 4.33. The cross-polarization levels are suppressed perfectly, and the phase design curve is linear.

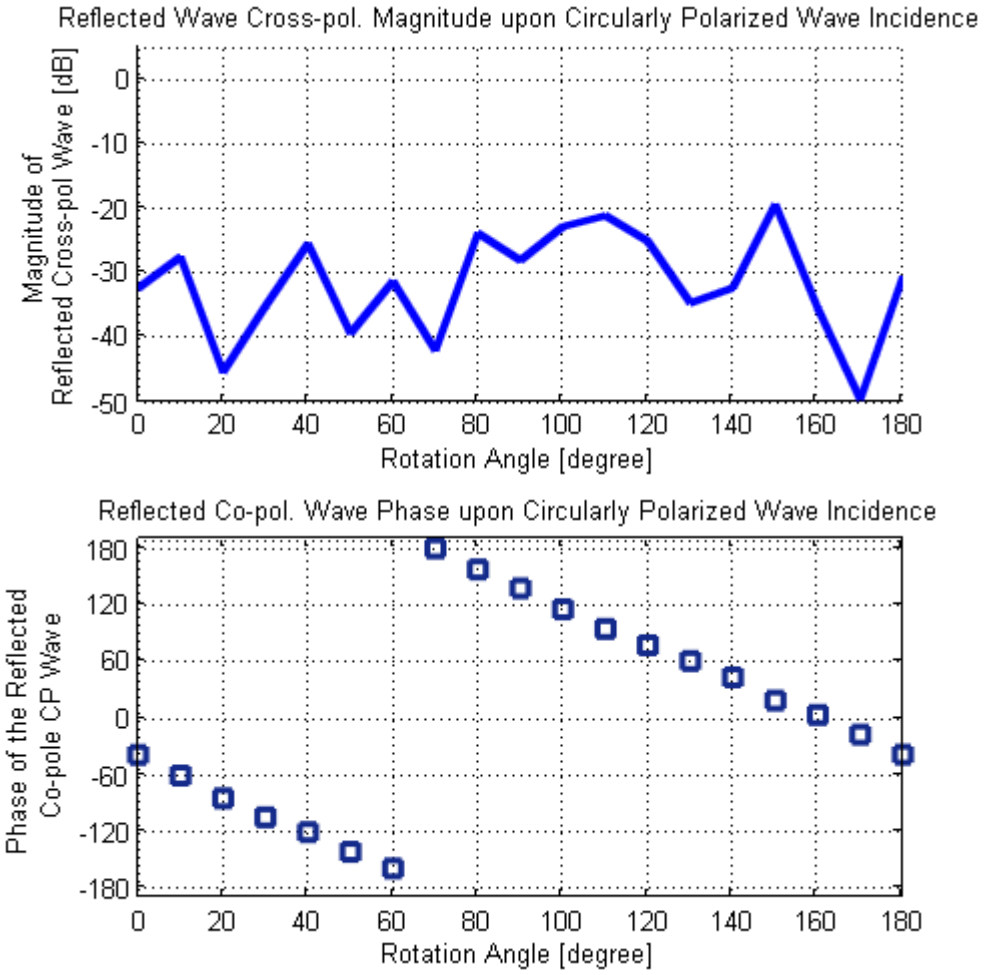

Figure 4.32 Magnitude of the reflected cross-pol. and the phase design curve at 22.65 GHz, for the element with impedance-boundary-modeled switches.

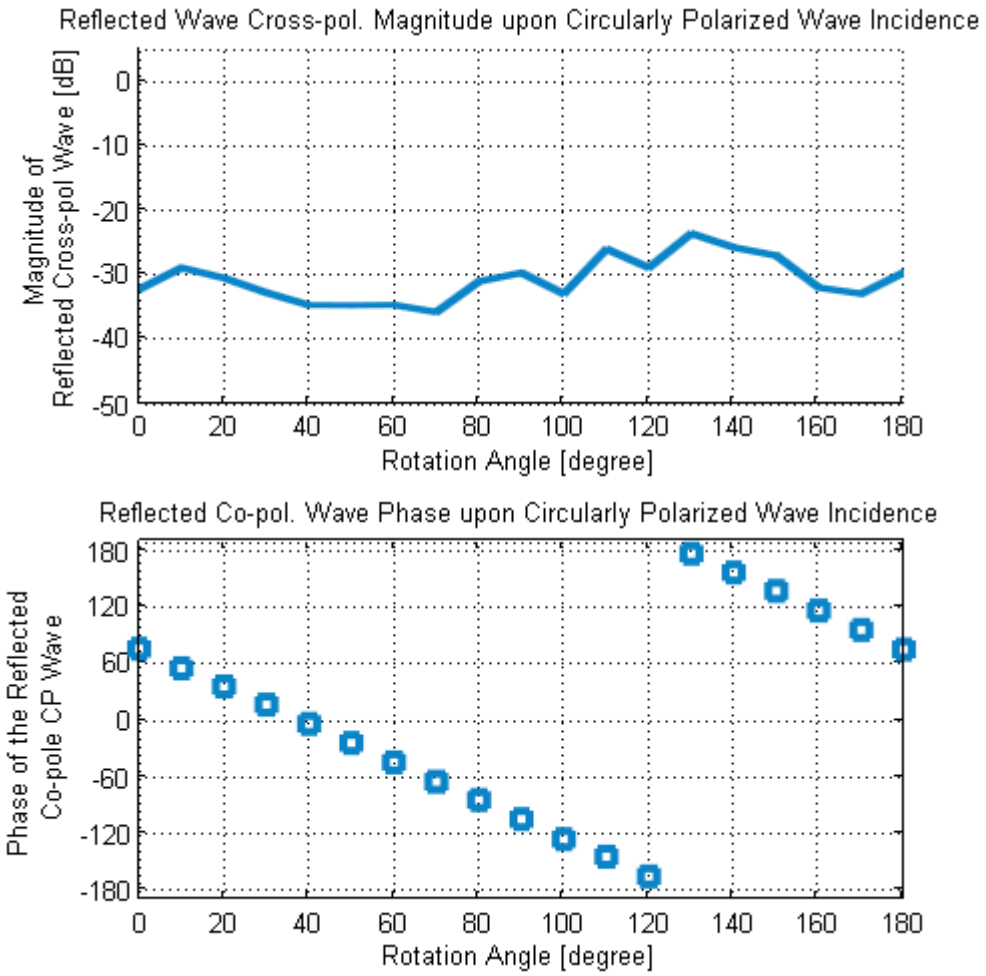

Figure 4.33 Magnitude of the reflected cross-pol. and the phase design curve at 34 GHz, for the element with impedance-boundary-modeled switches.

Although no bias lines were contributed to the simulations, it is helpful to mention bias line routing. If state of any ring is required to be set independently for electronic beam forming, via holes are the main solutions. However the technology is required and process can get harder. The bias lines from each pair of switches can thus be transferred to a printed circuit board. This is the most general solution, and the latter is left to the controlling circuitry. In this method, there has to be at least 3 bias feeds per ring as seen in Figure 4.34-(a), summing up to a high number of bias points. Moreover for verification aims of the antenna, the designer might opt out the independent operation in dual bands, and may narrow the capabilities to a switched

beam antenna. In this case as seen in Figure 4.34-(b), the routing is possible on the micromachined surface of the antenna. Then the antenna to be fabricated in this manner would switch the beam to 3 angles, however independent controlling of the beam direction in dual bands would not be possible. All these proposals are made with the assumption of maximum 2 levels crossing on top of each other. Process complexity may increase the possible routing schemes. And all these bias lines must be included in simulations to make sure the routing does not disturb required characteristic.

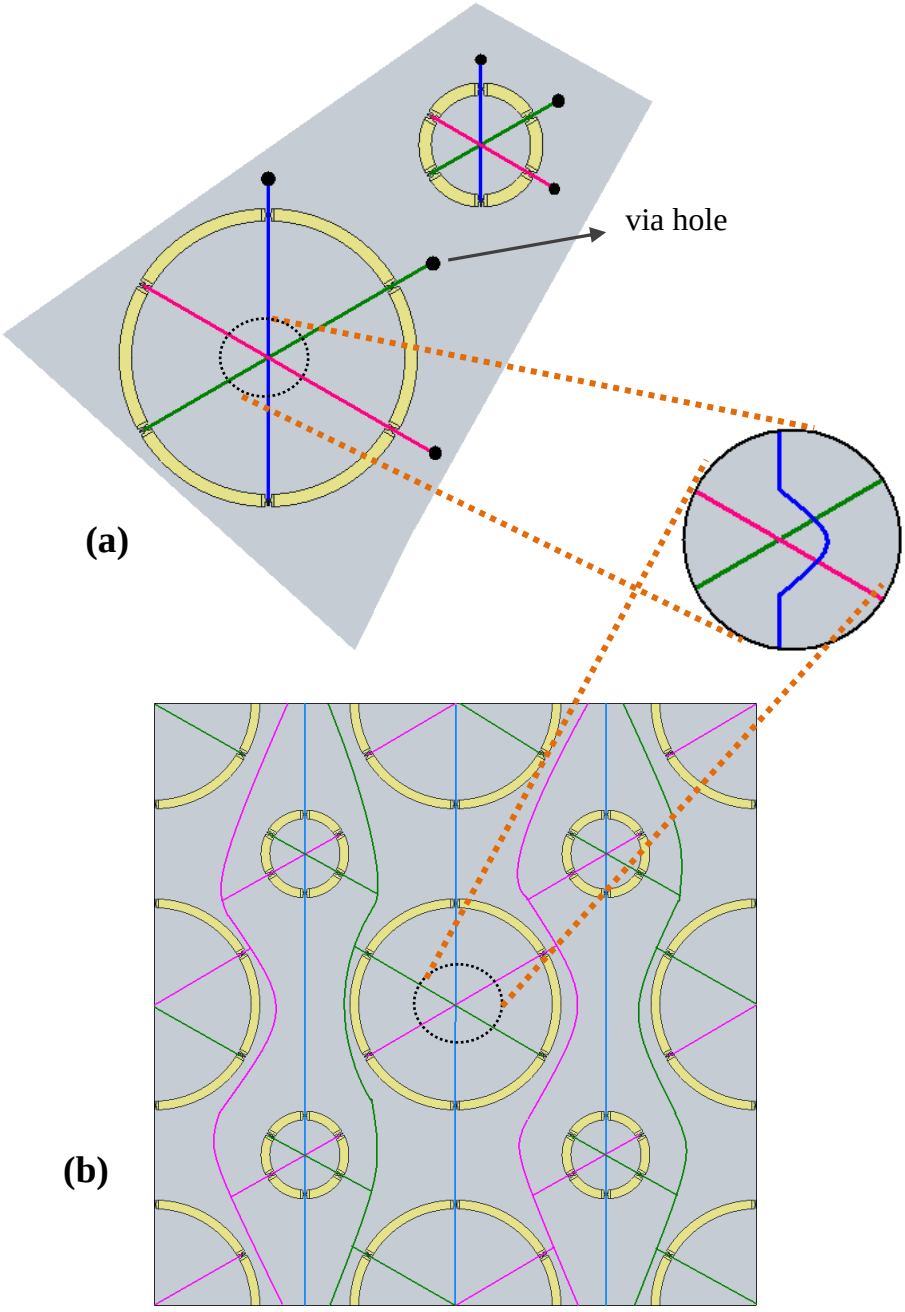

Figure 4.34 Two proposed biasing schemes.

4.3 Reflectarray Antenna Prototype

The full reflectarray antenna composing of the elements with the MEMS switches is the goal of the design. Beforehand designing and fabricating the full reflectarray antenna, it is essential to verify the concept in a prototype design. The prototype design is aimed to be simulated in HFSS and then fabricated, measured and compared to the simulations. Due to the long time requirements and high memory costs, to validate the design the reflectarray element integrated with RF MEMS, in a reflectarray antenna is not preferred. Also in the simulations of the reflectarray antenna, the aspect ratio of the metallization on the antenna surface is of high importance, for the meshing, thus the time increases drastically depending on the mesh detail. This is the reason that the prototype design of the reflectarray antenna utilizes the reflectarray element in Section 4.2.2. This element's fabrication is a simple base metal process available in METU MEMS Center. The on and off MEMS switches are modeled as perfect short and open.

The two RHCP horns at Ka and K bands available in METU mm-Wave Laboratories are taken as the illumination horns. The feed horn antennas are placed at their far-field distances with a 30° deviation from the normal of the wafer (antenna). The designed antenna is offset-fed; the elements are printed onto a 4-in. quartz wafer. The reflectarray elements have 3 states for each frequency, with phase resolution of 120°. These elements are combined in a manner that 3 states have progressive phase difference of 120° and -120° for steered beam and 0° for the broad-side.

The prototype is not reconfigurable; instead two antennas for the 0° and 120° progressive phase difference in y-direction (Figure 4.35) are fabricated with base-metal surface micromachining. The beam is steered on the YZ-plane. The reflect array antenna is composed of 109 and 124 elements respectively in Ka and K bands.

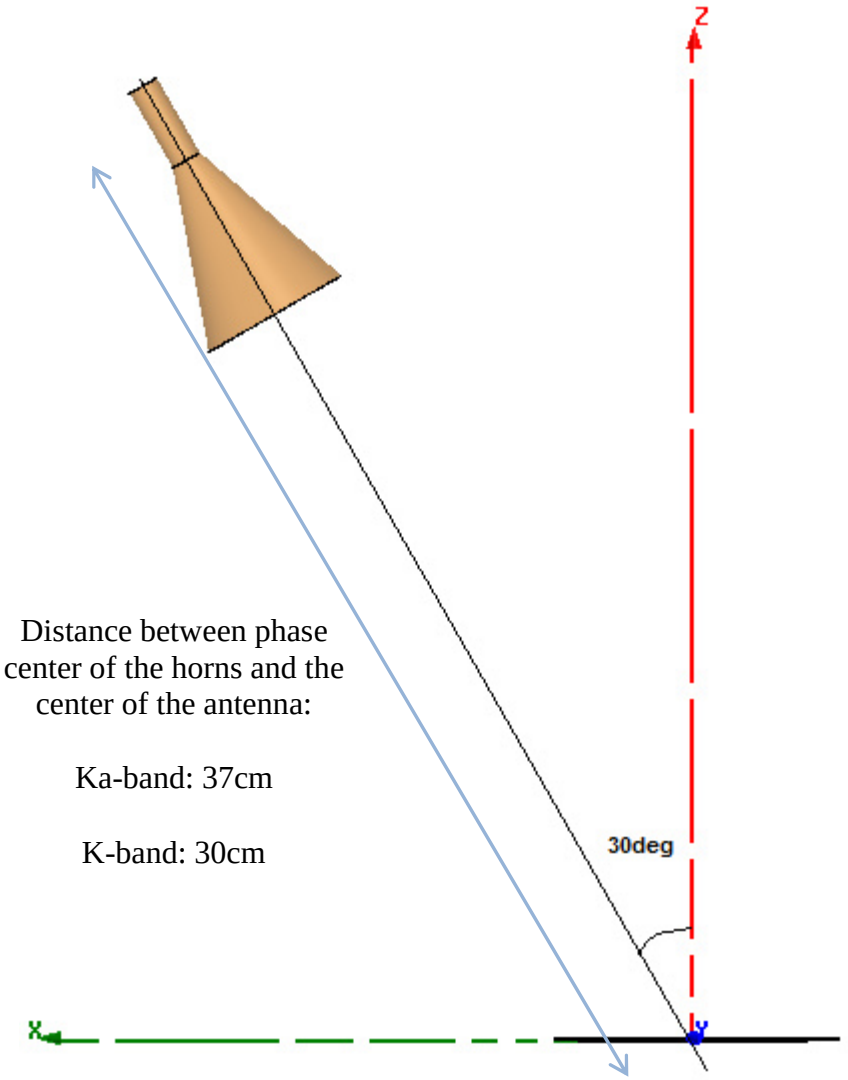

Figure 4.35 Horn placement.

4.3.1 Phase Compensation over the Reflectarray Antenna

The illumination phases due to the path differences between the illumination horn's phase center and the reflectarray elements, creates a phase distribution over the reflectarray surface. This phase is computed using the point source approach, and the split-rings in the broad-side state are put with an off-set angle to compensate the illumination phase and constitute a uniform phase distribution all over the reflectarray antenna. In the steered state, the elements are rotated to sustain 120°

progressive phase difference.

The phase of the incident field in front of elements is given as

$$\Phi_{incidence} = (x_{horn} - x_{elem.})^2 + (y_{horn} - y_{elem.})^2 + (z_{horn} - z_{elem.})^2 / \lambda_0 \qquad (4.1)$$

This phase can be compensated by rotation of split-rings in proper angles, knowing that the phase of an RHCP wave is linearly dependent on 2*ψ (ψ: rotation angle of the split-ring). By this method the phase difference between all the elements on the antenna are set to 0. The broad-side antenna prototype creates an equiphase plane upon reflection, perpendicular to the antenna normal.

4.3.2 Illumination Horn Placement

The horn antennas at K (24.4GHz) and Ka (35.5 GHz) bands are put with 30° oblique incidence respectively at 37cm and 30cm to maintain the far field condition and prevent the horns from obscuring the beam-steering plane (YZ) in Figure 4.35.

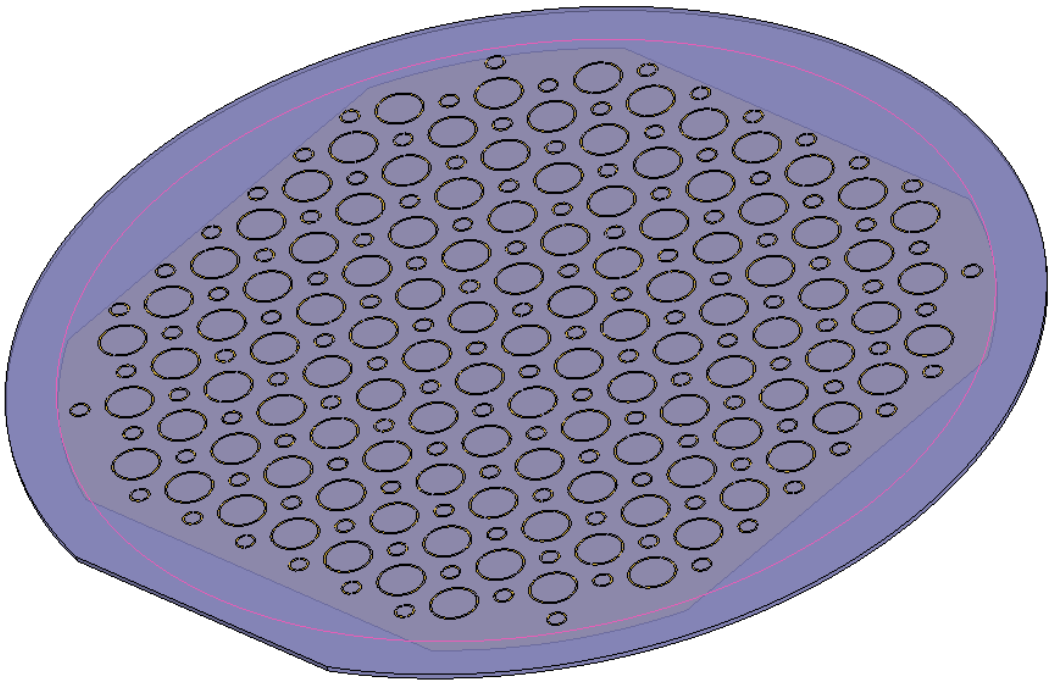

Figure 4.36 Overall view of the simulated reflectarray antenna.

4.3.3 Simulation Results of The Reflectarray Antenna

The antenna prepared for simulation and fabrication can be observed in Figure 4.36. The reflectarray is simulated with given horn distance and offset angle. Two designs have been employed to simulate and fabricate the broad-side and steered beam states with 120° progressive phase shift at 24.4 GHz and 35.5 GHz.

The simulations are done by building the horns and the reflectarray antenna in HFSS 3D modeler. The horns are simulated independently and far field link property in HFSS is utilized to simulate their illumination on the reflectarray antenna. This method forms the far field wave in a simulation set-up then applies it as incident field into another simulation. The simulations lasted more than 5 hr for a 4-inch reflectarray antenna in a 8GB RAM and 2.4GHz Core2 computer, but the high mesh number was reached before meeting the error energy below 10^{-3}.

Note that the element was 0.8λ spaced in higher frequency and 0.6λ spaced in lower frequency. The higher frequency is prone to high grating lobe levels. Anyway, the magnitude tapering naturally acquired from the horns and the frequency response degradation due to oblique incidence is thought to overcome the problem.

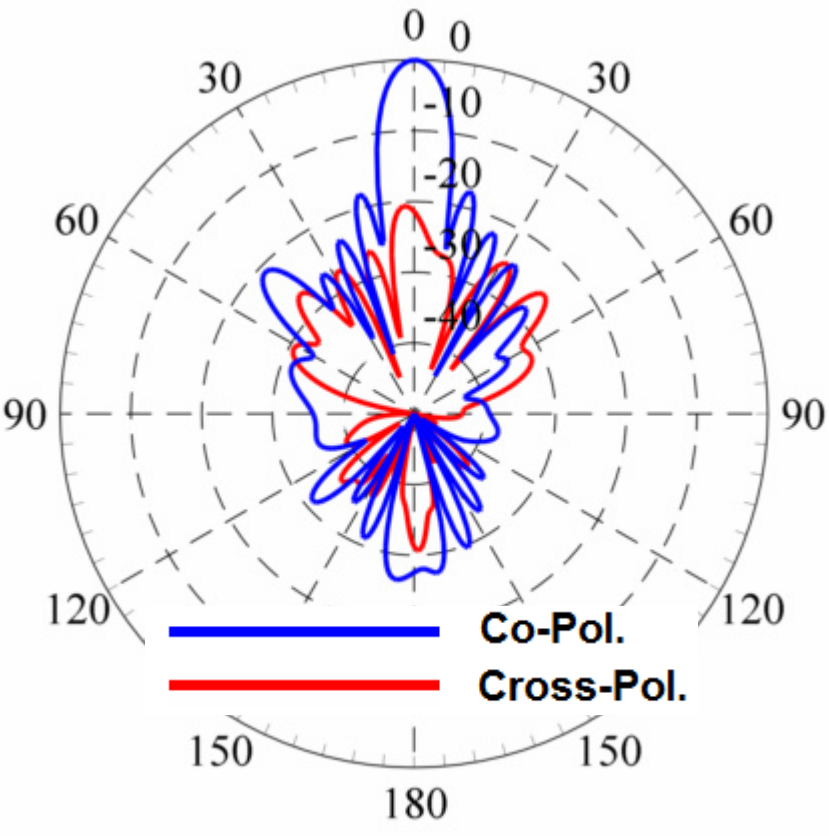

Figure 4.37 The radiation pattern at 24.4GHz, broad-side state.

The radiation patterns of the simulated reflectarray antenna in broad-side configuration at 24.4 GHz are given in Figure 4.37. It is observed that the phase compensation is accurate, the cross-pol. is suppressed as good as 20dB. Side-lobes are in -20dB and back-lobe levels are in -30dB.

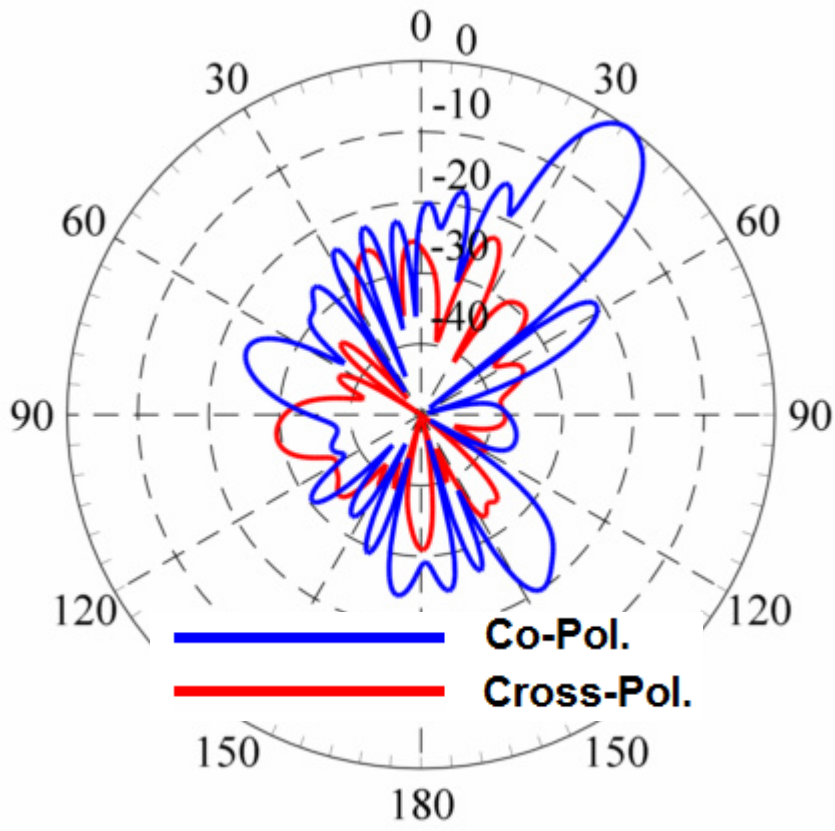

Figure 4.38 The radiation pattern at 24.4GHz frequency, steered-beam state.

The radiation patterns of the simulated reflectarray antenna in steered-beam configuration at 24.4 GHz are given in Figure 4.38. It is seen that the main beam is steered to 35° as expected. The cross-pol. is suppressed as good as 20dB. Side-lobe level is again preserved to be -20dB and back-lobe radiation is negligible.

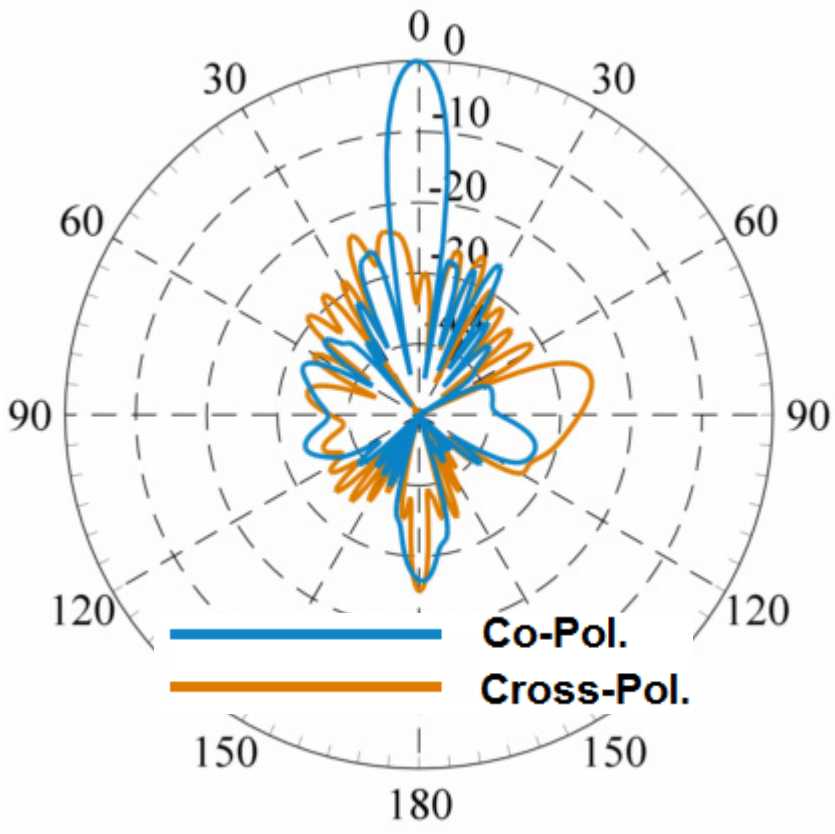

Figure 4.39 The radiation pattern at 35.5 GHz, broad-side state.

The radiation patterns of the simulated reflectarray antenna in broad-side configuration at 35.5 GHz are given in Figure 4.39. It is observed that the phase compensation is accurate thus the main beam points the broadside direction, the cross-pol. is suppressed as good as 20dB. Side-lobe level and back-lobe radiation are in the level of -20dB.

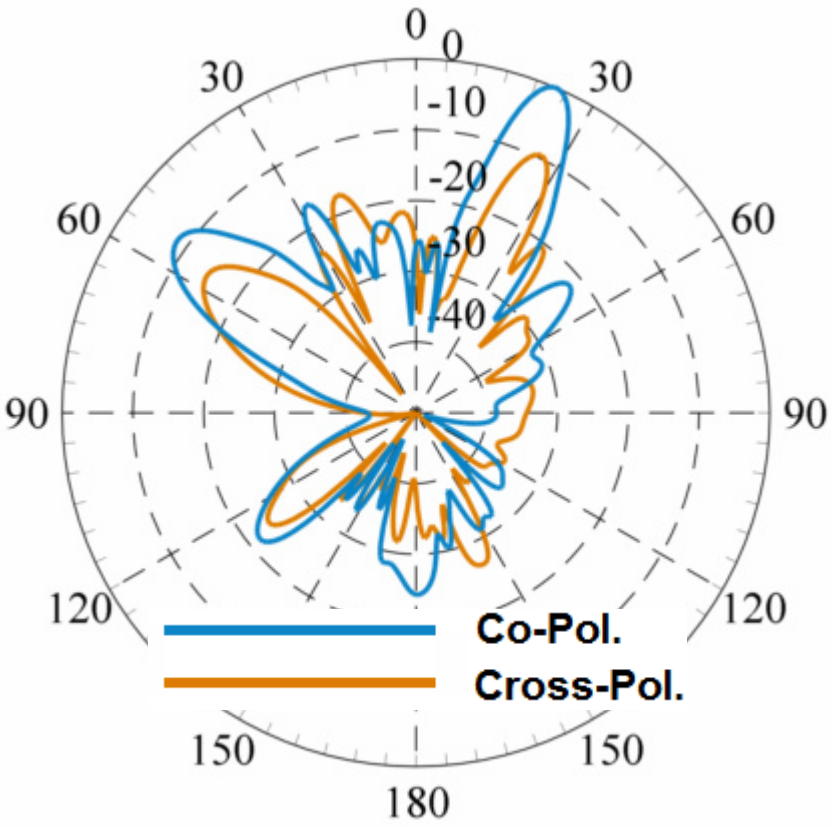

Figure 4.40 The radiation pattern at 35.5 GHz, steered-beam state.

The radiation patterns of the simulated reflectarray antenna in steered-beam configuration at 35.5 GHz are presented in Figure 4.40. It is observed that the main beam is steered to 24°. The cross-pol. is suppressed in levels of 10dB, which is not sufficient. The grating lobe emerged around 58 degrees at -10dB level. The performance of the antenna at higher frequency is not as desired.

4.3.4 Measurement Setup and Radiation Patterns

The radiation patterns of the antenna have been measured in the anechoic chamber of Department of Electrical and Electronics Engineering in METU. The measurement setup is composed of a linear rectangular horn antenna in the transmitting side, and

the designed reflectarray antenna at the receiving end, as seen in Figure 4.41.

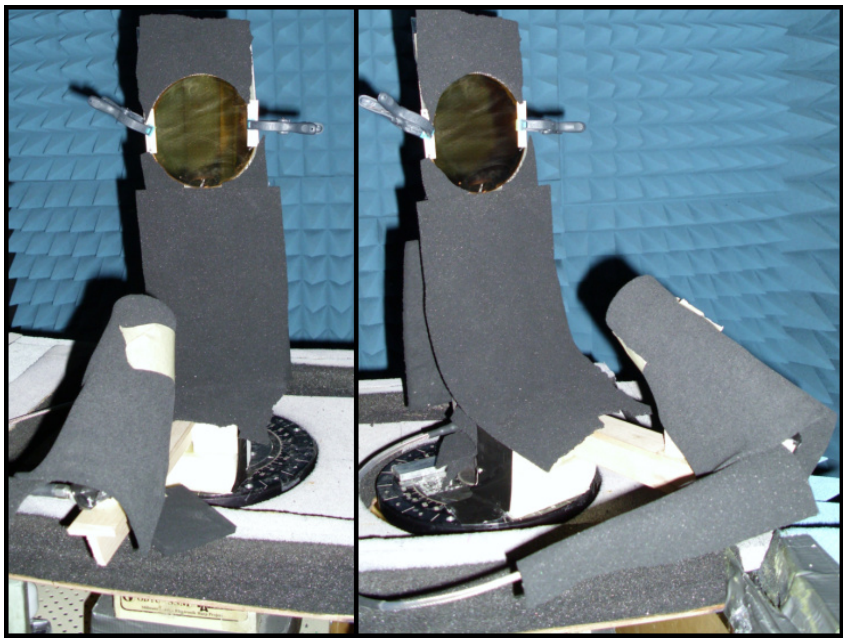

Figure 4.41 Reflectarray antenna and the illumination horn in the anechoic chamber.

It is evident that measurement of co- and cross-polarized components is not possible with this setup. What is measured using this setup can be well understood with the reciprocity theorem. The simulations were done for reflectarray antennas under circularly polarized wave, and the reception was both computed in co- and cross-polarized components. The reciprocity theorem implied that, if the illumination antenna of the reflectarray was linearly polarized and the antenna on the transmitting side of the setup was circularly polarized; the results would be intact. The equivalent case is the case that the cross- and co-polarized components in the simulation results are summed up to give the linear component. In another saying, the results found in the measurement setup include the cross-polarized component along with the desired co-polarized component. The simulation results are mathematically elaborated to be compared to the measurement results, according to the measurement setup. Only measurements of the fabricated switched beam prototype are available.

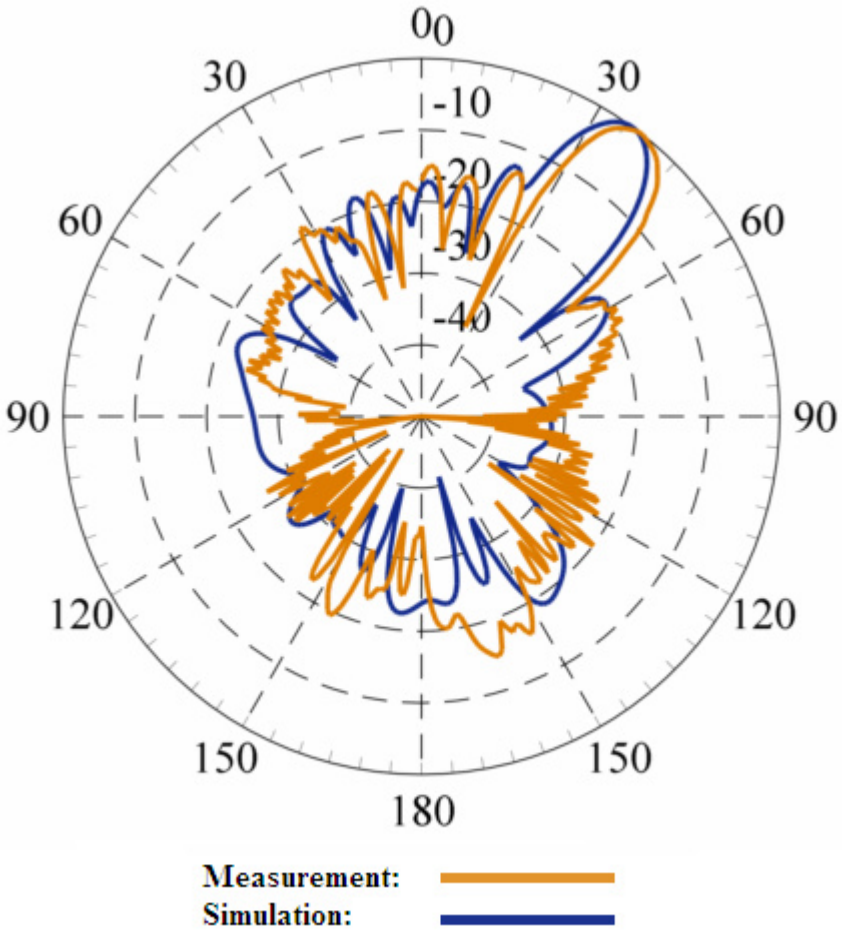

Figure 4.42 Comparison of simulation and measurements of normalized radiation pattern at 24.4 GHz.

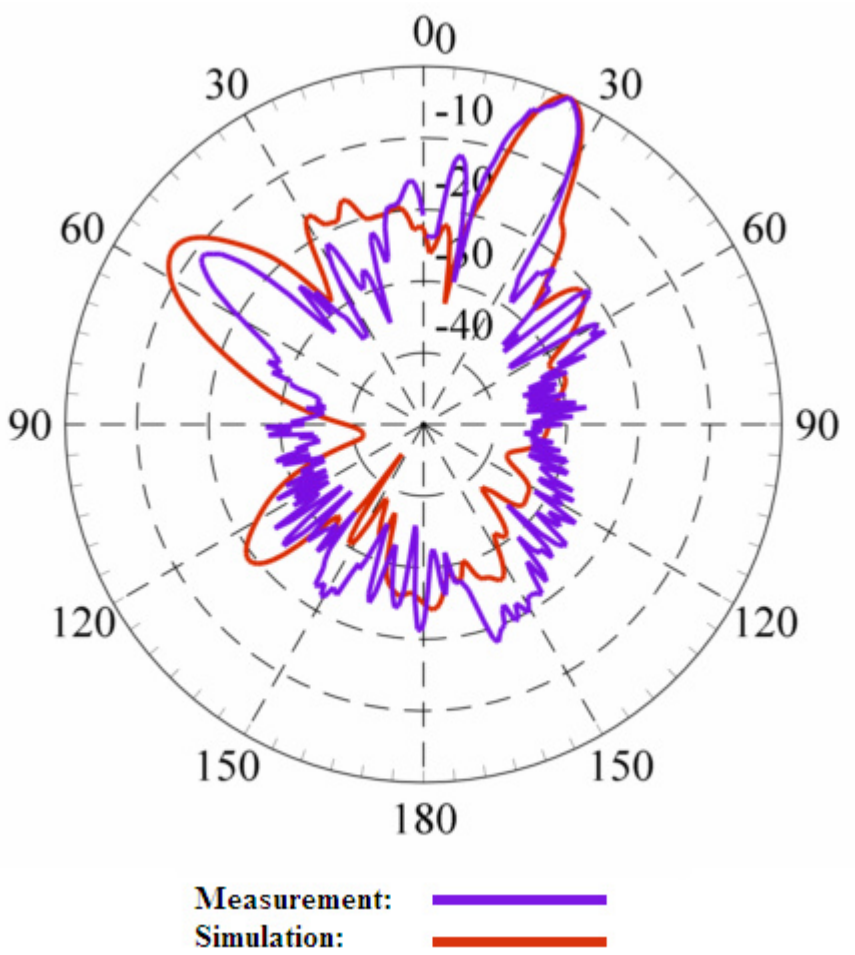

Figure 4.43 Comparison of simulation and measurements of normalized radiation pattern at 35.5 GHz.

The simulation and measurement results are consistent for the radiation patterns of the switched beam prototype. Figure 4.42 and Figure 4.43 show that the beam directions are in good agreement. One should keep in mind that the measurement setup is prone to errors in 1°-2° range. The simulation and measurement results prove the antenna design principles.

4.4 Conclusion

In this section, the dual band reflectarray element is designed and characterized in

various aspects. It is integrated with RF MEMS switches. Finally a reflectarray antenna prototype composing of the designed elements is simulated, the radiation patterns are given. The measurement results of the fabricated prototype are compared with those of the simulations.

CHAPTER 5

CONCLUSIONS AND FUTURE WORK

5.1 Conclusions

In this thesis, a circularly polarized reconfigurable reflectarray antenna capable of dual frequency operation is presented. The reflectarray antenna element was chosen to be split-rings on 0.5mm-thick quartz (ε_R=3.78) substrate over 0.6mm-thick air layer by a ground plane. The split-rings of two sizes were employed for independent operation in dual frequency. The rotational phase shift mechanism was used as the phase control technique which states that the reflection phase of a circularly polarized wave can be controlled by rotating the reflective element. When a circularly polarized wave is incident on a reflective element, the phase of the reflected wave with the same sense of circular polarization is linearly dependent on the physical angular position with a slope of 2. The realization of this principle to design a reconfigurable element was done with RF MEMS series ohmic contact switches. 6 switches were placed on a ring with 60° spacing. These were grouped into 3 pairs where a pair is composed of two switches on the same diameter. The split-ring is such realized with 3 pairs of switches when at each state only one pair is off. This corresponds to a 120° phase resolution between states in both bands. Such two rings with different sizes, on which there are 6 switches, are placed with an interleaved planar array design. These elements are used to design a reflectarray antenna on a 4in. quartz wafer. The conceptual design of the reflectarray was tested by a prototype antenna. The prototype antenna was design by modeling the RF MEMS switches in on and off states with short and open metallization. This antenna had 109 split-rings operating in Ka band and 124 split-rings operating in K band.

Each ring on the antenna is rotated by an initial offset angle to compensate for the phase difference emerging from different path lengths between the antenna plane and the feed horn. Thus the designed antenna in its 0-state directs the beam in the normal direction for both operation frequencies. And for the switched beam states, there is a ±120° progressive phase difference between elements. It is capable of beam switching to ±35° in Ka band, ±24° in K band.

The starting point was to mathematically derive the expression for the rotational phase shift principle. This derivation provided the in-depth interpretation of the principle that cross-polarization should be suppressed upon incidence for high gained and the incident field should be a perfect circularly polarized wave. Then a single frequency reflectarray antenna element composed of a split-ring was designed using unit cell approach. The rotational phase shift mechanism was thus proven with this element. The experience acquired from the single frequency element was transferred to the dual frequency composition. The split-rings in two different sizes were put together in an interleaved array configuration. The dual frequency element was tuned to suppress cross-polarized wave in Ka and K bands. Then in these bands it was shown that each ring could control the phase in its corresponding frequency independently. The RF MEMS switches were integrated into the design for reconfigurability. The simulation of the element with 12 RF MEMS switches was time consuming, for better and faster results the RF MEMS switches are modeled using impedance boundary conditions. Dual frequency element with RF MEMS switches is shown to control the reflection phase linearly over 360° phase range. The reflectarray prototype is simulated in HFSS, the results are presented. The radiation pattern measurements of fabricated prototype are shown to be in good agreement with the simulation results.

The designed element shows that the split-ring structure is a good option to be employed for dual band operation with circularly polarized waves. In addition the phase control mechanism by rotating the split-rings can be realized with RF MEMS technology. The simulations and the measurement results shows that the design

elements can be brought together in a straight forward manner to build a reflectarray antenna, and the antenna works as expected.

5.2 Future Work

The effort put forward in order to realize the novel dual band reconfigurable reflectarray antenna aimed in this thesis showed that the topology is capable of providing the desired quality. In the guidance of the analysis experience of this thesis and the results of the reflectarray prototype, the future works can be listed as follows:

- A monolithic fabrication with RF MEMS switches should be accomplished to present a novel and fully functioning reflectarray antenna.
- A larger antenna can provide narrower beam and lower spill-over and side lobes with a natural tapering.
- To increase the phase resolution, the number of states should be increased. This means more RF MEMS on the antenna. The yield and bias line routing solutions may be developed to achieve this.
- For an element-wise enhancement, the cross-pol. suppression bandwidth should be increased for better performance. This can increase the gain with reduced cross-pol. reflection contributing to the specular reflection.
- Different reflectarray cell configurations of split-rings can be tested to decrease the coupling and achieve a smaller element size to avoid the grating lobes.
- Different switch types may be implemented in the gaps of the split-rings to compare the performance of various reconfigurability choices.

As a result, the experience gained during the design, fabrication and measurement is a valuable contribution to the reconfigurable antenna, dual band antennas and the reflectarray antenna areas. The abilities of similar structures in reflectarray antennas can be studied further. Today's technology which drives the future of humanity towards the wireless communication systems makes it important to achieve

reconfigurable low profile antennas with low cost. This study and the results shown therein can be adopted to build high-end antennas as well as to define the necessary future tools to improve the reflectarray antenna design.

REFERENCES

[1] H. Phelan, "Spiraphase reflectarray for multitarget radar," *Microwave Journal,* vol. 20, p. 67, 1977.

[2] D. Berry, *et al.*, "The reflectarray antenna," *Antennas and Propagation, IEEE Transactions on,* vol. 11, pp. 645-651, 1963.

[3] C. Malagisi, "Microstrip disc element reflect array," in *Electronics and Aerospace Systems Convention*, 1978, pp. 186-192.

[4] D. M. Pozar and T. A. Metzler, "Analysis of a reflectarray antenna using microstrip patches of variable size," *Electronics Letters,* vol. 29, pp. 657-658, 1993.

[5] M. E. Bialkowski and K. H. Sayidmarie, "Investigations Into Phase Characteristics of a Single-Layer Reflectarray Employing Patch or Ring Elements of Variable Size," *Antennas and Propagation, IEEE Transactions on,* vol. 56, pp. 3366-3372, 2008.

[6] A. Kelkar, "FLAPS: conformal phased reflecting surfaces," in *Radar Conference, 1991., Proceedings of the 1991 IEEE National*, 1991, pp. 58-62.

[7] J. A. Encinar, "Design of two-layer printed reflectarrays using patches of variable size," *Antennas and Propagation, IEEE Transactions on,* vol. 49, pp. 1403-1410, 2001.

[8] J. A. Encinar and J. A. Zornoza, "Broadband design of three-layer printed reflectarrays," *Antennas and Propagation, IEEE Transactions on,* vol. 51, pp. 1662-1664, 2003.

[9] T. Metzler and D. Schaubert, "Scattering from a stub loaded microstrip antenna," in *Antennas and Propagation Society International Symposium, 1989. AP-S. Digest,* 1989, pp. 446-449 vol.1.

[10] A. W. Robinson, *et al.*, "An X-band passive reflect-array using dual-feed aperture-coupled patch antennas," in *Microwave Conference, 1999 Asia Pacific*, 1999, pp. 906-909 vol.3.

[11] E. Carrasco, *et al.*, "Aperture-coupled reflectarray element with wide range of phase delay," *Electronics Letters,* vol. 42, pp. 667-668, 2006.

[12] M. E. Bialkowski, *et al.*, "Design, development, and testing of X-band amplifying reflectarrays," *Antennas and Propagation, IEEE Transactions on,* vol. 50, pp. 1065-1076, 2002.

[13] O. Bayraktar, *et al.*, "Beam switching reflectarray with MEMS controls," in *Antennas and Propagation (EuCAP), 2010 Proceedings of the Fourth European Conference on*, 2010, pp. 1-4.

[14] O. Bayraktar, *et al.*, "Beam Switching Reflectarray using RF MEMS Technology," in *Antennas and Propagation, 2007. EuCAP 2007. The Second European Conference on*, 2007, pp. 1-6.

[15] O. Bayraktar, "Beam Switching Reflectarray with RF MEMS Technology," MS., Institute of Natural Sciences, Middle East Technical University, Ankara, 2007.

[16] J. Huang and R. J. Pogorzelski, "Microstrip reflectarray with elements having variable rotation angles," in *Antennas and Propagation Society International Symposium, 1997. IEEE., 1997 Digest*, 1997, pp. 1280-1283 vol.2.

[17] B. Subbarao, *et al.*, "Element suitability for circularly polarised phase agile reflectarray applications," *Microwaves, Antennas and Propagation, IEE Proceedings -*, vol. 151, pp. 287-292, 2004.

[18] H. Chulmin and C. Kai, "Ka-band reflectarray using ring elements," *Electronics Letters*, vol. 39, pp. 491-493, 2003.

[19] C. Han, *et al.*, "A C/Ka dual frequency dual Layer circularly polarized reflectarray antenna with microstrip ring elements," *Antennas and Propagation, IEEE Transactions on*, vol. 52, pp. 2871-2876, 2004.

[20] A. E. Martynyuk, *et al.*, "Spiraphase-type reflectarrays based on loaded ring slot resonators," *Antennas and Propagation, IEEE Transactions on*, vol. 52, pp. 142-153, 2004.

[21] B. Strassner, *et al.*, "Circularly polarized reflectarray with microstrip ring elements having variable rotation angles," *Antennas and Propagation, IEEE Transactions on*, vol. 52, pp. 1122-1125, 2004.

[22] D. F. Sievenpiper, *et al.*, "Two-dimensional beam steering using an electrically tunable impedance surface," *Antennas and Propagation, IEEE Transactions on*, vol. 51, pp. 2713-2722, 2003.

[23] J. Perruisseau-Carrier, "Dual-Polarized and Polarization-Flexible Reflective Cells With Dynamic Phase Control," *Antennas and Propagation, IEEE Transactions on*, vol. 58, pp. 1494-1502, 2010.

[24] R. Romanofsky, *et al.*, "A K-band linear phased array antenna based on $Ba_{0.60}Sr_{0.40}TiO_3$ thin film phase shifters," in *Microwave Symposium Digest., 2000 IEEE MTT-S International*, 2000, pp. 1351-1354 vol.3.

[25] A. Moessinger, *et al.*, "Electronically reconfigurable reflectarrays with nematic liquid crystals," *Electronics Letters*, vol. 42, pp. 899-900, 2006.

[26] R. R. Romanofsky, "Advances in Scanning Reflectarray Antennas Based on Ferroelectric Thin-Film Phase Shifters for Deep-Space Communications," *Proceedings of the IEEE*, vol. 95, pp. 1968-1975, 2007.

[27] R. Marin, *et al.*, "Realization of 35 GHz Steerable Reflectarray using Highly Anisotropic Liquid Crystal," in *Antennas and Propagation Society International Symposium 2006, IEEE*, 2006, pp. 4307-4310.

[28] A. Moessinger, *et al.*, "Investigations on 77 GHz tunable reflectarray unit cells with liquid crystal," in *Antennas and Propagation, 2006. EuCAP 2006. First European Conference on*, 2006, pp. 1-4.

[29] J. Perruisseau-Carrier and A. K. Skrivervik, "Monolithic MEMS-Based Reflectarray Cell Digitally Reconfigurable Over a 360° Phase Range," *Antennas and Wireless Propagation Letters, IEEE*, vol. 7, pp. 138-141, 2008.

[30] J. P. Gianvittorio and Y. Rahmat-Samii, "Reconfigurable patch antennas for steerable reflectarray applications," *Antennas and Propagation, IEEE Transactions on*, vol. 54, pp. 1388-1392, 2006.

[31] H. Rajagopalan, *et al.*, "RF MEMS Actuated Reconfigurable Reflectarray Patch-Slot Element," *Antennas and Propagation, IEEE Transactions on*, vol. 56, pp. 3689-3699, 2008.

[32] S. V. Hum, *et al.*, "Integrated mems reflectarray elements," in *Antennas and Propagation, 2006. EuCAP 2006. First European Conference on*, 2006, pp. 1-6.

[33] H. Legay, *et al.*, "A steerable reflectarray antenna with MEMS controls," in *Phased Array Systems and Technology, 2003. IEEE International Symposium on*, 2003, pp. 494-499.

[34] R. Sorrentino, "Reconfigurable reflectarrays based on RF MEMS technology," in *Microwaves, Radar and Remote Sensing Symposium, 2008. MRRS 2008*, 2008, pp. 16-21.

[35] J. Huang, "Bandwidth study of microstrip reflectarray and a novel phased reflectarray concept," in *Antennas and Propagation Society International Symposium, 1995. AP-S. Digest*, 1995, pp. 582-585 vol.1.

[36] WANG, *et al.*, *Generalised moment methods in electromagnetics* vol. 137. Stevenage, ROYAUME-UNI: Institution of Electrical Engineers, 1990.

[37] K. Topalli, *et al.*, "A Monolithic Phased Array Using 3-bit Distributed RF MEMS Phase Shifters," *Microwave Theory and Techniques, IEEE Transactions on*, vol. 56, pp. 270-277, 2008.

[38] G. M. Rebeiz and J. B. Muldavin, "RF MEMS switches and switch circuits," *Microwave Magazine, IEEE*, vol. 2, pp. 59-71, 2001.

[39] C. Cetintepe, "Development of MEMS Technology Based Microwave and Millimeter-Wave Components," MSc, Electrical - Electronics Eng., Middle East Technical University (METU), Ankara, 2010.

[40] H. Sedaghat-Pisheh, *et al.*, "A Novel Stress-Gradient-Robust Metal-Contact Switch," in *Micro Electro Mechanical Systems, 2009. MEMS 2009. IEEE 22nd International Conference on*, 2009, pp. 27-30.

[41] J. Perruisseau-Carrier, *et al.*, "Contributions to the Modeling and Design of Reconfigurable Reflecting Cells Embedding Discrete Control Elements," *Microwave Theory and Techniques, IEEE Transactions on,* vol. 58, pp. 1621-1628, 2010.

BEAM STEERABLE MEANDERLINE ANTENNA USING VARACTOR DIODES AND RECONFIGURABLE ANTENNA DESIGNS BY MEMS SWITCHES

A THESIS SUBMITTED TO
THE GRADUATE SCHOOL OF NATURAL AND APPLIED SCIENCES
OF
MIDDLE EAST TECHNICAL UNIVERSITY

BY

NİHAN GÖKALP

IN PARTIAL FULFILLMENT OF THE REQUIREMENTS
FOR
THE DEGREE OF MASTER OF SCIENCE
IN
ELECTRICAL AND ELECTRONICS ENGINEERING

AUGUST 2008

Approval of the thesis:

BEAM STEERABLE MEANDERLINE ANTENNA USING VARACTOR DIODES AND RECONFIGURABLE ANTENNA DESIGNS BY MEMS SWITCHES

submitted by **NİHAN GÖKALP** in partial fulfillment of the requirements for the degree of **Master of Science in Electrical and Electronics Engineering Department, Middle East Technical University** by,

Prof. Dr. Canan Özgen
Dean, Graduate School of **Natural and Applied Sciences** _____

Prof. Dr. İsmet Erkmen
Head of Department, **Electrical and Electronics Engineering** _____

Assoc. Prof. Dr. H. Özlem Aydın Çivi
Supervisor, **Electrical and Electronics Eng. Dept., METU** _____

Examining Committee Members:
Prof. Dr. Altunkan Hızal
Electrical and Electronics Engineering Dept., METU _____

Assoc. Prof. Dr. H. Özlem Aydin Çivi
Electrical and Electronics Engineering Dept., METU _____

Assoc. Prof. Dr. Şimşek Demir
Electrical and Electronics Engineering Dept., METU _____

Asst. Prof. Dr. Lale Alatan
Electrical and Electronics Engineering Dept., METU _____

(M.S.) M.Erim İnal
ASELSAN _____

Date: 22.08.2008

I hereby declare that all information in this document has been obtained and presented in accordance with academic rules and ethical conduct. I also declare that, as required by these rules and conduct, I have fully cited and referenced all material and results that are not original to this work.

Name, Last name : Nihan GÖKALP

Signature :

ABSTRACT

BEAM STEERABLE MEANDERLINE ANTENNA USING VARACTOR DIODES AND RECONFIGURABLE ANTENNA DESIGNS BY MEMS SWITCHES

GÖKALP, Nihan

M.S., Department of Electrical and Electronics Engineering
Supervisor : Assoc. Prof. Dr. H. Özlem AYDIN ÇİVİ

August 2008, 114 pages

Recently, reconfigurable antennas have attracted significant interest due to their high adaptation with changing system requirements and environmental conditions. Reconfigurable antennas have the ability to change their radiation pattern, frequency or polarization independently according to the application requirements.

In this thesis, three different reconfigurable antenna structures have been designed; beam-steerable meanderline antenna, dual circularly polarized meanderline antenna and dual-frequency slot-dipole array. Traveling wave meanderline antenna arrays are investigated in detail and a beam-steerable traveling wave meanderline antenna array has been introduced for X-band applications. Beam-steering capability of the antenna array has been achieved by loading the antenna elements with varactor diodes. Theoretical analysis and computer simulations of the proposed antenna have been verified with experimental results. Radiation direction of the 8-element meanderline

array can be rotated 10° by changing the varactor diode's bias voltage from 0V up to 20V. Also, a polarization-agile meanderline antenna array has been designed and simulated. Polarization of the circularly polarized meanderline array can be altered between right hand circularly polarized and left hand circularly polarized by using RF MEMS switches. The third type of reconfigurable antenna investigated in this thesis is a dual frequency slot-dipole array operating at X- and Ka-band. Electrical length of the slot dipoles has been tuned by using RF MEMS switches. Antenna prototypes have been manufactured for 'on' and 'off' states of RF MEMS switches and it has been shown that the operating frequency can be changed between 10 GHz and 15.4 GHz.

Keywords: Reconfigurable Antennas, Meanderline Antenna Arrays, Frequency Reconfigurable Antennas, Beam-Steerable Antennas, Polarization-Agile Antennas

ÖZ

VARAKTÖR DİYOTLU IŞIN HÜZMESİ YÖNLENDİRİLEBİLEN SUR BİÇİMLİ ANTEN VE MEMS ANAHTARLARLA AYARLANABİLİR ANTEN TASARIMLARI

GÖKALP, Nihan

Yüksek Lisans, Elektrik ve Elektronik Mühendisliği Bölümü

Tez Yöneticisi : Doç. Dr. H. Özlem AYDIN ÇİVİ

Ağustos 2008, 114 sayfa

Günümüzde, ayarlanabilir antenler değişen sistem ihtiyaçlarına ve çevre koşullarına yüksek uyumlulukları nedeniyle ilgi çekmektedir. Ayarlanabilir antenler uygulama gereksinimlerine göre ışınım huzmelerini, frekanslarını ve polarizasyonlarını bağımsız olarak değiştirme yeteneğine sahiptir.

Bu tezde, üç farklı ayarlanabilir anten yapısı tasarlanmıştır; ışınım huzmesi yönlendirilebilen sur biçimli anten, polarizasyonu ayarlanabilen sur biçimli anten ve çift frekanslı yarık dipol anten dizisi. Sur biçimli yürüyen dalga antenler ayrıntılı biçimde incelenmiş ve X-bant uygulamaları için ışınım huzmesi yönlendirilebilen sur biçimli yürüyen dalga anten dizisi tanıtılmıştır. Anten dizisine ışınım huzmesi yönlendirme özelliği, anten elemanları varaktör diyotlarla yüklenerek kazandırılmıştır. Önerilen anten dizisi ile ilgili gerçekleştirilen kuramsal tahminler ve bilgisayar benzetimleri deneysel ölçümlerle doğrulanmıştır. Varaktör diyotlara 0V'tan 20V'ta kadar besleme voltajı uygulandığında, 8 elemanlı sur biçimli anten

dizisinin ışınım yönü 10° dönmektedir. Bununla beraber, polarizasyonu ayarlanabilen sur biçimli anten dizisi tasarlanmış ve EM benzetimleri yapılmıştır. RF MEMS anahtarlar kullanılarak, dairesel polarizasyonlu sur biçimli antenin polarizasyonu sağ el dairesel polarizasyon veya sol el dairesel polarizasyon olarak değişebilmektedir. Bu tezde incelenen üçüncü tip ayarlanabilir anten. X- ve Ka-bant uygulama frekansı ayarlanabilen yarık-dipol anten dizisidir. Yarık-dipol antenlerin elektriksel uzunlukları RF MEMS anahtarlar kullanılarak ayarlanabilmektedir. RF MEMS anahtarların açık ve kapalı durumları için anten örnekleri üretilmiş ve çalışma frekansının 10GHz ve 15.4 GHz olarak değiştiği gösterilmiştir.

Anahtar Kelimeler: Ayarlanabilen Antenler, Sur Biçimli Antenler, Frekans Ayarlanabilen Antenler, Işınım Huzmesi Yönlendirilebilen Antenler, Polarizasyon Ayarlanabilen Antenler

To My Family

ACKNOWLEDGMENTS

I would like to thank Assoc. Prof. Dr. Özlem Aydın Çivi for her valuable supervision, support and tolerance throughout the development and improvement of this thesis.

I am grateful to Ali Günay Yıldız, Erhan Halavut, Tuncay Erdöl, Hakan Paruldar and Tülay Can for their support throughout the development and the improvement of this thesis. I would like to extend my special appreciation and gratitude to Volkan Öznazlı and my family and for their encouragement and understanding of my spending lots of time on this work.

I am also grateful to Aselsan Electronics Industries Inc. for the resources and facilities that I use throughout thesis.

I would also like to thank Turkish Scientific and Technological Research Council (TÜBİTAK) for their financial assistance during my graduate study.

Thanks a lot to all my friends for their great encouragement and their valuable help to accomplish this work.

TABLE OF CONTENTS

LIST OF TABLES

LIST OF FIGURES

CHAPTER I

INTRODUCTION

Antennas are crucial components of many systems such as radars, wireless communication systems, and remote sensing applications. There are different types of antennas that could satisfy the requirements of systems. For instance, traveling wave antennas are very suitable for radar applications due to their high directivity and side lobe control capabilities. Most of the time, to satisfy various system requirements, different antenna configurations are needed. At the basic antenna concept point of view, different system configurations need different antennas or large antenna units. Reconfigurable antenna concept adapts the antenna units depending on system configurations. Reconfiguration in antennas decreases the size of antenna units in systems and increases the operational capability of the antenna. Depending on system requirements; frequency, radiation pattern or polarization reconfigurations can be accomplished using electrical and mechanical mechanisms. Besides, planar surfaces are required to mount electrical reconfiguration components. Hence, microstrip antennas are good candidates for reconfigurable antenna applications.

In this thesis, three different reconfigurable antenna structures have been studied; beam-steerable meanderline antenna, polarization-agile meanderline antenna and dual-frequency slot-dipole array. Beam-steerable microstrip traveling wave antennas with varactor diodes have been analyzed, manufactured and tested. In addition, a polarization-agile meanderline array with RF MEMS (Radio Frequency MicroElectroMechanical Systems) switches has been designed. Lastly, frequency reconfigurable slot-dipole array has been designed and prototype structures have been manufactured and measured.

A detailed investigation of reconfigurability in antennas is presented in Chapter 2. Frequency, radiation pattern and polarization reconfigurable antennas are described and some examples are given. Furthermore, advantages and disadvantages of different reconfiguration mechanisms and methods are discussed.

General features of microstrip traveling wave antennas are given in Chapter 3. Electrical properties of different types of microstrip traveling wave antennas are explained. Since the main focus of the thesis is meanderline arrays, rest of the chapter is devoted to this subject. Radiation characteristics of the meanderline antenna are examined using different approaches and design parameters of meanderline array are obtained.

Chapter 4 describes design, simulation and measurement of the linearly polarized meanderline array operating at 10 GHz. According to design specifications, using commercial electromagnetic analysis tools Ansoft Designer and Ansoft HFSS, S-parameters, radiation pattern and surface current distributions of the meanderline array have been examined. Afterwards, the designed array has been manufactured and its S-parameters and radiation pattern have been measured. Measurement results in comparison with simulations are presented.

Chapter 5 presents a beam-steerable meanderline array operating at 10 GHz. In order to steer the beam to the specified direction, varactor diodes are employed on meanderline sections. Meanderline array loaded with varactor diodes has been manufactured. S-parameters and radiation pattern of the beam-steerable meanderline array have been measured at operating frequency.

In order to achieve more beam-steering, reflective type phase shifting mechanisms is proposed. Reflective type phase shifter is composed of a 3-dB branch-line coupler loaded with varactor diodes. This type of phase shifter has more phase tuning range than a single varactor diode. Analysis and simulations of meanderline array reflective type phase shifter are presented in this chapter.

A dual circularly polarized meanderline array is proposed in Chapter 7. Polarization of the proposed antenna can be altered by using SPDT (Single Pole Double Throw) RF MEMS switches between LHCP and RHCP.

A frequency reconfigurable slot dipole antenna array operating at X- and Ka- band is given in Chapter 7. Dual frequency operation of the slot dipole antennas is accomplished using SPST RF MEMS switches. MEMS switches are placed on the slot dipoles and electrical length of the dipoles changes with MEMS switches. Comparison of simulations and measurements is presented.

CHAPTER 2

RECONFIGURABLE ANTENNAS

Reconfigurable antennas have many advantages over traditional antenna elements and systems such as decreasing the size of the antenna units and increasing the degree of freedom in systems. Due to these benefits, reconfigurable antennas become more popular in many RF/microwave systems. Two different application areas can be considered while examining the functionality of the reconfigurable antennas. First application area is antenna arrays. Traditional antenna arrays have limited scan angle and frequency due to unit array elements. Unit elements of the array have fixed operating frequency and radiation pattern. Therefore, reconfigurability of the array unit elements enhances the operating frequency range of the array and beam scan angle. In addition to these, antenna arrays with fixed scan angle can be beam steerable with the advantage of reconfigurability. Second application area is portable wireless devices such as; cellular phones. These devices could demand different operating frequencies, diversity in transmission and reception. These properties can be satisfied by using different antennas in one system but due to size limitations of portable devices usually it is not desired. Main and effective solution to frequency and pattern reconfiguration is reconfigurable antennas. It is possible to obtain frequency or pattern reconfigurability by using reconfigurable antennas, also; the reconfigurability of the antennas increases the degree of freedom in the systems.

On the other hand, addition of the reconfigurability to the antenna units, increases complexity, requires signal processing and feedback circuitry. Reconfigurable antennas have more complicated fabrication processes compared to the traditional antennas.

In this chapter, first reconfigurability of the antenna's fundamental electrical

characteristics will be investigated and different reconfiguration mechanisms will be presented.

2.1 Reconfigurability for Antenna Elements

Antenna reconfigurability can be defined as the capacity to change the fundamental operating characteristics of the unit antenna element by means of electrical or mechanical [1]. For instance phasing of signals in an array in order to achieve beam forming or beam steering does not make the antenna reconfigurable because it does not change the fundamental electrical or mechanical characteristics of the antenna such as frequency response, radiation pattern etc. In addition to these if the antenna is said to be reconfigurable while its one of the electrical parameters changes, its other parameters should be kept constant.

Generally antennas are characterized with their input impedance characteristic over frequency (typically called the frequency response) and the radiation characteristic (or radiation pattern). Furthermore radiation pattern has the information about polarization, beam width, directivity, and beam scan angle of the antenna. Since the reconfigurability is the change of the fundamental operating characteristics, an antenna could be reconfigurable in frequency response, polarization or radiation pattern. In fact, radiation pattern is strongly correlated with frequency response in many antennas so there is a big challenge while constructing reconfigurable antennas. For example while designing a frequency reconfigurable antenna its radiation pattern should be identical for the entire band but it is not the case always. The following sections describe frequency response, polarization and radiation pattern reconfigurability of the antennas.

2.1.1 Frequency Reconfiguration

Frequency response of the antenna can be defined as its input impedance as a function of frequency. Antenna input impedance can be used to determine the

reflection coefficient (Γ) and related parameters, such as voltage standing wave ratio (VSWR) and return loss (RL), as function of frequency as given.

$$\Gamma = \frac{Z_{in}(\omega) - Z_0}{Z_{in}(\omega) + Z_0} \quad \textbf{(2.1)}$$

$$VSWR = \frac{1 + |\Gamma|}{1 - |\Gamma|} \quad \textbf{(2.2)}$$

$$RL = 20\log|\Gamma| \quad (dB) \quad \textbf{(2.3)}$$

where $\omega = 2 * \pi * f$

Z_{in}: Input impedance of the antenna,

Z_0: Characteristic impedance,

f: Operating frequency of the antenna.

Therefore in order to tune or reconfigure the antenna element its input impedance should be controlled in some manner. Input impedance in other means frequency response of the antenna elements can be changed continuously or discretely. Discretely tunable antennas have some kind of switching mechanisms that enable antennas to operate discrete frequency bands and continuous frequency tunable antennas has smooth transitions between operating bands without jump by using loading elements. Both discrete and continuous frequency tunable antennas have similar operation principle such as extending the effective length of the antenna element.

Frequency reconfiguration can be mainly applied to the resonant type antennas including linear antennas, slot antennas, and microstrip antennas. Effective electric length of these types of antennas can be tuned in order to obtain desired resonant frequencies [1]. There are different methods to achieve frequency reconfiguration:

First, it is possible to tune the antenna length by using switches. Dual frequency

operation of the antenna can be achieved by changing the electrical length of the antenna [2], [3], [4], [5]. An example of frequency reconfigurable antennas is 2-element frequency tunable slot dipole antenna array structure with MEMS switches as seen in Figure 2.1 [6]. The first resonance of the slot dipole antenna occurs when the switches are OFF. Electric length of the slot dipole antenna is decreased by making switches ON and operating frequency is shifted to higher frequency. Since the current distribution is same relative to the wavelength, radiation pattern does not change considerably. Design, prototype fabrication and measurements of 2-element frequency tunable slot dipole antenna array are in Chapter 7.

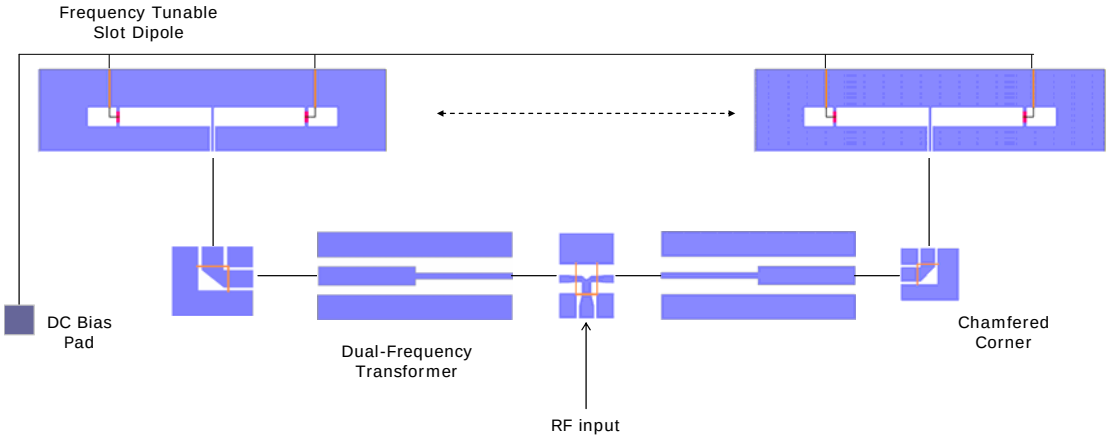

Figure 2.1 2-Element Frequency Tunable Slot Dipole Antenna Array Structure with MEMS Switches

Secondly, electrical length of the antenna can be changed by loading the antenna with variable capacitances. An example of the loaded antenna is a patch antenna with a stub loaded by RF MEMS variable capacitances [7]. The proposed antenna's operating frequency can be tuned between 15.75 GHz and 16.05 GHz.

2.1.2 Polarization Reconfiguration

Polarization of the antenna can be defined as the polarization of the wave transmitted (radiated) by the antenna. Electric field polarization of the antenna in the far field can be translated from the current flow on the antenna surface. Therefore, antenna polarization can be altered by controlling the current flow on the antenna surface. Polarization reconfigurations can occur between different types of linear polarizations, right and left hand circular polarizations, or between linear and circular polarizations. Polarization reconfiguration methods are generally similar with frequency reconfiguration methods although their implementations are different. Polarization reconfigurable antenna with a MEMS actuator has been introduced in [8]. The proposed antenna is a corner-fed nearly square patch antenna with two notches at two sides to generate 2 orthogonal modes. A MEMS actuator is placed on one of the notches and consists of a movable metal strip suspended over a metal stub. When the strip is suspended above the stub, the antenna has a circularly polarized pattern. When the actuator is down, the antenna is linearly polarized.

In addition, polarization reconfigurable circularly polarized meanderline array is designed and simulation results are given in Chapter 6. Antenna's polarization can be changed between RHCP (Right Hand Circularly Polarized) and LHCP (Left Hand Circularly Polarized) by using SPDT MEMS switches.

2.1.3 Radiation Pattern Reconfiguration

Antenna radiation pattern can be defined as a graphical representation of radiation properties of the antenna as a function of space coordinates. Radiation pattern is generally determined in the far field region and is represented as a function of directional coordinates. In fact radiation patterns are generally determined by the current distribution on the antenna structure. Therefore while achieving pattern

reconfigurability, it is hard to keep the frequency response of the antenna constant but not impossible. In order to achieve desired pattern reconfiguration magnitude and phase information of the current distribution should be analyzed in detail. After that for specific current distribution antenna structure is modified accordingly. While obtaining radiation pattern reconfigurability, to keep input impedance in other words frequency response more or less constant, tunable matching circuits can be used. In fact, reflector antennas and parasitically coupled antennas are more appropriate for pattern reconfiguration. Because reconfigured part is located in the feeding circuit so it is isolated from the radiated part. Therefore, it is easier to keep constant frequency response of the antennas.

There are many radiation pattern reconfigurable antennas reported in the literature [1], [9]. An example of a pattern reconfigurable antenna is planar 'V' antenna proposed in [11]. Arms of the 'V' antenna can be moved by using MEMS actuators, thus beam direction can be rotated or different beam shapes can be obtained. In addition, a rectangular spiral antenna with MEMS switches has been reported in [12]. Switches are located on the arm of the spiral. When these switches are activated, the spiral overall arm length is changed and as a result, its radiation beam direction is changed.

In Chapter 5, a beam-steerable meanderline array with varactor diodes is presented. Meanderline sections have been loaded with variable capacitors and beam direction is rotated. Design, manufacture and measurements of the proposed antenna are presented in Chapter 5.

2.2 Reconfiguration Mechanism for Antennas

Antenna reconfiguration can be accomplished by using number of mechanisms. Reconfiguration methods can be investigated in three groups: switches, diodes, mechanical and material changes. Each method has advantages and drawbacks and in some situations two or three methods are applied in the same design in order to achieved desired reconfiguration. In the following sections, a brief description will

be given for each method.

2.2.1 Switches

Switches are commonly used mechanisms in order to achieve any type of reconfigurations. There are many kinds of switches such as; optical switches, PIN diodes, FETs, and radio frequency micro electro mechanical system (RF MEMS) switches. Frequency tunability can be realized by changing the electrical length of the antenna by using switches. Also radiation pattern and polarization reconfiguration is obtained by controlling current distribution on the antenna surface using switches. Especially, pin diodes are preferable since they are easy to integrate and cost efficient. On the other hand, biasing circuits of the pin diodes has parasitic effects and has higher insertion loss compared to the RF MEMS switches. RF MEMS switches have low insertion, high linearity and low power consumption [13]. Besides, when the RF MEMS switches are fabricated on the same substrate with antenna it alleviates the packaging effects and other affects due to soldering and bonding [14].

In addition to these, optical switches have advantages over other kind of switches such as that can get rid of the some switch and bias line effects. In order to control the optical switches light from infrared laser diodes guided with fiber-optic cables can be used [15]. However, it should be noted that optical power used to activate the switches can affect the antenna gain and other parameters [16].

2.2.2 Variable Reactive Loading

Variable reactive loading is different from switch mechanism in a manner that it results in continuous reconfiguration while switches provide discrete changes. These continuous reconfigurations are commonly achieved by variable capacitor type mechanisms such as FETs, varactor diodes, RF MEMS variable capacitors. For instance, varactor diode capacitances change with respect to reverse applied voltage. By loading the antenna with tunable capacitance, it is possible to change its input

impedance and obtain frequency tunability. One example of the varactor loaded antenna is presented in [17]. In this structure, two varactor diodes have been connected between the main radiating edges of the antenna and the ground plane. With a reverse bias varying between 0 and 30 V, the varactors had capacitances between 2.4 and 0.4 pF. As the bias level changed, the capacitances at the edges of the patch tuned the electrical length of the patch. Continuous frequency tuning over a large band has been achieved.

Especially varactor diodes are packaged components and easy to integrate to the antenna elements. On the other hand biasing circuits of the varactor diodes can affect the electrical characteristics of the antenna. Hence, during the design of the antenna bias circuitry of the varactor diodes should be analyzed in detail.

In a similar manner, reactance of the FET components changes with applied voltage and this variable reactance can be used to tune the electrical length of the antenna or change the current phase and magnitude distribution of the antenna [18].

On the other hand tunable RF MEMS capacitors can also reduce parasitic effects, the losses, system size, and costs. A reconfigurable CPW-fed dual frequency rectangular slot antenna is given in [7]. In this structure, a rectangular slot antenna is integrated with MEMS cantilever type capacitors located on a stub. Capacitors are actuated by different voltage values and resonance frequency of the antenna can be changed.

2.2.3 Mechanical and Material Parameter Changes

Mechanical changes have more advantages over switches or variable reactive loading mechanisms because mechanical changes can create abrupt changes in frequency and radiation pattern reconfigurability. The main challenge using mechanical reconfiguration mechanisms is the actuation mechanism and the maintenance of other characteristics while changing the physical structure of the antenna abruptly [19], [20]. An example of mechanical changes is piezoelectric actuator systems which enable to control the distance between elements and makes possible to change

operating frequency or radiation pattern. It is stated that piezoelectric actuator systems changes other characteristics while achieving in one kind of reconfigurability [21].

Although it is known that current radiation characteristic of the antenna is dominantly determined by the conductor part of the antenna, it is possible to tune the antennas by changing material characteristics of substrates. For instance, ferro-electric materials relative permittivity can change with an applied static electric field and the permeability of the ferrite can change with an applied static magnetic field [22], [23], [24]. It is possible to change the effective length of the antennas by changing relative permittivity and permeability of the substrates. Also, the resonant current distributions on conductors can be arranged accordingly by changing permittivity and permeability of the ferrite or ferroelectric materials. Another example of mechanical reconfiguration mechanism is the electromagnetically actuated antenna proposed in [25]. By applying DC magnetic field, the patch can bend on the substrate surface at an angle which is called plastic deformation. The main advantage of changing characteristics of materials over other reconfiguration mechanisms is elimination of bias circuits commonly used for switches and variable reactive loading mechanisms. The main drawback of ferroelectric and ferrite materials is their high-conductivity resulting in high loss compared to other substrates and it decreases the efficiency of the antennas.

CHAPTER 3

TRAVELING WAVE ANTENNAS

Traveling wave antenna can be defined as an antenna whose conductors support a current distribution described by a traveling wave. It is possible to model a traveling wave antenna as a single wire transmission line (single wire over ground) which is terminated with a match load so no reflection at the end of the antenna as seen in Figure 3.1. Generally, the length of the transmission line is several wavelengths. Since, traveling wave antennas act as transmission line, they have constant input impedance over a very wide frequency range. On the other hand, their gain, efficiency and radiation pattern changes with frequency that limits operational bandwidth of the antennas.

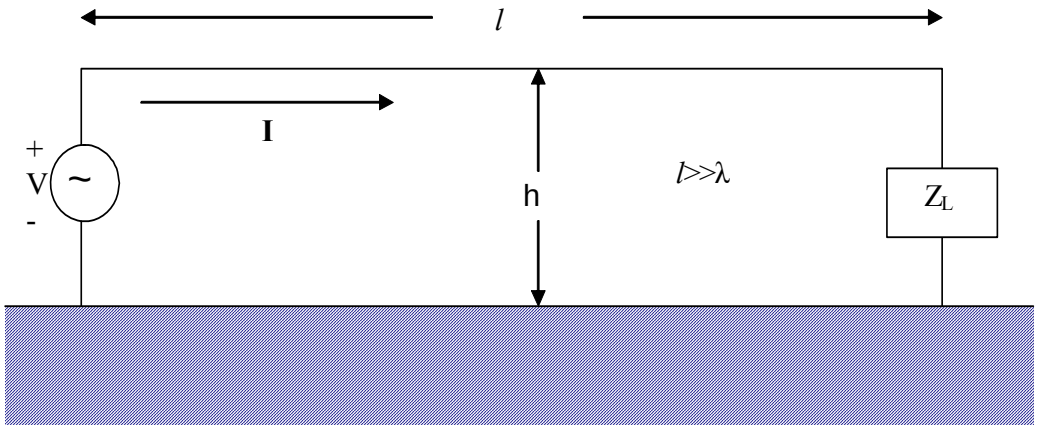

Figure 3.1 Single Wire Transmission Line over Ground Terminated with a Matched Load

Traveling wave antennas can be classified as a fast wave when the phase velocity of the wave is greater than the velocity of the light in free space and ($v_p / c > 1$) and slow wave if its phase velocity is equal or smaller than the velocity of light c in free space ($v_p / c \leq 1$). (Phase velocity is defined as, $v_p = \omega / k$, where ω is wave angular frequency, k is wave phase constant)

In general, there are two types of traveling wave antennas. First one is called leaky wave that couples power, either continuously or discretely, in a small increments per unit length from a traveling wave structure to free-space. An example of leaky wave antennas is a slotted rectangular waveguide antenna [26], [27]. Most of the leaky wave antennas are fast wave structures, they continuously loose energy due to the radiation and the fields decay along the structure in the direction of wave travel.

Second type of traveling wave antennas is surface wave antennas. Surface wave antennas radiate power from discontinuities in the structure that interrupt a bound wave on the antenna surface. Phase velocity of the traveling wave on the surface wave antenna is commonly equal to or less than velocity of light so that these antennas are also called slow wave structures. Radiation of the surface wave antennas are mainly occurs from discontinuities, curvatures, and non-uniformities. Discontinuities on the antenna surface can be discrete or distributed. In fact, most of the surface wave antennas are end-fire or near end-fire radiators. Practical configurations of surface wave antennas are curved, modulated structures, line and planar surfaces [29], [30].

3.1 Microstrip Traveling Wave Antennas

Printed microstrip antennas have many applications in satellite communications, radars, remote sensing, missile telemetry and other biomedical instruments. The advantages of microstrip antennas compared to other type of antennas are their light weight, low profile, easy to mount on systems and compatible with modular designs such as reconfiguration mechanisms; switches, phase shifters etc.

Microstrip traveling wave antennas have the advantages of both traveling wave antennas and microstrip antennas. Microstrip traveling wave antennas are slow wave structures. They consist of curved or chain shaped periodic conductors or an ordinary long TEM line on a substrate backed by a ground plane [28]. Traveling wave array structures are terminated with a matched load. There are number of microstrip configurations that have been used in the design of traveling wave antennas. These antennas are briefly described in this section.

Chain Antenna

Chain antenna is composed of rectangular loops which are chain shaped patterns on the grounded dielectric slab. End of the chain antenna is terminated with matched load as seen in Figure 3.2. Typically, the width of the rectangular loop, 2T, is in the order of one wavelength and the separation between chains, S, is slightly less than half a wavelength [29]. In order to obtain propagation along the chain antenna without reflections, the characteristic impedance of the line connecting the rectangular loops should be half of the impedance of the loop line and the effects of the discontinuities should be minimized [34].

As the wave propagates along the structure, the current along the chain structure attenuates due to radiation. The radiation occurs from the 'S' parts of the chain antenna which are parallel to the antenna axis whereas, radiation occurs from the T parts cancels each other since they have equal but opposite magnitudes. Therefore, the polarization of the chain antenna is parallel to the chain structure.

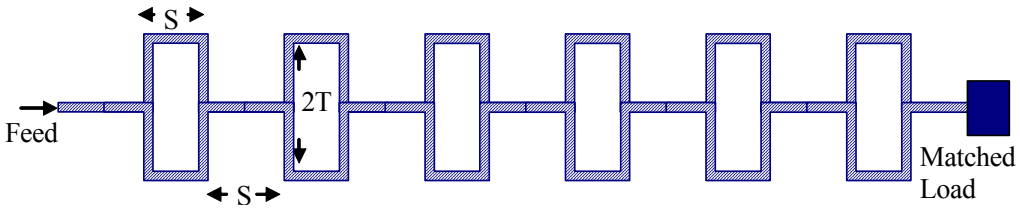

Figure 3.2 Rectangular Loop Type Microstrip Chain Antenna

TEM Line Antenna

TEM antenna is a microstrip type traveling wave antenna supporting TE_{01} coupled to a TEM mode along a microstrip line. Radiation mainly occurs at the frequencies not far above the cut-off frequency of the TE_{01}- mode since it is very loosely coupled to the line. As seen from Figure 3.3, the antenna is fed asymmetrically to excite the first higher order mode [29]. Also, it is possible to insert metal post on the antenna or create small slots on the antenna surface in order to suppress the fundamental mode. In addition, a matching transformer is used to match the antenna to the feed line.

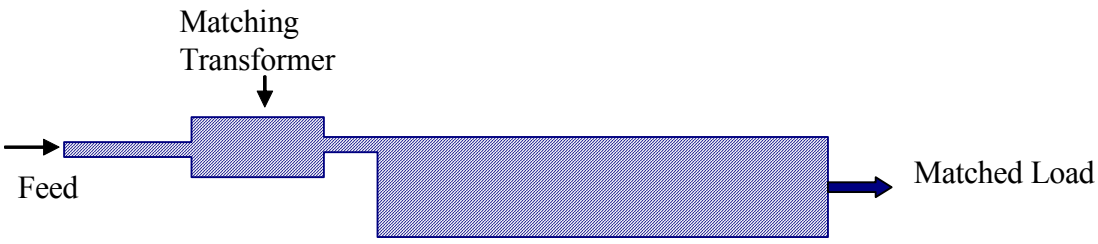

Figure 3.3 TEM Line Antenna Geometry

Series Microstrip Patch Antenna

The series microstrip patch traveling wave antenna consists of patch elements cascaded by high impedance transmission lines. Array of cascaded microstrip patches are terminated with a matched load as seen in Figure 3.4. The array input impedance is approximately same as the impedance connecting the elements because the internal reflections within the array add randomly in phase at the feed. In addition, series microstrip patch traveling wave antenna is a broadband structure [29].

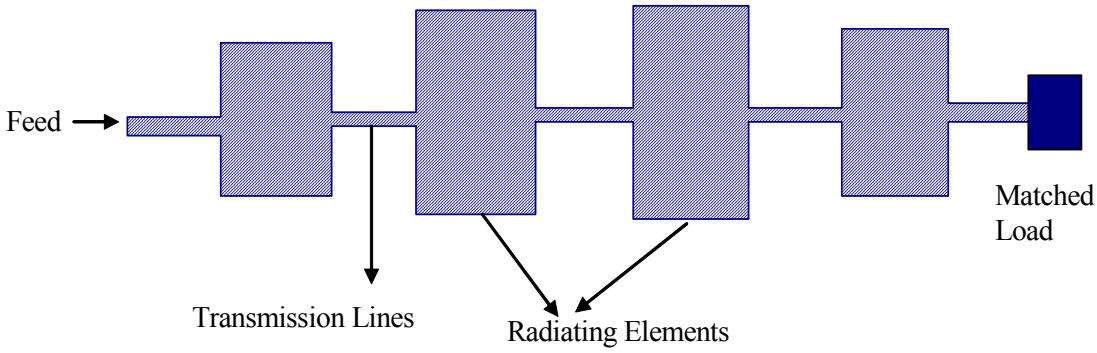

Figure 3.4 A Series Microstrip Patch Traveling-Wave Antenna Configuration

Combline Antenna

Another type of traveling wave antenna is a comb-line antenna shown in Figure 3.5. The antenna radiates from the open ended stubs or fingers. Stub lengths are approximately half a wavelength long, so that the radiation conductance is directly transferred to the feed line. Since the radiation conductance symbolizes the loading on the line, in order to obtain desired aperture distribution, the widths of the stubs are selected accordingly [29].

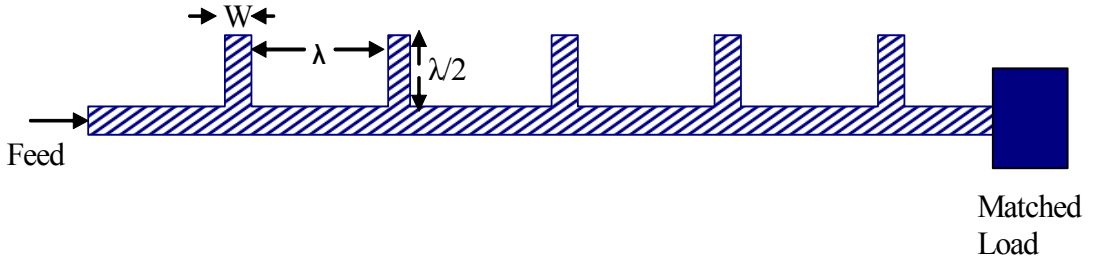

Figure 3.5 Combline Microstrip Traveling Wave Antenna

Franklin Type Antenna

Franklin type antenna configuration is shown in Figure 3.6. The antenna composed

of 50Ω microstrip line with a Franklin-antenna shape and open end of the antenna is terminated with a matched load or open circuit [29].

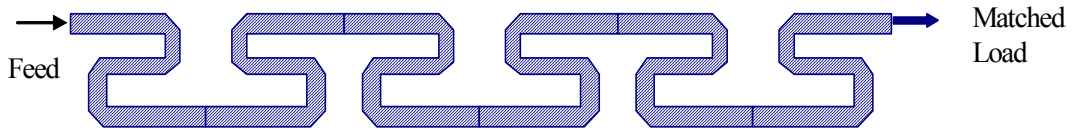

Figure 3.6 Geometry of a Franklin-Type Microstrip Traveling Wave Antenna

3.2 Meanderline Arrays (Rampart Antenna)

Meanderline arrays are another type of microstrip traveling wave antennas. Meanderline arrays have some advantages compared to other types of printed antennas, for instance their polarization and beam direction can be controlled by simply adjusting the spacing between the bends. Due to these features, meanderline arrays are good candidates of radar applications.

Meanderline arrays consist of a meandering microstrip line with a matched load at the end of the antenna as shown in Figure 3.7. A meanderline array composed of unit cells and each unit cell has six or four corners depending on the antenna polarization requirements as shown in Figure 3.8 (a) and (b) respectively. According to [28], radiation of the meanderline array mainly occurs from the right angle bends. In order to reduce the right-angled discontinuity susceptance and return loss, right-angled bends are chamfered. The radiation direction and the polarization can be controlled with the length, width and the period of the rampart cells. In the case of four cornered rampart cell, polarization radiated by the cell is controlled by two lengths s and d, and the third length l is used to control the required array scan angle.

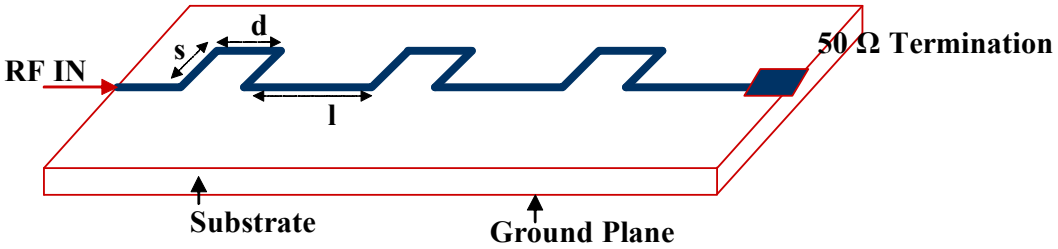

Figure 3.7 A Representation of Meanderline Array Section

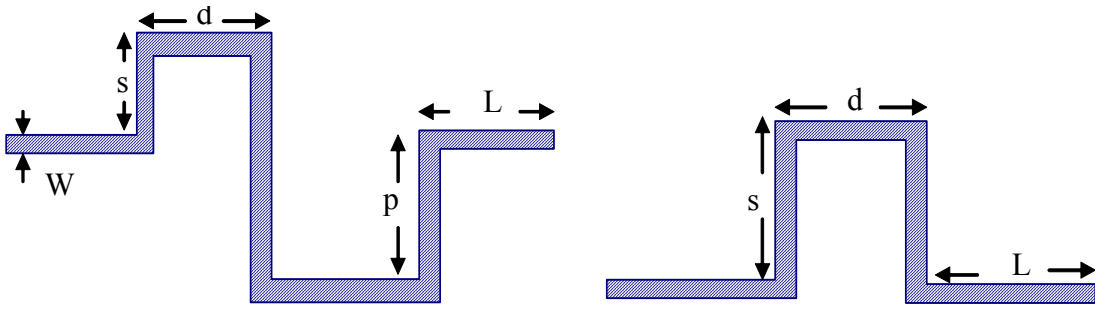

(a) **(b)**

Figure 3.8 Unit Cells of Different Types of Meanderline Array

(a) Six Cornered Meanderline Cell for Arbitrary Polarization

(b) Four Cornered Meanderline Cell for Linear or Circular Polarization

3.2.1 Radiation Mechanism of the Unit Meanderline Cell

As mentioned above radiation of the meanderline mainly occur from the right-angled bends. It is possible to model these right angled bends as magnetic current elements as seen in Figure 3.9(a), Since the current on the meanderline antenna travels a shorter path at inside edge than the outside edge, it creates an imbalance magnetic current [28]. Thus, the four cornered meanderline antenna cell can be modeled as an array of magnetic current elements which are fed in a phase progression for a traveling-wave array.

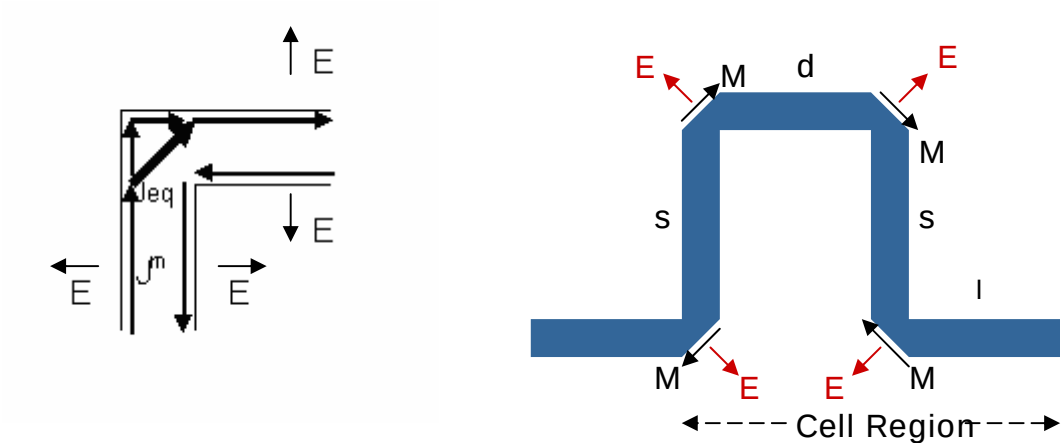

(a) **(b)**

Figure 3.9
(a) Equivalent Current Source Distribution at the Right Angle Bend
(b) Equivalent Model of Four Cornered Meanderline Cell

Since quasi TEM mode is excited on the meanderline structure as seen from Figure 3.9 (a), the E-field components on the straight lengths are oppositely directed and tend to cancel each other's radiation. As shown in Figure 3.9 (b) radiated electric field is diagonally placed to the corner and magnetic field is perpendicular to the electric field. The electric field and magnetic current distribution of the meanderline cell can be expressed in terms of electric and magnetic field elements.

$$\bar{J}^{e} = \hat{n} \times \bar{H} \tag{3.1}$$

$$\bar{J}^{m} = \bar{E} \times \hat{n} \tag{3.2}$$

where $\hat{n}$ is unit normal outward from the meanderline .

In Equations 3.1 and 3.2 electric field E and magnetic field H are associated with electric and magnetic type sources ($\bar{J}^{e}$ and $\bar{J}^{m}$) on the meanderline sections. Contribution of electric and magnetic current elements to the total radiation is equal [28], therefore while analyzing the radiated field only magnetic current element has

been used. Therefore, meanderline array is represented with magnetic current elements fed in a phase progression. Also, it is assumed that coupling due to surface waves and attenuation of the traveling wave on the line is negligible.

Formulation of the total radiated fields of the meanderline array is presented below:

As shown in Figure 3.10 antenna is placed on the y-z plane and magnetic current elements are represented with hertzian magnetic dipoles at the corners. Distance between magnetic current elements is equal to the length of the meander sections. Total magnetic current of the unit cell is equal to the summation of hertzian magnetic dipoles. First current element is located at the origin with zero phase and phase shift and the position of the other current vectors are written in terms of the first one.

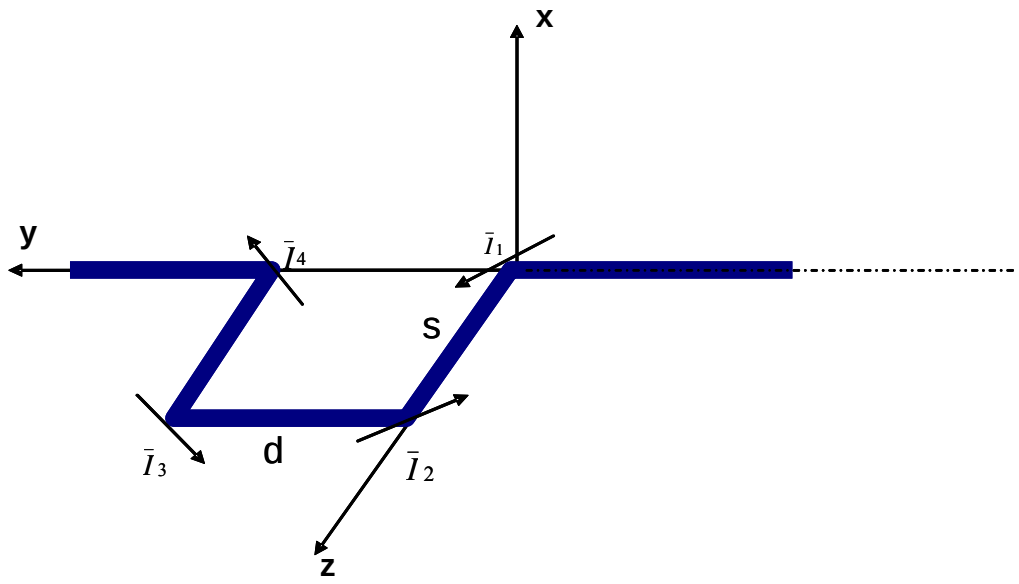

Figure 3.10 Magnetic Current Vectors on Meander Line Unit Cell

In order to calculate E and H fields of the meanderline array, it is possible to use induction equivalent modeling. It is assumed that the dominant part of the magnetic current J^m resides only in the front face of the conductor. From the image theory total magnetic current equals to $2J^m$ Therefore, by using $2J^m$ formulation given in

Equation 3.3, vector potential can be derived. J^m can be written in terms of current elements ($\bar{I}_1, \bar{I}_2, \bar{I}_3, \bar{I}_4$) defined at the corners of the meanderline cell.

$$\bar{A}_m = \frac{1}{4\pi}\int_V 2\bar{J}^m(x', y', z')\frac{e^{-jk_0R}}{R}\ dV' \tag{3.3}$$

$\bar{A}_m$ can be decomposed into $\bar{A}_m = \bar{A}_1^m + \bar{A}_2^m + \bar{A}_3^m + \bar{A}_4^m$

$$\bar{A}_1^m = (\hat{a}_y + \hat{a}_z)\frac{I}{\sqrt{2}}\frac{1}{2\pi}\frac{e^{-jk_0r}}{r} \tag{3.4-a}$$

$$\bar{A}_2^m = (-\hat{a}_y - \hat{a}_z)\frac{I}{\sqrt{2}}\frac{1}{2\pi}\frac{e^{-jk_0r}}{r}e^{-jk_0s\sin\theta\sin\phi}e^{-j\beta s} \tag{3.4-b}$$

$$\bar{A}_3^m = (-\hat{a}_y + \hat{a}_z)\frac{I}{\sqrt{2}}\frac{1}{2\pi}\frac{e^{-jk_0r}}{r}e^{-jk_0s\sin\theta\sin\phi}e^{-jk_0d\cos\theta}e^{-j\beta(s+d)} \tag{3.4-c}$$

$$\bar{A}_4^m = (\hat{a}_y - \hat{a}_z)\frac{I}{\sqrt{2}}\frac{1}{2\pi}\frac{e^{-jk_0r}}{r}e^{-jk_0d\cos\theta}e^{-j\beta(2s+d)} \tag{3.4-d}$$

where *I* equals to current flowing on each dipole.

In order to write magnetic vector potential in spherical coordinates $\hat{a}_x, \hat{a}_y, \hat{a}_z$ are written in terms of $\hat{a}_r, \hat{a}_\theta, \hat{a}_\varphi$ as shown in Equations 3.5 (a-b).

$$\hat{a}_y - \hat{a}_z = (Sin\theta Sin\phi - Cos\theta)\hat{a}_r + (Cos\theta Sin\phi - Sin\theta)\hat{a}_\theta + Cos\phi\,\hat{a}_\phi \tag{3.5-a}$$

$$\hat{a}_y + \hat{a}_z = (Sin\theta Sin\phi + Cos\theta)\hat{a}_r + (Cos\theta Sin\phi + Sin\theta)\hat{a}_\theta + Cos\phi\,\hat{a}_\phi \tag{3.5-b}$$

Therefore, in spherical coordinates at the far field $\bar{A}_m$ can be written as in Equations

3.6 and 3.7 (a-c).

$$A^m = A_r^m \hat{a}_r + A_\theta^m \hat{a}_\theta + A_\phi^m \hat{a}_\phi \tag{3.6}$$

$$A_r^m = \frac{I}{\sqrt{2}} \frac{1}{2\pi} \frac{e^{-jk_0 r}}{r} \begin{pmatrix} (\sin\theta\sin\phi - \cos\theta) \\ -(\sin\theta\sin\phi - \cos\theta)(e^{-jk_0 s\sin\theta\sin\phi} e^{-j\beta s}) \\ +(\sin\theta\sin\phi + \cos\theta)(e^{-jk_0 s\sin\theta\sin\phi} e^{-jk_0 d\cos\theta} e^{-j\beta(s+d)}) \\ -(\sin\theta\sin\phi + \cos\theta) e^{-j\beta(2s+d)} \end{pmatrix} \tag{3.7-a}$$

$$A_\theta^m = \frac{I}{\sqrt{2}} \frac{1}{2\pi} \frac{e^{-jk_0 r}}{r} \begin{pmatrix} (\cos\theta\sin\phi - \sin\theta) \\ -(\cos\theta\sin\phi - \sin\theta)(e^{-jk_0 s\sin\theta\sin\phi} e^{-j\beta s}) \\ +(\cos\theta\sin\phi + \sin\theta)(e^{-jk_0 s\sin\theta\sin\phi} e^{-jk_0 d\cos\theta} e^{-j\beta(s+d)}) \\ -(\cos\theta\sin\phi + \sin\theta) e^{-j\beta(2s+d)} \end{pmatrix} \tag{3.7-b}$$

$$A_\phi^m = \frac{I}{\sqrt{2}} \frac{1}{2\pi} \frac{e^{-jk_0 r}}{r} \begin{pmatrix} (\cos\phi) \\ -(\cos\phi)(e^{-jk_0 s\sin\theta\sin\phi} e^{-j\beta s}) \\ +(\cos\phi)(e^{-jk_0 s\sin\theta\sin\phi} e^{-jk_0 d\cos\theta} e^{-j\beta(s+d)}) \\ -(\cos\phi) e^{-j\beta(2s+d)} \end{pmatrix} \tag{3.7-c}$$

By using Far Field approximations, E-field at the far field can be derived.

$$\bar{E}_r \approx 0 \tag{3.8-a}$$

$$\bar{E}_\theta = -j\omega \bar{A}_\theta^m \tag{3.8-b}$$

$$\bar{E}_\phi = -j\omega \bar{A}_\phi^m \tag{3.8-c}$$

In order to obtain the azimuth pattern (E-plane) of the meanderline unit cell, take the ϕ=0 cut plane

So;

$$\bar{E}_\theta = -j\omega \bar{A}_\theta^m \Big|_{\phi=0} \tag{3.9-a}$$

$$E_\theta = j\omega \frac{I}{\sqrt{2}} \frac{1}{2\pi} \frac{e^{-jk_0 r}}{r} \sin\theta \left(1 - e^{-j\beta s} - e^{-jk_0 d\cos\theta} e^{-j\beta(s+d)} + e^{-j\beta(2s+d)}\right) \quad \textbf{(3.9-b)}$$

$$\bar{E}_\phi = -j\omega \bar{A}_\phi^m \Big|_{\phi=0} \quad \textbf{(3.10-a)}$$

$$E_\phi = -j\omega \frac{I}{\sqrt{2}} \frac{1}{2\pi} \frac{e^{-jk_0 r}}{r} \left(1 - e^{-j\beta s} + e^{-jk_0 d\cos\theta} e^{-j\beta(s+d)} - e^{-j\beta(2s+d)}\right) \quad \textbf{(3.10-b)}$$

After $\bar{E}_\theta$, $\bar{E}_\phi$ values of the meanderline unit cell is calculated as in Equations 3.9 and 3.10, array theory is applied in order to calculate the array pattern of the meanderline array.

$$\bar{E}_{tot} = \bar{E}_{unit} * AF \quad \textbf{(3.11)}$$

where $\bar{E}_{tot}$ is the total electric field of the meanderline array and $\bar{E}_{unit}$ is the radiation pattern of the meanderline array unit cell. *AF* is the array factor and can be defined as;

$$AF = \frac{SinN\frac{\psi}{2}}{NSin\frac{\psi}{2}} \quad \textbf{(3.12)}$$

Where N is the number of elements in the array and

$\psi = k_0(d+L)Cos\theta - (2s+d+L)\beta$

$\beta = \frac{2\pi}{\lambda_g}$

In conclusion, radiated E-Field at ϕ=0 plane (E-plane) at the far field for meanderline array has been calculated as;

$$\bar{E}_{tot} = \frac{SinN\frac{\psi}{2}}{NSin\frac{\psi}{2}} j\omega \frac{I}{\sqrt{2}} \frac{1}{2\pi} \frac{e^{-jk_0 r}}{r} \begin{bmatrix} (\sin\theta(1-e^{-j\beta s} - e^{-jk_0 d\cos\theta} e^{-j\beta(s+d)} + e^{-j\beta(2s+d)}))\bar{a}_\theta \\ +(-1+e^{-j\beta s} - e^{-jk_0 d\cos\theta} e^{-j\beta(s+d)} + e^{-j\beta(2s+d)})\bar{a}_\phi \end{bmatrix} \quad \textbf{(3.13)}$$

Polarization of the Meanderline Array

Total radiated electric field of the four corner meanderline array is calculated in the previous section. As seen from Equation 3.14, far field E-pattern of the antenna is controlled by s and d parameters of the unit meanderline cell. Polarization of the array can be analyzed in terms of the diagonally polarized fields and in this case, it is convenient to analyze the polarization of the meanderline array with ratio of E_θ and E_φ.

$$\frac{E_\theta}{E_\phi} = \frac{\sin\theta(1-e^{-j\beta s} - e^{-jk_0 d\cos\theta} e^{-j\beta(s+d)} + e^{-j\beta(2s+d)})}{(-1+e^{-j\beta s} - e^{-jk_0 d\cos\theta} e^{-j\beta(s+d)} + e^{-j\beta(2s+d)})} \quad \textbf{(3.14)}$$

In [29], it is stated that the radiation on the meanderline cell is diagonally polarized as seen from Figure 3.11.

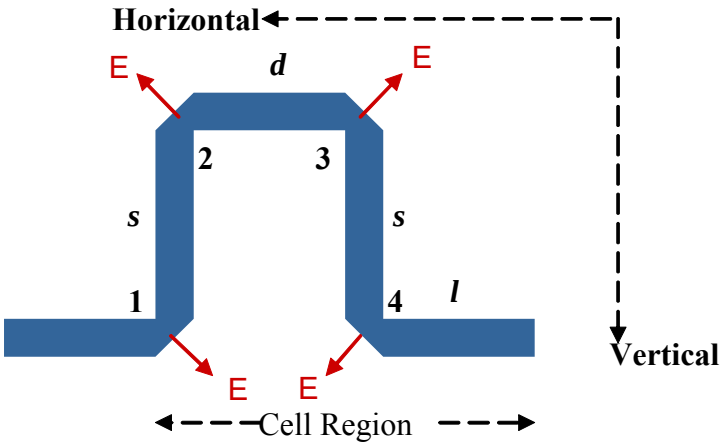

Figure 3.11 Diagonally Polarized E-Field Vectors of Meanderline Cell

The radiation from each bend in the cell can be decomposed into horizontal and vertical components; summation of these vertical and horizontal components gives the polarization of the meanderline array. While analyzing the polarization of the meanderline cell; vertical and horizontal components of the total radiated field at the first corner of the meanderline cell can be written in terms of P, where P is the radiation polarization field strength, after that, radiation components of other corners is calculated in terms of first corner, according to distance between radiation components i.e corners and direction of radiation vector at that corner.

Table 3.1 Polarization Components of a Meanderline Antenna

(a) Circular Polarization Case with s=λ/2, d= λ/4, and l=3 λ/4 Dimensions

Bend	**Polarization Component**	
	Vertical	Horizontal
1	P/√2	-P/√2
2	P/√2	-P/√2
3	jP/√2	jP/√2
4	jP/√2	jP/√2
Total	√2P(1+j)	j√2P(1+j)

(b) Vertical Polarization Case with s= λ/4, d=λ/4 and l=λ/4 Dimensions

Bend	**Polarization Component**	
	Vertical	Horizontal
1	P/√2	-P/√2
2	-jP/√2	jP/√2
3	P/√2	P/√2
4	-jP/√2	-jP/√2
Total	P(1-j) √2	0

As seen from Table 3.1 (a) total vertical and horizontal components of the

meanderline cell have a π/2 phase difference and thus produce circular polarization. Similarly, as seen from Table 3.1 (b) vertical polarization can be achieved with s= λ/4, d=λ/4 and l=λ/4 dimensions. In addition, s= 2λ/3, d= λ/3 and l= λ/3 provides horizontal polarization.

3.2.2 Lumped Approximate Network Model of the Meanderline Cell

In order to complete the electrical investigation of the meanderline array, a lumped approximate model of the meanderline is presented. This network model is developed in [28] by using two different methods, 'Transmission line Approach', and 'Two port Network Representation'. It is possible to calculate the input VSWR from the equivalent circuit representation. As shown from Figure 3.12, right angle bend of the meanderline element can be modeled with reactive elements, X_L ,X_c, and the radiation conductance of the bend is represented with G. Equations of X_L ,X_c and G are given in Equations 3.15, 3.16 and 3.17.

$$G = \frac{1}{90}\left(\frac{l}{\lambda_0}\right)^2 \tag{3.15}$$

where l is the length of the magnetic current element and approximated as $l = \sqrt{2}W_{eq}$, W_{eq} is the equivalent width of the microstrip line and is given.

$$W_{eq} = \frac{120\pi h}{Z_c\sqrt{\varepsilon_e}} \tag{3.16}$$

where h is the height of the dielectric, Z_c is the characteristic impedance of the antenna and ε_e is the effective dielectric constant.

$$X_L = \frac{W_{eq}}{\lambda_g}\left(1.756 + 4\left(\frac{W_{eq}}{\lambda_g}\right)^2\right) \tag{3.17}$$

$$X_C = -0.0865(\frac{W_{eq}}{\lambda_g}) \quad \textbf{(3.18)}$$

where λ_g is the guided wavelength.

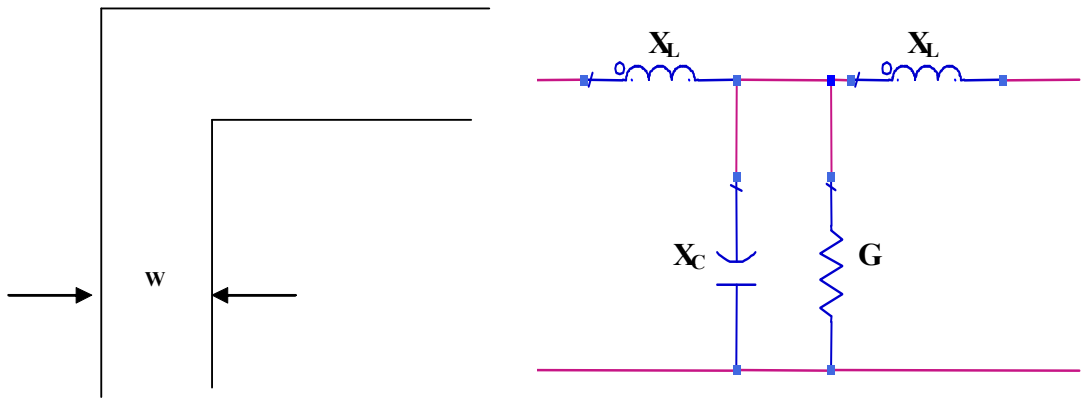

Figure 3.12
(a) Right Angle Bend of Meanderline
(b) Equivalent Circuit of Right Angle Bend

Overall meanderline array is composed of right angle bends and transmission lines. Therefore, according to the lumped equivalent network model overall meanderline array structure can be represented with right angled bend equivalent circuits cascaded with transmission lines that have similar lengths and impedance with microstrip lines of the meanderline array. Overall circuit of the meanderline array is shown in Figure 3.13.

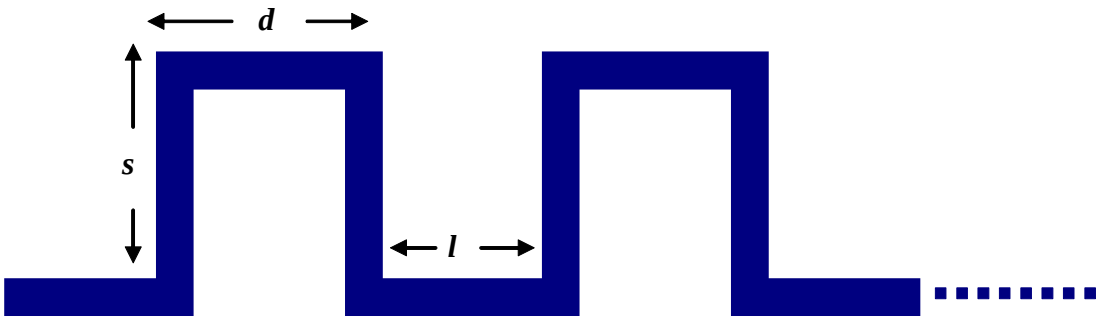

(a)

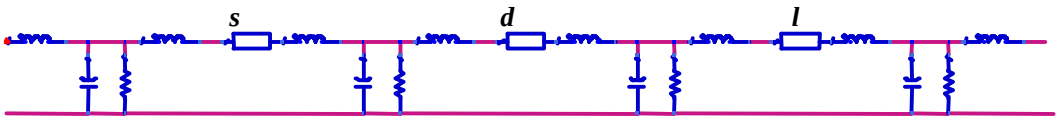

(b)

Figure 3.13
(a) Four Cornered Meanderline Array
(b) Equivalent Circuit Model of Four Corner Meanderline Array

Presented circuit model is an approximation to the meanderline array and can be used only VSWR analysis of the antenna. In order to obtain more realistic model, it is better to use full-wave EM simulators throughout the design of the antenna.

To sum up, electrical characteristics; radiation mechanisms, radiation pattern, polarization and lumped equivalent model of the meanderline array is analyzed in detail. It could be observed that s and d parameters of the meanderline array controls the polarization of the unit meanderline element and direction of the radiation depends on distance between unit cells i.e l parameter. In addition to these, as verified from total radiation pattern formulation of the meanderline array and the theory of traveling wave arrays, increasing number of elements in the array increases

directivity and efficiency because if the number of elements increases less power is dissipated at the load. Also, when the number of elements increases, side lobe levels of the antenna decreases since array elements are not fed uniformly.

CHAPTER 4

DESIGN OF LINEARLY POLARIZED TRAVELLING WAVE MEANDERLINE ARRAY

In the preceding section practical and theoretical background of four-corner meanderline has been investigated. By using the formulations and technical investigations, a linearly polarized traveling wave meanderline array operating at X-band has been studied. In this chapter, design, fabrication and the measurement procedures of the antenna have been presented in detail.

4.1 Design Specifications

Design specifications of linearly polarized traveling wave meanderline array for X-band applications are summarized below;

Operating frequency of the meanderline array is set to 10 GHz that is in X-band. In fact, one should be aware of that traveling wave antennas have very narrow bandwidth because when frequency sweeps electrical length between elements varies and electrical characteristics of the antenna i.e. polarization and beam scan angle changes.

Polarization of the meanderline array is set vertically polarized in order to receive both right and left hand circularly polarized fields.

Main beam direction of the meanderline array is set to 30° and antenna parameters are calculated according to beam scan angle.

Input impedance of the array is taken as 50 Ω in order to make the antenna

compatible with connectors and measurement systems.

Beam width of the meanderline array is expected to be 8° in Co-polarized plane and side lobe levels are below -13 dB. In fact, theoretically, it is stated in [28] that for uniform illumination of the meanderline array side lobe levels are around -13 dB and in the case of non-uniform illumination, side lobe levels decrease below -13 dB.

An initial design has been performed by using the formulations derived in the 3rd Chapter to satisfy the design requirements. Then full-wave EM (Electromagnetic) simulations have been performed to finalize the design.

4.2 Initial Design

Before theoretical analysis substrate of the antenna array has been taken under consideration. Many substrates do not operate properly at high frequencies and their performances degrade with increasing frequency. ROGERS 5880 Duroid has very low dissipation factor at high frequencies. According to test data sheet at 10 GHz its maximum dissipation factor equals to 0.0015 that is very low compared to the other substrates. Due to all these reasons, 15 mil ROGERS 5880 Duroid with ½ OZ. copper thickness has been used during design of the meanderline array. Dielectric constant (ε_r) of the substrate equals to 2.2.

Derivation of Microstrip Parameters

It is stated in the specification that the input impedance of the antenna and characteristic impedance of the meanderline sections will be equal to 50 Ω. In order to calculate the microstrip line parameters it is possible to use theoretical formulas given in Appendix A or ADS (Advanced Design System) which is an electromagnetic simulator.

Effective dielectric constant and the width of the microstrip line are calculated using "Line Calc" in ADS. In addition, guided wavelength is computed in order to use in calculating dimensions of the meanderline array. Calculated values are presented

below;

Effective Dielectric Constant; ε_e= 1.836
Guided Wavelength; λ_g=22.14 mm
50 Ω microstrip line width w=1.17 mm

Computing Parameters of Meanderline Array

In order to satisfy the specifications about polarization and radiation characteristics, initially, dimensions of the meanderline cell which defines the polarization of the antenna should be estimated. Afterwards, direction of the beam, beamwidth and side lobe levels are controlled by the array of meanderline cells and other design parameters are controlled by array formulations.

Polarization: As explained in Section 3.2.1 the polarization of the meanderline array can be investigated using vector addition of magnetic current elements at the corners of the meanderline cell. So, using Table 3.2.2, s and d values of the meanderline cell has been figured out $\lambda_g/4$. Since λ_g is derived as 22.14 mm s and d values equals to 5.535 mm.

Main Beam Scan Angle: Direction radiation of the meanderline array is controlled by the sections of the meanderline array as seen from Equation 4.1.

$$\psi = k_0(d+L)Cos\theta - (2s+d+L)\beta \qquad \textbf{(4.1)}$$

where $k_0 = \frac{2\pi}{\lambda_0}$ and $\beta = \frac{2\pi}{\lambda_g}$

Array factor takes its maximum value when ψ=2nπ (n=0,1,2…) so for a desired beam direction, it is possible to calculate s, d or l parameters when two of the parameters given.

For s and d values found from polarization calculations; l value of the antenna is

calculated as;
l=5.522mm

Meanderline array composed of 8 elements satisfies the beamwidth considerations.

In fact, during theoretical calculations, it is assumed that signal traveling on the meanderline array does not attenuate; therefore each magnetic current element has the same magnitude. In real case, wave traveling on the meanderline array attenuates so each radiation element of the meanderline array has different magnitudes. Final design parameters are obtained by performing full wave electromagnetic simulations using Ansoft Designer V2 and HFSS V10.

4.3 Full-wave EM Simulations

Throughout the simulations of meanderline array, commercial software programs; Ansoft Designer and Ansoft HFSS have been used. Each program uses different numerical tools and has advantages and disadvantages according to the application.

Ansoft Designer is a full-wave EM simulator based on Method of Moments and very efficient at microstrip antenna analysis. It is possible to insert N-port networks with S-parameters into the structure that will be analyzed. This property has been used during beam steerable meanderline antenna design. The other full wave EM analysis tool used in this thesis study is Ansoft HFSS which based on FEM (Finite Element Method). Designer can analyze only 2D or 2.5 D structures whereas HFSS can simulate 3D structures.

Linearly polarized meanderline array has been optimized using Ansoft Designer; schematic model of the array has been shown in Figure 4.1.

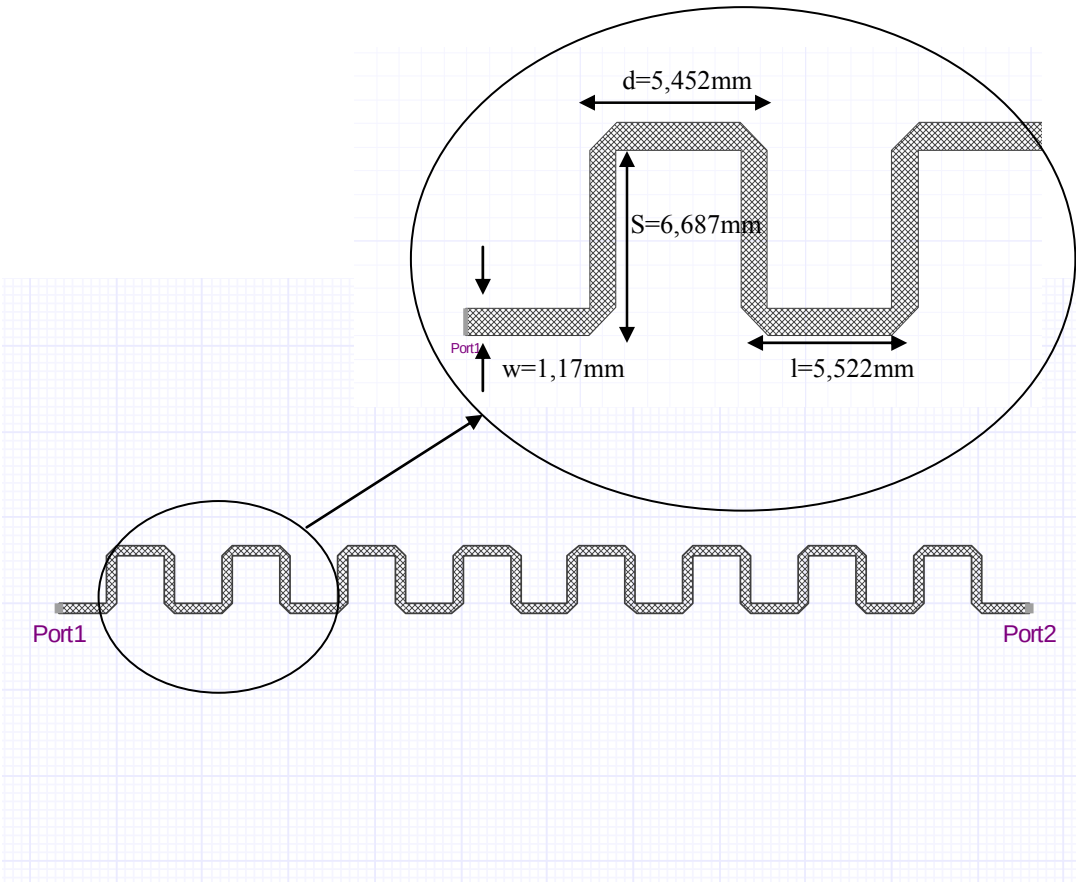

Figure 4.1 Ansoft Designer Schematic Model of Linearly Polarized 8 Element Meanderline Array

As shown in Figure 4.1, meanderline array is represented with meshes on the surfaces and there are two ports. First port is the excitation port and the second port is termination port. Optimized dimensions of the meanderline array are given on the simulation schematic model.

S-parameters of the meanderline antenna have been simulated between 9-11 GHz. E-plane radiation pattern of the array has been simulated at 10 GHz. Ansoft Designer simulation results of the meanderline array is compared with measurement results and presented in Sections 4.5.1 and 4.5.2.

Ansoft Designer simulates 2.5-D structures, i.e. it uses infinite substrate and ground plane. However, it is possible to analyze finite 3-D structures with HFSS. Therefore, meanderline array has been analyzed with Ansoft HFSS as well. The meanderline array is located in y-z plane in HFSS, S-parameters, E- and H-plane co- and cross-polarization patterns, three dimensional pattern and current distribution on the meanderline at 10 GHz have been investigated.

In addition, HFSS simulations have been compared with Ansoft Designer simulations. In Figure 4.2, S11 simulation of linearly polarized meanderline array is presented.

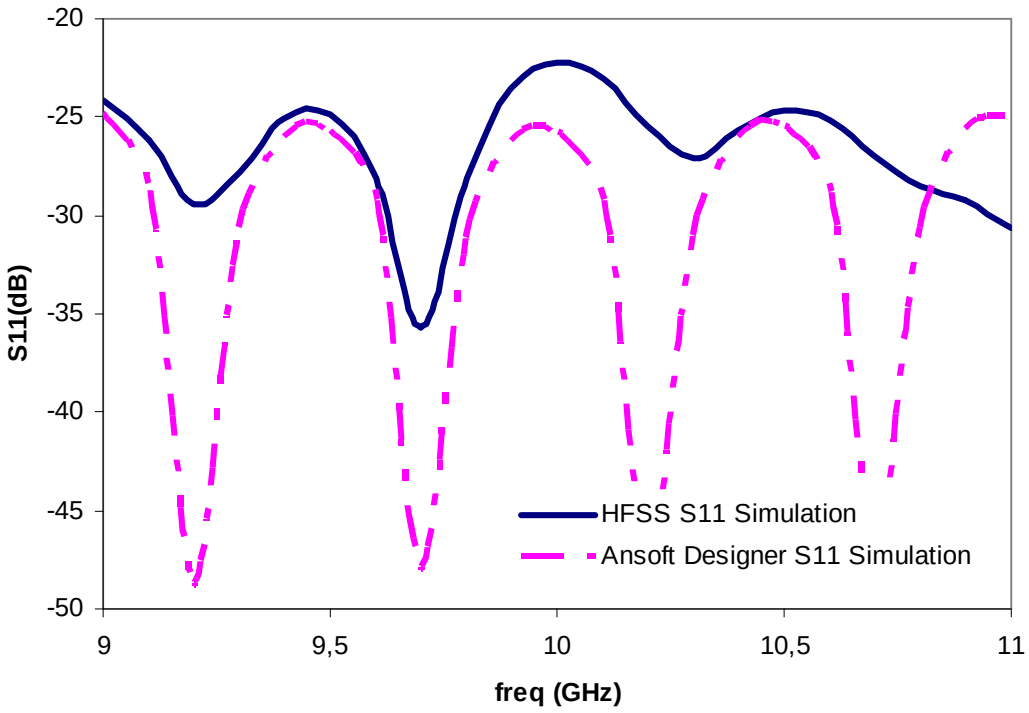

Figure 4.2 Ansoft Designer and HFSS S11 Simulations of Linearly Polarized Meanderline Array

As shown in Figure 4.3, E-plane pattern at Ansoft Designer and HFSS are similar, but there is a small shift at the maximum radiation direction. Maximum radiation direction is 32° at Ansoft HFSS and 30° at Ansoft Designer. Since HFSS defines finite dielectric in simulations, discrepancy between side lobe levels is expected.

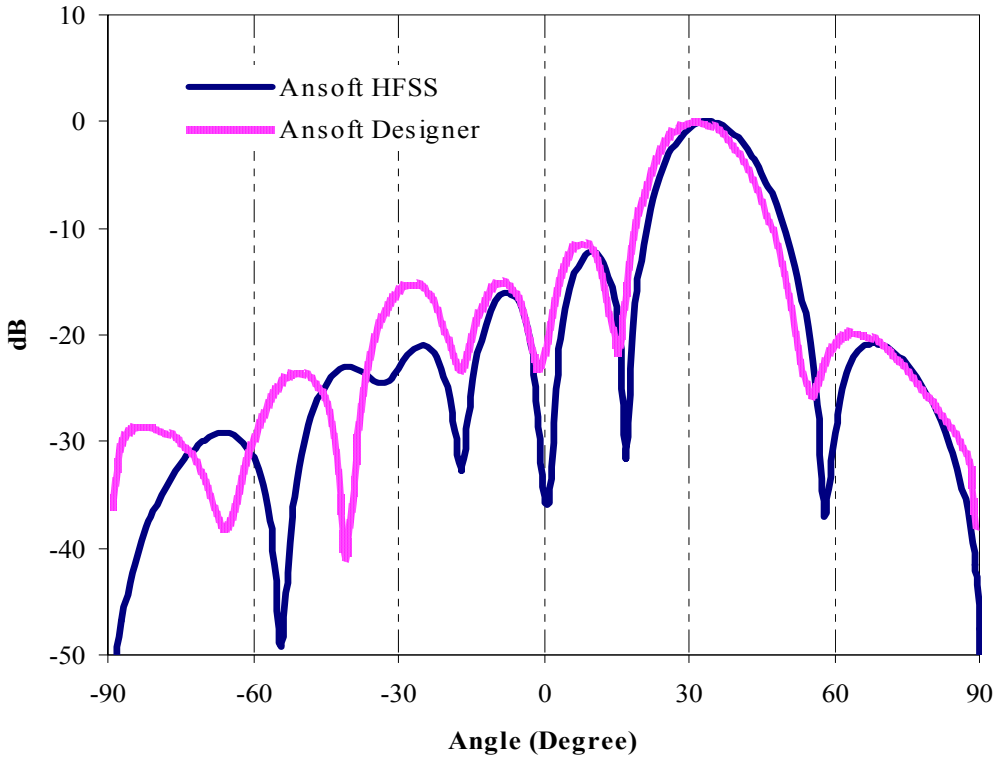

Figure 4.3 Ansoft Designer and HFSS E-plane Electric Field Pattern of Linearly Polarized Meanderline Array at 10 GHz

E-plane (X-Y) plane co- and cross-polarization patterns at 10 GHz are given in Figure 4.4. In simulations more than 20 dB cross-polarization level has been achieved at the maximum of the antenna main beam that satisfies the linearity requirement. Co-polarization of the antenna corresponds to z component of the E-field since the antenna is vertically polarized and cross-polarization of the antenna is y component of the electric field.

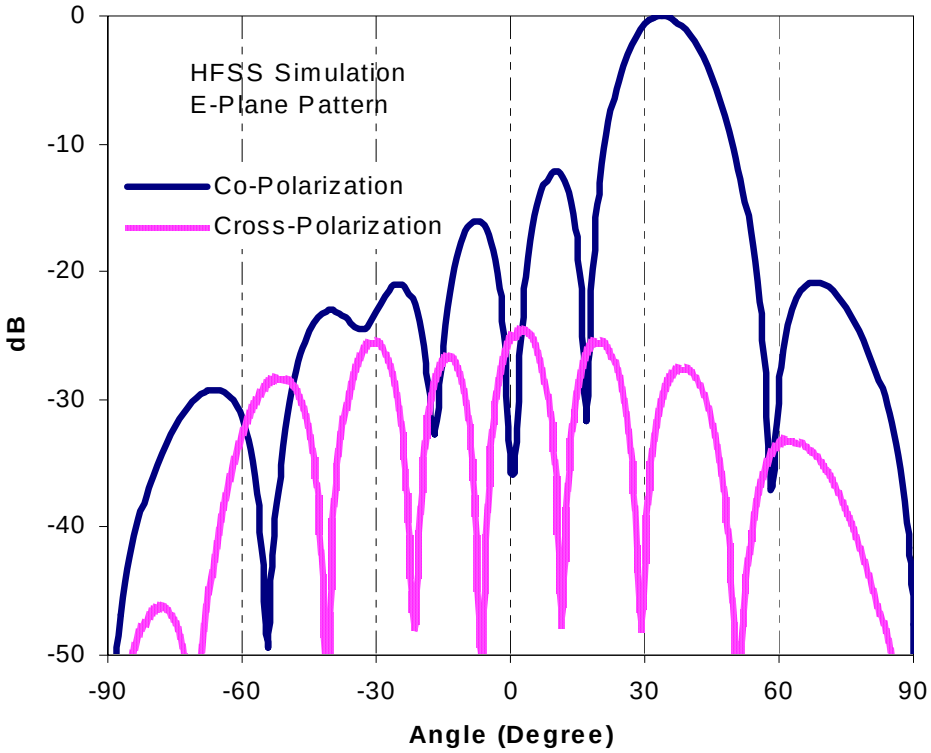

Figure 4.4 Co- and Cross-Polarization E-Plane Electric Field Patterns of Meanderline Array at 10 GHz

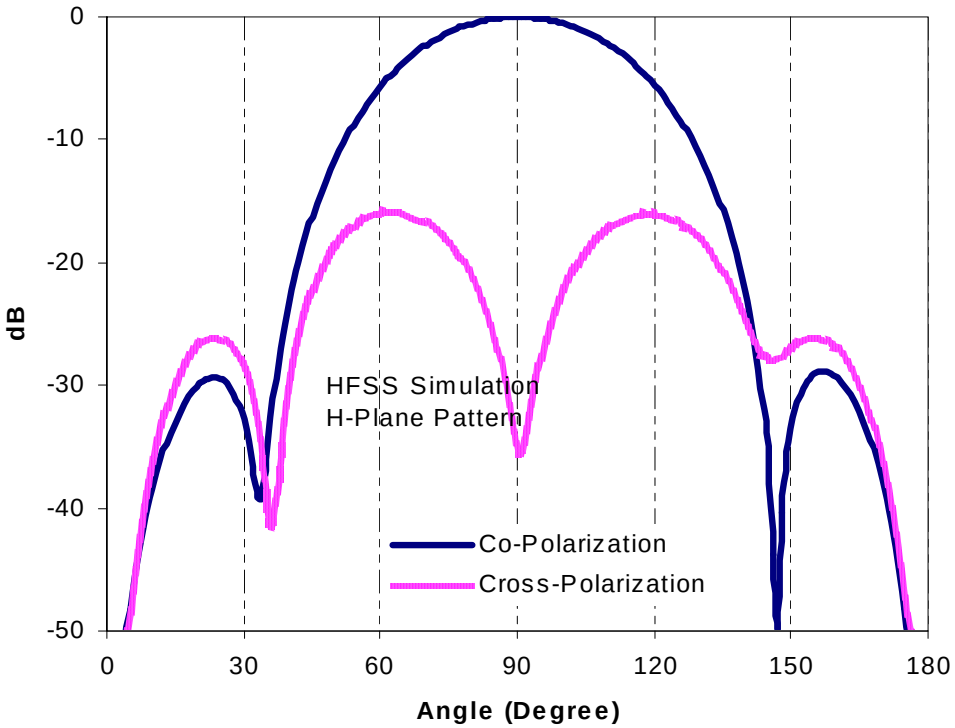

Figure 4.5 Co- and Cross-Polarization H-Plane Electric Field Patterns of Meanderline Array at 10 GHz

H-plane pattern of the meanderline array at 10 GHz is shown in Figure 4.5 and H-plane cut of the antenna corresponds to a cut for ϕ=32° (maximum of radiation at E-plane cut). Co- and cross-polarizations of the meanderline array are as seen from Figure 4.5 and there is more than 20 dB difference between co- and cross-polarization levels of the antenna.

3-dimensional radiation pattern of the meanderline array is shown in Figure 4.6. Main beam is directed towards 32° and side lobes of the antenna are shown clearly.

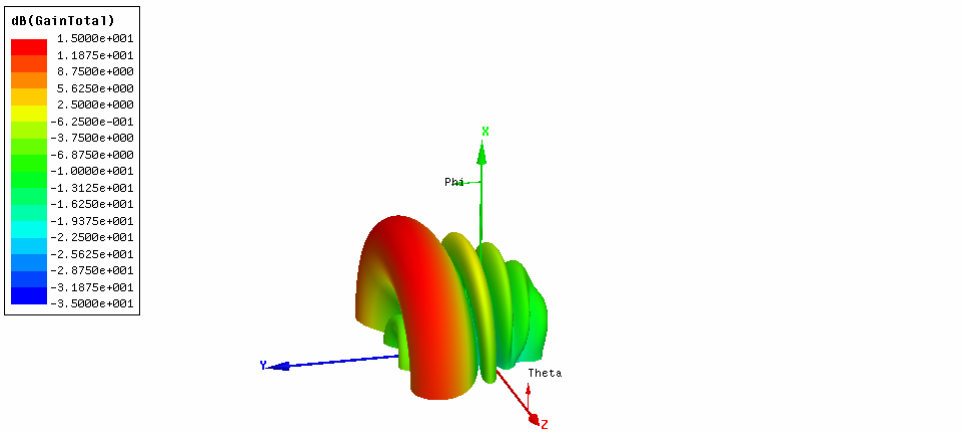

Figure 4.6 3-Dimensional Radiation Pattern of Meanderline Array

Surface current distribution of the meanderline array at 10 GHz and is presented as in Figure 4.7.

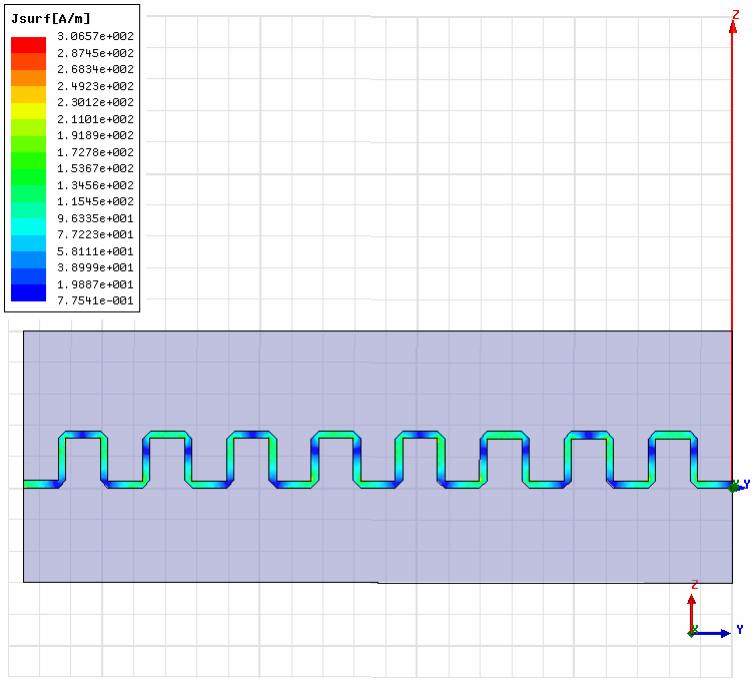

Figure 4.7 Surface Current Distribution of Meanderline Array

To sum up, linearly polarized meanderline array operating at 10 GHz has been investigated by using different simulation tools Ansoft Designer and Ansoft HFSS. Simulation results satisfy design criteria.

4.4 Fabrication of the Antenna

The designed linearly polarized meanderline array has been manufactured on 15 mil ROGERS 5880 Duroid with dielectric constant εr=2.2. Fabrication of the antenna has been performed by a LPKF 200 Machine in ASELSAN facilities. Photograph of the fabricated antenna is shown in Figure 4.8. Tyco/AMP SMA connectors operating from DC-18 GHz have been used at the two ports of the array. The first connector is RF-input connector and 50 Ω load is connected to the second port as shown in Figure 4.8.

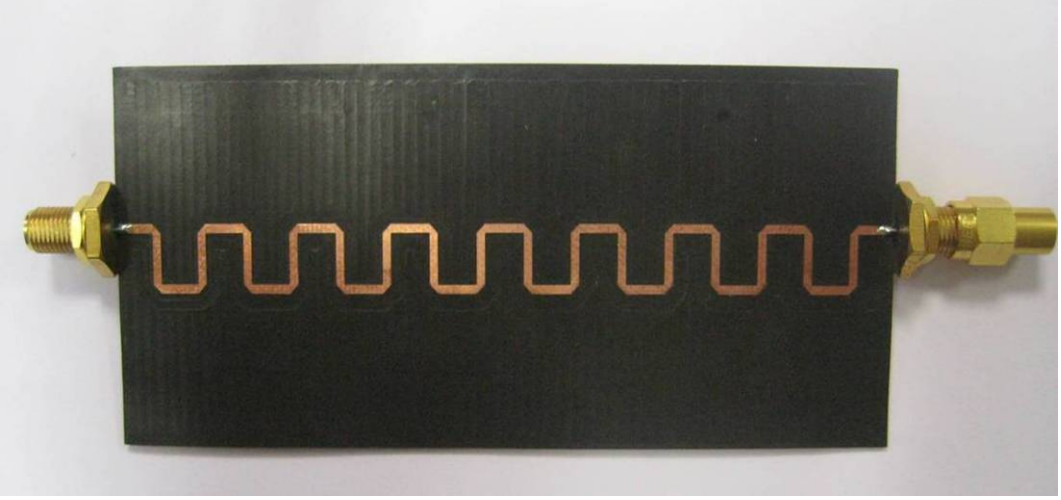

Figure 4.8 Prototype of Linearly Polarized Meanderline Array for X-band Applications

4.5 Measurements

S-parameters and radiation pattern of the meanderline array have been measured and compared with simulation results. Measurement set-ups and techniques are described briefly in the following sections. Measurement results are presented and compared with the simulation results.

4.5.1 S-Parameter Measurements of the Meander Line Array

The input return loss and S21 measurements of the meanderline array have been performed using Agilent E8364C PNA, 10 MHz to 50 GHz Vector Network Analyzer. Measurements have been carried out between 9-11 GHz. In order to measure S11 and S21 parameters of the antenna, network analyzer should be calibrated from the ports where the antenna will be connected. 3.5 mm Calibration Kit has been used for full two-port calibration. Before calibration, measurement frequency has been selected and IF bandwidth is set to 100 Hz and throughout the calibration open, short and load has been connected to each port of the network separately and lastly, two ports are connected with a through connection to complete

calibration.

After completion of calibration, S11 and S21 parameters of the antenna has been measured and compared to simulation results performed using Ansoft Designer.

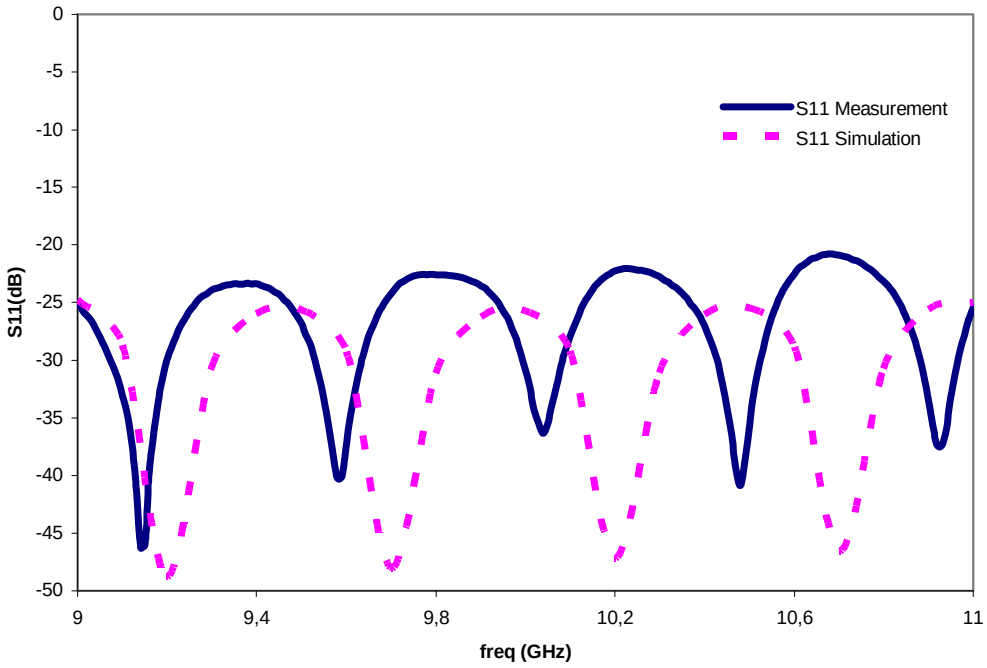

Figure 4.9 S11 (Return Loss) Measurement and Simulation Results of Linearly Polarized Meanderline Array

As shown in Figure 4.9, return loss is well below -20 dB in the band. In addition measurement and simulation results are similar except a slight shift in frequency.

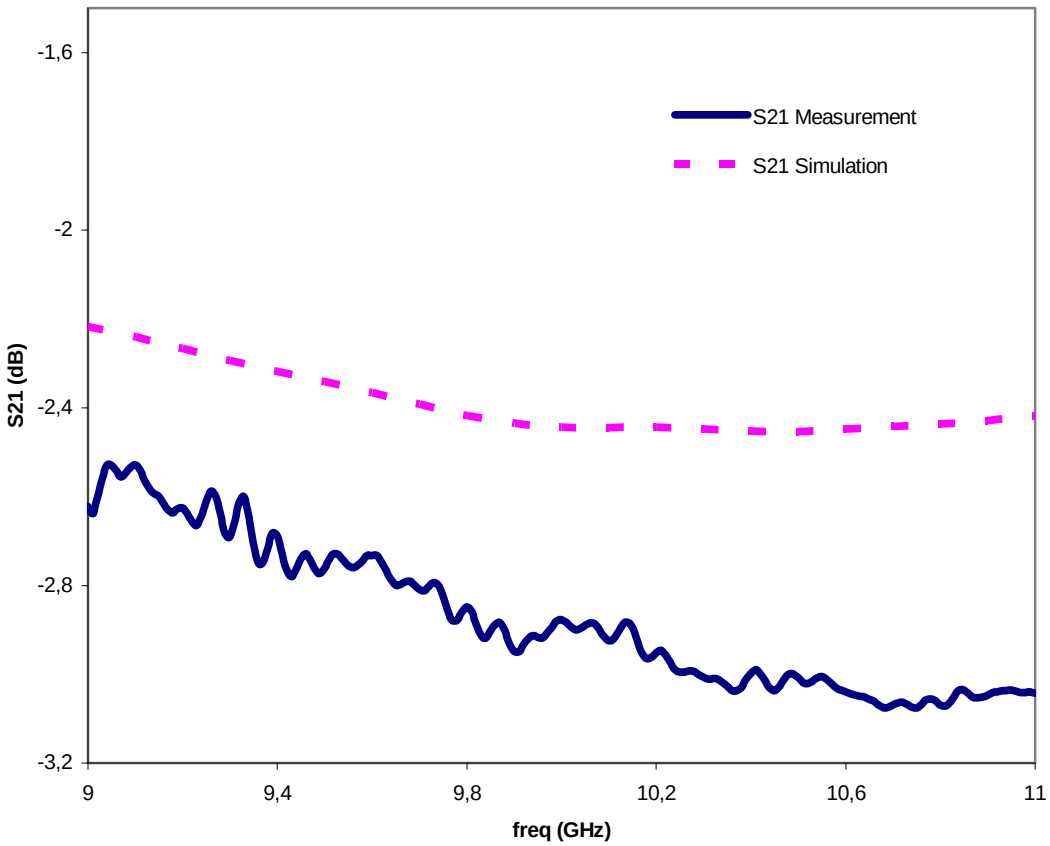

Figure 4.10 S21 Measurement and Simulation Results of Linearly Polarized Meanderline Array

In Figure 4.10, S21 measurements and Ansoft Designer simulations of meanderline array is shown. In Ansoft Designer simulations S21 is about 2.3 dB and in measurements it is approximately 2.6 dB; hence, there is a 0.3 dB difference between simulations and measurements. In fact, S21 of the meanderline array in simulations includes radiation losses and dielectric losses, on the other hand, connector losses and conductor losses have not been taken into account. Therefore, 0.3 dB difference in simulation and measurement is due to conductor and connector losses.

4.5.2 Radiation Pattern Measurements of the Meander Line Array

Radiation pattern of the array has been measured in tapered anechoic chamber at ASELSAN facilities. ASELSAN tapered anechoic chamber is described in Appendix C. Photograph of the meanderline array under test is shown in Figure 4.11.

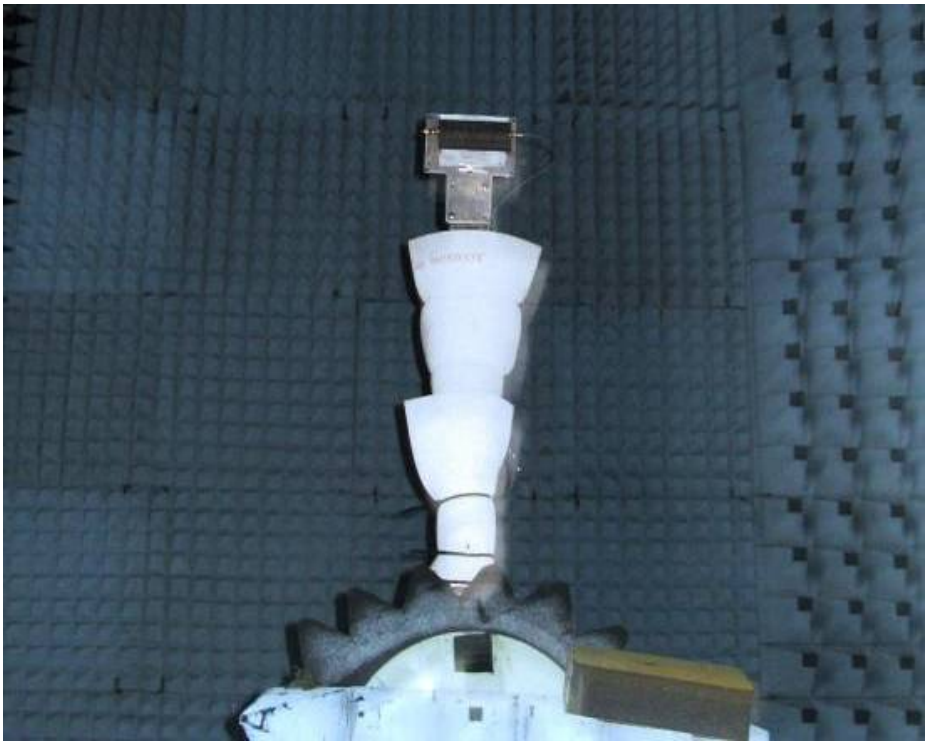

Figure 4.11 Linearly Polarized Meanderline Array under Test in Tapered Anechoic Chamber at ASELSAN Facilities

During measurements, meanderline array (AUT) is in receiver mode and the source antenna is transmitter mode. Source antenna is linearly polarized 2-18 GHz horn. So Co-polarized pattern of the meanderline array is measured when the source antenna is vertically placed in the test region and cross-polarized pattern of the meanderline array is measured by placing the feed antenna horizontally in the test region. Measurements have been performed at three frequencies; 9.5, 10 and 10.5 GHz.

Comparision of E-Plane Pattern Measurements and Simulations

Measured E-plane pattern of the antenna is compared with the simulations and presented in Figure 4.12 (a), (b), and (c) for 9.5, 10 and 10.5 GHz.

As shown from the Figure 4.12 (a), (b) and (c), measurements agree well with simulations. As the general characteristics of the meanderline array as frequency sweeps electrical length between elements varies so that main beam of the meanderline array sweeps. In Figure 4.12 (a) at 9.5 GHz beam direction is directed to 25°. At 10 GHz (Figure 4.12(a)) beam is directed to 32° and at 10.5 GHz (Figure 4.12(c)) beam is directed to 38°. Maximum side lobe levels at 9.5 GHz, 10 GHz and 10.5 GHz about 13 dB and satisfies design criteria.

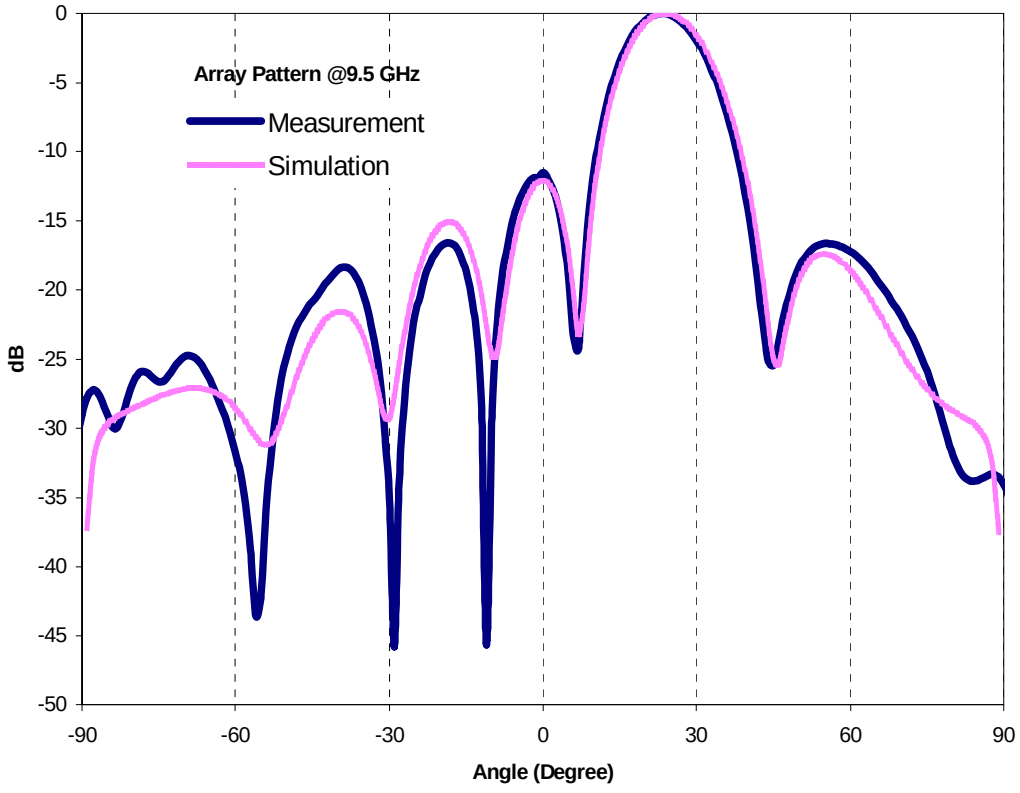

(a) at 9.5 GHz

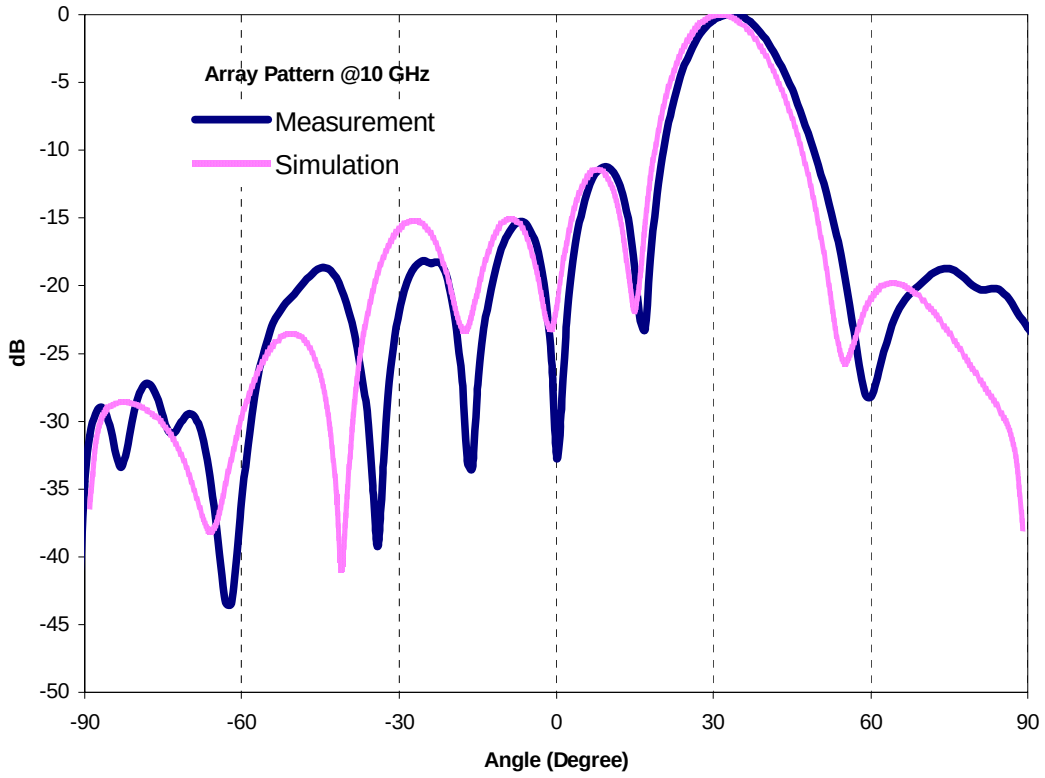

(b) at 10 GHz

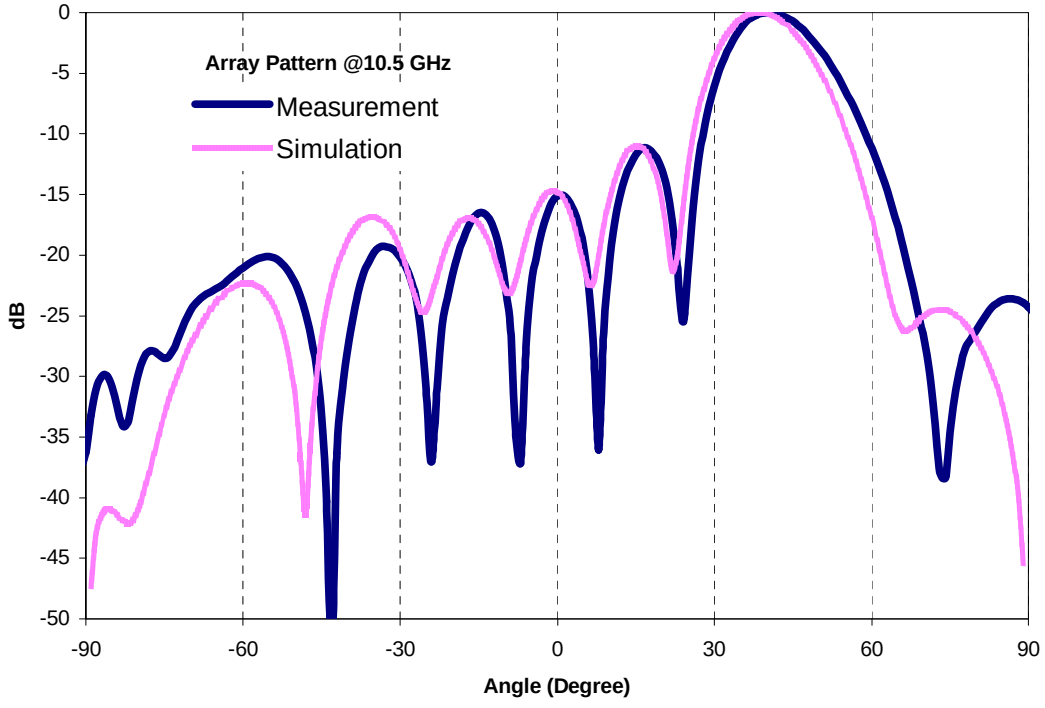

(c) at 10.5 GHz

Figure 4.12 Meanderline Array E-plane Electric Field Pattern Co-Polarization Measurement and Simulation Results

E-Plane & H-Plane Pattern Measurements

H-plane pattern of the meanderline array has been measured at three different frequencies. During H-plane measurement another rotator system has been used in order to measure the desired elevation cuts of the antenna. H-plane patterns as well as E-plane patterns are given in Figure 4.13 (a), (b) and (c). H-plane measurement results are similar to the H-plane patterns simulated in Ansoft HFSS

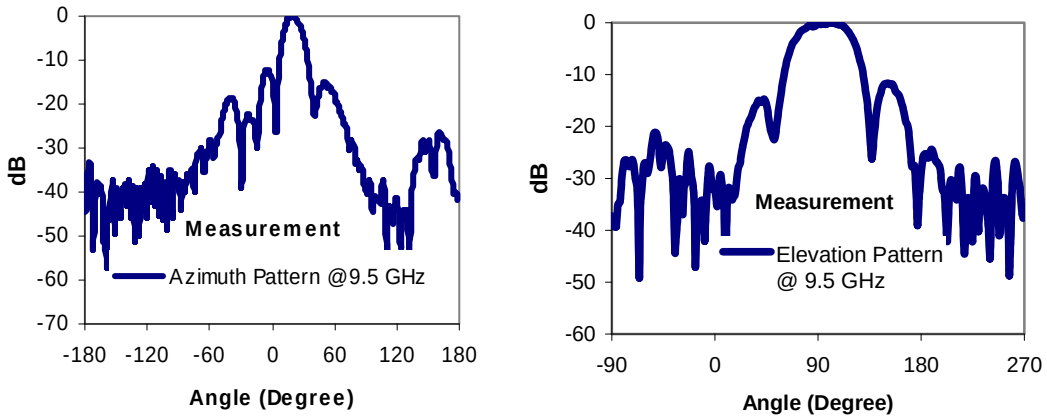

(a) at 9.5 GHz

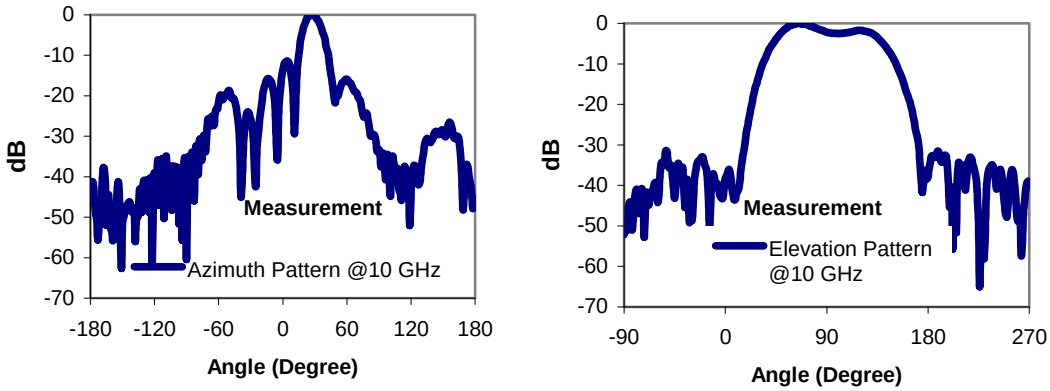

(b) at 10 GHz

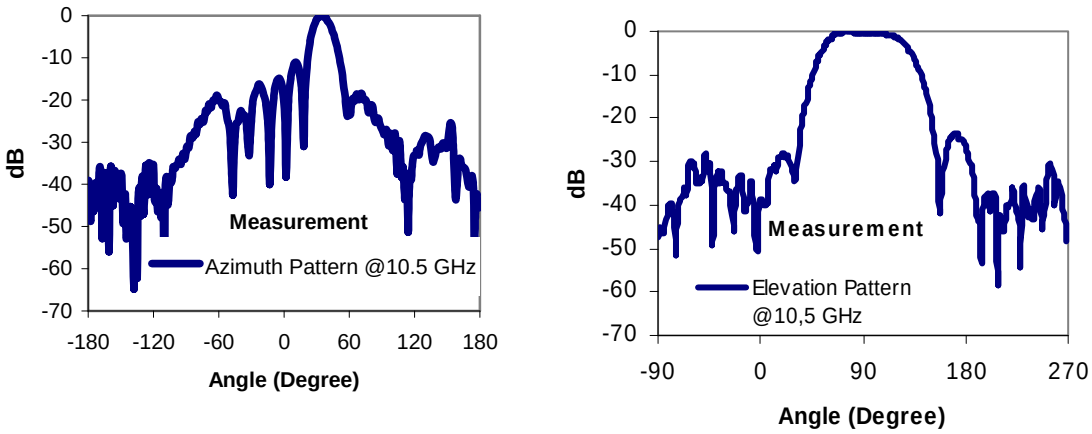

(c) at 10.5 GHz

Figure 4.13 Meanderline Array E-Plane and H-Plane Electric Field Pattern Measurement Results

Co- & Cross-Polarization Measurements

Measured cross polarized components of the patterns are given in Figure 4.14 in comparison with co-polarization patterns. There is more than 15 dB difference between co- and cross-polarization levels of the antenna, at 9.5 GHz and 10 GHz, whereas at 10.5 GHz difference between co- and cross-polarization levels decreases up to 10 dB. In other words, linear polarization of the meanderline array deteriorates while sweeping in frequency, because electrical length of the meanderline section varies and its inherent characteristic of traveling wave arrays.

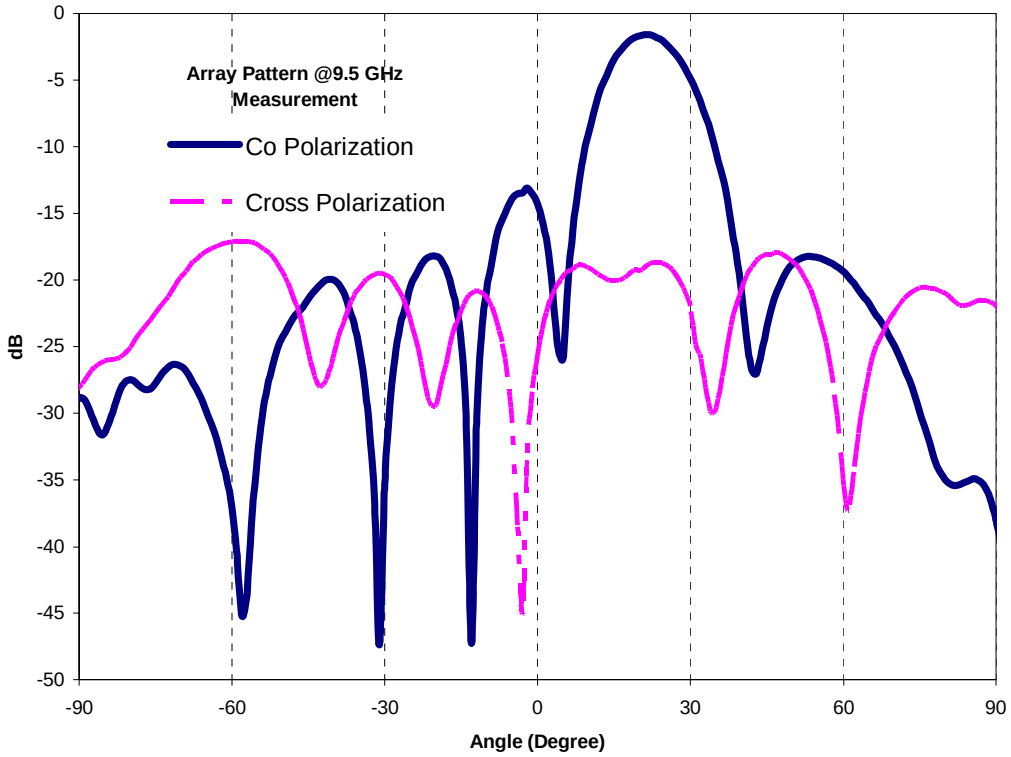

(a) at 9.5 GHz

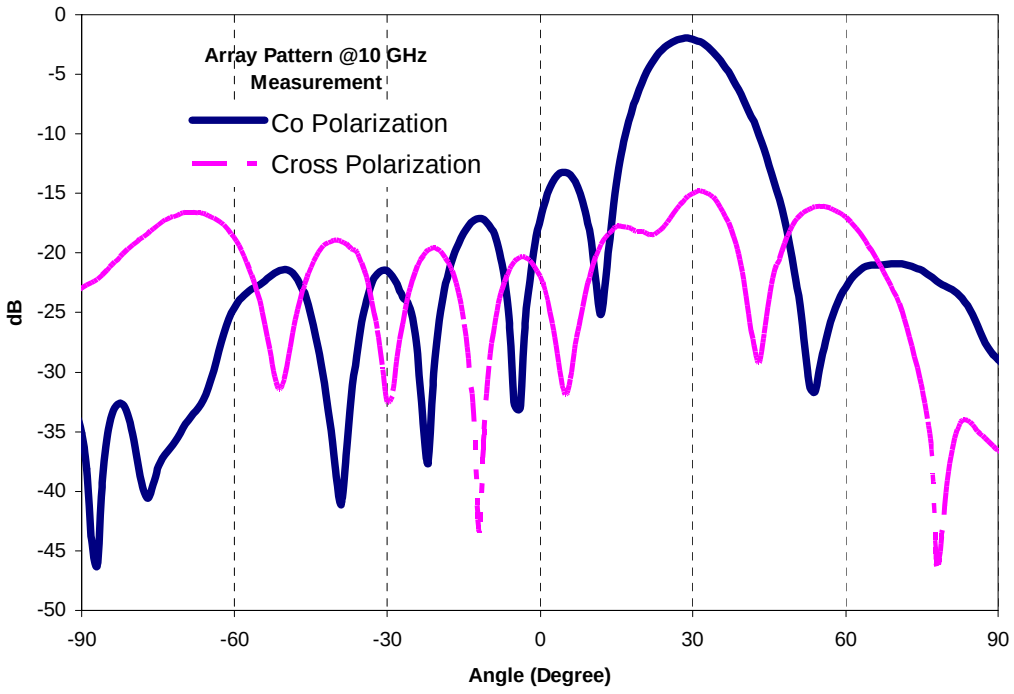

(b) at 10 GHz

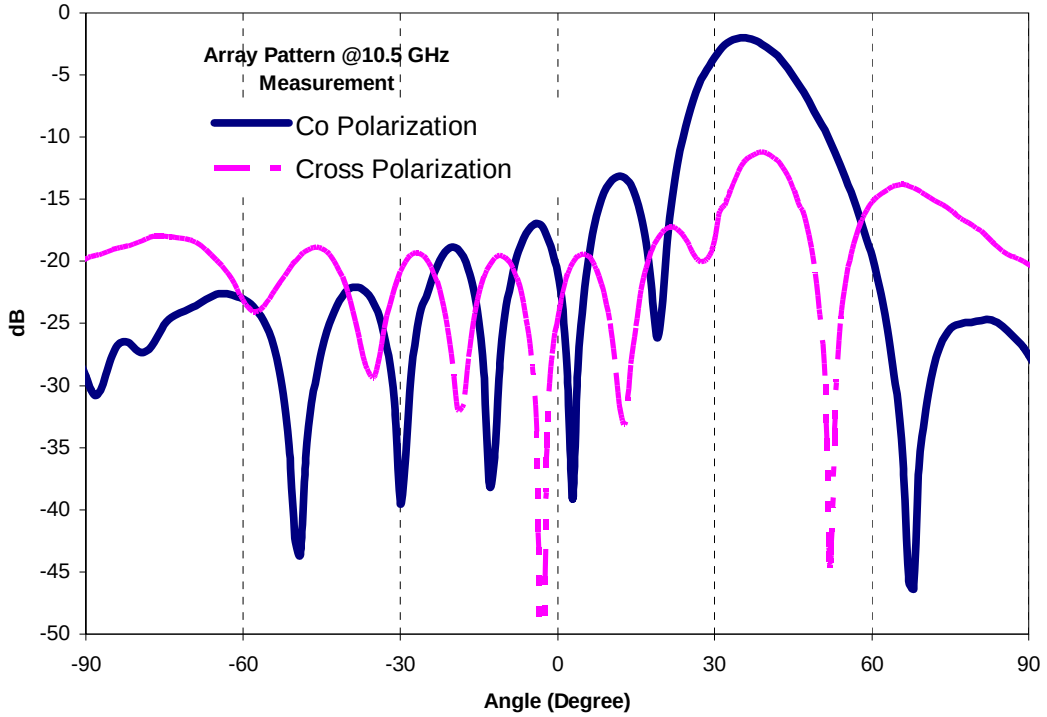

(c) at 10.5 GHz

Figure 4.14 Meanderline Array E-Plane Co-and Cross-Polarization Electric Field Pattern Measurement Results

In this chapter linearly polarized meanderline array theoretical and practical design procedures have been explained in detail. Antenna structure has been analyzed by Ansoft Designer and HFSS. Obtained simulation results have been compared with measurements.

CHAPTER 5

DESIGN OF BEAM-STEERABLE TRAVELING WAVE MEANDERLINE ANTENNA

In this chapter, a beam-steerable traveling wave meander line antenna has been introduced for X-band radar applications. Beam steering capability of the meander line antenna has been achieved by loading the antenna by varactor diodes.

The beam-steerable meander line antenna is composed of eight meanderline sections and eight varactor diodes placed on top of the meanderline elements as shown in Figure 5.1. Varactor diodes are voltage-controllable devices and the capacitance of the diodes varies with the reverse-bias voltage. Loading the meanderline antenna elements with varactor diodes, impedance and the electrical length of the meanderline can be tuned. As a result, main beam of the meanderline array steers with the applied bias voltage. Figure 5.1 shows the schematic diagram of the beam-steerable meanderline array with varactor diodes and DC bias pad.

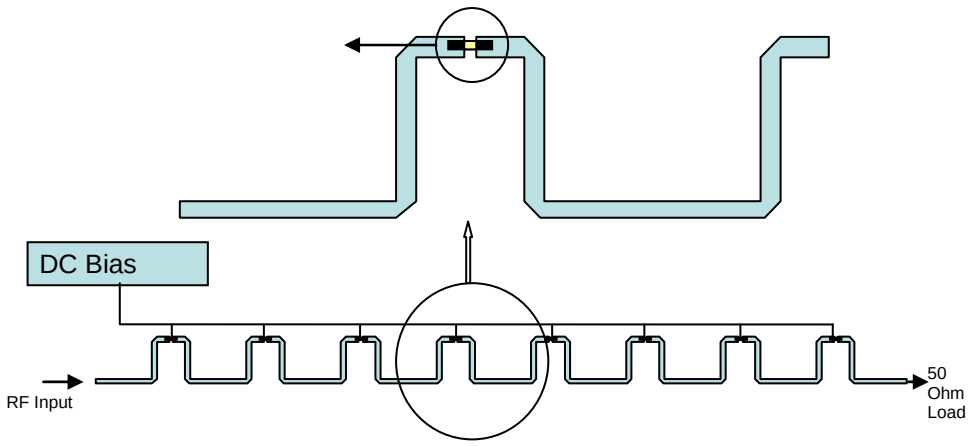

Figure 5.1 The Schematic View of Beam-Steerable Meanderline Antenna

Electrical properties of the beam-steerable meanderline array are similar to the properties of X-band linearly polarized meanderline array presented in Chapter 4. In the following sections, design aspects of beam steerable meanderline array and varactor diode phase shifting mechanism are given in detail. Afterwards, simulation results and measurements of the manufactured beam steerable array are presented.

5.2 Varactor Diode Phase Shifting Mechanism

Varactor diodes are voltage-controllable devices and are commonly used in electronic systems such as VCOs (Voltage Controlled Oscillators). By applying reverse-bias voltages, it is possible to obtain variable capacitance values. Besides, these features of varactor diodes are commonly used in phase shifting and capacitive loading mechanisms.

In this study, to rotate the beam of the meanderline antenna, meanderline is loaded with varactor diodes as shown in Figure 5.1.

Phase shift due to the varactor diodes directly depends on the capacitance variation controlled by the applied DC voltage. Many commercially available varactor diodes do not provide large capacitance variation, on the other hand; Microsemi MPV 2100 type varactors have very wide capacitance range under different bias voltages. Datasheet of Microsemi MPV 2100 varactor diode is given in Appendix C. Capacitance variation of varactor diodes with respect to different bias voltages given in datasheet is in Table 5.1.

Table 5.1 Microsemi MPV 2100 Type Capacitors Applied Voltage vs. Capacitance Values

Applied Voltage	Capacitance
0 V	2.7 pF
4 V	0.95 pF
20 V	0.3 pF

5.2.1 Characterization of Varactor Diode

In order to observe the phase shift provided by varactor diode, varactor diode on a microstrip line has been implemented on ROGERS 6010 Duroid with dielectric constant ε_r=10.2 and dielectric loss tangent δ=0.0023. Soldering pads of the varactor diode are placed on the back side; therefore silver epoxy has been used in order to mount the diode on the circuit board as shown in Figure 5.2.

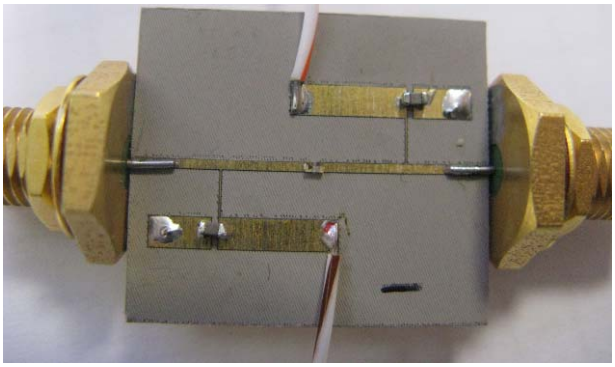

Figure 5.2 Bias Circuit of the Microsemi MPV2100 Varactor Diode Placed on the 50-Ω Microstrip Line

S-parameters of the varactor diode have been measured at 10 GHz using two-port network analyzer and given in Figure 5.3. S11 value is below -10 dB for different values of bias voltage and S21 values is around 2.5 dB.

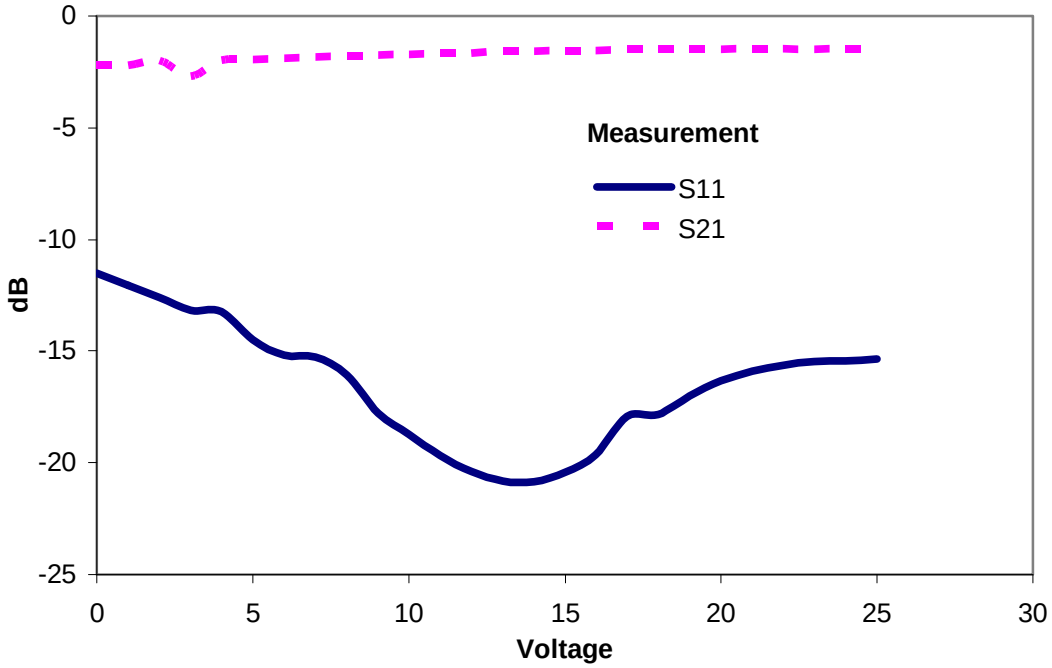

Figure 5.3 S-Parameter Measurement of Varactor Diode Bias Circuit

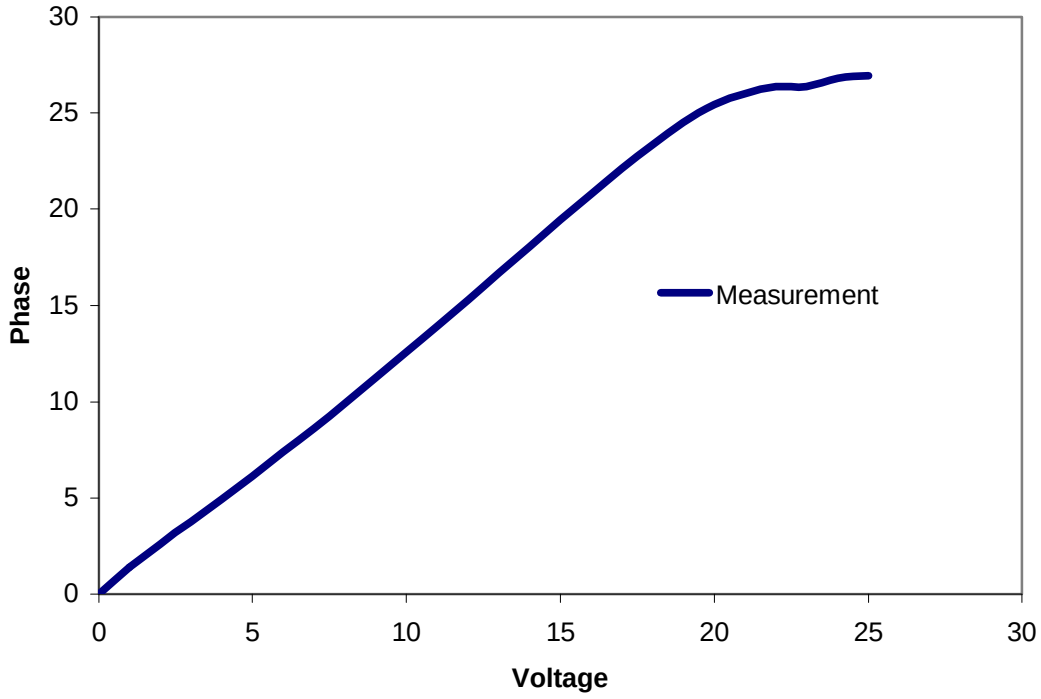

Figure 5.4 Measurement of Phase Variation with Respect to Different DC Bias Voltages

For different bias voltages, S21 phase values have been recorded and phase variation with respect to the bias voltage curve has been obtained and given in Figure 5.4. It is noticed that in measurements, more than 25° phase shift has been achieved. In addition, phase variation with respect to the bias voltage shows the linear change and this linear variation is an advantage during the design of beam-steerable meanderline array configuration since for constant increments of bias voltages, the direction of beam will sweep linearly.

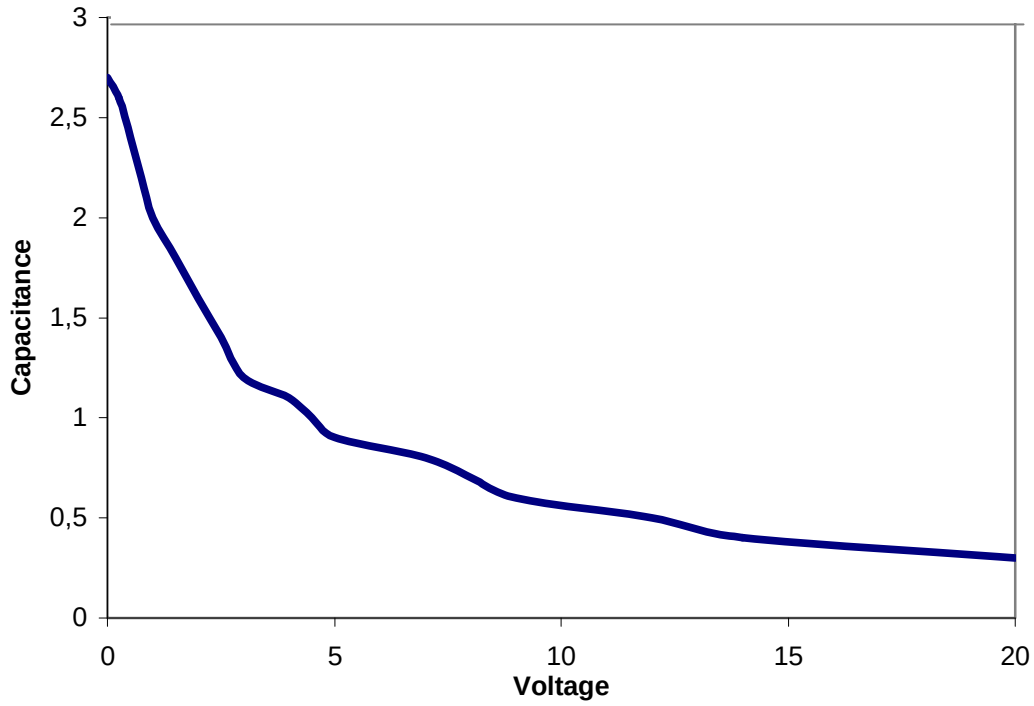

Figure 5.5 Relation between Applied Bias Voltage and Varactor Diode Capacitance

Furthermore, voltage versus capacitance curve of the varactor diode has been obtained in order to use during the design and measurement processes of beam-steerable meanderline array, as shown in Figure 5.5. It is observed that capacitance exhibits exponential variation with respect to the voltage as predicted from previous simulations and measurements.

5.3 Theoretical Investigations of Beam-Steerable Traveling Wave Antenna

Electrical parameters of the beam-steerable meanderline array are similar to those of linearly polarized meanderline array analyzed in Chapter 4. Therefore, theoretical analysis for polarization and direction of the radiation were not considered in this chapter. On the other hand, the design specifications of the beam-steerable meanderline array states that more than 10° beam variation is desired by applying corresponding phase shifts to the meanderline sections.

It is possible to analyze the beam variation of meanderline array by using array theory. Radiation direction of meanderline array can be found from

$$\psi = k_0(d+L)Cos\theta - (2s+d+L)\beta = 2n\pi \qquad \textbf{(5.1)}$$

where n=0,1,2… and θ=90° corresponds to broadside of the antenna array.

In Section 5.2, it is shown that 25° phase shift can be achieved using varactor diodes. Therefore, total beam steering for 25° phase shift has been calculated theoretically for given s, d and l parameters (s=5.452 mm, l=6.687 mm and d=5.522 mm). While calculating the radiation direction, width of the microstrip elements should be considered as well; because given s, l and d values are the edge dimensions of the meanderline array. In order to obtain corner-to-corner dimensions, width of the microstrip line should be incorporated in formulation as shown in Equation 5.2 so results will be more accurate.

Case 1: Phase=0°

$$\psi = (d+L+2w)Cos\theta - (2s+d+L+2w)\beta = 2n\pi \qquad \textbf{(5.2)}$$

After calculations, direction of radiation is found as θ=62°. It corresponds to 28° from broadside. Hence, the result is consistent with design specifications.

Case 2: Phase=25°

As shown in Equation 5.3, varactor diodes' phase shift should be added to the second part of the equation.

$$\psi = \frac{2\pi}{30}(d + L + 2w)Cos\theta - \{(2s + d + L + 2w)\beta + phase\} = 2n\pi \qquad \textbf{(5.3)}$$

After calculations, direction of radiation is found as θ=72.2°, it corresponds to 17.8° from broadside.

Theoretical analysis shows that it is possible to steer the beam 10° towards broadside by applying 25° phase shift using varactor diodes.

In the next section, theoretical investigations are verified with full wave EM simulations.

5.4 EM Simulation Results

Simulations of the beam-steerable meanderline array have been performed using two electromagnetic softwares; Ansoft Designer and Ansoft HFSS.

In Ansoft Designer, S-parameters of N-port devices obtained from linear simulations can be inserted in electromagnetic simulations. Therefore, during the simulations of beam-steerable meanderline array, instead of varactor diodes, S-parameters of different capacitance values are inserted into 2-port boxes and these boxes are connected to meanderline sections as shown in Figure 5.6.

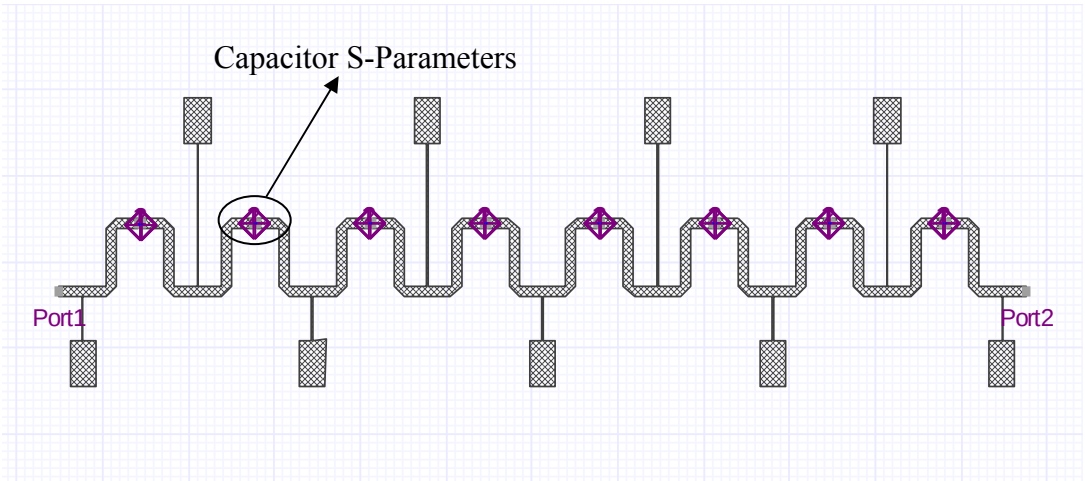

Figure 5.6 Ansoft Designer Model of the Beam Steerable Rampart Antenna with Varactor Diodes and Bias Lines

Dimensions of the beam-steerable meanderline array are similar to those of linearly polarized meanderline array mentioned in Chapter 4. In addition, varactor diodes' DC bias lines are reconfigured according to the geometrical structure of meanderline array. The unit element of meanderline array is illustrated in Figure 5.7 with dimensions s=6.687 mm, l=5.452 mm, d=5.522 mm, l1=16.35 mm, l2=5.45 mm, l3= 5.45 mm and l4= 5.45 mm.

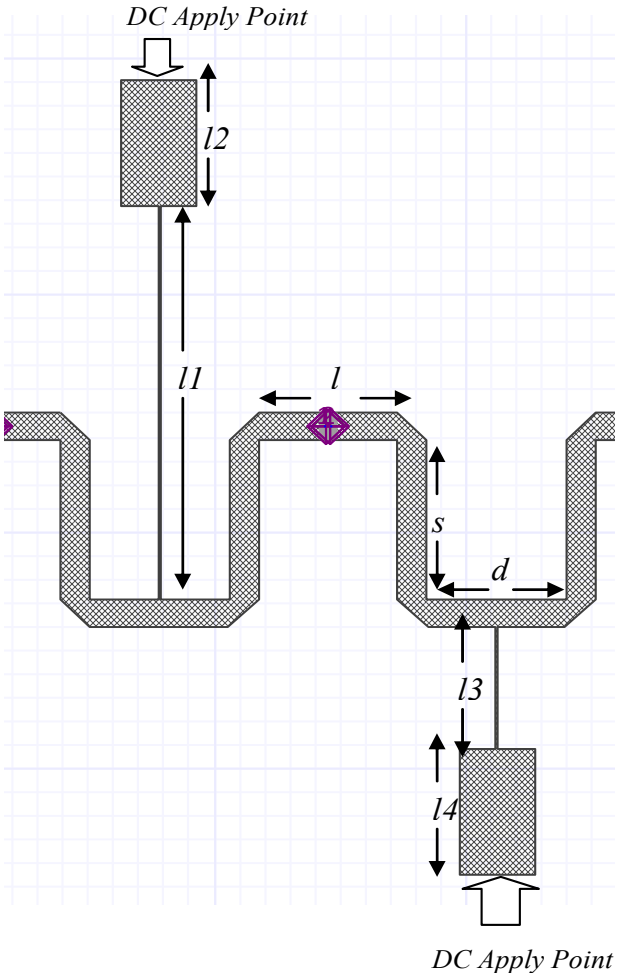

Figure 5.7 Unit Element of Beam-Steerable Meanderline Array

S-parameters obtained by Ansoft Designer is shown in Figure 5.8. As observed from the plots, for different values of varactor capacitance, return loss of beam-steerable array changes due to the impedance variation of the varactor diode. However, at 10 GHz, S11 value is well below -10 dB. Similarly, in Figure 5.9, S21 values for different capacitance values have been given and at 10 GHz, S21 value is about -3 dB.

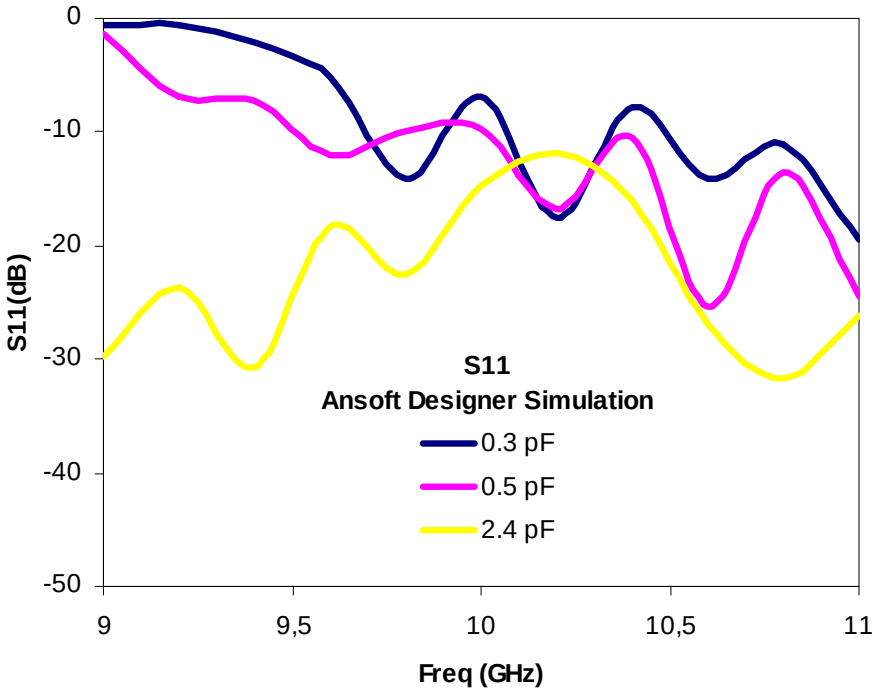

Figure 5.8 S11 Simulation of Beam-Steerable Meanderline Array for Various Capacitance Values

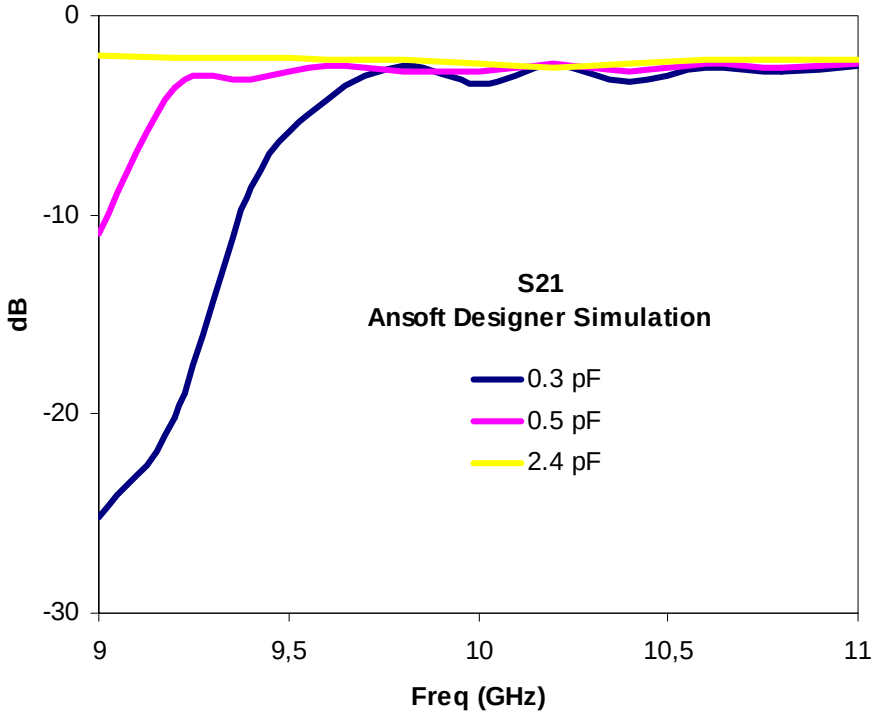

Figure 5.9 S21 Simulation of Beam-Steerable Meanderline Array for Various Capacitance Values

E-plane patterns for different values of varactor capacitances at 10 GHz is shown in Figure 5.10. The direction of the beam for 2.4-pF capacitance value is towards 30° and beam steers up to 19° for 0.3-pF capacitance value. Also, in Figure 5.11, beam variation with respect to varactor capacitance is presented. It could be derived from Figure 5.11 that beam steers more that 10° with corresponding varactor capacitance variation.

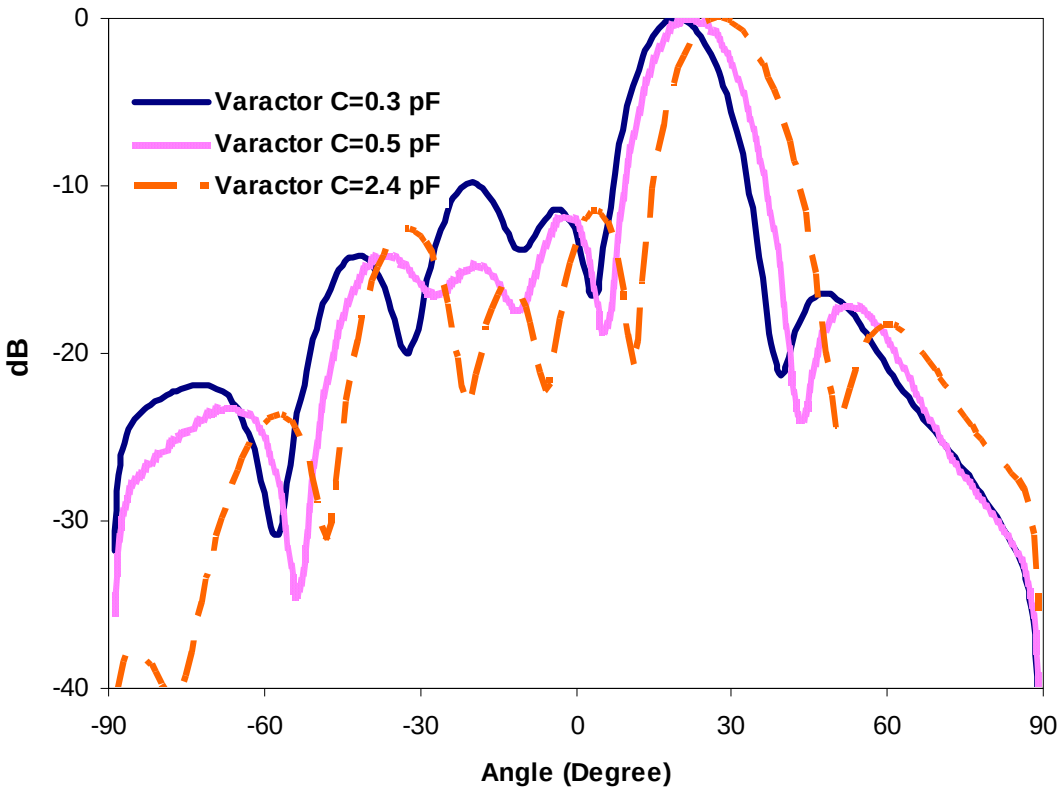

Figure 5.10 E-Plane Electric Field Pattern of Beam-Steerable Meanderline Array for Different Values of Varactor Capacitance (Ansoft Designer Simulation)

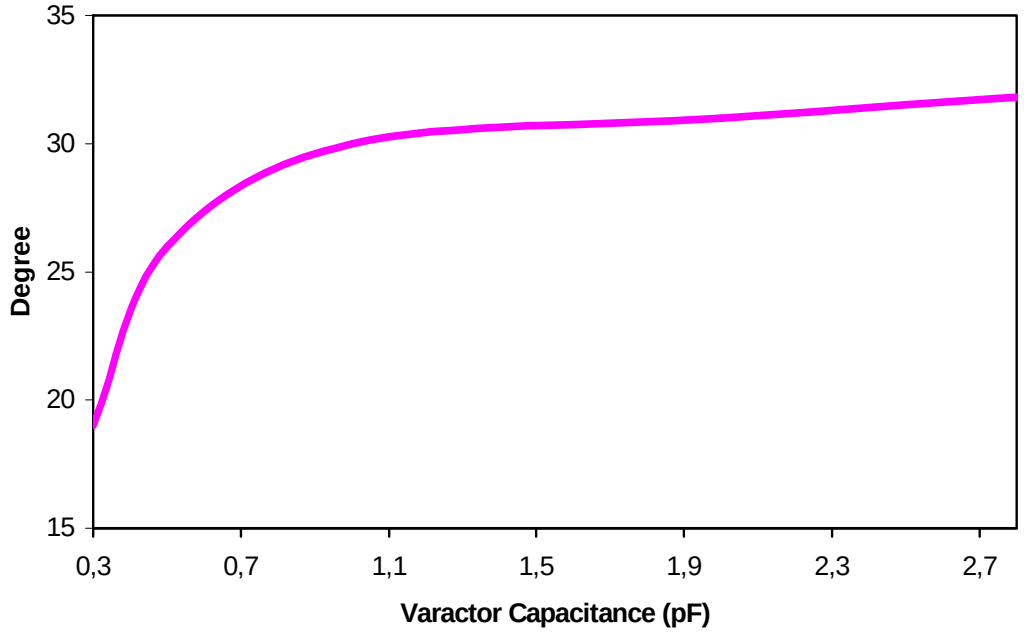

Figure 5.11 Beam Variation of Beam-Steerable Meanderline Array with respect to Varactor Capacitance Variation (Ansoft Designer Simulation)

E- and H-plane co- and cross-polarization patterns have been analyzed using Ansoft HFSS. Figure 5.12 shows E-plane co- and cross-polarization patterns of meanderline array. Since it is linearly polarized, there is more than 15 dB difference between co- and cross-polarizations' maximum values. H-plane radiation pattern of the meanderline array at 10 GHz has been illustrated in Figure 5.13. Difference between co- and cross-polarization levels is more than 15 dB which satisfies linearity requirements of beam-steerable meanderline array.

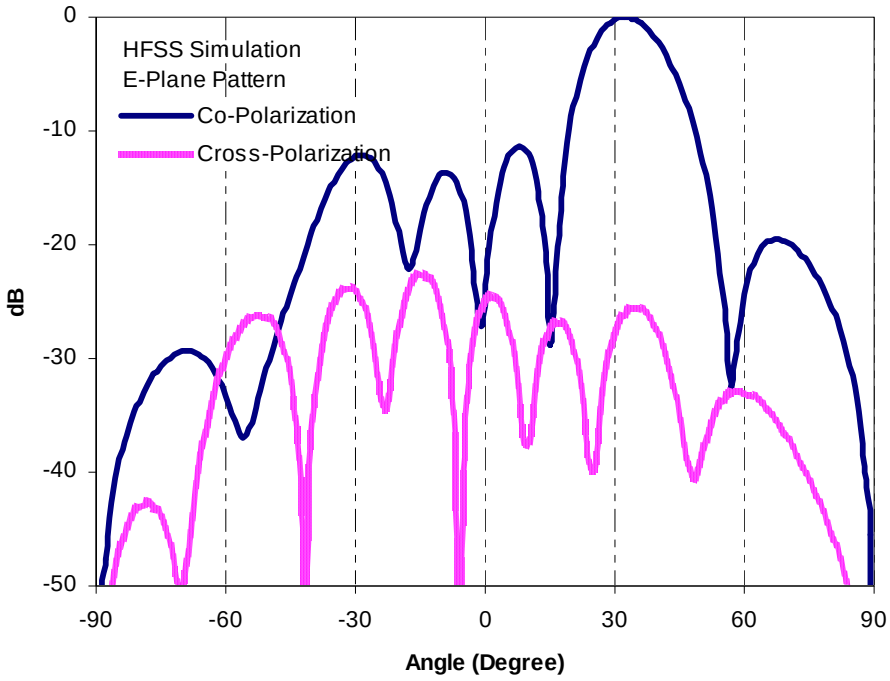

Figure 5.12 Co- and Cross-Polarization E-Plane Electric Field Patterns of Beam-Steerable Meanderline Array at 10 GHz

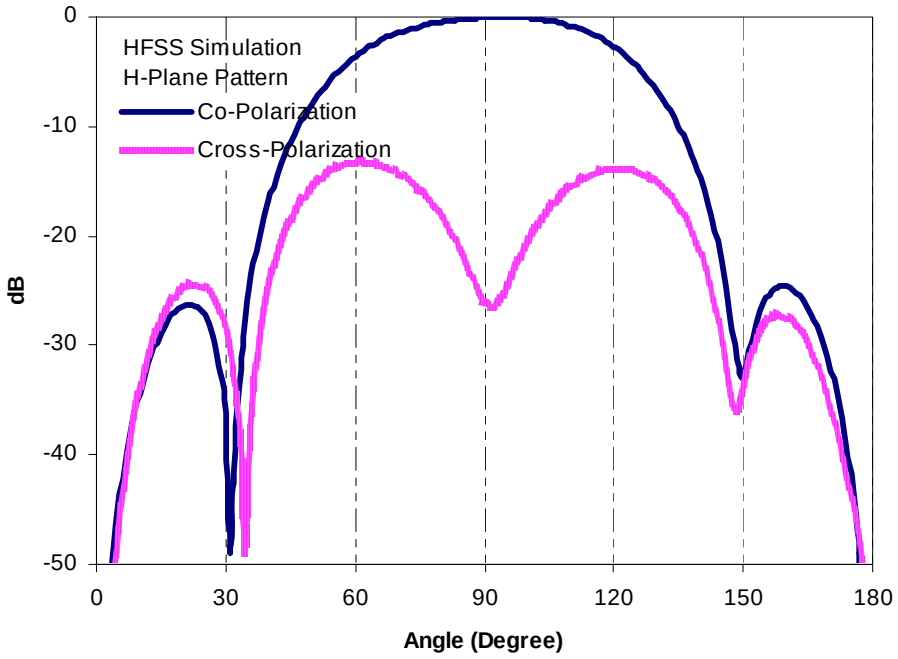

Figure 5.13 Co- and Cross-Polarization H-Plane Electric Field Patterns of Beam-Steerable Meanderline Array at 10 GHz

For different values of varactor capacitance, impedance of the varactor also changes; this affects the gain of the meanderline array. Ansoft Designer simulations show that the gain of the antenna decreases when the capacitance value of the varactor diode decreases.

Table 5.2 shows that for 2.4-pF varactor capacitance, gain of the meanderline array corresponds to 4.85 dB and it decreases down to 2.8 dB when the varactor capacitance equals 0.3 pF.

Table 5.2 Gain Variation of Meanderline Array for Different Values of Varactor Diodes Capacitance (Ansoft Designer Simulation)

Varactor Capacitance	**Gain**
0.3 pF	2.8 dB
0.5 pF	3.8 dB
2.4 pF	4.85 dB

To observe the effects of bias lines, surface current distribution obtained by HFSS is given in Figure 5.14 at 10 GHz. Current distribution demonstrates that no current flows on the bias paths, so meanderline array is not affected by varactor diodes' DC bias lines.

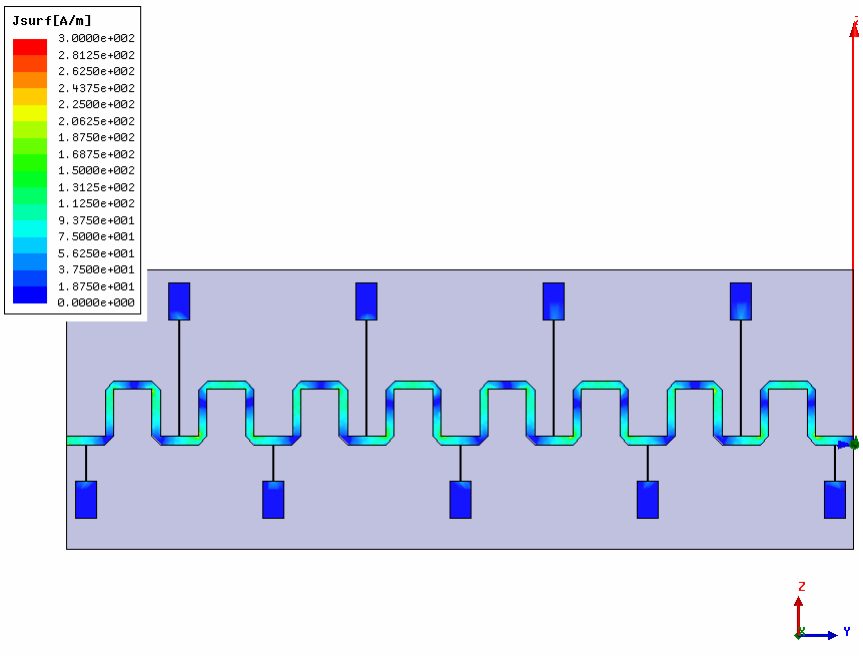

Figure 5.14 Surface Current Distribution of Meanderline Array

5.5 Production of Beam Steerable Antenna

Beam-steerable meanderline array has been manufactured on 15-mil thick ROGERS 5880 Duroid with dielectric constant ε_r=2.2 as shown in Figure 5.15. Tyco/AMP SMA type connectors have been used at the input and termination ports. During radiation pattern measurements, second port is terminated with 50-Ω load.

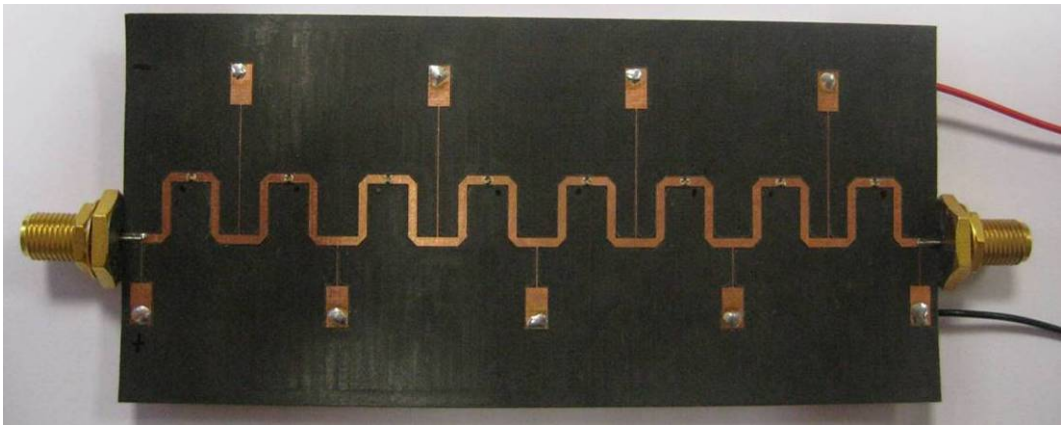

Figure 5.15 Prototype of Beam-Steerable Rampart Antenna with Varactor Diodes

In Figure 5.16, photograph of a unit cell of beam-steerable meanderline array with DC bias lines has been presented. Varactor diodes have been mounted on the meandering sections with silver epoxy cured at 150°C. Since ROGERS 5880 duroid is not suitable for plating, DC bias lines are connected to the DC pads placed on the ground plane by soldering.

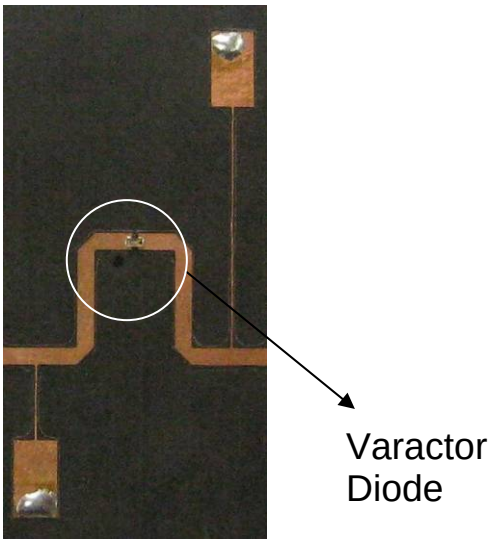

Figure 5.16 Unit Cell of the Beam Steering Rampart Antenna with DC Bias Pad

5.6 Measurements

In order to validate theoretical analysis and simulations performed in Ansoft Designer, S-parameters and radiation patterns of the meanderline array have been measured. In the following sections, measurement results will be presented.

5.6.1 S-parameter Measurements

S-parameter measurements of the beam-steerable meanderline array have been performed by using Agilent E8364C PNA, 10 MHz to 50 GHz Vector Network Analyzer. Two-port calibration has been carried out and antenna array has been measured between 9-11 GHz. Return loss of the beam-steerable meanderline array under different bias voltages has been measured to see the effect of capacitance variation to the S-parameters of the antenna. S11 measurements have been displayed in Figure 5.17. Return loss of the meanderline array is well below -10dB for different

values of bias voltages. Also, S21 parameter of the beam-steerable meanderline array has been measured and given in Figure 5.18. S21 parameter of the array is between -10 and -15 dB. Actually, S21 includes dielectric, copper, conductor, radiation losses and mainly varactor diodes' insertion losses. Furthermore, efficiency of the beam steerable meanderline array has been calculated at 10 GHz by using S-parameters.

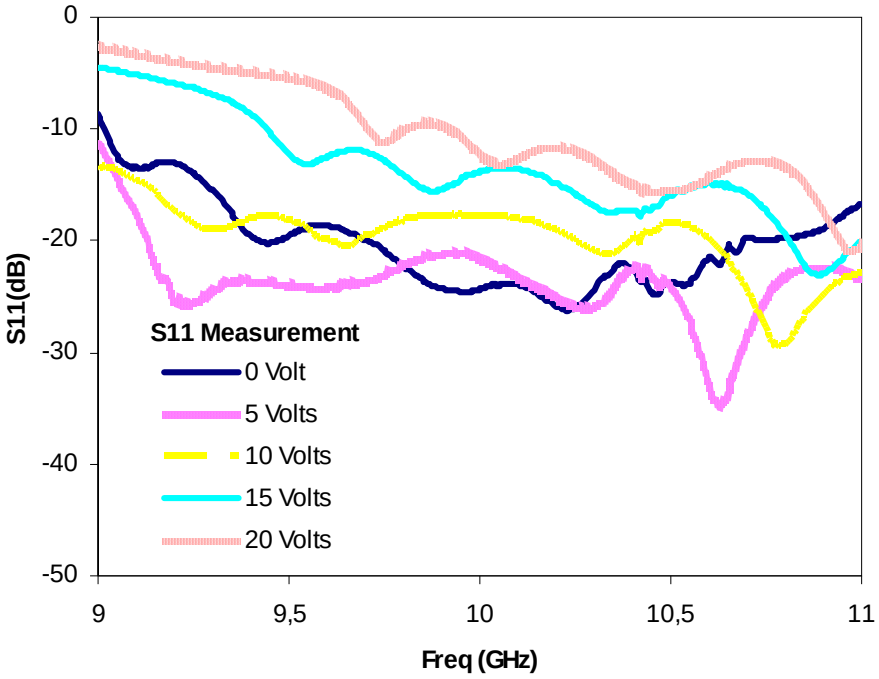

Figure 5.17 S11 Measurement of Beam-Steerable Meanderline Array Under Different Bias Voltages

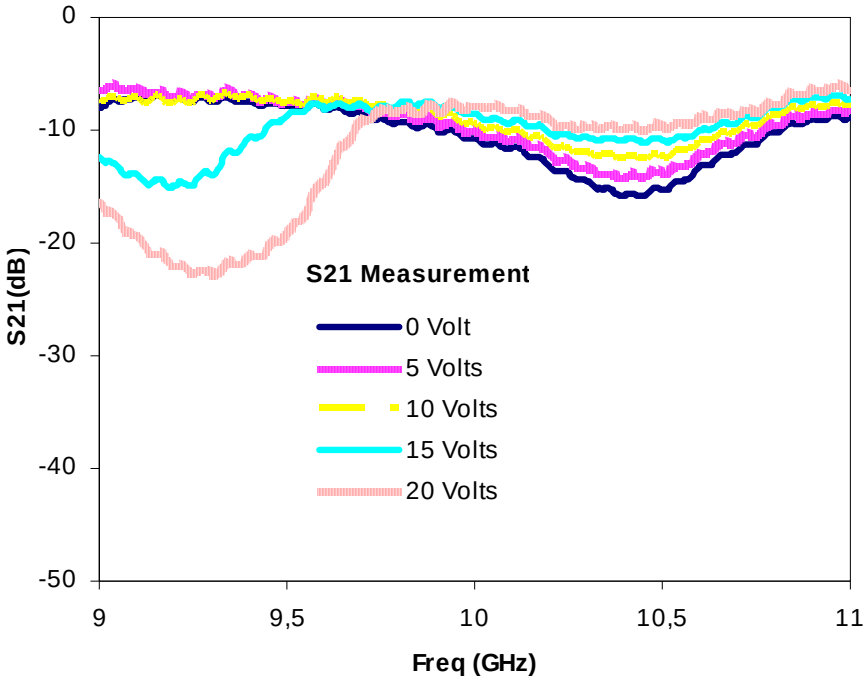

Figure 5.18 S21 Measurement of Beam-Steerable Meanderline Array under Different Bias Voltages

5.6.2 Radiation Pattern Measurements

Radiation patterns of beam-steerable meanderline array have been measured for different values of varactor diode bias voltage at 9.5, 10 and 10.5 GHz in tapered anechoic chamber at ASELSAN facilities

By using the relation between varactor capacitance vs. voltage derived in Section 5.2.2, simulations performed in Ansoft Designer are compared with measurements. Figure 5.5 indicates that 0-V bias voltage corresponds to 2.4-pF capacitance, therefore; in Figure 5.19, measured E-plane pattern under 0-V bias voltage is compared to the simulation with 2.4-pF capacitance case. It shows that simulations are consistent with measurements around the main beam. The difference at far side lobes is due to the effects of the platform on which the antenna is placed during measurement. In Figure 5.20 and Figure 5.21, simulations with different values of varactor capacitances are compared with measurements under 10-V and 20-V bias voltages. Reasonable agreement between simulations and measurements is observed.

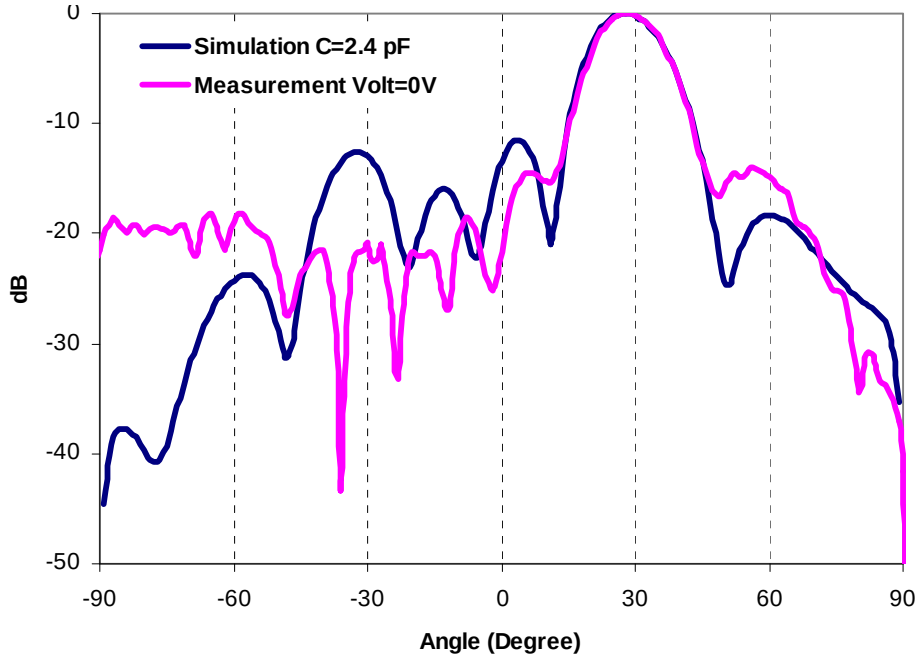

Figure 5.19 E-plane Electric Field Pattern Measurement under 0 Volt Bias Voltage and Ansoft Designer Simulation with 2.4 pF Varactor Capacitance

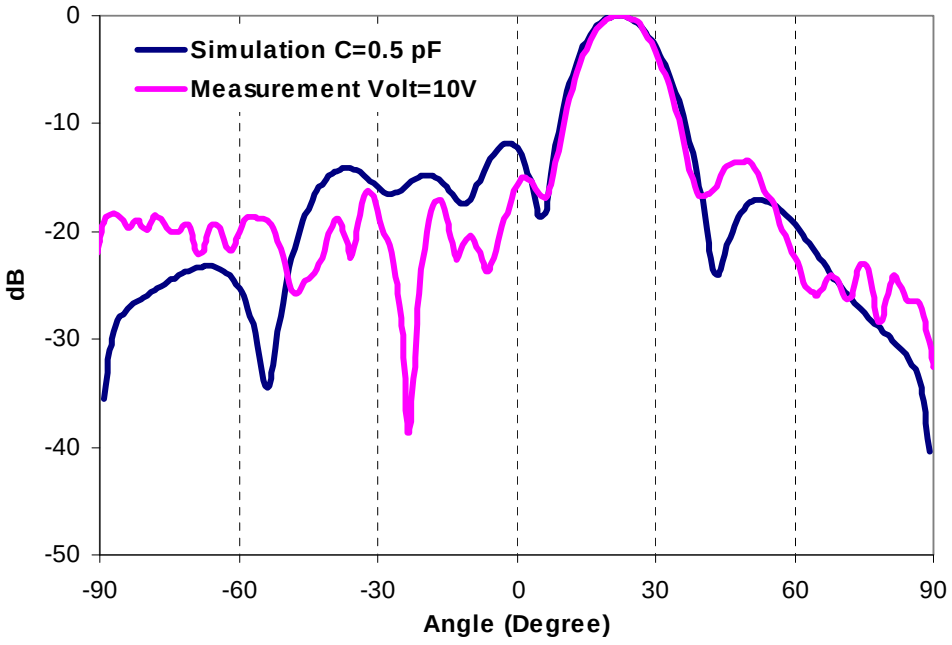

Figure 5.20 E-plane Electric Field Pattern Measurement under 10 Volt Bias Voltage and Ansoft Designer Simulation with 0.5 pF Varactor Capacitance

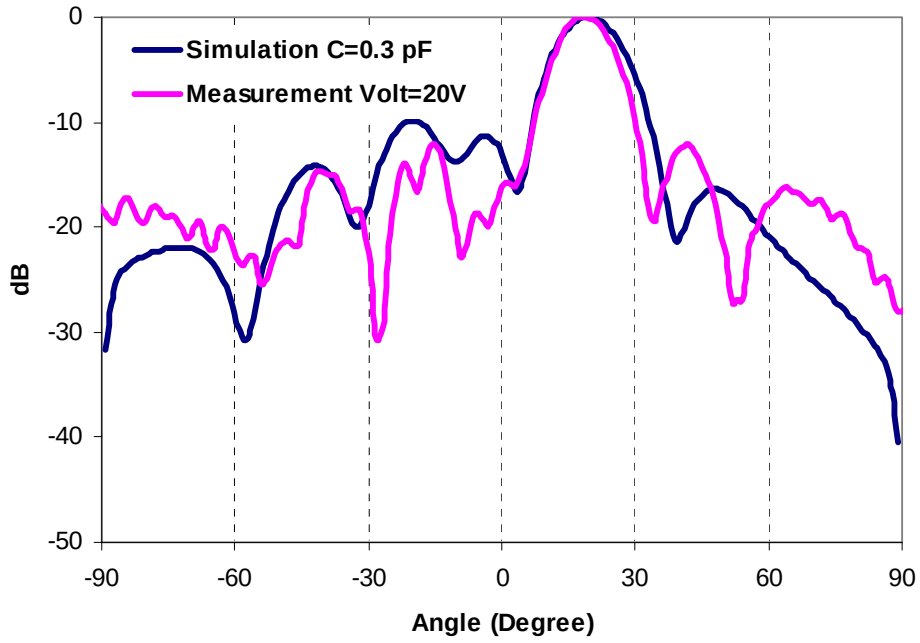

Figure 5.21 E-plane Electric Field Pattern Measurement under 20 Volt Bias Voltage and Ansoft Designer Simulation with 0.3 pF Varactor Capacitance

Furthermore, E- and H-plane measurements at 9.5, 10 and 10.5 GHz have been performed with different bias voltages. Results of E-plane measurements have been illustrated in Figure 5.22, Figure 5.23, and Figure 5.24. These figures show that the direction of the radiated beam steers linearly with respect to applied DC bias voltage. On the other hand, while the beam is steering, side lobes of the beam-steerable meanderline array also increase up to -10 dB. Also, as seen in Figure 5.22, Figure 5.23 and Figure 5.24, at different frequencies beam is steering at different angles. Electrical length between meanderline unit elements varies with frequency. Therefore, direction of radiation is steering with frequency as well.

H-plane measurements of beam-steerable meanderline array have been demonstrated in Figure 5.25, Figure 5.26, and Figure 5.27. H-plane pattern of the array does not change significantly with respect to the applied bias voltages. However, especially at 10.5 GHz, H-plane pattern is affected by the varactor diodes' bias lines.

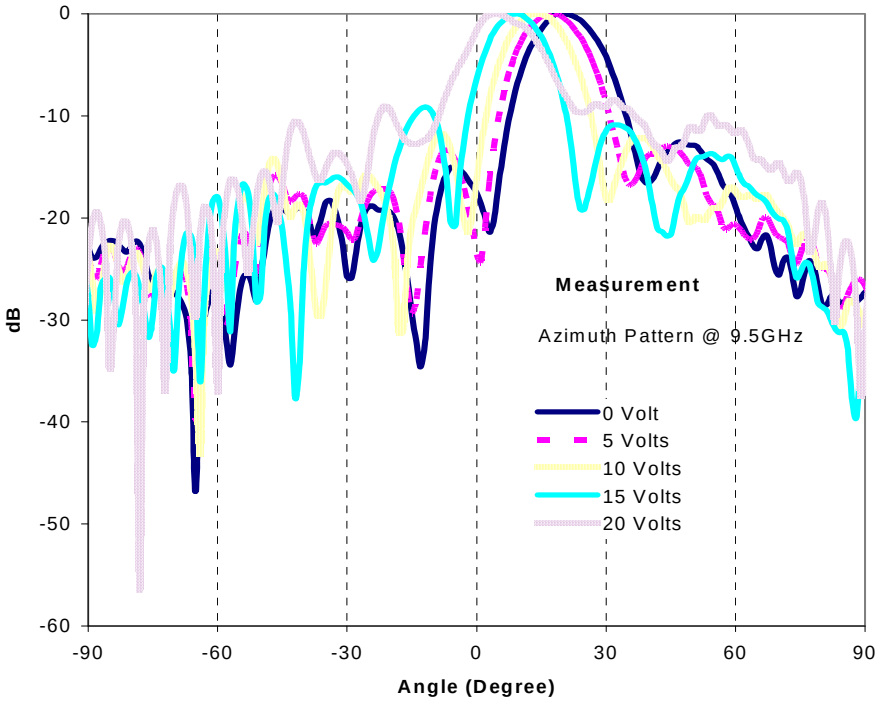

Figure 5.22 E-Plane Electric Field Pattern of Beam-Steerable Meanderline Array at 9.5 GHz Under Different Values of Bias Voltages

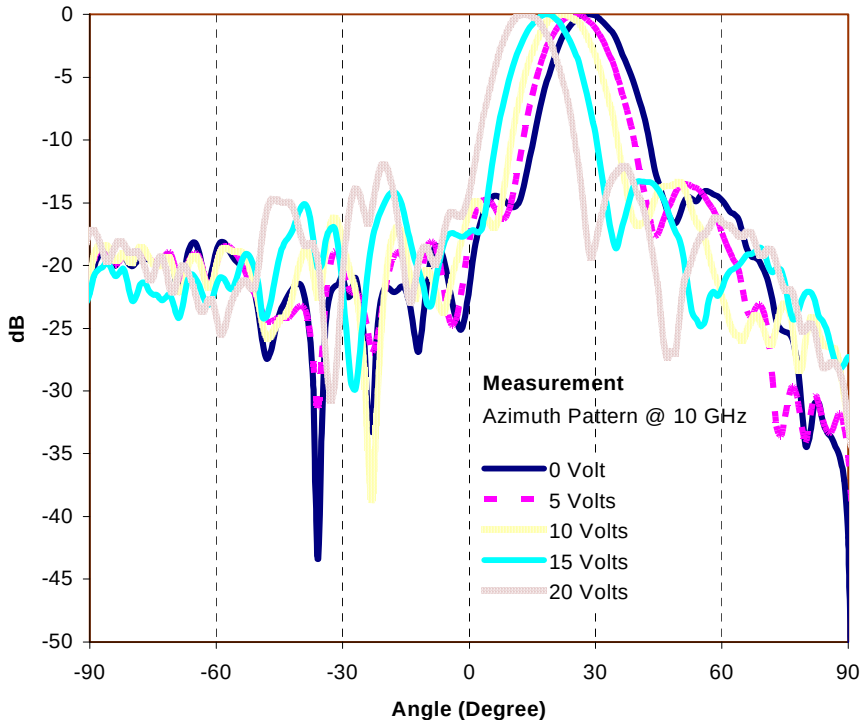

Figure 5.23 E-Plane Electric Field Pattern of Beam-Steerable Meanderline Array at 10 GHz Under Different Values of Bias Voltages

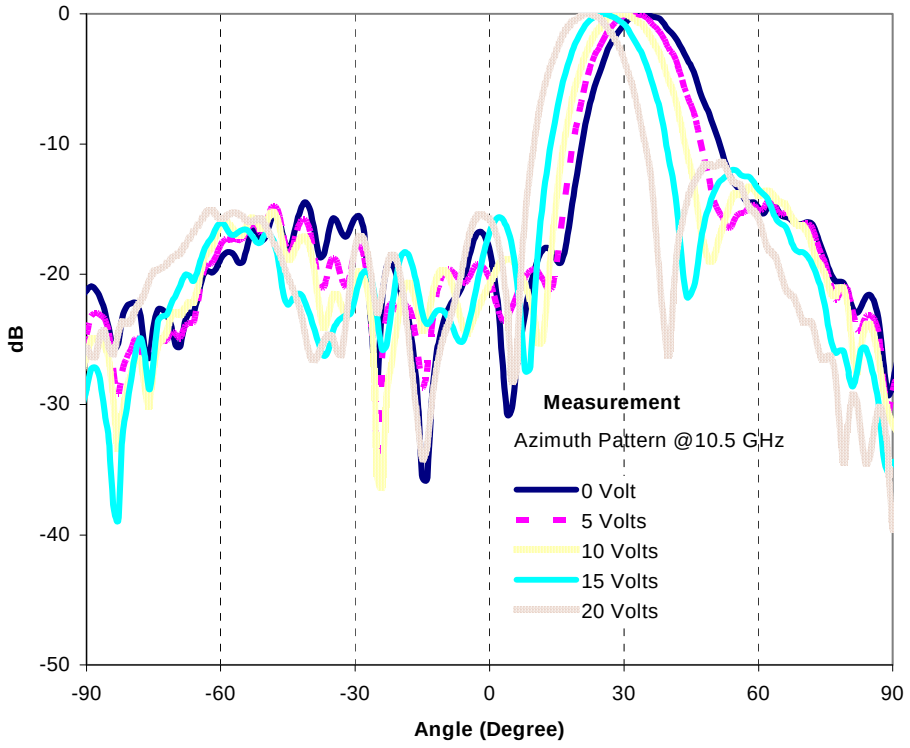

Figure 5.24 E-Plane Electric Field Pattern of Beam-Steerable Meanderline Array at 10.5 GHz Under Different Values of Bias Voltages

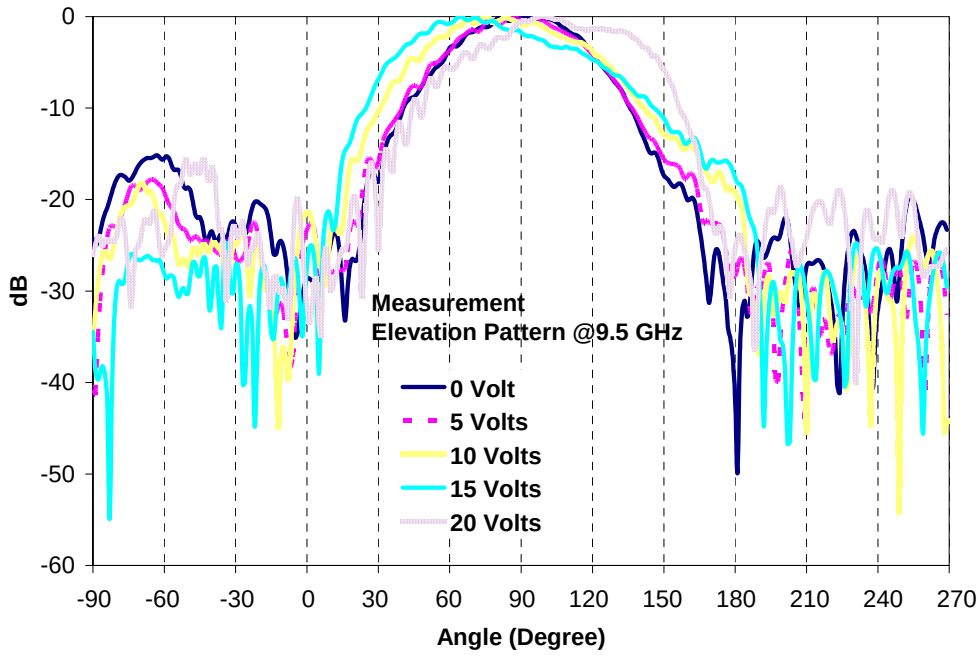

Figure 5.25 H-Plane Electric Field Pattern of Beam-Steerable Meanderline Array at 9.5 GHz Under Different Values of Bias Voltages

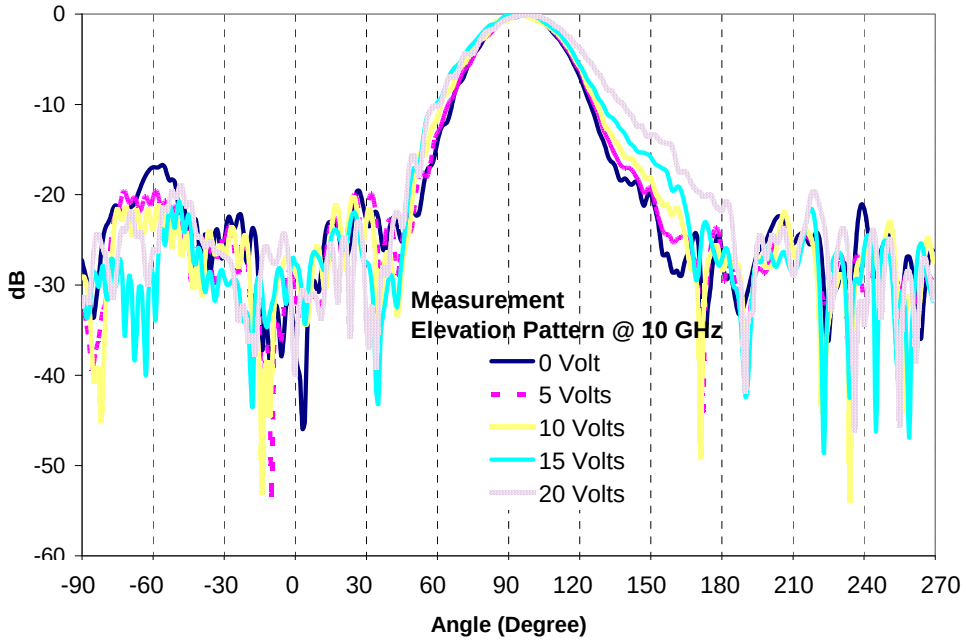

Figure 5.26 H-Plane Electric Field Pattern of Beam-Steerable Meanderline Array at 10.5 GHz Under Different Values of Bias Voltages

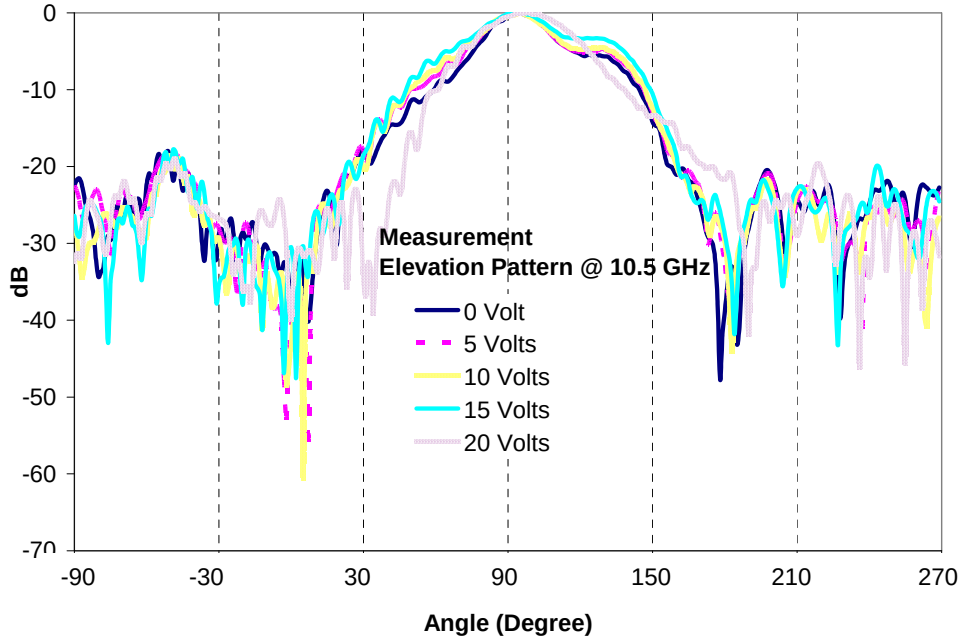

Figure 5.27 H-Plane Electric Field Pattern of Beam-Steerable Meanderline Array at 10.5 GHz Under Different Values of Bias Voltages

5.7 Further Investigations on Beam-Steerable Traveling Wave Meanderline Array

In previous section, it is shown that more than 10° beam steering can be achieved by loading the meandering sections with single varactor diode. As stated in Section 5.2, single varactor diode can provide 25° phase shift on the transmission line. On the other hand, in order to steer the beam of the meanderline array more than 10°, other phase shifting mechanisms can be used. In [32], it is stated that reflective type phase shifters can provide more than 60° phase tuning range.

To improve the beam scan range, a meanderline antenna with reflective type phase shifters has been designed. Reflective type phase shifter is composed of a hybrid-coupler and two identical tunable reflective loads. In order to realize tunable reflective loads, varactor diodes are utilized.

5.7.1 Varactor Diode Loaded Branch-Line Coupler Phase Shifters

Branch-line coupler is a narrowband device and can be used as power divider if it is designed as 3-dB directional coupler. In the case of 3-dB directional coupler which is called hybrid junction, power incident in port 1 is coupled to port 2 and port 3 but not into port 4 since it is the isolated port. Theoretical analysis of 3-dB branch-line coupler is investigated in detail in [31].

Design of narrowband branch-line coupler has been performed using Ansoft Designer. Operation frequency of the branch-line coupler has been set to 10 GHz. ROGERS 5880 Duroid with 15-mil thick ROGERS 5880 Duroid with dielectric constant ε_r=2.2 is selected as substrate due to its low dielectric loss.

Ansoft Designer schematic model of the branch-line coupler is illustrated as in Figure 5.28. Theoretically, to realize a 3-dB branch-line coupler, the impedance of the branches should be set as;

$$Y_1 = Y_0 * \sqrt{2}$$

$$Y = Y_0$$

Length of the branch-line sections should be equal to;

$l_1=l_2= \lambda_g/4$;

Therefore, dimensions of the branch-line coupler are; $l_1=l_2=$ 5.75 mm and w_1=1.17 mm, w_2=1.9 mm.

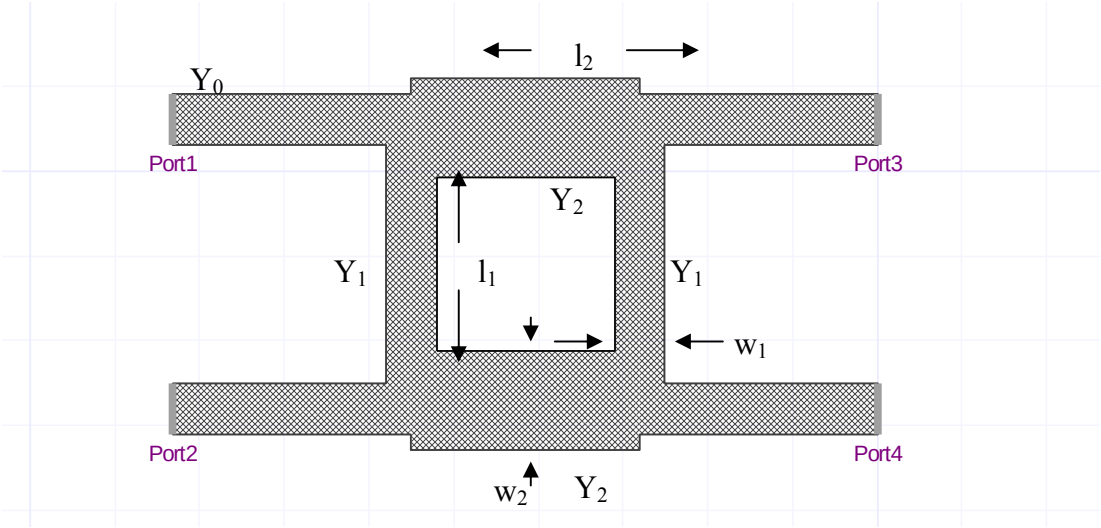

Figure 5.28 Ansoft Designer Model of 3-dB Branch-Line Coupler

Simulations of the 3-dB branch-line coupler have been performed between 6-15 GHz in Ansoft Designer. In Figure 5.28, S-parameters of branch-line couplers are presented. Return loss of the coupler (S11) is below -20 dB around 10 GHz. Power incident in port 1 is equally coupled to port 3 and port 4 and less than -20 dB of power is coupled to the isolated port (port 2).

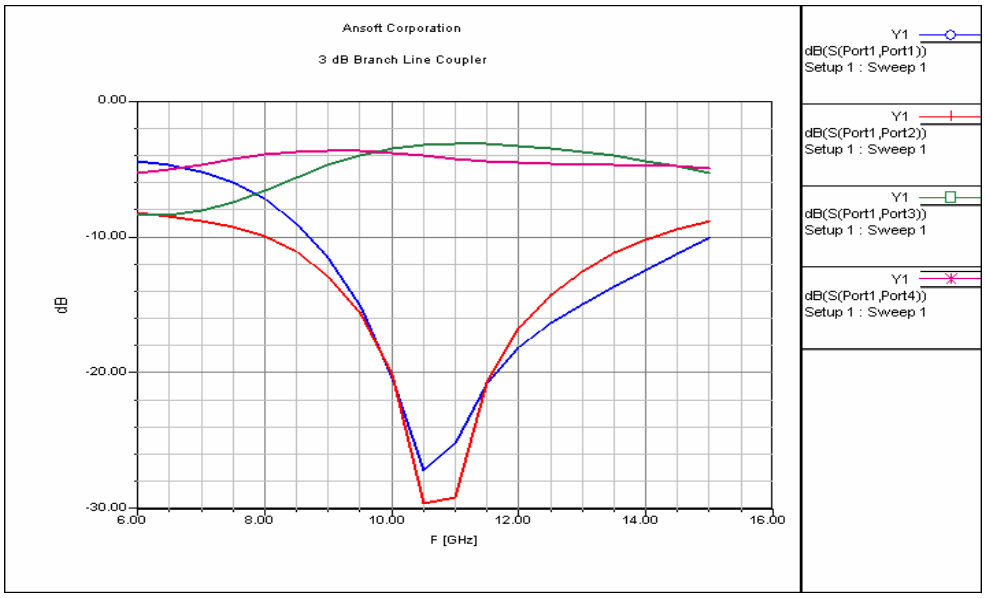

Figure 5.29 Ansoft Designer S-Parameter Simulation of 3-dB Branch-Line Coupler

As mentioned above, reflective type phase shifter is composed of 3-dB branch-line coupler loaded with varactor diodes. The analysis of reflective type phase shifter has been carried out in Ansoft Designer.

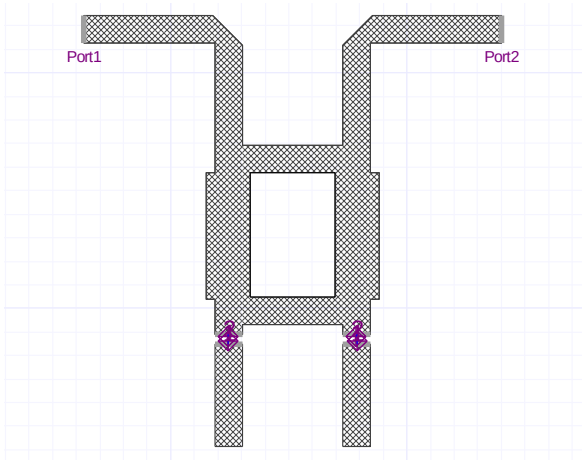

Figure 5.30 Ansoft Designer Model of Reflective Type Phase Shifter Loaded with Varactor Diodes

During the simulations of reflective type phase shifter, instead of varactor diodes, S-parameters of different capacitance values are inserted into 2-port boxes and these

boxes are connected to branch-line sections as shown in Figure 5.30. For different values of varactor capacitance, phase variation between port 1 and port 2 has been simulated. In simulations, varactor capacitance has been tuned between 0.3 pF to 2.7 pF and more than 70° phase variation has been observed as shown in Figure 5.31.

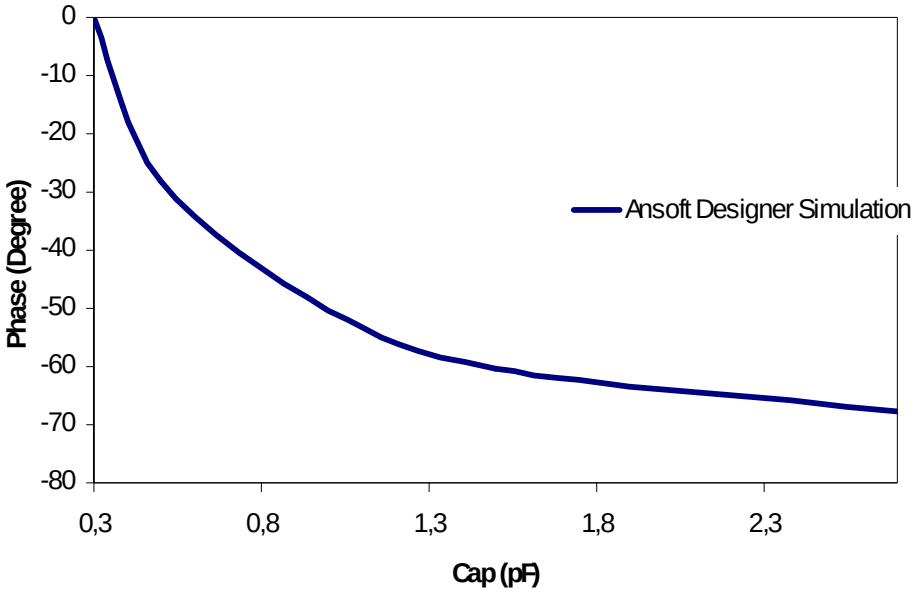

Figure 5.31 Ansoft Designer Simulation of Branch-Line Coupler Phase Variation with respect to Varactor Capacitance

5.7.2 Application of Phase Shifter on Traveling Wave Arrays

In order to achieve more beam-steering, varactor diodes in the previous design can be replaced by varactor diode loaded branch-line coupler type phase shifters, as shown in Figure 5.32.

Analysis of meanderline array with varactor diode loaded branch-line coupler type phase shifter has been performed using Ansoft Designer.

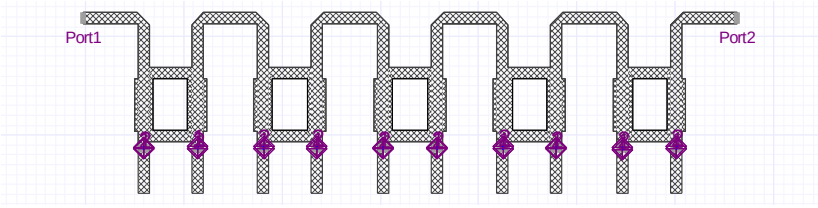

Figure 5.32 Meanderline Array with Varactor Diode Loaded Branch-Line Coupler Phase Shifter

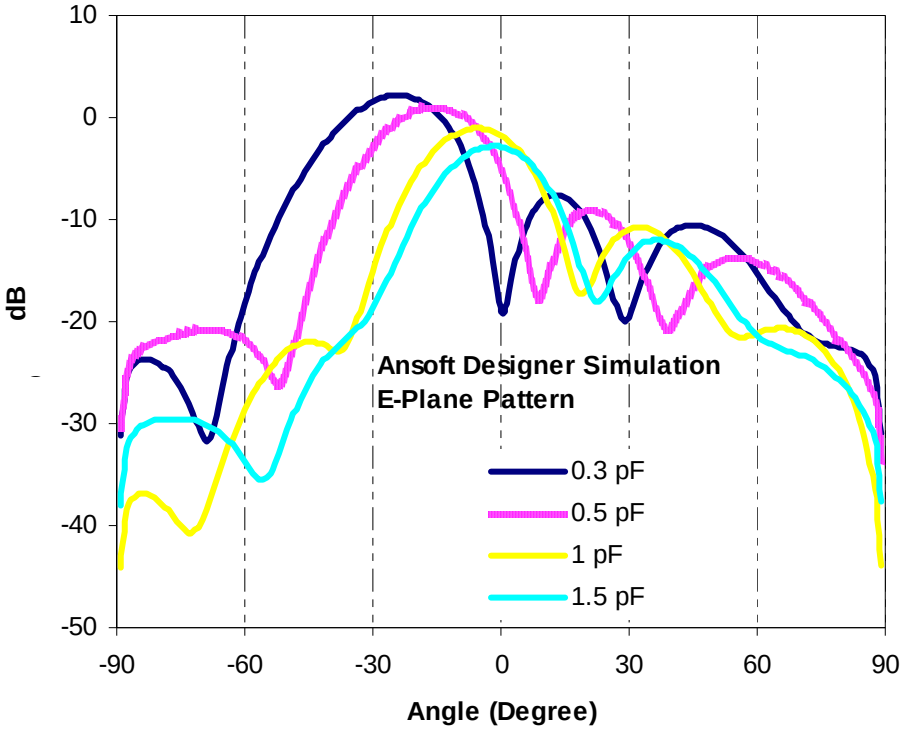

Figure 5.33 E-Plane Electric Field Pattern of Beam-Steerable Meanderline Array for Different Values of Varactor Capacitance (Ansoft Designer Simulation)

In Figure 5.33, patterns of the meanderline array with reflective type phase shifter are given for different capacitance value. Direction of the radiation beam steers from 24° to broadside 0°. On the other hand, while the beam is sweeping, the gain of the array decrease significantly.

To sum up, varactor diode loaded branch-line coupler phase shifters have wide phase-tuning range as shown in simulations. It is possible to use these types of phase

shifters in traveling wave meanderline arrays. However, since the branch-line coupler is physically large, placing the phase shifters between elements can be a problem. Furthermore, such a structure on the radiating part of the antenna may affect the radiation pattern as well. Thus, further investigations should be performed throughout the implementation processes.

CHAPTER 6

Dual CP Polarized Traveling Wave Meanderline Array using RF MEMS Technology for X-Band Applications

As mentioned in Chapter 2, polarization of the antenna is defined as the polarization of the wave transmitted (radiated) by the antenna and it is one of the important design parameters of the antennas in systems. Especially, polarization reconfigurability increases the degree of freedom of the antenna while sending and receiving signals with different polarizations. For instance, slant polarized antennas are able to receive both vertical and horizontal polarizations. It is possible to achieve polarization reconfigurability in antennas by using electrical and mechanical devices such as switches, loads etc. Particularly, RF MEMS switches have proven their usefulness, due to their small size, low insertion loss, high linearity and improved performance. RF MEMS devices are commonly used in frequency, polarization and radiation pattern reconfigurable antennas ([6], [7], [10])

Traveling wave meanderline arrays are microstrip structures and it is easy to integrate components on them. Consequently, it is rather easy to implement reconfigurable meanderline array structures as demonstrated in Chapter 5. Another advantage of meanderline arrays is that their polarizations can be controlled by tuning the dimensions of the meanderline sections. As explained in Section 3.2.1, if the dimensions of the meanderline array are $s=\lambda_g/2$, $d=\lambda_g/4$, and $l=3\lambda_g/4$, polarization of the meanderline array becomes circular.

In this chapter, a polarization-agile meanderline array has been investigated. Single meanderline array has been designed as circularly polarized antenna and by using RF MEMS switches its polarization can be set as either RHCP (Right Hand Circularly Polarized) or LHCP (Left Hand Circularly Polarized).

In Figure 6.1, schematic view of dual circularly polarized meanderline array is presented. Meanderline array consists of upper and lower meanderline sections and SPDT RF MEMS switches are placed at the connection point of meanderline sections. If the upper section of the meanderline array is switched, polarization of the array is RHCP and otherwise array is LHCP.

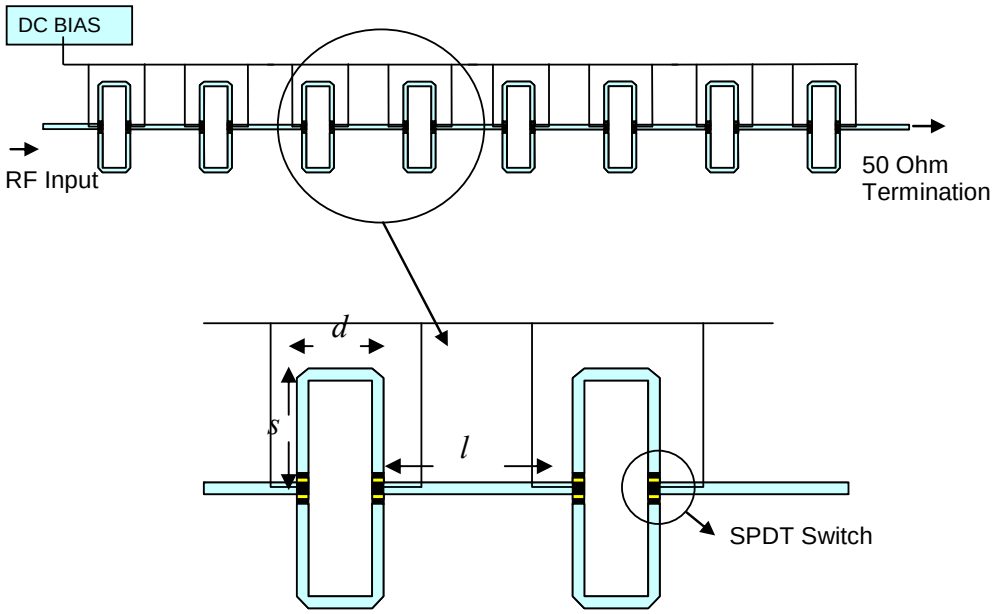

Figure 6.1 The Schematic View of Polarization-Agile Meanderline Array

Electromagnetic analysis of the polarization-agile meanderline array has been performed using Ansoft HFSS. Antenna has been designed on 15-mil thick ROGERS 5880 Duroid with ε_r=2.2. Operation frequency of polarization-agile meanderline array is set to 10 GHz and polarization is circular. Impedance of the meanderline sections are 50 Ω and the width of the microstrip segments is equal to 1.17mm. Dimensions of the meanderline sections are set as s=10.9mm, d=5.45mm and l=16.35mm to achieve circular polarization.

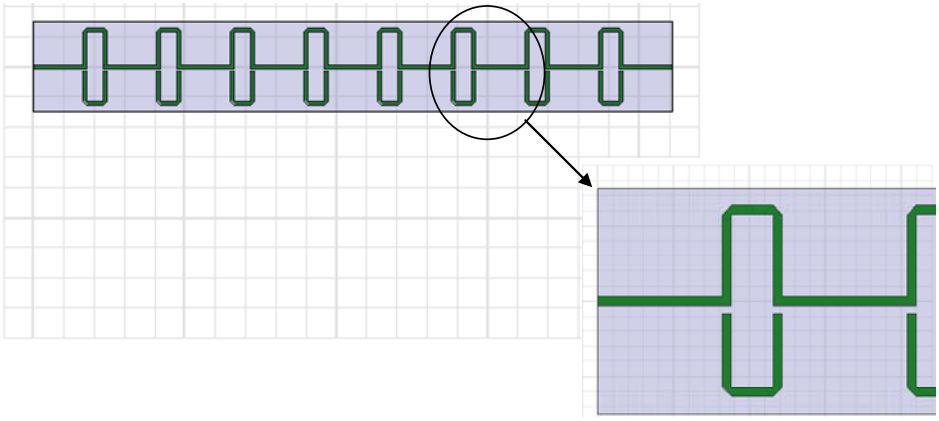

Figure 6.2 HFSS Model of the Polarization-Agile Meanderline Array

As illustrated in Figure 6.2, down states of MEMS switches are modeled by short metallic parts and up states of switches are left as open. S-parameter, radiation pattern and polarization characteristics of the polarization-agile array have been investigated at 10 GHz.

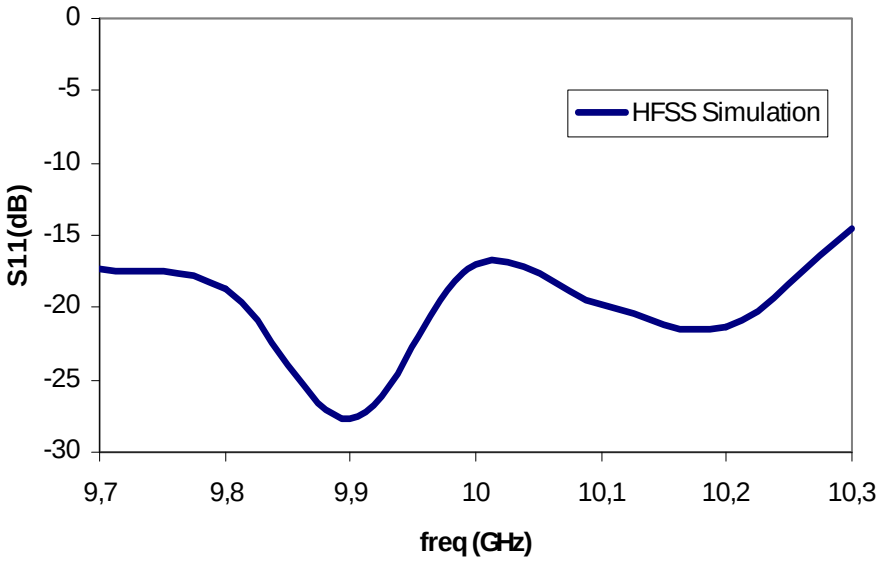

Figure 6.3 S11-Parameter Simulation of Polarization-Agile Meanderline Array

Return loss of the polarization-agile meanderline array is given illustrated in

Figure 6.3 between 9.7 to 10 GHz. Return loss of the array is well below -10 dB in the operation band.

E-plane pattern of the polarization-agile meanderline array at 10 GHz is shown in Figure 6.4. As seen from the pattern, the main beam of the array is directed toward 14° and 3-dB beam width is about 8°. Also, the shoulder around -100° is due to the placement of meanderline array elements. As mentioned in Chapter 3, meanderline array can be modeled with magnetic current elements. When the array factor of the array is calculated, grating lobes are observed.

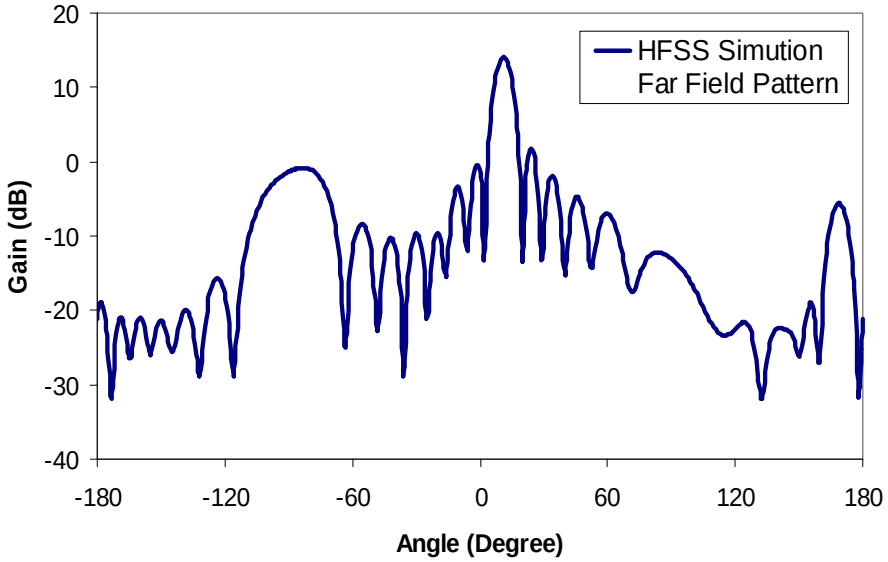

Figure 6.4 E-Plane Co-Polarization Pattern of Polarization-Agile Meanderline Array at 10 GHz

In addition, axial ratio of the meanderline array has been calculated around the main beam and given in Table 6.1. Around the main beam, axial ratio equals to 3 dB and axial ratio get worse towards 10°. In addition, when the switches select one array, other portion of the array will form open stubs. These sections disturb polarization of the array as well.

Table 6.1 Axial Ratio of the Polarization-Agile Meanderline Array around Main Beam at 10 GHz

Angle (Degree)	Axial Ratio (dB)
10°	3.24
11°	3.17
12°	3.07
13°	2.94
14°	2.77
15°	2.56
16°	2.28
17°	1.88
18°	1.3

As shown in Table 6.2, for the 1st state, upper part of the meanderline array is selected and the antenna is RHCP. In this case, the antenna receives RHCP signal with 16 dB of gain and LHCP signal 32 dB below. In a similar manner, when the 2nd state is selected, antenna is LHCP.

Table 6.2 Simulation of LHCP and RHCP values for the 1st and 2nd States of RF MEMS Switches

	1st State	2nd State
LHCP(dB)	-16 dB	16 dB
RHCP(dB)	16 dB	-16 dB

In summary, a polarization-agile meanderline array with SPDT RF MEMS switches has been proposed. Polarization of the meanderline array can be altered by selecting different paths of the meander line array. If the upper part of the array is selected by MEMS switches, antenna polarization becomes RHCP and if lower part of the meanderline array is selected, polarization turns out to be LHCP. Simulation of the polarization-agile array has been performed using Ansoft HFSS without MEMS switches and operation of the antenna has been verified.

CHAPTER 7

Dual Frequency Slot Dipole Array for X- and Ka- Band Applications

Frequency reconfigurable antennas are very attractive in many fields such as communication, radar and satellite applications. Reconfigurability can be provided by switches, loads etc. MEMS (MicroElectroMechanical Systems) devices have proven their usefulness in microwave applications with their reduced cost, improved performance, and miniaturized dimensions. A dual frequency reconfigurable slot dipole array with a CPW-based feed using RF MEMS technology for X- and Ka-band applications has been designed in [6]. In [6], the array has been designed on 500 μm-thick 4" glass substrate with εr=4.6 (tanδ=0.005) and MEMS switches are monolithically integrated on the glass substrate. Operation of MEMS switches is summarized in Appendix E. The antenna proposed in this thesis, based on [6], is designed on 25 mil-thick Rogers 6006 Duroid (ε_r=6.15) substrate and packaged MEMS switches will be implemented on the array. Prototype fabrication and measurements of single- and 2-element dual-frequency slot dipole antennas are introduced in this chapter.

The dual frequency array is composed of 2 linearly placed frequency-tunable slot dipole elements and a CPW-based feed network including 50-Ω/100-Ω dual-frequency transformers, chamfered CPW right-angle bends and T-junction. Coplanar waveguide (CPW) transmission lines have been used in the corporate feed network of 2-element linear array due to its advantages over a microstrip feeding network, such as low radiation losses, less dispersion, easier combination with active devices. Figure 7.1 shows the schematic view of the dual-frequency array.

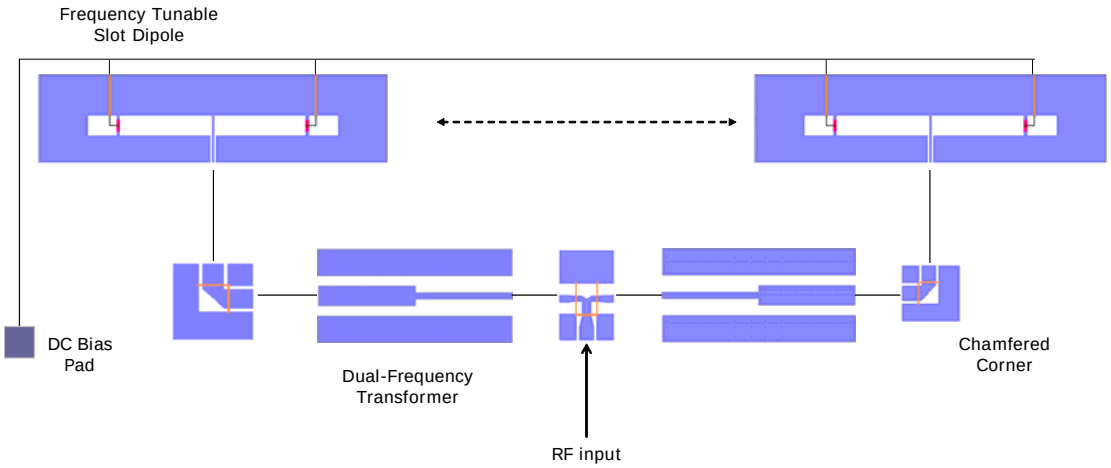

Figure 7.1 The Schematic View of 2-Element Reconfigurable Slot Dipole Antenna Array Structure with MEMS Switches

7.1 Reconfigurable Slot Dipole Antenna

Figure 7.2 shows the CPW fed slot dipole antenna structure used in the array [6]. For the implementation of these antennas, a 25 mil-thick Rogers 6006 Duroid (ε_r=6.15) substrate with 0.5 Oz Copper has been used. The slot dipole antennas can operate at X- and Ka- band with the aid of RF MEMS switches located on the slot arms. Operation frequency of the slot antennas is determined by the length of the slots. Also, it is stated in [6] that in addition to the length of the slots, height of the dielectric substrate controls the resonance frequency. Slot width and feed line parameters control the return loss level. In fact, slot dipole antennas exhibit 40-70Ω input impedance when the total length is about 0.8-0.9λ_g at the frequency of interest. The total length of the dipole is equal to 0.7λ_g (2*L1) when the switches are in up state and equal to 0.7λ_g (2*L2) when the switches are in down state.

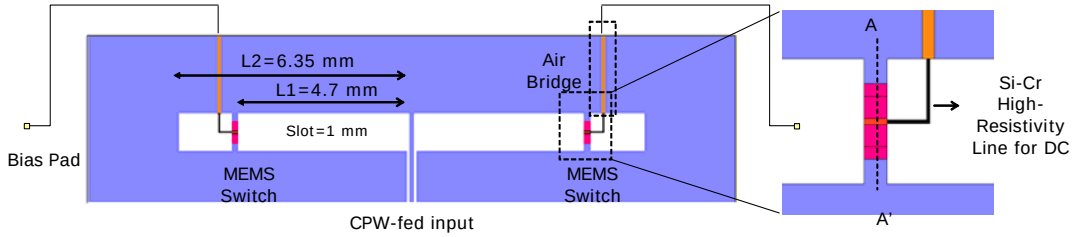

Figure 7.2 The Schematic View of Reconfigurable Slot Dipole Antenna with MEMS Switches Located on the Arms to Control Resonant Frequency

Throughout the design procedure of the antenna, the related analysis is performed using, Ansoft HFSS. Simulations are validated by comparing the measurements performed with the slot dipole antennas manufactured on the Rogers 6006 Duroid. Photographs of the fabricated antennas are given in Figure 7.3.

As shown in Figure 7.3, for up-state and down-state cases of RF MEMS switches two different prototypes have been manufactured. The down state case of the RF MEMS switches are modeled by short metallic parts as in Figure 7.3 (b) and up state of the switch is left as open as in Figure 7.3 (a).

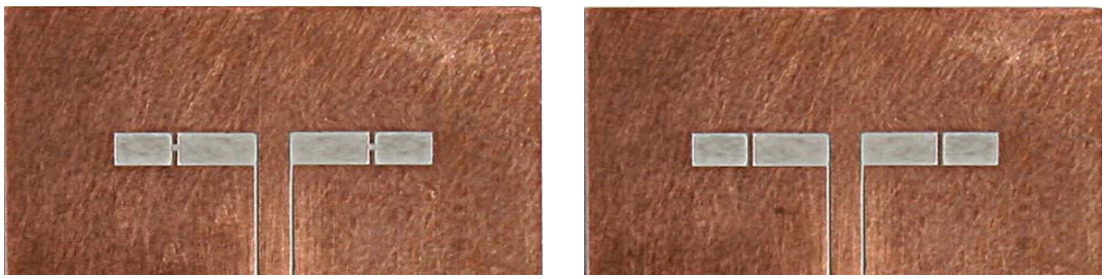

(a) **(b)**

Figure 7.3 Prototype structures of slot dipole antenna with metallic strips instead of RF MEMS switches
(a) Switches Up Position (b) Switches Down Position

S11 values obtained by measurements and HFSS simulations are given in Figure 7.4. As seen from the figure, simulation results are in good agreement with the measurements. The antenna manufactured for the up-state case of switches resonates

at 10 GHz and the antenna manufactured for the down-state case of switches resonates at 15.4GHz as expected.

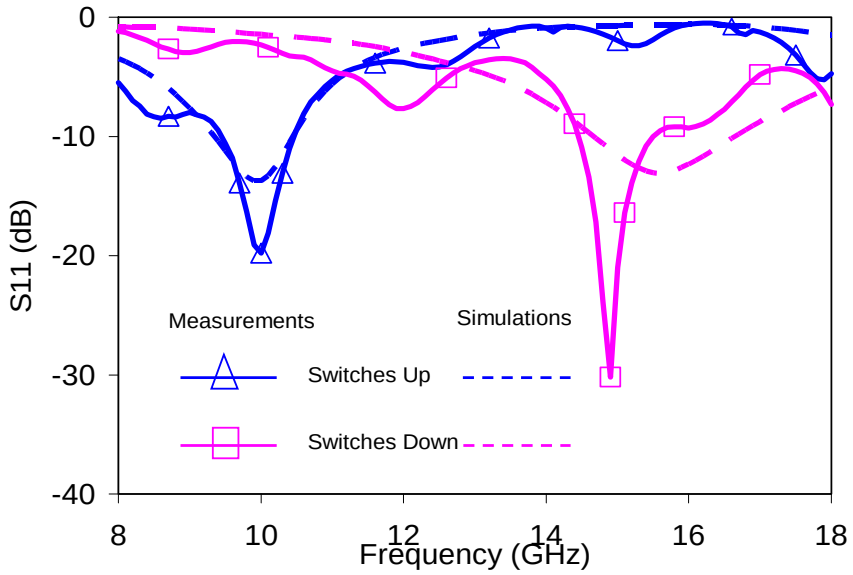

Figure 7.4 Measurement and simulation results of a slot dipole antenna with metallic strips instead of RF MEMS switches

Far field measurements of the prototype structures have been performed in the tapered anechoic chamber and shown in Figure 7.5-Figure 7.8. E-plane and H-plane measurements at 10 GHz for the up-state case and 15.4 GHz for the down-state case show good agreement with HFSS simulations.

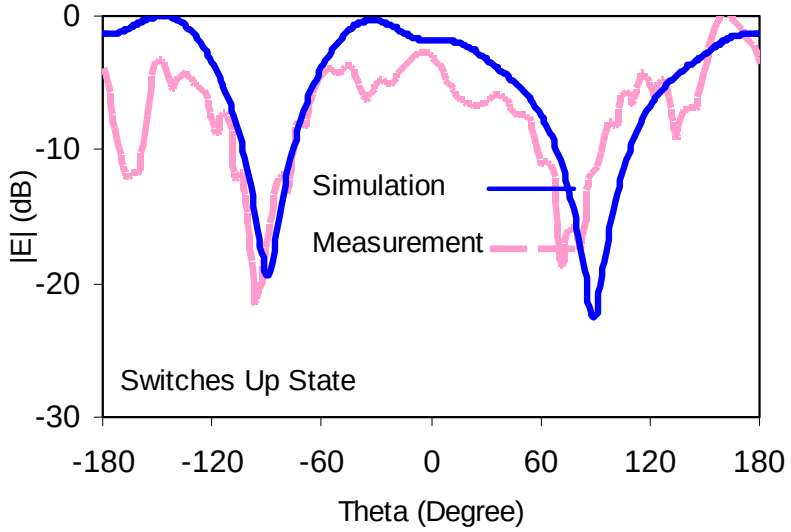

Figure 7.5 E-Plane Electric Field Pattern of Single Dipole Antenna at 10 GHz for the Switches are Up-State Case

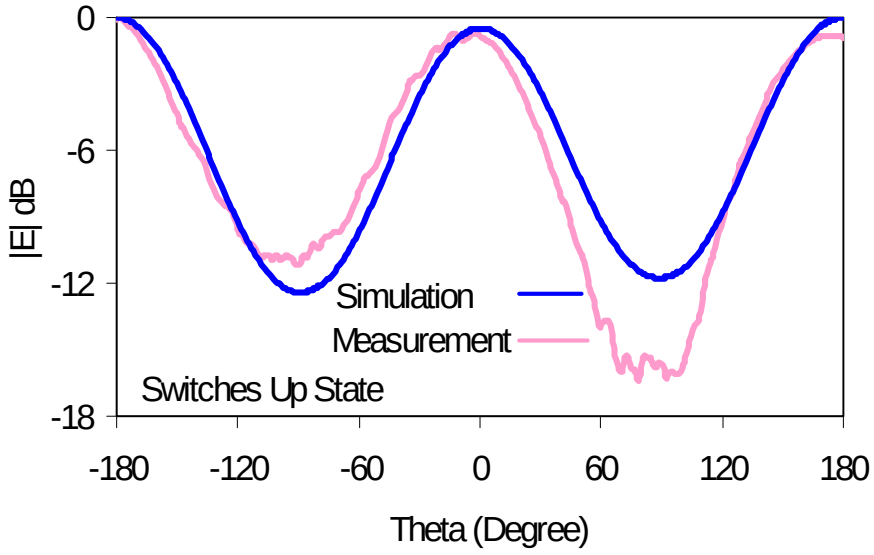

Figure 7.6 H-Plane Electric Field Pattern of Single Dipole Antenna at 10 GHz for the Switches are Up-State Case

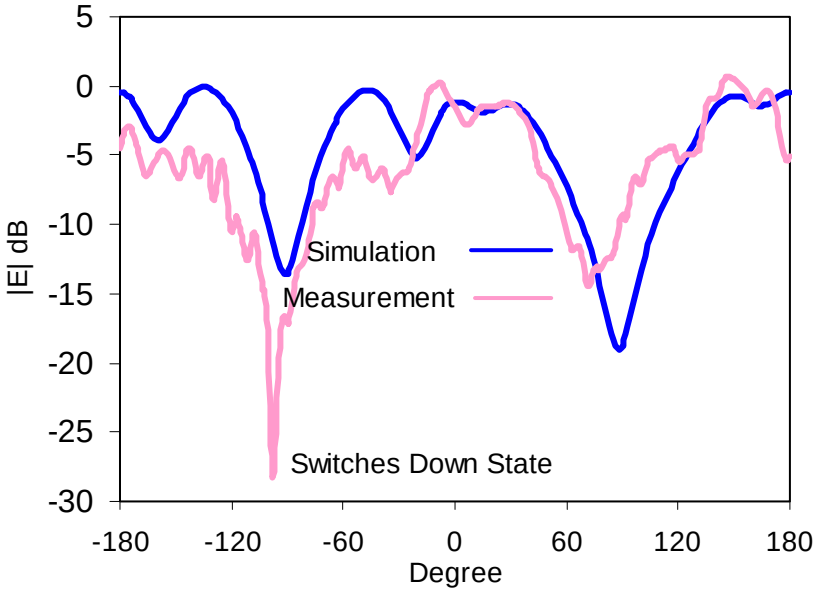

Figure 7.7 E-Plane Electric Field Pattern of Single Dipole Antenna at 15.4 GHz for the Switches are Down-State Case

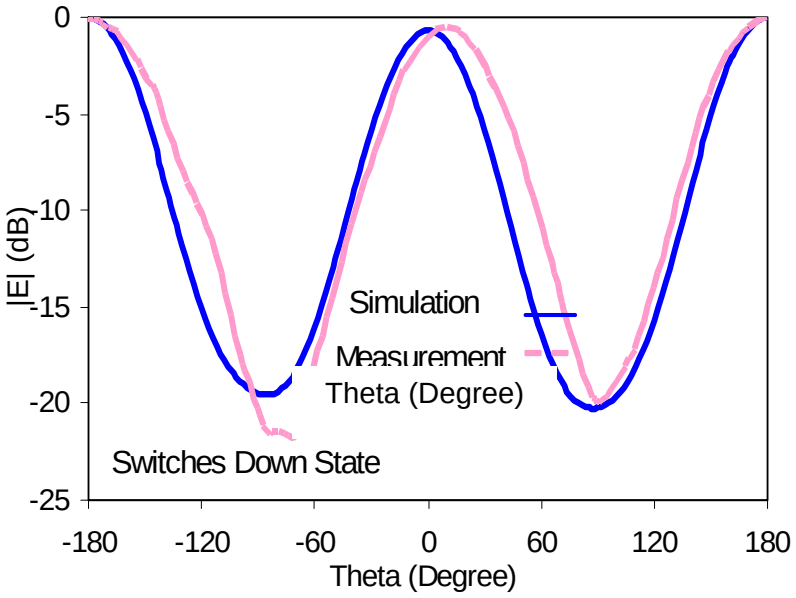

Figure 7.8 H-Plane Electric Field Pattern of the Single Dipole Antenna at 15.4 GHz for the Switches are Down-State Case

7.2 CPW-Based Feed Network

As mentioned in the introduction part, the feed network of the array is CPW-based that offers many advantages such as; low radiation losses, and less dispersion. The CPW-based feed network includes T-junctions, chamfered corners, and dual frequency transformers to match the input impedance at both resonant frequencies of the antennas.

Dual-frequency transformer

Generally, quarter-wave frequency transformers are used to match the impedance of a line at a single frequency. In fact, it is possible to design an electrically small transformer with two sections and achieve ideal impedance matching at two arbitrary frequencies. The dual frequency transformer presented in this study is used to transform 50-Ω input impedance of the antennas to 100-Ω impedance at the two ports of the T-junction [35]. Transformer has been designed on 500 μm-thick 4" glass substrate with εr=4.6 (tanδ=0.005) and manufactured in [35]. The transformer, which is designed to operate both in X- and Ka-band, is realized using two equal-length sections of CPW lines with different characteristic impedances. The circuit schematic and parameters of the designed transformer are given in Figure 7.9.

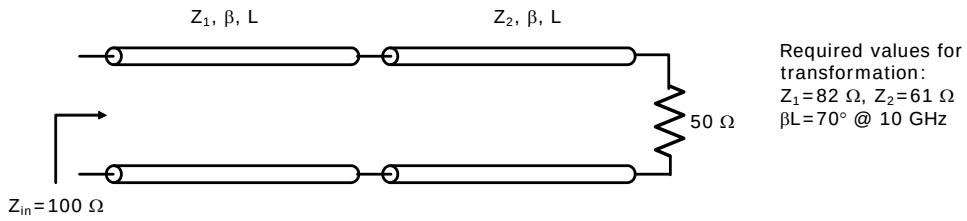

Figure 7.9 The Circuit Schematic View and Parameters of the Dual-Frequency Transformer

Also, dual frequency transformer has been manufactured and measurement results have been presented in [6]. As shown in Figure 7.10, HFSS simulations of the dual-frequency transformer are consistent with the measurements. Dual frequency

impedance transformers providing a return loss better than 15 dB at the frequency of interest.

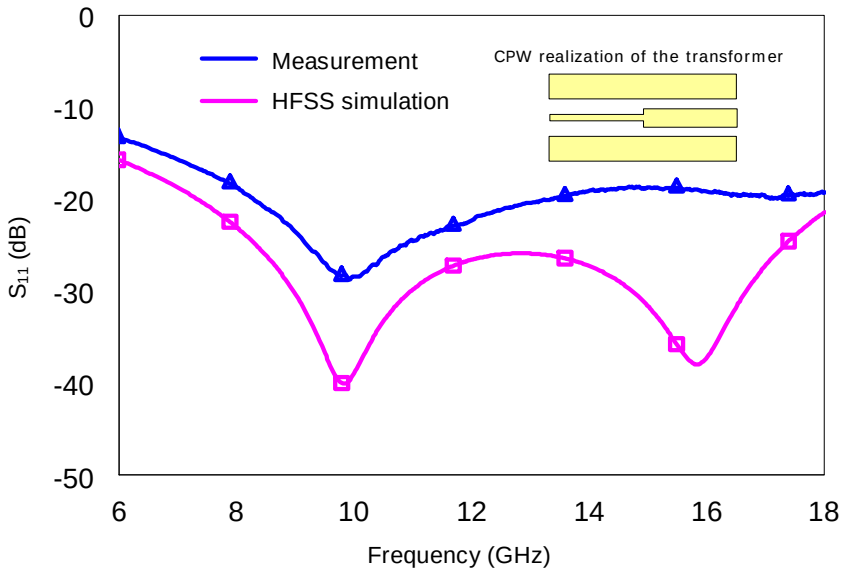

Figure 7.10 Measurement and simulation results of dual-frequency transformer operating at X- and Ka- Band

7.3 Two Element Slot Dipole Dual-Frequency Array Structure

Prototype structures of 2-element reconfigurable slot dipole antenna array structure have been manufactured on the 20 mil Rogers 6006 Duroid substrate. Photographs of the manufactured antennas for up-state and down-state cases of switches are given in Figure 7.11(a) and Figure 7.11 (b), respectively.

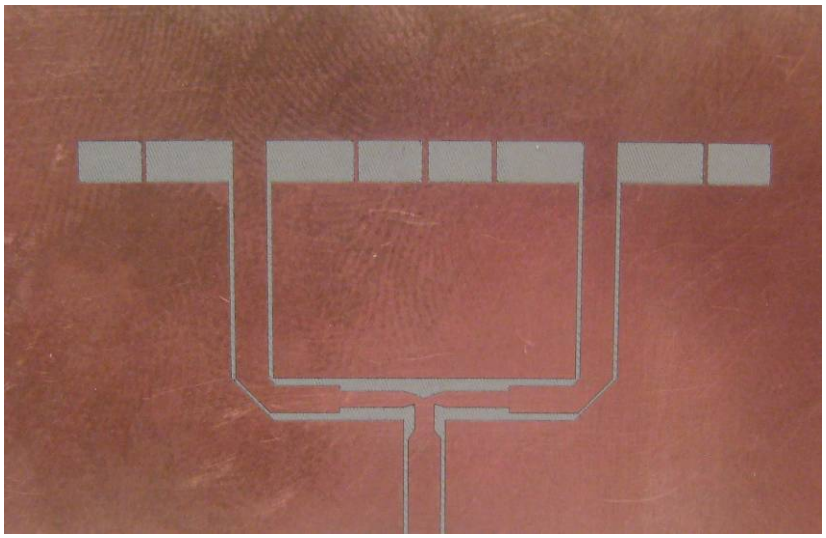

(a)

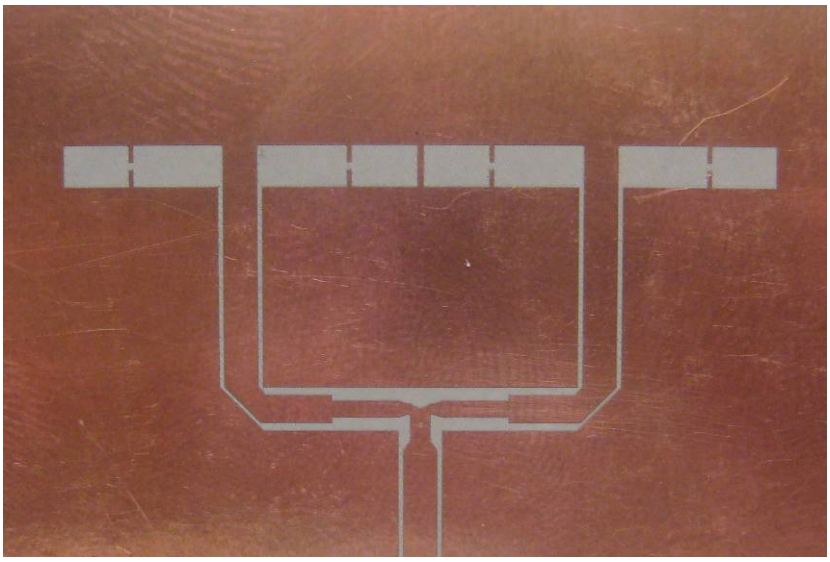

(b)

Figure 7.11 Prototype Structures of 2-Element Reconfigurable Slot Dipole Antenna Array with Metallic Strips Instead of RF MEMS Switches
(a) Switches Up-State Case. (b) Switches Down-State Case

The reflection coefficient measurements of the 2-element slot dipole antenna structure are performed using Agilent N5230A PNA-L 10 MHz-40GHz Network Analyzer. Figure 7.12 shows S11 measurements of the prototype structures for the up and down cases. For the up-state case resonance frequency of the antenna array is at

10.6 GHz and for the down-state case it is 15.9 GHz. However, there is a resonance around 10.5 GHz for the switches down state case. This resonance behavior should be investigated further.

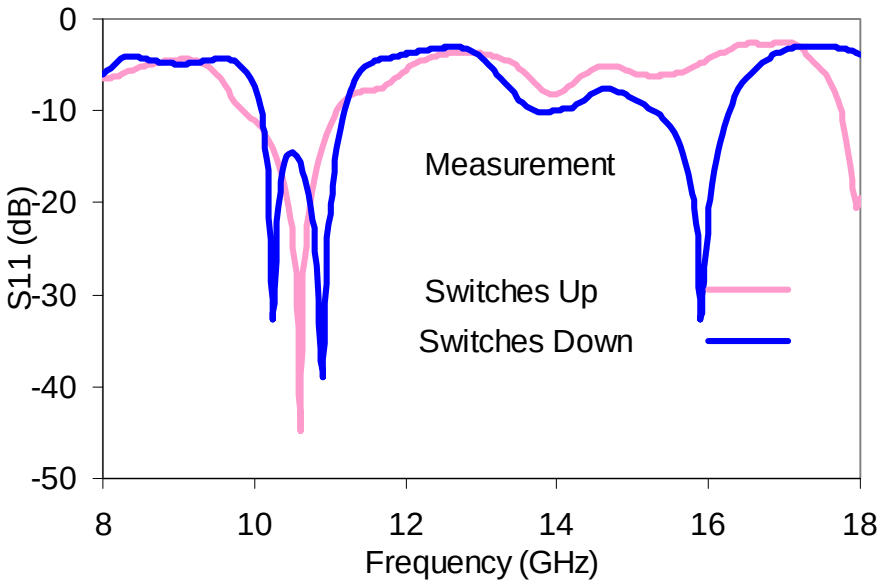

Figure 7.12 S11 Measurement Results of 2-Element Slot Dipole Antenna Array with Metallic Strips instead of RF MEMS Switches

Array structure far field pattern measurements have been performed in the tapered anechoic chamber. E-plane and H-plane patterns for the up-state and down-state cases are presented in Figure 7.14-Figure 7.16. For the up-state case E- and H- plane patterns have been measured at 10.6 GHz. As shown in Figure 7.13, E plane pattern of the array is similar to single slot dipole element. On the other hand, H-plane pattern of the array is more directive than a single element as expected. H-plane patterns at 15.9 GHz are consistent with the previous measurements. The asymmetry of the E-plane measurements can be attributed to feeding network.

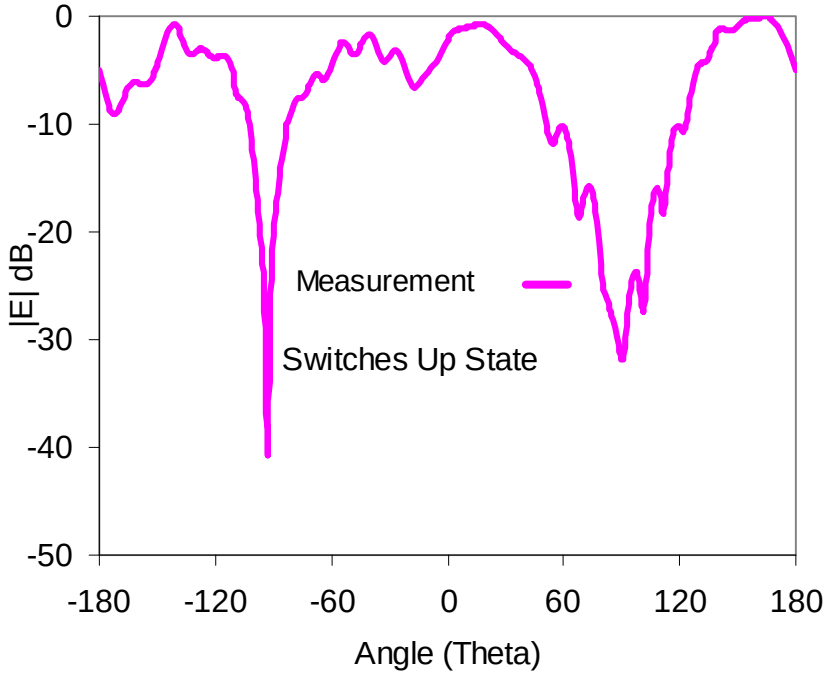

Figure 7.13 E-Plane Electric Field Pattern of 2-Element Antenna Array Structure at 10.6 GHz for the Switches are Up-State Case

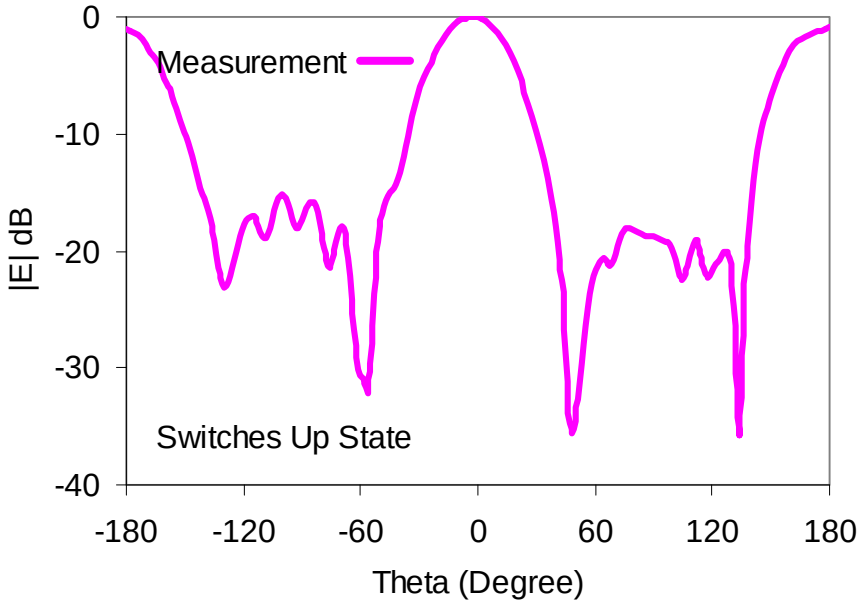

Figure 7.14 H-Plane Electric Field Pattern of 2-Element Antenna Array Structure at 10.6 GHz for the Switches are Up-State Case

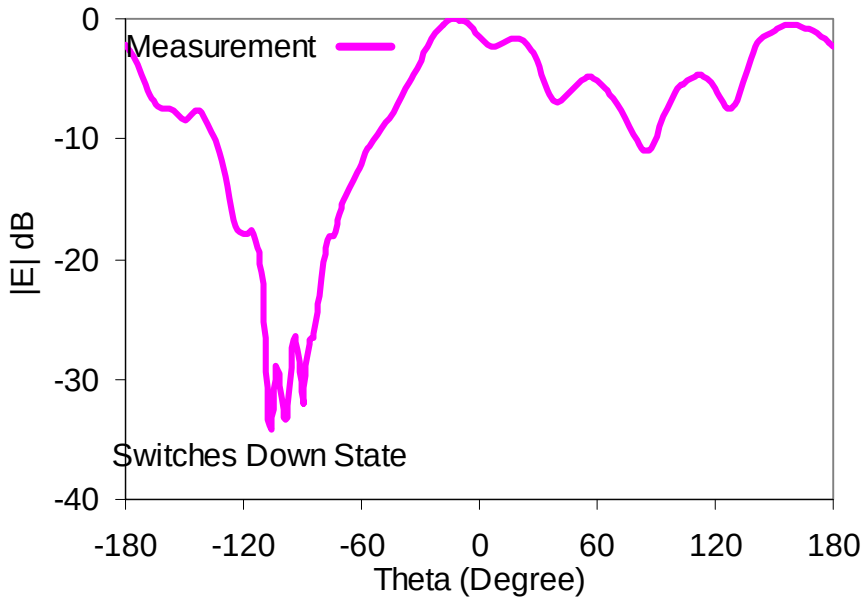

Figure 7.15 E-Plane Electric Field Pattern of 2-Element Antenna Array Structure at 15.9 GHz for the Switches are Down-State Case

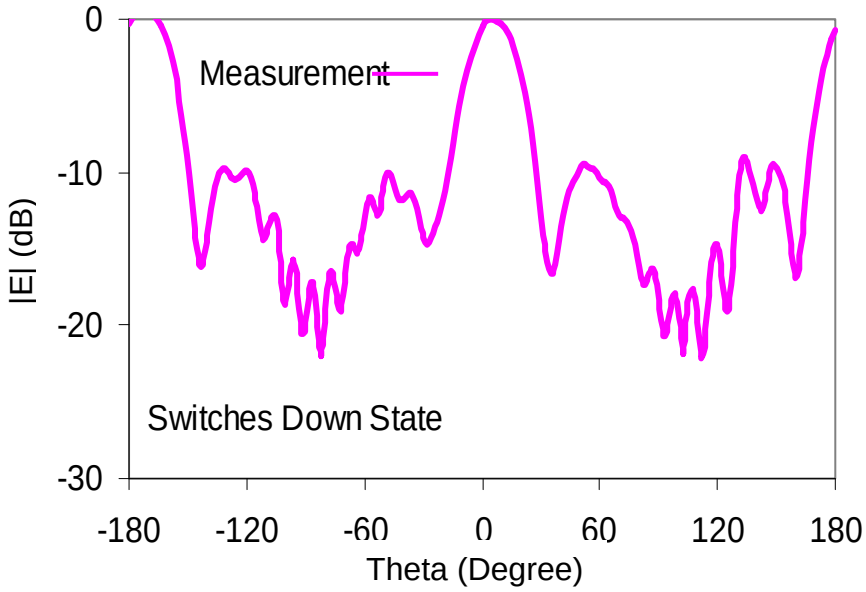

Figure 7.16 H-Plane Electric Field Pattern of 2-Element Antenna Array Structure at 15.9 GHz for the Switches are Down-State Case

In conclusion, a reconfigurable dual frequency slot dipole array operating at X- or Ka-band slot dipole antennas has been presented. It is possible to increase the number of elements in the array structure to enhance the directivity of the antenna array. In the future, commercial packaged MEMS switches will be integrated to the array.

CHAPTER 8

CONCLUSION

In this thesis, three different reconfigurable antenna structures, a beam-steerable traveling wave meanderline array with varactor diodes, dual circularly polarized meanderline array and frequency-tunable slot dipole array have been designed and investigated.

First, a linearly polarized meanderline array operating at 10 GHz has been designed by using previously introduced EM models. Then, final design parameters are obtained using full wave EM simulators, Ansoft Designer and Ansoft HFSS. Designed meanderline array has been manufactured and its S-parameters and radiation patterns have been measured. It has been shown that measurement results are in good agreement with the simulations.

Beam-steerable meanderline array has been designed, manufactured and measured. 10° beam scanning has been achieved by using reverse-biased varactor diodes. It has been shown that measurement results agree well with simulations. Since the varactor diodes are placed in series with the array, impedance of the varactor changes with applied voltage, so that return loss and S21 characteristics of the array change with applied voltage. In order to achieve beam-steering more than 10°, a reflective type phase shifter has been introduced. Reflective type phase shifter consists of a 3-dB branch-line coupler loaded with varactor diodes and has a phase tuning range of more than 60°. Reflective type phase shifters have been placed between meanderline unit cells and simulations have been performed. More than 20° beam-steering has been achieved in simulations. Reflective type phase shifters are commonly used in reconfigurable antennas. On the other hand, their sizes are large compared to wavelength making them inappropriate to use in small configurations.

A dual circularly polarized meanderline array has been designed and simulated in Ansoft Designer. Antenna polarization can be switched between LHCP and RHCP by using SPDT RF MEMS switches. In the simulations, down state of MEMS switches has been modeled by metallic parts replacing switches and in the up state switch locations have been left as open. Axial ratio around 3dB has been obtained, which is an acceptable value for circular polarization. Dual CP polarization has been verified by simulations.

Reconfigurable dual frequency slot dipole array has been designed for X- and Ka-band applications. Dual frequency operation of the antenna array has been achieved using RF MEMS switches located on slots. The corporate feed network of the array has been realized with coplanar wave transmission. Prototypes of single-element and two-element slot dipole array have been manufactured representing the corresponding structures with upstate and down state of MEMS switches. It has been shown that the array is operating at 10 GHz and 15 GHz for up state and down state of switches, respectively. The measurement results show very good agreement with the simulation results.

Dual Circularly polarized meanderline array and reconfigurable slot dipole array will be fabricated with packaged MEMS switches in a hybrid fashion. Packaged RF-MEMS switches are very recently available on the market. In fact, during the last months of this study there is only one company, RADANT MEMS Inc., which sells only SPST switches abroad. Therefore realization of dual CP antenna and dual frequency slot array will be performed in future.

REFERENCES

[1] J. T. Bernhard, ”Reconfigurable Antennas”, Morgan & Claypool Publishers series, 2007.

[2] J.Kiriazi, H.Ghali, H.Radaie, and H. Haddara, “Reconfigurable dual-band dipole antenna on silicon using series MEMS switches,” Proceedings of the IEEE/URSI International Symposium on Antennas and Propagation, vol.1, pp.403–406, 2003.

[3] M.A. Ali and P. Wahid, “A reconfigurable Yagi array for wireless applications,” Proceedings of the IEEE/URSI International Symposium on Antennas and Propagation, vol.1, pp. 466–468, 2002.

[4] S. Liu M-J. Lee, C. Jung, G-P. Li, and F. De Flaviis, ” A Frequency-Reconfigurable Circularly Polarized Patch Antenna by Integrating MEMS Switches”, Proceedings of the IEEE/URSI International Symposium on Antennas and Propagation, Vol. 2A, pp.413- 416, 3-8 July 2005.

[5] C.W. Jung, M-J. Lee, F. De Flaviis, “Reconfigurable dual-band antenna with high frequency ratio (1.6:1) using MEMS switches”, Electronics Letters, Vol.44, No.2, pp.76–77, January 17 2008.

[6] Kagan Topalli, Ozlem Aydin Civi, Simsek Demir, Sencer Koc, and Tayfun Akin, “Dual-Frequency Reconfigurable Slot Dipole Array with a CPW-Based Feed Network using RF MEMS Technology for X- and Ku-Band Applications,” *IEEE AP-S, 2007*

[7] E. Erdil, K. Topalli, O. Aydin Civi, and T. Akin, “Reconfigurable CPW-fed dual frequency rectangular slot antenna,” IEEE AP-S Symp. Digest, vol.2A, pp.392-395, 2005

[8] R.N. Simons, D. Chun, and L.P.B. Katehi, “Polarization reconfigurable patch antenna using microelectromechanical systems (MEMS) actuators,” Proceedings of the IEEE/URSI International Symposium on Antennas and Propagation, vol.1, pp.6–9, 2002.

[9] X-S. Yang, B-Z. Wang, Wu,and S. Xiao, “Yagi Patch Antenna With Dual-Band and Pattern Reconfigurable”, IEEE Antennas and Wireless Propagation Letters, Vol.6, pp.168-171, 2007.

[10] K. Topalli, O. Aydin Civi, S. Demir, S. Koc, and T. Akin, “A Monolithic Phased Array using 3-bit Distributed RF MEMS Phase Shifters,” IEEE Trans. MTT, pp. 270-277, Feb. 2007.

[11] J-C. Chiao, F. Yiton, M.C. Iao, M. DeLisio, and L-Y. Lin, “MEMS reconfigurable Vee antenna”, IEEE MTT-S International Microwave Symposium Digest, vol.4, pp.1515–1518, 1999.

[12] C. W. Jung, M-J. Lee, G. P. Li, and F. De Flaviis, “Reconfigurable Scan-Beam Single-Arm Spiral Antenna Integrated with RF-MEMS Switches”, IEEE Transactions on Antennas and Propagation, Vol.54, No.2, Part 1, pp.455–463, Feb. 2006.

[13] Kiriazi, J., Ghali, H., Radaie, H., and Haddara, H., “Reconfigurable dual-band dipole antenna on silicon using series MEMS switches,” Proceedings of the IEEE/URSI International Symposium on Antennas and Propagation, vol. 1, pp.403–406, 2003.

[14] Weedon, W.H., Payne, W.J., and Rebeiz, G.M., “MEMS-switched reconfigurable antennas,” Proceedings of the IEEE/URSI International Symposium on Antennas and Propagation, vol.3, pp. 654–657, 2001.

[15] Panagamuwa, C.J., Chauraya, A., and Vardaxoglou, J.C., “Frequency and beam reconfigurable antenna using photoconducting switches,” IEEE Transactions on Antennas and Propagation, vol. 54, pp. 449–454, February 2006.

[16] Freeman, J.L., Lamberty, B.J., and Andrews, G.S., “Optoelectronically reconfigurable monopole antenna,” Electronics Letters, vol. 28, no. 16, pp. 1502–1503, July 1992.

[17] Bhartia, P., and Bahl, I.J., “Frequency agile microstrip antennas,” Microwave Journal, vol. 25, pp. 67–70, October 1982.

[18] Kawasaki, S., and Itoh, T., "A slot antenna with electronically tunable length," Proceedings of the IEEE/URSI International Symposium on Antennas and Propagation, vol. 1, pp. 130–133, 1991.

[19] Kiely, E., Washington, G., and Bernhard, J.T., "Design and development of smart microstrip patch antennas," Smart Materials and Structures, vol. 7, no. 6, pp. 792–800, December 1998

[20] Kiely, E., Washington, G., and Bernhard, J.T., "Design, actuation, and control of active patch antennas," Proceedings of the SPIE International Society for Optical Engineering, vol. 3328, pp. 147–155, 1998.

[21] Bernhard, J.T., Kiely, E., and Washington, G., "A smart mechanically-actuated two-layer electromagnetically coupled microstrip antenna with variable frequency, bandwidth, and antenna gain," IEEE Transactions on Antennas and Propagation, vol. 49, pp. 597–601, April 2001.

[22] Pozar, D.M., and Sanchez, V., "Magnetic tuning of a microstrip antenna on a ferrite substrate," Electronics Letters, vol. 24, pp. 729–731, June 9, 1988.

[23] Mishra, R.K., Pattnaik, S.S., and Das, N., "Tuning of microstrip antenna on ferrite substrate," IEEE Transactions on Antennas and Propagation, vol. 41, pp. 230–233, February 1993.

[24] Mishra, R.K., Pattnaik, S.S., and Das, N., "Tuning of microstrip antenna on ferrite substrate," IEEE Transactions on Antennas and Propagation, vol. 41, pp. 230–233, February 1993.

[25] Langer, J.-C., Zou, J., Liu, C., and Bernhard, J.T., "Reconfigurable out-of-plane microstrip patch antenna using MEMS plastic deformation magnetic actuation," IEEE Microwave and Wireless Components Letters, vol. 13, pp. 120–122, March 2003.

[26] Eom, H.J., Lee, S.U., "Leaky Wave in a Slotted Rectangular Waveguide" Antenna Technology: Small Antennas and Novel Metamaterials, 2008. iWAT 2008. International Workshop, Page(s):103 – 106, 4-6 March 2008

[27] Tranquilly, J.M., Lewis, J.E., "On the Propagation of Leaky Waves in a Longitudinally Slotted Rectangular Waveguide" Microwave Theory and

Techniques, IEEE Transactions on Volume 28, Issue 7, Page(s):714 – 718, July 1980

[28] Dural,G., *Theory and Design of Microstrip Rampart Line Arrays*, Master Thesis, Metu, 1983

[29] I.J.Bahl and P. Bhartia, *Microstrip Antenns*, Artech House,Inc.,1980.

[30] J.R. James, P.S. Hall and C. WOOD, *Microstrip Antenna Theory and Design,* IEE Electromagnetic Waves Series 12, 1981.

[31] R. E. Collin, *Foundations for Microwave Engineering*, McGraw-Hill, Inc.,1992.

[32] S. Cheng, E. Öjefors, P. Hallbjörner, and A. Rydberg, "Compact Reflective Microstrip Phase Shifter for Traveling Wave Antenna Applications" IEEE Microwave and Wireless Components Letters, Vol.16, No.7, July 2006.

[33] R. Ratmon, I. Oz, C. J. Samson, "Comparision of Resonant and Travelling-Wave Meander-Line Antenna" Electrical & Electronics Engineers in Israel,1991, 17th Convebtion of. 5-7 March 1991 Page(s):149-151

[34] M. Tiuri, S. Tallqvist, S. Urpo, "*Chain Antenna*" 1974 Antennas and Propagation Society International Symposium, Volume 12, Jun 1974 Page(s):274 – 277

[35] C. Monzon, "A Small Dual-Frequency Transformer in Two Sections," IEEE Trans. Microwave Theory & Tech., vol.51, pp.1157-1161, April 2003.

[36] G.M. Rebeiz, J. B. Muldavin, "RF MEMS Switches and Switch Circuits" IEEE Microwave Magazine, pp. 59-71, December 2001.

[37] RADANT MEMS SPST Switch-http://www.radantmems.com/radantmems.data/Library/Radant-Datasheet200_1.5.pdf , Radant MEMS Inc, Hudson, MA, August,2008.

APPENDICES

A. Effective Dielectric Constant and Characteristic Impedance of Microstrip Lines

The Characteristic impedance of a microstrip line of width w over a dielectric substrate of dielectric constant ε_r and thickness h, at the frequency f is given below.

$$\varepsilon_e(f) = \varepsilon_r - \frac{\varepsilon_r - \varepsilon_e(0)}{1 + (f / f_a)^m}$$

$$\varepsilon_e(0) = \frac{\varepsilon_r + 1}{2} + \frac{\varepsilon_r - 1}{2}\left(1 + \frac{12h}{w}\right)^{-1/2} + F(\varepsilon_r, h) - 0.217(\varepsilon_r - 1)\frac{t}{\sqrt{wh}}$$

$$F(\varepsilon_r, r) = \begin{cases} 0.02(\varepsilon_r - 1)(1 - w/h)^2 & w/h \le 1 \\ 0 & w/h > 1 \end{cases}$$

$$f_a = \frac{f_b}{0.75 + (0.75 - 0.332\varepsilon_r^{-1.73})(w/h)}$$

$$f_b = \frac{299.7924562}{2\pi h\sqrt{\varepsilon_r - \varepsilon_e(0)}} \tan^{-1}\left[\varepsilon_r \sqrt{\frac{\varepsilon_e(0) - 1}{\varepsilon_r - \varepsilon_e(0)}}\right]$$

$$m = \begin{cases} m_0 m_c & m_0 m_c \le 2.32 \\ 2.32 & m_0 m_c > 2.32 \end{cases}$$

$$m_0 = 1 + \frac{1.4}{1 + \sqrt{w/h}} + \frac{0.32}{(1 + \sqrt{w/h})^3}$$

$$m_c = \begin{cases} 1 + \dfrac{1.4}{1 + w/h}\left[0.15 - 0.235e^{-0.45 f / f_a}\right] & w/h \le 0.7 \\ 1 & w/h > 0.7 \end{cases}$$

$$Z_c = \sqrt{\frac{\mu_0 \varepsilon_0}{\varepsilon_e} \frac{1}{C_a}}$$

where

$$C_c = \begin{cases} \dfrac{2\pi\varepsilon_0}{\ln(\dfrac{8h}{w} + \dfrac{w}{4h})} & w/h \le 1 \\ \varepsilon_0\left[\dfrac{w}{h} + 1.393 + 0.667\ln(w/h + 1.444)\right] & w/h > 1 \end{cases}$$

B. ASELSAN Tapered Anechoic Chamber Measurement System

The measurements and evaluation of the sinuous antennas are performed in an anechoic chamber (see Figure B.1). Anechoic chamber is a reflection free (i.e. the reflectivity levels of the absorbers covering the whole room are very low, about–20 dB) room inside of which is covered by absorbers.

The tapered anechoic chamber is designed in the shape of pyramidal horn that tapers from the small source end to a large rectangular test region, and with high quality absorbing material covering the side walls, floor and ceiling. The tapered anechoic chamber in the R&D department of Aselsan Inc. is used with an azimuth over elevation positioner holding up the antenna under test, a polarization positioner holding up the standard transmitter antenna, an Agilent PNA model vector network analyzer, and HP PII series computers using programs written in HP VEE program at Aselsan and which communicate with the above listed equipment through the aid of HP-IB's .Antenna measurement set up in anechoic chamber is shown in Figure B.2.

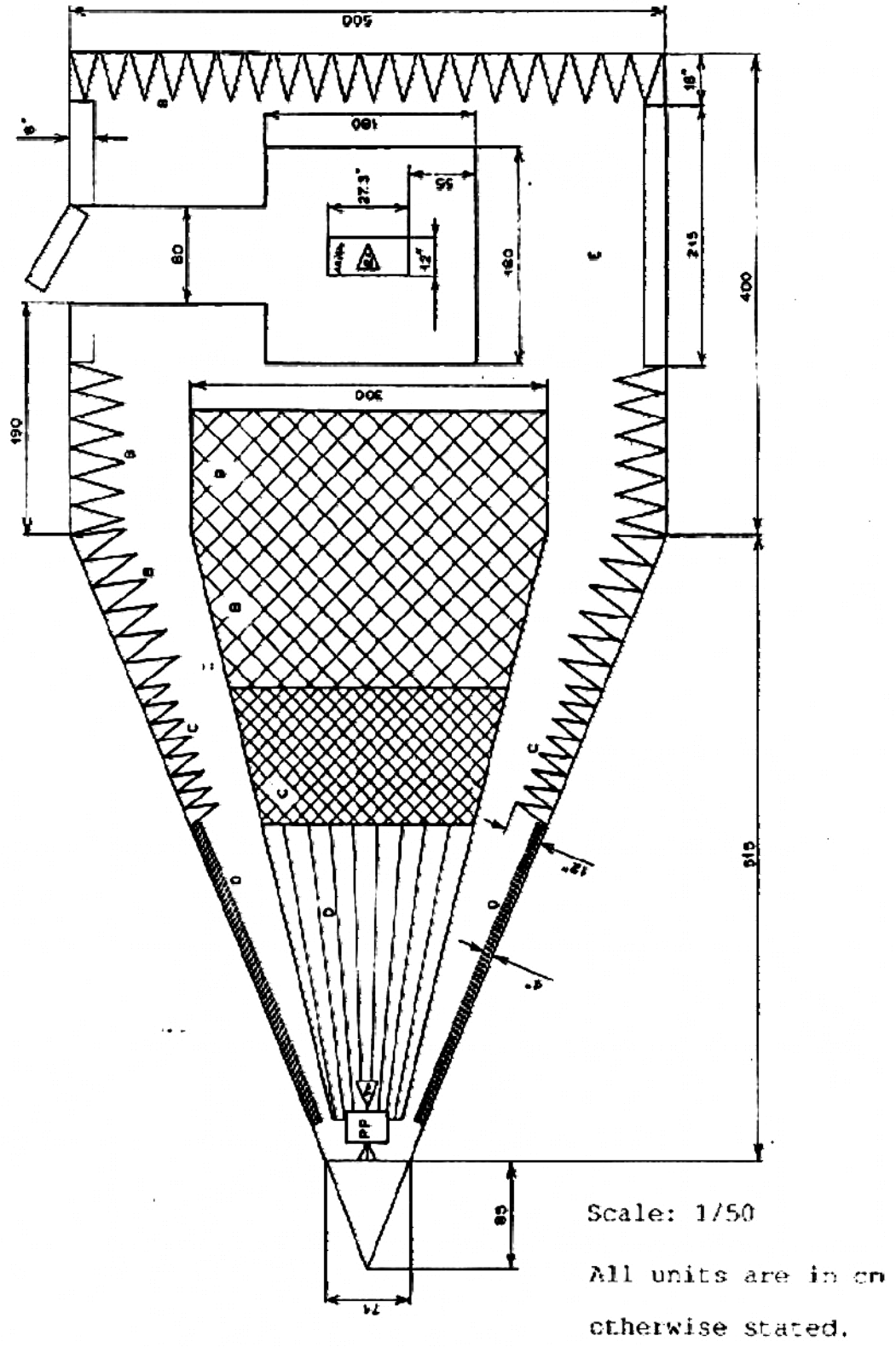

Figure B.1 Top view of the Tapered Anechoic Chamber in Aselsan Inc.

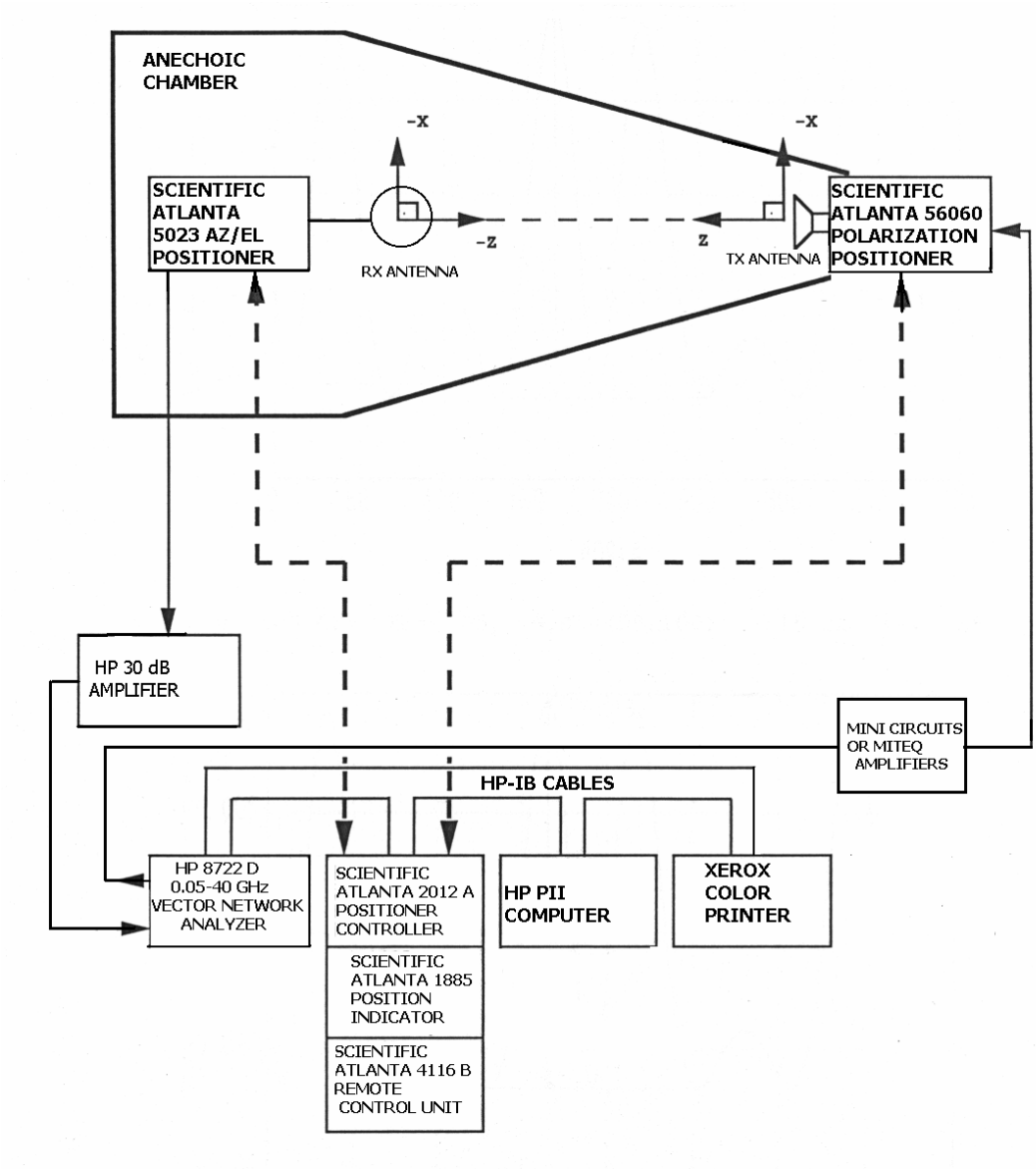

Figure B.2 Antenna Measurement Setup in Anechoic Chamber

C. RO5880 High-Frequency Laminate Datasheet

ROGERS CORPORATION

Advanced Circuit Materials

Advanced Circuit Materials Division
100 S. Roosevelt Avenue
Chandler, AZ 85226
Tel: 480-961-1382, Fax: 480-961-4533
www.rogerscorporation.com

Data Sheet
1.5000

RT/duroid®5870 /5880 High Frequency Laminates

Features:

- Lowest electrical loss for reinforced PTFE material.
- Low moisture absorption.
- Isotropic
- Uniform electrical properties over frequency.
- Excellent chemical resistance.

Some Typical Applications:

- Commercial Airline Telephones
- Microstrip and Stripline Circuits
- Millimeter Wave Applications
- Military Radar Systems
- Missile Guidance Systems
- Point to Point Digital Radio Antennas

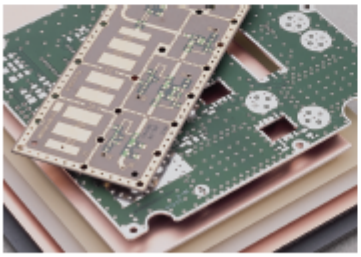

RT/duroid® 5870 and 5880 glass microfiber reinforced PTFE composites are designed for exacting stripline and microstrip circuit applications.

Glass reinforcing microfibers are randomly oriented to maximize benefits of fiber reinforcement in the directions most valuable to circuit producers and in the final circuit application.

The dielectric constant of RT/duroid 5870 and 5880 laminates is uniform from panel to panel and is constant over a wide frequency range. Its low dissipation factor extends the usefulness of RT/duroid 5870 and 5880 to Ku-band and above.

RT/duroid 5870 and 5880 laminates are easily cut, sheared and machined to shape. They are resistant to all solvents and reagents, hot or cold, normally used in etching printed circuits or in plating edges and holes.

Normally supplied as a laminate with electrodeposited copper of ¼ to 2 ounces/ft.^{2} (8 to 70µm) on both sides, RT/duroid 5870 and 5880 composites can also be clad with rolled copper foil for more critical electrical applications. Cladding with aluminum, copper or brass plate may also be specified.

When ordering RT/duroid 5870 and 5880 laminates, it is important to specify dielectric thickness, tolerance, rolled or electrodeposited copper foil, and weight of copper foil required.

Figure C.1 RO5880 High-Frequency Laminate Datasheet

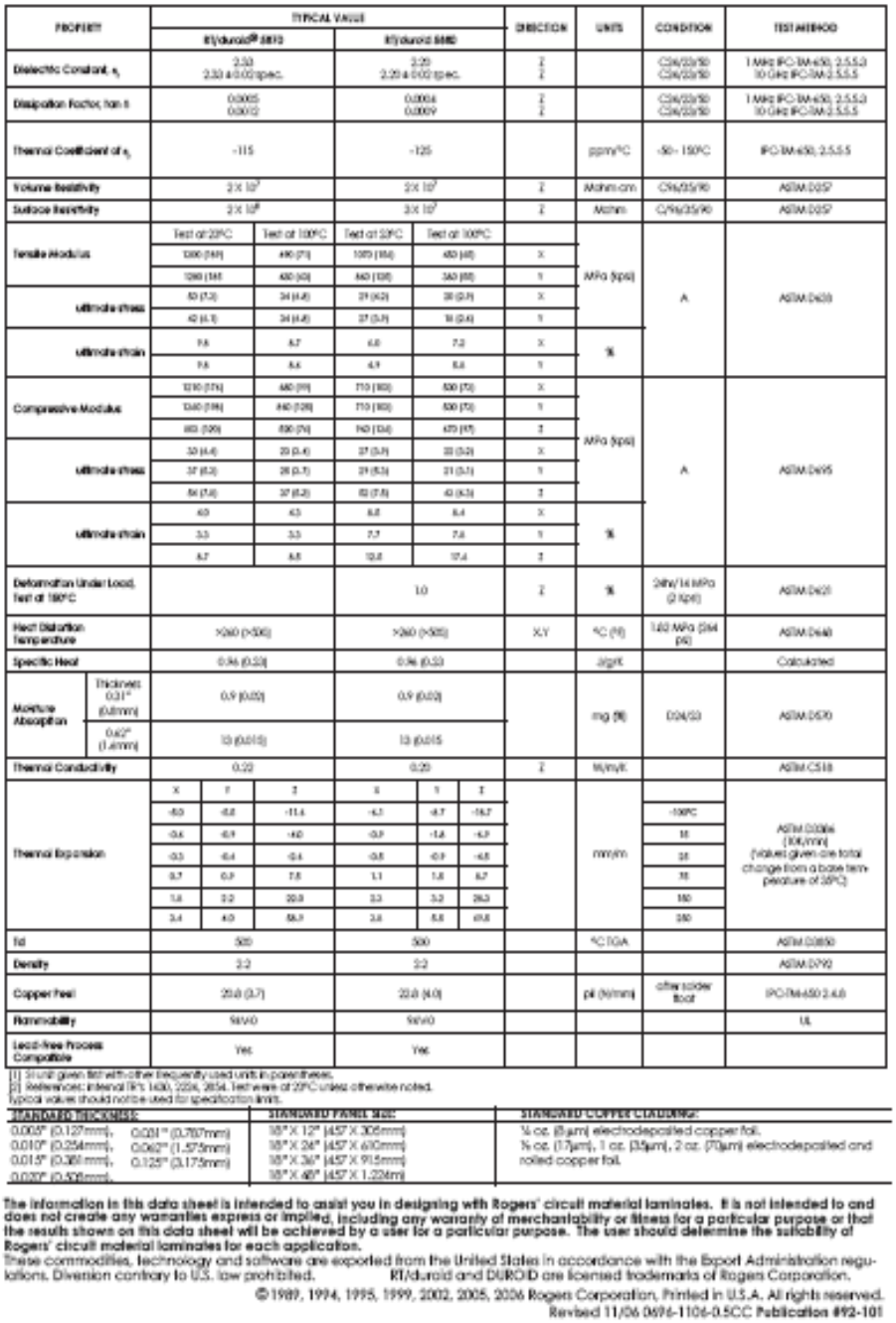

PROPERTY	TYPICAL VALUE				DIRECTION	UNITS	CONDITION	TEST METHOD
	RT/duroid® 5870		RT/duroid 5880					
Dielectric Constant, ε_r	2.33 2.33 ± 0.02 spec.		2.20 2.20 ± 0.02 spec.		Z Z		C24/23/50 C24/23/50	1 MHz IPC-TM-650, 2.5.5.3 10 GHz IPC-TM-2.5.5.5
Dissipation Factor, tan δ	0.0005 0.0012		0.0004 0.0009		Z Z		C24/23/50 C24/23/50	1 MHz IPC-TM-650, 2.5.5.3 10 GHz IPC-TM-2.5.5.5
Thermal Coefficient of ε_r	-115		-125			ppm/°C	-50 - 150°C	IPC-TM-650, 2.5.5.5
Volume Resistivity	2×10^7		2×10^7		Z	Mohm cm	C96/35/90	ASTM D257
Surface Resistivity	2×10^8		3×10^7		Z	Mohm	C/96/35/90	ASTM D257
Tensile Modulus	Test at 23°C	Test at 100°C	Test at 23°C	Test at 100°C				
	1300 (189)	490 (71)	1070 (156)	450 (65)	X	MPa (kpsi)	A	ASTM D638
	1280 (186)	430 (63)	960 (139)	360 (52)	Y			
Ultimate Stress	50 (7.2)	34 (4.8)	29 (4.2)	20 (2.9)	X			
	42 (6.1)	34 (4.8)	27 (3.9)	18 (2.6)	Y			
Ultimate Strain	9.6	8.7	6.8	7.2	X	%		
	9.8	8.6	6.9	8.8	Y			
Compressive Modulus	1210 (176)	680 (99)	710 (103)	530 (75)	X	MPa (kpsi)	A	ASTM D695
	1240 (180)	640 (128)	710 (103)	530 (75)	Y			
	850 (120)	530 (76)	960 (134)	670 (97)	Z			
Ultimate Stress	39 (5.6)	20 (2.8)	27 (3.9)	22 (3.2)	X			
	37 (5.3)	28 (3.7)	29 (4.2)	21 (3.1)	Y			
	56 (7.9)	37 (5.2)	50 (7.2)	42 (6.2)	Z			
Ultimate Strain	4.0	4.3	5.8	8.4	X	%		
	3.5	3.5	7.7	7.6	Y			
	6.7	6.8	12.8	17.4	Z			
Deformation Under Load, Test at 150°C			1.0		Z	%	24hr/14 MPa (2 kpsi)	ASTM D621
Heat Distortion Temperature	>260 (>500)		>260 (>500)		X,Y	°C (°F)	1.82 MPa (264 psi)	ASTM D648
Specific Heat	0.96 (0.23)		0.96 (0.23)			J/g/K		Calculated
Moisture Absorption	Thickness 0.31" (0.8mm)	0.9 (0.02)		0.9 (0.02)		mg (%)	D24/23	ASTM D570
	0.62" (1.6mm)	13 (0.015)		13 (0.015)				
Thermal Conductivity	0.22		0.20		Z	W/m/K		ASTM C518
Thermal Expansion	X	Y	Z	X	Y	Z		ASTM D3386 (10E/mm) (Values given are total change from a base temperature of 35°C)
	-8.0	-8.8	-11.6	-6.1	-8.7	-16.7	-100°C	
	-0.6	-0.9	-4.0	-0.9	-1.8	-6.9	35	
	-0.3	-0.4	-0.4	-0.8	-0.9	-4.8	35	
	8.7	8.9	7.8	1.1	1.8	8.7	35	
	1.8	2.2	20.8	2.2	3.2	26.3	150	
	3.4	4.0	58.9	3.8	5.8	69.8	250	
Td	500		500			°C TGA		ASTM D3850
Density	2.2		2.2					ASTM D792
Copper Peel	20.8 (3.7)		22.8 (4.0)			pli (N/mm)	after solder float	IPC-TM-650 2.4.8
Flammability	94V-0		94V-0					UL
Lead-free Process Compatible	Yes		Yes					

(1) SI unit given first with other frequently used units in parentheses.
(2) References: Internal TR's 1400, 2226, 2854. Test were at 23°C unless otherwise noted.
Typical values should not be used for specification limits.

STANDARD THICKNESS		STANDARD PANEL SIZE:	STANDARD COPPER CLADDING:
0.005" (0.127mm),	0.031" (0.787mm)	18" X 12" (457 X 305mm)	½ oz. (18µm) electrodeposited copper foil,
0.010" (0.254mm),	0.062" (1.575mm)	18" X 24" (457 X 610mm)	½ oz. (17µm), 1 oz. (35µm), 2 oz. (70µm) electrodeposited and
0.015" (0.381mm),	0.125" (3.175mm)	18" X 36" (457 X 915mm)	rolled copper foil.
0.020" (0.508mm),		18" X 48" (457 X 1.224m)	

Figure C.2 RO5880 High-Frequency Laminate Datasheet

D. MICROSEMI MPV-2100 Varactor Diode Datasheet

Microsemi
MICROWAVE PRODUCTS DIVISION

MPV1965, MPV2100

MONOLITHIC MICROWAVE SURFACE MOUNT VARACTOR DIODES

PRODUCT PREVIEW

DESCRIPTION

This series of surface mount Varactor diodes utilize new and unique monolithic MMSM technology. The technology is a package/device integration accomplished at the wafer fabrication level. Since the cathode and anode interconnections utilize precision photolithographic techniques rather than wire bonds, parasitic package inductance is tightly controlled. The package parasitics provide smooth non-resonant functionality through 12GHz.

IMPORTANT: For the most current data, consult MICROSEMI's website: http://www.microsemi.com

KEY FEATURES

- Tape and Reeled for Automatic Assembly
- Low Series Inductance (<0.2nH typical)
- Low Parasitic Capacitance (0.08 pf typical)
- Meets All Commercial Qualification Requirements
- 0204 Outline
- Very low thermal resistance

APPLICATIONS/BENEFITS

- 2.4 GHz PCS
- 5.7 GHz Wireless LANS
- VCO's (Voltage Controlled Oscillator)
- Tunable Filter
- Widest bandwidth of any commercial surface mounted devices
- Ultra tight parametric distribution

ELECTRICAL CHARACTERISTICS

Part #	Vb@10uA (min) Volts	Cr@1V (Pf)	Cr 1V/ Cr 3V (Pf)	Cr 1V/ Cr 6V (Pf)	Q (Min/4v/ 50MHz)	Outline Dwg Number	APPLICATION
MPV1965	15	2.6-3.8	1.4-2.2	2.6-3.6	1500	206	Low Voltage VCO

ELECTRICAL CHARACTERISTICS

Part #	Vb@10uA (min) Volts	Cr@4V Pf	Cr 0V/ (Typ) (Pf)	Cr @ 20V (Pf)	Q (Min/4v/ 50MHz)	Outline Dwg Number	APPLICATION
MPV2100	22	0.9-1.5	3.25	0.2-0.5	1500	206	Wide Bandwidth VCO

Microsemi
Microwave Products Division
75 Technology Drive, Lowell, MA 01851, 978-442-5600, Fax: 978-937-3748

Figure D.1 MICROSEMI MPV-2100 Varactor Diode Datasheet

Microsemi
MICROWAVE PRODUCTS DIVISION

MPV1965, MPV210

MONOLITHIC MICROWAVE SURFACE MOUNT VARACTOR DIODES

PRODUCT PREVIEW

DIMENSIONS

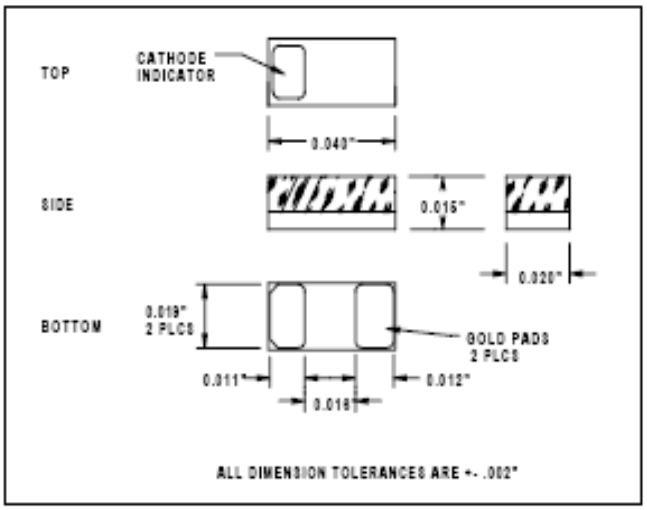

Figure D.2 MICROSEMI MPV-2100 Varactor Diode Datasheet

E. MEMS Switch Operation

RF MEMS switches are commonly used in phase shifters and switching networks up to 120 GHz due to their improved performance compared to p-i-n or field-effect transistor (FET) diode switches. RF MEMS application areas are in phase arrays and reconfigurable apertures for defense and telecommunication systems, switching networks for satellite communications.

MEMS switches are devices that use mechanical movement to achieve a short circuit or an open circuit in the RF transmission line. In order to achieve mechanical movement electrostatic, magnetostatic, piezoelectric, or thermal forces can be used. In fact, only electrostatic-type switch's operation has been verified at 0.1-100GHz with high reliability [36].

There are two types of RF MEMS switches: shunt switch and series switch. Shunt and series switches have two states; up and down state. Figure E.1 shows the up state of the series and shunt SPST MEMS switches. In the downs state, as seen from Figure E.2 the bridge collapses due to DC actuation to the switch mechanism.

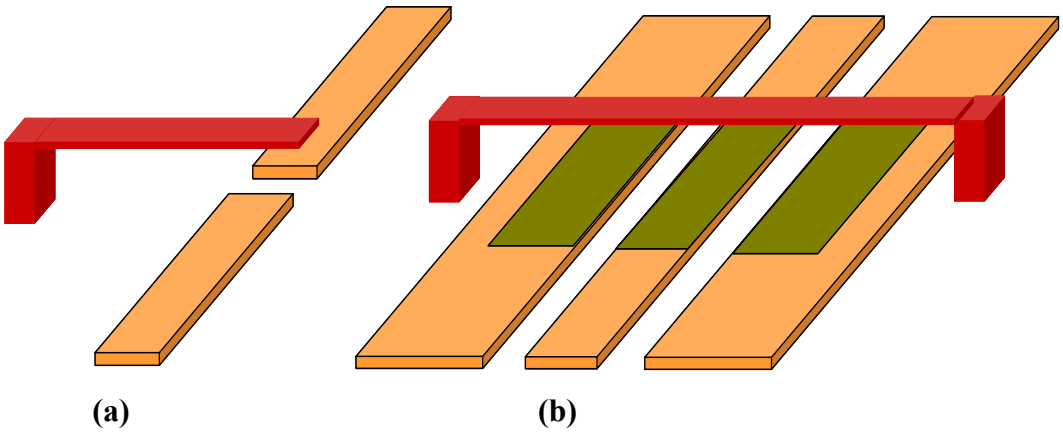

Figure E.1 Up State Schematic Models of (a) Series SPST Switch (b) Shunt SPST RF MEMS Switch

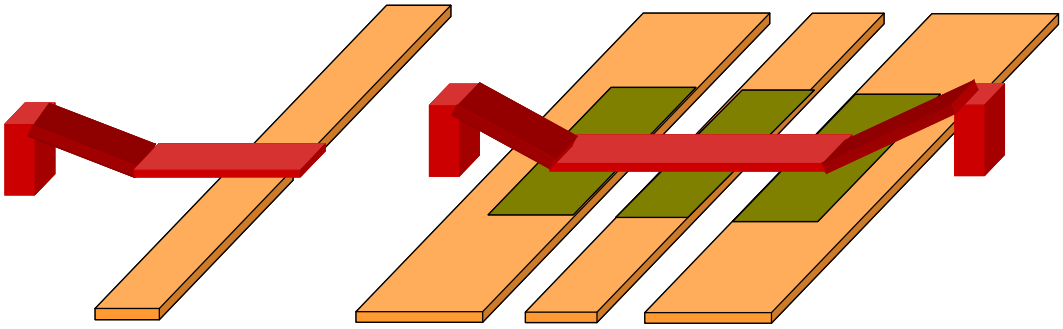

(a) **(b)**

Figure E.2 Down State Schematic Models of (a) Series SPST Switch (b) Shunt SPST RF MEMS Switch

The schematic model of the RADANT SPST MEMS shunt switch is shown in Figure E.3 [37]. A MEMS shunt switch has up- and down- states. In the down-state, a voltage is applied between the gate and source electrodes. The free end of the switch contacts the drain and completes an electrical path between the drain and the source. When the applied voltage is removed, the MEMS bridge returns back to its original position.

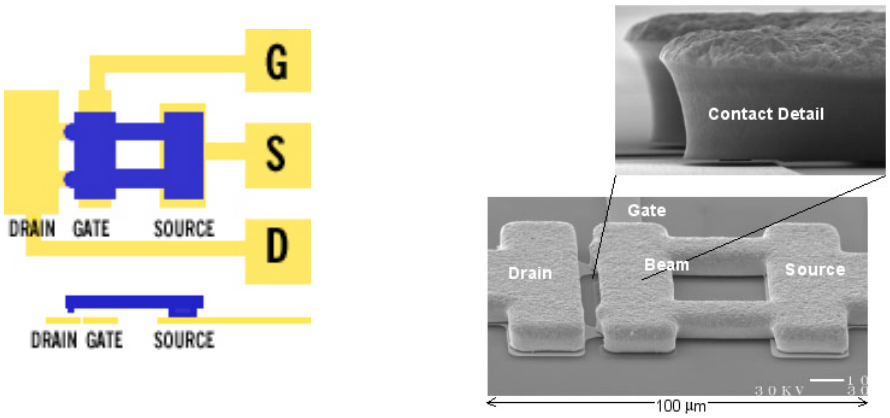

Figure E.3 Schematic Model and Photograph of RADANT SPST RF MEMS Shunt Switch

TÜBİTAK
PROJE ÖZET BİLGİ FORMU

Proje No:107E090 (COST IC0603)

Proje Başlığı: Bilgi Toplumu Teknolojileri için Anten Sistemleri ve Algılayıcılar

Proje Yürütücüsü ve Araştırmacılar: Prof. Dr. Özlem Aydın Çivi (yürütücü),
Doç.Dr. Şimşek Demir, Y.Doç.Dr. Lale Alatan, Prof. Dr. Altunkan Hızal, Arş.Gör. Caner Güçlü, Y. Müh. Aykut Cihangir, Y. Müh. Nihan Topallı
Prof.Dr. Tayfun Akın (danışman)

Projenin Yürütüldüğü Kuruluş ve Adresi: Orta Doğu Teknik Üniversitesi, Elektrik ve Elektronik Mühendisliği Bölümü, Ankara

Destekleyen Kuruluş(ların) Adı ve Adresi: TÜBİTAK, Ankara

Projenin Başlangıç ve Bitiş Tarihleri: 1.10.2007- 1.10.2010

Öz (en çok 70 kelime) Projede, yeniden şekillendirilebilir anten, elektronik taramalı dizi anten ve yansıtıcı dizi anten tasarlanmış, üretilmiş ve ölçülmüştür. X-band Sur Biçimli dizi antende varaktorler kullanılarak, huzmenin elektronik tarama yapabileceği gösterilmiştir. MM-Dalga sabit genişlikli ve doğrusal sönümlenen yarık antenler tasarlanıp, üretilmiş ve antenin şeklinin bu iki yapı arasında değiştirilmesi durumunda ışıma örüntüsünün değiştirilebileceği gösterilmiştir. K ve Ka bantlarında bağımsız çalışabilen, RF MEMS anahtarlarla yeniden şekillendirilebilir, ayrık halka elemanlı dairesel polarizasyonlu yansıtıcı dizi anten tasarlanmış, üretilmiş ve ölçülmüştür.

Anahtar Kelimeler: Faz dizili antenler, yansıtıcı antenler, yeniden şekillendirilebilir antenler, RF MEMS faz kaydırıcılar, RF MEMS devre bileşenleri, RF MEMS antenler

Fikri Ürün Bildirim Formu Sunuldu mu? **Evet** ☐ **Gerekli Değil** ☒
Fikri Ürün Bildirim Formu'nun tesliminden sonra 3 ay içerisinde patent başvurusu yapılmalıdır.

Projeden Yapılan Yayınlar:

Hakemli Dergilerde Yayınlanmış Makaleler

1. Nihan Gökalp, Ö.Aydın Çivi, "Beam Steerable Meanderline Antenna Using Varactor Diodes", *Microwave and Optical Technology Letters* dergisinde basılmak üzere kabul edildi, Aug, 2010.

Uluslararası Konferans Bildirileri

1. A. Cihangir, L. Alatan, " Reconfiguration in the Radiation Pattern of Tapered Slot Antennas," Proceedings of the 20th International Conference on Applied Electromagnetics and Communications (ICECOM) , Dubrovnik, Croatia, 20-23 Sept. 2010.
2. Caner Guclu, Julien Perruisseau-Carrier, and Ozlem Aydin Civi, "Dual Frequency Reflectarray Cell Using Split-ring Elements with RF MEMS Switches", 2010 IEEE AP-S International Symposium, Toronto, Canada, pp., 11-16 July 2010.

3. N. Gokalp, O. Aydin Civi, “Millimeter-Wave Frequency Reconfigurable Slot Dipole Array with Packaged RF-MEMS Switches”, 2009 European Conference on Antennas and Propagation EuCAP09, Berlin, Almanya, Proceedings pp.1334 –1336 , 23-27 Mart 2009.
4. N. Gokalp, Ö. Aydin Civi, “Beam steerable traveling wave meander line antenna using varactor diode for X-band applications”, IEEE 2008 Antennas and Propagation Society International Symposium, San Diego, ABD, pp.1 – 4, 5-11 July 2008.
5. K. Topalli, O. Bayraktar, M. Unlu, O. Aydin Civi, S. Demir, and T. Akin, “Reconfigurable antennas by RF MEMS technology,” 30th ESA Antenna Workshop on Antennas for Earth Observation, Science, Telecommunications and Navigation Space Missions, pp.497-500, Noordwijk, The Netherlands, 27-30 May 2008.

Ulusal Konferans Bildirileri

1. Caner Guclu, Julien Perruisseau-Carrier, and Ozlem Aydin Civi, “Çift Frekansta Çalışan Yeniden Yapılandırılabilir Ayrık Halka Yansıtıcı Dizi Anten Birim Hücre Tasarımı”, URSI Türkiye 5. Bilimsel Kongresi, pp.128-131, ODTÜ-KKK, 25-27 Ağustos 2010.

2. Nihan Gökalp, Özlem Aydın Çivi , “Işınım Huzmesi Yönlendirilebilen Sur Biçimli Mikroşerit Anten Dizisi”, URSI 4.Bilimsel Kongresi, pp. 208-211, Antalya, 20-22 Ekim 2008